DOE-ER-0313/56
Distribution
Categories
UC-423, -424

FUSION MATERIALS SEMIANNUAL PROGRESS REPORT FOR THE PERIOD ENDING

June 30, 2014

Prepared for
DOE Office of Fusion Energy Sciences
(AT 60 20 10 0)

DATE PUBLISHED: August 2014

Prepared by
OAK RIDGE NATIONAL LABORATORY
Oak Ridge, Tennessee 37831
Managed by
UT-Battelle, LLC
For the
U.S. DEPARTMENT OF ENERGY

FOREWORD

This is the fifty-sixth in a series of semiannual technical progress reports on fusion materials science activity supported by the Fusion Energy Sciences Program of the U.S. Department of Energy. It covers the period ending June 30, 2014. This report focuses on research addressing the effects on materials properties and performance of exposure to the neutronic, thermal and chemical environments anticipated in the chambers of fusion experiments and energy systems. This research is a major element of the national effort to establish the materials knowledge base for an economically and environmentally attractive fusion energy source. Research activities on issues related to the interaction of materials with plasmas are reported separately.

The results reported are the products of a national effort involving a number of national laboratories and universities. A large fraction of this work, particularly in relation to fission reactor irradiations, is carried out collaboratively with partners in Japan, Russia, and the European Union. The purpose of this series of reports is to provide a working technical record for the use of program participants, and to provide a means of communicating the efforts of fusion materials scientists to the broader fusion community, both nationally and worldwide.

This report has been compiled under the guidance of F. W. (Bill) Wiffen and Susan Noe, Oak Ridge National Laboratory. Their efforts, and the efforts of the many persons who made technical contributions, are gratefully acknowledged.

Peter J. Pappano
Research Division
Office of Fusion Energy Sciences

TABLE OF CONTENTS

1. FERRITIC/MARTENSITIC STEEL DEVELOPMENT

See also contributions 2.6, 7.3, 7.4, 8.3, 8.4, and 8.5.

A new RAFM steel has been designed to favor the formation of MC (M = metal) carbides because a recent study has shown superior stability of TaC over TaN and VN nanoprecipitates under thermal aging, creep testing, and Fe^{2+} ion irradiation at 500°C. A lab-scale heat of the new alloy has been fabricated in conventional normalization and tempering conditions. Tensile results for test temperatures up to 800°C exhibited yield strength significantly greater than P92 steel with decent total elongation. Four different TMT conditions have been developed on Grade 92 samples. One of the conditions with warm rolling after normalization followed by 2-step tempering was identified as having the best results in terms of tensile and Charpy impact properties; these conditions will be applied to the new alloy. Additionally, preliminary microstructural characterization of the high dose Fe^{2+}-irradiated TaC samples has produced some new observations.

Fracture toughness testing in high radiation areas using miniaturized specimens has become a major challenge in the evaluation of highly radioactive materials as it requires high precision recording of load-displacement data, including loading-unloading cycles, often in vacuum or controlled environments. A new testing and analysis procedure was established to test small disk compact tension (DCT) fracture specimens irradiated to high doses. This report summarizes the major components of the new procedure: a simplified testing technique to obtain minimum datasets needed for analysis and a simplified normalization method for evaluating crack resistance (J-R) data. In application, two sets of fracture test data obtained from 4.72 and 3.56 mm thick DCT specimens of nonirradiated low-activation ferritic-martensitic steels (F82H steels) were analyzed and the results are discussed focusing on the effect of side grooves and on the recommendation for data validity.

Ten tensile specimen holders from HFIR irradiation experiments JP28 and JP29 were successfully disassembled in the ORNL 3025E hot cell facility. Some holders needed to be cut along corners of the holder because specimens could not be easily pushed out of the holder. All tensile specimens from the disassembled holders were recovered and identified. The surfaces of the specimens irradiated at 673 and 773 K were oxidized during the irradiation and cannot be hardness tested without polishing. Vickers hardness was measured on some of the tensile specimens irradiated at 573 K.

TABLE OF CONTENTS

An RAFM steel and an ODS ferritic alloy (F82H.mod3+CW and 14YW, respectively) were irradiated as part of the HFIR-JP27 irradiation experiment conducted in the High Flux Isotope Reactor to explore He effects in structural alloys. The *in situ* He injection (ISHI) technique is used to implant He up to 9 μm below the surface of a NiAl coated sample at He/dpa levels up to ~50. This report summarizes the current status of TEM characterization of the two irradiated alloys. The He-implanted side of the RAFM alloy exhibited significant swelling due to bubble and void formation - within the matrix, on pre-existing dislocations, and at interfaces within the material. The 14YW alloy exhibited significant swelling even in the absence of implanted He, primarily through large voids that formed on the ODS particles. In addition, significant radiation-induced segregation of the Cr was observed around oxide particles and on lath boundaries and visible α′ particles could be detected via elemental mapping of the matrix of the 14YW alloy.

2. ODS AND NANOCOMPOSITED ALLOY DEVELOPMENT

See also contributions 1.4 and 8.7.

Four experimental ODS FeCrAl heats of composition Fe-12Cr-5Al were prepared by mechanical alloying with additions of Y_2O_3, Y_2O_3 + ZrO_2, Y_2O_3 + HfO_2 and Y_2O_3 + TiO_2. Characterization of the as-extruded and aged microstructures are in progress and are compared to a commercial ODS FeCrAl alloy, PM2000. An initial Pb-Li compatibility evaluation was performed at 700°C on the first three alloys. The fourth alloy with TiO_2 was recently produced and tensile properties have been measured from 25° to 800°C. This alloy had high strength but low ductility at 25° and 400°C consistent with its high hardness. Initial creep testing has begun on the alloy with HfO_2 at 800°C and 100 MPa.

A new Sc-based nanostructured ferritic alloy (NFA) was processed by ball milling gas atomized Fe alloy and Sc_2O_3 powders. Replacing Y with Sc was motivated by the fact that the latter has a much higher solubility in Fe compared to Y, possibly providing a melt processing path for producing Sc-based NFA. The milled powders were subject to four heat treatments: aging at both 850°C; aging at 1000°C; consolidation by spark plasma sintering (SPS) at a peak temperature of 1100°C; and SPS consolidation followed by annealing at 850°C for 3 hrs. Electron backscatter diffraction (EBSD) measurements showed fine grain sizes in both the 850°C and 1000°C aged powder conditions. Transmission electron microscopy (TEM) and atom probe tomography (APT) show that similar populations of $Sc_2Ti_2O_7$ complex oxide nano-features (NFs) also form at both aging temperatures. The microhardness was high for three conditions, and similar to that typically observed in Y-based NFA. However, the microhardness was much lower in the 1000°C powder aged condition. The reason for the low hardness is not yet understood.

TABLE OF CONTENTS

2.3 SEM and EBSD Characterization of Fe - {110} $Y_2Ti_2O_7$ INTERFACES – T. Stan, Y. Wu, G. R. Odette (University of California Santa Barbara) **45**

Nanostructured ferritic alloys (NFAs) are dispersion strengthened by a high density of 2-3 nm fcc pyrochlore $Y_2Ti_2O_7$ nano features (NFs). The interface between the bcc ferrite matrix and the $Y_2Ti_2O_7$ plays critical role in the radiation damage resistance of NFAs. However, details about the interfaces are difficult to determine from the nm-scale features themselves. To partially overcome this obstacle, and to complement other characterization studies of the actual NFs themselves, mesoscopic interfaces were created by electron beam deposition of Fe onto {110} oriented $Y_2Ti_2O_7$ bulk single crystal surfaces. We report characterization of Fe – {110}$Y_2Ti_2O_7$ interfaces using the Scanning Electron Microscopy (SEM) and Electron Backscatter Diffraction (EBSD) techniques. The polycrystalline Fe films had grains with three distinct orientation relationships (ORs). Notably, one 10 µm Fe grain had the favored {100}Fe||{110}$Y_2Ti_2O_7$ and <100>Fe||<100>$Y_2Ti_2O_7$ OR which is found in matrix embedded NFs. This work is continuing and while the mesoscopic interfaces may differ from those of the embedded NFs, the former will facilitate characterization of controlled interfaces, such as interactions with point defects and helium.

2.4 Fracture Behavior of Advanced ODS Alloy 9YWTV – T. S. Byun, D. T. Hoelzer (Oak Ridge National Laboratory), J. H. Yoon (Korea Atomic Energy Research Institute), and S. A. Maloy (Los Alamos National Laboratory) **50**

Latest studies on the high temperature fracture of nanostructured ferritic alloys (NFAs) have indicated that the microcracks formed within the alloys propagate by a low energy boundary decohesion mechanism and therefore resulted in low fracture toughness. A 9Cr NFA with improved fracture toughness was successfully developed by applying thermo-mechanical treatments (TMTs) designed to enhance grain boundary bonding. This article focuses on the static fracture behaviors of the newly developed 9Cr NFAs. Fracture mode and cracking resistance were compared among the materials treated through different controlled rolling (CR) routes. Optimal TMTs resulted in high fracture toughness at room temperature (> 250 MPa√m) and in retaining higher than 100 MPa√m over the wide temperature range 22–700°C. Significant differences were found in the fracture resistance (J-R) curves among the low and high fracture toughness NFAs.

2.5 Mechanical Properties Characterization of a Larger Best Practice Heat of 14YWT NFA1 – M.E. Alam, N. J. Cunningham, D. Gragg, K. Fields, G. R. Odette (UCSB), D. T. Hoelzer (ORNL) and S. A. Maloy (LANL) **63**

A new larger heat of best practice nanostructured ferritic alloy (NFA), designated FCRD NFA1, was produced by ball milling argon atomized Fe-14Cr-3W-0.4Ti-0.2Y (wt.%) and FeO powders followed by consolidation and thermo mechanical processing sequence of extrusion (850°C), annealing and cross-rolling (1000°C) steps. The microhardness of NFA1 averaged ≈ 376 ± 18 (kg/mm^2). The corresponding uniaxial tensile yield stress and ductility from 22 to 800°C are high at >1000 MPa at 22°C to >500 MPa at 600°C and 15-25%, respectively. K_{Jc}(T) fracture toughness curves were also measured from -196 to 22°C using pre-cracked 3-point bend (3PB) specimens. NFA1 manifests an exceptionally low fracture toughness transition temperature of ≈ -175°C in both LT and TL orientations. These results represent an *extraordinary combination* of strength and toughness. Extensive fractography provided insight on key fracture mechanisms.

2.6 Friction Stir Welding of ODS Steels and Advanced Ferritic Structural Steels — Z. Feng, X. Yu, W. Tang, D. Hoelzer, and L.T. Tan (Oak Ridge National Laboratory) **70**

Our research during this reporting period focused on (1) understanding the effects of post-weld heat treatment (PWHT) on the microstructure and property variations in friction stir welds of RAFM

TABLE OF CONTENTS

3. CERAMIC COMPOSITE STRUCTURAL MATERIAL DEVELOPMENT

See also Contributions 7.2, 8.9, and 8.10.

TABLE OF CONTENTS

indicate that observable Mg diffusion in 6H-SiC starts and a more rapid diffusion in CVD 3C-SiC occurs at 1573 K. The implanted Mg atoms tend to diffuse deeper into the undamaged CVD 3C-SiC. The microstructure with Mg inclusions in the as-implanted SiC has been initially examined using high-resolution STEM. The presence of Mg in the TEM specimen has been confirmed based on EDS mapping. Additional monocrystalline 3C-SiC samples have been implanted at 673 K to ion fluence 3 times higher than the previous one. RBS/C analysis has been performed before and after thermal annealing at 1573 K for 12 hrs. Isothermal annealing at 1573 K is being carried out and Mg depth profiles being measured. Microstructures in both the as-implanted and annealed samples are also being examined using STEM.

The neutron irradiation creep of near-stoichiometric SiC fibers was evaluated by bend stress relaxation (BSR) tests. The results indicate that the apparent stress exponent of the irradiation creep of the SiC fibers is near unity at ~500°C. The instantaneous creep compliance of the SiC fibers, which is the creep strain normalized to the applied stress and neutron flux, was estimated to be ~1×10^{-7} [MPa^{-1} dpa^{-1}] at ~6 dpa. The creep compliance values are orders of magnitude smaller than previously reported from light ion irradiation experiments. Quality of the fibers slightly affected the creep behavior: Hi-Nicalon^{TM} Type S fiber showed more creep than other fibers, including Tyranno^{TM} SA3, isotopically-controlled Sylramic^{TM} and Sylramic^{TM} iBN fibers at ~500°C to ~1 dpa.

Extended abstract of a paper accepted by the Journal of Nuclear Materials.

4. HIGH HEAT FLUX MATERIALS AND COMPONENT TESTING

See also Section 4.3.

A promising approach to increasing fracture toughness and decreasing the DBTT of a W-alloy is by ductile-phase toughening (DPT). In this method, a ductile phase is included in a brittle matrix to prevent fracture propagation by crack bridging. To examine the prospect of DPT, W-Cu three-point bend samples were deformed at several strain rates and temperatures. Data from these tests are used for the calibration of a dynamic crack-bridging model that can effectively predict elevated temperature crack growth in W-composites. The development and initial testing of a Cu-ligament bridging model based on a micromechanical flow stress model of Cu is discussed. Good agreement with the 3-point bend testing data is demonstrated along with future plans to improve the model.

TABLE OF CONTENTS

TABLE OF CONTENTS

Extended Abstract of an ICFRM-16 paper accepted for J. Nucl. Mater.

5. MAGNET AND DIAGNOSTIC SYSTEM MATERIALS

During this reporting period, electrical characterization work was completed on the ion irradiated superconducting films. Detailed electrical characterization of the materials response was performed at the University of South Alabama. This contribution highlights results of a forthcoming paper concluding the electrical characterization of the ion irradiated materials. Based on this work, the Zr-doped $(Y,Gd)Ba_2Cu_3O_{7-x}$ and $(Dy,Y)Ba_2Cu_3O_{7-x}$ (DyBCO) materials were selected for neutron irradiation studies. Ion irradiation results for the $GdBa_2Cu_3O_{7-x}$ conductor did not show a significant improvement over second-generation YBCO materials in terms of J_c improvement with irradiation. However, irradiated T_c remained higher than for YBCO. The neutron irradiation exposures are being planned for the July-August 2014 cycle at HFIR. Information on the irradiation capsules and preliminary results will be included in the next semi-annual report.

Specifically engineered Al_2O_3/SiO_2 and HfO_2/SiO_2 dielectric mirrors grown on sapphire substrates and exposed to neutron doses of 1 and 4 dpa at 458±10 K in the High Flux Isotope Reactor (HFIR), resulted in reductions in optical reflectance, indicating a failure of the multilayer coating. HfO_2/SiO_2 mirrors failed completely when exposed to 1 dpa, whereas the reflectivity of Al_2O_3/SiO_2 mirror reduced to 50%, eventually failing at 4 dpa. Transmission electron microscopy (TEM) observation of the Al_2O_3/SiO_2 specimens showed defects increase in size with irradiation dose from 1 to 4 dpa. Heavy interdiffusion leading to formation of Al-Si rich phase and cracking of some of Al_2O_3 layers was observed across the Al_2O_3/SiO_2 mirrors; however the interdiffusion is less evident in HfO_2/SiO_2 mirrors. Delamination at the interface between the substrate and first layer was typically observed in both 1 and 4 dpa HfO_2/SiO_2 specimens, where buckling type delamination was a major observation at all doses.

6. FUSION CORROSION AND COMPATIBILITY SCIENCE

Operation of the first thermal convection loop (TCL) using dispersion strengthened FeCrAl (Kanthal APMT) tubing and specimens was completed in this reporting period. The working fluid in the TCL was eutectic Pb-17at%Li, and the peak temperature (550˚) and temperature gradient (116˚C) was maintained without interruption for 1000 h. When operation was terminated, a problem with

TABLE OF CONTENTS

complete draining of the Pb-Li from the loop was encountered, which delayed retrieval of specimens exposed in the hot leg of the TCL; however, analysis of specimens from the cold leg has been initiated.

7. MECHANISMS AND ANALYSIS

7.1 **Effects of Ion Irradiation on BAM-11 Bulk Metallic Glass –** A. G. Perez-Bergquist[1,2], J. Brechtl[2], H. Bei[1], Y. Zhang[1,2] and S. J. Zinkle[1,2] ([1]*Oak Ridge National Laboratory,* [2]*University of Tennessee)* **184**

Bulk metallic glasses are intriguing candidates for structural applications in nuclear environments due to their good mechanical properties along with their inherent amorphous nature, but their radiation response is largely unknown due to the relatively recent nature of innovations in bulk metallic glass fabrication. Microstructural and mechanical property evaluations have been performed on as-cast and heat-treated $Zr_{52.5}Cu_{17.9}Ni_{14.6}Al_{10}Ti_5$ bulk metallic glass (BAM-11) irradiated with 3 MeV Ni^+ ions to 1 and 10 dpa. TEM showed no evidence of radiation damage or crystallization following ion irradiation, and changes in hardness and Young's modulus were 10-15%. In addition, irradiation-induced damage was seen to saturate at or below the 1 dpa dose level.

7.2 **Effects of Neutron Irradiation on Ti-Si-C Max-Phase Ceramic Microstructures** – A. G. Perez-Bergquist[1,2], Y. Katoh[1], C. Shih[1], and S. J. Zinkle[1,2] ([1]*Oak Ridge National Laboratory,* [2]*University of Tennessee)* **189**

MAX phase ceramics are intriguing candidates for structural applications in nuclear environments due to their unique mixture of metallic and ceramic properties. Specifically, their potential to retain adequate thermal conductivity after high levels of irradiation damage may make them an attractive alternative to SiC in fusion environments. In this study, we investigate samples containing MAX phase Ti_3SiC_2 after neutron irradiation to 3.4 and 5.0 dpa at temperatures of 500 and 800°C. Ti_3SiC_2 in the 500°C sample appeared to decompose into TiC under irradiation, whereas the Ti_3SiC_2 in the 800°C sample did not. Limited radiation damage was visible in the 800°C sample.

7.3 **Effects of Helium-DPA Interactions on Cavity Evolution in Tempered Martensitic Steels Under Dual Ion-Beam Irradiation** - Takuya Yamamoto, Yuan Wu, G. Robert Odette (University of California Santa Barbara), Sosuke Kondo, Akihiko Kimura (Kyoto University) **194**

Cavity evolution in normalized and tempered martensitic steel (TMS) F82H under Fe^{3+} and He^+ dual ion beam irradiation (DII) at 500°C was characterized over a wide range of dpa, He and He/dpa. Transmission electron microscopy (TEM) showed that DII up to ≈ 60 dpa and ≈ 2400 appm He produced a significant population of non-uniformly distributed cavities with bimodal sizes, ranging from ≈ 1 nm He bubbles to ≈ 20 nm faceted voids, resulting in observed swelling of up more than 3%. The incubation dpa for the onset of void swelling decreased linearly with increasing He/dpa in both IEA and mod.3 heats of F82H.

7.4 **Effects of Helium Atoms on the Strength of BCC Fe Grain Boundaries** – Xiaoxun Zhang, Jiansha Ji, Fang Ma (Shanghai University of Engineering Science), G. R. Odette (University of California Santa Barbara), R. J. Kurtz, F. Gao (Pacific Northwest National Laboratory) **201**

The effects of helium atoms and the formation of helium clusters on Σ3 <110> {111}, Σ3 <110> {112} and Σ5 <100> {310} symmetric tilt GBs in bcc iron were studied by the molecular dynamics simulation method. We found that helium atoms are deeply trapped at the GBs during annealing at 300 K, and that two or more helium atoms aggregate to form a small helium clusters. The helium

TABLE OF CONTENTS

atom and small clusters act as a failure initiation site under uniaxial straining. We show that helium atoms decreases cohesive strength and ductility of all the grain boundaries in bcc Fe that were studied.

8. **MODELING PROCESSES IN FUSION SYSTEM MATERIALS**

Molecular dynamics simulations are performed to investigate the effect of mass on displacement threshold energy in Cr, Mo, Fe and W. For each interatomic potential, the mass of the atoms is varied among those metals for a total of 16 combinations. The average threshold energy over all crystal directions is calculated within the irreducible crystal directions using appropriate weighting factors. The weighting factors account for the different number of equivalent directions among the grid points and the different solid angle coverage of each grid point. The grid points are constructed with a Miller index increment of 1/24 for a total of 325 points. For each direction, 10 simulations each with a different primary-knock-on atom are performed. The results show that for each interatomic potential, the average threshold energy is insensitive to the mass; i.e., the values are the same within the standard error. In the future, the effect of mass on high-energy cascades for a given interatomic potential will be investigated.

This is a work in progress and in this report we present basic implementation details of the first-passage time (FPT) approach to deal with very fast 1D diffusing SIA clusters in *KSOME* (kinetic simulations of microstructural evolution) and the status of its development.

An equation of state that accurately reproduces the pressure-volume relationship of helium is necessary to understand and predict the behavior of He-vacancy defects in irradiated materials. We have used *ab initio* calculations to determine the energetics of helium-vacancy clusters and applied the results to develop a new three-body interatomic potential that describes the behavior of helium in iron. The potential was employed in molecular dynamics simulations to determine the conditions for mechanical equilibrium between small helium-stabilized bubbles and an iron matrix, and to systematically map the pressure-volume relationship for the bubbles at a range of temperatures. These atomistic results are compared to an existing equation of state and a modification is proposed for bubbles with high helium densities.

Extended Abstract of an ICFRM-16 paper submitted to J. Nucl. Mater.

TABLE OF CONTENTS

TABLE OF CONTENTS

9. **IRRADIATION METHODS, EXPERIMENTS, AND SCHEDULES**

TABLE OF CONTENTS

technical and safety issues were addressed at a level appropriate for a 30% design. Specific recommendations were addressed in the feasibility study report appendices.

Other highlights of the FMITS 30% design progress during the past 6 months include a completed preliminary seal mock-up test, improved remote handling tooling and procedures, and a completed project resource-loaded schedule and contingency analysis.

1.1 DEVELOPMENT OF ADVANCED REDUCED ACTIVATION FERRITIC/MARTENSITIC STEELS —

L. Tan (Oak Ridge National Laboratory)

OBJECTIVE

Develop alloy composition and thermomechanical treatment (TMT) to produce high density of nanoprecipitates, high temperature-capable, more manufacturable, and affordable reduced-activation ferritic/martensitic (RAFM) steels.

SUMMARY

A new RAFM steel has been designed to favor the formation of MC (M = metal) carbides because a recent study has shown superior stability of TaC over TaN and VN nanoprecipitates under thermal aging, creep testing, and Fe^{2+} ion irradiation at 500°C. A lab-scale heat of the new alloy has been fabricated in conventional normalization and tempering conditions. Tensile results for test temperatures up to 800°C exhibited yield strength significantly greater than P92 steel with decent total elongation. Four different TMT conditions have been developed on Grade 92 samples. One of the conditions with warm rolling after normalization followed by 2-step tempering was identified as having the best results in terms of tensile and Charpy impact properties; these conditions will be applied to the new alloy. Additionally, preliminary microstructural characterization of the high dose Fe^{2+}-irradiated TaC samples has produced some new observations.

PROGRESS AND STATUS

Introduction

Recent investigations on the evolution of TaC, TaN, and VN nanoprecipitates under thermal aging at 600 and 700°C, creep testing at 600°C, and Fe^{2+} ion irradiation up to ~49 dpa at 500°C indicated the superior stability of TaC over TaN and VN [1,2]. This finding sheds a light on developing new RAFM steels favoring the formation of MC carbides rather than nitrides. The MC-type precipitates are believed to be beneficial for maintaining high temperature strength of this class of steels. Therefore, a new alloy, designated as TT1, has been designed and prepared to test its performance. In the meantime, TMT processes have been explored to identify an appropriate process for property improvements of the alloy. Additionally, microstructural characterization of the high dose Fe^{2+}-irradiated samples of TaC, TaN, and VN has been initiated.

Experimental Procedure

Computational thermodynamics was employed to design new RAFM steels with an increased amount of MC-type precipitates. One of the new alloys, TT1, has been fabricated using vacuum arc melting and drop casting, yielding a small experimental heat (~1 lb.). Part of the cast alloy was subjected to hot rolling followed by standard normalization (N) and tempering (T) heat treatment. Several routes of TMTs involved with warm rolling (WR) have been conducted on a Grade 92 heat to investigate the effect of WR on tensile properties and Charpy impact resistance.

Tensile testing was conducted using miniature specimens (type SS-3: 25.4 x 4.95 x 0.76 mm), machined along the rolling direction of the plate, at a nominal strain rate of 0.001 s^{-1}. Half-size Charpy specimens were used to assess ductile-brittle transition temperature and upper shelf energy of the processed samples. The microstructures of the samples were characterized using optical microscopy, scanning electron microscopy (SEM), and transmission electron microscopy (TEM). A FEI CM200 field-emission-gun TEM/STEM equipped with an EDAX energy dispersive X-ray spectroscopy (EDS) detector was primarily used to characterize the Fe^{2+}-irradiated samples. TEM specimens, perpendicular to the surfaces, were lifted out and thinned to electron-transparent using focused ion beam (FIB) on a Hitachi

NB5000. Specimen thickness of the characterized regions was estimated using convergent beam electron diffraction (CBED) technique.

Results

The calculated phase mole fraction of the new alloy TT1 as a function of temperature is shown in Figure 1 (left). Only three types of precipitates, i.e., $M_{23}C_6$, MC, and Laves phase, exist in this alloy. The amount of MC is increased to be higher than that including M(C,N) in other developed RAFM steels, leading to the reduced amount of $M_{23}C_6$ in the alloy. Tensile testing results with yield strength and total elongation as a function of testing temperatures up to 800°C are shown in Figure 1 (right). The NIMS data of P92 tested using regular size specimens are included for comparison. Two N&T conditions with a slight difference in normalization temperature were conducted on alloy TT1. The yield strength of the new alloy is significantly higher than P92, e.g., ~290 and ~130 MPa greater than P92 at room temperature and 800°C, respectively. The total elongation of alloy TT1 is greater than 14%. According to the ASTM standard A335-11, the minimum elongation value of type SS-3 specimens is determined to be 10.95% by $E = 1.25t + 10.00$ for P92 miniature specimens with thickness $t = 0.76$ mm. Thus, the elongation of alloy TT1 is greater than the minimum elongation requirement of P92. Detailed microstructural characterization and thermal aging experiments of the samples of alloy TT1 are in progress.

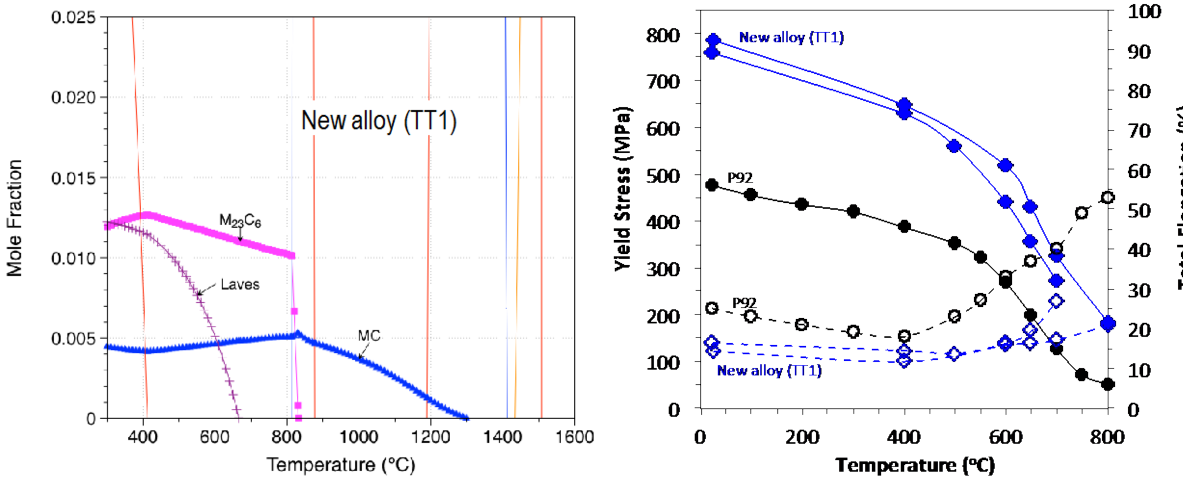

Figure 1. Temperature-dependent of calculated phase fraction (left) and tested yield strength and total elongation using type SS-3 specimens (right) of the newly developed alloy TT1. The NIMS data of P92 are included for comparison.

Four types of TMT conditions, involving the application of WR and tempering, have been developed on Grade 92 samples. Yield strength of the four TMT conditions, i.e., N+T+WR (C1), N+T+WR+T (C2), N+WR+T (F1), and N+WR+2T (F2), as a function of testing temperatures up to 650°C is shown in Figure 2. The WR after N&T (C1) noticeably increased strength, but the followed T (C2) significantly decreased strength, suggesting the occurrence of significant recovery. Although strength is decreased in the C2 condition, it is still noticeably higher than P92 as shown in Figure 1 (right). The application of WR between N and T (F1) exhibited strength between the C1 and C2 conditions. The application of a secondary tempering (F2) did not result in noticeable difference from the F1 condition. However, Charpy impact testing results indicated the lowest DBTT of the F2 (-43°C) and the highest DBTT of the C1 (35°C). Therefore, the F2 condition would be the best TMT in the four conditions, which will be applied to alloy TT1.

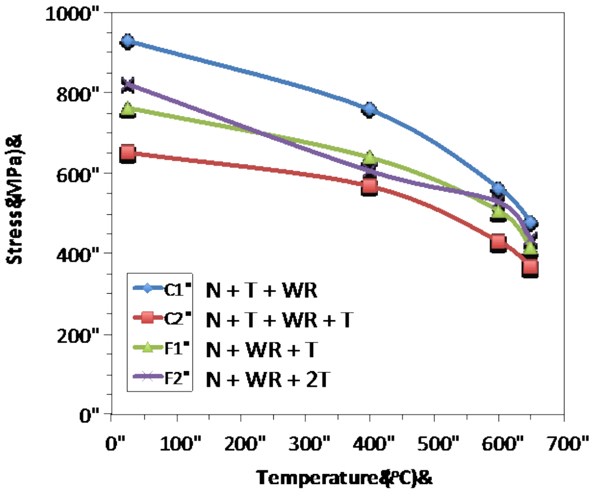

Figure 2. Effect of TMT on temperature-dependent yield strength of Grade 92.

The stability of TaC nanoprecipitates in ferritic steel under Fe^{2+} ion irradiation to ~246 dpa at 500°C was characterized using scanning-transition electron microscopy (TEM/STEM). The left high-angle annular dark field (HAADF) image in Figure 3 was taken at ~1 μm from the TEM specimen surface, which corresponds to ~150 dpa according to SRIM (Stopping and Range of Ions in Matter) calculations [3] with input parameters recommended by Stoller *et al.* [4]. Compared to the right HAADF image taken from a non-irradiated zone (~2.5 μm from the TEM specimen surface), the size of the TaC particles (in white) was significantly reduced. Additionally, a few irradiation induced cavities, e.g., black spheres in the left HAADF image, were observed in the high dose irradiation samples; these were not observed in previous low dose irradiated samples. Statistical analysis of the results is in process.

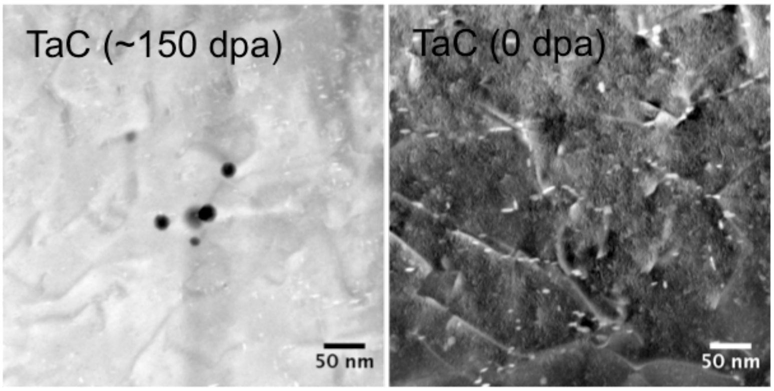

Figure 3. HAADF-STEM images of TaC nanoprecipitates in the ~150 dpa Fe^{2+}-irradiated (left) and non-irradiated (right) zones.

REFERENCES

[1] L. Tan, Y. Kotah, L.L. Snead, Stability of the strengthening nanoprecipitates in reduced activation ferritic steels under Fe^{2+} ion irradiation, J. Nucl. Mater. 445 (2014) 104-110.
[2] L. Tan, T.S. Byun, Y. Katoh, L.L. Snead, Stability of MX-type strengthening nanoprecipitates in ferritic steels under thermal aging, stress and ion irradiation, Acta Materialia 71 (2014) 11-19.
[3] The Stopping and Range of Ions in Matter (SRIM) (http://www.srim.org).
[4] R.E. Stoller, M.B. Toloczko, G.S. Was, A.G. Certain, S. Dwaraknath, F.A. Garner, On the use of SRIM for computing radiation damage exposure, Nuclear Instruments and Methods in Physics Research B 310 (2013) 75-80.

1.2 FRACTURE TESTING AND EVALUATION PROCEDURES FOR MINIATURE F82H DCT SPECIMENS – T. S. Byun (Oak Ridge National Laboratory) and D. Hamaguchi (Japan Atomic Energy Agency)

OBJECTIVE

Fracture testing and evaluation of highly radioactive fusion reactor materials require miniaturized specimens and simplified test techniques. The goal of this work is to establish a new fracture testing and evaluation procedure for highly radioactive F82H disk compact tension (DCT) specimens.

SUMMARY

Fracture toughness testing in high radiation areas using miniaturized specimens has become a major challenge in the evaluation of highly radioactive materials as it requires high precision recording of load-displacement data, including loading-unloading cycles, often in vacuum or controlled environments. A new testing and analysis procedure was established to test small disk compact tension (DCT) fracture specimens irradiated to high doses. This report summarizes the major components of the new procedure: a simplified testing technique to obtain minimum datasets needed for analysis and a simplified normalization method for evaluating crack resistance (J-R) data. In application, two sets of fracture test data obtained from 4.72 and 3.56 mm thick DCT specimens of nonirradiated low-activation ferritic-martensitic steels (F82H steels) were analyzed and the results are discussed focusing on the effect of side grooves and on the recommendation for data validity.

PROGRESS AND STATUS

Introduction

The structural materials for fusion reactors require excellent performance at high temperatures and high doses as the reactor designs aim at increasingly higher thermal efficiency and longer lifetime. Materials evaluation procedures need to handle very high dose (>10 dpa) specimens that can limit specimen size for reasonable cost and efficiency of work in radiation area. Compared to the evaluation of current pressurized water reactor (PWR) materials, therefore, more extreme miniaturization techniques are required for the property evaluation of high dose materials. More restricted testing conditions such as high temperature and environmental control can further aggravate the difficulties in the evaluation procedure in high radiation areas. For the fracture testing in a high temperature vacuum furnace, for instance, instrumentation for displacement measurement from a miniature fracture specimen is extremely difficult and thus needs to be minimized. This research aimed to establish miniaturized fracture testing and evaluation techniques that can remove some of the experimental difficulties in high radiation area.

A simplified procedure for static fracture testing and dada analysis was established to test miniature disk-compact tension (DCT) specimens irradiated to high doses. The standard fracture testing procedure needs a high precision recording on loading-unloading cycles. In reality, however, we often experience that the measurements of unloading compliance from miniature specimens become highly inaccurate at elevated or high temperature because of significant friction and plastic deformation at contact surfaces. Therefore, the major change made in the testing procedure is removing the attachment of external (clip-on) gage. In data analysis the issues caused by this change were resolved by adopting the curve normalization method for J-R curve construction and by modifying other detailed calculation steps accordingly. This report summarizes the major components of the new procedure.

In addition, to demonstrate the applicability of the new procedure, the new procedure has been applied to the baseline tests for nonirradiated low-activation ferritic-martensitic steels (F82H steels). Two sets of fracture test data obtained, respectively, from the 4.72 and 3.56 mm thick DCT specimens of were analyzed and the results are discussed. Application results demonstrated that the newly established procedure can produce nearly identical J-R curve as the traditional unloading compliance method. It was also shown that the miniature DCT specimens without side grooves can induce significant variation or overestimation in the fracture toughness of the test material.

Experimental and Analysis Procedures

Simplification of data acquisition for fracture test in high radiation area

In the post-irradiation fracture tests using remote manipulator in hotcells, any data acquisition through direct connections to specimens can cause major drawbacks in addition to the general difficulties in handling miniature specimens. Use of some sensing devices becomes prohibitively difficult in the miniature specimen tests in a controlled environment. It should be therefore considered if the test technique that uses gage lead or electrode directly attached to the specimen can be avoided. Since the normalization method requires the simplest datasets to obtain a J-R curve, i.e., the load-displacement curve and optical measurements of initial and final crack lengths, it was chosen for the fracture testing of miniature DCT specimens. Further, simplification in data acquisition has been pursued based on the consideration that the measurement of highly accurate displacement may not be needed as explained below.

In typical fracture test systems, a precision displacement gage, such as Wheatstone bridge type clip gage or linear variable differential transducer (LVDT), is usually attached to the fracture specimen to measure the specimen-mouth displacement in compact tension specimens or the axial displacement (deflection) in bend-bar type specimens. In actual J-R curve calculation (*ASTM Standard Test Method E1820)*, the J-integral is divided into two components of elastic and plastic works. The elastic J component is a well-defined function of load, crack length, and elastic constants, none of which requires displacement measurement. The plastic J component indeed requires displacement data but plastic component only. These detailed practices in J-evaluation indicate that the elastic component of measured displacement is not used in any methods of J-R curve calculation except for compliance data in the unloading compliance method. In the normalized curve method, in particular, the plastic displacement at each point can be easily separated from total displacement using the initial slope of load-displacement curve and updated compliance value, which is calculated by a function of crack length.

In a displacement control mode, most mechanical testing systems are controlled by the displacement reading from built-in devices: an LVDT is usually embedded in the actuator of a servohydraulic test system, and the rotation encoding signal is converted to the crosshead movement or displacement in motor-driven systems. These displacement data obtained from the built-in devices include the displacement components of all parts and contacts in the entire load train, and therefore, are usually not accurate enough to be used in the unloading compliance method, where an accurate measurement of elastic unloading slopes is essential for converting those to crack length data. In the normalization method, however, any non-plastic components of total displacement can be easily removed in the J-R curve calculation procedure: the displacement reading from a built-in device can be used to extract the necessary plastic component of displacement. In this work, therefore, a major simplification was made in the testing setup: attachment of additional gage such as clip gage was eliminated. The following sections describe the normalization method modified for the simple data acquisition along with application examples of F82H ferritic-martensitic steel specimens.

Materials and specimens

The test material used for this development is the Japanese low-activation ferritic-martensitic (LAFM) steel H82H with a nominal composition of Fe-8Cr-2W-0.2V-0.04Ta-0.1C (in wt.%). The steel was in normalized (at 1040°C for 40 min) and tempered (at 1040°C for 1 h) condition. As listed in Table 1, two sizes of miniature DCT specimens were tested: four 3.56 mm thick DCTs and five 4.72 mm thick DCTs. The smaller DCT specimens do not have size grooves but one specimen, while the larger specimens have a 10% side groove at each side. The flow stress (the average of YS & UTS) and the Young's modulus (*E*) used for calculations were typical values measured for the material. Also, the initial and final crack lengths, a_0 and a_f, were measured from the boundaries of the surfaces from precracking, stable crack growth on J-R testing, and post-test fracture. The initial crack length is determined by the average of nine point measurements on the front line of precracking growth. The final crack lengths were measured in the same manner, but either heat tinting or fatigue cracking was applied to the as-tested specimens before final separation for making the stable and final fracture surfaces discernible.

Table 1. Dimensions and basic properties of DCT specimens

Specimen I.D.	S_Y [MPa]	*B* [mm]	*Bn* [mm]	*Be* [mm]	*W* [mm]	*E* [GPa]	a_0 [mm]	a_f [mm]	*Dia.* [mm]
F82H 0.14DCT-22C-A	586	3.56	3.56*	3.56	8.13	206.8	3.31	5.21	9.6
F82H 0.14DCT-22C-B	586	3.56	3.56*	3.56	8.13	206.8	3.80	5.50	9.6
F82H 0.14DCT-22C-C	586	3.56	3.56*	3.56	8.13	208	3.65	4.90	9.6
F82H 0.14DCT-22C-D	586	3.56	2.63**	3.32	8.13	208	4.25	5.10	9.6
F82H 0.18DCT-22C-A	586	4.72	3.78	4.54	9.25	206.8	4.58	6.05	12.5
F82H 0.18DCT-22C-B	586	4.72	3.78	4.54	9.25	206.8	4.55	6.27	12.5
F82H 0.18DCT-22C-C	586	4.72	3.78	4.54	9.25	206.8	4.93	6.55	12.5
F82H 0.18DCT-22C-D	586	4.72	3.78	4.54	9.25	206.8	4.92	6.55	12.5
F82H 0.18DCT-22C-E	586	4.72	3.78	4.54	9.27	208	4.65	5.87	12.5

Note A: S_Y = flow stress, B, Bn, Be = gross, net, and effective thickness, W = width of specimen
*Note B: *no side groove, **13% side groove at each side; all 0.18 DCTs have 10% side grooves.*

The modified curve normalization method

The descriptions given below follow those of the standard test method ASTM E1820. Only exception is the process to use the displacement data either from a built-in device or from cross-head movement. The same equations and definitions as in the standard are used below for being easily recognized by readers.

Record load-displacement data: The first step of the procedure is to produce load-displacement curve (P_i – v_i dataset). In this work the load-displacement data were recorded with or without attachment of clip gage. Each static fracture test was performed at a displacement rate of about 0.5 mm/min at room temperature until the load decreases to about 50% of the maximum load. Figure 1 displays an example for the load-displacement curve obtained from a 4.7 mm thick F82H DCT specimen.

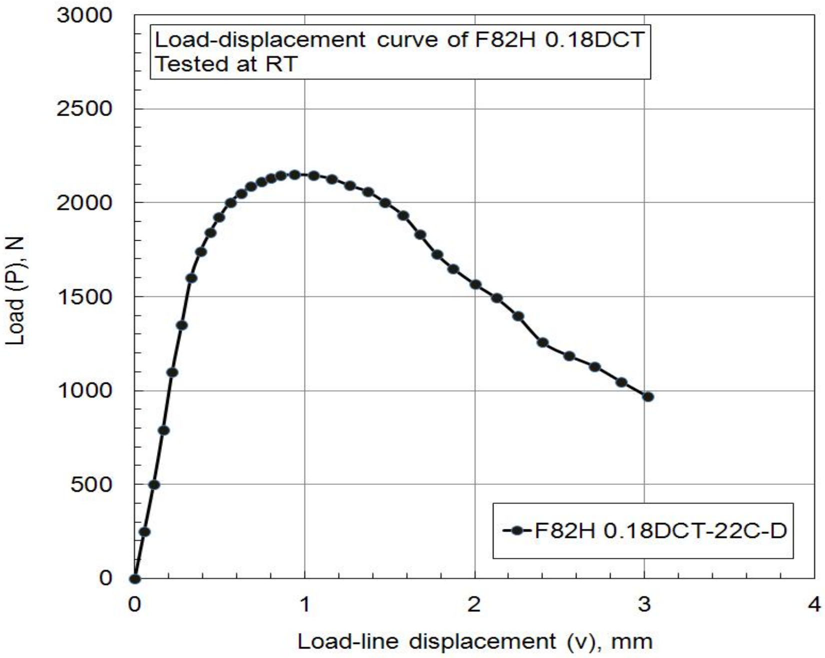

Figure 1. A load-displacement curves for a 4.7 mm thick DCT specimen. The displacement was recorded using a clip gage and this curve is after removing the loading-unloading lines.

Calculation of J-integral: Although different techniques are used for evaluation of crack length, common equations are used for calculation of *J*-integral and stress intensity factor *K* (ASTM E1820). Those equations are summarized first as below since many of them are intermingled in the application of normalized curve method. The total J-integral at point (i) is defined as the sum of elastic and plastic components ($J_{e(i)}$ and $J_{p(i)}$):

$$J_{(i)} = J_{e(i)} + J_{p(i)} = \frac{K_{(i)}^2(1-\nu^2)}{E} + J_{p(i)} \tag{1}$$

where *E* is the elastic modulus, *v* the Poisson ratio (=0.28), and K the stress intensity factor or linear-elastic component of fracture toughness. When all load-displacement and geometrical parameters are known, the plastic component J_p can be calculated by

$$J_{p(i)} = \frac{\eta A_p}{B_N b} \tag{2}$$

where the A_p is the plastic energy applied to the specimens or area below load-plastic displacement curve, Δa crack length dependent dimensional parameter, B_N the net specimen thickness, and *b* the uncracked ligament (=*W*-*a*; *W* is the specimen width). In practical calculations, however, a discretized equation is used:

$$J_{p(i)} = \left[J_{p(i-1)} + \left(\frac{\eta_{(i-1)}}{b_{(i-1)}}\right)\frac{A_{p(i)}-A_{p(i-1)}}{B_N}\right]\left[1-\gamma_{(i-1)}\frac{a_{(i)}-a_{(i-1)}}{b_{(i-1)}}\right] \tag{3}$$

where $a_{(i)}$ and $b_{(i)}$ are the crack length and uncracked ligament at point (i), respectively. Note that in this article all parameters at point (i) and (i-1) are defined in the same manner. Also, the η and γ parameters, and plastic energy increment are defined as below:

$$\eta_{(i-1)} = 2.0 + 0.522 b_{(i-1)}/W \qquad (4)$$

$$\gamma_{(i-1)} = 1.0 + 0.76 b_{(i-1)}/W \qquad (5)$$

$$A_{p(i)} - A_{p(i-1)} = \frac{\left[P_{(i)} + P_{(i-1)}\right]\left[v_{p(i)} - v_{p(i-1)}\right]}{2} \qquad (6)$$

The stress intensity factor $K_{(i)}$ is given as a function of load P and geometrical parameters only:

$$K_{(i)} = \frac{P_{(i)}}{(EB_N W)^{1/2}} \frac{\left[(2 + a_{(i)}/W)(0.76 + 4.8(a_{(i)}/W) - 11.58(a_{(i)}/W)^2 + 11.43(a_{(i)}/W)^3 - 4.08(a_{(i)}/W)^4\right]}{(1 - a_{(i)}/W)^{3/2}} \qquad (6)$$

Calculation of normalized P-v curve up to the maximum load point: This section of a load-displacement curve corresponds to the crack blunting regime or the initial section of a J-R curve with a steep slope of $2\sigma_Y$. As described in the standard test method, the normalized load and displacement ($P_{N(i)}$, $v'_{p(i)}$) are defined as generalized parameters that are insensitive to the geometry of test specimen and given in stress and strain units, respectively. The normalized load and displacement up to, but not including the maximum load is calculated by:

$$P_{N(i)} = \frac{P_{(i)}}{\mathrm{WB}\left[\frac{W - a_{(i)}}{W}\right]^{\eta_{(i)}}} \qquad (7)$$

$$v'_{p(i)} = \frac{v_{p(i)}}{\mathrm{W}} = \frac{v_{(i)} - C_{(i)} P_{(i)}}{\mathrm{W}} \qquad (8)$$

Here, the crack length $a_{(i)}$ and compliance $C_{(i)}$ ($=C_{LL(i)}$ if measured with load-line displacement) calculated by:

$$a_{(i)} = a_0 + \frac{J_{(i)}}{2\sigma_Y} \qquad (9)$$

$$C_{LL(i)} = \frac{1}{EB_e}\left(\frac{1 + a_{(i)}/W}{1 - a_{(i)}/W}\right)^2 \left[2.0462 + 9.6496\left(\frac{a_{(i)}}{W}\right) - 13.7346\left(\frac{a_{(i)}}{W}\right)^2 + 6.1748\left(\frac{a_{(i)}}{W}\right)^3\right] \qquad (10)$$

As can be quickly realized in practical calculation, the evaluation of these equations requires to solve circular references among parameters: in the above four equations, for example, the $a_{(i)}$ needs to be evaluated first to calculate others such as $\eta_{(i)}$, $J_{(i)}$, $C_{LL(i)}$, and then $P_{N(i)}$. Therefore, we need to adopt an iteration technique or a simpler technique of using previously calculated values for the (i-1)th point. In this work, the latter technique is used as data acquisition interval can be easily adjusted to be very small so that the error from using the values of the (i-1)th point instead of those of the (i)th point becomes negligible.

Calculation of normalized load and displacement from the max-load point to final point: A major modeling is needed in this step, representing the major crack growth to final failure, as the crack blunting line (eq. 9) cannot be used. The accuracy of the model depends on how we connect the maximum load point with the final point (known from the measurement of final crack length) in the normalized load-displacement curve ($P_{N(i)}$-$v'_{p(i)}$ curve).

A line should be drawn from the final normalized load-displacement pair tangent to the curve around the maximum load point calculated in the previous step. The connection with a simple linear line can provide highly accurate outcome for J-R curve in most cases although use of a normalization function with four fitting coefficients is recommended in the standard method. A simpler but non-linear four parameter function was suggested by the author and has been used for high strength steels:

$$P_{N(i)} = \frac{P_{N(m)}+x\left[v'_{p(i)}-v'_{p(m)}\right]}{1+y\left[v'_{p(i)}-v'_{p(m)}\right]^2} \qquad (11)$$

where the point denoted by the subscript '*m*' is the maximum load point, and the variables *x* and *y* are changed until the best fit curve is reached. Among the four parameters to be determined the x and y are true variables while the other two are determined at the maximum load (m) point.

Two criteria used for searching the best fitting function are (a) if the functional continuity between the fitting function and the calculated data using the blunting line ($J=2\Delta_Y\Delta a$) is achieved around the maximum load point and (b) if the normalized load by the fitting function matches the value calculated from the measured final crack length. An example displayed for a normalized load versus displacement curve for the 4.7 mm thick DCT specimen is provided in Figure 2, which corresponds to the non-normalized curve given in Figure 1.

Calculation of crack lengths from the max-load point to final point: As the full normalized load versus displacement is established, the crack extension beyond the crack blunting regime can be easily calculated by an inverse function of equation (7):

$$a_{(i)} = W\left\{1-\left[\left(\frac{P_{(i)}}{P_{N(i)}}\right)\left(\frac{1}{WB}\right)\right]^{1/\eta_{(i)}}\right\} \qquad (12)$$

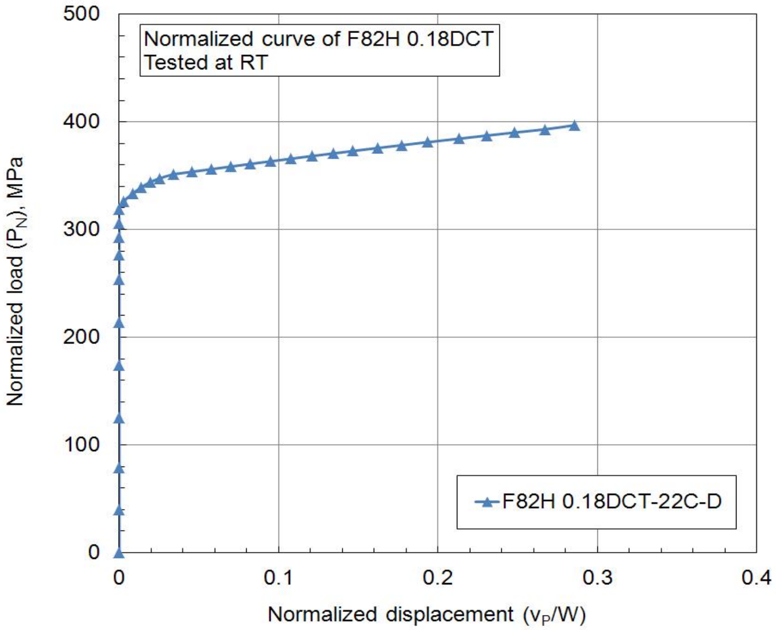

Figure 2. A normalized load versus displacement curve for a 4.7 mm thick DCT specimen

Construction of J-R curve: In the process of calculating crack lengths using normalization, the *J-R* curve, i.e., *J-Δa* curve is simultaneously obtained at each data point since the crack extension amount *Δa* is simply given by $a_{(i)}$- a_0. The J-R curve obtained for the present example case is displayed in Fig. 4. The comparison with the curve from the standard unloading complication method indicates that the J-integral values from the two methods agree well.

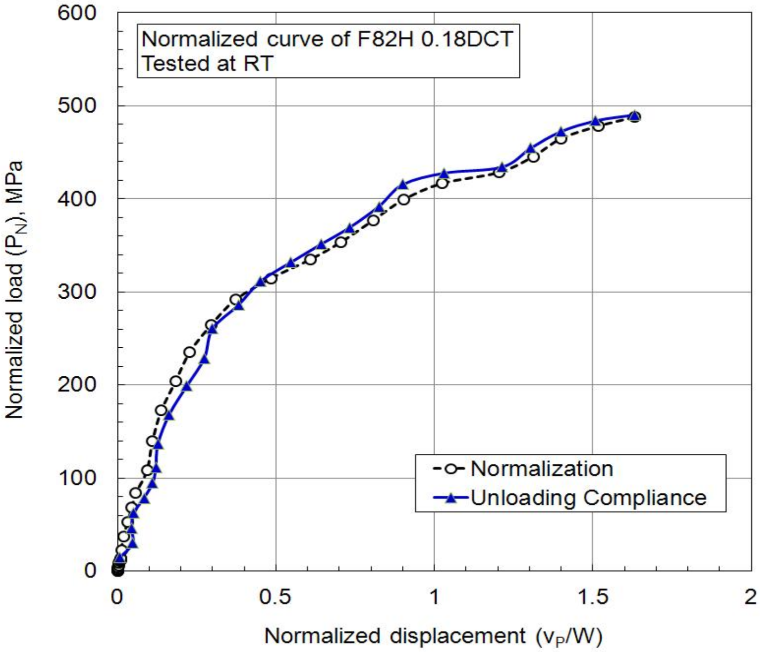

Figure 3. An example of J-R curve obtained by the normalization method. It is compared to the curve from the standard unloading compliance method (for specimen F82H 0.18DCT-22C-D).

Results and discussion

Load line-displacement and J-R curves

Figures 5 and 6 display the load versus displacement curves for the DCT specimens. It should be noted that the curves for the first two cases, F82H-0.18DCT-22C-A and –B, were recorded with clip-on gage, while the other curves without the gage. Significantly different load-displacement traces were recorded from the DCT specimens primarily due to the differences in initial crack length and net thickness. Further, the smaller DCT specimens without side grooves (A & B) also incurred larger plasticity zone.

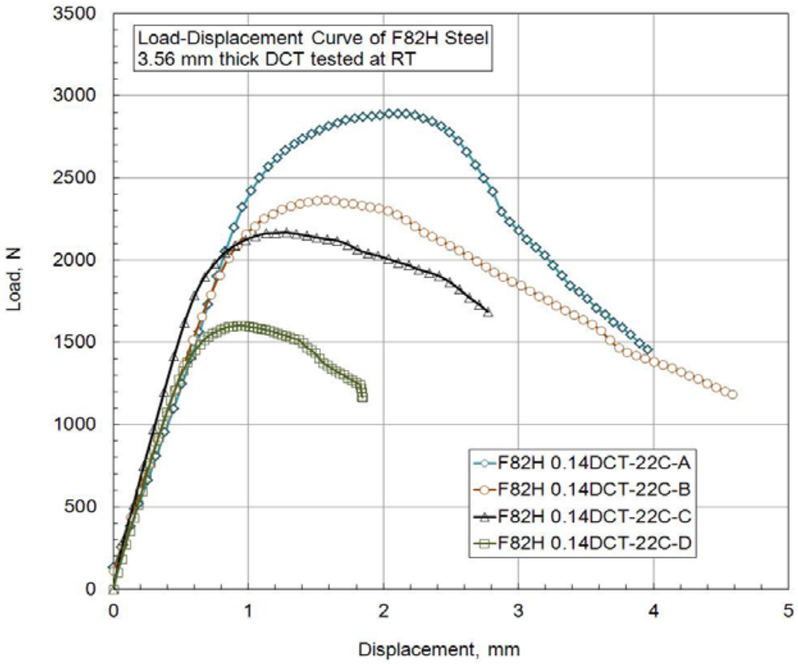

Figure 4. Load-displacement curves for 3.56 mm thick DCT specimens. Note that no clip-on gage was used: the displacement data were obtained from cross-head movement. No side groove was machined to the three specimens F82H 0.14DCT-22C-A to C but had side 13% grooves in the D specimen.

Figures 7 and 8 present the J-R curves constructed from the specimen geometry data (Table 1) and the load-displacement curves (Figs. 6 and 7) using the simplified curve normalization method described in Section 2. The J-R curves from the first two smaller DCTs (F82H 0.14DCT-22C-A&B) show slightly different behaviors. The J-integral value of the specimen A increased to higher values in low crack extension (Δa) range but it went lower than the curve for specimen B from Δa = ~0.7 mm. As a result, the specimen A displayed lower slope or tearing modulus. Since these smaller specimens did not have side grooves, the development of plasticity zone should be less uniform between the specimens when compared to the side grooved specimens. It is believed that the differences in plastic zone size and initial crack length have caused such different J-R behaviors in the 3.6 mm thick DCT specimens.

In Figure 6, the other smaller DCT specimens (F82H 0.14DCT-22C-C&D) showed similar J-R curves although they were tested with and without side grooves (see Table 2). Compared to the specimen C, the specimen D showed lower load-displacement curve due to larger initial crack length and side grooves; however, both J-R traces are similar for both specimens. In general, the specimen with a larger initial crack length results in a steeper increase, especially in J value in the later part of J-R curve. It is interesting, however, to observe that the slope in the later part of J-R curve in D is not higher than that of the specimen C. This is believed to be because of the constrained development of plastic zone in the specimen D with side grooves. It is also very evident that these specimens (F82H 0.14DCT-22C-C&D) have much lower J-R curves than the other two specimens (F82H 0.14DCT-22C-A&B). The difference is too large to explain with specimen geometry reasons; a metallurgical difference is expected to be found between these seemingly two different materials.

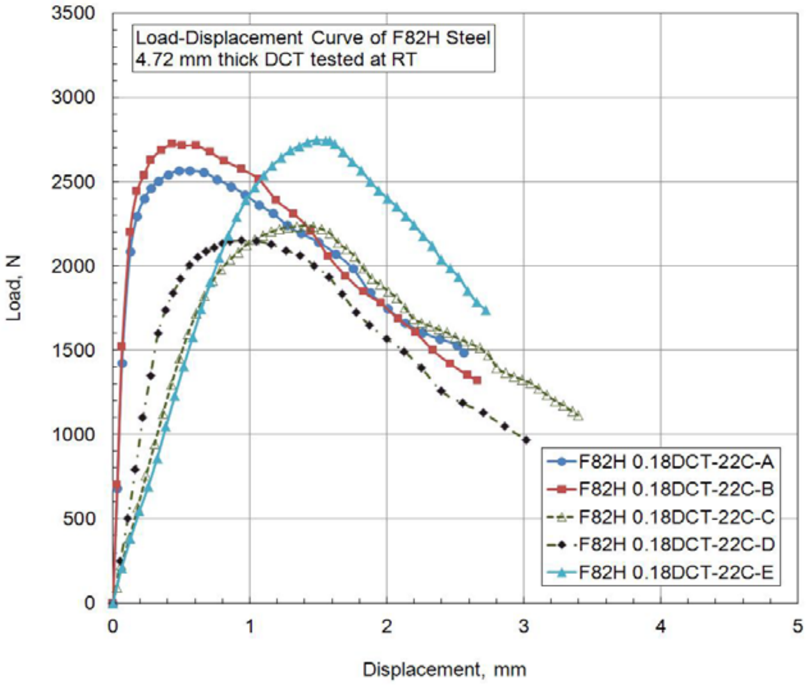

Figure 5. Load-displacement curves for 4.72 mm thick DCT specimens. Note (1) that the curves for the first two cases, F82H-0.18DCT-22C-A and B, were recorded with clip-on gage, while the other curves without the gage and (2) that all the 0.18DCT specimens have a nominal thickness of 0.18 inch (~4.7 mm) and 10% side groove at each side.

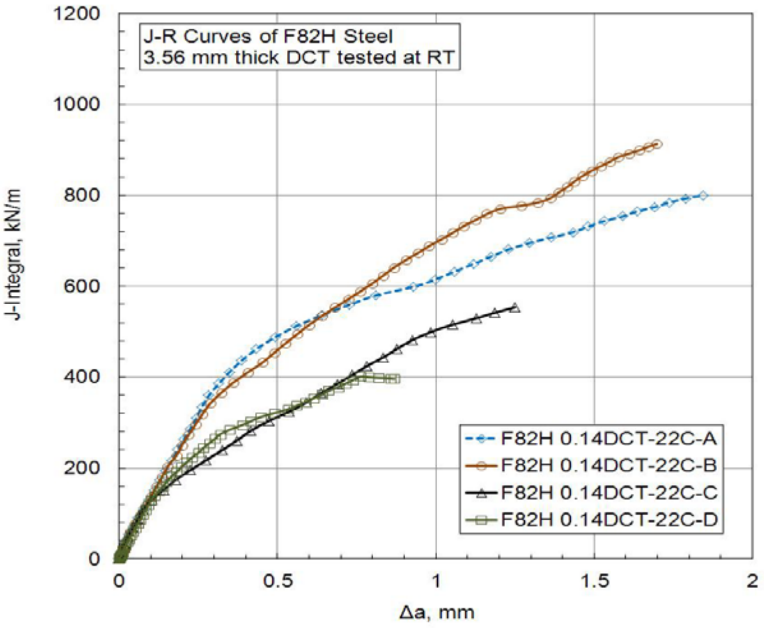

Figure 6. J-R curves generated for F82H 0.14DCT specimens.

For the 4.7 mm thick DCTs with side grooves, Figure 7 confirms that the different load-displacement curves result in similar J-R curves. This might be because the side grooves have caused more orderly crack extension and thus smaller plastic zones developed in these specimens are relative uniform. This result also confirms that the J-evaluation process using pure plastic displacement only has been correctly developed.

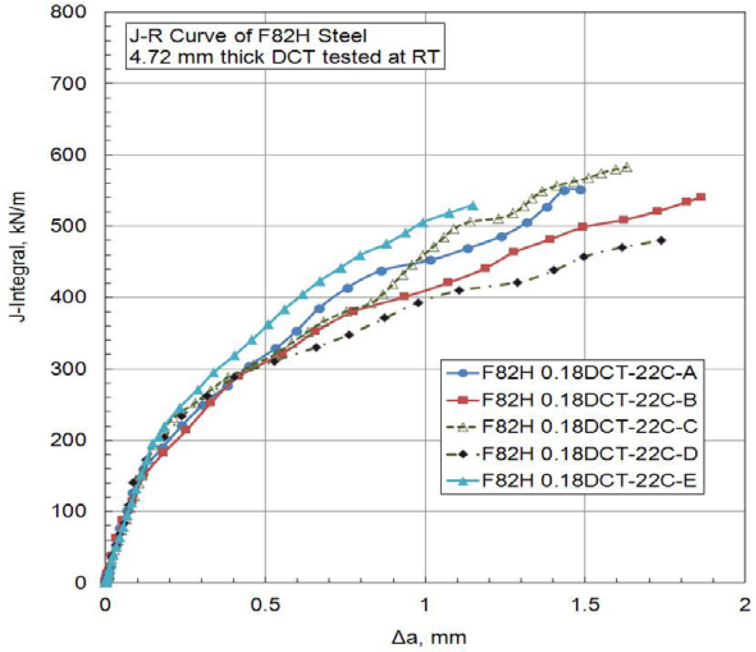

Figure 7. J-R curves generated for F82H 0.18DCT specimens.

The final step of fracture evaluation procedure is to determine fracture toughness values. Following the ASTM standard method E1820, the interim fracture toughness values (J_Q) were determined at the intersection of the constructed J-R curves and the 0.2 mm offset line of the blunting line ($=2\sigma_Y\Delta a$). The final fracture toughness data are also given in the form of stress intensity factor, K_{JQ}, which can be converted from the J_Q data using the following relationship:

$$K_{JQ} = \sqrt{(J_Q \cdot E)/(1-\nu^2)}, \qquad (13)$$

The results of this toughness determination process are summarized in Table 2. Comparing the values in Table 2, the side grooved 4.7 mm thick specimens have yielded relatively uniform fracture toughness values. The maximum difference among K_{JQ} values was only 19 MPa√m, which is about 7% of the fracture toughness values listed.

The last column lists the slope *dJ/da* for reference. These values can be easily converted to the tearing modulus *dJ/(Eda*). Further, it is worth knowing that the fracture toughness values corresponding to the intersection of J-R curve with a 0.1 mm shifted line can be approximately calculated form the fracture toughness data provided in Table 2 using these slope data.

It is worth noting that the fracture toughness parameters in Table 2 are still in ‘interim’ status as the validity check is not performed for the data. The toughness values for the specimens without side grooves, in particular, are expected to be invalid mainly because of the curved crack front line and overly higher plasticity. It is advised to use these data for comparison purposes only and a scaling process using a size effect model is needed prior to use in engineering analyses.

Table 2. Fracture toughness parameters

Specimen	*J_Q [N/mm or kJ/m^2]	K_{JQ} [MPa√m]	dJ/da [GPa]
F82H 0.14DCT-22C-A	513	341	275
F82H 0.14DCT-22C-B	495	335	503
F82H 0.14DCT-22C-C	282	253	389
F82H 0.14DCT-22C-D	312	266	238
F82H 0.18DCT-22C-A	277	251	365
F82H 0.18DCT-22C-B	253	240	308
F82H 0.18DCT-22C-C	297	260	273
F82H 0.18DCT-22C-D	288	256	210
F82H 0.18DCT-22C-E	319	269	409

*Determined at the intersection between 0.2 mm offset blunting line and J-R curve ($J_Q = J_{0.2mm}$)

CONCLUSIONS

A modified procedure for fracture testing and J-R curve construction has been developed to test miniature disk compact tension (DCT) specimens in high radiation areas. Fracture testing procedure was simplified by eliminating any externally-attached displacement gage. In the J-integral evaluation procedure, the load-displacement curve normalization method for calculation of crack lengths was modified to accommodate the experimental simplification.

The application to the H82H ferritic-martensitic steel DCT specimens confirmed that the newly established procedure can produce nearly identical J-R curve as the traditional unloading compliance method. With the side grooved DCT specimens, where the crack extension and development of plastic zone are strongly guided, highly close J-R curves could be obtained for the DCT specimens with different initial crack sizes.

The application results also indicated that the miniature DCT specimens without side grooves can induce significant variation or overestimation in the fracture toughness of the test material. Introducing side groves is highly recommended in using miniature fracture specimens.

Acknowledgements

This research was sponsored by U.S. Department of Energy, Offices of Fusion Energy Sciences and Nuclear Energy, under Contract DE-AC05-00OR22725 with UT-Battelle, LLC.

1.3 DISASSEMBLY OF HFIR JP28&29 TENSILE HOLDERS AND VICKERS HARDNESS RESULTS ON F82H IRRADIATED AT 573 K

— M. Ando, D. Hamaguchi and H. Tanigawa (Japan Atomic Energy Agency), R. G. Bowman, G. C. Morris, J. P. Robertson and Y. Katoh (Oak Ridge National Laboratory)

OBJECTIVE

The objective of this work was to disassemble ten tensile specimen holders from JP28&29 capsules and perform Vickers hardness measurements on 573 K -irradiated SS-J3 specimens. This work is part of the U.S. Department of Energy – Japan Atomic Energy Agency fusion materials collaboration.

SUMMARY

Ten tensile specimen holders from HFIR irradiation experiments JP28 and JP29 were successfully disassembled in the ORNL 3025E hot cell facility. Some holders needed to be cut along corners of the holder because specimens could not be easily pushed out of the holder. All tensile specimens from the disassembled holders were recovered and identified. The surfaces of the specimens irradiated at 673 and 773 K were oxidized during the irradiation and cannot be hardness tested without polishing. Vickers hardness was measured on some of the tensile specimens irradiated at 573 K.

PROGRESS AND STATUS

Introduction

This experiment is being carried out within the fourth phase framework of the U.S. DOE-JAERI Collaboration on Fusion Materials. The goals of the experiment include the investigation of the effects of helium on microstructural evolution, the impact of helium on fracture properties, and the development of engineering data on the fusion candidate material F82H. The HFIR JP28&29 capsules began neutron irradiation in HFIR in 2005 [1]. The capsules achieved an irradiation dose of 80dpa in 2013 and were removed from the reactor after completing (44 cycles). Higher-dose irradiation data on RAFM is very significant for the design of a fusion DEMO reactor [2]. However, mechanical property data for RAFM with high-dose neutron irradiation, above 80 dpa, are not available.

This report summarizes results of the disassembly of the JP28&29 tensile specimen holders and the Vickers hardness measurements for some specimens irradiated at 573 K.

Disassembly of JP28&29 tensile specimen holders

In this work, two plans were prepared for the disassembly of tensile specimen holders:
Plan 1; Hold the holder with one manipulator and use a special tool to try to push out the center circular spring pin.
Plan 2; Mount the holder in the special cutting machine in cell 6 and cut along the corners on each side of the holder.

At first, plan 1 was tried for each holder. If it could not be disassembled easily, then plan 2 was performed.
These disassembly results are summarized in table 1. Figure 1 shows an example of this cutting process in the hot cell.

Table 1. Disassembly results for JP28&29 tensile holders

No	Holder No.	Irrad. Temp.	Dose	Cut	SS-J3	APFIM/MMPC	Passive TM
		(K)	(dpa)	Number of specimens (missing), [broken]			
1	JP28 #7	673	85.4	1	16 (0)	17 (0)	8 [0]
2	JP28 #9	773	81.8–83.4	2	16 (0)	16 (0)	8 [0]
3	JP29 #7	573	85.9–86.8	–	16 (0)	16 (0)	8 [0]
4	JP29 #10	573	76.9–79.9	1	17 (0)*	17 (0)	8 [0]
5	JP29 #13	573	46.9–52.9	3	16 (0)	16 (0)	8 [0]
6	JP29 #2	673	45.7–51.8	1	16 (0)	16 (0)	7 [1]
7	JP28 #3	573	66.8–70.8	–	16 (0)	13 (3)	7 [1]
8	JP28 #1	673	41.7–47.9	1	16 (0)	15 (1)	7 [1]
9	JP29 #3	773	58.7–63.7	1	16 (0)	15 (1)	8 [0]
10	JP29 #12	573	58.7–63.7	–	16 (0)	14 (2)	8 [0]

* Including 3 SSJ2 specimens

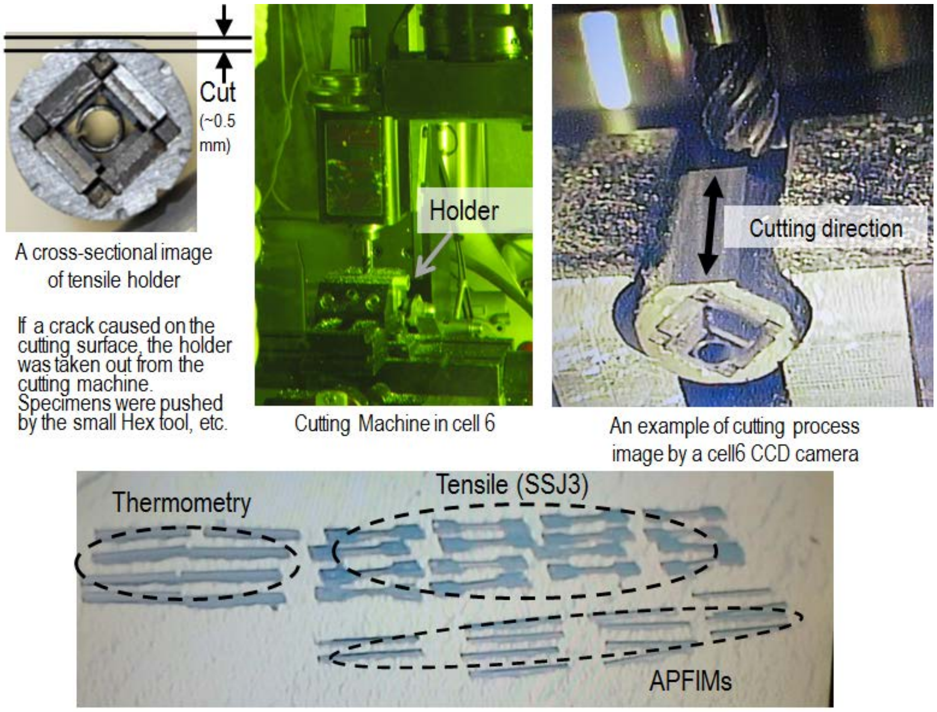

A cross-sectional image of tensile holder

If a crack caused on the cutting surface, the holder was taken out from the cutting machine. Specimens were pushed by the small Hex tool, etc.

Cutting Machine in cell 6

An example of cutting process image by a cell6 CCD camera

Figure 1. An example of the disassembly process for tensile holder by using cutting machine in hot cell

Experimental

The materials were F82H IEA heat, F82H Modify-3 and Nickel-doped F82H provided by Japan Atomic Energy Agency. The chemical compositions of these materials are reported elsewhere [3,4,5]. Nickel-doped F82H steels were provided to investigate the effect of helium on mechanical properties. In this experiment, two types of Nickel-doped F82H were prepared [4]. One is 1.4%^{58}Ni-F82H which produced helium atoms by the reaction $^{58}\mathrm{Ni}(\mathrm{n}_{\mathrm{Thermal}}, \gamma)^{59}\mathrm{Ni}(\mathrm{n}_{\mathrm{Thermal}}, \alpha)^{56}\mathrm{Fe}$ during irradiation. The other is 1.4%^{60}Ni-F82H which did not produce helium atoms.

In this work, the hardness tests were performed for tensile (SS-J3 type) specimens irradiated in position 7 in the JP29 capsule. The hardness of these specimens was measured by a Vickers hardness tester (Mitsutoyo AAV-500) at cell2 in Building 3025E, Oak Ridge National Laboratory (ORNL). The hardness tests were performed on a tab section of each tensile specimen (near the engraved ID).

Results and Discussion

Table 2 shows results of Vickers hardness for tensile specimens irradiated at 573 K up to 80 dpa.

Table 2. Vickers hardness of tensile specimens from JP29 position 7

Capsule	**Pos.**	**ID**	**Material**	**Irr. Temp K**	**dpa**	**Hv**				
						Max	Min	Range	Avg	Stdev
JP29 #7	UI	560	F82H+1.4%Ni58	573+	85.9	386	349	36	**372**	12
JP29 #7	UI	561	F82H+1.4%Ni58	573+	85.9	413	376	37	**396**	13
JP29 #7	UI	562	F82H+1.4%Ni58	573+	85.9	406	382	24	**400**	7
JP29 #7	UI	563	F82H+1.4%Ni58	573+	85.9	417	382	35	**399**	11
JP29 #7	UO	060	F82H IEA	573-	85.9	392	369	23	**383**	7
JP29 #7	UO	061	F82H IEA	573-	85.9	Not tested				
JP29 #7	UO	062	F82H IEA	573-	85.9	420	382	37	**401**	10
JP29 #7	UO	063	F82H IEA	573-	85.9	424	388	36	**407**	11
JP29 #7	DI	660	F82H+1.4%Ni60	573+	86.8	370	321	49	**348**	13
JP29 #7	DI	661	F82H+1.4%Ni60	573+	86.8	Not tested				
JP29 #7	DI	662	F82H+1.4%Ni60	573+	86.8	357	320	37	**339**	10
JP29 #7	DI	663	F82H+1.4%Ni60	573+	86.8	396	349	47	**383**	12
JP29 #7	DO	H60	F82H Mod3	573-	86.8	Not tested				
JP29 #7	DO	H61	F82H Mod3	573-	86.8	Not tested				
JP29 #7	DO	H62	F82H Mod3	573-	86.8	385	345	40	**362**	13
JP29 #7	DO	H63	F82H Mod3	573-	86.8	Not tested				

One of the purposes of a hardness test is to confirm the irradiation temperature by reference to other available hardness value. In the holders containing the tensile specimens, the SS-J3 specimens are groups in two sets of eight specimens each. In the upper section (U) of each holder, there are four inner specimens (UI) surrounded by four outer specimens (UO). In the lower section of each holder (D), there are also four inner specimens (DI) surrounded by four outer specimens (DO). The average hardness for specimens in lower positions had a tendency to be lower than the average hardness of the upper position specimen. However, these results need to be compared to another holder which has a similar irradiation condition. A record of the irradiation temperature also should be examined by analyzing passive temperature monitors.

The irradiation hardening data from this work are shown in comparison to data from the JP25, 26 and 27 capsules in Figure 2. Additionally, 50 dpa irradiation data for F82H will be also obtained in the future from recently completed high dose (50 dpa) rabbit capsule irradiation experiments with similar materials. From reported data [6], the yield stress (σ_y) is close to the ultimate strength (σ_{UTS}) for F82H irradiated at 573 K. Therefore, it is expected that σ_y for F82H irradiated at 573 K, to- 80 dpa is about ~1100 MPa at room temperature. The hardness testing will be completed on all SS-J3 specimens prior to tensile testing.

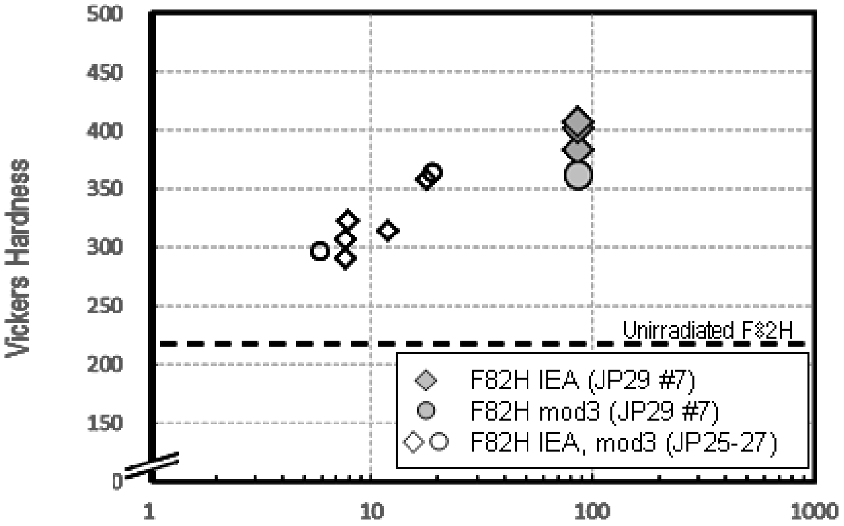

Figure 2. Dose dependence of Vickers hardness for F82H irradiated at ~573 K in HFIR.

Acknowledgements

This research was sponsored by Japan Atomic Energy Research Institute and the Office of Fusion Energy Sciences, U.S. Department of Energy, under contracts NFE-10-02779 and DE-AC05-00OR22725, respectively, with UT-Battelle, LLC. The authors would like to acknowledge the assistance by Patrick S. Bishop in Building 3025 hot cell facility to the experimental work and the supports of FMNS Gr staffs.

REFERENCES

[1] D. K. Felde et al., DOE/ER-0313/38 (2005) 164-182.
[2] H. Tanigawa et al., J. Nucl. Mater. 417 (2011) 9–15.
[3] K. Shiba, et al., JAERI-Tech 97-038 (1997).
[4] K. Shiba et al,. J. Nucl. Mater. 329–333 (2004) 243–247.
[5] T. Sawai et al,. Fusion Science & Technology 44 (2003), 201-205.
[6] K. Shiba et al., DOE/ER-0313/28 (2000) 131-135.

1.4 ANALYTICAL TEM CHARACTERIZATION OF MODIFIED F82H and 14YW UNDER SIMULTANEOUS HELIUM AND NEUTRON IRRADIATION COMPARED TO ONLY NEUTRONS AT 500°C

- H.J. Jung, D. J. Edwards, B. Yao, R. J. Kurtz (Pacific Northwest National Laboratory), G. R. Odette, T. Yamamoto, Y. Wu (University of California Santa Barbara)

OBJECTIVE

To characterize the microstructure and chemical evolution of a reduced activation ferritic/martensitic (RAFM) steel and an oxide dispersion strengthened (ODS) alloy irradiated to 21.2 dpa at 500°C and simultaneously injected with 1230 appm of He via an *in situ* He injection (ISHI) technique.

SUMMARY

An RAFM steel and an ODS ferritic alloy (F82H.mod3+CW and 14YW, respectively) were irradiated as part of the HFIR-JP27 irradiation experiment conducted in the High Flux Isotope Reactor to explore He effects in structural alloys. The *in situ* He injection (ISHI) technique is used to implant He up to 9 µm below the surface of a NiAl coated sample at He/dpa levels up to ~50. This report summarizes the current status of TEM characterization of the two irradiated alloys. The He-implanted side of the RAFM alloy exhibited significant swelling due to bubble and void formation - within the matrix, on pre-existing dislocations, and at interfaces within the material. The 14YW alloy exhibited significant swelling even in the absence of implanted He, primarily through large voids that formed on the ODS particles. In addition, significant radiation-induced segregation of the Cr was observed around oxide particles and on lath boundaries, and visible α′ particles could be detected via elemental mapping of the matrix of the 14YW alloy.

PROGRESS AND STATUS

Introduction

Reduced activation ferritic/martensitic (RAFM) steels and oxide-dispersed strengthened (ODS) alloys are being evaluated as structural materials with high swelling-resistance for first-wall materials for future fusion reactors [1,2]. The materials used in the first wall will inevitably endure a harsh thermal and neutron-irradiation environment, an environment made even more difficult by the presence of high levels of He production (10 appm He per dpa) from transmutation [3]. The high levels of He impacts the mechanical properties of ferritic-based alloys through He embrittlement and the formation of He bubbles and voids in the matrix, at lath boundaries, grain boundaries, and at particle-matrix interfaces [4], which can lower the high-temperature tensile and creep properties. A further consequence of the He accumulation is that the bubbles can grow large enough to eventually transition to unstably growing voids, thereby leading to significant swelling [5]. In order to mitigate the rate at which He bubbles transition to voids, alloy microstructures are being designed to provide a high density of nanoscale trapping sites that keep He gas atoms broadly dispersed [1]. Research efforts are currently investigating the effectiveness of different oxide dispersions, as well as understanding the mechanisms of He transport, trapping, and interaction with various defects and interfaces present in irradiated ferritic based alloys.

Due to practical difficulties of assessing material performance in a neutron irradiation environment under conditions relevant to a fusion reactor, a novel approach, the *in-situ* He injection (IHSI) technique, has been used to investigate the effects of simultaneous neutron irradiation and He injection on microstructural evolution of candidate materials, as described in detail [7]. Here we present analytical transmission electron microscopy (TEM) characterization on neutron irradiated and He-injected samples of a modified F82H (RAFM steel) and 14YW (ODS alloy) with a 4 µm thick NiAl layer bonded to one surface. When irradiated with neutrons, the ^{59}Ni isotope undergoes a ^{59}Ni(n, α) reaction and injects some fraction of the energetic He into the ferritic alloy. The samples were irradiated to a dose of 21.2 dpa at 500°C in the JP-27 experiment in the HFIR reactor, which injected an estimated 1230 appm of He into the sample over a uniform depth of 9 µm. Cross-sectional TEM samples were prepared by FIB to characterize microstructure related features such as He bubbles/voids, dislocation loops/line dislocation, and oxide or carbide particles.

Experimental Procedure

The compositions of the RAFM steel and ODS alloy characterized in this effort are listed in Table 1. Sample F82H-mod.3+CW was modified to reduce the N and Ti levels to 14 ppm and 0.001%, respectively, and add 0.1% Ta. It was austenitized at 1040°C for 30 min, normalized (air-cooled), and tempered at 740°C for 1.5 h. Before the irradiation, 20% cold work was applied to the modified F82H specimen to generate a high dislocation density. 14YW is ODS alloy fabricated through powder metallurgical procedures, described in Ref. 7. All samples were neutron irradiated to a dose of 21.2 dpa at 500°C in the High Flux Isotope Reactor at Oakridge National Laboratory. The thickness of NiAl is 4.7 µm, which gives a He concentration of about 1230 appm in the ferritic matrix extending to a depth of ~9 µm away below the NiAl coating.

Table 1. Composition of examined RAFM/ODS alloys

Alloy	Composition (wt.%) with Fe balance										
	Cr	Ti	$Y(Y_2O_3)$	C	Al	Ta	W	Mn	Si	Ni	V
F82H-mod.3+CW	8.16	<0.005	-	0.097	-	0.1	1.98	0.13	0.10	0.01	0.20
14YW	14.00	-	0.25	-	-	~	3.00	-	-	-	-

Cross-sectional TEM samples, prepared by a FIB (FEI Quanta 3D), were finalized with low-energy surface cleaning (2 keV Ga^+ ion) at ±2° tilt angles. Further surface cleaning to remove FIB artifacts was conducted using low-energy Ar^+ ion beam by a Fischione Model 1040 NanoMill, detailed in Table 2.

Table 2. Nanomilling cleaning condition

High tension (eV)	Beam current (nA)	Time (min)	Milling size (µm)	Tilt angle (°)	Temperature (°C)
900	165	20 (each side)	40 × 20	± 10	-165

The analytical TEM characterization was performed using a newly installed Cs-corrected JEOL ARM 200CF microscope equipped with various detectors, including a Centurio silicon drift detector (SDD) for energy dispersive X-ray spectroscopy (EDS), a Gatan Dual EELS (electron energy loss spectroscopy) system, and HAADF (high angle annular dark field) and BF (bright field) STEM detectors. This instrument can achieve spherically aberration-corrected sub-nanometer and sub-Å probes with high beam currents because of the cold field emission gun (CFEG), allowing enhanced spatial resolution EDS mapping. TEM sample thickness was determined through convergent-beam electron diffraction (CBED). Bright-field TEM images of He bubbles and voids were acquired at an over/under-focus, and this measured value is about 87% of the actual bubble size at a under-defocus of 750 nm [8]. The dislocation loops and line dislocations were imaged using multiple diffraction vectors at two-beam conditions based on both crystallographic projections [9].

Results and Discussion

A surprising observation was the presence of small 1-2 nm cavities at a density of $\sim 10^{22}$ per m^3 that were distributed in the matrix of F82H-mod.3+CW that experienced only neutron irradiation (Figure 1-a). With no He injection on this side, it is likely that relatively small levels of He, up to 10-15 appm, were formed from the ^{54}Fe (n,α) reaction in the alloy and transmutation of potential B impurities, the latter of which creates He from the ^{10}B isotope [10]. In the absence of a high density of trapping sites, this alloy nucleated visible bubbles with only a relatively small amount of He. Assuming that about 10 appm He is generated from ^{54}Fe and B impurities and all of this He is contained in the visible bubble population, then the estimated He to vacancy ratio is ~0.44, which is about the level expected for bubbles at equilibrium pressure.

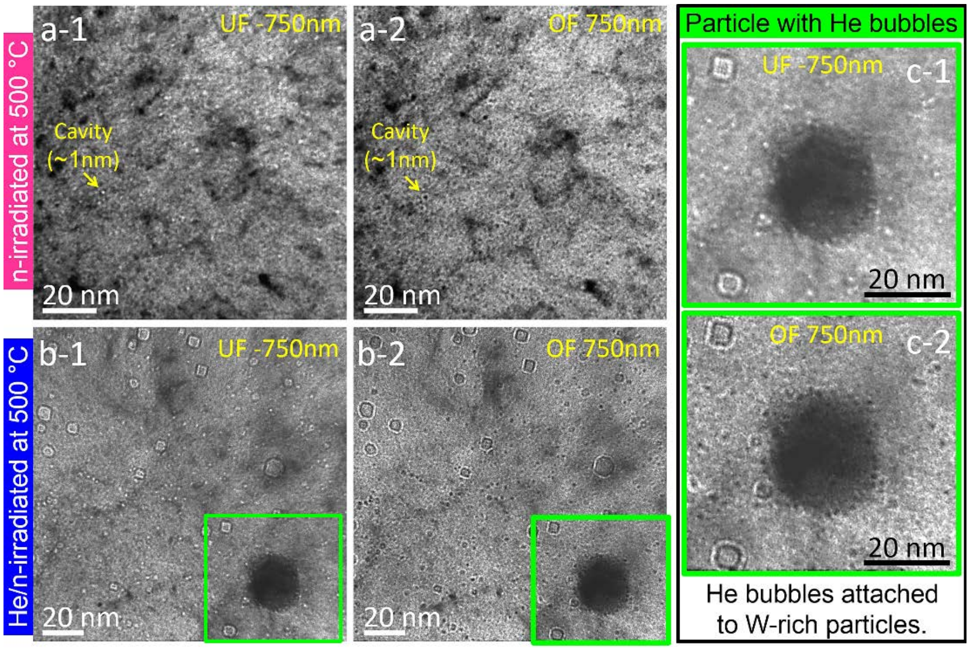

Figure 1. Cavities and He bubbles are visible in F82H-mod.3+CW based on BFTEM images taken at 750 nm of under/over-focus from (a) the side with no He-injection and (b) the side with in-situ He injection. The images in (c) show He bubbles (1~2 nm) and voids (>2nm) forms at W-rich particle/matrix interface. Note that small cavities of 1~2 nm are observed in neutron-irradiated side.

Another transmutation reaction worth noting concerns the W. Substantial Os peaks and lower than expected levels of W were observed in the EDS spectra from both the SEM and TEM analysis of the irradiated samples, and a search of the literature revealed that W converts to roughly 30% Os by 25 dpa in HFIR [11]. This loss of W has been reported by other researchers looking into the effect of W transmutation on the first wall W armor and irradiation hardening of W by Os [12,13]. This reaction occurred equally in both of the samples examined in this study.

As expected, He bubbles ranging in size from 1-3 nm with a density of ~10^{23} per m^3 and larger voids (3~15 nm) are observed in the He-injected side of the neutron irradiated F82H.mod3 alloy (Figure 1-b) as shown using bright-field TEM at an under/over-defocus of ±750nm. A more complete analysis of the cavity distribution is ongoing, but the initial results are summarized in Table 3. A magnified view (Figure 1-c) of the round particle (green box in Figure 1-b), identified as a W-V carbide using EDS mapping, shows He bubbles and voids have nucleated at the interface of the particle. The Cr-rich carbides were found to contain significant levels of W (~12 wt%), and Os (~5 wt%), and lower amounts of V (~1.5 wt%). In our previous work, a high density of small He bubbles less than 2 nm are consistently located at the lath boundaries in conjunction with a large fraction of voids dispersed over the matrix [14]. Furthermore, it has been reported that F82H-mod.3 with cold work exhibits a smaller number of large voids and larger number of small He bubbles than that without cold work when irradiated to 380 appm He / 9 dpa at 500°C [15].

Table 3. Statistics of Cavities in the Two Alloys

Alloy	Non-Implanted Side		He-implanted Side	
	Density (x 10^{23} m^{-3})	Mean Size (nm)	Density (x 10^{23} m^{-3})	Mean Size (nm)
F82H-mod	0.21	1.3	1.1	2.7
14YW	0.06	11.6	1.1	3.1

The non-injected side of the 14YW sample contained relatively large cavities (5 to 30 nm diameter) attached to faceted Y-rich oxide particles (see Figure 2-a), suggesting that the small levels of He produced from the ^{54}Fe reaction accumulated preferentially at the particle/matrix interface and eventually transitioned to large cavities. The He-injected side of the neutron-irradiated 14YW exhibited not only the same association between voids and large Y-rich oxide particles, but a much higher density of small He bubbles (1-3 nm) and large voids (3~30 nm) in matrix as shown in Figure 2-b and Figure 3. Interestingly, several examples were found of He bubbles and voids aligned to <100> directions in the matrix when imaged near an 001 zone axis, indicated as yellow dotted lines in Figure 3. Different from the faceted Y-rich particles, elongated Cr-rich carbide particles nucleated He bubbles and large voids both inside the particle and at the particle/matrix interface. Whether the voids (or cavities) within the elongated particles contain He or not still remains in question and attempts will be made to verify this using EELS. The formation of voids in 14YW shows that coarse scale oxides are not as effective as the nano-oxides in true nano-structured ferritic alloys (NFA) like 14YWT and MA957. Indeed the presence of large voids in 14YW suggests that there may be good and bad oxide microstructures.

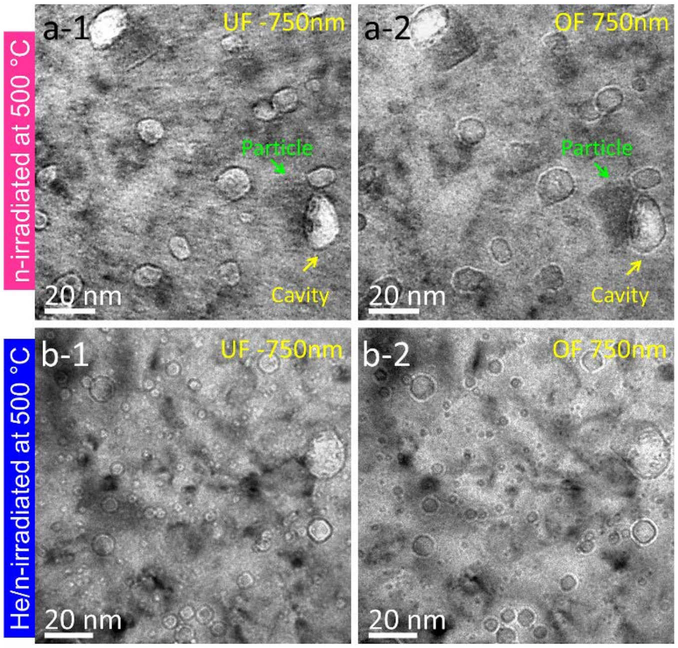

Figure 2. Cavities and He bubbles of 14YW on two sets of BFTEM images at under/over-focus from (a) non-injected side and (b) the in-situ injected side. Note that large cavities ranging from 5 to 30 nm in size are associated with each Y-rich oxide particles.

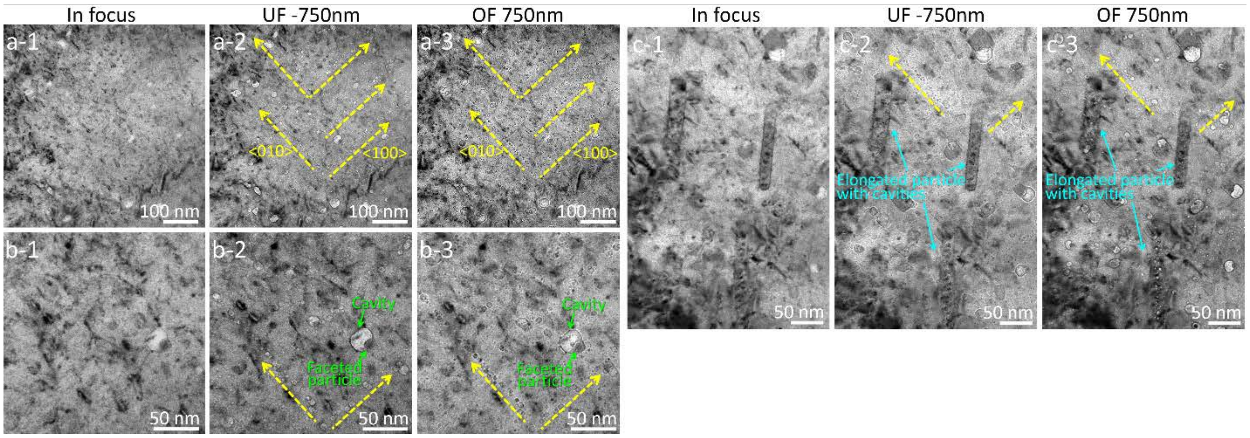

Figure 3. Three sets of through-focus BFTEM images taken near an [001] zone axis in in the He-injected side of alloy 14YW show (a) He bubbles and cavities aligned to <100> directions (along yellow arrow), (b) large cavities (green) attached to rounded rectangular particle surface, and (c) large cavity and He bubbles (light blue) formed at elongated particles inside (c). Note that there are two different particles, one is a round Y-rich oxide phase and the other are elongated Cr-rich carbides.

In order to identify the particle composition and explore chemical evolution during irradiation, EDS elemental mapping was conducted, the results of which are presented in Figs. 4 through 8. Figure 4-a presents an overview of particle distribution predominantly located at lath boundaries in the non-injected side of F82H-mod.3+CW based on bright-field/dark-field TEM images. Figure 4-b shows bright field (BF)/HAADF STEM images with corresponding elemental EDS mapping. There are two types of particles revealed in the maps: a very low density of small W-C carbides (rounded shape) and large Cr-rich carbide particles (elongated shape). Figure 5 provides a comparable set of images and elemental maps from the He-injected side of the neutron irradiated F82H-mod.3+CW, demonstrating the same evidence of chromium carbides and spherical W-V carbides as observed in Figure 1-c.

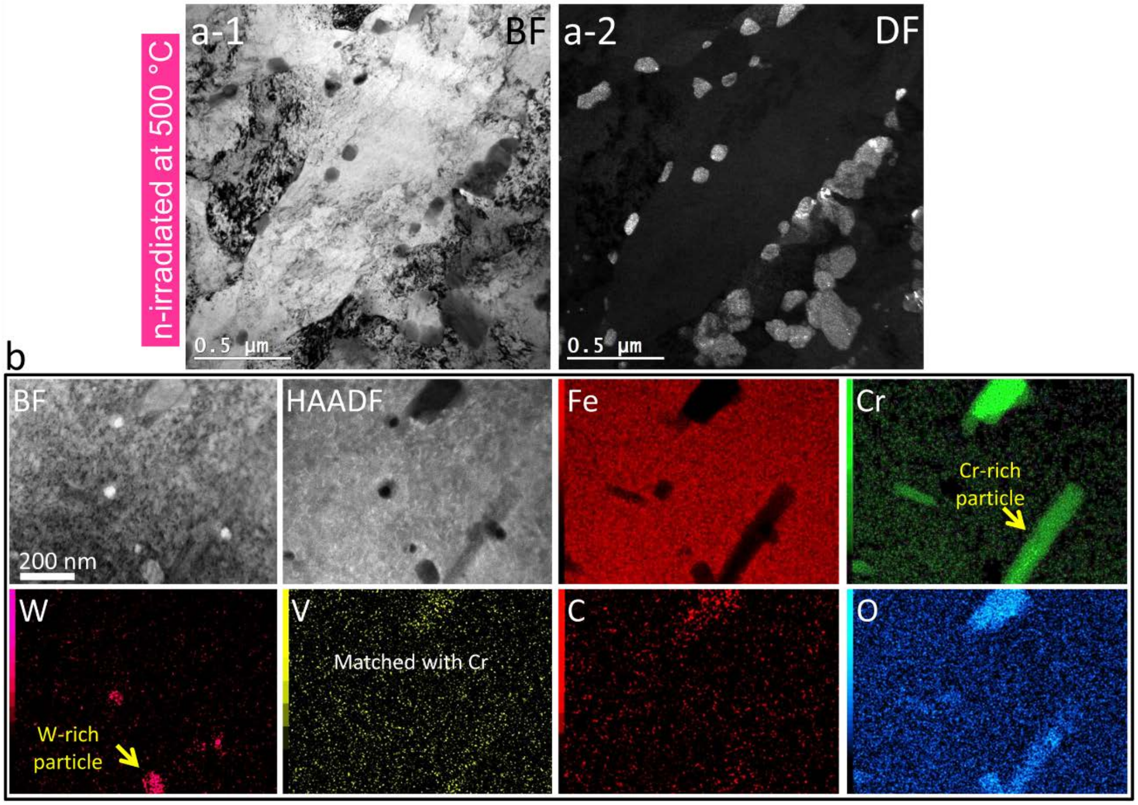

Figure 4. (a) BF and DF TEM images showing Cr-rich carbide particles formed predominately on the lath boundaries in the neutron-irradiated F82H-mod.3+CW. BF and HAADF STEM images with elemental EDS mapping are provided in (b). Note that there are W-rich oxide particles and Cr-rich particles, with the Cr-rich particles generally much larger than the W-rich particles. Vanadium is segregated in Cr-rich particles.

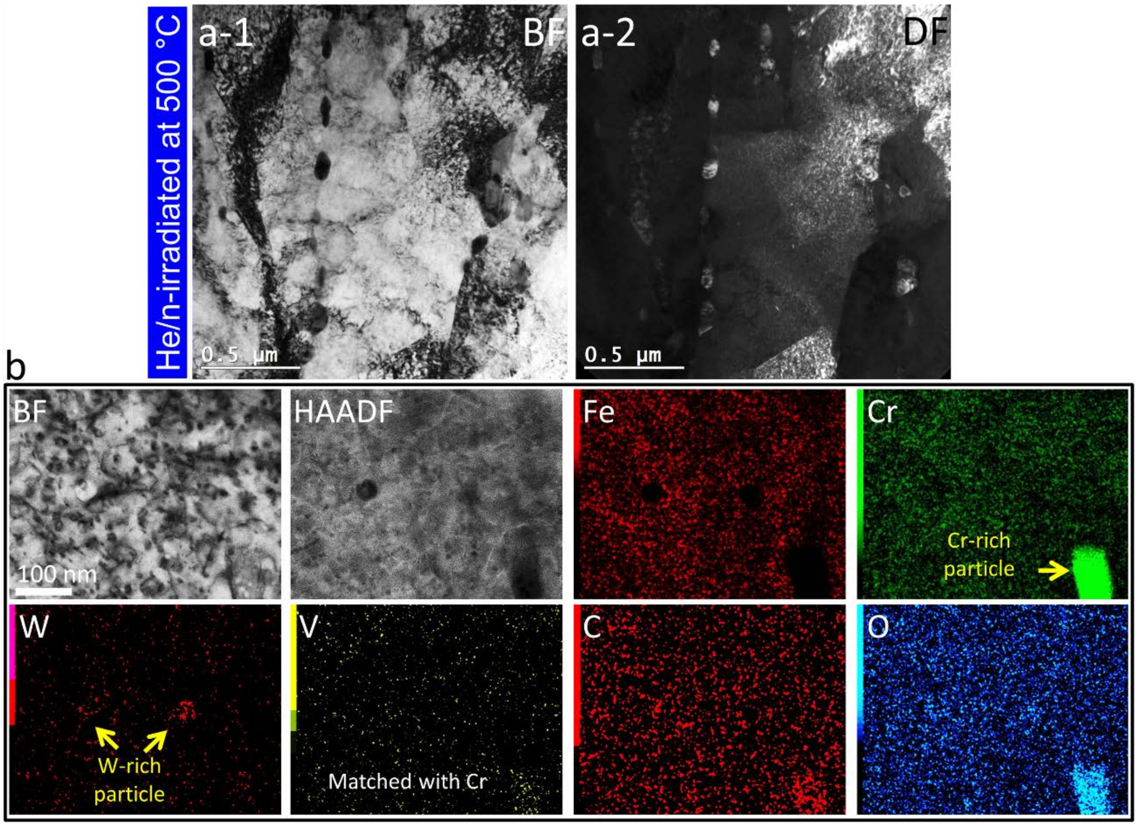

Figure 5. (a) BF and DF TEM images showing particles formed predominately at lath boundaries in the He injected side of F82H-mod.3+CW. (b) BF and HAADF STEM images with elemental EDS mapping reveal the phases in this alloy. Note that there are small W-rich particles and Cr-rich carbides, but no evidence of α′ formation in this alloy.

Figure 6-a displays BFTEM images showing particles from neutron-irradiated 14YW. BF and HAADF STEM images at low and high magnification (6-b and 6-c respectively) with elemental EDS mapping of the indicated elements. There are 3 types of particles identified from EDS mapping. The first are large Cr-rich carbides of 50-500 nm located predominately at grain boundaries. The other two are small spherical W-rich oxide particles of 10-50 nm and small Y-rich oxide particles of 10-50nm, both of which are located in the grain interior. The Y-rich oxide particles are present in a much more uniform distribution and higher number density than the W-rich oxide particles, and contain significant Si, suggesting the oxide particles are actually a Y-Si-O phase. Vanadium, formed due to transmutation, is agglomerated in Cr-rich particles. Phase separation of Cr-rich α’ (bcc) at high magnification (Cr map in Figure 6-c) is verified in the elemental maps, as well as segregation to lath boundaries and around oxide particles. In contrast, no α’ formation was detected using elemental mapping in the F82H-mod.3+CW.

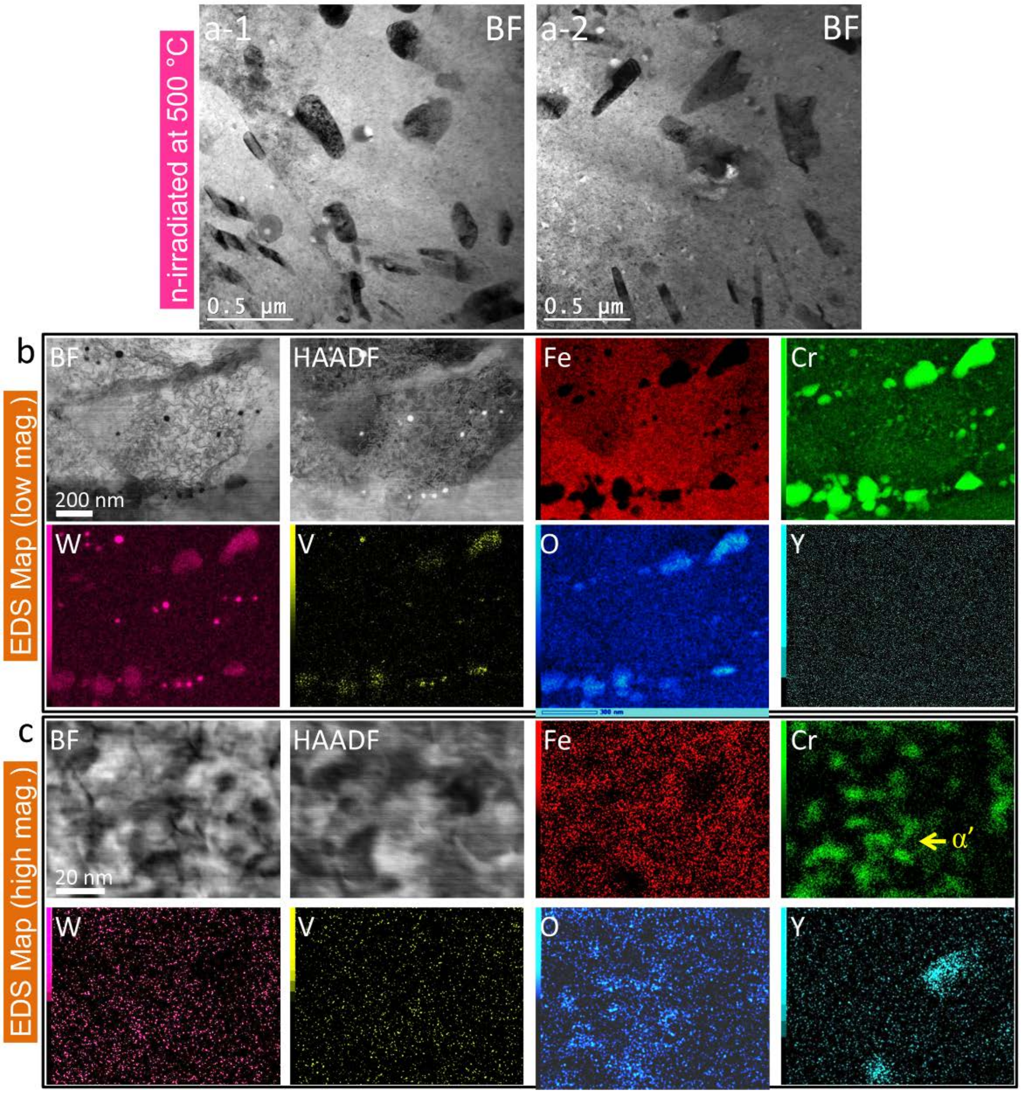

Figure 6. (a) BFTEM images showing particles from the non-injected side of the neutron-irradiated 14YW. BF and HAADF STEM images at (b) low and (c) high magnification with elemental EDS mapping. These maps reveal the presence of several phases, including significant evidence for α′ formation. See text for explanation.

A comparable set of images and STEM-EDS maps were obtained to investigate the particle types and chemical evolution in the He-injected side of 14YW. The results, presented in Figure 7, revealed no major differences compared to the side with no He injection. Small W-V carbides could be found at random in a very low density, while the larger Cr-rich particles are commonly present at lath boundaries. The small Y-rich oxide particles are dispersed more evenly and densely than the other particle types. Interestingly as can be seen in Figure 8, the W-V carbide particles contain a reasonable degree of Cr and V, whereas Cr-rich particles have very low W and V. The W-V carbide particles often exhibit a core-shell structure consisting of a Cr-rich outer shell surrounding a W and V-rich core, raising the possibility that Cr diffuses to the particle interface along with the He and vacancies. This was also found to occur in the F82H.mod3 alloy.

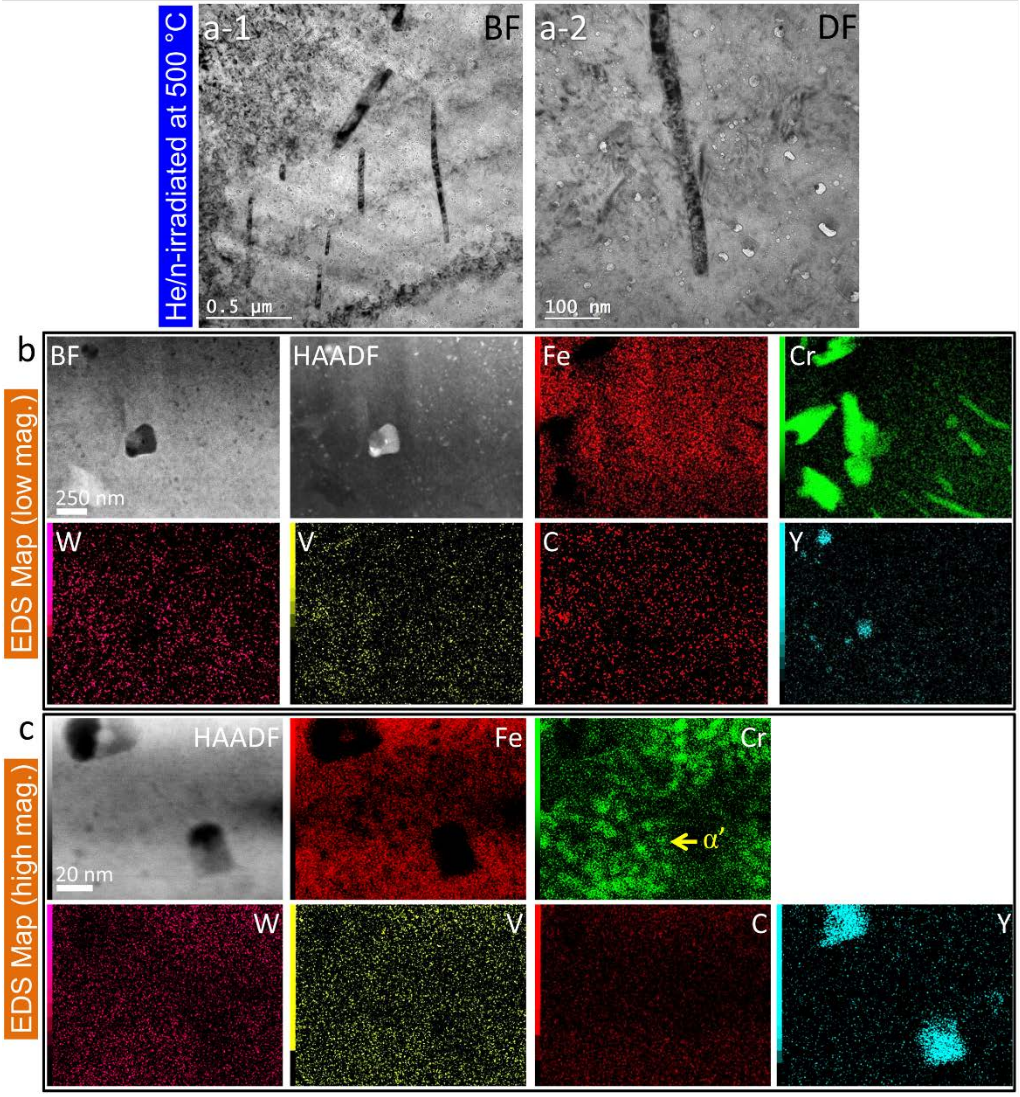

Figure 7. (a) BFTEM images showing particles from He/neutron-irradiated 14YW. BF and HAADF STEM images at (b) low and (c) high magnification with elemental EDS mapping of Fe (red), Cr (green), W (purple), V (yellow) and O (blue), and Y (light blue). There are three types of particles present based on these maps, and Cr-rich α' (Cr map at c) and Y-O matches (Y and O map at c) at high magnification are verified. See text for explanation.

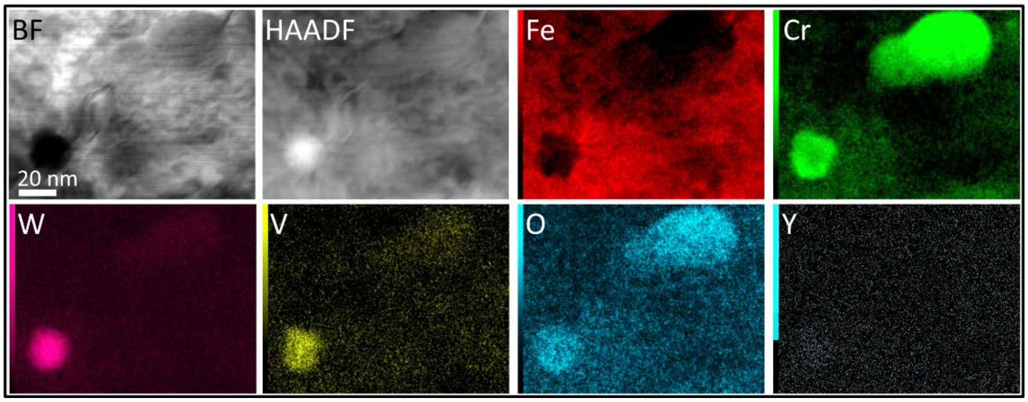

Figure 8. BF and HAADF STEM images with elemental maps taken from the He injected side of the neutron-irradiated 14YW reveal two types of particles: an elongated Cr-rich carbide phase with low concentration of W and V (top right) and a spherical W-rich oxide particle with a moderate concentration of Cr and V (bottom left). Note that W and V are concentrated at core of the W-rich particle, but Cr is concentrated in a shell around the core of the particle.

Figures 9 and 10 reveal line dislocations and dislocation loops of F82H-mod.3+CW and 14YW respectively on two sets of BFTEM images at under/in/over-focus from both sides of the TEM discs. The through-focal series is used to highlight the distribution of cavities with respect to the dislocation structure. Measured densities of line dislocations at each case are given in Table 4, and show that the densities of line dislocations are not significantly different for the two alloys, ranging from 1 to 3×10^{-14} m^{-2}. The BFTEM images indicate that the He-injected side has a higher density of loops than in the non-injected side, and this is currently being investigated in more detail. In our previous report, measured densities of dislocation loops of two samples (regardless of loop types) on the He-implanted side are similar with a range of $3\sim5\times10^{21}$ m^{-3} [11], but the non-injected side had not yet been characterized.

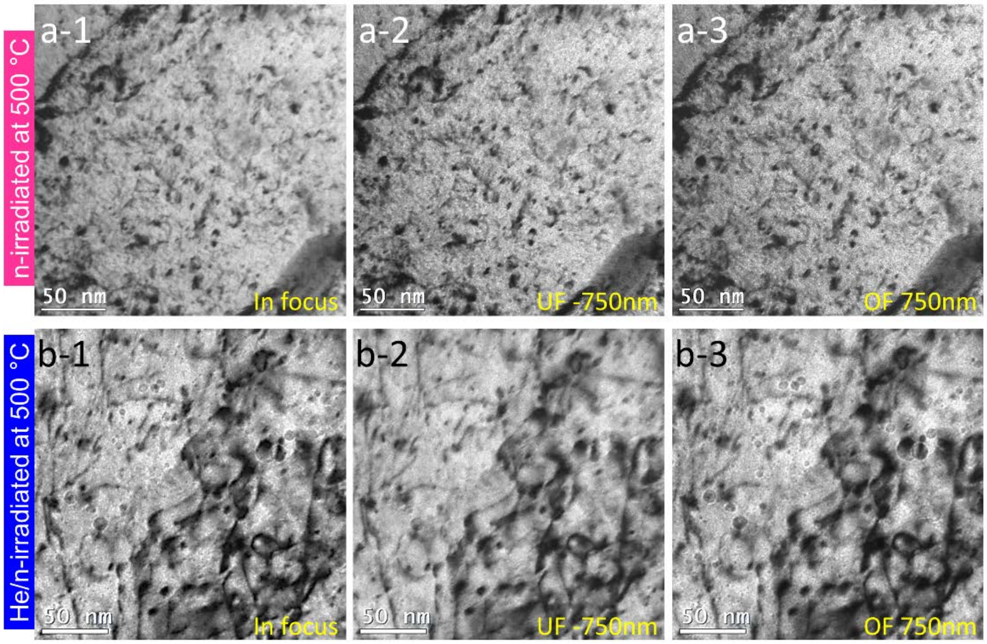

Figure 9. The dislocation structure is shown in two sets of BFTEM images of F82H-mod.3+CW taken at under/in/over-focus from (a) the non-He injected side and (b) the He-injected side

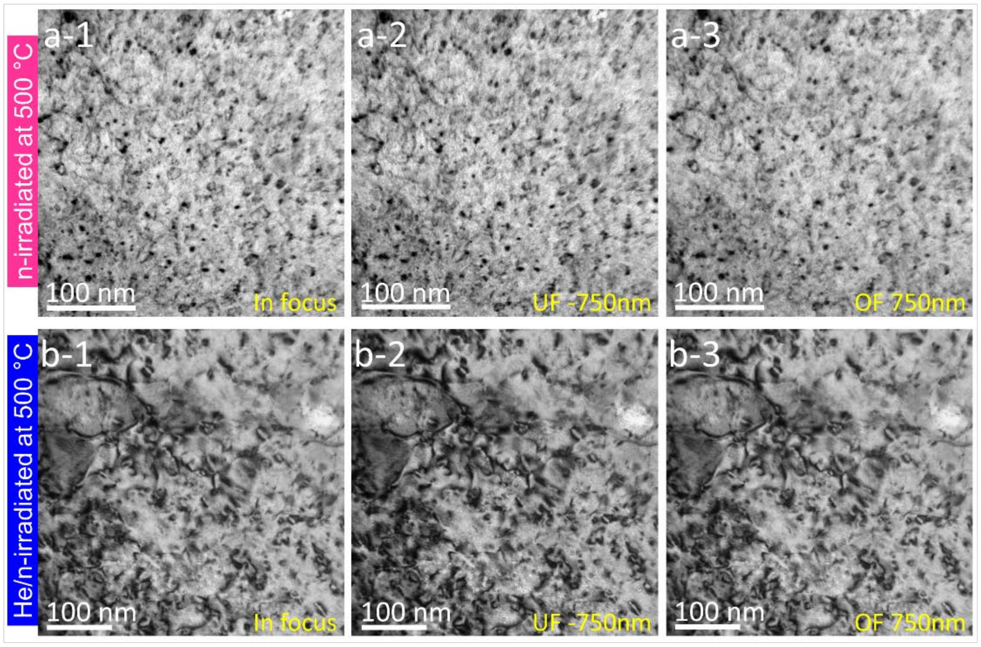

Figure 10. The dislocation structure is show in two sets of BFTEM images taken of the neutron-irradiated 14YW alloy at under/in/over-focus from (a) the non-He injected side and (b) the He-injected side.

Table 4. Density (m^{-2}) of line dislocations in two alloys

Alloy	He-Implanted Side	Non-implanted Side
F82H-mod	2.7×10^{14}	3.0×10^{14}
14YW	2.4×10^{14}	1.6×10^{14}

Acknowledgments

This research was supported by the U. S. Department of Energy, Office of Fusion Energy Sciences, under contract DE-AC06-76RLO1830.

REFERENCES

[1] G. R. Odette, M. J. Alinger, and B. D. Wirth, Annu. Rev. Mater. Res. 38 (2008) 471.
[2] R. J. Kurtz, A. Alamo, E. Lucon, Q. Huang, S. Jitsukawa, A. Kimura, R. L. Klueh, G. R. Odette, C. Petersen, M. A. Sokolov, P. Spätig, and J. W. Rensman, J. Nucl. Mater. 386-388 (2009) 411.
[3] N. Baluc, K. Abe, J. L. Boutard, V. M. Chernov, E. Diegele, S. Jitsukawa, A. Kimura, R. L. Klueh, A. Kohyama, R. J. Kurtz, R. Lässer, H. Matsui, A. MÖslang, T. Muroga, G. R. Odette, M. Q. Tran, B. van der Schaaf, Y. Wu, J. Yu, and S. J. Zinkle, Nucl. Fusion 47 (2007) S696.
[4] H. Ullmaier, Nucl. Fusion. 24 (1984) 1039
[5] R. E. Stoller and G. R. Odette, J. Nucl. Mater. 131 (1985) 118.
[6] R. Schäeublin and Y. L. Chiu, J. Nucl. Mater. 362 (2007) 152
[7] G. R. Odette, P. Miao, D. J. Edwards, T. Yamamoto, R. J. Kurtz, and H. Tanigawa, J. Nucl. Mater. 417 (2011) 1001.
[8] B. Yao, D. J. Edwards, R. J. Kurtz, G. R. Odette, and T. Yamamoto, Fusion Materials Semiannual Progress Report for Period Ending December 31, 2011, DOE/ER-0313/51, U.S. Department of Energy, 85.
[9] B. Yao, D. J. Edwards, and R. J. Kurtz, G. R. Odette, and T. Yamamoto, Maps of dislocation loops in irradiated bcc Fe–based steels. To be submitted.

[10] L. R. Greenwood, B. M. Oliver, S. Ohnuki, K. Shiba, Y. Kohno, A. Kohyama, J. P. Robertson, J. W. Meadows, and D. S. Gelles, J. Nucl. Mater. 283-287 (2000) 1438.
[11] L. R. Greenwood and F. A. Garner, J. Nucl. Mater. 212-215 (1994) 635.
[12] T. Noda, M. Fujita, and M. Okada, J. Nucl. Mater. 258-263 (1998) 934.
[13] T. Tanno, A. Hasegawa, J-C He, M. Fujiwara, S. Nogami, M. Satou, T. Shisido, and K. Abe, Mater. Trans. 48, (2007) 2399.
[14] B. Yao, D. J. Edwards, R. J. Kurtz, G. R. Odette, and T. Yamamoto, Fusion Materials Semiannual Progress Report for Period Ending December 31, 2012, DOE/ER-0313/44, U.S. Department of Energy, 26.
[15] T. Yamamoto, G. R. Odette, P. Miao, D. J. Edwards, and R. J. Kurtz, Fusion Materials Semiannual Progress Report for Period Ending December 31, 2008, DOE/ER-0313/44, U.S. Department of Energy, 44.

2.1 DEVELOPMENT OF ODS FeCrAl FOR FUSION REACTOR APPLICATIONS – B. A. Pint, K. A. Unocic, S. Dryepondt and D. T. Hoelzer (Oak Ridge National Laboratory, USA)

OBJECTIVE

The dual coolant lead-lithium (DCLL) blanket concept requires improved Pb-Li compatibility with ferritic steels in order to demonstrate viable blanket operation in a DEMO-type fusion reactor. The goal of this work is to develop an oxide dispersion strengthened (ODS) alloy with improved compatibility with Pb-Li and excellent mechanical properties. The current focus is characterizing the performance of a group of ODS alloys based on Fe-12Cr-5Al.

SUMMARY

Four experimental ODS FeCrAl heats of composition Fe-12Cr-5Al were prepared by mechanical alloying with additions of Y_2O_3, Y_2O_3 + ZrO_2, Y_2O_3 + HfO_2 and Y_2O_3 + TiO_2. Characterization of the as-extruded and aged microstructures are in progress and are compared to a commercial ODS FeCrAl alloy, PM2000. An initial Pb-Li compatibility evaluation was performed at 700°C on the first three alloys. The fourth alloy with TiO_2 was recently produced and tensile properties have been measured from 25° to 800°C. This alloy had high strength but low ductility at 25° and 400°C consistent with its high hardness. Initial creep testing has begun on the alloy with HfO_2 at 800°C and 100 MPa.

PROGRESS AND STATUS

Introduction

The DCLL blanket concept (Pb-Li and He coolants) is the leading U.S. design for a test blanket module (TBM) for ITER and for a DEMO-type fusion reactor.[1] With reduced activation ferritic-martensitic (FM) steel as the structural material, the DCLL is limited to ~475°C metal temperature because Fe and Cr readily dissolve in Pb-Li above 500°C and Eurofer 97 plugged a Pb-Li loop at 550°C.[2-3] For a higher temperature blanket for DEMO, structural materials with enhanced creep and compatibility are needed. ODS FeCrAl alloys are one possibility to meet this objective and considerable research on ODS FeCr alloys has shown an excellent combination of creep strength and radiation resistance.[4-7] However, these ODS FeCr alloys do not have adequate compatibility with Pb-based coolants, such as Pb-Bi eutectic (LBE) [8-11]. With the addition of Al, isothermal compatibility tests have shown low mass losses at up to 800°C.[12] Therefore, a materials development effort is underway, specific to this application. ODS FeCrAl was commercialized in the 1970's for its high temperature (>1000°C) creep and oxidation resistance [13] and other research groups are currently investigating new FeCrAl alloy compositions for fission and fusion applications with liquid metals.[14-16]

Previous initial work [17-19] had identified Fe-12wt.%Cr-5Al as a target composition with low Cr to minimize α' formation during irradiation [20], while maintaining 5%Al for Pb-Li compatibility.[17,21] Using diffusion couples, combinations of oxides also were identified that could form stable ternary compounds. The properties of this first generation composition are being measured with a second generation being designed based on this information.

Experimental Procedure

Four experimental ODS FeCrAl ferritic alloys were produced by mechanical alloying (MA). Powder of specified composition Fe-12.1wt.%Cr-5.0Al and particle size range ~45-150 µm was prepared by Ar gas atomization by ATI Metal Powders. The FeCrAl powder was blended with 0.3%Y_2O_3 powder (17-31 nm crystallite size, produced by Nanophase, Inc.) and subsequent 1kg batches included additions of 0.4ZrO_2, 0.22HfO_2 and 0.2TiO_2 powders (<100 nm diameter from American Elements). Each batch was ball milled for 40 h in Ar gas atmosphere using the Zoz CM08 Simoloyer ball mill. After ball milling, the powders were placed in mild steel cans, degassed at 300ºC under vacuum and sealed. The cans were equilibrated at 950ºC for 1 h and then extruded through a rectangular shaped die. Table 1 shows the as-extruded compositions of each alloy. The alloys with additional ZrO_2, HfO_2 and TiO_2 oxide additions showed higher O contents and the Cr and Al contents were lower than the starting powder. Other typical impurities were Co, Cu, Ni and Mn at the 0.01-0.02% level and the C and N pickups from the milling process were acceptable. Tensile tests were performed using SS-3 type tensile specimens fabricated with the gage section (7.62 mm long and 0.762 mm thick) parallel to the extrusion axis of the ODS FeCrAl heats. The tensile tests were conducted in an MTS hydraulic frame at temperatures ranging from 25ºC-800ºC and a strain rate of 10^{-3} s^{-1}. Creep tests were performed at 800°C on similar size specimens with a 2 x 2 mm gage section.

Static Pb-Li capsule tests were performed using Mo (inert to Pb-Li) inner capsules and type 304 stainless steel (SS) outer capsules to protect the inner capsule from oxidation. The ODS FeCrAl specimens were ~1.5 mm thick and 4-5 cm^2 in surface area with a 600 grit surface finish and were held with 1 mm diameter Mo wire. The capsules were loaded with 125 g of Pb-Li in an Ar-filled glove box. The Pb-Li was melted and cast at ORNL and had Li contents of 15.6-16.5 at%. The Mo and SS capsules were welded shut to prevent the uptake of impurities during the isothermal exposure. After exposure, residual Pb-Li on the specimen surface was removed by soaking in a 1:1:1 mixture of acetic acid, hydrogen peroxide and ethanol for up to 72 h. Mass change was measured with a Mettler-Toledo balance with an accuracy of 0.01 mg/cm^2. Post-test specimen surfaces were examined using x-ray diffraction (XRD) and secondary electron microscopy (SEM) equipped with energy dispersive x-ray (EDX) analysis. After surface characterization, the specimens were metallographically sectioned and polished and examined by light microscopy, SEM and electron probe microanalysis (EPMA) using wavelength dispersive x-ray analysis.

The as-extruded and aged microstructure was characterized using a Hitachi S4800 Field Emission Gun (FEG) Scanning Electron Microscope (SEM) equipped with X-ray Energy Dispersive Spectroscopy (XEDS). Specimens for Transmission Electron Microscope (TEM) analysis were prepared by Focused Ion Beam (FIB, Hitachi model NB500) using the in-situ lift-out method from the polished specimens. A Philips model CM200 FEG-TEM/STEM (Scanning TEM) with XEDS and EELS (Electron Energy Loss Spectroscopy) was used for analysis. Bright-Field (BF) and High Angle Annular Dark Field (HAADF) STEM and Energy Filtered TEM (EFTEM) imaging methods were used in the microstructural investigations. For high resolution imaging a JEOL 2200FS-AC FEG STEM 200kV probe corrected microscope (using CEOS Cs-Corrector) was used that has 0.7Å resolution in STEM mode equipped with a Bruker XFlash® 6|30 silicon drift detector (SDD) that combines excellent energy resolution with the larger solid angle of a 30 mm^2 active chip area. Electron diffraction patterns and fast Fourier transform (FFT) were used for phase identification. Vickers hardness was measured using a 200 or 500g load.

Table 1. Alloy chemical compositions (mass% or ppmw) by inductively coupled plasma analysis and combustion analysis.

Material	Fe%	Cr%	Al%	Y%	O	C	N	S	Other
Powder	82.8	12.1	5.0	<	64	31	11	<3	0.004Si
125Y	83.3	11.4	4.8	0.19	842	380	455	20	0.05W, 0.02Si, 0.01Ti
125YZr	82.8	11.5	4.9	0.18	1920	250	161	10	0.30Zr, 0.01Hf, 0.01Si
125YHf	82.3	11.7	4.8	0.17	2280	220	110	10	0.68Hf, 0.01Zr, 0.01Si
125YTi	82.4	12.0	4.9	0.16	2220	350	135	30	0.20Ti,0.01Si
PM2000	74.1	19.1	5.5	0.39	2480	14	86	8	0.48Ti, 0.02Si

< indicates below the detectability limit of <0.01%

Results and Discussion

Previously the general microstructure features were reported such as average grain size and the oxide precipitate size distribution of the new ODS alloys.[19] In the first three alloys characterized, a high number density of small (~3nm) particles were distributed uniformly throughout the matrix and showed dark contrast relative to the surrounding matrix in HAADF STEM images. The current work is focused on identifying the oxide phases that formed in the as-extruded 125YZr with Y_2O_3 + ZrO_2 (Figure 1) and 125YHf with Y_2O_3 + HfO_2 (Figure 2) alloys and the latter alloy after thermal ageing (Figure 3) using high resolution TEM techniques. In 125YZr, a few large bright contrast particles were observed that contained only Zr. These precipitates were identified as ZrO using a combination of EDS and FFT analyses (Figure 1) from which interplanar spacing and angles were measured and compared with the JCPDS values. The formation of metastable ZrO suggests the as-extruded structure is not at equilibrium. In as-extruded 125YHf, a trimodal particle size distribution was observed and phase identification is still in progress with examples shown in Figure 2. After ageing at 1000°C for 1 and 100 h, both the bright Hf-rich particles and the dark Al-rich oxides appeared to coarsen, Figure 3. The particles with mixed dark and bright areas began to disappear and small Y+Hf oxides appeared (EDS maps associated with Figure 3d).

Ageing experiments were conducted on all of the alloys at 800°, 1000° and 1200°C. However, it was not feasible to perform TEM after all conditions. Therefore, hardness was used as an indication of the microstructure stability. Figure 4 summarizes the measurements made at 800° and 1000°C with

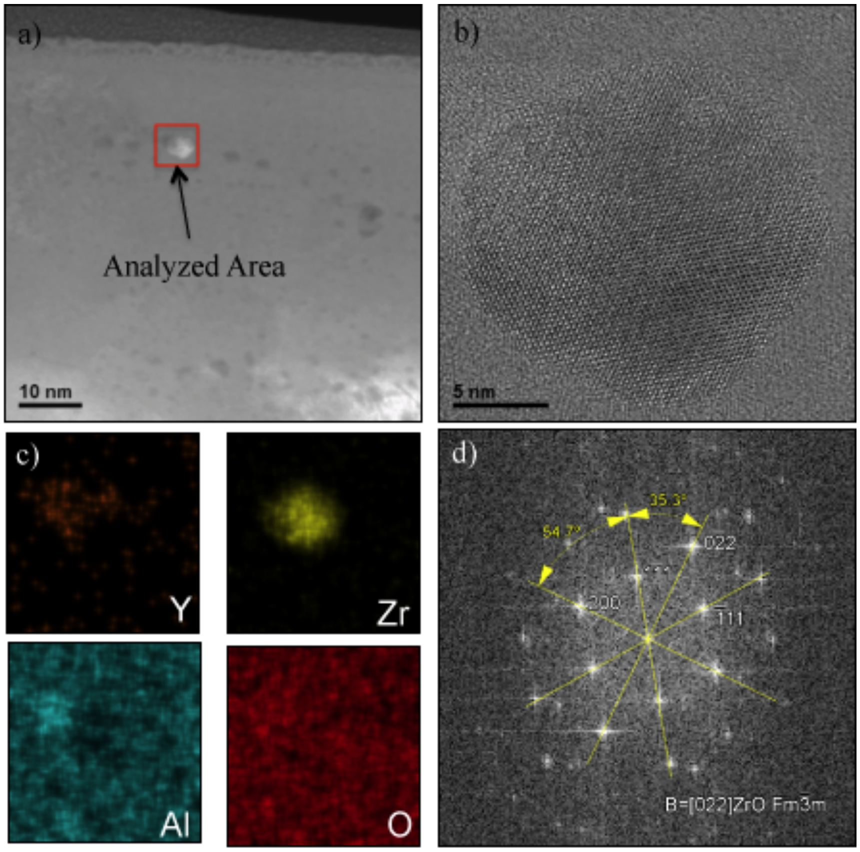

Figure 1. a) HAADF image of the 125YZr as-extruded (lift-out FIB) microstructure. b) High resolution BF-STEM of the Zr-rich particle (from the area marked in 1a) identified using c) EDS Map and d) FFT as ZrO.

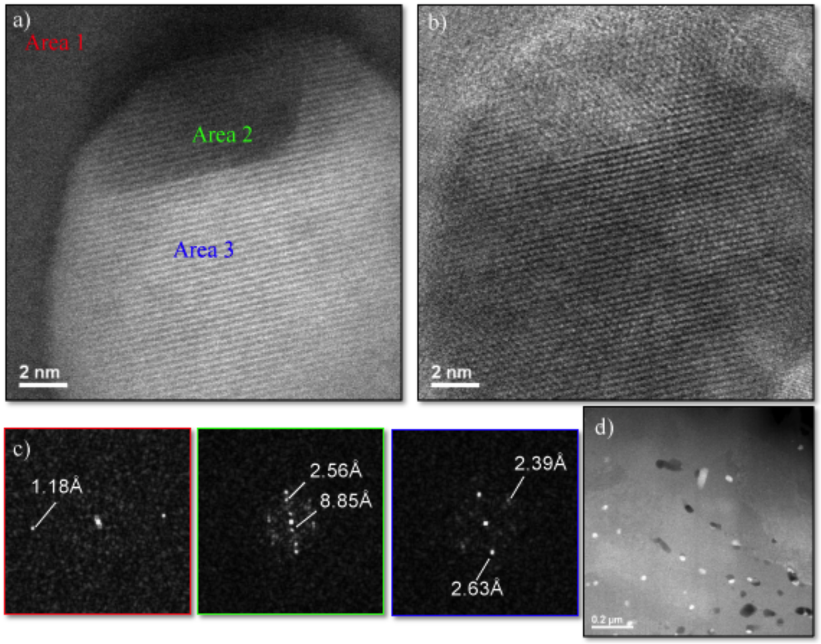

Figure 2. High resolution (a) HAADF and b) BF-STEM images of a typical “double” particle from 125YHf after extrusion with c) FFT and d) low magnification HAADF image showing the microstructure.

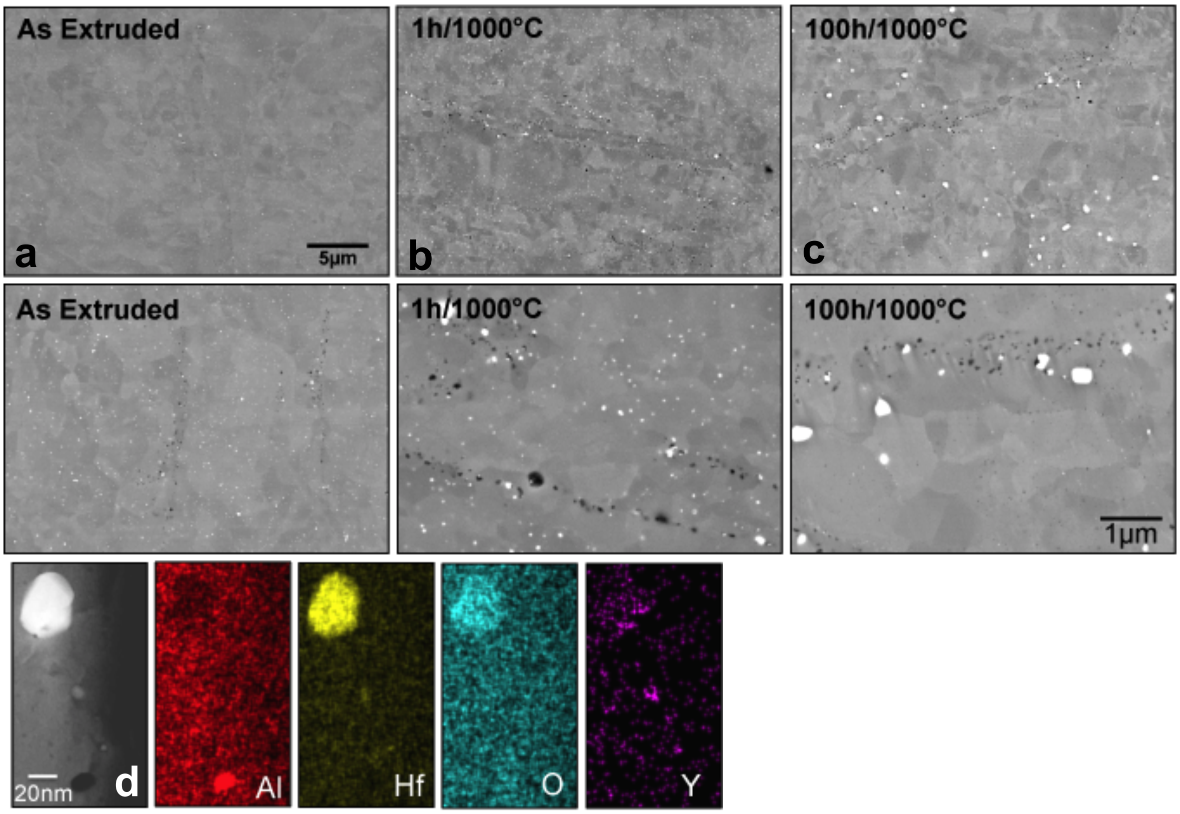

Figure 3. SEM backscattered electron images of 125YHf, a) as-extruded, b) after 1 h at 1000°C, and c) 100 h at 1000°C at two magnifications. The Hf-rich (bright) and Al-rich (dark) particles coarsen with exposure time. (d) HAADF image with associated XEDS Al, Hf, O and Y maps from area in (c).

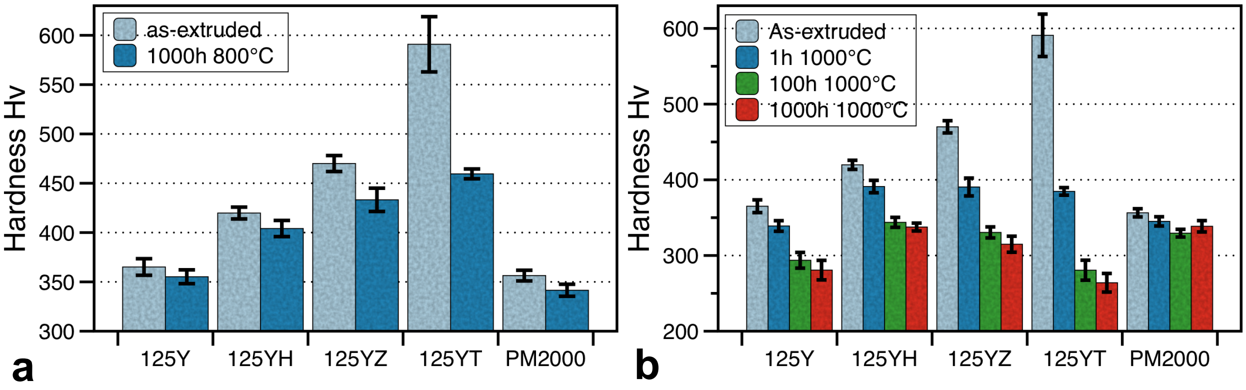

Figure 4. Vickers hardness values as a function of aging time at (a) 800°C and (b) 1000°C.

unrecrystallized PM2000 used as a comparison. While the alloy with Y_2O_3 + TiO_2 had the highest starting hardness, it also experienced a large drop after annealing at both 800° and 1000°C. After 1000h at 1000°C, it had the lowest hardness of any of the alloys. The other ODS alloys experienced relatively small decreases in hardness after 1000h at 800°C, and larger drops after annealing at 1000°C. There was little statistical difference between the hardness values measured after 100 and 1000 h at 1000°C, suggesting that the microstructures had stabilized. Based on these hardness measurements, PM2000 showed the highest microstructural stability. The as-extruded hardness for PM2000 was relatively low but the decrease after annealing was relatively minor at both temperatures. The hardness measurements at 1200°C are in progress.

The mass change data for the new ODS alloys after 1000 h at 700°C in static Pb-Li is summarized in Figure 5.[22] For reference, the mass change for several cast FeCrAl alloys [21] is shown as well as commercial ODS FeCrAl alloy, PM2000, Table 1. When Al was present in the alloy, a $LiAlO_2$ layer

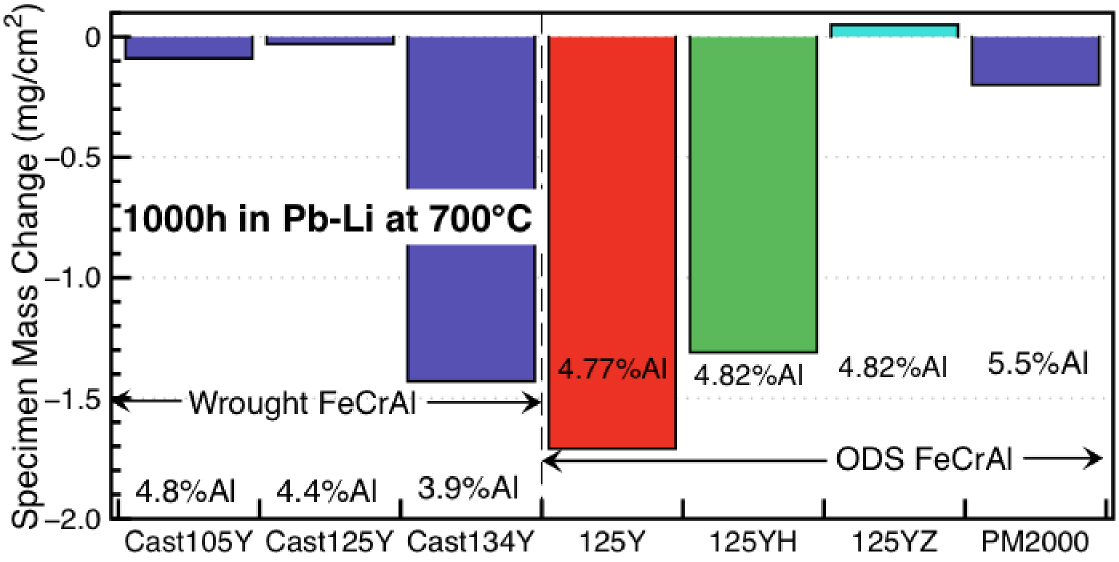

Figure 5. Specimen mass change for alloy specimens exposed for 1000h at 700°C in static Pb-Li.

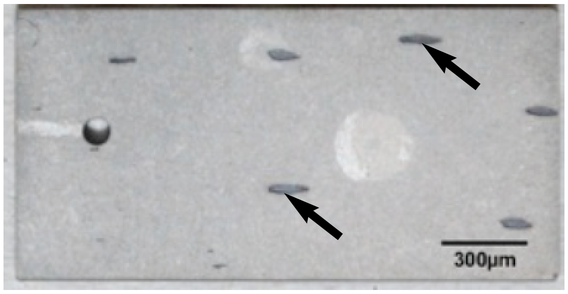

Figure 6. Light microscopy of the 125Y specimen after 1000 h in Pb−Li at 700°C with arrows pointing to the large surface pits.

(identified by XRD) formed on each specimen [12,23] from O impurities in the Pb-Li (200-400ppmw as cast) and this layer inhibited dissolution of the alloy into the liquid metal. The high mass loss for the Y_2O_3 specimen (125Y) was linked to ~300μm deep pits in the surface (arrows in Figures 6 and 7a), which suggested that powder with little or no Al was incorporated in this first batch of ball milled material and was selectively dissolved from the specimen. Similar extreme behavior was observed when an aluminized 9Cr steel specimen was exposed with one cut (uncoated) face [24]. Both Fe and Cr have a high solubility in Pb-Li and without the Al to form a stable oxide, dissolution occurred rapidly without the liquid reaching saturation thereby slowing the dissolution rate. Surprisingly, the Y_2O_3 + HfO_2 specimen (125YH) also showed similar mass loss as the 125Y specimen. There was no indication of significant dissolution but spallation near the specimen edges was observed. The Y_2O_3 + ZrO_2 specimen (125YZ) showed the lowest mass change, which was consistent with the cast FeCrAl alloys of similar composition, Figure 5. The higher mass loss for the cast alloy with only 4 wt.%Al indicated that the Al content could not be reduced below ~5wt.%Al for this application. Figure 7 shows cross-sections of each of the new ODS alloys exposed with little observable difference between the specimens with HfO_2 and ZrO_2. Further characterization using EPMA, found some Al depletion in the substrate with a small Al gradient measured ~75μm beneath the surface, but similar for all of the materials, Figure 8. The depletion of 0.5-1at%Al near the surface is more than had been observed previously for PM2000 exposed for the same conditions.[12] The most severe depletion was observed beneath one of the surface pits (Figure 6 or 7a). A Pb-Li exposure for a specimen of the Y_2O_3 + TiO_2 alloy is in progress.

Figure 9 summarizes all of the tensile data for this group of alloys, with the recent addition of the data for

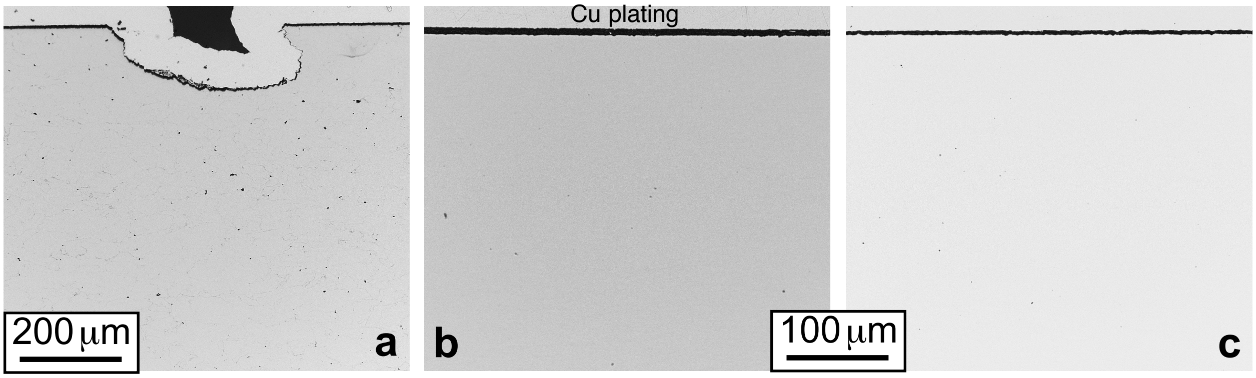

Figure 7. Light microscopy of polished cross-sections after 1000 h in Pb-Li at 700°C of (a) 125Y, (b) 125YHf and (c) 125YZr.

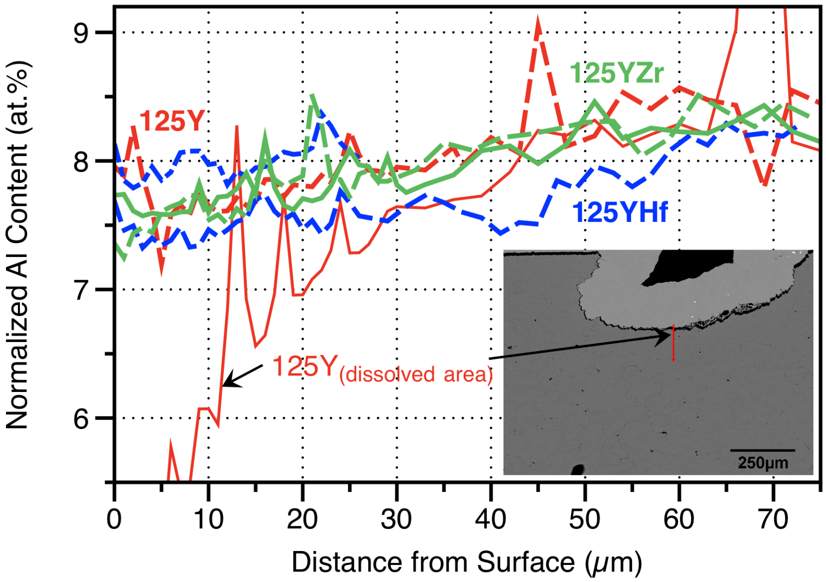

Figure 8. EPMA Al composition profiles from the alloy beneath the surface oxide formed after 1000 h at 700°C in Pb-Li. Two profiles are shown for each ODS alloy.

the alloy with Y_2O_3 + TiO_2. The results are compared to data for unrecrystallized PM2000. This material had the highest yield stress (σ_{ys}) and ultimate tensile strength (σ_{uts}) at 25°-600°C but also showed lower ductility at 25° and 400°C. Measurement of the tensile properties after ageing is in progress.

The alloy with Y_2O_3 + HfO_2 was selected for creep studies at 800°C and 100 MPa. The first creep test showed an initial drop in strain, likely due to a measurement error. After the rate had stabilized, the stress was increased to 120 MPa but the specimen then failed after < 50h. This suggested that 100 MPa was

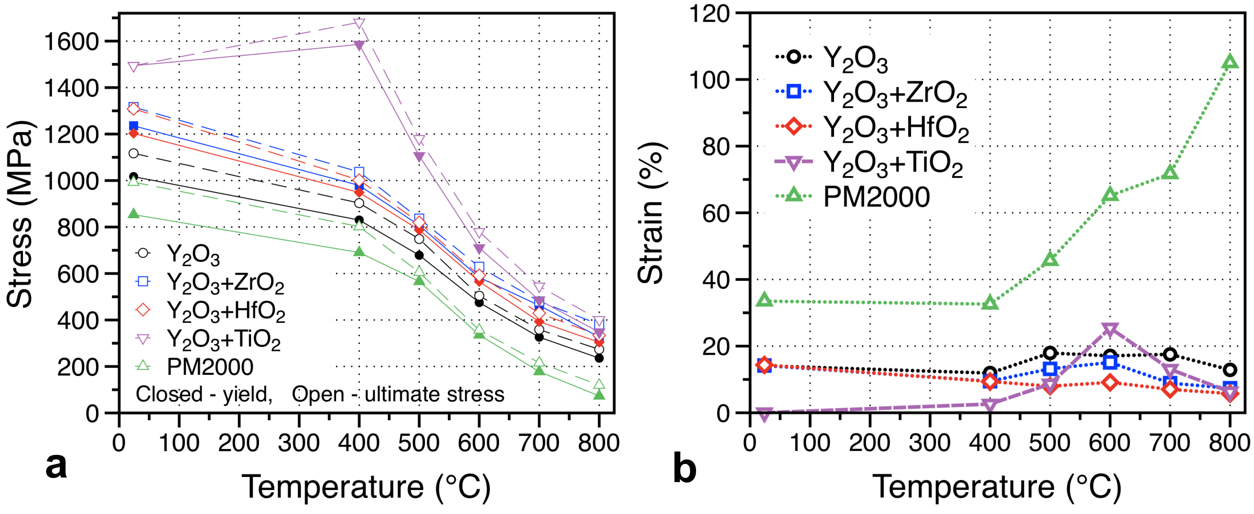

Figure 9. Tensile properties of the ODS FeCrAl heats as a function of test temperature. (a) yield stress and ultimate tensile strength and (b) total elongation.

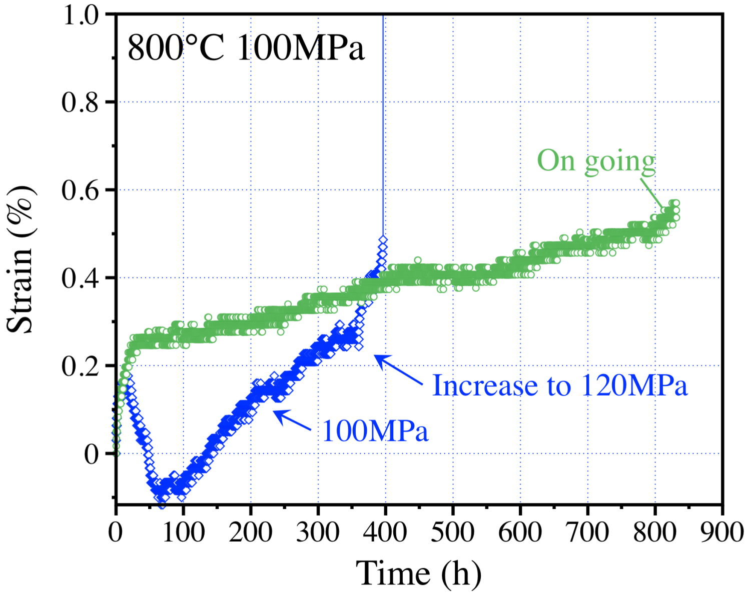

Figure 10. Strain as a function of exposure time for two 125YHf specimens tested at 800°C/100 MPa.

near the threshold stress for this alloy at 800°C. A second creep test at 800°C/100 MPa is in progress with steady behavior past 800 h. Additional testing will be conducted on unrecrystallized PM2000 and the Y_2O_3 + ZrO_2 alloy for comparison.

References

[1] M. Abdou, D. Sze, C. Wong, M. Sawan, A. Ying, N. B. Morley and S. Malang, Fus. Sci. Tech., 47 (2005) 475.

[2] O. K. Chopra, D. L. Smith, P. F. Tortorelli, J. H. DeVan and D. K. Sze, Fusion Technol., 8 (1985) 1956.

[3] J. Konys, W. Krauss, J. Novotny, H. Steiner, Z. Voss and O. Wedemeyer, J. Nucl. Mater. 386-88 (2009) 678.

[4] S. Ukai and M. Fujiwara, J. Nucl. Mater. 307 (2002) 749.

[5] G. R. Romanowski, L. L. Snead, R. L. Klueh, D. T. Hoelzer, J. Nucl. Mater., 283-287 (2000) 642.

[6] R. L. Klueh, J. P Shingledecker, R. W. Swindeman, D. T. Hoelzer, J. Nucl. Mater. 341 (2005) 103.

[7] D. A. McClintock, M. A. Sokolov, D. T. Hoelzer and R. K. Nanstad, J. Nucl. Mater., 392 (2009) 353.

[8] T. Furukawa, G. Müller, G. Schumacher, A. Weisenburger, A. Heinzel and K. Aoto, J. Nucl. Mater. 335 (2004), 189.

[9] P. Hosemann, H.T. Thau, A.L. Johnson, S.A. Maloy and N. Li, J. Nucl. Mater. 373 (2008) 246.

[10] C. Schroer, J. Konys, T. Furukawa and K. Aoto, J. Nucl. Mater. 398 (2010) 109.

[11] A. Weisenburger, K. Aoto, G. Müller, A. Heinzel, G. Schumacher and T. Furukawa, J. Nucl. Mater. 358 (2006) 69.

[12] B. A. Pint, L. R. 122012) 129.

[13] J. D. Whittenberger, Met. Trans. 9A (1978) 101.

[14] J. Lim, H.O. Nam, I.S. Hwang and J.H. Kim, J. Nucl. Mater. 407, (2010), 205.

[15] A. Kimura, et al., J. Nucl. Mater. 417, (2011), 176.

[16] S. Takaya, et al., J. Nucl. Mater. 428, (2012), 125
[17] B. A. Pint, D. T. Hoelzer, D. Shin, J. O. Kiggans, Jr., K. A. Unocic, DOE/ER-0313/53 (2012) 10.
[18] B. A. Pint, D. T. Hoelzer and K. A. Unocic, DOE/ER-0313/54 (2013) 27.
[19] D. T. Hoelzer, K. A. Unocic, S. Dryepondt and B. A. Pint, DOE/ER-0313/55 (2013) 5.
[20] C. Capdevila, M.K. Miller, K.F. Russell, J. Chao, J.L. González-Carrasco, Mater. Science and Engineering A, 490, (2008), 277.
[21] K. A. Unocic and B. A. Pint, J. Nucl. Mater. in press.
[22] K. A. Unocic, D. T. Hoelzer and B. A. Pint, Mater. High Temp. in press.
[23] B. A. Pint and K. L. More, J. Nucl. Mater. 376 (2008) 108.
[24] B. A. Pint and K. A. Unocic, J. Nucl. Mater. 442 (2013) 572.

2.2 A NEW SCANDIUM-BASED NANOSTRUCTURED FERRITIC ALLOY

– T. Stan, S. Pun, N. J. Cunningham, Y. Wu and G. R. Odette (University of California Santa Barbara)

OBJECTIVE

The objective of this work is to synthesize, characterize and, eventually, determine the thermal stability of a new type of nanostructured ferritic alloy (NFA) with much higher solubility Sc replacing the basically insoluble Y, potentially opening a melt processing path.

SUMMARY

A new Sc-based nanostructured ferritic alloy (NFA) was processed by ball milling gas atomized Fe alloy and Sc_2O_3 powders. Replacing Y with Sc was motivated by the fact that the latter has a much higher solubility in Fe compared to Y, possibly providing a melt processing path for producing Sc-based NFA. The milled powders were subject to four heat treatments: aging at both 850°C; aging at 1000°C; consolidation by spark plasma sintering (SPS) at a peak temperature of 1100°C; and SPS consolidation followed by annealing at 850°C for 3 hrs. Electron backscatter diffraction (EBSD) measurements showed fine grain sizes in both the 850°C and 1000°C aged powder conditions. Transmission electron microscopy (TEM) and atom probe tomography (APT) show that similar populations of $Sc_2Ti_2O_7$ complex oxide nano-features (NFs) also form at both aging temperatures. The microhardness was high for three conditions, and similar to that typically observed in Y-based NFA. However, the microhardness was much lower in the 1000°C powder aged condition. The reason for the low hardness is not yet understood.

BACKGROUND

Nanostructured Ferritic Alloys (NFAs) are Fe-Cr based ferritic stainless steels that traditionally contain an ultrahigh density of Y-Ti-O nanofeatures (NFs). NFAs have high tensile, creep and fatigue strengths, unique thermal stability and are irradiation tolerant [1-3]. The major thrust of this research is to explore a new NFA variant by replacing Y with Sc. Both Y and Sc are group III elements with similar chemical properties. However Sc is a much smaller atom than Y and has an enormously higher solubility with a maximum of 3 at% at 1280°C [4]. Thus, in principle, it should be possible to produce Sc-based NFA by more conventional melt processing paths. However, it is noted that that due to current high cost of Sc, this would be too expensive.

PROGRESS AND STATUS

Experimental Methods

An atomized Fe-based alloyed powder ball milled with Sc_2O_3 powders for 10 hours in a SPEX Mill 8000M, using 6 and 8 mm diameter balls, yielding a nominal powder composition of (in wt%) 14Cr, 3W, 0.4 Ti, 0.18Sc, bal Fe. Approximately 20 g batches of the milled powders were aged for 3 hours at 850°C and 1000°C. A third 20 g batch was consolidated by spark plasma sintering (SPS) under vacuum, using the conditions shown in Figure 1. The red curve is the temperature, the green curve is the applied pressure, held at 75 MPa, and the blue curve is the actuator displacement. The consolidated pellet was also subsequently annealed for 3 h at 850°C.

Microhardness data on the 850°C and 1000°C conditions was obtained from mounted powder samples with a LECO M-400A semi-automated indenter using a 500 g load. The microhardness was measured directly on polished disks for both the 1100°C as-SPS and SPS plus annealed conditions. A FEI Quanta 400F field-emission environmental scanning electron microscope (SEM) with an electron backscatter diffraction (EBSD) detector was used to obtain grain size and crystallography information. EBSD was carried out on the 850°C and 1000°C annealed powders that were mounted in Bakelite and polished by first using a series of sandpapers down to 1200 grit, then 6 μm and 0.5 μm diamond powder on a fast-wheel, and finally with 0.02 μm colloidal silica. A FEI Helios focused ion beam (FIB) tool was used to micro-machine <30 nm thick electron transparent lift-outs for transmission electron microscopy (TEM). A 300 keV FEI Titan was used to obtain TEM and energy dispersive x-ray spectroscopy (EDS) information. Atom probe tomography (APT) was performed on an IMAGO LEAP 3000X HR microscope.

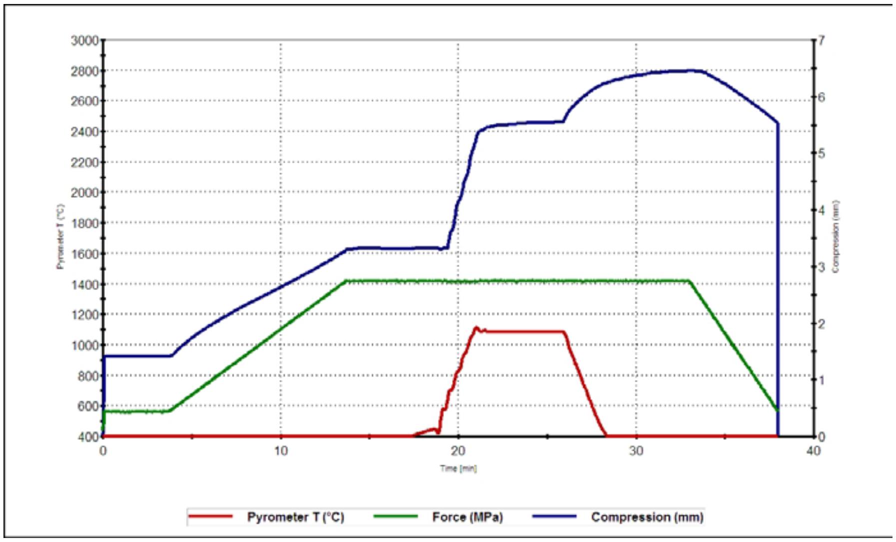

Figure 1. The SPS processing parameters used to consolidate the alloyed powder.

Results and Discussion

The microhardness data versus processing temperature for the Sc-based NFAs (blue) compared to typical values for Y-based NFA (red) are shown in Figure 2. Overall, the Y-based and Sc-based NFAs have similar hardness values. Surprisingly, the hardness of the 1000°C annealed Sc-NFA was lower than both of the 850°C anneal and the 1100°C SPS samples. This difference is not understood, but may be due to an artifact of measuring the hardness of the powders.

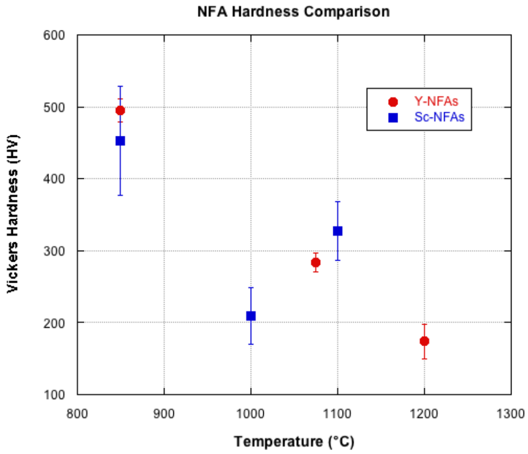

Figure 2. Microhardness of the Sc-NFAs (blue squares) and Y-NFAs (red diamonds).

Figure 3 shows EBSD pole figure maps. Figures 3a and 3b show the out of plane orientations of the 850°C and 1000°C aged powders, respectively. Red, green, and blue grains have out of plane orientations close to {100}, {110}, and {111}, respectively. The black/grey streaks in Figure 3b are areas where the grain orientation could not be determined. Pole figures (not shown) do not indicate crystallographic texturing in either case and both contain similar bimodal distributions of grain sizes, that range from <0.2 μm (fine) to >2 μm (coarser). Most of the larger grains were not uniformly colored which implies some plastic deformation. Grain size is not be the reason for the surprisingly low hardness 1000°C annealed condition.

Bright field TEM images for the 850°C and 1000°C powders are shown in Figures 4a and 4b, respectively. The dark features are precipitates that span a range of sizes. The average precipitate diameter in the 850°C and 1000°C samples is 3.3 nm and 2.9 nm, respectively. The number densities were also similar for the 850°C and 1000°C aged powders at 8.5x10^{22} m^{-3} (850°C) and 7.5x10^{22} m^{-3} (1000°C). APT measurements, illustrated in Figure 5, on the 850°C aged powders showed a higher density ≈ 2.6x10^{22} m^{-3} of somewhat smaller ≈ 2.1 nm precipitates.

Table 1 compares the precipitate sizes found in the Sc-based versus Y-based NFAs in various conditions and using various techniques (TEM, APT and SANS). The precipitates in the Sc-NFAs are similar in size and number density to those in Y-NFAs. EDS was used to measure the compositional information of the precipitates as summarized in Table 2 for the 850°C and 1000°C aged powder conditions. The precipitate diameters ranged from 7 nm to 52 nm in the 850°C aged powder condition with Sc/Ti ratios ranging from 0.5 to 1.2, averaging 0.72 ± 0.21. The corresponding (Sc + Ti)/O ratio ranged from 0.10 to 0.32 averaging 0.15 ± 0.37. There was no clear effect between precipitate size and Sc/Ti ratio and the (Sc + Ti)/O ratio. The precipitates in the 1000°C aged condition ranged from 5 nm to 40 nm, with similar Sc/Ti ratios ranging from 0.26 to 1.34, averaging 0.83 ± 0.39. The corresponding (Sc + Ti)/O ratio ranged from 0.08 to 0.24 averaging 0.17 ± 0.05. However in the 1000°C case, the smaller precipitates have larger Sc/Ti ratios. In both cases, the precipitates also contained trace amounts of W and Cr (not shown). The corresponding compositions found in APT characterization of the 850°C aged powder were Sc/Ti ≈ 0.83 and (Sc + Ti)/O ≈ 0.88. The APT and EDS Sc/Ti are in good agreement. The APT (Sc + Ti)/O are lower than found by EDS. However this is consistent with previous results on Y-based NFA. Overall the precipitates in the annealed Sc-alloys appear to be Sc-Ti-O complex oxides, perhaps $Sc_2Ti_2O_7$, and the deviations in the nominal O are due to various limitations and artifacts in the techniques.

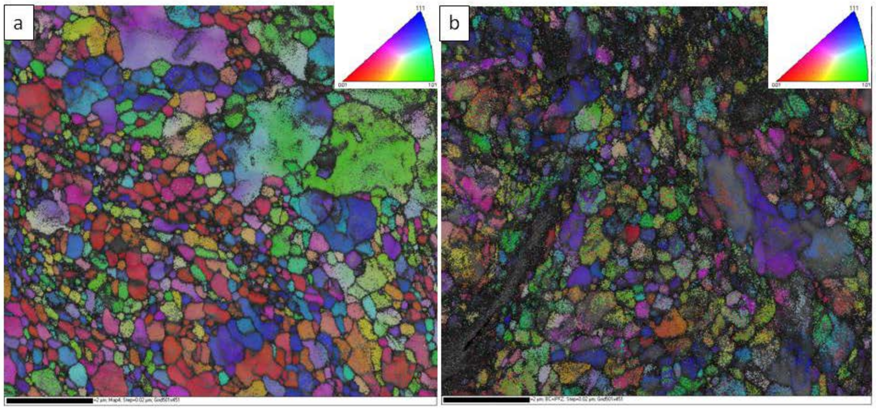

Figure 3. EBSD pole figure maps showing grain size from 850°C annealed powder (a) and from 1000°C annealed powder (b).

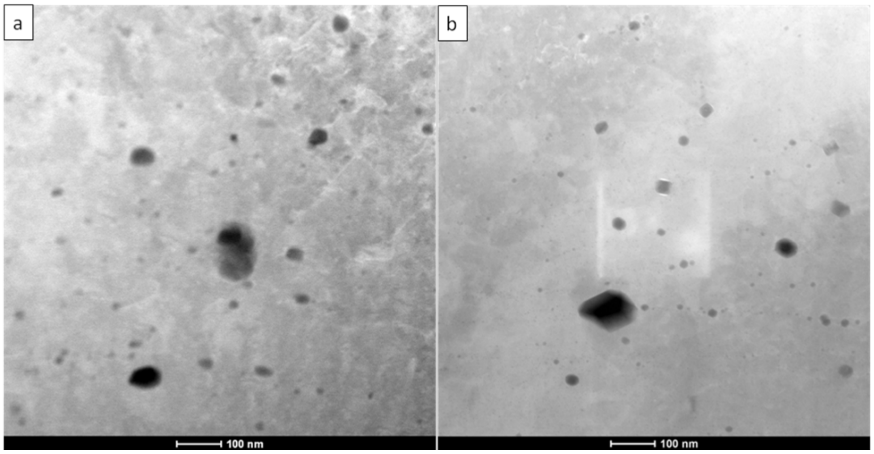

Figure 4. TEM micrographs for powders aged at 850°C (a) and 1000°C (b) for 3 hrs.

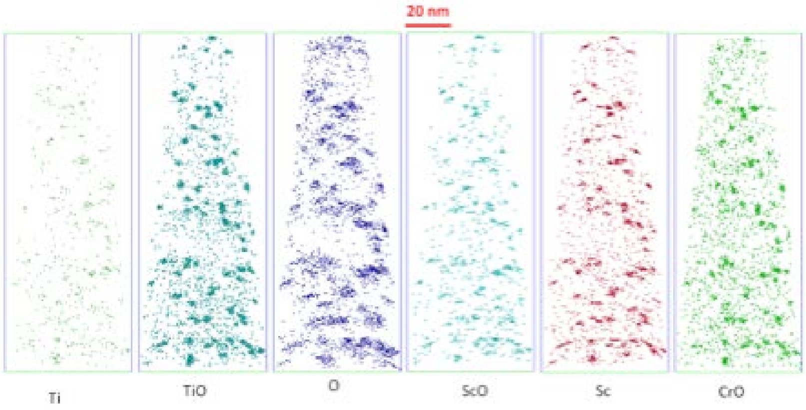

Figure 5. APT maps showing Sc-T-O oxide precipitates in the Sc-based NFA powders aged at 850°C.

Table 1. Precipitate sizes and number densities in the Sc-based versus Y-based (in various conditions) NFAs and using various techniques.

NF Parameters	Technique	US-MA957	Fr-MA957	LTTA	FSW	FSW + Anneal	14SWT 850° C 3 hr	14SWT 1000° C 3 hr
Average diameter (nm)	TEM	3.0	-	-	2.9	3.0	3.3	2.9
	APT	2.3	3.1	2.6	2.2	-	2.1	
	SANS	2.7	2.6	3.9	2.5*	-		
Number density (m^{-3})	TEM	6.6×10^{22}	-	-	1.1×10^{23}	1.1×10^{23}	8.5×10^{22}	7.5×10^{22}
	APT	1.8×10^{23}	6.0×10^{23}	6.7×10^{23}	1.6×10^{23}	-	2.6×10^{22}	
	SANS	9.4×10^{23}	7.6×10^{23}	2.3×10^{23}	3.5×10^{23}*	-		

Table 2. Average EDS precipitate compositions in the annealed powders.

Anneal Temp (°C)	Avg Sc (at%)	Avg Ti (at%)	Avg O (at%)	Sc/Ti	(Sc+Ti)/O
850	1.68±1.23	2.36±1.47	25.88±4.53	0.72±0.21	0.15±0.07
1000	2.07±0.86	3.17±2.08	30.48±7.37	0.83±0.40	0.17±0.05

Continuing and Future Research

Here we summarize some very preliminary and limited results the potential for replacing Y with Sc in NFA. The next steps will be to: a) SPS consolidate additional batches of milled Sc-based powders at 850°C, 1000°C and 1150°C; b) complete the characterization of all the consolidated NFA conditions; c) determine the reasons for the low hardness in the 1000°C aged powder condition; d) carry out thermal aging studies to assess the stability of Sc-based NFA.

REFERENCES

[1] G. R. Odette, M.J. Alinger, B.D. Wirth, Annu. Rev. Matter. Res. 38 (2008) 471.
[2] G. R. Odette, et al., J. Nucl. Mat., (2011).
[3] Y. Dai, G. R. Odette, T. Yamamoto, Comp. Nucl. Mater., 1 Chap. 6 (2012) 141.
[4] H. Okamoto, J. Phase Equilib. 33 (2012) 80.

2.3 SEM AND EBSD CHARACTERIZATION OF Fe - {110} $Y_2Ti_2O_7$ INTERFACES – T. Stan, Y. Wu, G. R. Odette (University of California Santa Barbara)

OBJECTIVE

The objective of this work is to create mesoscopic scale interfaces which help further understand the role of Y-Ti-O nano-features in the bcc Fe-Cr ferrite matrix found in nanostructured ferritic alloys (NFAs).

SUMMARY

Nanostructured ferritic alloys (NFAs) are dispersion strengthened by a high density of 2-3 nm fcc pyrochlore $Y_2Ti_2O_7$ nano features (NFs). The interface between the bcc ferrite matrix and the $Y_2Ti_2O_7$ plays critical role in the radiation damage resistance of NFAs. However, details about the interfaces are difficult to determine from the nm-scale features themselves. To partially overcome this obstacle, and to complement other characterization studies of the actual NFs themselves, mesoscopic interfaces were created by electron beam deposition of Fe onto {110} oriented $Y_2Ti_2O_7$ bulk single crystal surfaces. We report characterization of Fe – {110} $Y_2Ti_2O_7$ interfaces using the Scanning Electron Microscopy (SEM) and Electron Backscatter Diffraction (EBSD) techniques. The polycrystalline Fe films had grains with three distinct orientation relationships (ORs). Notably, one 10 μm Fe grain had the favored {100}Fe||{110}$Y_2Ti_2O_7$ and <100>Fe||<100>$Y_2Ti_2O_7$ OR which is found in matrix embedded NFs. This work is continuing and while the mesoscopic interfaces may differ from those of the embedded NFs, the former will facilitate characterization of controlled interfaces, such as interactions with point defects and helium.

BACKGROUND

Materials in fusion reactor environments are subject to intense radiation fields, large time-varying stresses, high temperatures, and chemically reactive environments [1]. Transmutation reactions produce helium (He) which interacts with displacement damage to drive complex microstructural evolutions. Notably, He precipitates as gas bubbles which help nucleate growing voids and creep cavities, and embrittle grain boundaries. Nanostructured Ferritic Alloys (NFAs) are radiation tolerant due to the ultrahigh density of Y-Ti-O nanofeatures (NFs) which trap He in harmless fine-scale bubbles that suppress void swelling and embrittlement. The interface between the matrix and NFs also act as sinks for defect annihilation and provide high creep strength due to dislocation pinning [2].

Numerous Transmission Electron Microscopy (TEM) studies have shown that NFs are complex oxides, primarily fcc cubic pyrochlore $Y_2Ti_2O_7$ [3-8]. Wu et al. reported a comprehensive TEM characterization study of an NFA variant (MA957) in different conditions, using various techniques [9]. The work showed that extracted NFs are structurally consistent with $Y_2Ti_2O_7$ and are generally near stoichiometric with Y/Ti ratios from 0.5 to 1. The dominant in-foil interface was found to be parallel to the {100} planes in Fe, although the oxides themselves could not be indexed due to their small size (≈ 2 nm). This paper also discusses some other work in the literature that did not find the pyrochlore $Y_2Ti_2O_7$. Henceforth, $Y_2Ti_2O_7$ will be referred to as YTO.

A study by Ribis et al. on 1100°C annealed Fe-Cr-W-Y-Ti-O alloys reported ≈ 10 nm YTO type NFs [10]. The orientation relationships (ORs) between these NFs and the matrix are: {100}Fe||{100}YTO and <100>Fe||<100>YTO. Finally, a high resolution TEM (HRTEM) study by Cisten et al. confirmed that the in-foil NF in the same friction stirred weld variant of MA957 are $Y_2Ti_2O_7$ [11]. This study using TEAM 0.5 HRTEM showed that the dominant NF in-foil interface OR is {100}Fe||{100}YTO and <100>Fe||<110>YTO. This OR is different from the one found by Ribis et al. by a 45 degree bulk rotation of the oxide within the matrix. The observations by Ciston et al. indicate that the NFs have two interfacial ORs. The first happens to be the same as the bulk OR: {100}Fe||{100}YTO and <100>Fe||<110>YTO. The second is: {100}Fe||{110}YTO and <100>Fe||<100>YTO.

NFs embedded in a matrix are difficult to study due to their small size, of order 2-3 nm. Thus larger scale interfaces were created by electron beam deposition of Fe onto oriented YTO single crystal surfaces. Preliminary studies on {111} YTO surfaces show that the character of the Fe film is affected by the YTO surface crystallographic orientation, YTO surface topology, and Fe deposition rate [12]. This work has now been extended to {110} YTO surfaces. While these interfaces may differ from those for embedded NFs, creating a variety of mesoscopic surrogates with self-selected ORs will facilitate developing an understanding of metal-oxide interfaces in NFAs, especially with respect to their structures and functional properties.

PROGRESS AND STATUS

Experimental Methods

The details of how samples were fabricated and what instruments were used for characterization are covered in a previous publication [12] and a Fusion Semiannual Report [13]. In summary, a pure single crystal of $Y_2Ti_2O_7$ was {110} oriented and a 2 mm thick wafer was cut using a wire saw. An Allied Multi-prep instrument was used to polish the wafer using a sequence of diamond lapping films, followed by a final 15 minute polishing step using a 0.02 μm non-crystallizing silica suspension. An electron beam system was used to deposit Fe on the $Y_2Ti_2O_7$ crystal at 6.2×10^{-6} torr and 800°C. The deposition rate was 8 nm/s for 250 s, producing an Fe layer thickness of ≈ 2 μm. The sample was then cooled to room temperature at a rate of ≈ 0.16°C/s.

Results and Discussion

Scanning Electron Microscope (SEM) and Electron Backscatter Diffraction (EBSD) Characterization

Figure 1(a) is a Scanning Electron Microscope (SEM) image taken from the Fe film on {110} $Y_2Ti_2O_7$. There are three types of surface topologies (marked 1, 2 and 3 on the figure). Area 1 is flat and has ripples and ridges across the surface. This area coalesced as one continuous film and did not have clear grain boundaries. However, there are some surface cracks in this area. About most of the $Y_2Ti_2O_7$ surface was covered by this kind of Fe film. The sample also has ≈ 2 μm pointed grains which are marked with 2 in Figure 1(a). Some of these grains were isolated within the cracks in the flat areas, while others were found in groups. These grains occupy about a very small fraction of the total area of the sample. The final topology is marked with 3 in Figure 1(a). This ≈ 10 μm grain is smooth and flat, and is the only one found on the entire sample. It is surrounded by both type 1 and type 2 Fe.

Figure 1(b) shows Electron Backscatter Diffraction (EBSD) data taken from the area marked by a green rectangle in Figure 1(a). Each out-of-plane crystallographic orientation of Fe is assigned a color based on the legend in the top right of Figure 1(b). Fe with an {100} surface orientation are marked with red, Fe with an {110} surface orientation are marked with green, Fe with a {111} surface orientation are marked with blue, and other orientations can be indexed using the legend. White areas in Figure 2(b) represent locations where the crystallographic information could not be acquired. This is often due to interference from grain boundaries, rough surface topology, or surface contamination such as dust.

Figure 2(b) appears to show that area 1 has surface orientations marked with green and blue. However, further analysis (not shown) indicates that the blue parts were miss-indexed by the EBSD software and should be green. Thus, the large areas marked with 1 have the same out-of-plane orientation close to {110}. The peaked grains marked with 2 are all purple and have an orientation close to {112}. The large red grain marked with 3 is {100} oriented.

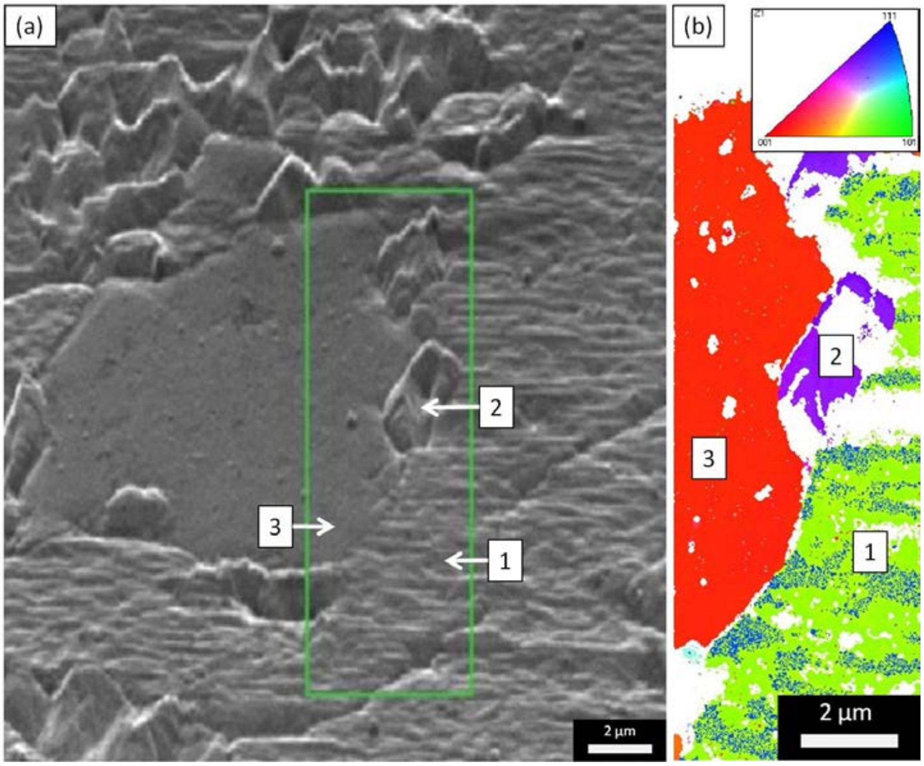

Figure 1. (a) An SEM image of the Fe film. Three surface topologies are marked by 1, 2, and 3. (b) EBSD image showing out-of-plane orientations of the Fe grains.

The EBSD data from Figure 1(b) is also represented as pole figures in Figure 2. Each part of Figure 2(a-d) shows the name of the material, four pole figures representing the 111, 110, 100, and 112 reflections, and a 3D cube showing the full crystallographic orientation. The green diamonds on the pole figures indicate the surface orientation, while the blue hexagons show the in-plane orientation. Figure 1(a) shows the crystallographic orientation of the YTO substrate. The green diamond in the center of the {110} pole figure and the accompanying 3D cube show that the substrate was {110} oriented.

Figure 2(b) shows EBSD data taken from the flat Fe film, referred to as area 1 in Figure 1. The film does not have a clear out-of-plane OR with the substrate. The Fe film likely has a high-index orientation close to {110}. By observing the overlap between the hexagons in the 100 Fe pole figure and the 110 YTO pole figure, the following in-plane OR is obtained: <100>Fe||<110>YTO.

Figure 2(c) shows EBSD data from the paked grains marked with 2 in Figure 1. These grains are clearly {112} surface oriented. By overlapping the diamonds and hexagons from the YTO substrate (Figure 2a) and those from the Fe grains (Figure 2c), the following OR is obtained: {112}Fe||{110}YTO and <111>Fe||<110>YTO. This OR has not been observed in any previous study on embedded NFs, nor on Fe depositions.

Figure 2(d) shows EBSD data from the large flat grain marked with 3 in Figure 1. The OR between this grain and the substrate is: {100}Fe||{110}YTO and <100>Fe||<100>YTO. Notably, this is one of the same ORs that was found in the study by Ciston et al. [11]. This result is significant since it shows that some surrogate interfaces can be created to have the same ORs as those found in embedded NFs. Further studies are required to show what fabrication conditions lead to specific ORs.

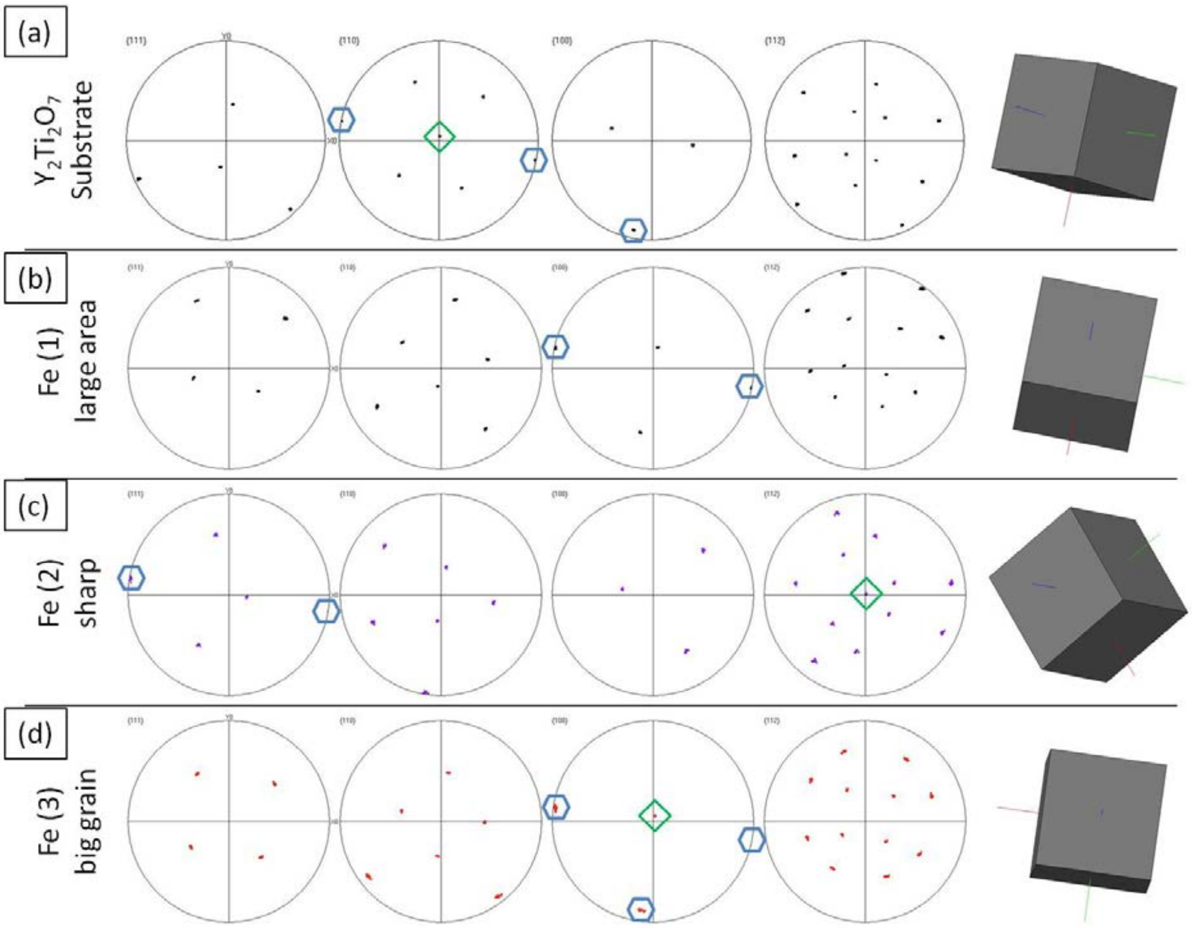

Figure 2. EBSD pole figures from the $Y_2Ti_2O_7$ substrate (a) and from the three types of Fe grains (b – d). Green diamonds show surface orientations while blue hexagons show in-plane orientations. The cubes next to the pole figures represent the full 3D orientation.

Continuing and Future Research

This work is continuing and will be extended to other oxide surface orientations and different deposition conditions. Scanning transmission electron microscopy (STEM) was done on two of the ORs found from the Fe-{110}YTO samples and the results are still being analyzed. It is not yet known what experimental parameters affect the orientation of the Fe film. Ideally, future samples will contain the same interfacial ORs as those found in the embedded NFs. Furthermore, the CrystalMaker software is being used to analyze the three types of interfaces found in the Fe-{110}YTO sample. Perhaps the three ORs have similar atomic matching. There will also be studies of the interface interactions with irradiation induced defects and He.

Acknowledgements

The authors acknowledge the contributions of Gareth Seward, Mark Cornish, Deryck Stave, and Stephan Kraemer for help with various parts of the research. The work performed at UCSB was supported by the U. S. Department of Energy, Office of Fusion Energy Sciences, under grant DE-FG03-94ER54275.

REFERENCES

[1] G.R. Odette, M.J. Alinger, B.D. Wirth, Annu. Rev. Matter. Res. 38 (2008) 471.
[2] Y. Dai, G.R. Odette, T. Yamamoto, Comp. Nucl. Mater., 1 Chap. 6 (2012) 141.
[3] H. Sakasegawa, L. Chaffron, F. Legendre, et al. J. Nucl. Mater. (2009) 384.
[4] S. Yamashita, S. Ohtsuka, N. Akasaka, et al. Phil. Mag. Lett. (2004) 84.
[5] S. Yamashita, N. Akasaka, S. Ohnuki, J. Nucl. Mater. (2004) 329.
[6] M. Klimiankou, R. Lindau, A. Möslang, J. Nucl Mater (2004) 329.
[7] M. Klimiankou, R. Lindau, A. Möslang, Micron (2005) 36.
[8] T. Okuda, M. Fujiwara, J. Mater. Sci. Lett. (1995) 14.
[9] Y. Wu, E.M. Haney, N.J. Cunningham, et al., Acta Mater. 60 (2012) 3456.
[10] J. Ribis, Y. de Carlan, Acta Mater. 60 (2012) 238.
[11] J. Ciston, Y. Wu, G. R. Odette, et al., Fus. Mat. Semiann. Prog. Rep. (2012) DOE-ER-0313/51.
[12] T. Stan, Y. Wu, G.R. Odette. et al., Metal. and Mater. Trans. A, 44 (2013) 10.
[13] Fusion Semiannual Report, DOE/ER 0313/54, 7.3.

2.4 FRACTURE BEHAVIOR OF ADVANCED ODS ALLOY 9YWTV –

T. S. Byun, D. T. Hoelzer (Oak Ridge National Laboratory), J. H. Yoon (Korea Atomic Energy Research Institute), and S. A. Maloy (Los Alamos National Laboratory)

OBJECTIVE

Nanostructured ferritic alloys (or advanced ODS alloys) have been considered as primary candidate materials for fusion reactors because of their excellent high temperature creep strength and irradiation resistance. This research aims at characterizing and understanding the fracture behaviors of newly developed 9YWTV alloy with improved fracture toughness.

SUMMARY

Latest studies on the high temperature fracture of nanostructured ferritic alloys (NFAs) have indicated that the microcracks formed within the alloys propagate by a low energy boundary decohesion mechanism and therefore resulted in low fracture toughness. A 9Cr NFA with improved fracture toughness was successfully developed by applying thermo-mechanical treatments (TMTs) designed to enhance grain boundary bonding. This article focuses on the static fracture behaviors of the newly developed 9Cr NFAs. Fracture mode and cracking resistance were compared among the materials treated through different controlled rolling (CR) routes. Optimal TMTs resulted in high fracture toughness at room temperature (> 250 MPa√m) and in retaining higher than 100 MPa√m over the wide temperature range 22–700°C. Significant differences were found in the fracture resistance (J-R) curves among the low and high fracture toughness NFAs.

PROGRESS AND STATUS

Introduction

In the past decade, the nanostructured ferritic alloys (NFAs) with ultra-high strength (1–2 GPa) have been developed for various nuclear reactor applications such as the first-wall structure of gas-cooled fusion reactors and advanced sodium-cooled fast reactor for their excellent high temperature creep strength and high dose irradiation resistance [1-13]. One of the major issues that we inevitably face in developing such ultra-high strength materials is the resulting low toughness and low ductility. However, although high initial toughness and ductility are essential for preventing cracking for both manufacturing and delaying the onset of radiation-induced embrittlement, this key engineering requirement has not been a focus of development efforts in major research programs. A series of studies of deformation and fracture mechanisms using 14YWT NFA indicate that the microcracks tend to propagate along grain boundaries without significant plastic deformation, resulting in low energy grain boundary decohesion and low fracture toughness [14-22].

It has been proposed that strengthening grain bonding could be achieved through thermo-mechanical treatments (TMTs) specially designed to enhance grain boundary inter-diffusion [22]. Recently, 9Cr NFAs with high toughness have been successfully developed by applying optimum TMTs to as-consolidated NFAs [15-25]. Since a proper fracture resistance is a key requirement for any engineering grade material, the purpose of the detailed study on the newly developed 9Cr NFAs was set to elucidate and characterize the static fracture behaviors focusing on high temperature fracture resistance and mechanism.

In search of high fracture toughness conditions, two series of TMTs, i.e., isothermal annealing and controlled rolling treatments, have been applied to two as-extruded NFAs with normal chemistry of Fe(bal)-9Cr-2W-0.4Ti-0.2V-(0.05 and 0.12)C-0.3Y_2O_3 [24]. These different TMTs were supposed to produce widely different fracture behaviors. A three-point bar (TPB) type miniature fracture specimen with dimensions of 15 mm×5 mm×2.5 mm (thickness) was used for static fracture (J-R) testing. Fracture tests on the miniature TPB specimens have been performed at 22 – 700 °C at a nominal gage speed of 0.05 mm/min [26-32]. Process dependence of J-R curve and fracture toughness is the focus of discussion in this article. Fracture test result showed that some optimum TMTs resulted in fracture toughness similar to those of conventional quenched and tempered ferritic-martensitic steels. Fracture surfaces and J-R curves are compared to find the origin of such a significant improvement in fracture toughness.

Experimental

Base materials and thermomechanical treatments

Two new Fe-9Cr nanostructured alloys have been developed to improve fracture toughness by integrating the best practices in the mechanical milling-based steel-making technology. Details of the integrated processing technology can be found in earlier publication [33] and a summarized description is provided here. The alloy powders were produced in the ATI Powder Metals Co. in Pittsburgh, PA, using an integrated process of vacuum induction melting and argon gas atomization. The product chemistries of the two Fe-9Cr-alloy powders were Fe-8.84Cr-2.04W-0.38Ti-0.21V-0.05C (heat L2476) and Fe-9.02Cr-2.11W-0.38Ti-0.21V-0.11C (heat L2477), which correspond to 10% and 11.5% Cr-equivalents, respectively. The yttrium oxide (Y_2O_3) powder to be mixed with these alloy powders for mechanical milling was purchased from the Nanophase Technology Co. and has particle sizes ranging from 17 to 31 nm.

In the production of NFAs, the mechanical milling process is designed to provide a completely-alloyed status of the material without any precipitation or evident elemental segregation. The two alloy powders have been mechanically-milled in Zoz GmbH CM08 attritor milling machine after being mixed with 0.3 wt.% yttrium oxide (Y_2O_3) powder. Each of the loads for milling comprised 997 g of an alloy powder and 3 g of Y_2O_3 powder and was milled for 40 hours in static argon environment in water cooled chamber. For consolidation, the mechanically-alloyed powders were filled into mild steel cans with 50 mm inner diameter and evacuated to a vacuum of ~1 Pa at ≤ 400 °C. The consolidation process, i.e., hot extrusion operation, was performed in the Watson-Stillman unit at ORNL with a capacity of 1.25 kilotons. During the extrusion operation a peak force of ~900 tons was taken to extrude a 90 mm (outer) diameter can containing ~1 kg mixed powder. The two as-extruded NFAs were designated as 9YWTV-PM1 (with higher carbon) and 9YWTV-PM2 (with lower carbon). Up to this step, the processing details were the same as those developed for 14YWT [27].

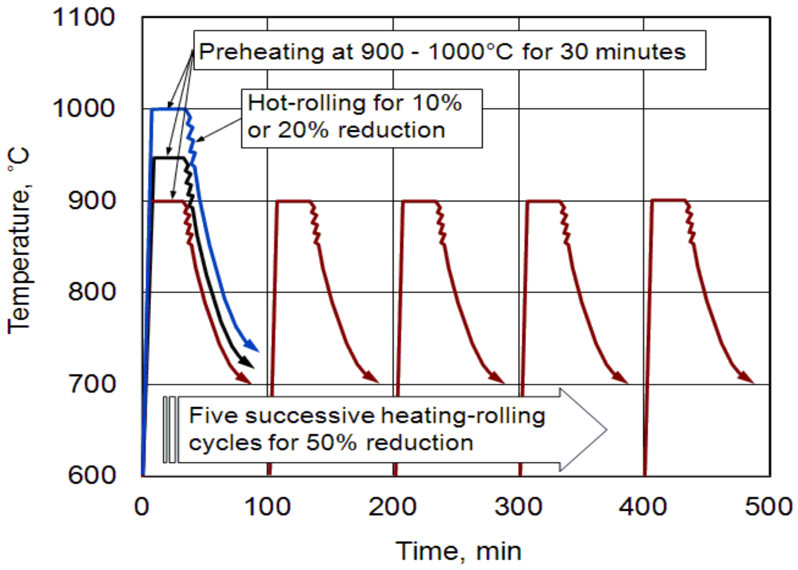

Figure 1. Controlled rolling (CR) processes applied to 9Cr NFAs [33]. Note that the 20% reduction was made by one-step rolling and the 50% rolling was made by five 10% reductions and that the rolling temperatures are believed to be close to the annealing (or rolling initiation) temperatures as the coupons were still cladded with 4–6 mm thick mild steel (can material).

The final processing step was controlled rolling (CR) or repeated rolling treatment in two-phase temperature region: the as-extruded or base NFAs were controlled-rolled at 900, 925, 950, 975, and 1000 °C for 20 or 50% total reduction (i.e., isothermally annealed and rolled down on cooling in air). The hot-rolling treatments have been applied to ~5 cm long coupons after heating to 900–1000 °C for 30 minutes; this temperature range was chosen considering the temperature range for α to γ transformation (850–1000°C), hot formability of NFAs (> ~900°C), and prevention of abnormal grain growth (< ~1100°C) [33]. Since the coupons were still cladded by the mile steel can material and thus cooling in the meat NFA was limited during the rolling, the actual rolling temperatures for the NFAs were believed to be very close to the specified ones in 900 – 1000 °C. Figures 1 illustrates schematic routes of CR treatments applied to the two base NFAs.

Specimen preparation

For the two NFAs treated in various conditions, static fracture testing was performed in an MTS servo-hydraulic testing machine with a vacuum furnace at select temperatures in the range of 22(room temperature)–700 °C using miniature bend bar specimens with nominal dimensions of 15 mm in length and 5 mm in width and 2.5 mm in gross thickness. These specimens had a 1.5 mm long wire-cut notch and 0.25 mm deep side groove in each side, as illustrated in Figure 2. All specimens had L-T orientation, in which the loading direction is in the extrusion direction and crack extension occurs in the perpendicular direction. Prior to the fracture testing, precracking to produce sharp crack tip was carried out for each specimen under a nominal cyclic load of at 500 ± 450 N at 20 - 30 Hz. Precracking was made until the machined notch (1.5 mm) extended by 0.5–1.2 mm; the nominal crack length-to-specimen width ratio (a/W) was about 0.46 after the precracking.

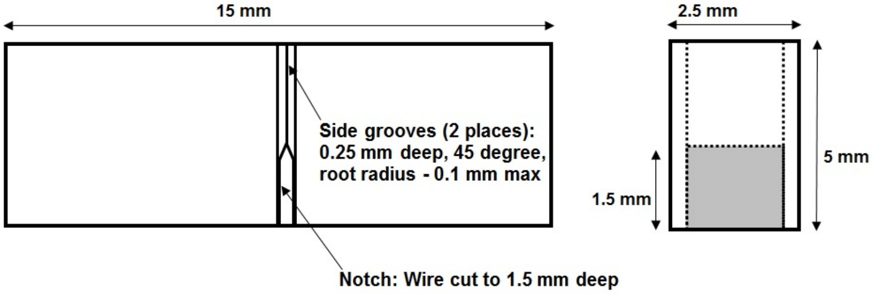

Figure 2. Dimensions of three-point bend bar fracture specimen.

Static fracture resistance (J-R) testing and analysis

Fracture resistance (J-R) tests in quasi-static mode were carried out at a crosshead speed of 0.005 mm/s with a temperature control within ±1°C. For each TMT condition, 2 - 7 J-R tests were conducted at select temperatures of 22, 200, 300, 400, 500, 600, and 700°C and in a vacuum of ~10^{-4} Pa (~10^{-6} torr), except for the room temperature (22°C) tests in air. Each specimen was soaked at a desired temperature for 5 – 10 minutes prior to the initiation of each J-R test. All of the J-R fracture tests were run in a displacement-controlled three-point bending mode, and the static fracture testing and evaluation were performed following the standard procedure described by the ASTM Standard E1820-09, Standard Test Method for Measurement of Fracture Toughness. As the normalized method was applied to the construction of fracture resistance (J-R) curves, the monotonic load-displacement curves without loading-unloading cycles were recorded. In each test loading was stopped when the load decreased to about 50% of maximum load or a catastrophic failure occurred before the 50% load point. After each J-R test, the tested specimen was fatigue-loaded in air to make a mark for the final crack length before the complete separation of the specimen. The initial and final crack lengths were then measured optically. Figure 3 displays examples for the optical photographs of fracture surface, in which the white portions were formed by high cycle fatigue loading and provides easily discernible crack surface regions. The dark area between the lower and higher white areas is the surface formed by the stable fracture testing. The Figure 3(a) is an exception that has experienced brittle failure [35-42].

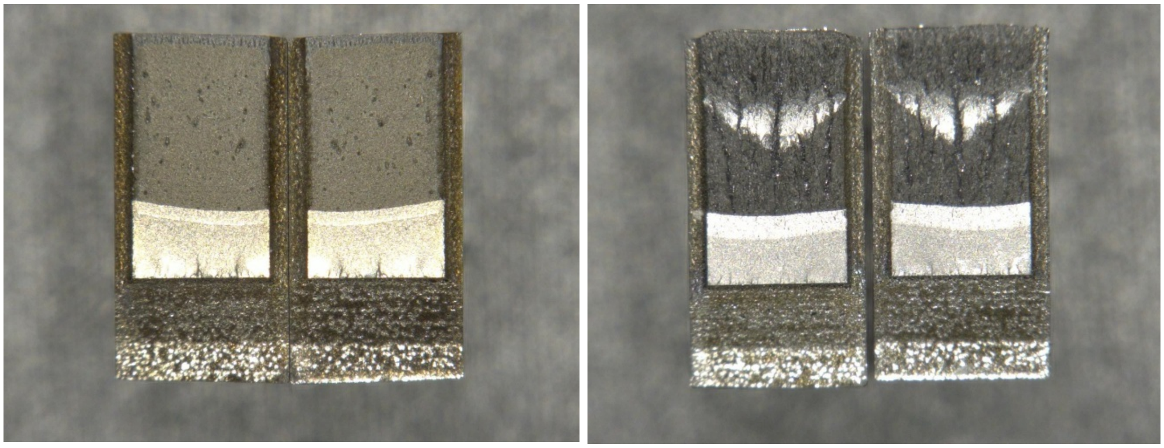

(a) 9YWTV-PM1 as-extruded, tested at 600 °C

(b) 9YWTV-PM2 as-extruded, tested at 200 °C

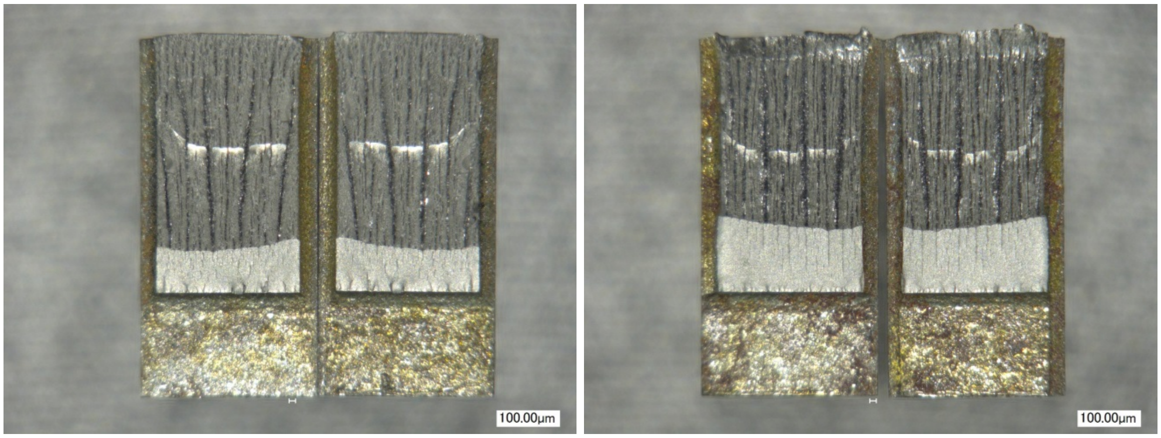

(c) 9YWTV-PM1 50% rolled at 1000 ^{o}C, tested at RT

(d) 9YWTV-PM2 50% rolled at 1000 ^{o}C, tested at RT

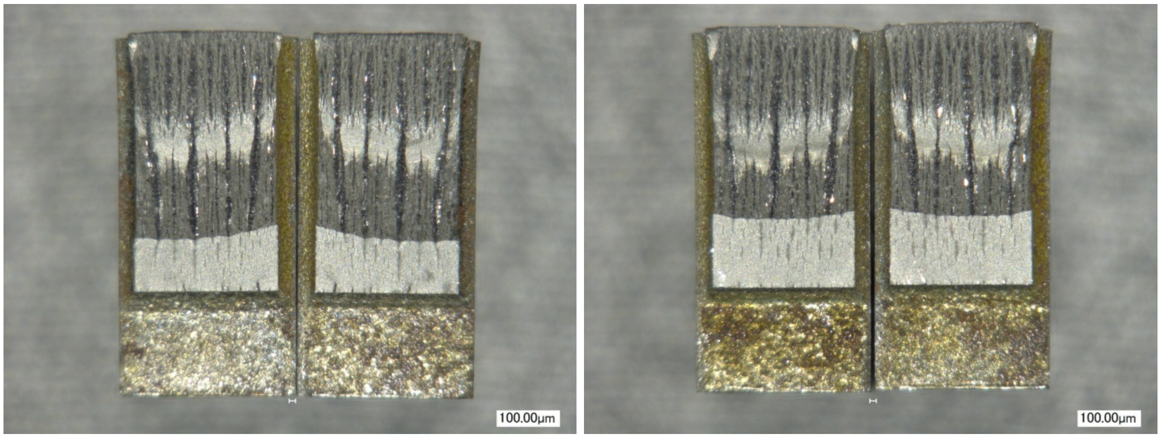

(e) 9YWTV-PM2 50% rolled at 975 ^{o}C, tested at RT

(f) 9YWTV-PM2 50% rolled at 975 ^{o}C, tested at 500 ^{o}C

Figure 3. Examples for the optical photographs of fracture surfaces. The white portions are from fatigue loading, which were used for crack length measurement.

In the data analysis procedure to construct the J-Resistance curve (or J-integral versus Δa curve), the crack growth values were obtained using the normalization curve method. This simplified J-R curve calculation method is described in the ASTM Standard. To use the normalization curve method, two datasets need to be obtained: a load-displacement curve of up to ~50% of the maximum load, and the initial and final crack lengths, both of which were obtained during testing and microscopy as aforementioned. For each J-R curve, the interim fracture toughness value (J_Q) is determined at the intersection of the J-R curve and the 0.2 mm offset line of the blunting line using the formula and procedure described in the ASTM standard [34]. The final fracture toughness data are also given in the form of stress intensity factor, K_{JQ}, which can be converted from the J_Q data using the following relationship:

$$K_{JQ} = \sqrt{J_Q E/(1-\nu^2)} \qquad (1)$$

where E is the Young's modulus at given temperature (T in °C) (=218 – 0.045T-0.0001T^2 GPa) and v the Poisson ratio (=0.28, assumed temperature-independence).

It is worth noting that the fracture toughness data (K_{JQ}) produced in this study remain as interim values (K_{JQ}) because the curvature at crack frontline and the limitation imposed by small specimen volume and thickness cannot satisfy some of the standard requirements for the validation towards formal fracture toughness (K_{IC}). It is also important to note that the standard practice used leads to an overestimation when small specimens are used [43-48]. Such overestimation originates from application of the standard practice of using the 0.2 mm shifted crack blunting line to the different uncracked ligaments: the present miniature TPB specimen has a nominal uncracked ligament of ~2.5 mm, which is very small compared to any types of standard fracture specimens. As indicated in Figure 3, the excessive plasticity or loss of stress constraint, which is often observed in soft material miniature specimens, is not a cause for the overestimation.

Results and discussion

Characteristics of fracture resistance (J-R) behavior

A J-integral versus Δa curve, which is obtained from load-displacement data using either curve normalization method or unloading compliance method, can represent the fracture resistance (J-R) of an alloy during crack growth. Cracking resistance at or near the initiation is usually defined as fracture toughness (J_{IC} for example) and is considered as the most important fracture parameter, however, the slope and height of the J-R curve after the initial portion can also be useful in characterizing overall cracking resistance of the material as a growing crack tends to stop earlier with higher J-value. This section compares the J-R curves of the two 9Cr NFA materials in various conditions.

The J-R curves in as-irradiated condition are compared in Figure 4. First of all, it is noted in this figure that four of eight J-R curves are buried in the initial linear line (blunting line) as those specimens have fractured in either linear elastic or crack blunting region. It is worth remembering that such buried lines exist in the following plots. Among the J-R curves with crack extension, the 9YWTV-PM2 alloy tested at low temperatures, room temperature and 200 °C, displayed strong fracture resistance. However, the other two curves obtained from high temperatures, 9YWTV-PM1 at 500 °C and 9YWTV-PM2 at 700 °C, showed much lower resistance. As these base NFA specimens fracture without crack growth or experience crack growth at a low resistance, resulting fracture toughness at a high temperature ≥ 500 °C seems to be as low as those of the reference material 14YWT-SM10 [33].

At room temperature, the 9YWTV-PM2 alloy after CR displays much higher fracture resistance when compared to the base material, Figure 5. The two J-R curves of 9YWT-PM2 after 900 °C rolling show extraordinary long blunting lines, from which high fracture toughness values are measured as they are determined at maximum. In such cases with long blunting lines, the contribution of high strength to fracture toughness (J_Q) becomes significant. The other two curves of 9YWTV-PM2 alloy after CR at 975 and 1000 °C display high J-values with relatively high slopes (dJ/da). It is obvious that the 9YWTV-PM1 alloy has relatively lower fracture resistance as the two J-R curves after 975 and 1000 °C CR are located lower than those of 9YWTV-PM2 alloy and the specimens after 900 °C CR have failed without stable crack growth and curves are buried in linear portion.

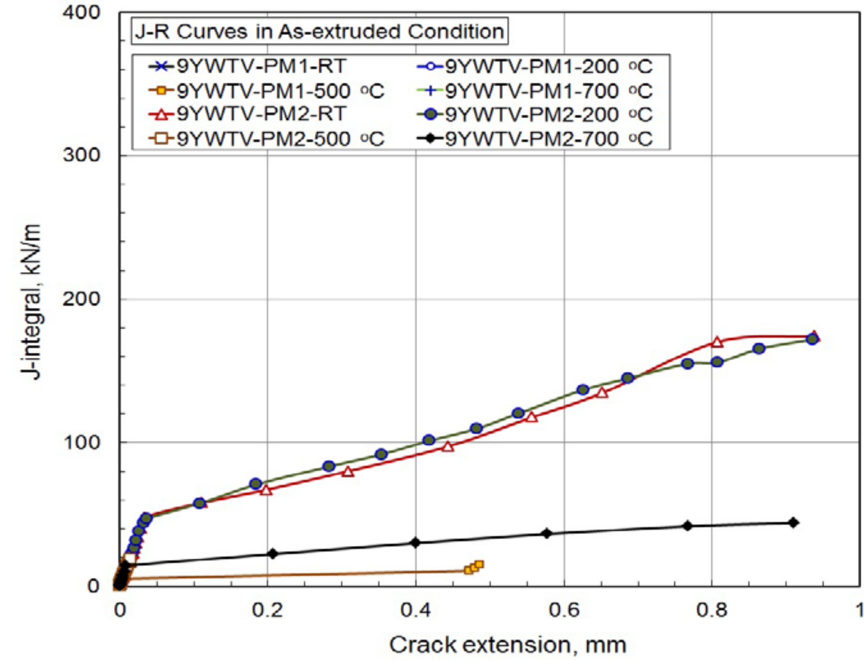

Figure 4. J-R curves from the miniature bend specimens of 9YWTV-PM1 and -PM2 in as-extruded condition.

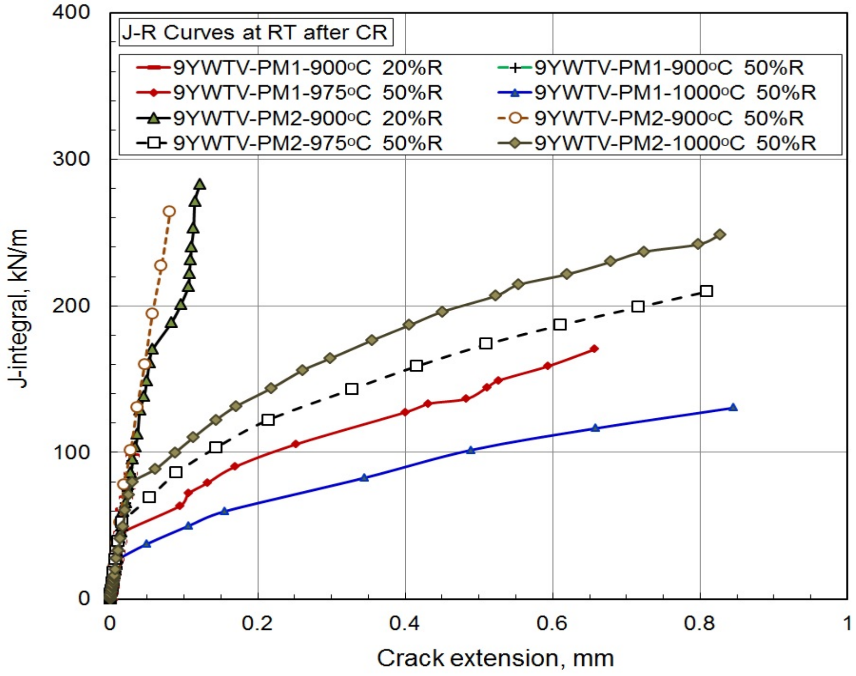

Figure 5. J-R curves from the miniature bend specimens of controlled rolling (CR) treated 9YWTV-PM1 and -PM2 tested at room temperature.

High temperature fracture resistances are compared in Figures 6 and 7. The J-R data in Figure 5 indicate fracture resistance is relatively higher at 500 °C than at 700 °C. There are also exceptions: in the two cases of 9YWTC-PM1 after CR at 900 °C, the all J-values contained on the blunting line. Meanwhile, as seen in the room temperature data, the 9YWTV-PM2 after CR at 900 °C has noticeably higher fracture resistance compared to the other alloy or CR conditions.

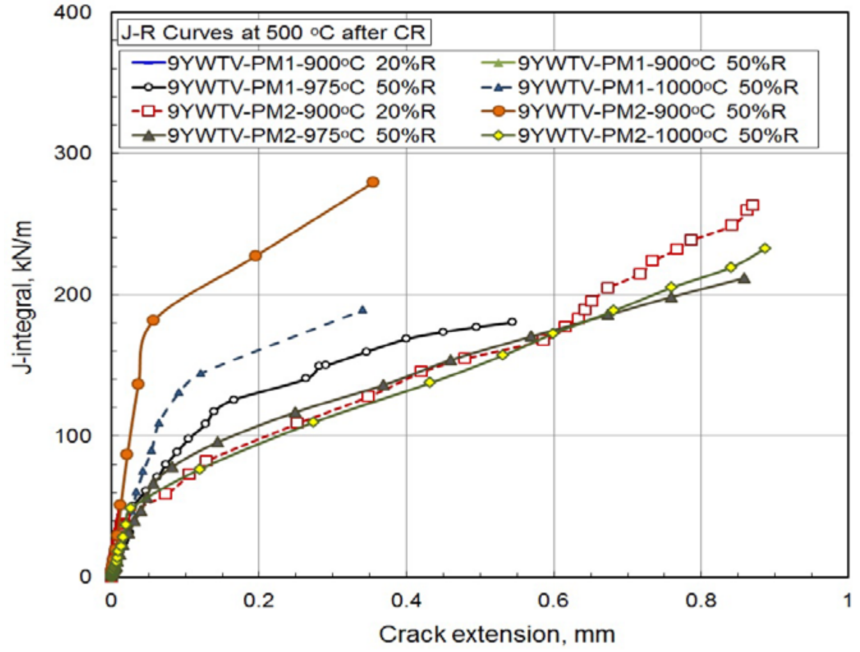

Figure 6. J-R curves from the miniature bend specimens of controlled rolling (CR) treated 9YWTV-PM1 and -PM2 tested at 500 °C.

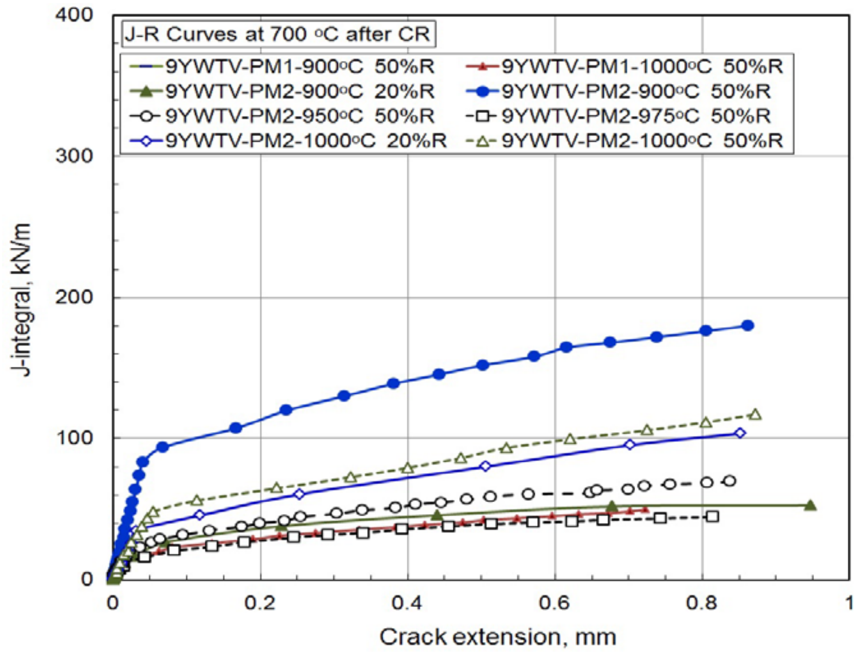

Figure 7. J-R curves from the miniature bend specimens of controlled rolled 9YWTV-PM1 and -PM2 tested at 700 °C.

For both materials, relatively lower fracture resistances were measured at 700 °C as illustrated in Figure 7. The higher carbon alloy 9YWTV-PM1 yielded low fracture resistance as the specimen after 900 °C CR has failed in brittle mode, and the J-R curve after CR at 1000 °C runs low although crack growth was stable. It is confirmed again that the 9YWTV-PM2 after CR at 900 °C has highest fracture resistance in the two materials in different TMT conditions.

Temperature dependence of fracture toughness (K_{JQ})

In earlier publication [33] fracture toughness (K_{JQ}) data obtained at room temperature and 500 °C were used to determine effective TMT conditions that can produce high toughness NFAs. In Figures 8 and 9 the temperature dependence of K_{JQ} over a wide range of temperature up to 700 °C is discussed for the CR treated NFAs. In the background the K_{JQ} values of ferritic-martensitic (FM) steels, HT9 (12Cr-1MoWV) and NF616 (9Cr-2WVNb), are displayed in the upper band (colored light pink) and those of two 14YWTs and two base 9Cr NFAs are in the lower band (light blue). These datasets in two distinctive bands are used as benchmark data for improvement as the ultimate goal of this research was to develop a 9Cr NFA with fracture toughness comparable to those of the melting-based FM steels.

As displayed as the upper band, the K_{JQ} of FM steels is typically in the range of 200 – 300 MPa√m at room temperature. Room temperature is believed to be in the upper shelf region of fracture toughness, and the ductile-brittle transition temperature (DBTT) of typical quenched and tempered FM steel is below room temperature [12]. Above room temperature the fracture toughness of FM steels slowly decreases with test temperature. The band widens, to a 100 – 260 MPa√m range at 700 °C because the K_{JQ} difference between the toughest NF616 and the classic HT9 grows with temperature. Meanwhile, the K_{JQ} data of 14YWTs and base 9YWTVs fall within the band of lower fracture toughness. Up to ~200 °C 14YWT-SM10 and 9YWTV-PM2 in as-extruded condition have 100–140 MPa√m, however, between 200 and 300 °C the K_{JQ} for those NFAs dropped to well below 100 MPa√m, about a half of the peak toughness, and remained at the level in the range of 300–700 °C. Others, 14YWT-SM11 and 9YWTV-PM1 in as-extruded condition, show even lower toughness within the band.

In Figure 8 the K_{JQ} values of 9YWTV-PM1 alloy after various CR treatments, larger data markers, are compared to the back ground data. For the majority of the data for CR-treated 9YWTV-PM1, the treatment did not help to improve fracture toughness. The only exception was the case of 975 °C CR treatment, which resulted in high fracture toughness in 100–600 °C span. A maximum toughness of ~240 MPa√m was measured in the 200–300 °C region and it decreased with temperature above 300 °C. The increase of K_{JQ} in the RT–300 °C region may be considered as a toughness transition region, if not data scattering. Also, this standing out case with high K_{JQ} over entire test temperature range is believed to be as an experimental error resulting from an inhomogeneity in material sampling; but further examination needs to be made for confirmation. Temperature dependence behaviors after 900 and 1000 °C CR-treatments are close to those of the low toughness back ground data.

As displayed in Figure 9, the improvement of fracture toughness by CR treatments is significantly more pronounced and consistent in the 9YWTV-PM2 alloy. The room temperature K_{JQ} values were in the range of 150–280 MPa√m and the CR-treated PM2 alloy retained similar level of fracture toughness up to at least 300 °C. Obvious decrease with temperature started above 300 °C, but the sudden decrease of fracture toughness in 200– 300 °C region, which is often observed in high strength NFAs, did not occur in the CR-treated 9YWTV-PM2. At the highest temperature of 700 °C the K_{JQ} value after 20% rolling at 900 °C and 50% rolling at 900 °C decreased slightly below 100 MPa√m. Except for a few data points at room temperature and 700 °C, the fracture toughness data of the CR-treated 9YWTV-PM2 fall within the band of FM steels. Overall temperature dependence of these CR-treated NFAs is also similar to that of FM steels.

Among the CR-treatments the 50% rolling at 900 °C demonstrated the highest fracture toughness, which retained high K_{JQ} of >150 MPa√m over the entire test temperature range. The main reason for such high toughness is believed to originate from its high strength combined with appropriate ductility [45-49].

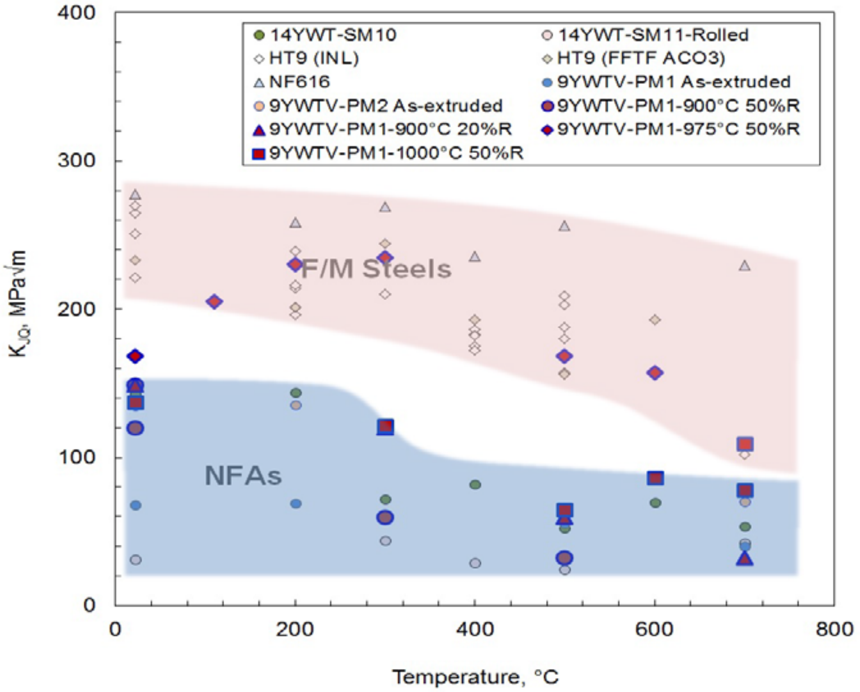

Figure 8. Temperature dependence in the fracture toughness (K_{JQ}) of 9YWTV-PM1 controlled rolled at various conditions. Data are compared with those of FM steels in pink (upper) shadowed area and those of lower toughness NFAs in blue (lower) shadowed area.

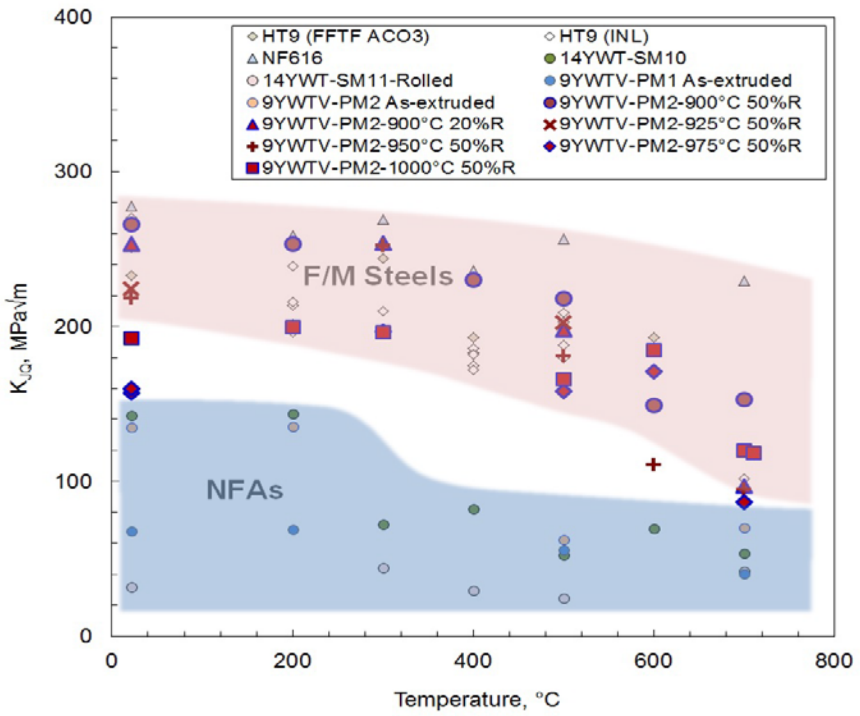

Figure 9. Temperature dependence in the fracture toughness (K_{JQ}) of 9YWTV-PM2 controlled rolled at various conditions. Data are compared with those of FM steels in pink (upper) shadowed area and those of lower toughness NFAs in blue (lower) shadowed area.

SUMMARY

Fracture resistance behaviors have been characterized in detail for the newly developed 9YWTV alloys after various controlled rolling (CR) treatments.

Fracture resistance (J-R) tests have been carried out for the CR-treated 9YWTV-PM1 and 9YWTV-PM2 alloys over a wide temperature range of RT–700 °C and the data were analyzed using a simplified normalization method.

The fracture toughness of CR-treated 9YWTV-PM2 was as high as those of non-ODS F/M steels. In particular, the 9YWTV-PM2 controlled-rolled at 900°C demonstrated the best fracture toughness among NFAs, which were above 150 MPa√m over the entire test temperature range.

Acknowledgement

This research was jointly sponsored by the Fuel Cycle R&D Program of the Office of Nuclear Energy, as well as by the Fusion Materials Program of Office of Fusion Energy, the U.S. Department of Energy, under Contract DE-AC05-00OR22725 with UT-Battelle, LLC. The authors express special thanks to Dr. Xiang Chen for his thorough review and thoughtful comments.

REFERENCES

[1] S.J. Zinkle, G.S. Was, Acta Mater. 61 (2013) 735–758.
[2] B. Z. Margolin, A. I. Murashova, V. S. Neustroev, Strength of Mater. 44 (2012) 223-240.

[3] T.R. Allen, J.I Cole, C.L Trybus, D.L Porter, H. Tsai, F. Garner, E.A. Kenik, T. Yoshitake, J. Ohta, J. Nucl. Mater., 348 (2006) 148-164.
[4] I.I. Balachov, E.N. Shcherbakov, A.V. Kozlov, I.A. Portnykh, F.A. Garner, J. Nucl. Mater., 329–333 (2004) 617–620.
[5] S.A. Maloy, M. Toloczko, J. Cole, T.E. Byun, J. Nucl. Mater., 415 (2011) 302-305.
[6] V.S. Neustroev, F.A. Garner, J. Nucl. Mater., 386–388 (2009) 157–160.
[7] Y. Mutoh, K. Ichikawa, K. Nagata, M. Takeuchi, Journal of Materials Science, 30 (1995) 770–775.
[8] T.S. Byun, K. Farrell, J. Nucl. Mater., 318 (2003) 292-299.
[9] R.L. Klueh, D.R. Harris, High-chromium Ferritic and Martensitic Steels for Nuclear Applications, ASTM (2001), ISBN 0-803102090-7.
[10] T.R. Allen, J.T. Busby, R.L. Klueh, S.A. Maloy, M.B. Toloczko, JOM, 60 (2008) 15-23.
[11] R. Chaouadi, G. Coen, L. Lucon, V. Massaut, J. Nucl. Mater., 403 (2010) 15-18.
[12] T.S. Byun, M. Li, K. Farrell, Met. & Mat. Trans. A, 44 (2013) 84-93.
[13] S.A. Maloy, M. Toloczko, J. Cole, T.S. Byun, J. Nucl. Mater., 415 (2011) 302–305.
[14] J.S. Cheon, C.B. Lee, B.O. Lee, J.P. Raison, T. Mizuno, F. Delage, J. Carmack, J. Nucl. Mater., 392 (2009) 324-330.
[15] L. Tan, D.T. Hoelzer, J.T. Busby, M.A. Sokolov, R.L. Klueh, J. Nucl. Mater., 422 (2012) 45–50.
[16] J. Chen, M.A. Pouchon, A. Kimura, P. Jung, W. Hoffelner, J. Nucl. Mater., 386–388 (2009) 143–146.
[17] P. Lours, S. Le Roux, G. Bernhart, J. Adv. Mater., 33 (2001) 11-20.
[18] P. Krautwasser, A. Czyrska-Filemonowicz, M. Widera, F. Carsughi, Mater. Sci. Engi., A 177 (1994) 199-208.
[19] J. Chen, P. Jung, W. Hoffelner, H. Ullmaier, Acta Materialia, 56 (2008) 250–258.
[20] A Wasilkowska, M Bartsch, U Messerschmidt, R Herzog, A Czyrska-Filemonowicz, J. Mater. Process. Tech. (2003) 218-224.
[21] A. Czyrska-Filemonowicz, B. Dubiel, J. Mater. Process. Tech. 64 (1997) 53-64.
[22] T.S. Byun, J.H. Kim, J.H. Yoon, D.T. Hoelzer, J. of Nucl. Mater*.,* 407 (2010) 78-82.
[23] R.L. Klueh, J.P. Shingledecker, R.W. Swindeman, D.T. Hoelzer, J. Nucl. Mater., 341 (2005) 103–114.
[24] M.B. Toloczko, D.S. Gelles, F.A. Garner, R.J. Kurtz, K. Abe, 329–333 (2004) 352–355.
[25] P. Miao, G.R. Odette, T. Yamamoto, M. Alinger, D. Klingensmith, J. Nucl. Mater., 377 (2008) 59–64.
[26] M.K. Miller, D.T. Hoelzer, E.A. Kenik, K.F. Russell, J. Nucl. Mater., 329–333 (2004) 338–341.
[27] D.T. Hoelzer, J. Bentley, M.A. Sokolov, M.K. Miller, G.R. Odette, M.J. Alinger, J. Nucl. Mater., 367-370 (2007) 166-172.
[28] M.J. Alinger, G.R. Odette, D.T. Hoelzer, Acta Mater., 57 (2009) 392-406.
[29] G.R. Odette, M.J. Alinger, B.D. Wirth, Ann. Rev. Mater., Res. 38 (2008) 471-503.
[30] M.K. Miller, D.T. Hoelzer, E.A. Kenik, K.F. Russell, Intermetallics 13 (2005) 387-392.
[31] S. Ukai, S. Ohtsuka, T. Kaito, H. Sakasegawa, N. Chikata, S. Hayashi, S. Ohnuki, Mater. Sci. Engi., A 510-511 (2009) 115-120.
[32] H. Sakasegawa, S. Ukai, M. Tamura, S. Ohtsuka, H. Tanigawa, H. Ogiwara, A. Kohyama, M. Fujiwara, J. Nucl. Mater., 373 (2008) 82–89.
[33] T.S. Byun, J.H. Yoon, D.T. Hoelzer, J. Nucl. Mater*.,* (2012) in press.
[34] H.S. Cho, R. Kasada, A. Kimura, J. Nucl. Mater., 367 (2007) 239-243.
[35] H. Kishimoto, R. Kasada, O. Hashitomi, A. Kimura, J. Nucl. Mater., 386 (2009) 533-536.
[36] N. Akasaka, S. Yamashita, T. Yoshitake, S. Ukai, A. Kimura, J. Nucl. Mater., 329 (2004) 1053-1056.
[37] P. Olier, J. Malaplate, M.H. Mathon, D. Nunes, D. Hamona, L. Toualbi, Y. de Carlan, L. Chaffron, J. Nucl. Mater., 428 (2012) 40-46.
[38] S. Ukai, M. Harada, H. Okada, M. Inoue, S. Nomura, S. Shikakura, K. Asabe, T. Nishida, M. Fujiwara. J. Nucl. Mater., 204 (1993) 65-71.
[39] S. Ukai, T. Nishida, T. Okuda, T. Yoshitake, J. Nucl. Mater., 258 (1998) 1745-1749.
[40] A-L. Rouffié, P. Wident, L. Ziolek, F. Delabrouille, B. Tanguy, J. Crépin, A. Pineau, V. Garat, B. Fournier, J. Nucl. Mater., 433 (2013) 108–115.
[41] A. Steckmeyer, M. Praud, B. Fournier, J. Malaplate, J. Garnier, J.L. Béchade, I. Tournié, A. Tancray, A. Bougault, P. Bonnaillie, J. Nucl. Mater., 405 (2010) 95–100.

[42] J.H. Kim, J.H. Lee, J.Y. Min, S.W. Kim, C.H. Park, J.T. Yeom, T.S. Byun, J. Alloys and Compounds, (2013), in press.
[43] D.K. Mukhopadhyay, F.H. Froes, D.S. Gelles, J. Nucl. Mater., 258-263 (1998) 1209-1215.
[44] D.A. McClintock, D.T. Hoelzer, M.A. Sokolov, R.K. Nanstad, J. Nucl. Mater., 386 (2009) 307-311.
[45] D.A. McClintock, M.A. Sokolov, D.T. Hoelzer, R.K. Nanstad, J. Nucl. Mater., 392 (2009) 353-359.
[46] J.H. Kim, T.S. Byun, D.T. Hoelzer, J. of Nucl. Mater*.,* 407 (2010) 143-150.
[47] J.H. Kim, T.S. Byun, D.T. Hoelzer, S.W. Kim, B.H. Lee, Mat. Sci. Eng. A, 559 (2013) 101-110.
[48] J.H. Kim, T.S. Byun, D.T. Hoelzer, C.H. Park, J.T. Yeom, J.K. Hong, Mat. Sci. Eng. A, 559 (2013) 111-118.
[49] J.H. Kim, T.S. Byun, D.T. Hoelzer, J. Nucl. Mater*.,* 425 (2012) 147-155.

2.5 MECHANICAL PROPERTIES CHARACTERIZATION OF A LARGER BEST PRACTICE HEAT OF 14YWT NFA1 – M.E. Alam, N. J. Cunningham, D. Gragg, K. Fields, G. R. Odette (UCSB), D. T. Hoelzer (ORNL) and S. A. Maloy (LANL)

OBJECTIVES

The objective of this study is to characterize the microhardness, tensile properties and fracture toughness of a newly developed larger best practice heat of 14YWT nanostructured ferritic alloys.

SUMMARY

A new larger heat of best practice nanostructured ferritic alloy (NFA), designated FCRD NFA1, was produced by ball milling argon atomized Fe-14Cr-3W-0.4Ti-0.2Y (wt.%) and FeO powders followed by consolidation and thermomechanical processing sequence of extrusion (850°C), annealing and cross-rolling (1000°C) steps. The microhardness of NFA1 averaged ≈ 376 ± 18 (kg/mm^2). The corresponding uniaxial tensile yield stress and ductility from 22 to 800°C are high at >1000 MPa at 22°C to >500 MPa at 600°C and 15-25%, respectively. K_{Jc}(T) fracture toughness curves were also measured from -196 to 22°C using pre-cracked 3-point bend (3PB) specimens. NFA1 manifests an exceptionally low fracture toughness transition temperature of ≈ -175°C in both LT and TL orientations. These results represent an *extraordinary combination* of strength and toughness. Extensive fractography provided insight on key fracture mechanisms.

BACKGROUND

Advanced fission and future fusion energy depends on developing new, high performance structural materials that can sustain extended component lifetimes under extreme conditions. Nanostructured ferritic alloys (NFA) are well known for their unique features such as exceptional thermal stability, outstanding high temperature strength and remarkable irradiation tolerance, including managing high concentrations of helium. These outstanding attributes are provided by an ultrahigh density of nm-scale Y–Ti–O rich oxide nanofeatures (NFs) [1]. The conventional NFA processing path is ball milling to mechanically alloy Y_2O_3 in the Fe-Cr(-W-Ti) matrix, which is an expensive process and often leads to heterogeneous distributions of NFs [2]. To try to overcome these limitations, an alternative processing path in which Y is included in the melt prior to gas atomization and rapid solidification was developed in collaboration with partner institutions including Oak Ridge National and Los Alamos National Laboratories, under the sponsorship of the DOE Office of Nuclear energy. ATI Powder Metals provided atomized Fe-14Cr-3W-0.4Ti0.2Y powders. However, the Y was phase separated after atomization, this low interstitial alloy powder variant was ball milled for 40 hours with FeO to increase the O content, by Zoz GMBH (Germany). The milled powders were processed at ORNL by canning, degassing and extruding at 850°C, followed by annealing (0.5 h) and cross-rolling (50% thickness reduction) at 1000°C. The larger scaled up alloy of 14YWT, called FCRD NFA1, followed the same processing route as a previous smaller developmental heat called 14YWT-PM2 [3]. Microstructural characterization studies on PM2 and NFA1, including SANS, APT, TEM, have been previously reported [2]. Mechanical property characterizations that included microhardness, tensile and fracture toughness are reported here. Fracture surfaces were also characterized by SEM fractography.

EXPERIMENTAL

Microhardness testing was performed on the flat and polished surfaces using a Vickers indenter and 500g load on a LECO M-400A semi-automated hardness tester. Seven randomly selected specimens were chosen and 10 to 15 indents were made in each specimen. Tensile testing was performed on the dog-bone shaped SSJ2 (5.0x1.2x0.5 mm^3) specimens both at longitudinal (L) and transverse (T) directions (Figure 1) at temperatures ranging from 22 to 800°C using a 810 MTS servo-hydraulic universal testing machine with a crosshead speed of 0.12 mm/min (strain rate of 4 x 10^{-4}/s). Fracture tests were conducted from -196 to 22°C on fatigue pre-cracked single-edged notch three point bend (3PB) bars (3.33x3.33x18 mm^3) (Figure 1). The tests were conducted in general accordance with the ASTM 1921 standard practice. The K_{Jc} were calculated at the maximum load, often coincident with a small pop-in load drop, in an otherwise stable crack growth load-displacement curve. Extensive fractography was performed on both tensile and 3PB specimens to provide insight on the fracture mechanisms at different temperature range using SEM (FEI xL30).

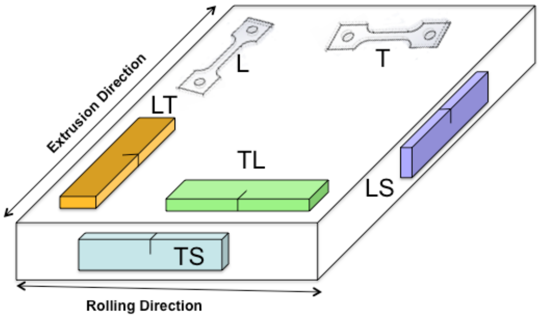

Figure 1. NFA1 test specimen orientations with respect to extrusion and cross-roll directions.

STATUS AND PROGRESS

Microhardness

Vicker's microhardness (H_v) data for several NFA are summarized in Table 1. H_v averages 376 ± 18 (kg/mm^2) for NFA1, which is slightly lower than for PM2 (401 H_v) and higher than for one heat of MA957 (336 Hv), respectively. These differences can probably be partly attributed to the respective alloy grain sizes.

Table 1. Microhardness and grain size of NFA1, PM2 and MA957.

Materials	NFA1	PM2	MA957
Grain Size (nm)	454	424	1470 x 630
Microhardness (Hv)	376 ± 18	401 ± 15	336 ± 8

Tensile Properties

NFA1 tensile properties are summarized in Figure 2 both for L and T orientations from ≈ 22 to 800°C. The alloy is both strong and ductile with little to modest effects of orientation. However, the overall the L orientation has slightly better properties than in the T orientation. The tensile properties are typical of NFA.

SEM fractographs for the L orientation reveals dimple-like features for all the samples confirming ductile fracture (Figs. 3a, 3b and 3c). Room temperature fracture sample showed large flat dimples. Surface cracks formed parallel to the loading direction (Figure 3d). The dimples are much finer at 400°C and the surface cracks have directions both somewhat parallel and angled with respect to the tensile axis (Figs. 3b and 3e). Typical microvoid coalescence is also observed at 800°C but details are masked by extensive oxidation, while crack are observed perpendicular to the loading axis (Figs. 3c and 3f). Macroscopic views of the fracture surface are shown in Figs. 3g, 3h and 3i. At 22°C, a large amount of necking is observed and the surface cracks are seen to connect with through thickness delaminations parallel to the thin dimension of the gauge section. At 400 and 800°C there is slightly less necking and no delaminations are observed. Generally similar observations apply to tensile tests in the T orientation. Figure 4 shows the geometry of the delaminations observed at 22°C in both orientations.

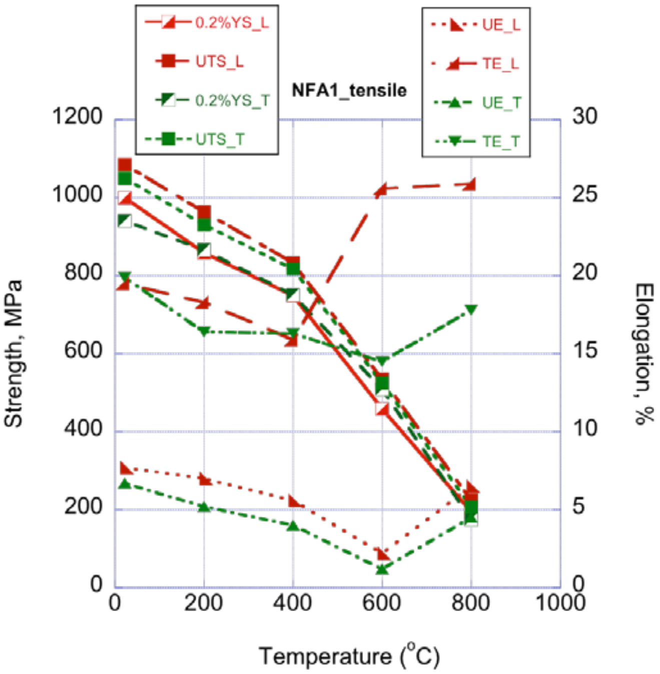

Figure 2. Tensile properties of NFA1 in the L and T orientations as a function of temperature.

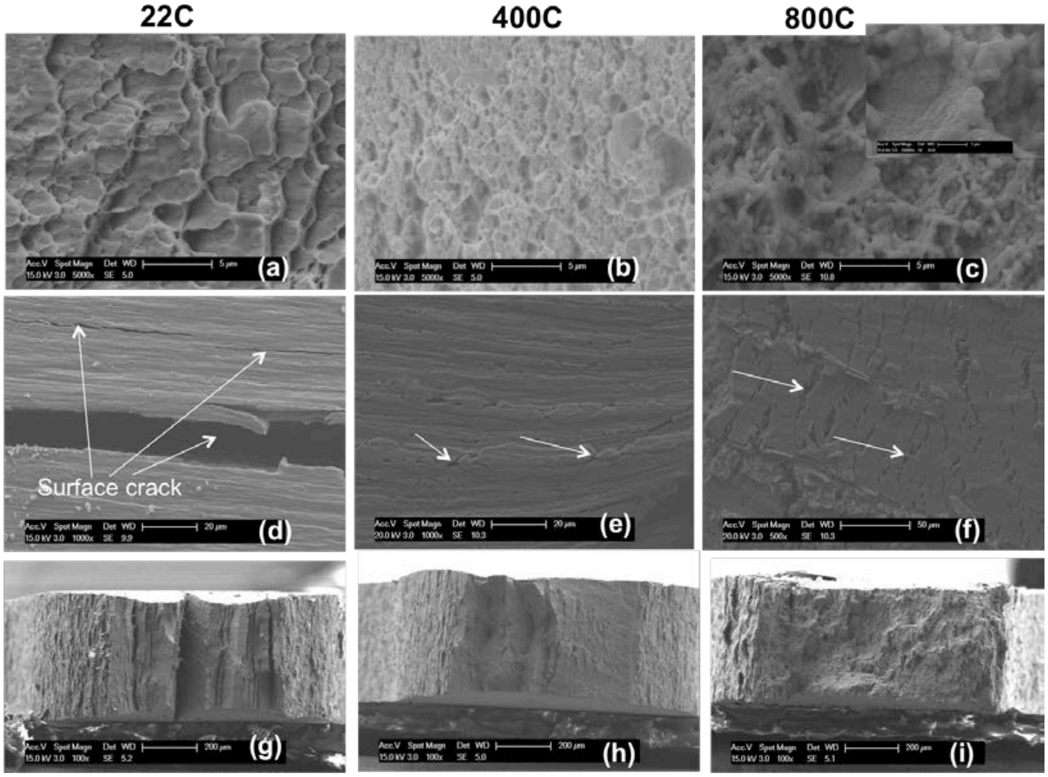

Figure 3. SEM fractographs of NFA1 showing: (a-c) shear-lips @ 22°C, (b) dimples at 400°C and (c) microvoid coalescence at 800°C, respectively; (d-f) wide direction surface cracks; and, (g-i) a macro-view of the fracture surfaces.

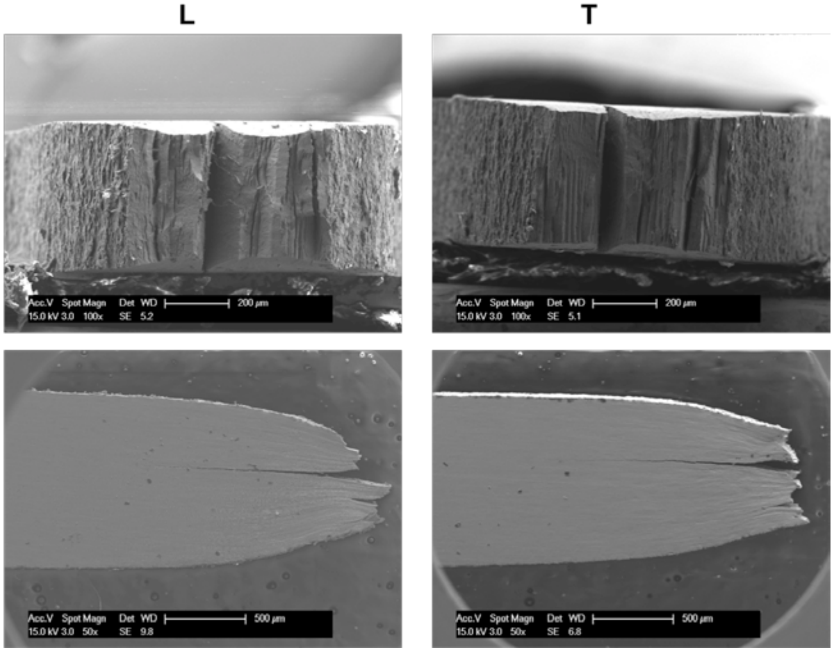

Figure 4. Delamination in the L and T orientations at room temperature.

Fracture Toughness

Typical fracture load displacement curves are illustrated in Figure 5. Figure 5a shows a load displacement curve characteristic of tests at all but the lowest temperature, indicating stable crack growth signaled by a gradually decreasing post maximum load. Figure 5b shows a load displacement curve for linear elastic brittle fracture at -196°C. The fracture toughness (K_{Jc}) results are shown in Figure 6. The upper shelf toughness lies in the vicinity of 100 MPa$\sqrt{m}$, indicating only modest tearing resistance compared to conventional 9Cr tempered martensitic steels. However, the transition from ductile tearing to cleavage initiation takes place at a remarkably low temperature at (LT) and (TL) below ≈ -175°C. There is little effect of specimen orientation. This can be attributed to the nearly equiaxed grain morphology of NFA1 in the crack propagation plane [2]. However, on average the upper shelf toughness and transition temperature are both slightly higher in the LT orientation.

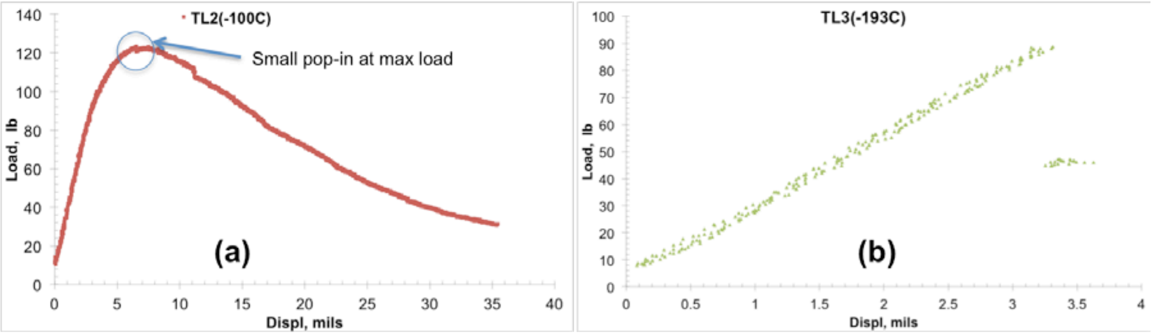

Figure 5. Load-displacement curves of TL 3PB fracture samples at: (a) -100^{o}C and (b) -196^{o}C, respectively.

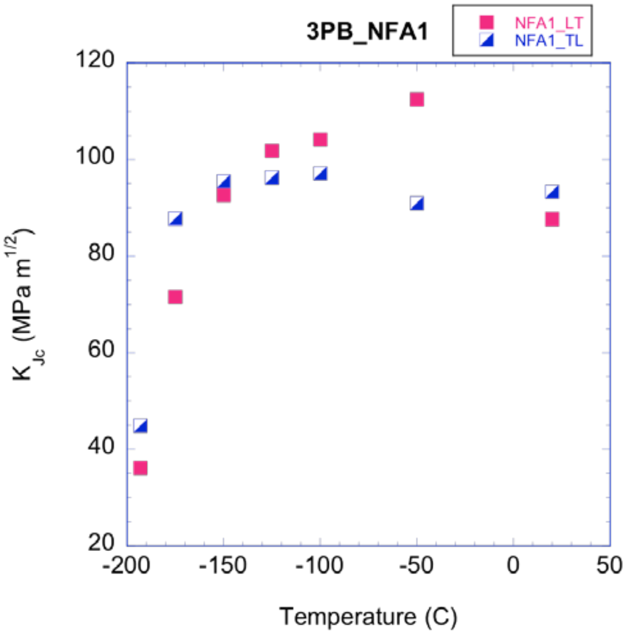

Figure 6. Fracture toughness of FCRD NFA1 as a function of test temperature.

Figure 7 shows the macroscopic view of the fractured surfaces in the two orientations and at various temperatures. The fractured surfaces are dominated by the delaminations (splits) from room temperature down to -150°C (LT) and -175°C (TL) orientation. Shear lips and dimple ductile microvoid coalescence is observed between the delaminations that grow in plane parallel to and out of plane perpendicular to the crack propagation direction. The delamination planes are perpendicular to both the extrusion and cross rolling directions, likely along prior particle boundaries between the broader faces of the compressively deformed powders.

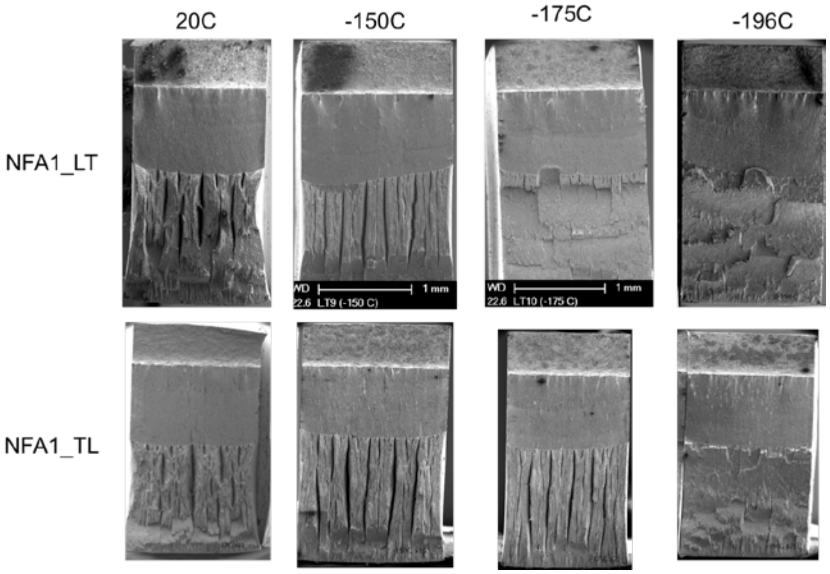

Figure 7. SEM fractographs of NFA1 fracture surfaces both for LT and TL orientations.

These observations provide insight on the reason for the low transition temperature in FCRD NFA-1. The initial lateral triaxial stress component parallel to the crack front is sufficient to cause the delaminations. However once the delaminations occur the lateral stress is relaxed and deformation occurs under plane stress rather than plane strain conditions resulting in a major decrease in the crack tip stress fields and much higher toughness by a ductile rather than a cleavage mechanism. However, at the lowest temperature cleavage initiation occurs before delamination.

Discussion and Summary

We believe that the properties of NFA1 represent a truly extraordinary, and perhaps unique, combination of high strength, ductility and fracture toughness. The high strength is provided by a combination of small grains, high dislocation densities and a very large number of nano-oxide dispersion strengthening features. These properties are remarkably isotropic in the key orientations pertinent to structural performance. Perhaps the most notable property is the fracture toughness with a transition to cleavage fracture at or below ≈ -175°C. Perhaps the main contribution to high toughness is triaxial stress driven delaminations that alter the blunting crack tip stress fields from plain strain to plane stress states. A further beneficial attribute of NFA1 (and other alloys in this class) is its ability to sustain stable crack growth up to very large amounts of deformation. That is cracked structures will be highly ductile, and thus forgiving in service. Further, while the tearing toughness is modest the load capacity of NFA1 will be close to net section limit conditions as governed yield and flow stress constitutive properties. However, it must be emphasized that we have explored mainly low temperature or static properties. Future research will emphasize: a) time-dependent, high temperature properties including creep crack growth; b) development of fully microstructurally informed micormechanical models or NFA deformation and fracture; c) optimization of NFA to further improve their mechanical properties; and, d) detailed evaluation of the advantages and disadvantages of NFA under realistic in service structural applications.

Acknowledgments

This work is part of a multi-laboratory collaboration between LANL, UCSB and ORNL. The DOE Office of Fusion Energy Sciences supported some of the mechanical testing reported here. NFA-1 was produced with the sponsorship of the DOE Office of Nuclear Energy under both a NEUP grant and the FCRD program.

REFERENCES

[1] G.R. Odette, D.T. Hoelzer, “Irradiation-tolerant nanostructured ferritic alloys: Transforming helium from a liability to an asset,” JOM. 62, 84 (2010).
[2] N.J. Cunningham, Y. Wu, G.R. Odette, D.T. Hoelzer, S.A. Maloy, “ Characterization of a larger best practice heat of 14YWT in annealed powder, HIP consolidated and extruded forms,” DOE/ER-0313/54 (2013), DOE Fusion Reactor Materials Program Semiannual Progress Report (2013).
[3] N.J. Cunningham, Y. Wu, G.R. Odette, D. Gragg, K. Field, D.T. Hoelzer, S.A. Maloy, “Characterization of the final precursor alloy to a larger best practice heat of 14YWT,” DOE/ER-0313/53 (2012), DOE Fusion Reactor Materials Program Semiannual Progress Report (2012).

2.6 FRICTION STIR WELDING OF ODS STEELS AND ADVANCED FERRITIC STRUCTURAL STEELS

— Z. Feng, X. Yu, W. Tang, D. Hoelzer, and L.T. Tan (Oak Ridge National Laboratory)

OBJECTIVE

This project aims to address the critical technology gap of joining oxide dispersion strengthened (ODS) steels, nanostructured ferritic alloys (NFAs), reduced-activation ferritic/martensitic (RAFM) steels, and dissimilar metal joining of ODS/NFAs and RAFM steels through friction stir welding technology. The research focuses on understanding the stability of the strengthening phases in the weld region, and the bonding mechanisms between dissimilar structural steels as a function of FSW process conditions.

Specific project objectives are (i) developing the process parameter space to consistently produce defect-free welds of the same and dissimilar metals, (ii) developing the knowledge base and practical applicable approaches to tailor and optimize the microstructure features in the weld to match the properties of the base metal through process innovation, and (iii) producing representative weld joints and welded components to support future testing and evaluation at high temperature and irradiation environments in collaboration with JAEA and other international teams.

SUMMARY

Our research during this reporting period focused on (1) understanding the effects of post-weld heat treatment (PWHT) on the microstructure and property variations in friction stir welds of RAFM steels, (2) developing the PWHT schedule to homogenize and restore the weld properties to match these of base metal, and (3) understanding the effect of the extreme thermal and deformation conditions associated with FSW on the nano oxide strengthening particles in MA956 ODS alloy. Major findings included the development of a PWHT schedule to produce uniform microstructure and a homogeneous hardness distribution in the weld region that is identical to base metal. Initial atom probe maps of FSWed MA956 revealed complete dissolution of the nano oxide particles, which has major implications on the fundamental understanding the stability of nano-oxide particles under extreme thermal-mechanical process conditions, as well as potential solutions to restore the creep strength of the weld region.

PROGRESS AND STATUS

Post-Weld Heat Treatment Study of RAFM FSW

Previously, friction stir welding trials were carried out on two RAFM steels (EUROFER97 and experimental RAFM steel with a composition of Fe-9Cr-1.48W-0.13Ta-0.09C). The as-welded microstructure within stir zone (SZ) and heat-affected zone (HAZ) are distinctively different (Figure 1 (a)-(c)), which led to a highly inhomogeneous distribution of mechanical property, e.g., hardness, within the welds. Due to high hardenability of RAFM steels, the stir zone was predominately martensite with its characteristic higher hardness. Softening was found in the HAZ due to over-tempering of the hardened phases and/or the formation of pre-eutectoid ferrite in the inter-critical region. Post-weld heat treatment (PWHT), which is commonly used for such type of steels, was considered as an option to restore the microstructure and properties in the weld region to these of the base metal. Results from the following three representative PWHT cases are presented.

- Case 1: Tempering at 760°C for 0.5hr followed by air cooling
- Case 2: Tempering at 800°C for 0.5hr followed by air cooling
- Case 3: Normalizing at 980°C for 0.5hr and quench, followed by tempering at 760°C for 0.5hr with air-cooling.

Case 3 represents the typical heat treatment conditions applied to a RAFM steel in producing the optimal high-temperature properties. In the other two cases, PWHT temperature was progressively increased in an attempt to temper the martensite in the stir zone but without re-austenizing the material.

Microstructures of PWHT specimens within the stir zone (SZ), thermo-mechanically affected zone (TMAZ), and HAZ were examined under optical microscope. Hardness mapping was also performed on the cross section of the welds using LM100AT micro-hardness tester, in order to reveal the effect of PWHT on the mechanical property. Sample surface was grinded, polished, and etched with a mixture of 30ml HCl and 10ml HNO_3, to reveal the microstructure and to exam the welding defects.

The microstructure and microhardness of FSWed EUROFER92 are shown in Figures 1 and 2 respectively. The effects of PWHT on the experimental RAFM steel are shown in Figures 3 and 4. First of all, the as-welded microstructures and hardnesses are drastically different from the base metal. Tempering only PWHT (at least for the time duration studied in this performance period) was not able to homogenize the microstructure in the stir zone and the HAZ. On the other hand, applying the heat treatment conditions of the base metal restored the microstructure and hardness to these of the base metal (with some minor variations in EUROFER92 weld). This suggested the advantage of FSW – since no additional materials (filler metal) is used in FSW, the weld region has essentially the same chemistry as the base metal so that it is possible to restore the microstructure and properties of the weld region to these of the base metal through proper heat treatment. This is the primary goal of the project.

In the next few months, additional heat treatment studies and FSW process conditions will be further studied, with the objective of developing effective approaches to tailor and optimize the microstructure features in the weld to match the properties of the base metal.

The restoration of a homogeneous microstructure and microhardness through PWHT forms a sound foundation for further testing the high-temperature mechanical properties of the FSWed RAFM steel and comparing with the base metal properties. Mechanical property testing is planned in the next few months.

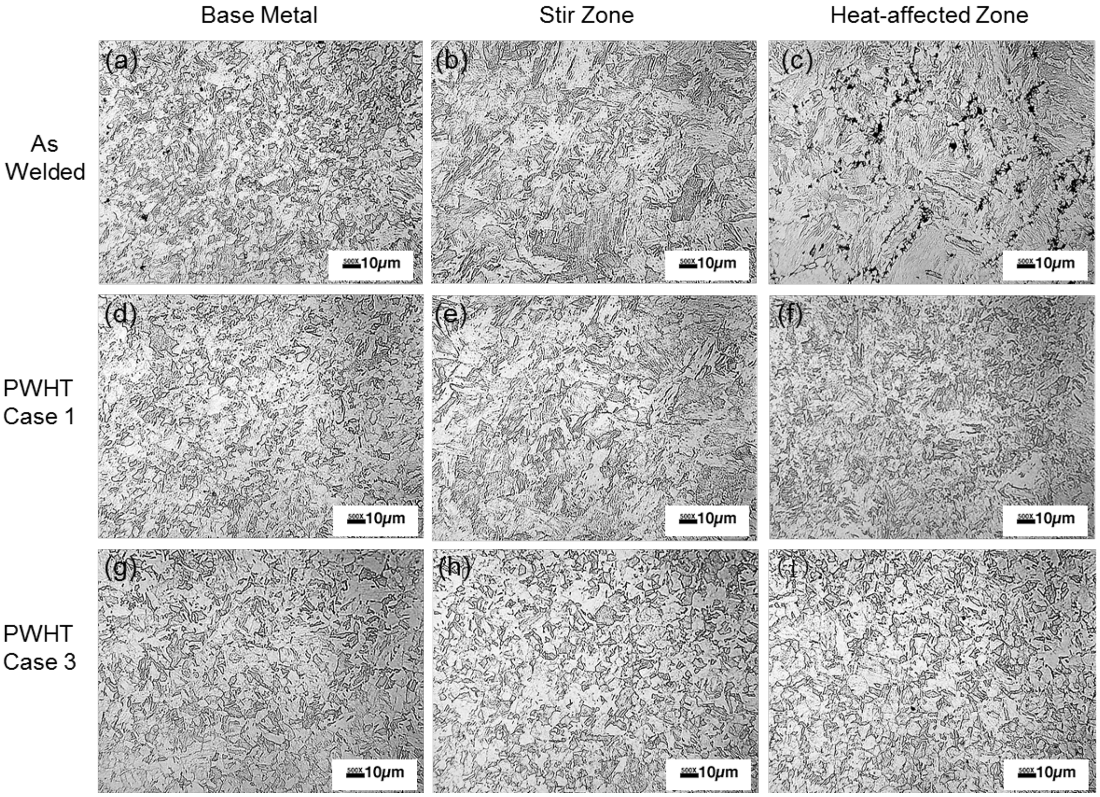

Figure 1. Optical micrographs of the as-welded (a)-(c) and PWHTed EUROFER 97 samples under conditions of Case 1 (d)-(f) and Case (3) (g)-(i) within base metal, stir zone and heat-affected zone, respectively.

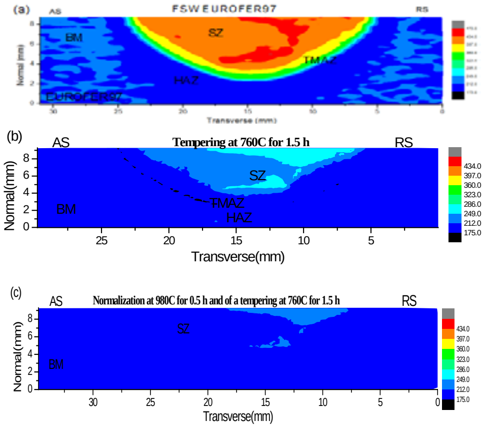

Figure 2. Hardness mappings of the FSW EUROFER97 steel as-welded (a), PWHT Case 1 (b) and 3 (c)

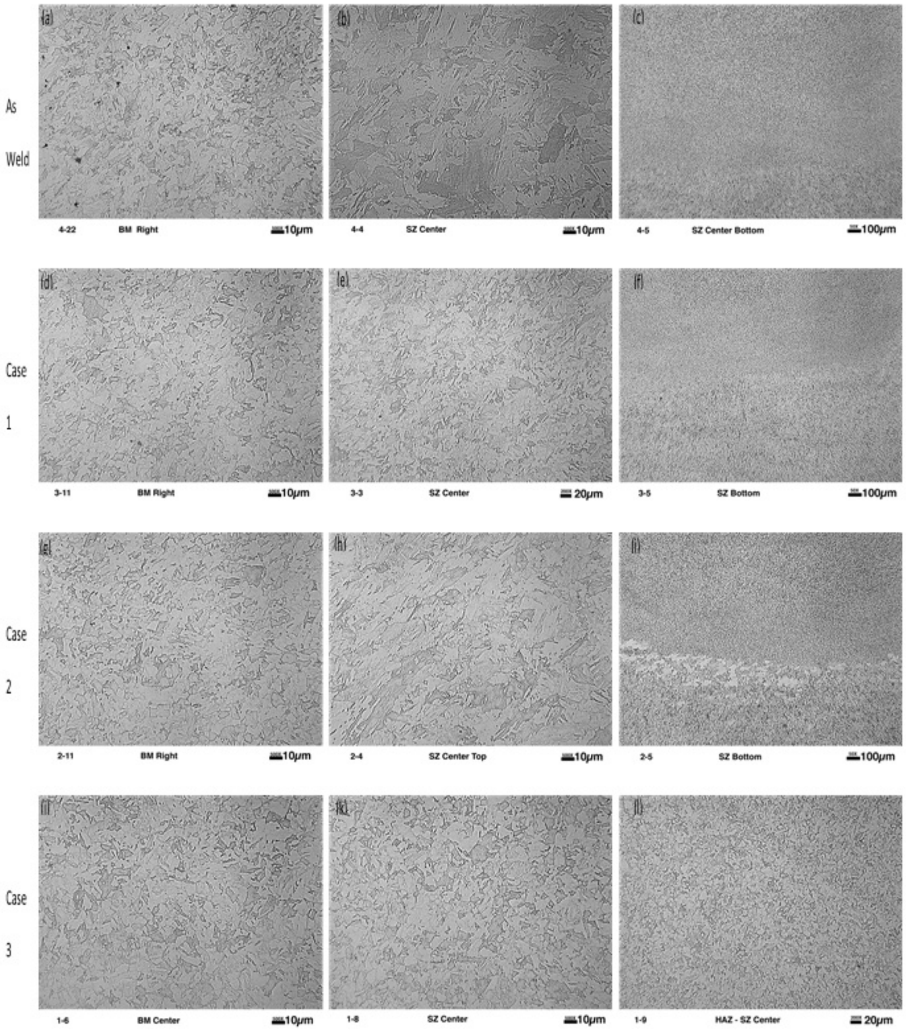

Figure 3. Optical micrographs of the as-welded (a)-(c) and PWHTed experimental RAFM steel samples under conditions of Case 1 (d)-(f) , Case (2) (g)-(i) and Case 3 (j)-(l) within base metal, stir zone respectively.

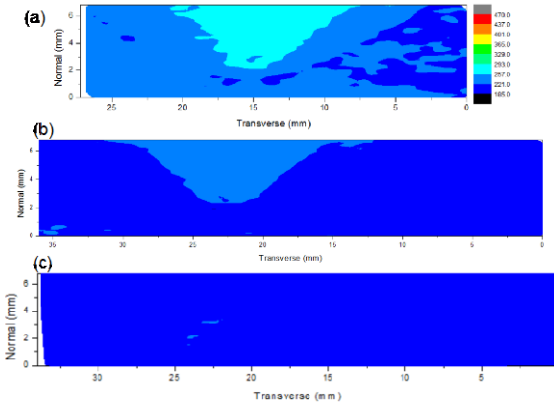

Figure 4. Hardness mappings of the FSWed experimental RAFM steels after PWHT in Cases 1-3 (a)-(c)

Additional FSW welds on RAFM steel for planned mechanical property testing

Additional friction stir welds were made on RAFM steel in this period, using the welding parameters developed which results in defect free welds. These welds are planned for further studying of post weld heat treatment and mechanical property testing. Due to the limited availability of the RAFM steel, the mechanical testing will be on a limited scoping study.

Figure 5 shows the apparent of the FSW made. Note the surface was painted for DIC measurement of stress/strain distribution during welding. Also shown in the figure are the thermocouples used to calibrate the temperature field measurement by Infrared thermography. The strain field during the friction stir welding process is being analyzed and will be corroborated with the temperature field measurement to further our understanding of the FSW process in joining creep resistance materials.

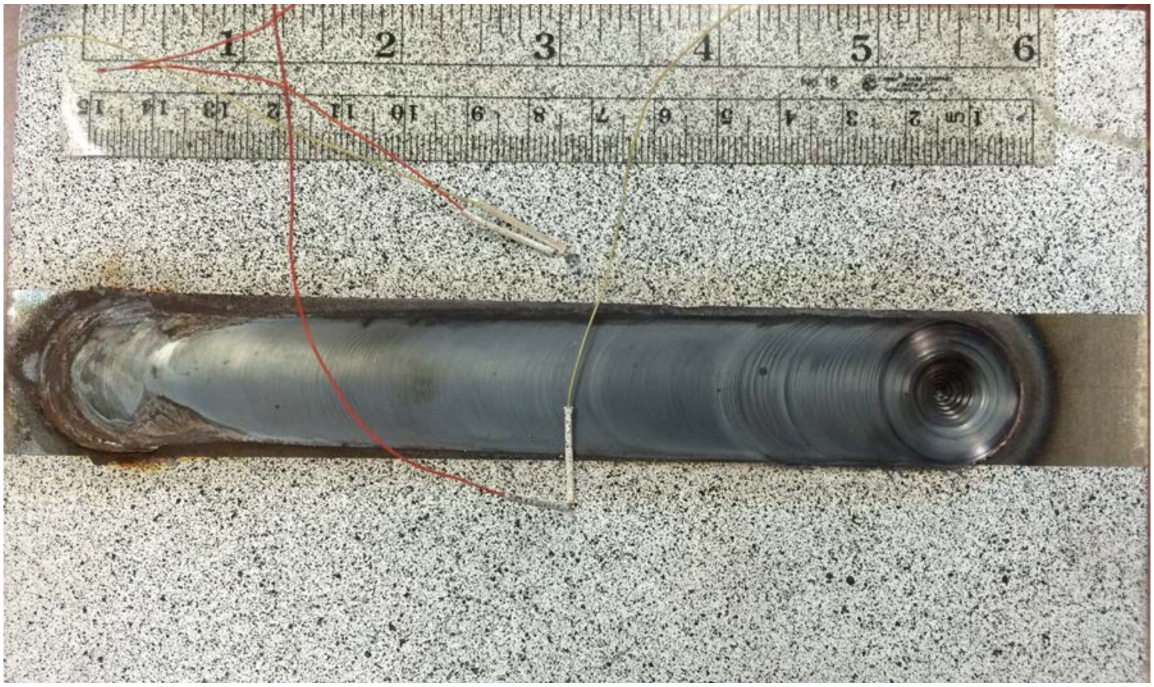

Figure 5. Surface appearance of RAFM FSW.

Characterization of Nano Oxide Particles in MA956 ODS Alloy Friction Stir Weld

As reported previously, defect-free FSW between MA956 ODS alloy and RAFM steels were successfully produced in this project. However, the stir region of MA956 ODS alloy showed considerable reduction of microhardness compared to the base metal. Systematic investigations of the underlying microstructure changes are on-going. Initial atom probe tomography (APT) analysis revealed some very interesting results, as shown in Figure 6 and Figure 7. In Figure 6, the clusters of nano-sized oxide particles are clearly observed in the base metal of MA956. The particles, with size between 10-50 nm, are enriched with in O, Y, and Al. However, as shown in Figure 7, these particles, at least for the regions examined so far, are near completely resolved (or re-solutionized) in the stir zone, as evidenced by no spherical oxide found. It should be noted the absence of Y element in Figure 7. Such absence will be further investigated in the next round of experiment. It is worth noting the absent of Yttrium element in the matrix, which is difficult to comprehend at this moment. Such observations were very different from recent work by others where FSW tends to coarsen the nano particles or nano-features in different ODS alloys. Unlike the coarsening case, the resolution of nano particles is significant in that it offers the possibility to form the nano-particles through appropriate post weld heat treatment. This aspect will be investigated in the next few months.

It is important to recognize that the stability of the nano-particles is dependent on the chemistry and nature of these particles. Other type of nano-particles or nano-clusters such as those in 14YWT ODS alloys which do not have Al may have different stability during FSW. This aspect is being investigated.

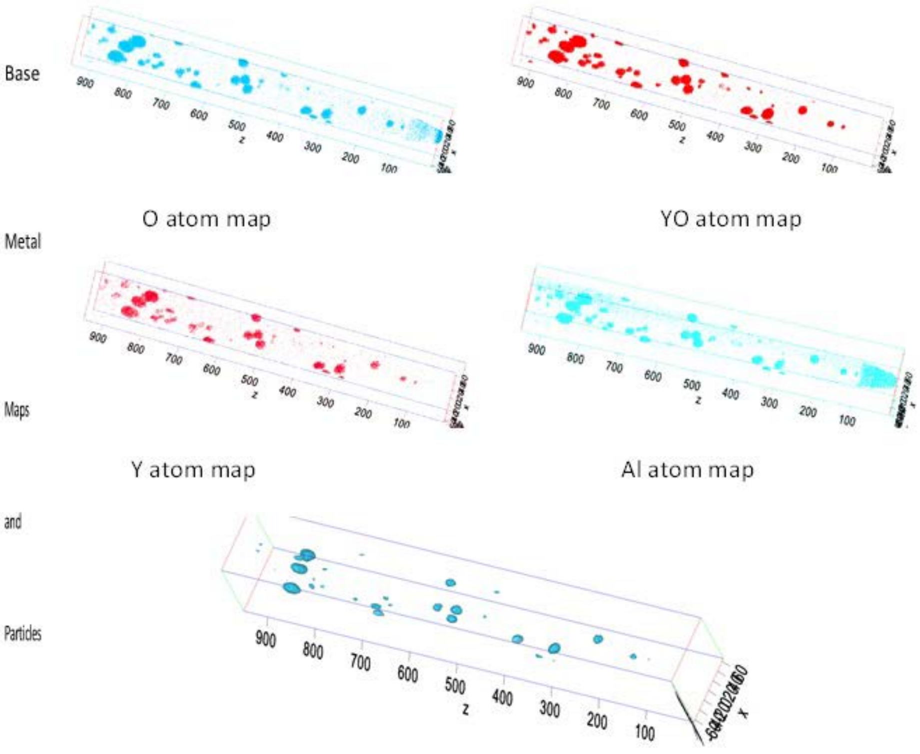

Figure 6. Atom maps and particles distribution in the base metal of ODS steel MA956.

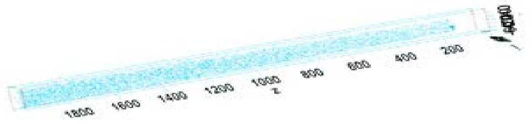

O atom map

Al atom map

Y atom map

C atom map

Figure 7. Atom maps showing the relatively uniform and dispersive distributions of major nano-oxide particle elements in the stir zone of ODS MA956.

Characterization of 14YWT

In ATP analysis of 14YWT, we used 5 at.% Ti iso-concentration surface to characterize nanoclusters since Ti is the major component in these nanoclusters. The result from base metal and stir zone is shown in Figure 7 and Figure 8 respectively. Stir zone shows much coarser nanocluster than base metal. Quantitative analysis on the nanoclusters shows the average radius of nanoclusters in base metal is 1.86 nm, comparing 2.83 nm in stir zone. There are two hypotheses on the coarsening of nanoclusters in stir zone. First, since friction stir welding is a process with high temperature and high deformation, there is a significant amount of vacancies generated in the stir zone during welding. Vacancies generated will accelerate the diffusion by several order of magnitude, which will lead to coarsening of nanoclusters in a very short period of time (several seconds). Second, nanoclusters may dissolve during stirring and re-precipitate during cooling. Vacancy-oxygen has a low bonding energy in steel. Excessive vacancies created by FSW increase the number of vacancy-oxygen and therefore increase the O solubility in steels. As a result, nanoclusters may dissolve during stirring as it was seen in MA956. As the temperature decrease during cooling, number of vacancies decrease. Nanoclusters may re-precipitate.

Synchrotron X-ray diffraction was also performed to characterize secondary phase in 14YWT. Figure 10 shows the comparison result between base metal and weld metal. Since the nanoclusters are very small, current study by X-ray diffraction did not reveal any O enriched nanoclusters. $M_{23}C_6$ carbides, on the other hand, were captured by X-ray diffraction in base metal. X-ray result shows fully dissolution of $M_{23}C_6$ carbides in the stir zone.

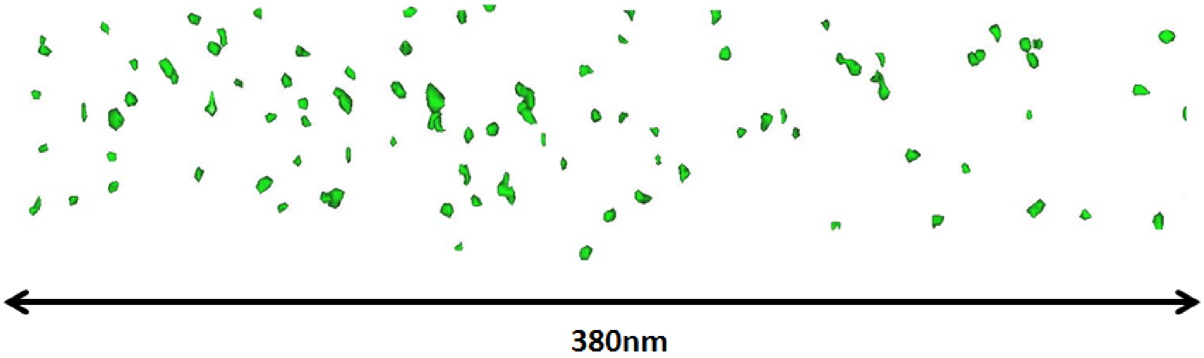

Figure 8. 5 at.% Ti iso-concentration surface of base metal showing nanoclusters enriched with Ti, Y and O

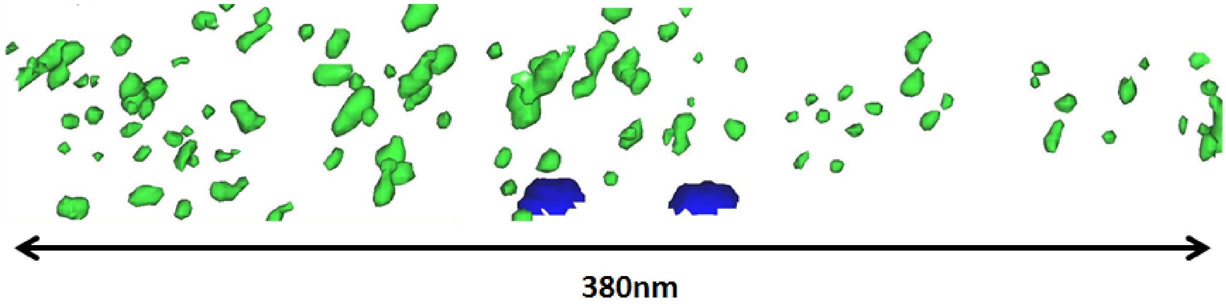

Figure 9. 5 at.% Ti iso-concentration surface of stir zone showing larger precipitates and inhomogeneous distribution

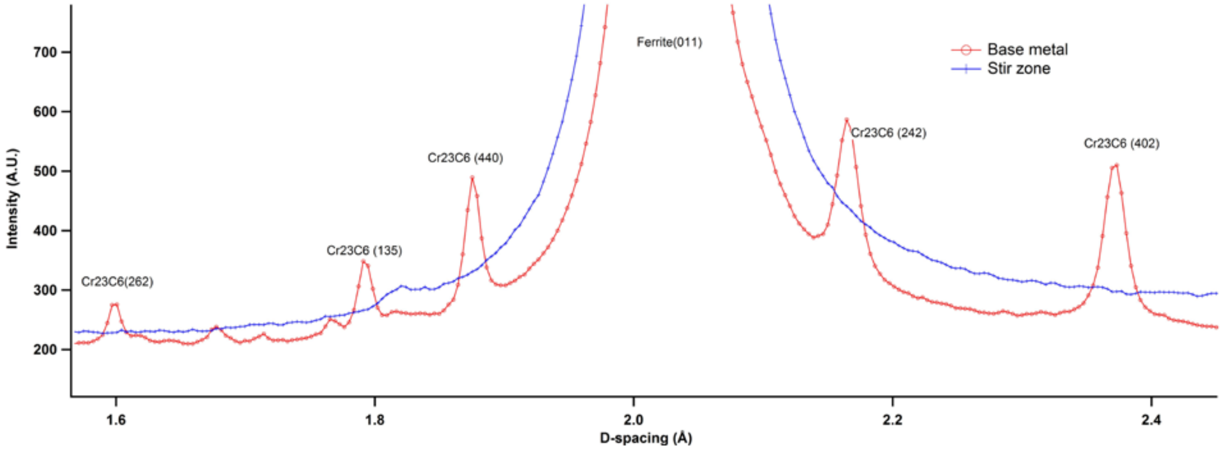

Figure 10. Synchrotron X-ray diffraction results from base metal and stir zone

Future Work

Consistent with the overall project plan, the following major activities are planned for the next 6 months:

- Additional FSW welds on RAFM steels will be produced with fine-tuned welding process conditions to further develop the basic understanding of process-microstructure-property relationship.
- Prepare for mechanical property testing including long-term creep testing, under the as-welded and different PWHT conditions.
- Additional in-situ DIC and IR measurements during FSW to obtain the temperature and stress information during FSW under different process conditions.
- Further APT characterization of nano particles/clusters in the friction stir welded ODS alloys (MA956 and 14YWT) including the effect of post weld heat treatment.
- Continue to investigate the bonding mechanisms between ODS alloys and RAFM steels through detailed microstructure characterization.
- Computation modeling to simulate the temperature and deformation history experience by the ODS and RAFM alloys.

Overall, the project is on schedule, without major technical issues.

REFERENCES

[1] D.T. Hoelzer, K.A. Unocic, M.A. Sokolov, and Z. Feng, "Joining of 14ywt and F82h by Friction Stir Welding," J. Nucl. Mater., 442 (1–3, Supplement 1) (2013) S529-S534.

[2] Z. Yu, Z. Feng, D.T. Hoelzer, L. Tan, M.A. Sokolov, “Friction Stir Welding of ODS Steels and Advanced Ferritic Structural Steels,” ICFRM16, Oct 20-26, 2013, Beijing, China.

[3] D.T. Hoelzer, K.A. Unocic, M.A. Sokolov, and Z. Feng, "Joining of 14ywt and F82h by Friction Stir Welding," ICFRM-15 15th (International Conference on Fusion Reactor Materials), 442, (2013), S529-S534.

[4] Z. Yu, Z. Feng, D.T. Hoelzer, L. Tan, M.A. Sokolov, “Similar and Dissimilar Friction Stir Welding of ODS and RAFM Steels,” TMS Annual Meeting, Feb 16-20, 2014, San Diego, CA.

[5] X. Chen, Z. Yu, and Z. Feng, “FSW of Reduced Activations Steels with PWHT,” Accepted, 10th International Friction Stir Welding Symposium, May 20-22, 2014, Beijing, China.

3.1 LOW ACTIVATION JOINING OF SiC/SiC COMPOSITES FOR FUSION APPLICATIONS: MODELING MINIATURE TORSION TESTS—

C.H. Henager, Jr., B.N. Nguyen, R.J. Kurtz, T. Roosendaal, and B. Borlaug (Pacific Northwest National Laboratory, Richland, WA, USA); M. Ferraris and A. Ventrella (Politecnico di Torino, Torino, Italy); and Y. Katoh (Oak Ridge National Laboratory, Oak Ridge, TN, USA)

OBJECTIVE

The results of torsion shear tests, examinations of joint failures, and mechanics models are presented to rationalize observed torsion test results and to help formulate a path forward with joint testing and analysis for nuclear SiC materials.

SUMMARY

The use of SiC and SiC-composites in fission or fusion environments appears to require joining methods for assembling systems. The international fusion community has designed miniature torsion specimens for joint testing and for irradiation in HFIR. Therefore, miniature torsion joints were fabricated using displacement reactions between Si and TiC to produce Ti_3SiC_2 + SiC joints with CVD-SiC that were tested in shear prior to and after HFIR irradiation. However, these torsion specimens fail out-of-plane, which causes difficulties in determining shear strength for the joints or for comparing unirradiated and irradiated joints. A finite element damage model has been developed that indicates fracture is likely to occur within the joined pieces to cause out-of-plane failures for miniature torsion specimens when a certain modulus and strength ratio between the joint material and the joined material exists. The implications for torsion shear joint data based on this sample design are discussed.

PROGRESS AND STATUS

Introduction

Joining of SiC and SiC-composites has been identified as a critical technology for the use of these materials in either future fusion reactors or in fission power reactors [1-11]. The international fusion materials community is currently irradiating several joint types and compositions in the HFIR reactor at ORNL [1]. PNNL is working with Politecnico di Torino and ORNL using miniature torsion specimens (hourglass samples) that have been specifically designed for pre- and post-irradiation joint shear strength testing (see Figure 1) [12]. The PNNL joints, which are synthesized using displacement reactions between TiC and Si, fail out-of-plane, or in the base CVD-SiC material, during torsion testing. Therefore, this study was undertaken to determine if some simple modifications to the miniature torsion specimen could be used to fix this problem. The first step was to reduce the joined surface area of the torsion samples by dimpling one of the surfaces with either a 2.3 or 3.1-mm diameter dimple using a diamond slurry drill. The samples were fabricated at PNNL and tested at Politecnico di Torino. To elucidate how and where cracks can initiate and propagate in the torsion joint specimens, finite element analyses of these specimens subjected to torsion were performed using a continuum damage mechanics (CDM) model previously developed at PNNL for elastic damage materials [13]. The CDM model was implemented in the ABAQUS® finite element code via user subroutines. Comparative analyses of the torsion joints using ABAQUS® and the damage model were conducted considering typical mechanical properties of CVD-SiC and different mechanical behaviors of the joint material manifested through the assumed stress/strain responses up to failure. Such analyses are very valuable to help understand the conditions for failure in the joint and/or in the CVD-SiC and provide guidance to make improved joints.

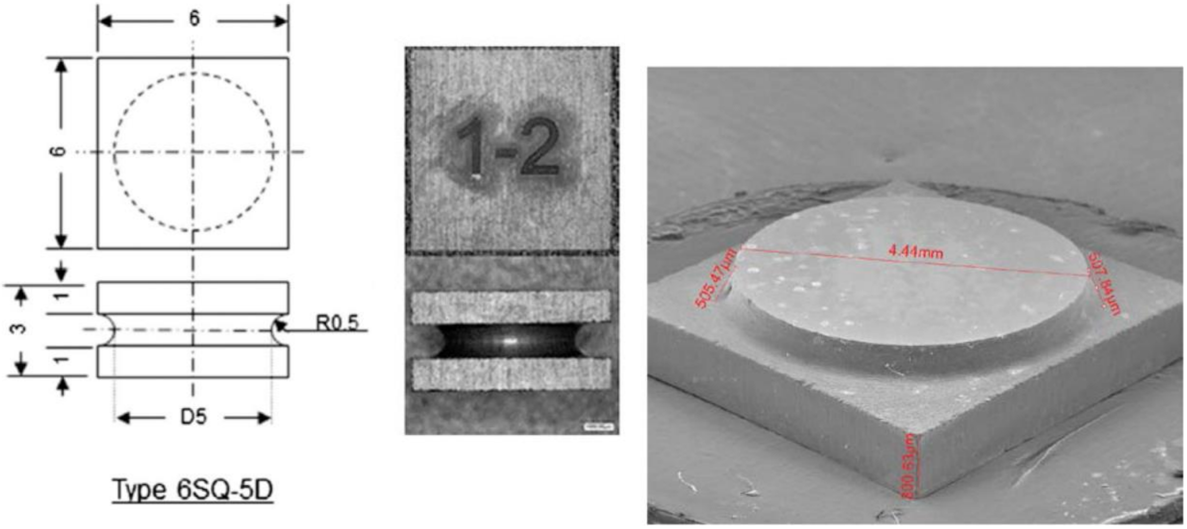

Figure 1. Torsion joint specimen geometries and dimensions (in mm).

Experimental

Joint Synthesis

Strong joints between miniature torsion halves of CVD-SiC were made using solid-state displacement reaction joining methods discussed previously [2, 14, 15]. Joints are processed at 1425˚C (1698 K) for 2h at either 30 or 40 MPa of applied pressure during the 2-hour joining process. Joints were observed to consist of a dual-phase interpenetrating microstructure with SiC-platelets interpenetrating Ti_3SiC_2 particles with about 40% SiC by area fraction analysis. The joints are strongly bonded at the CVD-SiC-Ti_3SiC_2/SiC interface due to the in-growth of SiC from the CVD-SiC during the displacement reaction processing, which is explained by the CVD-SiC surfaces being favorable nucleation sites for the SiC-phase produced during the displacement reaction.

As will be discussed in more detail below, joining pressures of 5, 10, and 20 MPa were also used to produce test samples in addition to the higher pressures of 30 and 40 MPa. Full-bonded joints were made in which the full 5-mm diameter joint half was bonded to produce full-bonded miniature torsion samples at these varying pressures. In addition, circular dimples of 2.3 or 3.1-mm diameter were created in one of the joint halves so that, for these cases, an annular bond was created with correspondingly reduced bonded surface area. These joints, both the reduced joining-pressure joints and the reduced joined-area joints, were created to help troubleshoot test difficulties that were occurring with the miniature torsion joint specimens when joint strength is high.

Joint Microstructures and Porosity

Representative joints synthesized at each of the five joining pressures were cross-sectioned and examined using OM and SEM. The joints were analyzed for porosity content using standard metallography methods of counting separate phases based on contrast differences. Pores in these materials were separated from the dual phase microstructure based on image contrast and the area fraction determined and the information for each type of joint is shown in Table 1. The joint porosity content was then used to compute an effective elastic modulus based on the relation

$$E = E_0 e^{-CV_p} \tag{1}$$

where E is Young's modulus, V_p is volume fraction porosity (area fraction), and C is a constant that is equal to 3.57 for CVD-SiC [16]. Although this equation is used for the joint material Ti_3SiC_2/SiC and C for this material is not known we will use the value of C = 3.57 for these estimates of modulus reduction due to porosity. The dense Young's modulus for the joint material is estimated to be E_0 = 341 GPa and that for dense CVD-SiC is 460 GPa [16]. From Table 1 it can be seen that the effective joint moduli range from 340 for a fully dense joint synthesized at 40 MPa joining pressure to 116 GPa for a 5-MPa joint. These data are plotted in Figure 2 as effective moduli as a function of joining pressure. These data will be more meaningful when the joint fracture model is discussed.

Table 1. Joint Porosity and Effective Modulus Calculations

Joining Pressure (MPa)	Measured Joint Area (%)	Total Porosity (%)	Effective Modulus (GPa)
40	-	0	340
30	99	3	308
20	99	9	248
10	99	24	146
5	99	30	116

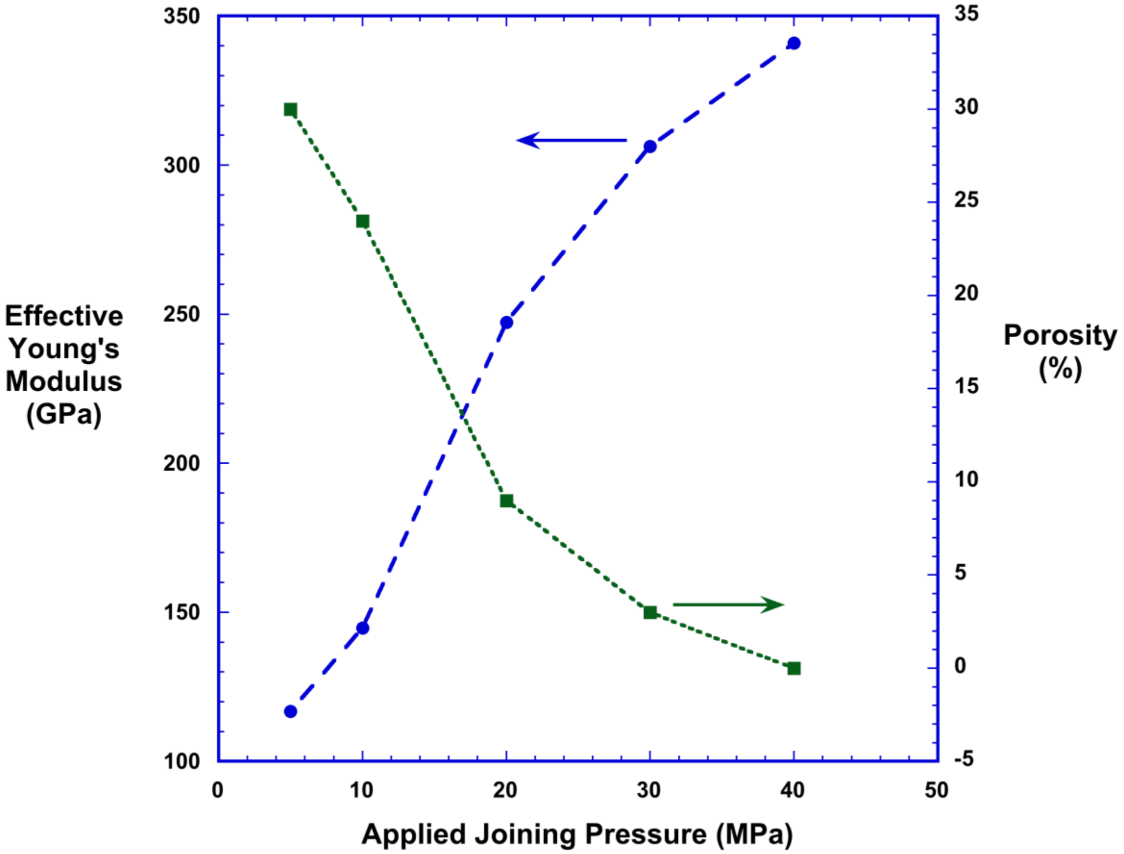

Figure 2. Calculated effective joint modulus as a function of applied joining pressure. The modulus defect occurs due to porosity, which is also shown as a function of joining pressure.

Joint Testing (Politecnico di Torino)

Miniature torsion joint tests were performed at Politecnico di Torino by Prof. M. Ferraris and her co-workers using a universal testing machine (ZWICK 100), where the load was applied until fracture occurred. The torsion load was applied using a rotating disk fixture. The crosshead speed was 0.5 mm/minute with an estimated rotation speed of about 0.010 rad/minute. The torque was obtained using the force measured at specimen fracture. No stress concentration factor caused by the curvature radius was used in this work. Joint failure locations were noted and samples imaged optically and in the SEM after testing. Samples were photographed at PNNL prior to testing in Torino. The torsion test apparatus used in Torino is shown in Figure 3

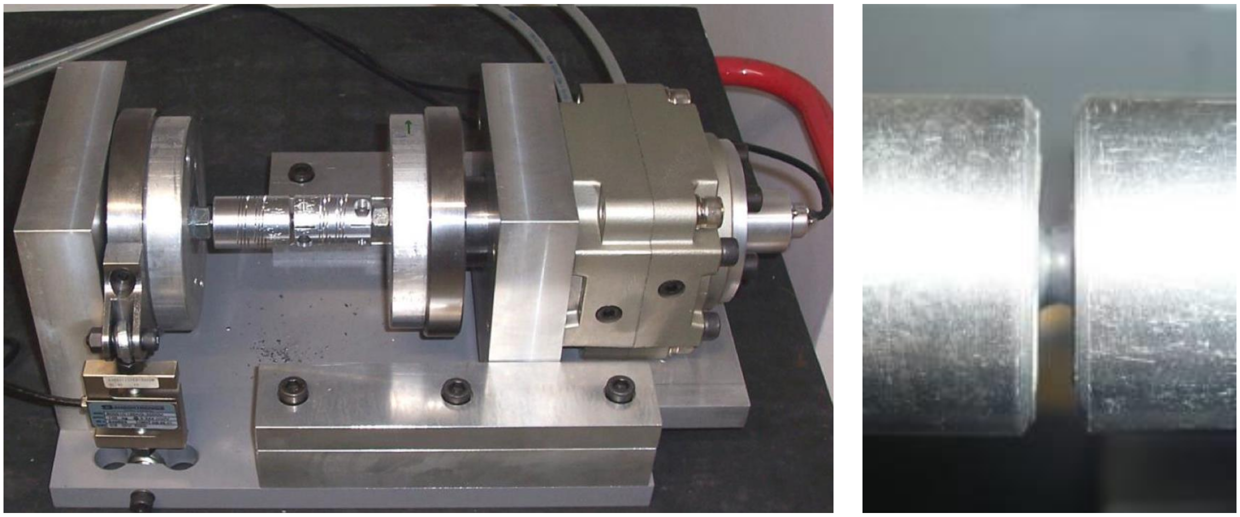

(a) (b)

Figure 3. Torsion testing setup at Politecnico di Torino for the miniature joint testing program. Shown in (a) is the test apparatus and in (b) is a close-up image of a sample in the tester grips prior to testing.

Joints were tested in torsion at ambient temperature and the results are reported in terms of shear strength with notations as to the location of failure or fracture. Joints that fail by shattering the sample, which happens most often, should be considered as having a strength that is better defined as the torsion resistance of these joined structures, and they can be safely used to compare torsional failure resistance of SiC hourglasses joined by several different materials. However, the term shear strength will be used instead of torsion resistance of joined structure for brevity [1]. The shear strength (torsional resistance) is found by using Eq. 2.

$$\tau = \frac{16T}{\pi d^3} \tag{2}$$

where T is the applied torque and d is the diameter of the joined circular region, which is 5 mm for the full bonded joints. For annular bonded joints, or reduced area joints, the following expression is used:

$$\tau = \frac{16T}{\pi(d^3 - d_i^3)} \tag{3}$$

where d_i is the inner annulus diameter.

Table 2 lists the joints that were tested and summarizes the results. Figure 4 is a graph showing some of the results, including some of the unirradiated full-bonded joints tested at ORNL using similar equipment and test parameters as Torino. The full-bonded joints all fail in the base material where the entire sample is failed and, thus, any strength values are considered as torsional resistance values. For the CVD-SiC material and machining condition used in this study this strength value is about 80 to 120 MPa. This is true for the reduced area joints as well and these base material failures typically involve fracture of the entire torsion specimen. Figure 5 shows some sample remnants after such failures.

Table 2. Joint Testing Summary[1]

Joint Type	Pressure (MPa)	Failure Mode	Test Efficiency (Joint/Total)	Shear Strength[2] (MPa)
Full Bonded	40	Base	0/18 (Torino)	~ 80
Full Bonded	40	Base	0/6 (ORNL)	117 ± 10
Full Bonded	30	Base	0/3 (Torino)	83 ± 16
Full Bonded	20	Base	0/3 (Torino)	77 ± 5
Full Bonded	10	Base, Joint	2/3 (Torino)	49 ± 21 (35 ± 10)
Full Bonded	5	Joint	6/6 (Torino)	(37 ± 16)
Reduced (2.3 mm)[3]	40	Base	0/3 (Torino)	70 ± 7
Reduced (3.1 mm)	40	Base	0/2 (Torino)	89 ± 19

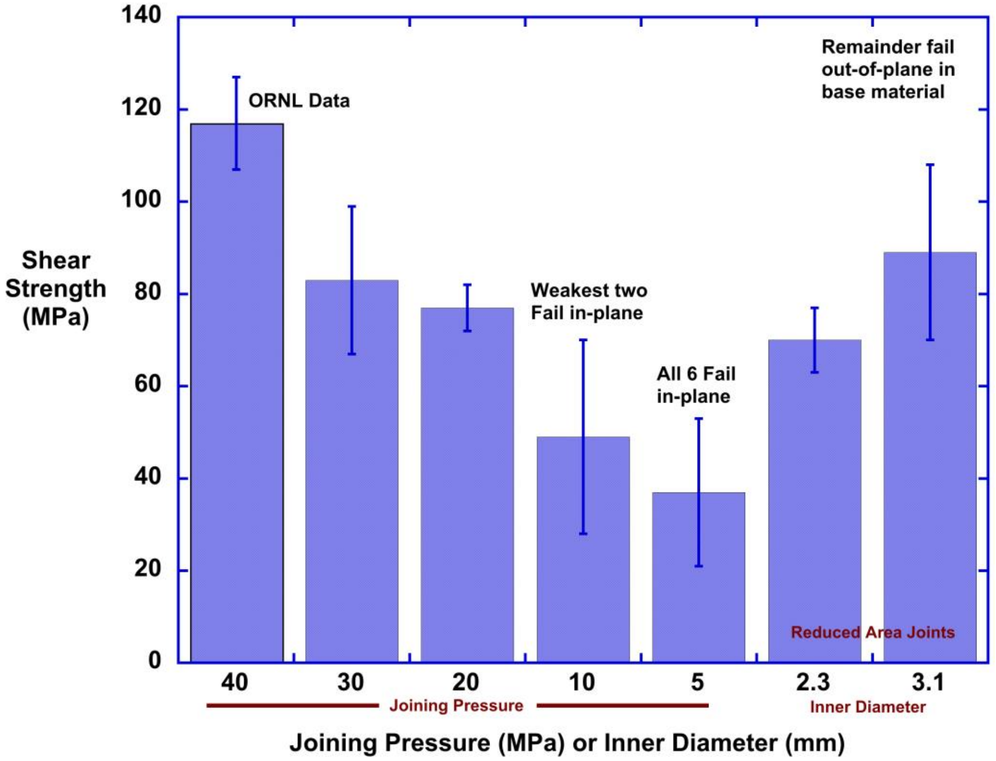

Figure 4. Joint strength data combining ORNL unirradiated dataset with Torino data as a function of joining pressure or inner diameter for reduced joining area joints. All joints processed at 1698 K (1425 ˚C) for 2 h from the same tape cast lot. There is a transition from base to in-plane joint failures between 10 and 5 MPa joining pressure.

For reduced pressure joints it is also observed that base material failures occur for 30 and 20 MPa applied joining pressures. However, for 10 MPa and 5 MPa applied joining pressures there is a transition from base material failure to true shear in-plane joint failures. For 10 MPa pressure this does not always occur and 1 out of 3 joints fail in the base material. For 5 MPa pressure all of the joints fail in-plane and

---

[1] Base refers to fracture of entire sample, Joint refers to fracture in-plane in the joint region. Test efficiency refers to the number of in-plane joint failures (Joint) compared to the total number of tests.

[2] Numbers in parentheses are the true shear strength for in-plane joint failures.

[3] Numbers refer to inner diameter.

have a shear strength of 46 ± 10 MPa. Figure 6 shows a sample of such a failure with joining material bonded to either face of the tested miniature torsion specimen.

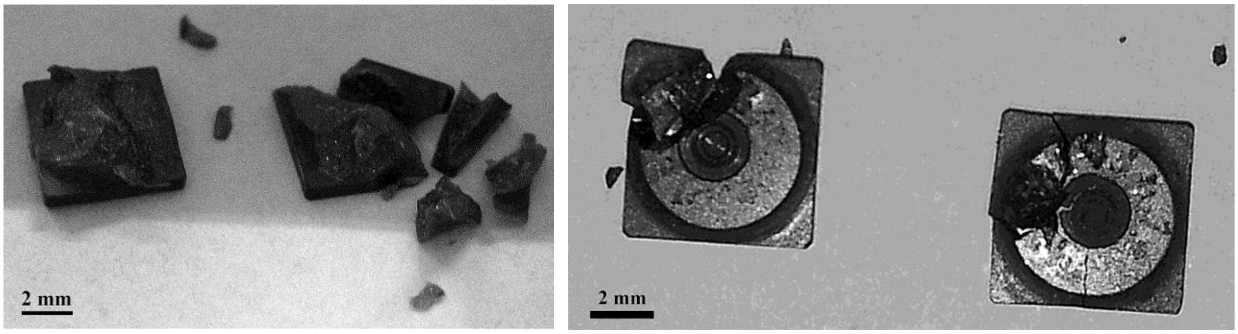

(a) (b)

Figure 5. Optical images of fractured specimens where the fracture is in the base material. Shown in (a) is a full-bonded joint and in (b) is a reduced area joint. Both joints are produced using 30 to 40 MPa of joining pressure that creates a high strength joint. All such failures for tested miniature torsion specimens occur in the base material.

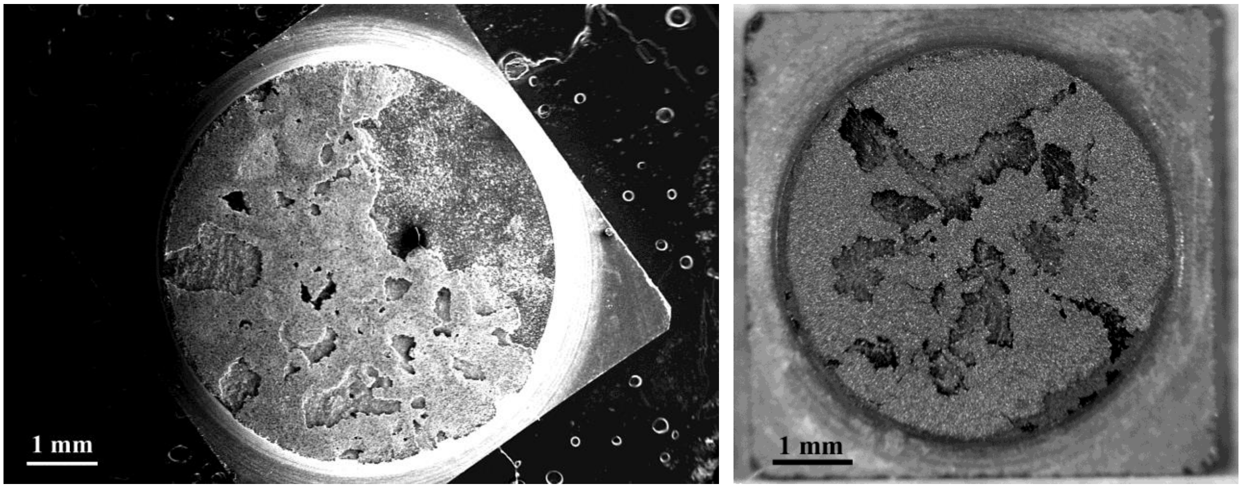

(a) (b)

Figure 6. Torsion fracture surfaces of 5 MPa joining pressure samples. Shown in (a) is an SEM image after testing in Torino showing the in-plane failure mode with joining material residue on surface of tested miniature specimen. In (b) is an optical image of a sample tested at PNNL with similar results.

The experimental data clearly show that weak joints, such as the 5 MPa and some of the 10 MPa reduced joining pressure joints, fail in-plane whereas stronger joints, including those made at 20 MPa joining pressure and higher, only fail in the base material and do not give reliable joint shear strengths. Rather, the torsion strength measured when the base material fails is best described as the torsion shear resistance of the miniature joined specimen [1].

Model Formulation

Approach

$$C_{ijkl} = C_{ijkl}(D) \tag{4}$$

Using the concepts of thermodynamics of continuous media [17, 18], a thermodynamic potential is defined to derive the constitutive relations and the thermodynamic force (conjugate variable) associated with the damage variable. This damage model uses the density of the elastic deformation energy as the thermodynamic potential that provides a coupling between damage and elasticity

$$\Phi(\varepsilon_{ij}, D) = \frac{1}{2} C_{ijkl}(D)\, \varepsilon_{ij} \varepsilon_{kl} \tag{5}$$

From the potential in Eq. 5, the constitutive relations and the thermodynamic force associated with *D* are obtained as

$$\sigma_{ij} = \frac{\partial \Phi(\varepsilon_{ij}, D)}{\partial \varepsilon_{ij}} = C_{ijkl}(D)\, \varepsilon_{kl} \tag{6}$$

$$F = \frac{\partial \Phi(\varepsilon_{ij}, D)}{\partial D} = \frac{1}{2} \frac{\partial C_{ijkl}(D)}{\partial D} \varepsilon_{ij}\, \varepsilon_{kl} \tag{7}$$

where σ_{ij} and ε_{ij} denote the stress and strain tensors, respectively. As damage is an irreversible process, the Clausius-Duhem inequality that expresses the total dissipation must be positive [1]

$$-F.\dot{D} \geq 0 \tag{8}$$

From inequality in Eq. 8, it is clear that if $F < 0$, then $\dot{D} > 0$: damage progresses. If $F \geq 0$ then $\dot{D}$ must be zero, and damage is stable. Finally, using a damage criterion dependent on a damage threshold function, $F_c(D)$

$$f(D) = F_c(D) - F \tag{9}$$

the damage evolution law is obtained by the consistency condition: $f = 0$ and $\mathrm{d}f = 0$

$$\mathrm{d}D = \frac{-\dfrac{\partial C_{ijkl}(D)}{\partial D} \varepsilon_{ij}\, \mathrm{d}\varepsilon_{kl}}{\dfrac{1}{2} \dfrac{\partial^2 C_{ijkl}(D)}{\partial D} \varepsilon_{ij} \varepsilon_{kl} - \dfrac{\partial F_c(D)}{\partial \mathrm{D}}} \tag{10}$$

If the elastic modulus is assumed to be reduced by damage in a linear manner, $E\,(D) = E^0(1 - D)$ with E^0 being the initial elastic modulus, the damage evolution law in Eq. 10 becomes

$$\mathrm{d}D = \frac{\dfrac{\partial C_{ijkl}(D)}{\partial D}\varepsilon_{ij}\,\mathrm{d}\varepsilon_{kl}}{\dfrac{\partial F_{\mathrm{c}}(D)}{\partial \mathrm{D}}} \tag{11}$$

Damage evolves with the deformation according to the damage evolution law until a critical (saturation) state at which $D=D_{\mathrm{cr}}$ $(0< D_{\mathrm{cr}} <1)$ and failure occurs. D_{cr} is small for brittle materials, and this is the case for ceramic materials studied in this work. The occurrence of failure implies that the failed material can no longer carry loads. In this work, failure at damage saturation ($D=D_{\mathrm{cr}}$) leading to crack initiation and propagation is modeled by a vanishing finite element technique [19] that reduces the stiffness and stresses of the failed "integration points" of an element to zero in number of load steps according to the Nguyen et al.'s model [13, 20]

$$\begin{aligned} &n<K: \;\; C_{ijkl}^{\mathrm{failed}} = C_{ijkl}(D_{\mathrm{cr}}) - \frac{nC_{ijkl}(D_{\mathrm{cr}})}{K} \\ &n\geq K: \;\; C_{ijkl}^{\mathrm{failed}} = \alpha_{ijkl} \\ &\sigma_{ij} = C_{ijkl}^{\mathrm{failed}}\,\varepsilon_{kl} \end{aligned} \tag{12}$$

where *n* is the load step number starting from the step at which failure occurs, and *K* is a prescribed constant, which represents the crack resistance of the material. The components of α_{ijkl} are taken to be very small (~10^{-8} MPa) to represent a vanishing stiffness. The patterns of failed elements represent propagated cracks.

Computational Procedure

The damage model was implemented in PNNL's EMTA-NLA tool [21] that functions as a set of user subroutines of ABAQUS®. The *User Material* option of ABAQUS® must be selected for analyses using the damage model. For the execution of the damage model, we must determine a priori the stiffness reduction law, $C_{ijkl}(D)$ in Eq. 4 and the damage threshold function, $F_{\mathrm{c}}(D)$ whose derivatives with respect to the damage variable govern the damage evolution law in Eq. 10. For the materials studied in this work, a linear reduction of the elastic modulus with the damage variable was assumed, and as a result, the stiffness reduction law is directly obtained as:

$$C_{ijkl} = C_{ijkl}^{0}(1-D) \tag{13}$$

where C_{ijkl}^{0} denotes the initial elastic stiffness tensor of the undamaged material. $C_{ijkl}(D)$ can generally have a more complex expression than the simple linear relationship. For materials with distributed damage like microcracks, $C_{ijkl}(D)$ can be determined via micromechanical modeling. The damage threshold function $F_{\mathrm{c}}(D)$ can be discretely computed for the damage variable values in the [0, D_{cr}] interval by means of the thermodynamic force associated with the damage variable in Eq. 9 and the uniaxial stress/strain data. The increment of the damage variable is computed in term strains and strain increments using the damage evolution law to update the damage variable for the current loading. Next, the current stresses are computed using the constitutive relations. Damage can evolve with the deformation until reaching the saturation state characterized by $D=D_{\mathrm{cr}}$ and at which failure is predicted to occur. Failure is modeled by the finite element vanishing technique associated with the failure model described in the previous section in Eq. 12.

Results

Model Results

The damage model was used in the ABAQUS® finite element analysis of the torsion joint specimens shown in Figure1 In order to investigate the specimen failure including conditions for crack initiation and propagation for different types of joints ranging from much stronger to much weaker than the CVD-SiC, different mechanical behaviors of the joint were considered and were reflected through the assumed stress/strain responses up to failure. In addition, typical mechanical properties of CVD-SiC in the experimentally observed range were assumed. Figure 7 and Table 3 present all the mechanical properties assumed in this parametric study. There are 3 different behaviors (named 1, 2, and 3) considered for the Ti_3SiC_2/SiC composite. In addition, the analysis was also performed for an epoxy joint specimen. The damage variable value at saturation was taken to be 0.2 for all the ceramics while it was considered to be 0.4 for the epoxy leading to the epoxy strength of 120 MPa and failure strain of 0.02 that are achievable values for a structural epoxy.

Table 3. Mechanical properties of the CVD-SiC and joint material assumed for the analysis.

Material	Elastic Modulus (GPa)	Poisson Ratio	Strength (MPa)	Failure Strain	Damage Variable Critical Value
CVD-SiC	**460**	**0.2**	**368**	**0.001**	**0.2**
Ti_3SiC_2/SiC (1)	**380**	**0.2**	**608**	**0.002**	**0.2**
Ti_3SiC_2/SiC (2)	**200**	**0.2**	**320**	**0.002**	**0.2**
Ti_3SiC_2/SiC (3)	**100**	**0.2**	**160**	**0.002**	**0.2**
Epoxy	**10**	**0.3**	**120**	**0.02**	**0.4**

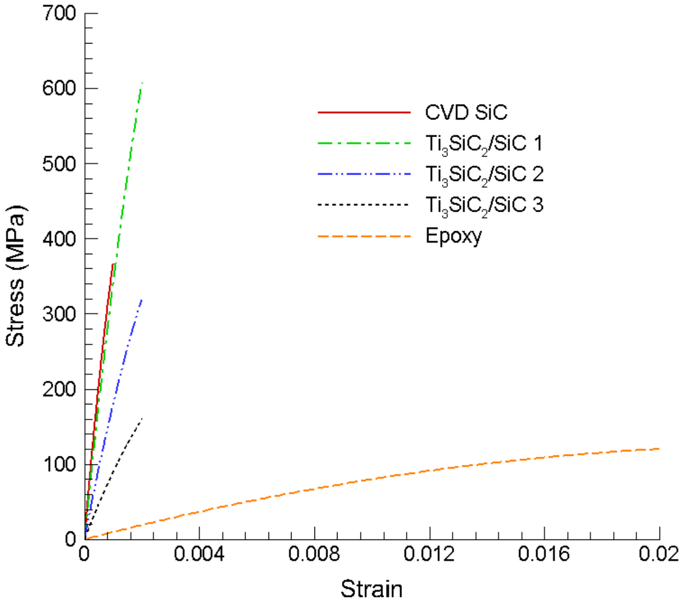

Figure 7. Uniaxial stress/strain responses considered for the CVD-SiC and different types of joint material.

Figure 8 shows the three-dimensional (3D) finite element model with assigned material behaviors for the analysis of the torsion joint specimen illustrated in Figure 1 The joint was 10 microns thick and finely discretized. The top and bottom regions of the specimen were modeled assuming elastic CVD-SiC material while the central region includes the elastic damage CVD-SiC parts joined by an elastic damage Ti_3SiC_2/SiC layer. The bottom surface of the specimen was completely fixed (zero-displacements and zero-rotations). Zero-normal displacement and uniform rotation about the specimen vertical axis were imposed on the top surface to achieve the torsion loading about this axis.

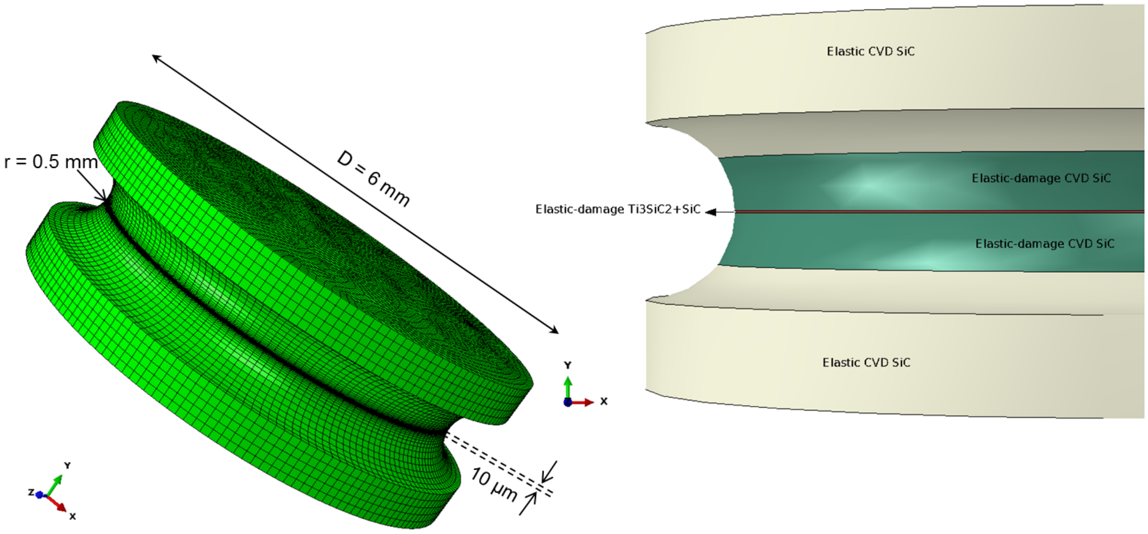

Figure 8. 3D finite element model for the torsion joint specimen with assigned material behaviors.

Figure 9 (a) shows the damage distribution (contour of the damage variable) in the specimen with the Ti_3SiC_2/SiC (1) joint at the initiation of fracture that happened at the neck. This joint material is less stiff but is much stronger than the CVD-SiC (Table 3). Failure occurred when the damage attained the critical value. A close examination of the fracture initiation region (Figure 9 (b)) reveals that fracture occurred in the CVD-SiC and did not happen in the joint where the values of the damage variable were well below the critical value. (Figure 10) shows an advanced state of fracture where the failed regions extended deeper in the CVD-SiC joined materials. The predicted fracture location agrees well with the experimental fracture observation for this type of very strong joint that exhibits out of plane fracture.

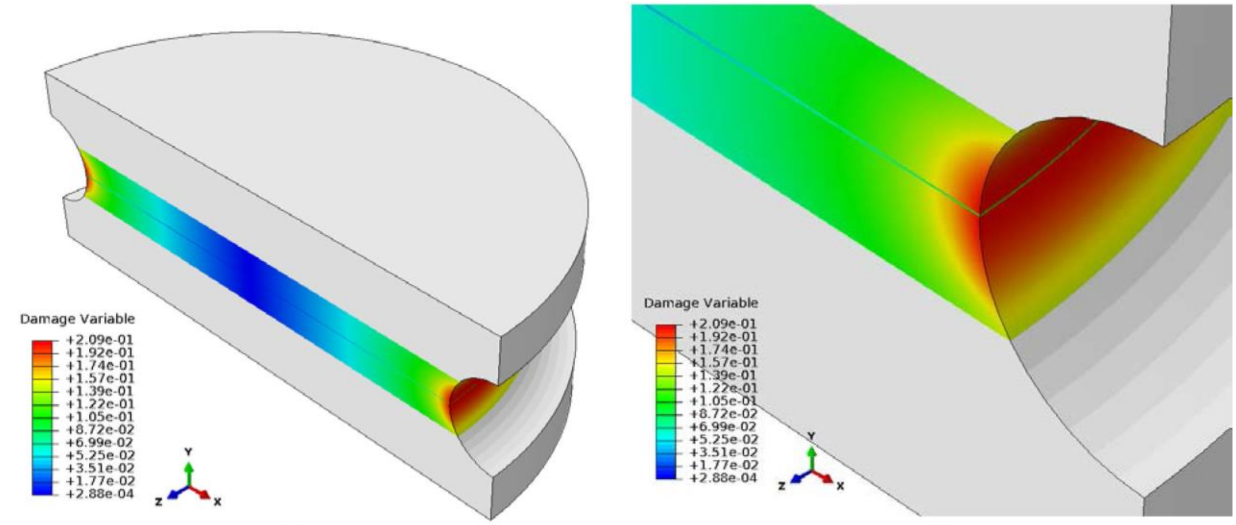

(a) (b)

Figure 9. (a) Damage accumulation at fracture initiation in the specimen with Ti_3SiC_2/SiC (1) joint, (b) a snapshot showing fracture initiation at the neck and in the CVD-SiC joined materials.

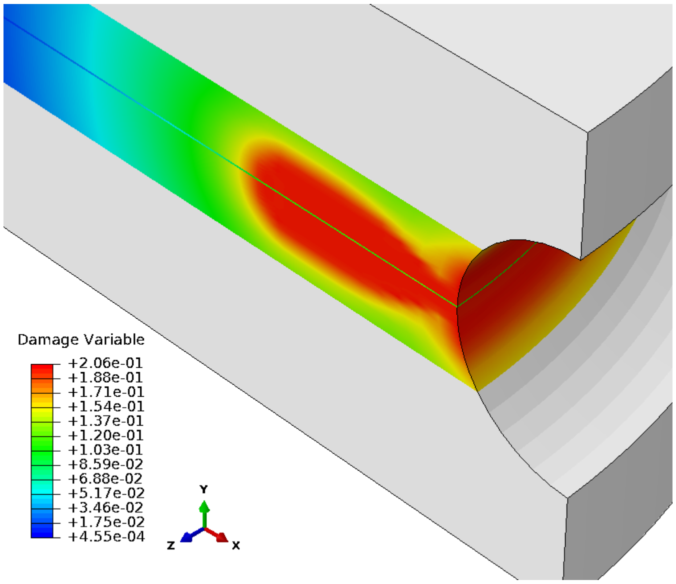

Figure 10. Predicted advanced state of damage and fracture showing failure of the joined CVD-SiC materials occurring in the base material due to damage accumulation within the CVD-SiC.

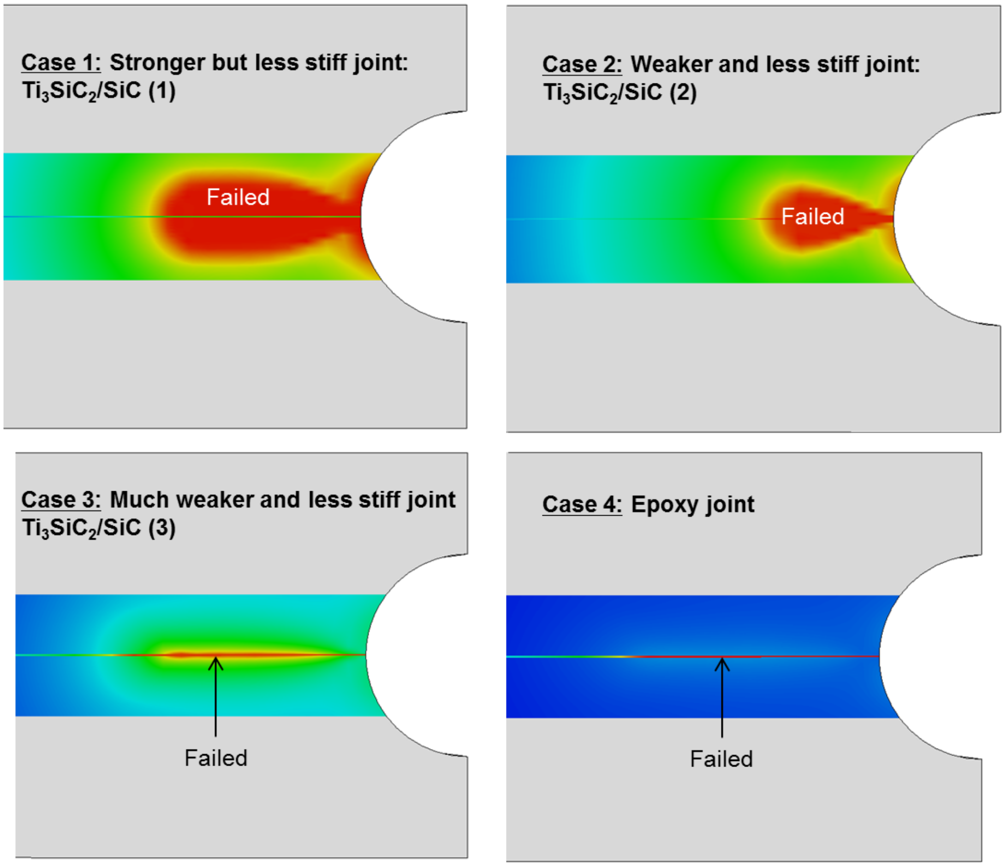

Figure 11. Predicted fracture patterns (red regions) for the torsion joint specimens made of different joint materials with mechanical properties listed in Table 3.

Similar analyses were conducted for the torsion joint specimens made of the materials listed in Table 3. The predicted failure patterns for all the studied cases are gathered in Figure 11 Case 1 for the Ti_3SiC_2/SiC (1) joint has been discussed above. Case 2 is related to the Ti_3SiC_2/SiC (2) joint that is weaker and less stiff than the joined CVD SiC materials. For Case 2, failure is predicted to initiate in the joint but then develop into the joined materials resulting in out-of-plan failure. Case 3 for the Ti_3SiC_2/SiC (3) joint that is much weaker and less stiff than the CDV-SiC develops in-plane failure. The epoxy joint (Case 4) also exhibits in-plane failure. The results illustrated in Figure 11 suggests that there is a joint-to-CVD SiC modulus and/or strength ratio below which the fracture mode switches from out-of-plane failure to in-plane failure.

Figure 12 shows the predicted evolutions of the maximum shear stresses at the neck of the specimen and in a plane perpendicular to the specimen vertical axis for all the cases studied in this work. The maximum shear stress is highest (104 MPa) for the specimen with the Ti_3SiC_2/SiC (1) joint (Case 1).

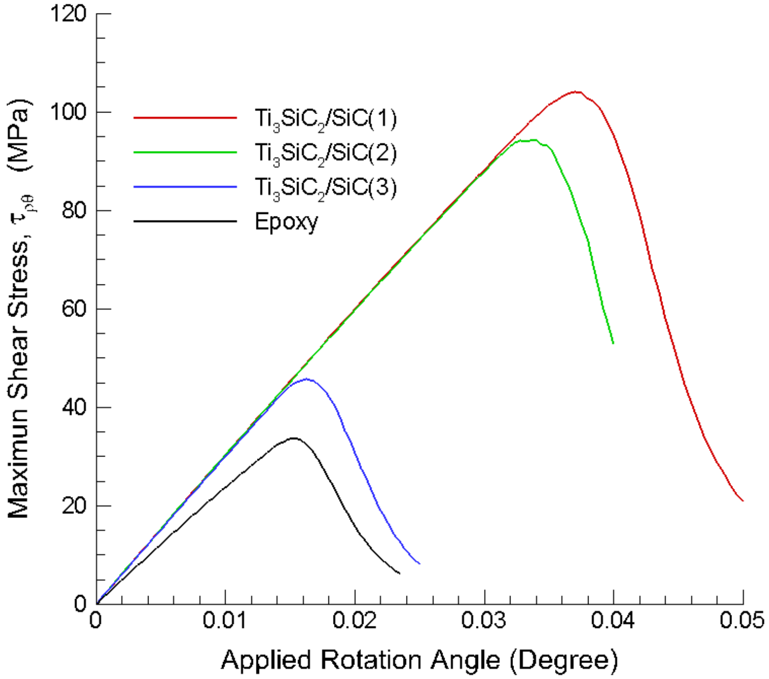

Figure 12. Predicted evolution of the maximum in-plane shear stresses with the applied rotation angle for the material cases studied here and shown in Table 3.

Discussion

Model Predictions and Comparisons

The damage model was created to be able to help understand the fracture results from the miniature torsion specimens that clearly exhibited a transition from planar to non-planar fracture (joint to base material fracture). A critical part of the damage model was to be able to model the stress-strain curves for the constitutive materials. The curves shown in Figure 7 using the data in Table 3 are very reasonable assumptions for this approach and capture the material elastic constants as well as the failure strengths. The accuracy of the model is then predicated on the accuracy of the stress-strain data and, even though this model data is not completely precise, the expected results from carefully applying the model are expected to show the desired effects. Namely, is there a transition from planar to non-planar fracture for a range of elastic moduli and strength values? Intuitively it is anticipated that low modulus epoxy will behave much differently compared to high modulus Ti_3SiC_2/SiC in terms of load sharing with the CVD-SiC base material. In fact, one thought (gedanken) experiment at the extreme of this type of thinking is to imagine the entire miniature torsion specimen machined from a single piece of CVD-SiC and then to try to predict where it will fail. Probabilistic brittle fracture mechanics tells us that it will fail somewhere in the specimen that contains a combination of the largest flaw and the highest tensile stresses, which will not necessarily coincide with the central plane of the torsion specimen. Thus, a high strength, high modulus joint may not either. As is shown in Figure 11 load sharing with the CVD-SiC forces the highest damage to occur within the base CVD-SiC material and failure is predicted to occur out-of-plane of the joint.

The model predicts a high degree of load sharing and CVD-SiC damage for a joint modulus greater than about 200 GPa and a minimal amount of load sharing with highly localized (planar) fracture for moduli 100 GPa and lower (Figure 10). This is in good agreement with the observed experimental data for the joints tested at Torino. In addition, the predicted failure strengths in shear match quite well with measurements from ORNL and Torino. The ORNL data for the unirradiated Ti_3SiC_2/SiC joints indicated a torsional shear resistance value of 117 GPa ± 10 GPa, which agrees well with the model data of 104 GPa. The epoxy joined data from Politecnico di Torino indicates shear fracture strength of 36 MPa, which agrees well with the model prediction of about 35 GPa[4]. In fact, this is a great strength of the model that predicts quite accurate shear strength failures for CVD-SiC based on assumed tensile stress-strain data.

Data Interpretation and Torsion Test Future

Since the model predicts that high strength, high modulus joints will likely not fail in such a manner as to provide a true shear strength for the joints then an obvious point of discussion is what to make of the miniature torsion test? First, the miniature torsion specimen is ideal for in-reactor experiments and will still provide a vehicle for obtaining valuable microstructural evolution data for experimental joints for fusion. The specimen can still help us deal with both microstructural evolution leading to differential strains, environmental exposures, and radiation damage differentials. This became clear in the HFIR data recently obtained at ORNL [1].

Second, changes in joint strength or moduli due to radiation damage can still be revealed during post-irradiation joint testing. It is worth noting that the Ti_3SiC_2/SiC joints survived after 800˚C (1073 K) and 5 dpa but that the torsion shear failure location changed from base material failure to in-plane joint failure as noted in Ref. [1]. This suggests that a major change had occurred in the joined specimens and post-irradiation microscopy revealed a degree of interface cracking and microcracking within the joint material. This is thought to be due to either thermal expansion or swelling mismatches between the joint material and the CVD-SiC. Thus, both shear strength and shear failure location can be used to help understand joining for fusion materials. The role of the model in this understanding can be to guide experimental data interpretation by allowing various parameters to be controlled and varied. It is important to realize that many of these parameters can also be independently quantified so that the model can be refined as needed.

The HFIR results from ORNL also display a failure mechanism that was not included in the model yet, namely, the failure of the joint/CVD-SiC interface. The model here assumed a strongly bonded interface between the joint and CVD-SiC and there was no evolution of that bond allowed. Future model implementations will treat the interface as a separate material region with an identifiable strength.

Future Work

The model will be improved to treat joint/base material interfaces and model parameters will be adjusted to match more closely to experimental mechanical property data. Torino has performed several calibration studies of the miniature torsion specimens and this calibration data will be shared with PNNL so that the model can be improved accordingly.

Acknowledgments

This research was supported by Office of Fusion Energy Sciences, U.S. Department of Energy (DOE) under Contract DE-AC05-76RL01830.

REFERENCES

[1] Y. Katoh, L. L. Snead, T. Cheng, C. Shih, W. D. Lewis, T. Koyanagi, T. Hinoki, C. H. Henager Jr, and M. Ferraris, J. Nucl. Mater., 448 (1-3) (2014) 497.

[2] C. H. Henager Jr. and R. J. Kurtz, J. Nucl. Mater. 417 (1-3) (2011) 375.

[3] M. Ferraris, M. Salvo, V. Casalegno, S. Han, Y. Katoh, H. C. Jung, T. Hinoki, and A. Kohyama, J. Nucl. Mater., 417 (1-3) (2011) 379.

[4] C. H. Henager Jr., Y. Shin, Y. Blum, L. A. Giannuzzi, B. W. Kempshall, and S. M. Schwarz, J. Nucl. Mater., 367-370(1) (2007) 1139.

---

[4] Personal Communication from Prof. M. Ferraris of Politecnico di Torino. They used AV119 Epoxy with an elastic modulus of 2.8 GPa and Poisson ratio of 0.4. They obtained accurate, in-plane shear failures for all tests and a shear strength of 36 MPa ± 8 MPa.

[5] B. Riccardi, C. A. Nannetti, T. Petrisor, J. Woltersdorf, E. Pippel, S. Libera, and L. Pilloni, J. Nucl. Mater. 329-333 (2004) 562.
[6] M. Ferraris, P. Appendino, V. Casalegno, F. Smeacetto, and M. Salvo, Adv. Sci. technol. 33 (2003) 141.
[7] C. A. Lewinsohn, M. Singh, T. Shibayama, T. Hinoki, M. Ando, Y. Katoh, and A. Kohyama, J. Nucl. Mater. 283-287B (2000) 1258.
[8] P. Colombo, B. Riccardi, A. Donato, and G. Scarinci, J. Nucl. Mater. 278(2) (2000) 127.
[9] P. Colombo, V. Sglavo, E. Pippel, and J. Woltersdorf, J. Mater. Sci. 33(9) (1998) 2405.
[10] R. H. Jones and C.H. Henager Jr, J. Nucl. Mater. 26-36 (1996) 233.
[11] M. Ferraris, C. Badini, M. Montorsi, P. Appendino, and H. W. Scholz, J. Nucl. Mater. 212-1(pt B) (1994) 1613.
[12] H.-C. Jung, T. Hinoki, Y. Katoh, and A. Kohyama, J. Nucl. Mater. 417(1-3) (2011) 383.
[13] B. N. Nguyen, B. J. Koeppel, S. Ahzi, M. A. Khaleel, and P. Singh, J. Am. Ceram. Soc. 89(4) (2006) 1358.
[14] C. H. Henager, J., R. J. Kurtz, N. L. Canfield, Y. Shin, W. G. Luscher, J. T. Mansurov, T. J. Roosendaal, and B. A. Borlaug, Fusion Reactor Materials Program Semiannual Progress Reports for Period Ending December 31, 2013, DOE/ER00313/55, U.S. Department of Energy, 23.
[15] C. H. Henager Jr., R. Kurtz, and M. Ferraris, Fusion Reactor Materials Program Semiannual Progress Report for Period Ending December 31, 2010, DOE/ER00313/49, U.S. Department of Energy, 25.
[16] L. L Snead, T. Nozawa, Y. Katoh, T.-S. Byun, S. Kondo, and D. A. Petti, J. Nucl. Mater. 371(1-3) (2007) 329.
[17] J. Lemaitre and J. L. Chaboche, Journal de Mecanique Appliquee, 2(3) (1978) 317.
[18] G. A. Maugin, The Thermomechanics of Plasticity and Fracture (Cambridge University Press, Cambridge, UK, 1992).
[19] V. Tvergaard, Int. J. Fract. 31 (1986) 183.
[20] B. N. Nguyen, V. Kunc, J. H. Phelps, C. L. Tucker III, and S. K. Bapanapalli, J. Compos. Mater. 43(3) (2009) 217.
[21] B. N. Nguyen, EMTA User’s Guide, PNNL-19997 (Pacific Northwest National Laboratory, Richland, WA, 2010).

3.2 PROCESS DEVELOPMENT AND OPTIMIZATION FOR SILICON CARBIDE JOINING AND IRRADIATION STUDIES-IV— Takaaki Koyanagi, James Kiggans, Chunghao Shih, Yutai Katoh (Oak Ridge National Laboratory)

OBJECTIVE

The objective of this task is to develop and optimize joining processes for silicon carbide (SiC) ceramics and its composites for fusion energy applications.

SUMMARY

Processing and characterization of SiC ceramics joined by the pressureless transient eutectic-phase (PL-TEP) method were conducted. Apparent shear strengths of ~100 MPa was demonstrated by torsion test on the PL-TEP joint formed with SiC nano-powder, oxide additives, and organic agents. The fracture behavior was typical of robust joints. In addition, the joints are expected to have high densities based on sintered densities of monolithic SiC representing the PL-TEP joint layer. Irradiation of SiC joints made with different bonding materials is being conducted in HFIR.

PROGRESS AND STATUS

Introduction

The development of SiC joints that retain adequate mechanical and functional properties in a fusion reactor environment is essential for the use of SiC and its composites as the primary structural material [1]. Effects of neutron irradiation on the material performance are among the most critical factors in a fusion reactor environment. TEP method, which is a specific type of liquid phase sintering, is one of the fabrication routes used to obtain dense and radiation-resistant SiC-matrix composites [2, 3]. The TEP process involves the use of SiC nano-powder and a reduced amount of sintering additives such as the yttrium-alumina system. The TEP process is also used to join SiC ceramics [4].TEP joining is attractive for nuclear application because this joining method can provide SiC base joint layer with dense microstructures, high strengths, and expected irradiation tolerance. In fact, a pressurized TEP process was used to join SiC materials, and the excellent irradiation-tolerance and adequate shear strength was demonstrated following neutron irradiation at low to intermediate fluence [5]. However, requirement of the external pressure during heat treatment is a major factor that dictates applicability of a specific joining method to integration of components with large sizes and complex geometries. To overcome this problem, previous work demonstrated feasibility of robust PL-TEP joining without the use of loads during heat treatment [6]. Present work presents processing and characterization of PL-TEP joints to optimize the processing.

This report also provides current progress of the neutron irradiation experiments in HFIR.

Experimental Procedure

Materials

The PL-TEP joints were formed using the powder mixtures consisting of SiC nano-powder (average diameters ~30 nm) or combined SiC nano- and micron-powders, and sintering additives (Al_2O_3 powder and Y_2O_3 powder), with or without organic agents such as Polyvinylpyrrolidone (PVP) and acrawax. The total amount of the oxide additives was 6 or 10 wt.%. The total amount of the organic agents was ~3.5 wt.%. The PL-TEP joints were formed by sandwiching mixed powder between chemical vapor deposited (CVD) plates followed by cold-pressing at ~10 MPa in graphite die to partially densify the powder. The sandwiched materials were then heat-treated at 1875^{o}C for 1 h in a flowing argon atmosphere in the graphite die without external loading. The dimension of the pair of CVD SiC plates was 21.0 mm (w) ×

31.2 cm (l) × 6.2 mm (t). Process conditions and specimen ID are summarized in Table 1. This is updated table as was shown in a previous report [6].

PL-TEP SiC monoliths, representing the bonded layer of the PL-TEP joints, were also fabricated to estimate density of the joint layers. The feedstock of the monolithic forms was the same as that used for the PL-TEP joints, except for additional use of carbowax as an organic agent for pressing the compacts. A steel die was used for cold pressing of the test pellets. The typical SiC monolithic cylindrical pellets before sintering had dimensions ~8 mm diameter and ~10mm thickness. The sintering was performed at 1875^{o}C for 1 h in a flowing argon atmosphere. Density measurements were conducted by weighting and measuring before sintering and by Archimedes density measurement after sintering. Specimen ID and processing conditions for the PL-TEP SiC is listed in Table 2.

Table 1**.** Processing conditions, apparent shear strength, and fracture behavior of CVD-SiC joined by PL-TEP method.

Material	**Specimen ID**	**Alias**	**Processing Conditions**				**Joint Strength**			
			Starting Materials	Atm.	Temp. (^{o}C)	Time (h)	Test method	Apparent shear strength (MPa) [1]	Fracture location	# of tests
PL-TEP joint	TEP-6A	RUN 34	SiC nano and micron powder, 6wt.% oxide additives, 3.5 wt% PVP and acrawax	Ar	1875	1	DNS [2]	113±52	Joint layer	3
	TEP-6B	RUN 36	SiC nano powder, 6wt.% oxide additives, 3.5 wt% PVP and acrawax	Ar	1875	1	DNS	163±43	Substrate	3
		RUN 37C					Torsion	104±23	Substrate	4
	TEP-6C	RUN 35	SiC nano powder, 6wt.% oxide additives,	Ar	1875	1	N.D. [3]			
	TEP-10B	RUN 38	SiC nano powder, 10wt.% oxide additives, 3.5 wt% PVP and acrawax	Ar	1875	1	DNS	224±18	Substrate	3

[1] Average strength ±one standard deviation
[2] Double notch shear test
[3] Not determine

Table 2. Processing conditions and apparent density of PL-TEP SiC monoliths.

Material	Specimen ID	Starting materials	Apparent Density Before Sintering (%)	Apparent Density After Sintering (%)
Pressureless TEP SiC	P53a	Same for TEP-6B	31.70	94.73
	P53b	SiC nano-powder, 6 wt.% oxide additives, 3.5wt.% acrawax and carbowax	30.33	93.38
	P57	SiC nano-powder, 10 wt.% oxide additives, without organic agents	29.07	95.89
	P57a	Same for TEP-10B	28.91	94.20
	P57b	SiC nano-powder, 10 wt.% oxide additives, 3.5wt.% acrawax and carbowax	31.07	96.38

Shear strength determination

The shear strengths of the SiC joints were determined by double-notch shear (DNS) test [7] and torsional shear test. The DNS test was used for a quick estimation of the shear strength due to the ease of specimen preparation, and the torsion test was used for a more accurate strength evaluation because this test can provide uniform stress states at the joints. Details of the DNS test used in this work can be found elsewhere [6]. The dimensions of the torsional test specimen were 6 mm × 6 mm × 3 mm, with the diameter of the neck 4 mm as shown in Figure 1. The torsional test was conducted using TestResources 160GT-125Nm torsion system with flexible couplers and sample grips (Figure 2). Aluminum-alloy tabs were installed at the square grip sections to obtain uniform stress distributions there. The rotation speed was 0.15 deg/min. Nominal shear strength values (τ) in this work are given by following equation,

$$\tau = 16T/\pi d^3 \qquad (1)$$

where T is the applied torque and d is the specimen diameter of the neck. Number of the torsion tests was four. Further description of details of the test method can be found elsewhere [8]. All mechanical tests were conducted at room temperature.

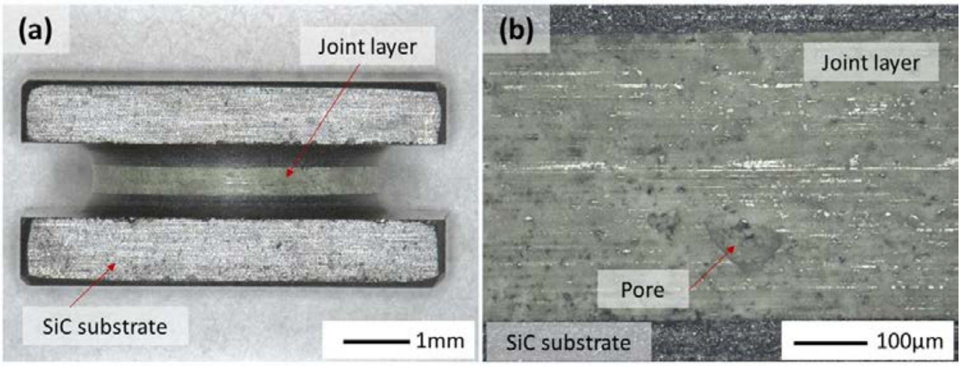

Figure 1. Optical micrograph of the torsional test specimen of PL-TEP joint:
(a) Side-view image, and (b) magnified images of the joint region.

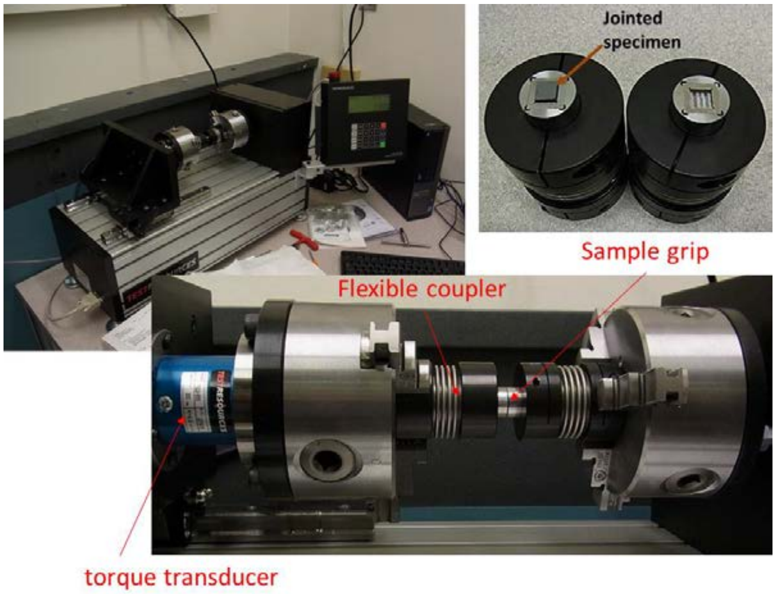

Figure 2. Overview of the torsional testing machine.

Metallographic examinations

Microstructures of the bonded regions were characterized using optical microscope (Keyence, VHX-1000) and field-emission scanning electron microscope (SEM, Hitachi, S4800) equipped with energy dispersive spectroscopy (EDS).

Results

Shear strength investigation of PL-TEP joints

The DNS tests on the TEP-10B joints and the torsion tests on the TEP-6B joints were conducted. The average DNS strengths and the one standard deviation of the TEP-10B joint were 224 and 18 MPa, respectively. The cracks ran through the SiC substrates based on the observation of the tested

specimens. The apparent DNS strength of over 150 MPa and the substrate failure observed in the TEP-10B were typical for a strong joint as observed in the TEP-6B joint and metallic diffusion-bonded SiC joints [6, 9].
For the torsion specimen, ~50 µm sized pores was observed on the surface of bonded zone of the TEP-6B joint (Figure 1 (b)). The apparent shear strengths of ~100 MPa were demonstrated by the torsional test with that joint. The bonded zone of the specimen got shattered into pieces after the test. Visual observations of the fractured areas show that the cracks ran through both the joint layer and SiC substrates as shown in Figure 3. The failure within the SiC base material was typically observed in robust SiC joints determined by the torsional shear test on hourglass specimens [5].

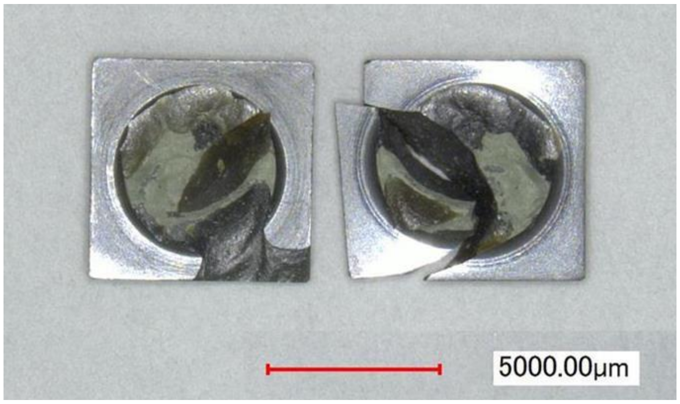

Figure 3. Photograph of pieces of the torsional tested specimens

To understand the fracture behavior, crack observations were conducted using optical microscopy on the partially broken torsion tested samples, as shown in Figure 4. Note that the torsion test was stopped after detection of ~30% decreased in applied torque during the testing. The apparent shear strength of the torsion “tested” sample was very weak (~10 MPa). The crack ran through the SiC substrate and bonded zone as shown in Figure 4. The crack near the joint region typically runs at an angle of approximately 45° to joint interface, which appeared to be perpendicular to the tensile stress component in the shear-loaded specimen. It was difficult to identify the crack initiation site, but the stress state during the testing suggests the possible initiation site is surface defects of bonded zone such as pre-existing pores, [4].

In summary of shear strength determinations, both TEP-6B and 10B joints exhibited a fracture behavior characteristic of robust joints. This indicates that both joints are promising from the point of view of strength.

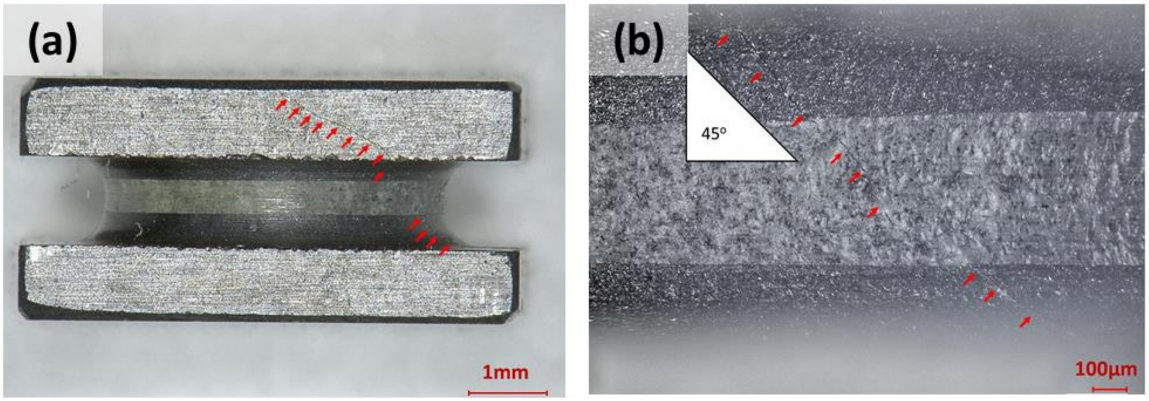

Figure 4. Micrographs of torsion tested PL-TEP joint (TEP-6B): (a) low-magnification image, and (b) high-magnification image. Cracks caused by the torsion test are arrowed.

Processing and characterization of PL-TEP SiC monolith

Due to the difficulty of accurate density measurement of the joint layer, the apparent densities of the PL-TEP SiC in pellet form were performed. Results of the density measurements are summarized in Table 2. The data of the PL-TEP SiC with 6 wt.% oxides and without organic agent is absent because of chipping of the weak powder-compact before sintering. Relative densities before and after sintering were ~30% and ~95%, respectively, for all samples. The effect of the amount of oxide additives on the density of the PL-TEP SiC was insignificant in this work. In addition, the effect of organic agents on the density was not clear.

SEM images of the PL-TEP SiC are shown in Figure 5. Pores with a few tens micron size were observed in the PL-TEP SiC with 6 wt.% oxides and 3.5 wt.% organic agents. The size of pore was decreased by use of 10 wt.% oxide additives and 3.5 wt.% organic agents. The pore size was the smallest in case of the PL-TEP SiC without organic agents, while the difference of the densities between the PL-TEP SiC pellets was not significant.

The results of the density measurements and the microstructural observations provide the following implications: (1) organic agents caused the large pore, and (2) increased amount of the oxide additives reduced the pore size. However, note that the organic agents are necessary during the cold pressing to form robust PL-TEP joints, as indicated in previous work [6]. The use of the organic agents represents a trade-off between the addition of pores and the needed strength provided to the pre-sintered materials. More work may be needed to investigate the effect of the organic agents. In summary, high density (~95% relative density) is potentially expected for the bonded zone of PL-TEP joints with both 6 and 10 wt.% oxide additives, though the amount of oxide additives and use of the organic agents affected the morphology of pore structure.

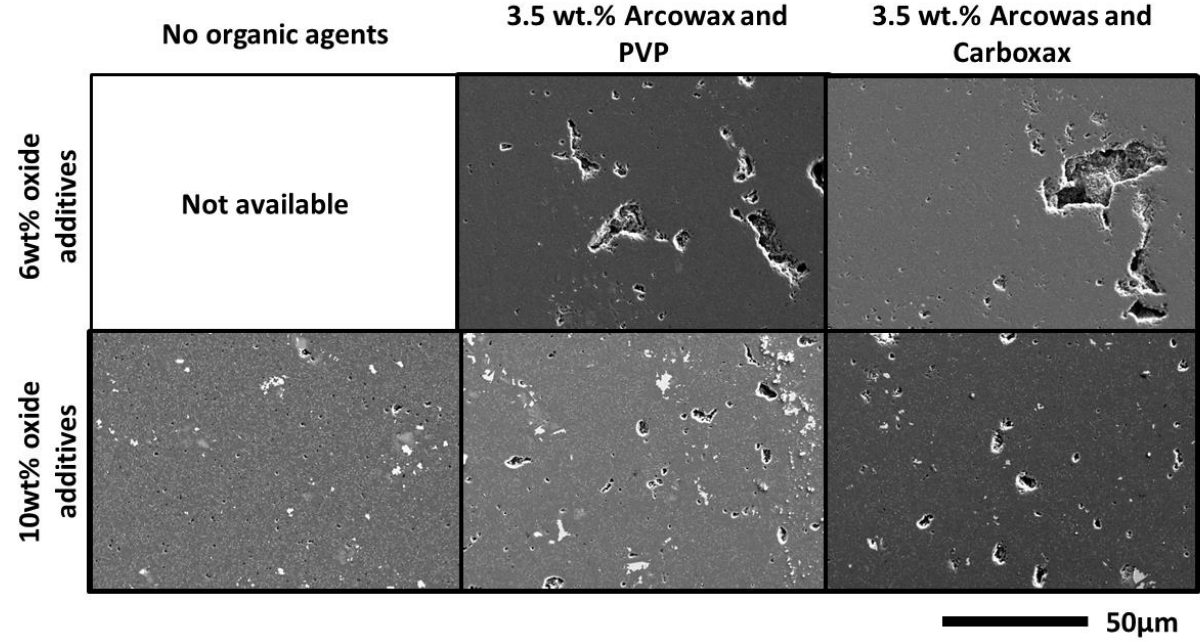

Figure 5. Secondary electron images of the various PL-TEP SiC.

Current progress of neutron irradiation experiments

Rabbit capsules containing SiC joint specimens are being irradiated in HFIR to study effects of neutron irradiation on the shear strength. Five capsules containing a total of 80 samples are being irradiated under three different irradiation conditions. The materials and the irradiation conditions are summarized in Table 3 and 4. The target irradiation conditions are: 500^{o}C to 3 dpa, 500^{o}C to 10 dpa, and 1000^{o}C to 3 dpa. The bonded material is high-purity CVD SiC. The joints were fabricated by pressureless or pressurized methods. The pressureless joined materials are MAX phase joints provided by Rolls-Royce HTC and ORNL, PL-TEP joints by ORNL, and CA glass ceramics joints by Politecnico di Torino. The pressurized-method joined materials are metallic diffusion-bonding using Ti and Mo by ORNL, MAX phase tape casting by PNNL, spark plasma sintering (SPS) by Queen Mary University of London, and TEP using slurry and tape casting by Kyoto University. The joint phases nominally include Ti-Si-C system in the Ti diffusion and the MAX phase joints, metallic Ti in the SPS joint, SiC with Y-Al oxide phases in the TEP joints, Mo-Si-C system in the Mo diffusion joint, and calcia-alumina glass in the glass ceramic joint. Regarding post-irradiation experiments, torsional tests using the Test Resources 160GT-125Nm torsion system is planned. Observation of the fracture appearance will also be conducted. In addition the actual irradiation temperatures will be evaluated by dilatometry of CVD SiC temperature monitors that are internal components of the capsules containing the SiC joints. Torsion tests on control specimens are ongoing.

Table 3.Irradiation test matrix for various SiC joints.
The checks denote test conditions planned in this work.

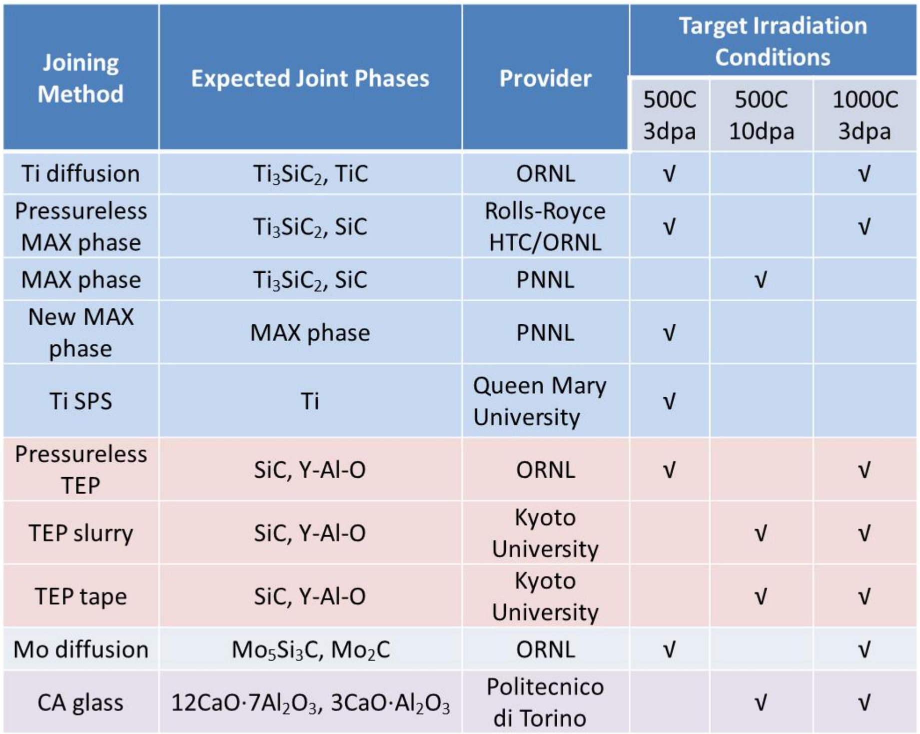

Joining Method	Expected Joint Phases	Provider	Target Irradiation Conditions		
			500C 3dpa	500C 10dpa	1000C 3dpa
Ti diffusion	Ti_3SiC_2, TiC	ORNL	√		√
Pressureless MAX phase	Ti_3SiC_2, SiC	Rolls-Royce HTC/ORNL	√		√
MAX phase	Ti_3SiC_2, SiC	PNNL		√	
New MAX phase	MAX phase	PNNL	√		
Ti SPS	Ti	Queen Mary University	√		
Pressureless TEP	SiC, Y-Al-O	ORNL	√		√
TEP slurry	SiC, Y-Al-O	Kyoto University		√	√
TEP tape	SiC, Y-Al-O	Kyoto University		√	√
Mo diffusion	Mo_5Si_3C, Mo_2C	ORNL	√		√
CA glass	$12CaO{\cdot}7Al_2O_3$, $3CaO{\cdot}Al_2O_3$	Politecnico di Torino		√	√

Table. 4 Irradiation conditions for HFIR rabbit capsules containing various SiC joints.

Rabbit ID	Rabbit ID2	TEMPERATURE (°C)	HFIR POSITION		TARGET FLUENCE (10^{21} n/cm^2)	FAST FLUX (n/cm^2-s)	NUMBER OF CYCLES	FAST FLUENCE PER CYCLE (n/cm^2)	EXPECTED TOTAL FLUENCE (n/cm^2)
SCJ2-10	FTS1	500	TRRH	7	3	7.00E+14	2	1.45E+21	2.90E+21
SCJ2-11	FTS3	500	TRRH	7	10	7.00E+14	7	1.45E+21	1.02E+22
SCJ2-12	FTS2	500	TRRH	7	3	7.00E+14	2	1.45E+21	2.90E+21
SCJ2-16	FTS4	1000	PTP	5	3	1.11E+15	1	2.30E+21	2.30E+21
SCJ2-17	FTS5	1000	PTP	5	3	1.11E+15	1	2.30E+21	2.30E+21

REFERENCES

[1] Y. Katoh, L.L. Snead, I. Szlufarska, W.J. Weber, J. Nucl. Mater., 16 (2012) 143.
[2] Y. Katoh, S.M. Dong, A. Kohyama, Fusion Eng. Des., 61–62 (2002) 723.
[3] T. Koyanagi, K. Ozawa, T. Hinoki, K. Shimoda, Y. Katoh, J. Nucl. Mater., 448 (2014) 478.
[4] H.-C. Jung, T. Hinoki, Y. Katoh, A. Kohyama, J. Nucl. Mater., 417 (2011) 383.
[5] Y. Katoh, L.L. Snead, T. Cheng, C. Shih, W.D. Lewis, T. Koyanagi, T. Hinoki, C.H. Henager Jr., M. Ferraris, J. Nucl. Mater., 448 (2014) 497.
[6] T. Koyanagi, J.O. Kiggans, T. Cheng, Y. Katoh, Fusion Materials Semiannual Progress Report for Period Ending December 31, 2013, DOE/ER-0313/55, U. S. Department of Energy, 22.
[7] ASTM C1292-10, (2010).
[8] H.-C. Jung, T. Hinoki, Y. Katoh, A. Kohyama, J. Nucl. Mater., 417 (2011) 383.
[9] T. Koyanagi, J. Kiggans, C. Shih, Y. Katoh, Proceedings of 38th Int'l Conf & Expo on Advanced Ceramics & Composites (ICACC 2014), Manuscript ID: 1789424.R1.

3.3 DIFFUSION OF MAGNESIUM AND MICROSTRUCTURES IN Mg$^+$ IMPLANTED SILICON CARBIDE

— W. Jiang, D. J. Edwards, H J. Jung, Z. Wang, Z. Zhu, T. J. Roosendaal, S. Hu, C. H. Henager, Jr., R. J. Kurtz (Pacific Northwest National Laboratory), and Y. Wang (Los Alamos National Laboratory)

OBJECTIVE

Magnesium is predicted as one of the major metallic transmutation products in silicon carbide under high-energy neutron irradiation. As a candidate material for fusion reactor designs, SiC is investigated in this experimental study to obtain data and gain a basic understanding of defect microstructures and Mg diffusion in Mg$^+$ ion implanted SiC.

SUMMARY

Following our previous reports [1-3], further isochronal annealing (2 hrs.) of the monocrystalline 6H-SiC and polycrystalline CVD 3C-SiC was performed at 1573 and 1673 K in Ar environment. SIMS data indicate that observable Mg diffusion in 6H-SiC starts and a more rapid diffusion in CVD 3C-SiC occurs at 1573 K. The implanted Mg atoms tend to diffuse deeper into the undamaged CVD 3C-SiC. The microstructure with Mg inclusions in the as-implanted SiC has been initially examined using high-resolution STEM. The presence of Mg in the TEM specimen has been confirmed based on EDS mapping. Additional monocrystalline 3C-SiC samples have been implanted at 673 K to ion fluence 3 times higher than the previous one. RBS/C analysis has been performed before and after thermal annealing at 1573 K for 12 hrs. Isothermal annealing at 1573 K is being carried out and Mg depth profiles being measured. Microstructures in both the as-implanted and annealed samples are also being examined using STEM.

PROGRESS AND STATUS

Introduction

Silicon carbide composites (SiC/SiC) have been proposed for structural materials [4] and flow channel inserts [5] in fusion reactor designs. Upon exposure to high-energy neutrons, SiC undergoes nuclear transmutations accompanied with generation of atomic displacements. Sawan et al. [6] has predicted that at a fast neutron dose of ~100 dpa (displacements per atom), there will be ~0.5 at.% Mg generated in SiC among other major transmutation products that include 0.15 at.% Al, 0.2 at.% Be, 0.01 at.% P, 2.2 at.% He and 0.84 at.% H. The impacts on structural stability and property degradation from the displacement damage and the presence of the transmutation impurities in SiC are currently unknown. They need to be investigated and fully evaluated prior to an informed decision for SiC to be utilized in fusion reactors. High-energy neutron irradiation in a prototypical fusion environment would be ideal for investigating the response of SiC microstructures. However, a fusion relevant neutron source capable of generating a meaningful amount of Mg and other elements in SiC for study through transmutation reactions is currently not available. This experimental study uses ion implantation to introduce Mg into the SiC microstructure; post-implantation thermal annealing is applied to recover implantation damage in the structure. Reported here are some of the initial data on Mg diffusion, microstructures with Mg inclusions, and defect accumulation and recovery in Mg$^+$ ion implanted SiC. Further on-going study of isothermal annealing at 1573 K will lead to determination of the Mg diffusion coefficient in SiC. Microstructural features with Mg inclusions will also be examined. The data may provide a useful basis for modeling and simulation to further understand the physical and chemical processes of Mg interaction with SiC.

Experimental Procedure

The previous monocrystalline (0001)-oriented 6H-SiC and polycrystalline CVD 3C-SiC implanted at 773 K with 200 keV Mg$^+$ ions to 2.5×10^{16} and 3.2×10^{16} ions/cm^2, respectively, have been further annealed isochronally (2 hrs.) at higher temperatures up to 1673 K. The Mg depth profiles in the SiC samples were measured after each annealing step using time-of-flight secondary ion mass spectrometry (ToF-SIMS) with 2 keV O_2^+ ions as the sputtering beam and 25 keV Bi^+ ions as the analyzing beam. The depth scale for monocrystalline 6H-SiC with a smooth surface was calibrated by measuring the crater depth with a Veeco Dektak 150 stylus profilometer, while that for polycrystalline CVD 3C-SiC samples is determined based on the same sputtering rate in units of nm/(nA·sec) from 6H-SiC. The microstructure in the implanted depth region of epitaxial (001)-oriented 3C-SiC film (~2 µm thick) on Si has been examined using an FEI aberration-corrected Titan 80-300 scanning electron transmission microscope (STEM). Energy dispersive spectroscopy (EDS) for Mg in the sample has also been conducted using a new JEOL JEM-ARM200CF aberration-corrected STEM with greatly enhanced analytical capability.

In addition, two (001)-oriented 3C-SiC films on Si were implanted 7° off normal with 200 keV Mg^+ ions to an ion fluence of 9.6×10^{16} ions/cm^2 at 673 K. Unlike the previous implantation at 773 K, surface exfoliation of the 3C-SiC films did not occur at the lower temperature (673 K). The ion fluence corresponds to ~6 at. % Mg at the peak maximum according to a SRIM simulation [7]. Although the relative ion fluences are expected to be reasonably accurate, the absolute values could be subject to a large error bar. The implanted sample was cleaved to smaller pieces for different thermal treatments. One piece was annealed at 1373 K for 2 h and the other at 1573 for 12 h to study defect recovery and Mg behavior. The furnace anneals were performed in flowing Ar gas with the sample placed in a chimney of Zr metal foils to minimize or prevent surface oxidation of the SiC sample. For the sample annealed at 1573 K, the center region was covered with flakes of Zr oxide, which was removed prior to making measurements. Two edges of the sample formed unintentional, irremovable layers of Zr oxide. SIMS measurements for Mg profiles in both the center and edge areas were conducted. In addition, the ion-channeling method based on 2.0 MeV He^+ Rutherford backscattering spectrometry (RBS/C) was used to analyze the lattice disorder on the Si sublattice in the center area. The edge area was too small to be probed with RBS/C. The annealed SiC at 1573 K and the as-implanted sample are currently being examined under TEM. Isothermal annealing at 1573 K for times ranging up to 12 h is currently being conducted and ToF-SIMS is being followed to measure the Mg depth profile after each anneal.

Results and Discussion

The normalized SIMS depth profiles of the implanted Mg in 6H-SiC and CVD 3C-SiC annealed at 1573 and 1673 K, together with some of the previous data for lower temperatures are shown in Figure 1. Based on the ion fluences, the peak maxima for the Mg profiles in 6H-SiC and CVD 3C-SiC correspond to ~1.6 at.% and ~2.0 at.% Mg, respectively. The Mg profile in the as-implanted 6H-SiC in Figure 1(a) is located at 255 nm with a full width half maximum (FWHM) of 103 nm. Annealing at higher temperatures up to 1473 K does not lead to a significant change in the peak width [1]; further isochronal annealing at 1573 and 1673 K for 2 h each results in an observable Mg diffusion, as shown in Figure 1, which is somewhat similar to Ag behavior in 6H-SiC [8]. The Mg diffusion is still insignificant with an increase in the peak width (FWHM) from 104 nm at 1473 K to 125 nm at 1673. The Mg profile in 6H-SiC remains somewhat Gaussian up to 1673 K. Compared to its monocrystalline 6H-SiC counterpart, the Mg peak width in as-implanted polycrystalline CVD 3C-SiC below 1473 K is systematically larger by 20-30%, as shown in Figure 1(b). This behavior could be attributed to diffusion enhancing impurities or porosity at the grain boundaries. Similar interpretations have been proposed for Ag diffusion in CVD-SiC [911]. The data in Figure 1(b) suggest that there might be some modest Mg diffusion starting at 1473 K [1]. More rapid Mg diffusion occurs with an increase in the width from 147 nm at 1473 K to 317 nm at 1673 K. Furthermore, the Mg atoms tend to diffuse deeper into the polycrystalline host, making its depth profile highly skewed towards the bulk. The half width of the Mg profile at the greater depth is 136 nm (vs. 102 nm for the other half towards the surface) in CVD 3C-SiC at 1573 K, and 192 nm (vs. 125 nm) at 1673 K. This preferred Mg diffusion into the undamaged crystal is not yet fully understood, but could be associated with implantation induced effects near the surface region. Similar behavior was observed for Ag in CVD-SiC [12]. It should be noted that shifts in peak positions in both 6H-SiC and CVD 3C-SiC are observed and all the peaks except for that in CVD 3C-SiC at 1673 K are repositioned to 255 nm. The peak shifts could originate from various contributors, including SiC surface oxidation [observed for CVD 3C-SiC at 1573 and 1673 K (data not shown)], deposition and redistribution of Zr oxide on SiC surface, and possible sublimation or etching of ion-implanted SiC at high temperatures [13,14]. We are currently performing vacuum anneals to investigate the associated issues.

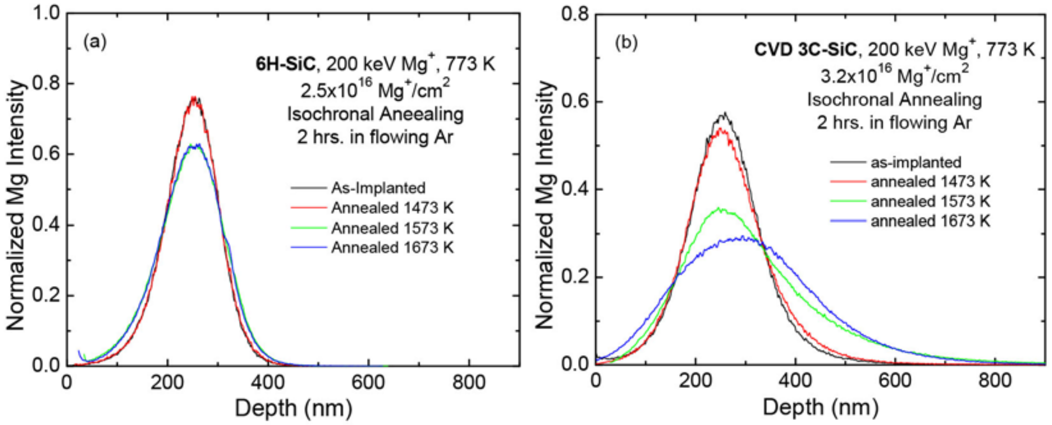

Figure 1. ToF-SIMS depth profiles of Mg in (a) monocrystalline 6H-SiC and (b) polycrystalline CVD 3C-SiC implanted with Mg$^+$ ions at 773 K and annealed isochronally (2 hrs.) up to 1673 K in Ar environment.

Figure 2 shows two high-angle annular dark field (HAADF) STEM images with different magnifications for 3C-SiC implanted with 200 keV Mg$^+$ to 3.2×10^{16} ions/cm^2 at 773 K. The lowerresolution image in Figure 2(a) shows a buried implantation band located at depths between 170 and 330 nm. The atomic-level resolution image shown in Figure 2(b) was taken in the depth region near the Mg profile maximum (~255 nm). Some image contrast on the 3C-SiC (110) plane is observed. In-situ EDS analysis has ruled out the possibility of major surface contamination from Ga during the focused ion-beam (FIB) process for TEM specimen preparation. However, either EDS or EELS in the Titan 80-300 STEM system has not detected Mg at 300 keV. The Mg atomic concentration is expected to be ~2 at.% in the depth region from SRIM simulation for an ion fluence of 3.2×10^{16} ions/cm^2, but we cannot exclude the possibility of a large error in the absolute value of the ion fluence at this time. The image contrast is not yet fully understood, but could originate from a number of factors, including Mg aggregation or replacement, presence of vacancies in the darker atomic columns, a change in the local atomic density, and possible electron diffraction due to a part of coherent electron beam under the high-angle geometry. Implantation to a higher ion fluence is needed for a better understanding. An additional implantation (by tripling the ion fluence) and subsequent thermal treatments have been performed. Preliminary characterizations have also been conducted (see below).

In order to confirm the retention of Mg in the TEM specimen, further EDS analysis at 200 keV was performed using an enhanced EDS system in a new JEOL JEM-ARM200CF STEM. The system has an improved sensitivity due to a larger solid angle of an x-ray detector that has a larger area and is located closer to the specimen than a conventional one. The microscope provides a high-intensity electron beam to facilitate EDS analysis as well as microscopy. The EDS spectra from the implanted depth region clearly show a well-resolved Mg Kα line (data not shown). EDS mapping for the TEM specimen was carried out with the data shown in Figure 3. By integrating counts, the Mg depth profile has been obtained and is plotted in Figure 3. This profile is consistent with that determined by SIMS for the as-implanted sample (Figure 1). The result indicates that Mg redistribution in the implanted SiC is insignificant during the FIB process.

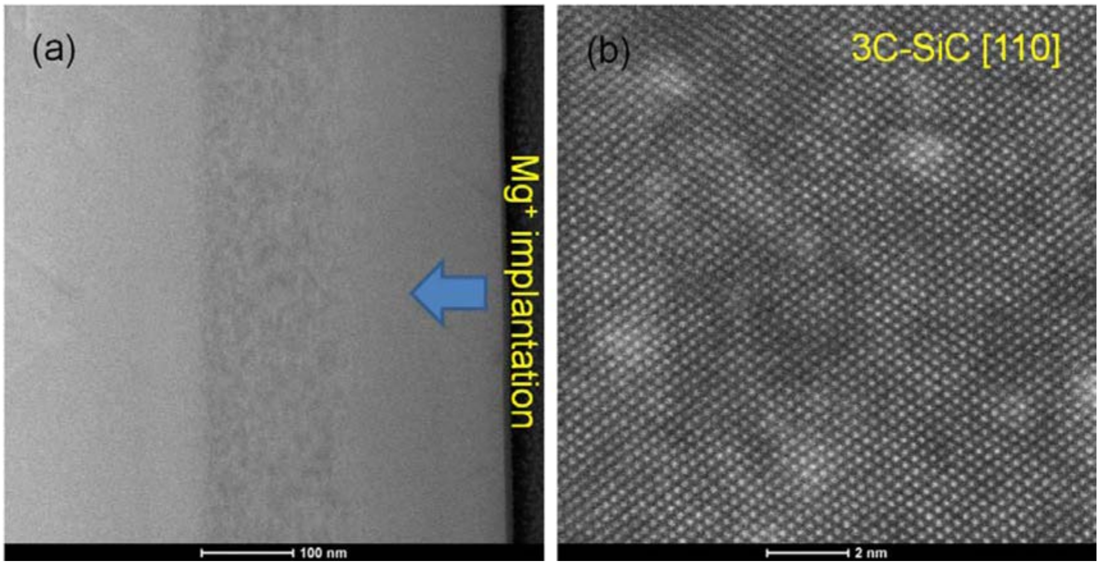

Figure 2. (a) Low-resolution and (b) atomic-level resolution HAADF STEM images for 3C-SiC implanted with 200 keV Mg^+ to 3.2×10^{16} ions/cm^2 at 773 K.

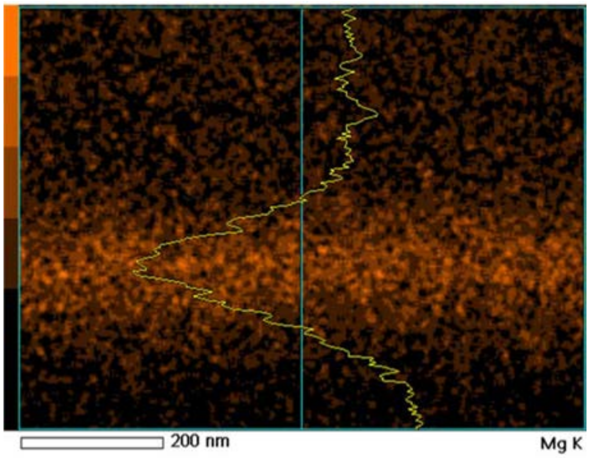

Figure 3. EDS map and depth profile of Mg in 3C-SiC implanted to 3.2×10^{16} Mg^+/cm^2 at 773 K.

Figure 4 shows RBS/C spectra for 3C-SiC implanted to 9.6×10^{16} Mg^+/cm^2 at 673 K, 2 h post-implantation annealed at 1373 K, and 12 h at 1573 K. Channeling and random spectra from an unirradiated area are also included in the figure. It is apparent that the intensity of the damage peak decreases after annealing at 1373 K, indicating that the thermal annealing leads to observable defect recovery. In contrast, the Mg depth profile from SIMS does not change (data not shown), which is consistent with the results for the lower ion fluence reported previously [1]. Further annealing at 1573 for 12 h leads to a nearly complete recovery of the implantation damage. Although the overall dechanneling yield is still slightly higher than that from the unimplanted sample, the damage peak in the annealed sample disappears and the surface peak is comparatively small, suggesting that the surface lattice displacements are also well discovered. It should be noted that in this depth region, the Mg concentration is an order of magnitude smaller than in the as-implanted sample, as shown in Figure 5. The sample surface was covered with Zr oxide flakes after the thermal annealing, which were removed prior to the RBS/C analysis. Possible Mg diffusion to and subsequent release from the surface, SiC sublimation [13,14], or both during the thermal annealing process might be responsible for the low Mg concentration. Unexpectedly, some edge areas were covered with irremovable Zr oxide layers, where Mg was still retained in SiC without a significant loss. This unintentional layer of Zr oxide may serve as a diffusion barrier to minimize Mg loss. Diffusion of Zr into SiC occurred during the thermal annealing (data not shown), which could affect the Mg migration path in the disordered SiC. The results could be of scientific interest and technological impact, but this is not the focus of the current study. The edge area is being used for STEM study, in addition to the as-implanted sample. A sequence of isothermal annealing at 1573 K up to 720 min, followed by SIMS measurement of Mg depth profile in SiC after each anneal, is also being performed to determine Mg diffusion coefficient in SiC. The data, together with the TEM results will be reported elsewhere at a later time.

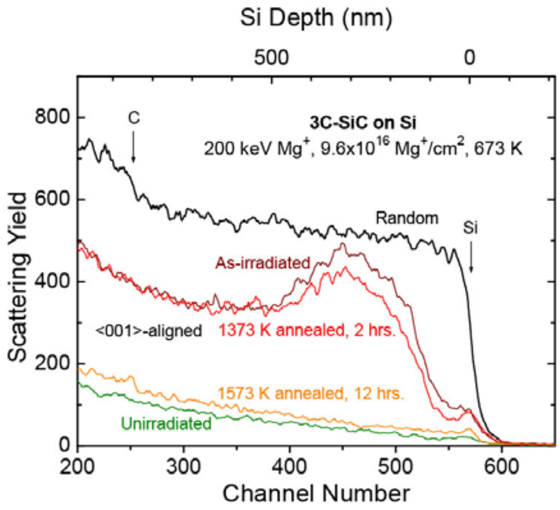

Figure 4. 2.0 MeV He^+ RBS/C spectra along the <001> axis in 3C-SiC implanted with 200 keV Mg^+ ions to 9.6×10^{16} ions/cm^2 at 673 K and post-annealed at higher temperatures. Also included are random and channeling spectra from an unirradiated area.

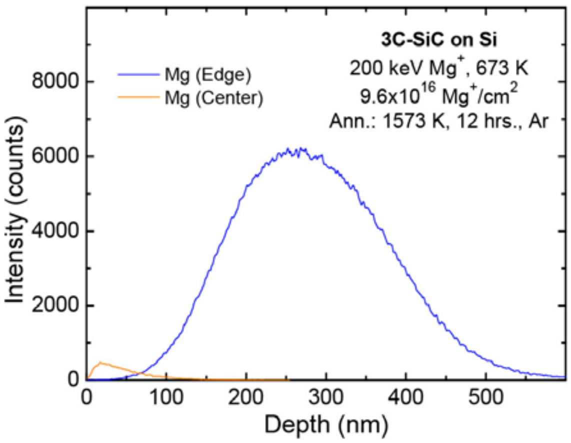

Figure 5. ToF-SIMS depth profiles of Mg in 3C-SiC implanted to 9.6×10^{16} Mg^+/cm^2 at 673 K and annealed at 1573 K for 12 hrs. The center area had flakes of Zr oxide that were removed prior to analysis, while the edge area had an irremovable Zr oxide layer (depth scale corrected).

Acknowledgments

This research was supported by Office of Fusion Energy Sciences, U.S. Department of Energy (DOE) under Contract DE-AC05-76RL01830. A portion of the research was performed using EMSL, a national scientific user facility sponsored by the DOE's Office of Biological and Environmental Research and located at PNNL. Jiang likes to thank Robert Colby for his early TEM effort and Alicia Certain for her early FIB work. Ion implantation was conducted at Ion Beam Materials Laboratory through a partial support from Center for Integrated Nanotechnologies in Los Alamos National Laboratory.

REFERENCES

[1] W. Jiang, Z. Zhu, T. Varga, M. E. Bowden, S. Manandhar, T. Roosendaal, S. Y. Hu, C. H. Henager, Jr., R. J. Kurtz, and Y. Wang, Fusion Materials Semiannual Progress Report for Period Ending June 30, 2013, DOE/ER-0313/54, U. S. Department of Energy, 70.
[2] S. Y. Hu, W. Setyawan, R. M. Van Ginhoven, W. Jiang, C. H. Henager, Jr., and R. J. Kurtz, J. Nucl. Mater. 448 (2014) 121.
[3] S. Y. Hu, W. Setyawan, W. Jiang, C. H. Henager, Jr., and R. J. Kurtz, Fusion Materials Semiannual Progress Report for Period Ending December 31, 2013, DOE/ER-0313/55, U. S. Department of Energy, 149.
[4] A. R. Raffray, R. Jones, G Aiello, M. Billone, L. Giancarli, H. Golfier, A. Hasegawa, Y. Katoh, A. Kohyama, S. Nishio, B. Riccardi, and M. S. Tillack, Fusion Eng. Des. 55 (2001) 55.
[5] C. P. C. Wong, M. Abdou, M. Dagher, Y. Katoh, R. J. Kurtz, S. Malang, E. P. Marriott, B. J. Merrill, K. Messadek, N. B. Morley, M. E. Sawan, S. Sharafat, S. Smolentsev, D. K. Sze, S. Willms, A. Ying, and M. Z. Youssef, Fusion Eng. Des. 85 (2010) 1129.
[6] M. E. Sawan, Y. Katoh, and L. L. Snead, J. Nucl. Mater., 442 (2013) S370.
[7] J. F. Ziegler, J. P. Biearsack, and U. Littmark, The stopping and Range of Ions in Solids (Pergamon Press, New York, 1985); available from: http://www.SRIM.org.
[8] W. Jiang, W. J. Weber, V. Shutthanandan, L. Li, and S. Thevuthasan, Nucl. Instrum. Method Phys. Res. B 129-220 (2004) 642.
[9] E. Friedland, T. Hlatshwayo, and N. van der Berg, Phys. Status Solidi C 10 (2013) 208.
[10] E. J. Olivier and J. H. Neethling, J. Nucl. Mater., 432 (2013) 252.
[11] E. López-Honorato, H. Zhang, D. Yang, and P. Xiao, J. Am. Ceram. Soc. 94 (2011) 3064.
[12] E. Friedland, J. B. Malherbe, N. G. van der Berg, T. Hlatshwayo, A. J. Botha, E. Wendler, and W. Wesch, J. Nucl. Mater., 389 (2009) 326.
[13] M. A. Capano, S. Ryu, J. A. Cooper Jr., M. R. Melloch, K. Rottner, S. Karlsson, J. Elec. Mater., 28 (1999) 214.
[14] T. T. Hlatshwayo, J. B. Malherbe, N. G. van der Berg, A. J. Botha, and P. Chakraborty, Nucl. Instrum. Method Phys. Res. B 273 (2012) 61.

3.4 IRRADIATION CREEP OF NEAR-STOICHIOMETRIC SILICON CARBIDE FIBERS

— T. Koyanagi, K. Ozawa (Oak Ridge National Laboratory), T. Hinoki (Kyoto University), L.L. Snead, Y. Katoh (Oak Ridge National Laboratory)

OBJECTIVE

The objective of this work is to evaluate the irradiation creep behavior of near-stoichiometric silicon carbide (SiC) fibers to aid in the understanding of the performance of SiC composite as fusion reactor structural components.

SUMMARY

The neutron irradiation creep of near-stoichiometric SiC fibers was evaluated by bend stress relaxation (BSR) tests. The results indicate that the apparent stress exponent of the irradiation creep of the SiC fibers is near unity at ~500°C. The instantaneous creep compliance of the SiC fibers, which is the creep strain normalized to the applied stress and neutron flux, was estimated to be ~1×10^{-7} [MPa^{-1} dpa^{-1}] at ~6 dpa. The creep compliance values are orders of magnitude smaller than previously reported from light ion irradiation experiments [1]. Quality of the fibers slightly affected the creep behavior: Hi-Nicalon$^{\mathrm{TM}}$ Type S fiber showed more creep than other fibers, including Tyranno$^{\mathrm{TM}}$ SA3, isotopically-controlled Sylramic$^{\mathrm{TM}}$ and Sylramic$^{\mathrm{TM}}$ iBN fibers at ~500°C to ~1 dpa.

PROGRESS AND STATUS

Introduction

The service life of ceramic matrix composites (CMC) is often governed by a slow crack growth phenomenon [2]. For continuous SiC fiber reinforced CMC in high radiation operating environments, the slow crack growth is expected to be governed by irradiation creep of bridging fibers and environmentally-induced recession of exposed interphase. Recently, the irradiation creep of high-purity CVD SiC was shown to operate very slowly compared to metals [3]. The underlying mechanism for the primary transient irradiation creep was reported to be swelling-coupled creep caused by anisotropic evolutions of the multi-dimensional defect clusters under applied stresses [3]. However, the irradiation creep of SiC fibers is only poorly understood. The neutron-irradiation creep has not been reported, though a few papers report data on the creep behavior under ion and proton irradiations [4-6]. This report presents data concerning the evaluation of the creep behavior of near-stoichiometric SiC fibers under neutron irradiation.

To evaluate the irradiation creep strain, the BSR test was used. This is one of bend type test techniques, which can evaluate creep properties of ceramic fibers [7]. The BSR method is useful for neutron irradiation experiments because it enables the application of stress to miniature specimens under irradiation, and it requires only very simple post-irradiation measurement. The quantitative evaluation and mechanistic study of irradiation creep of monolithic SiC materials has been reported using this method [3, 8]. However, there are limitations for this test: Applied stress is not constant and uniform in sample during the experiment. The applied stress approaches zero during testing. Therefore, the determination of the creep is impossible after the initial stress is fully relaxed. The non-uniform stress state in test specimens makes the analysis difficult in a certain case. All the data concerning creep rate and stress exponent (*n*) of creep can be obtained from BSR test if the specimen exhibits a uniform isotropic microstructure and creep behavior linear with stress. Because the experimental results showed that the creep behavior of the fibers appeared linear to the applied stress, the quantitative analysis of the irradiation creep was conducted in this study, assuming that the microstructures of the fibers are uniform. Microstructural analyses on the near-stoichiometric SiC fibers were reported by Dong et al. and Sauder et al. [9, 10]. Based on their results, microstructure of Hi-Nicalon$^{\mathrm{TM}}$ Type S fiber is uniform. On the other hand, the uniformity of microstructure in Tyranno$^{\mathrm{TM}}$ SA fibers depends on the batch. Slyramic$^{\mathrm{TM}}$ fiber has a slightly different microstructure between near the fiber edge at the core.

Experimental Procedure

Materials

The materials used in this work were Hi-Nicalon^{TM} Type S (Nippon Carbon Co., Tokyo, Japan, lot number: 407203 March 2005), Tyranno^{TM} SA3 (Ube Industry Ltd., Tokyo, Japan, type: S1I16PX, lot number: 4303), experimental-grade Sylramic^{TM} (COI Ceramics, Inc., California, USA, lot number: 4240, spool 01A), and experimental-grade Sylramic^{TM} iBN (COI Ceramics, Inc., California, USA, lot number: 4630, spool 01B) SiC-based fibers. The key properties of these fibers are presented in

Table **1**. The properties other than grain size were obtained from material data sheet provided from the venders. Information of the grain size can be found elsewhere [10, 11]. Note that the Sylramic^{TM} and Sylramic^{TM} iBN fibers in this work are isotopically-controlled, which mainly contain ^{11}B instead of ^{10}B. The properties of these two fibers are assumed to be same as those of commercial ones except for the type of the isotope.

Table 1. Properties of near-stoichiometric SiC fibers.

Materials	**Elemental Composition [wt.%]**	**Carbon Impurity [wt.%]**	**Average Diameter [µm]**	**Young's Modulus [Gpa]**	**Grain Size [nm]**
Tyranno™-SA3	67 Si + 31 C + <1 O + <2 Al	2.3	7.5	380	200
Hi-Nicalon™ Type S	69 Si + 31 C + 0.2 O	1.4	12	420	50
Experimental Sylramic™	67 Si + 29 C + 0.8 O + 2.3 ^{11}B + 0.4 N + 2.1 Ti	0.3	10	372	100
Experimental Sylramic^{TM}-iBN	67 Si + 29 C + 0.8 O + 2.3 ^{11}B + 0.4 N + 2.1 Ti	0.3	10	372	>100

BSR test

The fiber bundles were attached to a fixture with three different curvature radiuses of 2, 3, and 6 mm to apply flexural stress, and then were irradiated as shown in

Figure 1. The fixture was fabricated from near-stoichiometric graphite to avoid chemical reaction between the fibers and the fixture. The initial bending stress levels systematically ranged from ~200 to ~1400 MPa. Relaxation creep was evaluated using the BSR ratio (m), which is the ratio of final stress (σ_a) to initial stress (σ_0). The BSR ratio can be expressed as Eq. (1), where E, ε, and R are the elastic modulus, flexural strain, and curvature radius of the specimen, respectively.

$$m = \frac{\sigma_a}{\sigma_0} = \frac{E_a(\varepsilon_0 - \varepsilon_c)}{E_0\varepsilon_0} = \frac{E_a}{E_0}(1 - \frac{R_a}{R_0}) \qquad (1)$$

The subscripts a, 0, and c stand for the initial state, final state, and creep, respectively. The BSR ratio varies between 0 and 1, where 0 indicates complete relaxation and 1 indicates no relaxation. The effect of irradiation on the Young's modulus is assumed to be same as that for CVD SiC [12]. The BSR ratio was evaluated by measuring the curvature radius of the specimen. The curvature radiuses before and after irradiation were obtained using analysis of the images of an individual fiber. The imaging was conducted using KEYENCE, VHX-1000 optical microscope. The creep strain was obtained from the BSR ratio and initial flexural strain according to Eq. (1). Details about the BSR testing procedure can be found elsewhere [7].

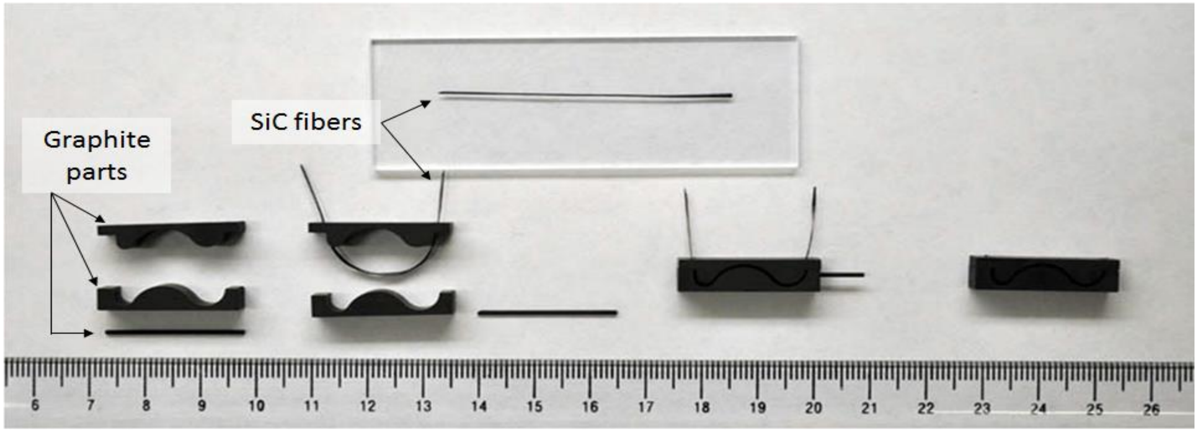

Figure 1. Appearance of the BSR test fixture and SiC fiber specimens.

<u>Neutron irradiation</u>

Neutron irradiation was in the High-Flux Isotope Reactor (HFIR). The specimens were irradiated at 480–1180°C to 0.97–11.87 dpa for SiC (0.97–11.87 × 10^{25} n/m^2, E > 0.1 MeV; and the conversion 1.0 × 10^{25} n/m^2 = 1 dpa is used). The damage rate was ~1.1 × 10^{-6} dpa/s. Experiments to determine the irradiation creep were conducted in an inert-gas atmosphere. The irradiation temperature was determined by dimensional changes on annealing of CVD SiC parts irradiated with the BSR fixture, using a dilatometer. As the SiC parts were designed to be in direct contact with the BSR fixture during irradiation, this measurement represents an accurate sample temperature during irradiation.

Results

Figure 2 shows appearance of the SiC fiber bundles after irradiation at ~500°C to ~1 dpa. The fibers are constrained by the graphite fixture in unirradiated condition as shown in **Figure 1**, and the constraint is removed after irradiation as shown in Figure 2. The presence of irradiation creep was clearly observed for all kinds of the fibers at this condition due to the curved appearance. If the irradiation creep was absent, the fibers remained straight as observed in unirradiated condition. The irradiation creep also existed under the other irradiation conditions at ~500°C to ~10 dpa, and at ~1200°C to ~1 dpa.

Stress dependence of the BSR ratios measured in this work is shown in Figure 3. The horizontal error bars indicate the range of flexural stress during irradiation with the highest at the beginning of irradiation and the lowest at the end of irradiation. The vertical error bar is due to the measurement scatter of the pre-irradiation curvatures. Relationship between the stress dependence and the stress exponent (*n*) of the irradiation creep is also presented. The stress exponent is unity if the BSR ratio is independent on applied stress. When the stress exponent is over 1, the BSR ratio decreases with increasing the applied stress. The stress dependence becomes marked with increasing the stress exponent as shown in Figure 3 (e). The stress dependences of the BSR ratio appeared to be insignificant at ~500°C, indicating the apparent stress exponents of the irradiation creep were near unity for the SiC fibers. At ~1200°C, the BSR ratios of Hi-Nicalon^{TM} Type S fiber were independent on applied stress level. However, the stress dependence can exist for the other fibers. The stress dependence of the BSR ratio at ~1200°C will be discussed with additional data points with the neutron fluence of ~10 dpa.

The BSR ratios ranged over approximately 0.3–0.6 under irradiation at 500 and 1200°C to 1 dpa, and 0–0.2 at 500°C to 10 dpa for all fibers. Note that the BSR ratios were similar following irradiation at 500°C to 1 dpa and at 1200°C to 1 dpa, though the temperature was significantly different. Since the contribution of thermal creep to irradiation creep increases at higher temperature, the irradiation-induced creep appeared to be more significant at 500°C.

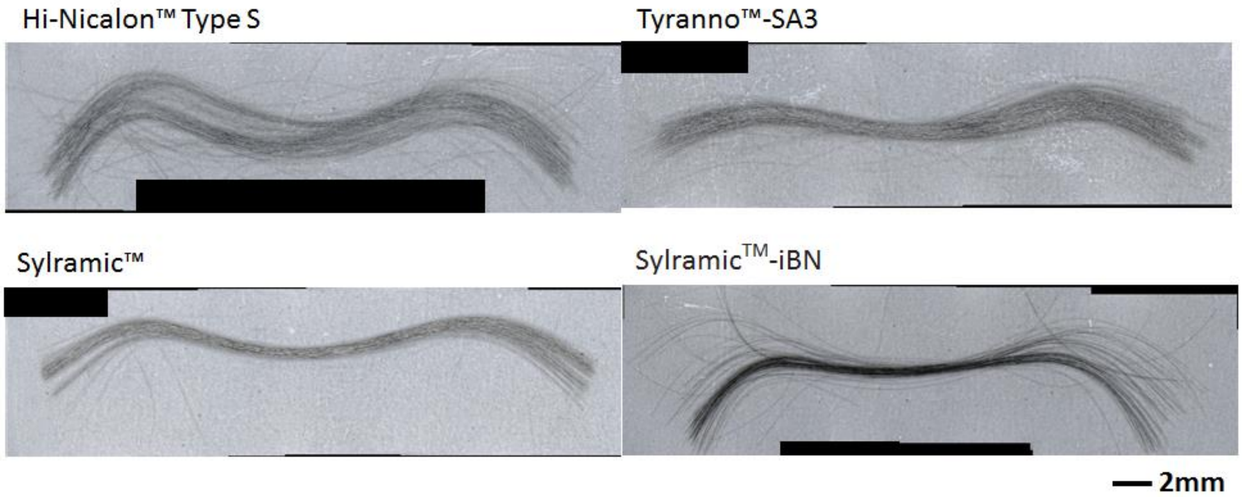

Figure 2. Optical micrographs of SiC fibers following irradiation at ~500°C to ~1 dpa

Table 2. Results of the BSR experiments. Standard deviations in parentheses. Irradiation temperatures determined by dimensional change during annealing of CVD SiC irradiated with the SiC fibers.

Materials	**Irradiation Temperature [°C]**	**Fluence [dpa]**	**Rabbit Capsule ID**	**Number of Measured Curvature**	**Average BSR ratio**
Tyranno™-SA3	560	0.97	TTN16	15	0.59 (0.04)
HI-Nicalon™ Type S	560	0.97	TTN16	24	0.35 (0.06)
Developmental Sylramic™	560	0.97	TTN16	23	0.55 (0.09)
Developmental Sylramic™-iBN	560	0.97	TTN16	24	0.51 (0.06)
Tyranno™-SA3	500	11.87	TTN17	0	
HI-Nicalon™ Type S	500	11.87	TTN17	11	0.08 (0.06)
Developmental Sylramic™	500	11.87	TTN17	11	0.10 (0.07)
Developmental Sylramic™-iBN	500	11.87	TTN17	13	0.11 (0.06)
Tyranno™-SA3	1110	0.97	TTN19	8	0.51 (0.09)
HI-Nicalon™ Type S	1110	0.97	TTN19	11	0.46 (0.04)
Developmental Sylramic™	1110	0.97	TTN19	10	0.61 (0.09)
Developmental Sylramic™-iBN	1110	0.97	TTN19	11	0.56 (0.08)

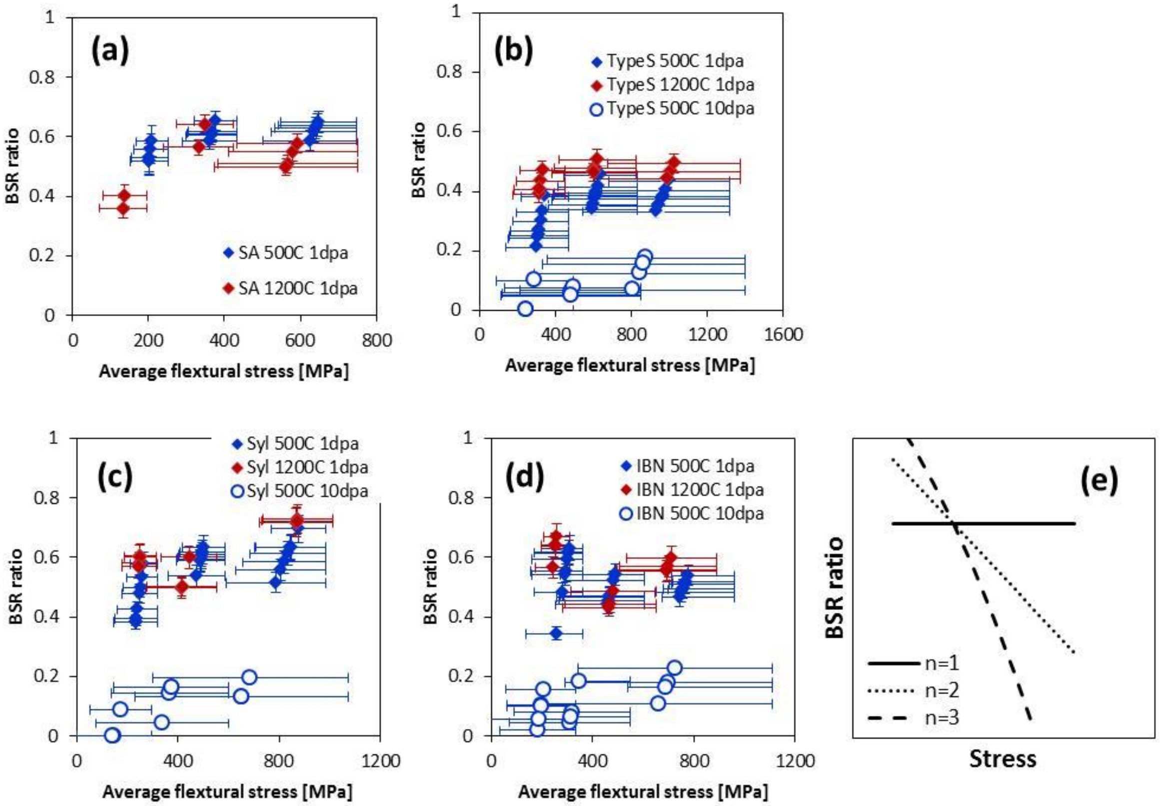

Figure 3. Effect of stress magnitude on BSR ratio in Tyranno™-SA3 (a), Hi-Nicalon™ Type S (b), experimental Sylramic™ (c), and experimental Sylramic^{TM}-iBN (d) during neutron irradiation. The horizontal error bars indicate the range of flexural stress during irradiation with the highest at the beginning of irradiation and the lowest at the end of irradiation. The relationship between the stress dependence and the stress exponent (*n*) is also presented (e).

Irradiation fluence dependences of the BSR ratios of the SiC fibers are shown in Figure 4. The graph also contains the data plots of CVD SiC materials including Rohm & Hass polycrystalline 3C SiC having columnar grains with ~1 µm of the column width and with a moderate amount of stacking fault and, CoorsTek polycrystalline 3C SiC having highly faulted columnar grains with ~10 µm of the column width, and Cree 4H single crystal SiC [3]. The data points for the CVD SiC at ~10 dpa have not been published. At ~500°C, the BSR ratios of both the SiC fibers and CVD SiC decreased with increasing fluence, meaning that the irradiation creep occurred till 10 dpa. The BSR ratios of the fibers were clearly smaller than those of CVD SiC ceramics, i.e. the fibers crept more than the CVD SiC materials. Effects of the material quality of the SiC fibers on the BSR ratio was observed at ~500°C to ~1dpa: the Hi-Nicalon^{TM} Type S SiC fiber crept more than the other fibers. On the other hand, the material quality did not affect the creep behavior of CVD SiC, though the poly-type, grain size (the order of micron), and density of the pre-existing stacking fault were different. Since the fibers had different grain-size (the order of nano) and impurities as shown in Table 1, these differences potentially caused the differential creep of the fibers.

In case of the creep at ~1200°C, the BSR ratio was similar among the fibers, considering the error bars. The stress relaxation of the fibers was similar level to polycrystalline CVD SiC provided by Rohm and Haas Company. In contrast to the SiC fiber, differential creep behavior of the CVD SiC materials has been reported, and is considered to be caused by different degree of the grain-boundary sliding and the basal slip among the materials [3]. At this temperature, the thermal creep of the SiC fibers can have non-negligible contribution to the irradiation creep [11,13].

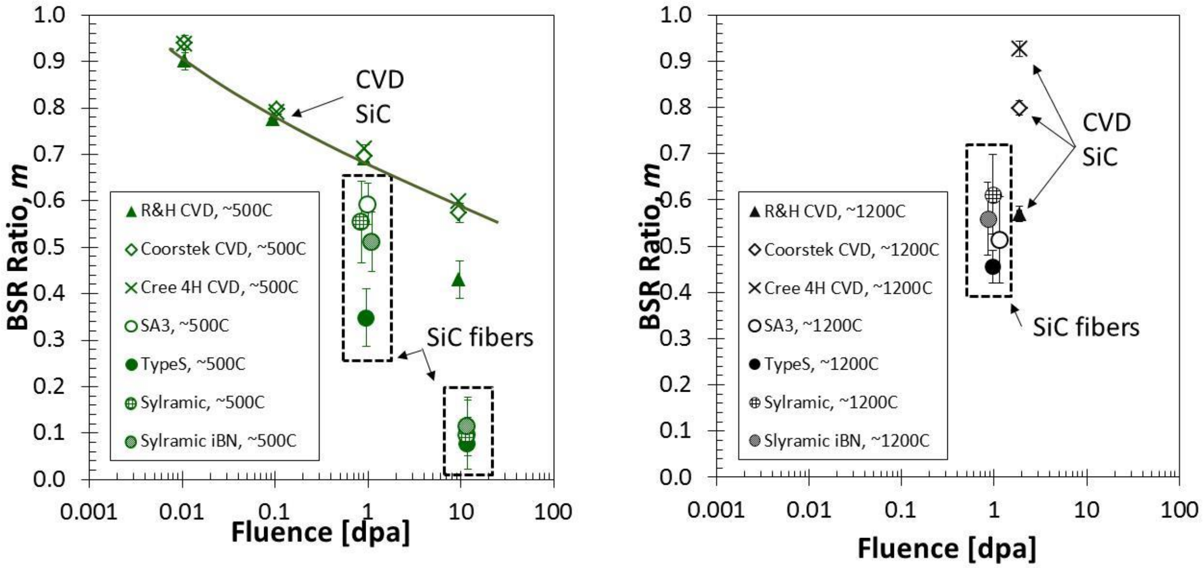

Figure 4. The effect of neutron fluence on the BSR ratio of the SiC fibers. Error bars indicate one standard deviation. The data plots of the fibers were laterally-shifted for visual purpose. The data of CVD SiC is also plotted.

Creep coefficient, which is normalized creep strain with respect to the stress and the neutron fluence is used to compare creep behavior of different materials at low fluence level [14]. The instantaneous creep coefficient (K) is defined by:

$$K \cong \frac{\varepsilon_2 - \varepsilon_1}{\sigma(\gamma_2 - \gamma_1)} \qquad (2)$$

where γ_1 and γ_2 ($\gamma_1 < \gamma_2$) are neutron fluences, σ is average stress during irradiation, and ε_1 and ε_2 are irradiation creep strains following irradiation at a fluence of γ_1 and γ_2, respectively. Figure 5 shows the fluence dependence of the instantaneous creep coefficient of the SiC fibers. The highest and lowest error bars indicate the fluence of γ_1 and γ_2 for each data point, respectively. The instantaneous creep coefficient of Tyranno$^{\mathrm{TM}}$ SA3 is absent in the figure due to the luck of the creep data. That is expected to be a comparable to those of the experimental-grade Sylramic$^{\mathrm{TM}}$ and Sylramic$^{\mathrm{TM}}$ iBN fibers based on the similar creep behavior among them in Figure 4. The figure also shows the instantaneous creep coefficient of Rohm & Hass CVD SiC, and the swelling-coupled creep model of CVD SiC at ~300–~500°C [3]. The creep coefficients of the SiC fiber have values of ~1×10^{-7} [MPa^{-1} dpa^{-1}] at ~6 dpa, which is within one order of magnitude of that of CVD SiC. In other words, creep behavior was not dramatically different between the CVD SiC and the SiC fibers, though the SiC fibers crept more than the CVD SiC as shown in Figure 4. Note that the creep coefficient was very small comparing to those of stainless steels (in the order of ~1×10^{-6} [MPa^{-1} dpa^{-1}]) [14]. The swelling-creep coupled model can explain the creep behavior of CVD SiC at the initial transient region (up to ~1 dpa) [3], but cannot explain the creep after the transient. This result indicates the existence of a differential creep mechanism, such as steady state creep. The instantaneous creep coefficient for the steady state creep of the CVD SiC would be ~1×10^{-7} [MPa^{-1} dpa^{-1}], if it exists. A similar steady state creep rate is expected for the SiC fibers.

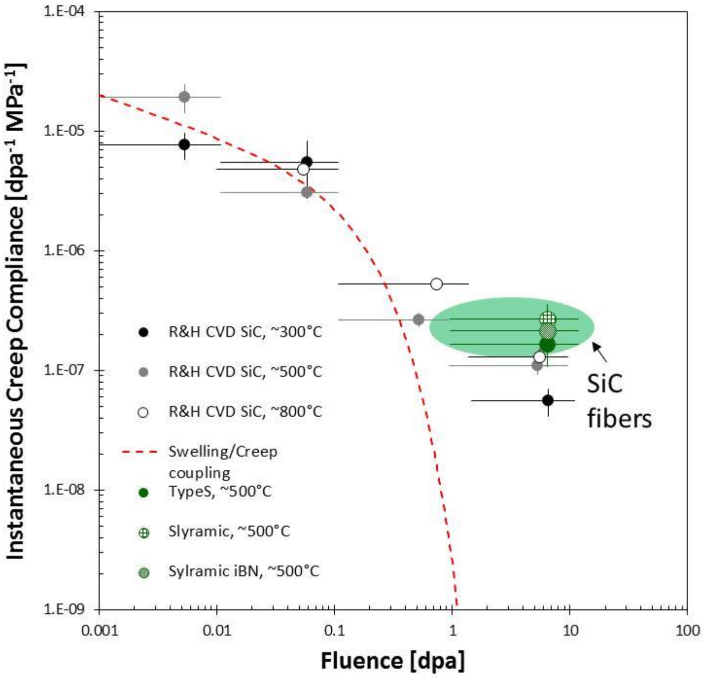

Figure 5. Neutron fluence dependence of instantaneous creep coefficients of SiC fibers. The data for CVD SiC, and the creep coefficients for swelling-coupled creep are included.

References

---

[1] R. Scholz, G.E. Youngblood, J. Nucl. Mater., 283 (2000) 372.
[2] S. Zhu, M. Mizuno, Y. Kagawa, Y. Mutoh, Composites Science and Technology, 59 (1999) 833.
[3] Y. Katoh, L.L. Snead, C.M. Parish, T. Hinoki, J. Nucl. Mater., 434 (2013) 141.
[4] J. Huguet-Garcia, A. Jankowiak, S. Miro, Y. Serruys, J.M. Costantini, Nuclear Instruments and Methods in Physics Research B, 327 (2014) 93.
[5] R. Scholz, J. Nucl. Mater., 258 (1998) 1533.
[6] R. Scholz, G.E. Youngblood, J. Nucl. Mater., 283 (2000) 372.
[7] G.N. Morscher, J.A. Dicarlo, J. Am. Ceram. Soc., 75 (1992) 136.
[8] T. Koyanagi, K. Shimoda, S. Kondo, T. Hinoki, K. Ozawa, Y. Katoh, J. Nucl. Mater., 455 (2014) 73.
[9] S.M. Dong, G. Chollon, C. Labrugère, M. Lahaye, A. Guette, J.L. Bruneel, M. Couzi, R. Naslain, D.L. Jiang, J. Mater. Sci., 36 (2001) 2371.
[10] C. Saude, J. Lamon, J. Am. Ceram. Soc., 90 (2007) 1146.
[11] J.A. DiCarlo, H.-M. Yun, (2005), Non-oxide (Silicon Carbide) Fibers, Handbook of Ceramic Composites, N. P. Bansal, Ed., Springer Science+Business Media, Inc., 33–52.
[12] L.L. Snead, T. Nozawa, Y. Katoh, T.-S. Byun, S. Kondo, D.A. Petti, J. Nucl. Mater., 371 (2007) 329.
[13] J.J. Sha, J.S. Park, T. Hinoki, A. Kohyama, Mechanics of Materials 39 (2007) 175.
[14] K. Ehrlich, J. Nucl. Mater. 100 (1981) 149.

3.5 HIGH DOSE NEUTRON IRRADIATION OF HI-NICALON TYPE S SILICON CARBIDE COMPOSITES, PART 1: MICROSTRUCTURAL EVALUATIONS

- A. G. Perez-Bergquist, T. Nozawa, C. Shih, K. J. Leonard, L. L. Snead, Y. Katoh (Oak Ridge National Laboratory)

Extended abstract of a paper accepted by the Journal of Nuclear Materials

ABSTRACT

Over the past decade, significant progress has been made in the development of silicon carbide (SiC) composites, composed of near-stoichiometric SiC fibers embedded in a crystalline SiC matrix, to the point that such materials can now be considered nuclear grade. Recent neutron irradiation studies of Hi-Nicalon Type S SiC composites showed excellent radiation response at damage levels of 30-40 dpa at temperatures of 300-800°C. However, more recent studies of these same fiber composites irradiated to damage levels of >70 dpa at similar temperatures showed a marked decrease in ultimate flexural strength, particularly at 300°C. Here, electron microscopy is used to analyze the microstructural evolution of these irradiated composites in order to investigate the cause of the degradation. While minimal changes were observed in Hi-Nicalon Type S SiC composites irradiated at 800°C, substantial microstructural evolution is observed in those irradiated at 300°C. Specifically, carbonaceous particles in the fibers grew by 25% compared to the virgin case, and severe cracking occurred at interphase layers.

HIGHLIGHTS

- Hi-Nicalon Type S SiC fiber composites were neutron irradiated to >70 dpa at 300, 500, and 800°C.
- The composites irradiated at low temperature showed substantial degradation in ultimate flexural strength. Strengths dropped from 335 MPa in the unirradiated state to 205 MPa at 800°C, 200 MPa at 500°C, and 95 MPa at 300°C. Similarly, proportional limit stress dropped to 128 MPa at 500°C and 91 MPa at 300°C.
- Fibers exhibited no change in phase as measured by electron diffraction, and size of SiC grains within the fibers was consistent before and after irradiation.
- Fibers were found to contain excess free carbon in small pockets evenly distributed throughout. These carbonaceous pockets were found to increase in size with irradiation at low temperature, from 14.8 nm in diameter in the unirradiated condition to 18.5 nm in diameter after 300°C irradiation. Pockets did not grow after 800°C irradiation.
- EELS analysis showed a slight shift in the carbon spectrum between the unirradiated, 300, 500, and 800°C samples, indicating a possible phase shift in the carbon located in the amorphous pockets.
- Interphase layers were not noticeably changed after 800°C irradiation, but layers at 300°C exhibited severe cracking and degradation. SiC layers were partially amorphized and showed a clear drop in thickness. PyC layers had changed from turbostratic to amorphous and had grown at the expense of the SiC layers.

Matrix regions surrounding the SiC fibers appeared unchanged in all irradiated samples, with no cracking, porosity, phase changes, or severe microstructural changes or accumulation of defect structures.

REFERENCE

[1] A. G. Perez-Bergquist, T. Nozawa, C. Shih, K. J. Leonard, L. L. Snead, Y. Katoh, High Dose Neutron Irradiation of Hi-Nicalon Type S Silicon Carbide Composites, Part 1: Microstructural Evaluations. J. Nucl. Mater., In Revisions.

4.1 RECENT PROGRESS IN THE DEVELOPMENT OF DUCTILE-PHASE TOUGHENED TUNGSTEN FOR PLASMA-FACING MATERIALS –

C. H. Henager, Jr., R. J. Kurtz, T. J. Roosendaal, B. A. Borlaug, W. Setyawan, and K. B. Wagner (Pacific Northwest National Laboratory), G. R. Odette, K. H. Cunningham, K. Fields, D. Gragg, and F. W. Zok (University of California, Santa Barbara)

OBJECTIVE

The objective of this study is to develop the materials science of fiber-reinforced tungsten composites as candidates for plasma-facing components in future fusion reactors. A dynamic bridging model for W-Cu is introduced and discussed.

SUMMARY

A promising approach to increasing fracture toughness and decreasing the DBTT of a W-alloy is by ductile-phase toughening (DPT) [1-3]. In this method, a ductile phase is included in a brittle matrix to prevent fracture propagation by crack bridging. To examine the prospect of DPT, W-Cu three-point bend samples were deformed at several strain rates and temperatures. Data from these tests are used for the calibration of a dynamic crack-bridging model that can effectively predict elevated temperature crack growth in W-composites. The development and initial testing of a Cu-ligament bridging model based on a micromechanical flow stress model of Cu is discussed. Good agreement with the 3-point bend testing data is demonstrated along with future plans to improve the model.

PROGRESS AND STATUS

Background

Tungsten (W) and W-alloys are the solid materials of choice for the plasma-facing components (PFCs) of future fusion reactors, such as the International Thermonuclear Experimental Reactor (ITER) and Demonstration Power Plant (DEMO), due to their high melting point, strength at high temperatures, high thermal conductivity, low coefficient of thermal expansion, and low sputtering yield [4-8]. However, W and most W-alloys exhibit low fracture toughness and a high ductile-brittle transition temperature (DBTT) that would render them as brittle materials during reactor operations [4, 6, 9]. The DBTT for unirradiated W-alloys typically ranges from 573K to 1273K (300 to 1000˚C) and in a reactor environment radiation hardening would further elevate this range [6, 10, 11]. Metallurgical approaches to toughen W-alloys, including rhenium (Re)-alloying and severe plastic deformation (SPD), have resulted in modest DBTT decreases [10, 12]. However, they would be difficult or impossible to implement, due to high costs and implications to irradiation hardening (Re alloys) or extremely complex processing demands (SPD) [13-15]. To prevent mechanical failure, a toughening mechanism is needed for W before it can be considered effective plasma facing component material (PFCM). W-alloys toughened by engineered reinforcement architectures, such as ductile-phase toughening (DPT), are strong candidates for PFCs. In DPT, a ductile phase is included in a brittle matrix to prevent fracture propagation. This is accomplished by the formation of an intact bridging zone behind the crack tip, which provides reinforcement, resulting in an increase in the remote load stress intensity for continued crack growth with increasing crack length [16, 17]. In Figure 1a, optical evidence of the crack bridging property of DPT can be seen in a W-Cu alloy.

The principles of DPT are illustrated in Figure 1b, which shows a schematic of ductile bridging ligaments stretching across an open crack in a brittle matrix material, such as W [16, 17]. For a brittle material containing a suitable volume fraction of a ductile phase, a highly effective resistance curve toughening mechanism develops as the crack extends. As the crack propagates through a brittle matrix, it leaves a bridging zone of ductile ligaments over a length $\boldsymbol{L}$ behind the crack tip. As the crack extends, $\boldsymbol{L}$ increases. For small scale bridging (SSB), when the bridging zone is much smaller than the length of the crack, $\boldsymbol{L}$ reaches a steady state ($\boldsymbol{L} = \boldsymbol{L_{SSB}}$). The ligaments act in opposition to the applied loading stress intensity factor, $\boldsymbol{K_{Applied}}$. This reduces the crack tip stress intensity factor so that: $\boldsymbol{K_{Tip}} < \boldsymbol{K_{Applied}}$. The crack opening (u) increases with increasing distance behind the crack-tip until the reinforcement breaks at a critical u*.

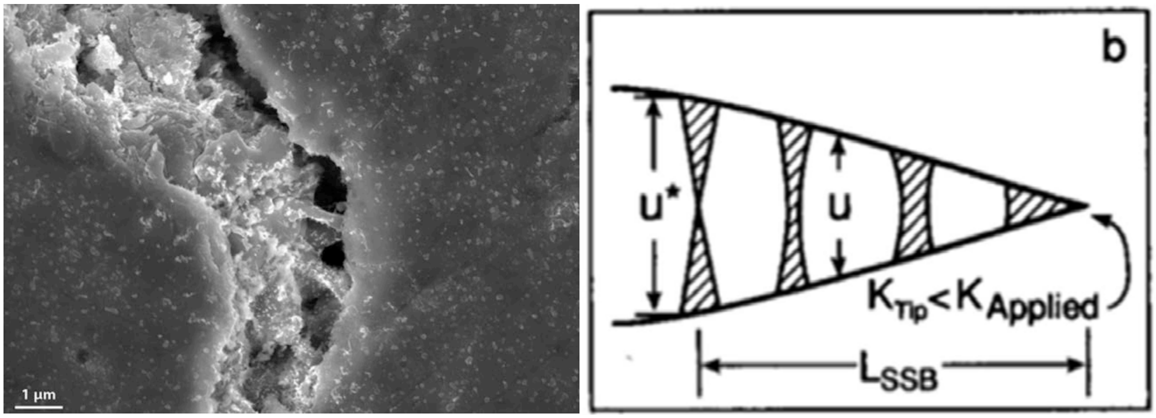

Figure 1. a) SEM image of W-Cu fracture where the ductile phase (Cu) is effectively bridging the crack. b) A steady-state bridging zone shown schematically in 2D [17].

Experimental

Elevated temperature testing of notched and pre-cracked three-point bend specimens was performed in a tube furnace at ½ T_m, ⅔ T_m, and room temperature, where T_m is the melting point of the reinforcement (ductile) phase. Displacement rates of 0.0002, 0.002, 0.02, 0.2, and 2.0 mm/min were employed. Purified Ar gas flowed through the tube furnace to prevent specimen oxidation. W-Cu alloys were evaluated using fracture mechanics test methods to gather quantitative data on the effects of DPT. Similar tests on monolithic W were performed to provide a baseline for comparison to these materials [18].

The W-Cu System

The W-Cu system served as a model system for the initial exploration of DPT in W-alloys [18]. Although not a plausible choice for nuclear applications due to Cu's low melting temperature, it was chosen with the goal of maximizing the plastic $\sigma(u)$ of the Cu reinforcement. The data gathered would be used to develop a fully quantitative model of DPT in the W-Cu system that will aid in future research to develop an effective W-based PFC. A working hypothesis for this composite material is that the fracture properties are determined by the ductile-phase mechanical properties, which in this case is the Cu phase.

The W-25% Cu (by weight) composite, Copelmet®, was purchased by UCSB and sent to PNNL in the form of 3.30mm x 1.67mm x 16.05mm bend bars for mechanical testing [18]. The bars were EDM notched to a depth (a_n) over bar width (w) ratio of a_n/w =0.2. Slight variances in specimen geometry (including notch depth) were accounted for by computing the peak-load linear elastic stress intensity factor (K_{peak}).

Three-Point Bend Testing

Testing was conducted on an Instron 5582 test frame with the following parameters: 1) Test temperatures were ambient, ½ T_m and ⅔ T_m, and 2) Strain rates were 0.0002 to 2 mm/min covering each decade. All high temperature testing was conducted in flowing purified argon (Ar) to prevent oxidation of the sample.

Peak Stress Intensity Calculation

Calculations of K_{Peak} were made from the 3-point SENB data using the peak load and equations A3.1 and A3.2 in ASTM-E399-12, "Standard Test Method for Linear-Elastic Plane-Strain Fracture Toughness KIC of Metallic Materials" [19]. At this stage of research, K_{Peak} provides an approximate toughness-based method for comparing the mechanical properties of W-composites by accounting for differences in specimen and crack geometry. The results are not meant to be interpreted as fracture toughness data.

Model Development

Model Methodology

A dynamic bridging model was constructed based on previous fiber bridging models with time-dependent deformation, including fiber creep and fiber/matrix interphase oxidation [20-23]. The bridges are now considered to be Cu particles intercepted by cracks in the W matrix. The toughening of the W-Cu alloy has been documented elsewhere [24] but is summarized in Figure 2 showing the dependence of the peak stress intensity, K_{peak}, on 3-point bend sample displacement rate and temperature.
The basic framework of the model is to solve for the set of bridging forces acting on a set of compliant elastic-plastic bridges spanning a crack in a brittle matrix in 2-dimensions (2D) and to treat these forces as crack closure forces that impart a measure of fracture toughness to the brittle matrix material by virtue of having to be deformed plastically as the crack extends. The solution makes use of the weight function for 4-point bending of a bar and is detailed in Ref. [22]. Each Cu bridge is assigned a compliance that is used to compute the bridge force. At this time, we have only implemented the bridge being loaded to its ultimate tensile strength after which it is considered to be a broken bridge and to contribute nothing to crack closure forces.

The model makes use of a published Cu flow stress model [25] to compute the entire flow stress curve to the ultimate strength as a function of strain rate and temperature, which are explicitly built into the flow stress model. In this way, the effects of test strain rate and temperature are accounted for. For the 3-point bend test geometry the experimental displacement rates were converted into an effective tensile strain rate using the 3-point bending formula. These were the strain rates that are used in conjunction with the Cu flow stress model implementation.

Implementation with Cu Flow Stress Model

The flow stress model for Cu as derived in Ref. [25] is implemented. In the model, the stress has an exponential dependence on the strain as follows:

$$\sigma = \sigma_y + \frac{m^2 \alpha G}{\omega c_L}\left(1 - e^{-\omega \varepsilon/2}\right) \tag{1}$$

where σ_y is the yield strength where plastic deformation starts, *m* the Taylor factor, *G* the shear modulus,

$\alpha = (1-\nu/2)/2\pi(1-\nu)$ (ν is the Poisson's ratio), and $\omega = \frac{m}{b} d_{int}\left(2 - \frac{1}{n_{slip}}\right)$. The interaction distance between dislocations where they start to combine, d_{int} is taken to be 2.5 times the Burger's vector magnitude *b*. The number of slip systems n_{slip} in Cu is 12. The parameter c_L is related to the "spurt" distance, *L*, which a dislocation moves when it is released during deformation:

$$c_L = L\sqrt{\rho} \tag{2}$$

where ρ is the dislocation density. The value of c_L is calculated from the stationary dislocation density ρ_{stat}. From the balance of dislocation density due to work hardening and dynamic recovery model:

$$\rho_{stat} = \left(\frac{m}{b c_L \omega}\right)^2 \tag{3}$$

On the other hand, the balance of dislocation density due to work hardening and static recovery model gives

$$\mathrm{M}\rho_{\mathrm{stat}}^{3/2} = \frac{\mathrm{m}\dot{\varepsilon}}{2\mathrm{bc_L}}\left(\frac{2}{\mathrm{Gb}^2}\right) \tag{4}$$

where *M* is the dislocation mobility, which depends on temperature, *T*, and dislocation density. Using Equation 3 and 4, c_L can be solved numerically. The dislocation mobility for climb and glide is given by

$$\mathrm{M}(\mathrm{T},\sigma) = \frac{\mathrm{D_{so}b}}{\mathrm{k_B T}}\exp\left(\frac{\sigma \mathrm{b}^3}{\mathrm{k_B T}}\right)\exp\left(-\frac{\mathrm{Q}}{\mathrm{RT}}\left[1-\left({}^{\sigma}/_{\sigma_{\mathrm{back}}}\right)^2\right]\right) \tag{5}$$

The meaning and value of the constants are given in Table 1. The stress is related to the dislocation density as

$$\sigma = \sigma_{\mathrm{y}} + \mathrm{m}\alpha\mathrm{Gb}\sqrt{\rho} \tag{6}$$

The dependence of the shear modulus on temperature is taken to be $G = 4.75\mathrm{x}10^4 - 17T$, where *G* is in MPa and *T* in K. The temperature and strain rate dependence of the yield strength is expressed as

$$\sigma_{\mathrm{y}}(\mathrm{T},\dot{\varepsilon}) = \sigma_{\mathrm{y}}(\mathrm{T_0},\dot{\varepsilon_0})\left[\left(1-\left(\frac{\sigma}{\sigma_{\mathrm{back}}}\right)^2\right)\left(\frac{\sigma}{\sigma_{\mathrm{CLo}}}\right)+\left(\frac{\sigma}{\sigma_{\mathrm{back}}}\right)^2\frac{\mathrm{G}}{\mathrm{G_0}}\right]\left(\frac{\dot{\varepsilon}}{\dot{\varepsilon}_0}\right)^{1/\mathrm{n}} \tag{7}$$

where the subscript 0 denotes the reference temperature of 293 K and reference strain rate of 0.0001. The Norton exponent, n, can be determined from the stationary creep rate as follows:

$$\dot{\varepsilon} = \frac{2\mathrm{bc_L}}{\mathrm{m}}\frac{\mathrm{Gb}^2}{2}\mathrm{M}(\mathrm{T},\sigma)\left(\frac{\sigma}{\alpha\mathrm{mGb}}\right)^3 \tag{8}$$

$$\mathrm{n} = \mathrm{d}\ln(\dot{\varepsilon})\,/\mathrm{d}\ln(\sigma) \tag{9}$$

This model provides a set of equations that can be solved at a given strain rate or temperature to provide a stress-strain curve, either true strain or engineering strain, that is used to represent the Cu bridges in the dynamic bridging model. At the present time, the bridges are only allowed to reach their ultimate tensile strength and then break. No time-dependent creep deformation is treated at this time, rather the strain rates are accounted for explicitly in the flow stress model. Norton exponents range from 120 at room temperature and fast strain rates to about 6 as slower strain rates and high temperatures. In addition, a strengthening factor, sfact, is introduced into the model to account for bridge size effects and tri-axial constraint. This factor linearly scales the stress strain curve to account for these effects that can act to greatly increase the fracture strength of small, constrained bridges. In this preliminary work, the linear scaling is applied with a constraint that the Young's modulus remains unchanged. Scaling of the Young's modulus will be investigated in the future.

Table 1. Parameters used in the implementation of the copper flow stress model.[1]

Parameter	Value	Description
$\dot{\varepsilon}_0$	0.0001	Reference strain rate
σ_{back}	257 MPa	Maximum back stress
σ_{CL0}	209 MPa	Reference tensile strength
σ_{y0}	74 MPa	Reference yield strength
m	3.06	Taylor factor
α	0.19	Coefficient in Equation 1
D_{s0}	1.31×10^{-5} m^2/s	Coefficient for self diffusion
Q	198000 J/mol	Activation energy for self diffusion
b	2.56×10^{-10} m	Burger's vector magnitude
k_B	1.381×10^{-23} J/K	Boltzmann's constant
R	8.314 J/mol/K	Gas constant

Approach

In an attempt to compare model results to experimental data, an equivalent dataset was considered. The model begins by considering an initial applied K, a_{K0}, for a known specimen geometry and a_0/w, where a_0 is the initial crack length and w is the specimen width. For the case treated here, a_0 was 0.7 mm and w was 3.3 mm and the bar was loaded in 4-point bending. The value of *sfact* was obtained by arbitrarily assuming that a bridged crack that was 1-mm long existed in the sample at each strain rate and temperature. The value of *sfact* that achieved this stable bridged crack at $2/3T_m$ and a strain rate of 1.47×10^{-5} s^{-1} was equal to 4.7. Thus, the computed flow stress for Cu using the flow stress model was scaled by 4.7 to account for size and constraint effects in the Cu bridges. A bridge radius of 50 µm was assumed with a Cu volume fraction of 0.4 to match previous SEM data on Cu area fraction in polished cross-sections.

Results

Model Results

The model was run at all strain rates and temperatures to match the experimental dataset (see Table 2) so that a maximum applied K (a_{K0}) was found for each temperature and strain for which the crack was still bridged and stable after 1-mm of crack growth. The criteria for crack growth was a_{Kcrit} = 8 MPa√m so that a crack will arrest when a_{Ktip} falls below 8 MPa√m. Determining the maximum applied K (a_{Kmax}) for which crack arrest will still occur is roughly equivalent to measuring the K_{peak} in the experiments, and allows for a direct comparison of datasets, one experimental and one model. Several steps were taken in order to determine this value for each strain rate and temperature. In addition to recording a_K, other calculated values were recorded as well: a_{Ktip} and the difference between a_K and a_{Ktip}, which is ΔK. ΔK represents the closure force caused by the bridges, or the toughening due to the bridges. The model dataset is shown in Table 1 and the maximum values of a_K (a_{Kmax}) are plotted as a function of applied displacement rate (strain rate) and temperature in Figure 3 for comparison with Figure 2.

---

[1] The reference condition corresponds to strain rate of 0.0001 at 293 K.

Table 2. Model results showing computed values of critical parameters for stable bridged cracks

Temp (K)	**Displ. Rate (mm/min)**	**Strain Rate (1/s)**	**sfact**	**Max a_{K0} (MPa√m)**	**Number of bridges**	**a_{Ktip} (MPa√m)**	**Max a_K = a_{Kmax} (MPa√m)**	**ΔK (MPa√m)**
293	2	0.17	4.7	19.61	29	7.99	34.82	26.83
293	0.2	0.017	4.7	19.39	30	7.44	35.13	27.69
293	0.02	0.0016	4.7	19.31	30	7.80	34.99	27.19
293	0.002	0.000155	4.7	19.13	30	7.99	34.66	26.67
293	0.0002	1.47E-05	4.7	18.8	30	7.99	34.06	26.08
679	2	0.056	4.7	17.72	31	7.85	32.77	24.92
679	0.2	0.0051	4.7	16.94	31	7.99	31.33	23.34
679	0.02	0.000459	4.7	16.52	32	7.99	31.29	23.30
679	0.002	3.97E-05	4.7	15.47	32	7.99	29.31	21.32
679	0.0002	3.45E-06	4.7	14.75	35	7.99	29.77	21.77
905	2	0.035	4.7	16.25	32	7.99	30.68	22.69
905	0.2	0.0029	4.7	15.04	33	7.99	29.09	21.10
905	0.02	0.00024	4.7	13.88	35	7.99	28.01	20.02
905	0.002	1.87E-05	4.7	12.42	38	7.99	26.86	18.87
905	0.0002	1.37E-06	4.7	10.15	39	7.93	22.45	14.52

Experimental Data for W-Cu

At room temperature, the peak stress intensity of W-Cu (≈20-24 MPa√m) is approximately three times greater than that of monolithic W (≈8 MPa√m) [18]. Figure 2 shows the effects of temperature and deformation rate on the peak stress intensity of W-Cu as determined in experiments in flowing Ar in 3-point bending. As expected the greatest toughening occurs for the highest strain rates and the lowest temperatures, corresponding to where the Cu reinforcement phase is the strongest. The least toughening occurs for the slowest strain rates and higher temperatures.

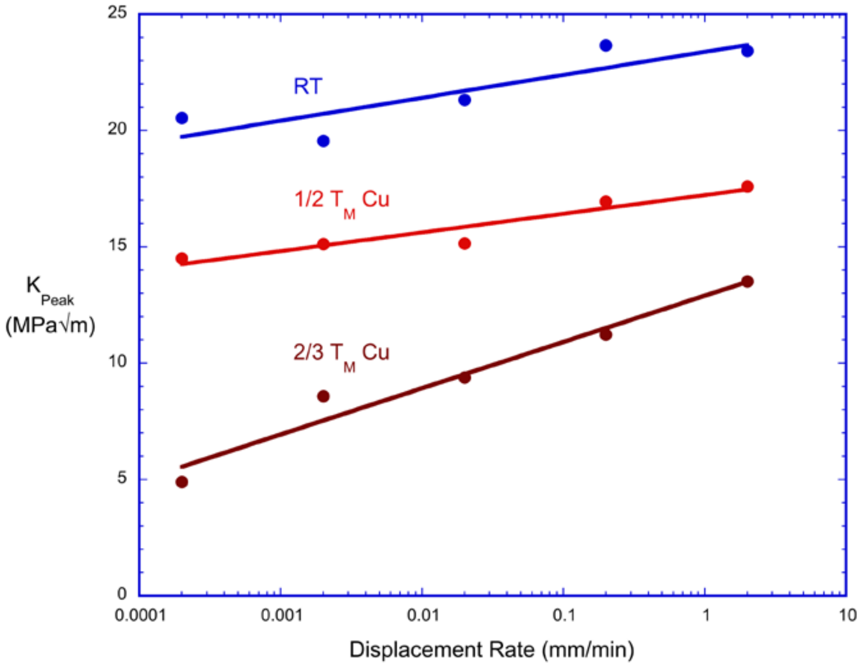

Figure 2. Dependence of peak stress intensity of the W-Cu composite on deformation rate and test temperature.

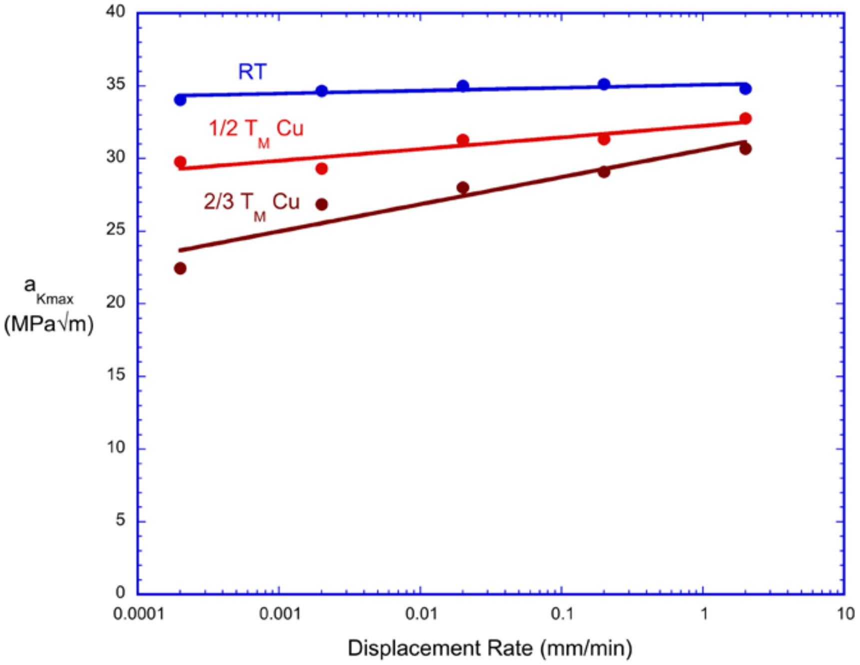

Figure 3. Dependence of computed a_{Kmax} for W-Cu bridged model on strain rate and temperature.

<u>Discussion and Comparison</u>

The model results are rather arbitrary in terms of initial conditions but the trends are encouraging. In order to examine the trends more carefully, the model results are put onto the same scale as the experimental data by applying a simple constant correction. The model a_{Kmax} is scaled to the experimental data by applying a correction of 22.45 – 4.9 = 17.55 MPa√m offset to account for the differences between the model a_{Kmax} and experimental K_{peak} at the slowest strain rate and highest temperature. This scaled result is shown in Figure 4. This data plot demonstrates that the Cu flow stress model captures the effects of strain rate and temperature rather well. The agreement is especially encouraging at the highest temperatures where the slopes of the two datasets as a function of strain rate are very similar. This is attributed to the high quality of the strain rate dependence built to the flow stress model as discussed in Ref. [25]. The two sets of data are not as similar for the room temperature data.

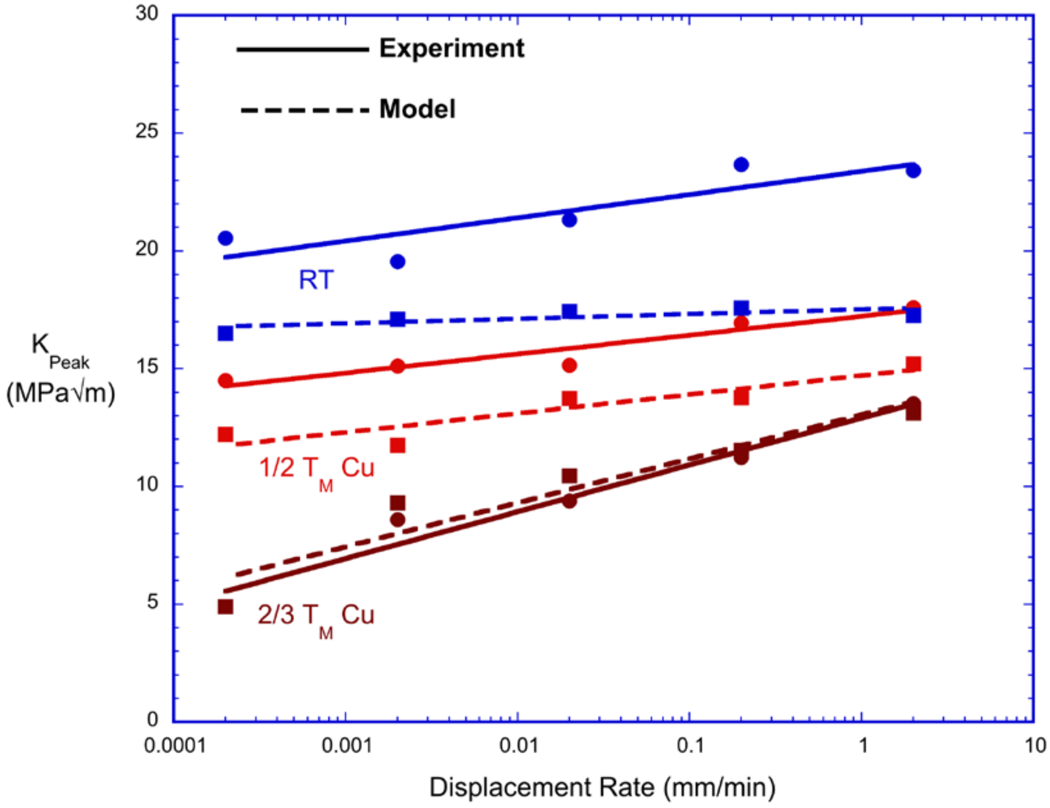

Figure 4. Single point scaled model data compared to experimental data. Solid lines are experiment and dashed lines are model data. The single point scaling places only the two points at the lower left of the plot (slowest strain rate and highest temperature) in coincidence by simple subtraction.

The similarity in slopes at the highest temperatures reflects the accuracy of the Cu flow stress model in capturing the effects of strain rate on ultimate tensile strength. However, it is not clear why this agreement is not as good at room temperature unless the current neglected contributions to bridge deformation (see below) have a larger effect at lower temperatures. Indeed, it may be that we are not capturing the complete work of fracture at room temperature due to the competition between work hardening and plastic instability. At higher temperatures, work hardening is lessened and creep deformation plays an increasingly important role. This work is preliminary and reflects a first-cut at dynamic ductile bridging model development. More details are required.

FUTURE WORK

The representation of the Cu bridges needs to be improved by taking into account the following aspects of ductile bridging as follows:

1. The ductile bridges need to be able to shed load and to neck as seen in experiments [2, 26-28].
2. The ductile bridges need to undergo creep deformation at high temperatures and slow strain rates.
3. The ductile bridges need to be able to debond as required.

REFERENCES

[1] H. E. Deve, A. G. Evans, G. R. Odette, R. Mehrabian, M. L. Emiliani, and R. J. Hecht, Acta Metall. Mater. 38 (1990) 1491.
[2] F. Erdogan and P. F. Joseph, J. Am. Ceram. Soc. 72 (1989) 262.

[3] L. S. Sigl, P. A. Mataga, B. J. Dalgleish, R. M. McMeeking, and A. G. Evans, Acta Metall. 36 (1988) 945.
[4] M. Rieth, J. L. Boutard, S. L. Dudarev, T. Ahlgren, S. Antusch, N. Baluc, M. F. Barthe, C. S. Becquart, L. Ciupinski, J. B. Correia, C. Domain, J. Fikar, E. Fortuna, C. C. Fu, E. Gaganidze, T. L. Galan, C. Garcia-Rosales, B. Gludovatz, H. Greuner, K. Heinola, N. Holstein, N. Juslin, F. Koch, W. Krauss, K. J. Kurzydlowski, J. Linke, C. Linsmeier, N. Luzginova, H. Maier, M. S. Martinez, J. M. Missiaen, M. Muhammed, A. Munoz, M. Muzyk, K. Nordlund, D. Nguyen-Manh, P. Norajitra, J. Opschoor, G. Pintsuk, R. Pippan, G. Ritz, L. Romaner, D. Rupp, R. Schaublin, J. Schlosser, I. Uytdenhouwen, J. G. Van Der Laan, L. Veleva, L. Ventelon, S. Wahlberg, F. Willaime, S. Wurster, and M. A. Yar, J. Nucl. Mater. 417 (2011) 463.
[5] R. A. Pitts, A. Kukushkin, A. Loarte, A. Martin, M. Merola, C. E. Kessel, V. Komarov, and M. Shimada, Phys. Scripta T (2009) 014001.
[6] P. Mertens, T. Hirai, M. Knaup, O. Neubauer, V. Philipps, J. Rapp, V. Riccardo, S. Sadakov, B. Schweer, A. Terra, I. Uytdenhouwen, and U. Samm, Fusion Eng. Des. 84 (2009) 1289.
[7] A. Gervash, R. Giniyatulin, T. Ihli, W. Krauss, A. Makhankov, I. Mazul, P. Norajitra, and N. Yablokov, J. Nucl. Mater. 367-370 B (2007) 1472.
[8] M. Merola, W. Danner, and M. Pick, Fusion Eng. Des. 75-79 (2005) 325.
[9] P. Mertens, V. Philipps, G. Pintsuk, V. Riccardo, U. Samm, V. Thompson, and I. Uytdenhouwen, Phys. Scripta T (2009) 014032.
[10] B. Gludovatz, S. Wurster, A. Hoffmann, and R. Pippan, Int. Journal of Refractory Metals and Hard Materials 28 (2010) 674.
[11] S. J. Zinkle and N. M. Ghoniem, Fusion Eng. Des. 51-52 (2000) 55.
[12] M. Faleschini, H. Kreuzer, D. Kiener, and R. Pippan, J. Nucl. Mater. 367-370 A (2007) 800.
[13] T. Tanno, A. Hasegawa, J. C. He, M. Fujiwara, M. Satou, S. Nogami, K. Abe, and T. Shishido, J. Nucl. Mater., 386-388 (2009) 218.
[14] T. Tanno, A. Hasegawa, M. Fujiwara, H. Jian-Chao, S. Nogami, M. Satou, T. Shishido, and K. Abe, Mater. Trans. 49 (2008) 2259.
[15] T. Tanno, A. Hasegawa, H. Jian-Chao, M. Fujiwara, S. Nogami, M. Satou, T. Shishido, and K. Abe, Mater. Trans. 48 (2007) 2399.
[16] K. T. Venkateswara Rao, G. R. Odette, and R. O. Ritchie, Acta Metall. Mater. 42 (1994) 893.
[17] G. R. Odette, B. L. Chao, J. W. Sheckherd, and G. E. Lucas, Acta Metall. Mater. 40 (1992) 2381.
[18] K. H. Cunningham, K. Fields, D. Gragg, F. W. Zok, J. C. H. Henager, R. J. Kurtz, and T. Roosendaal, Fusion Materials Semiannual Progress Report for Period Ending June 30, 2013, DOE/ER-0313/54, U. S. Department of Energy, 95.
[19] Author, Standard Test Method for Linear-Elastic Plane-Strain Fracture Toughness KIC of Metallic Materials, E399-12 (ASTM International, West Conshohocken, PA, 2012).
[20] C. H. Henager Jr., J. Nucl. Mater., 367-370 (2007) 742.
[21] R. H. Jones and C. H. Henager Jr, J. Eur. Ceram. Soc. 25 (2005) 1717.
[22] C. H. Henager Jr. and R. G. Hoagland, Acta Mater. 49 (2001) 3739.
[23] C. H. Henager Jr., R. H. Jones, C. F. Windisch, Jr., M. M. Stackpoole, and R. Bordia, Metall. Mater. Trans. 27A (1996) 839.
[24] C. H. Henager Jr., R. J. Kurtz, T. J. Roosendaal, B. A. Borlaug, G. R. Odette, K. H. Cunningham, K. Fields, D. Gragg, and F. W. Zok, Fusion Materials Semiannual Progress Report for Period Ending December 31, 2013, DOE/ER-0313/55, U. S. Department of Energy, 23.
[25] R. Sandstrom and J. Hallgren, J. Nucl. Mater. 422 (2012) 51.
[26] M. Bannister, H. Shercliff, G. Bao, F. Zok, and M. F. Ashby, Acta Metall. Mater. 40 (1992) 1531.
[27] B. N. Cox, Acta Metall. Mater. 39 (1991) 1189.
[28] M. F. Ashby, F. J. Blunt, and M. Bannister, Acta Metall. 37 (1989) 1847.

4.2 RECENT PROGRESS IN THE FABRICATION AND CHARACTERIZATION OF DUCTILE-PHASE-TOUGHENED TUNGSTEN COMPOSITES FOR PLASMA-FACING MATERIALS –

K. H. Cunningham, G. R. Odette, K. Fields, D. Gragg, and F. W. Zok (University of California, Santa Barbara), C. H. Henager, Jr., R. J. Kurtz, T. J. Roosendaal, and B. A. Borlaug (Pacific Northwest National Laboratory)

OBJECTIVE

The objective of this study is to develop ductile-phase-toughened tungsten composites as candidates for plasma-facing components in future fusion reactors.

SUMMARY

A promising approach to increasing fracture toughness and decreasing the DBTT of a W-alloy is by ductile-phase toughening (DPT). In this method, a ductile phase is included in a brittle matrix to prevent crack propagation by bridging. Composite specimens were fabricated by two methods: 1) sintering W powders together with carburized W wires, and 2) hot pressing W and Cu foils together with W wires. These composites were tested in tension and three-point bending.

PROGRESS AND STATUS

Background

Background information and previous progress have been discussed in earlier semi-annual reports [1-2].

Experimental

W-Wires and W and Cu Foils as Reinforcements

We have previously reported the tensile properties of tungsten wire, which motivated an investigation of using W-wire as reinforcement. Table 1 summarizes the tensile properties of W-wire of various diameters. [2] A general trend of increased strength and decreased ductility is observed as the wire diameter decreases. The ultimate strength reaches a remarkable value of ≈ 4.25 GPa in the 15-µm diameter wire, with about 1.0% total elongation. While the strengths are lower for the larger diameter wires the total elongations are about 1.7 and 2.4% respectively.

The 250-µm W wires, used to make the composites described below, were characterized to quantify how their properties evolved after several of the high-temperature processing steps used in composite fabrication. After processing at 1900°C for 5 minutes during the carburization process described below, only modest effects on the grain structure and texture of the wires were observed in EBSD measurements, which require further quantitative analysis. The hardness of the wire decreased about 9% after processing treatments of hot pressing the laminate in vacuum at 900°C for 5 minutes as well as performing an oxide reduction for 360 minutes in H_2 at 900°C, followed by a second hot pressing step under the same conditions as the first for a total of 370 min at temperature.

Table 1. Average values of W wire properties from tensile testing. [2]

Wire Diameter (µm)	Yield Stress (GPa)	Ultimate Tensile Strength (GPa)	Total Elongation (%)	Reduction in Area (%)
15	3.58	4.24	1.0	N/A
250	1.78	2.30	1.7	29.9
500	1.34	2.16	2.4	27.1

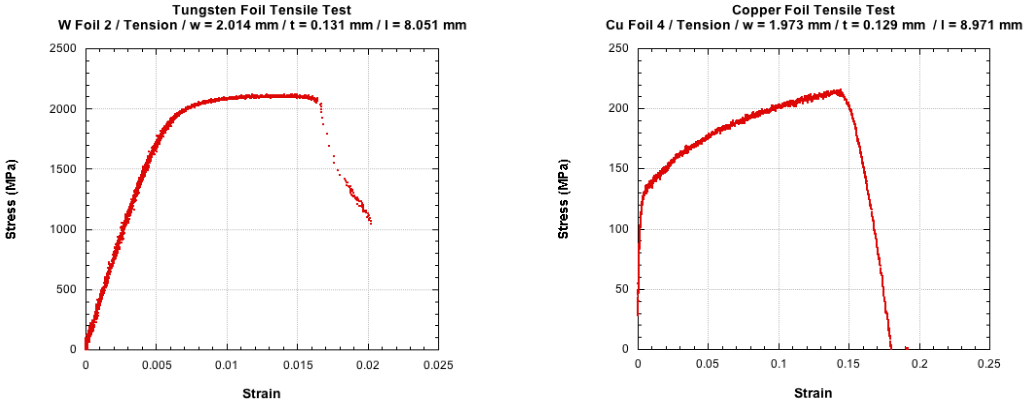

Figure 1. Representative stress-strain curves for tungsten (left) and copper (right) foils. Note the order-of magnitude differences for both the stress and strain axes between graphs.

We also tested pure W and Cu foils with nominal thickness 127 µm. These foils were used to fabricate a laminate composite as discussed below. Tensile tests were performed at a strain rate of 0.011 min^{-1} at ambient temperature in air, with a gauge length and width of 9 mm and 2 mm, respectively. Strain was measured with a laser extensometer. Representative stress-strain curves for the pure tungsten and copper foils are shown in Figure 1. The tensile properties are summarized in Table 2. The W-foil has a high strength and limited ductility. The Cu-foil has low strength, but high ductility.

Table 2. Summary of tensile data for tungsten and copper foils (nominal thickness = 127 µm).

	Yield Stress (MPa)	Ultimate Tensile Strength (MPa)	Total Elongation (%)
W	1997.7 ± 10.5	2119.4 ± 4.5	3.4 ± 1.3
Cu	130.2 ± 4.6	218.7 ± 4.9	16.9 ± 3.3

The W-WC Sintered Composite System

Fiber-reinforced composites were explored with unidirectional coated W wires in a W matrix. Efforts to use a Cu coating on the W wire have been reported previously. [2] Tungsten carbide (WC) was investigated as a potential highly stable debonding layer since it is even more brittle than W and because C is a suitable element for the divertor in terms of low neutron activation and reduced potential for plasma contamination. 250-µm diameter W wires were placed apart in loose graphite powder, and then compacted at 35 MPa at ambient temperature in the SPS system. The compact was heat treated at 1800°C for 1 minute with a heating ramp of 300°C/min under a minimum load of 9 MPa. The resulting WC layer on the wire was 12 µm thick. To consolidate a sample from which two test specimens containing one embedded wire could be prepared, two coated wires were then laid separately and parallel in W powder of particle size 4-6 µm. The wires and powder were sintered at 1900°C for 15 minutes at 50 MPa. Notched specimens of the sintered composite were tested in three-point bending with the goal of observing debonding behavior during crack propagation. Notched three-point bend test samples were EDM cut with a test span, width, thickness, and notch depth of 10 mm, 3.6 mm, 3.6 mm, and 0.5 mm, respectively. The crack propagation direction was perpendicular to the wire direction. Bend testing was performed with a crosshead displacement rate of 0.05 mm/min at ambient temperature in air.

The W-Cu Hot-Pressed Composite System

To avoid the issue of Cu melting and wicking during the sintering of a W matrix, a hot-pressing fabrication route was developed for W wires sandwiched between W and Cu foils, as illustrated in Figure 2a. The top and bottom layers were 127-µm W foils. The inner layers were the 127-µm Cu foils, while the middle layer contained 250-µm W wires. The laminate was 5cm x 5cm, with an average of 50 µm at the shortest distance between the parallel fibers. After hot pressing at 900°C at 38 MPa for 5 minutes, the W-wires were embedded in the Cu, forming a 3-layer sandwich. Tensile test samples of the reinforcement were EDM cut with a gauge length, width, and thickness of 6.4 mm, 2.45 mm, and 0.8 mm, respectively. The tensile direction was parallel to the wire direction. Tensile testing was performed with crosshead displacement rates of 0.1 and 0.1125 mm/min at ambient temperature in air.

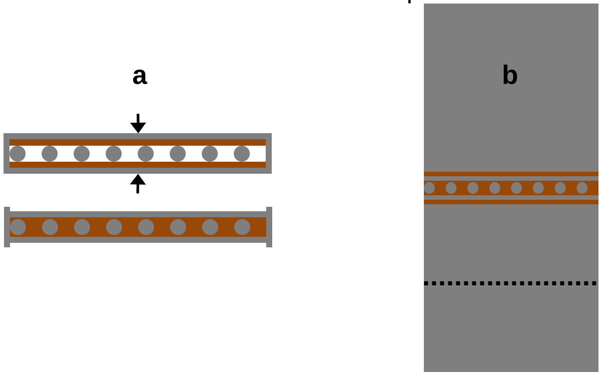

Figure 2. a) Schematic diagram of reinforcement cross-section before (top) and after (bottom) hot pressing. b) Schematic diagram of laminate bend specimen cross-section. Dashed line indicates notch depth.

The W-foil//Cu//W-wire sandwich reinforcement was then hot pressed between 4-mm thick W plates, as illustrated in Figure 2b. Since the surface roughness of the reinforcement was ≈ 100 µm, reflecting the underlying topology of the stronger W-wires, a Cu bond layer of 127-µm foil was used between the W-plates and sandwich. However, in spite of this extra layer the volume/atom fraction of Cu is much lower at ≈ 10% in the laminate, compared to ≈ 50% in the heavy metal W-Cu composites studied previously. Notched three-point bend test samples were EDM cut with a test span, width, thickness, and notch depth of 27.6 mm, 8.9 mm, 3.1 mm, and 2 mm, respectively. The crack propagation direction was perpendicular to the wire direction. Bend testing was performed with a crosshead displacement rate of 0.02 mm/min at ambient temperature in air.

RESULTS

W-WC Sintered Composite

No bridging was observed in the W-WC sintered composite, since the cracks ran directly though the coated wire without any debonding. Despite the presence of some porosity at the WC-matrix interface, this may be due to the fact that the WC layer was strongly bonded to both the W matrix and wire. A representative load-displacement curve shown in Figure 3 illustrates the brittle response of the material.

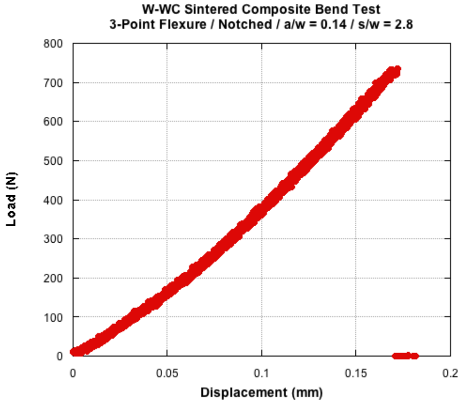

Figure 3. Representative load-crosshead displacement curve for notched 3-point bend tests on W-WC sintered composite, showing brittle failure.

W-Cu Hot-Pressed Composite

Reinforcement Tensile Testing

A representative stress-crosshead displacement curve and images of two different broken test specimens are shown in Figure 4. Note that the plot shows one curve with a discontinuity, as the test was paused and resumed after the W foils cracked. The reinforcement showed some evidence of fiber pullout but no indication of plasticity in the W-wires. The outer W-foils cracked at the peak stress, followed by fracture of the W-wires. Deformation occurred in the Cu layer at a much lower stress until up to ductile failure. Determination of the stress contribution from wire pullout is in progress.

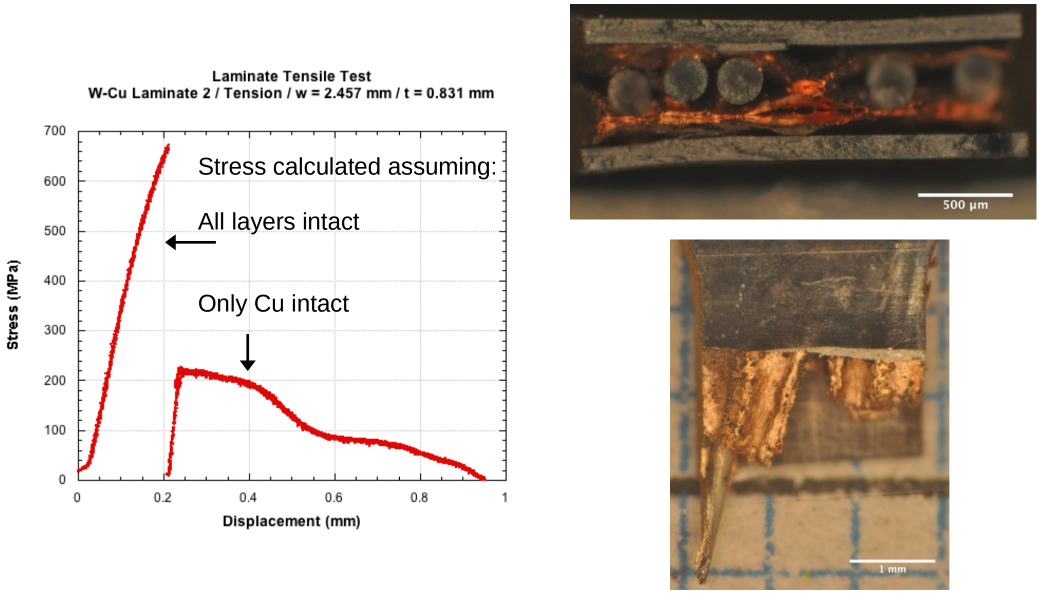

Figure 4. Left: stress-displacement curve for laminate tensile test 2. Top right: fracture surface of specimen 1. Bottom right: protruding W wire from specimen 2 suggests energy dissipation by pullout.

Laminate Notched Three-Point Bend Testing

The results are summarized in Figure 5. The stress was calculated using the applied load and initial geometry of the test specimen. In one test (specimen 1), the crack propagated through the W plate up to the embedded laminate and re-nucleated on the other side, leaving the reinforcement sandwich intact. At this point the specimen could only sustain a low load, of ≈ 130 N. In a second test (specimen 2), cracks grew from the notch parallel to the sandwich, before branching with one crack deflecting 90° and propagating up to the sandwich at the first pop-in stress drop. This crack arrested and the stress increases again until the crack re-nucleated at the back of the sandwich marked by the second stress drop. However, the laminate composite was still able to sustain a significant load in this case, which actually then increased prior to a gradual drop-off associated with continued deformation of the sandwich layer. Removing the Cu using an acid bath showed that several of the W wires had fractured approximately 0.075 to 1.4 mm away from the bending point, indicating that fiber pullout could play a role in the mechanical response of the composite. Peak-load stress intensity factor values ranged from 20 to 34 MPa√m. These results are very encouraging and suggest that sandwich reinforcements could provide a route to developing tough W composites.

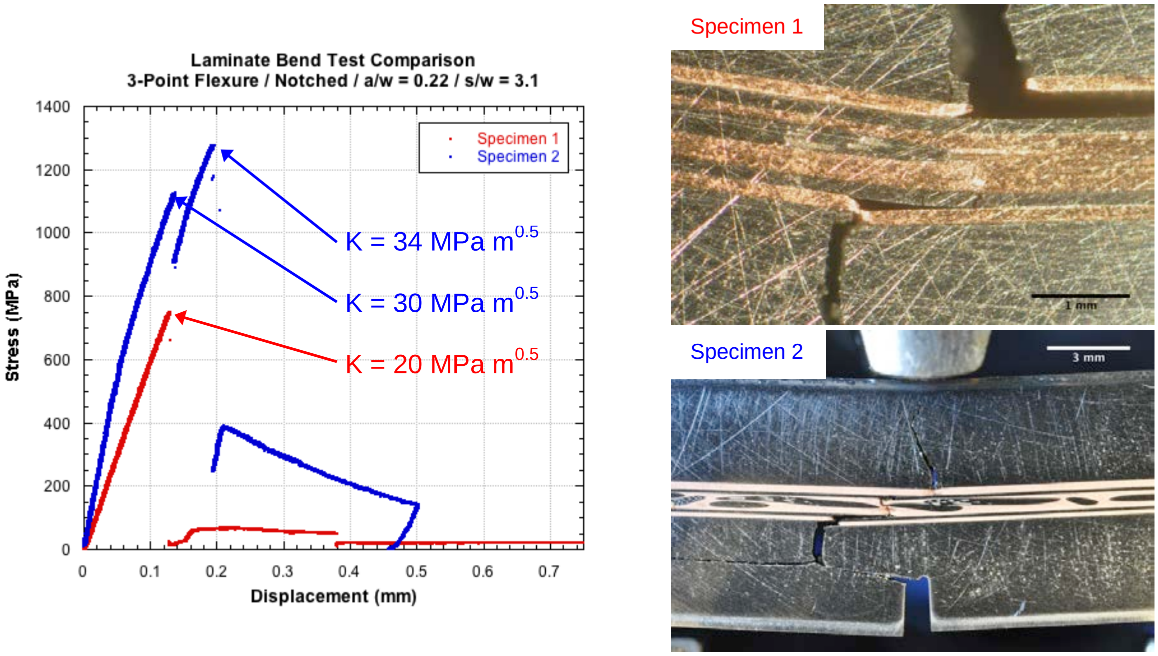

Figure 5. Stress-displacement curves for two bend specimens. Right top: specimen 1 after testing Right bottom: specimen 2 after testing.

ONGOING AND FUTURE WORK

The next steps underway are to fabricate multilayer laminate composites by hot pressing 1-mm W plate with various metallic foils, including copper, iron, stainless steels, and vanadium. These composites will be notched, precracked, and tested in three-point bending to measure relative resistance to crack growth. These experiments will be complemented by bridging model calculations. The model, along with fracture data, the method and cost of synthesis, and microstructure examinations will be used to guide the future design of improved W-composites. We will link our composite development effort to thermal-mechanical simulations of W-based divertor components and will attempt to fabricate and evaluate some divertor-type components. Ultimately, a clear understanding of the materials science of W-composites will be developed with relation to: a) the choice and behavior of the ductile phase; b) the synthesis, processing, and fabrication of composites; and c) the composite’s microstructure as it evolves during service.

REFERENCES

[1] K.H. Cunningham, K. Fields, D. Gragg, F.W. Zok, C.H. Henager, Jr, R.J. Kurtz, and T. Roosendaal, Recent Progress in the Development of Ductile-Phase Toughened Tungsten for Plasma-Facing Materials, in DOE/ER-0313/54 - Volume 54, Semiannual Progress Report, June 30, 2013. 2013, US DOE: ORNL, TN.

[2] C.H. Henager, Jr, R. J. Kurtz, T. J. Roosendaal, B. A. Borlaug, G. R. Odette, K. H. Cunningham, K. Fields, D. Gragg, and F. W. Zok, Recent Progress in the Development of Ductile-Phase Toughened Tungsten for Plasma-Facing Materials, in DOE/ER-0313/55 - Volume 55, Semiannual Progress Report, Dec. 31, 2013. 2013, US DOE: ORNL, TN.

4.3 SPECIMEN PREPARATIONS FOR MECHANICAL TESTING AND HYDROGEN PERMEATION OF NANO W-1Ti-0.5TiC — X. Wang and Z. Zak Fang (University of Utah)

OBJECTIVE

The objective of this work is to prepare specimens for evaluating mechanical properties and hydrogen permeation of Nano W-1Ti-0.5TiC for fusion reactor materials applications.

SUMMARY

During the last reporting period, processing for making nano W with grain size near 100 nm was developed. The ongoing work in this reporting period is focused on evaluating mechanical properties and hydrogen permeation of the nano W alloys. So far, the specimen preparation for testing is being really difficult due to cracking problems during pressing and sintering, which originated from the special characteristics of the high energy milled nano W powders made in this project. Attempts have been made to make crack-free specimens for property evaluations of Nano W.

PROGRESS AND STATUS

Introduction

For fusion reactors, the material of choice must have well-established and high performance mechanical properties before and after irradiation. During the last reporting periods, we have developed processing for making nano W with grain size near 100 nm [1, 2]. First of all, the mechanical properties of the developed nano-W alloys at unirradiated state need to valid. However, the large samples after the processing showed some laminate cracks and radial cracks. For evaluating mechanical properties of nano W developed, the cracking problems of large samples have to be eliminated.

In this work, control of the processing parameters was investigated to eliminate cracking. Basically, the characteristics of nano-W powders with high specific surface area result in low and non-uniform density distributions in the large green compact to a great extent. Furthermore, the densification rate for the nano W powder made in this project can be really fast [1]. These lead to rapid and non-uniform shrinkage of the sintered compact, causing cracking. For achieving a high quality fully sintered testing specimen, the cracking problem may be solved via deceasing density inhomogeneity throughout the green compact and slow heating during sintering. The most sensitive parameters including compaction pressure, the heating rating of sintering, the pressing methods and the amount of binders were attempted for removing the cracks.

Experimental Procedure

Commercial tungsten powders with average particle size of ~ 100 nm were used as the raw materials. Commercially available Titanium Hydride (TiH_2) powders (average particle size of -45 µm) were used as the second phase element Ti and Titanium carbide (TiC) as the grain growth inhibitor. The powder W-1Ti-0.5TiC (in wt%) was milled in unique high energy ball milling machine [1] for 6 hours in a mixture of heptane and ethanol (15 vol%). Tungsten carbides (~ 1 mm) were used as the grinding media. Polyethylene glycol (PEG) and paraffin wax with different weight ratios were added as plastic binders and lubricants. The milled nano tungsten powders were dried in a vacuum desiccator and then were compacted using a uniaxial press and a cold isostatic press (CIP) at different pressures. The green compacts were then treated in hydrogen at different temperatures (250, 650, and up to 1100 ◦C) with different time durations and heating rates (1-10 ◦C/min) for debinding, reducing, and sintering.

Density measurements of the green and sintered specimens were conducted by simple geometric and mass measurements, as well as by the Archimedes technique using distilled water as the displacement medium. The microstructures of the fractured surface of the sintered samples were observed using Scanning Electron Microscopy (SEM). Tungsten grain sizes were determined from the SEM micrographs by using the linear intercept method.

Results

Previously, only small samples for microstructural analysis and hardness testing were made. Figure 1(a) shows a photo of the small sample which is free of cracks. For measuring a wide range of properties of Nano W, large specimens with two shapes, rod and disc, have been made.

Rod specimens

Table 1 lists the process parameters tested for CIPed and uniaxial pressed nano W rods. At first, there were no plastic binders in the powers. Cracks were observed at each processing steps as shown in Table 2. As expected, the lower the pressure and the slower heating rate, the less and the finer the cracks. There were, however, still cracks for the pre-sintered rod (in Figure 1(b)) with a pressure of 50 MPa and a heating rate of 1 °C /min.

On uniaxial pressing, zinc stearate in ethanol as lubricant was coated on die wall. ~ 20 vol %, 45 vol % and 70 vol % plastic binder were added. For sintering, the heating rate was 1 °C /min. The observation of cracking during processing is give in Table 3. The higher amount of binders and the lower pressure, the smaller the crack size. The cracks moved from the end to the middle, indicating the decease of the density inhomogeneity. There was still very fine crack in the middle of the sample, see Figure 1(d) .
In short, we need to further adjust our processing to prepare high quality large samples for measuring mechanical properties.

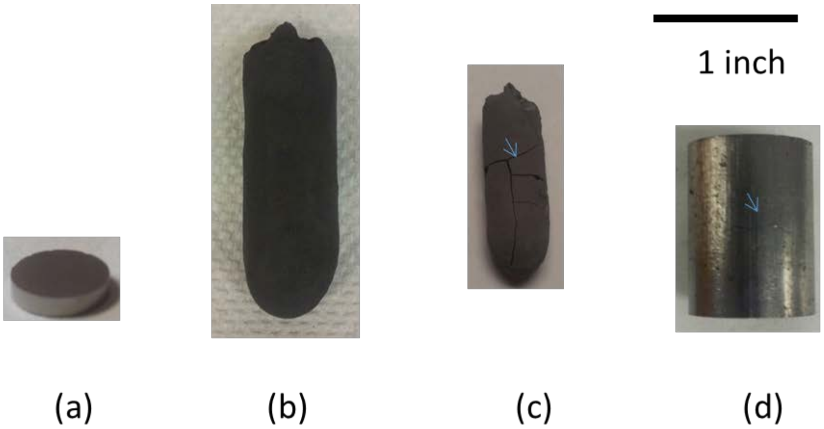

Figure 1. W rods (a) small specimen with height ~3 mm, sintered at 1100°C for 1 hour, Heating Rate=10°C/min. (b) CIPed under 100 MPa (b) CIPed (b) and then sintered at 1000°C. (d) 70 vol% binder, uniaxial pressed 80 MP, sintered at 1000°C.

Table 1. Process parameters tested for CIPed rods

CIPing pressure (MPa)	Heating rates (°C /min)
300	10
150	5
100	1
50	

Table 2. Observations of cracking for CIPed rods

CIPing pressure (MPa)	Heating rate °C /min	After CIPing	After reduction at 650 °C for 2h	Crack after pre sinter
300	10	N	Y	Y
300	1	N	Y	
100	1	N	Y	
50	1	N	N	Y

Table 3. Observations of cracking for uniaxial pressed rods

binder vol%,	After debinding	after reducing at 650C	Crack after pre sinter?
20%	Y		
45%	N	Y	
70%	N	N	Y

Disc specimens

The nano-W alloys are expected to have good resistance to radiation damage such as hydrogen blistering. 1" thin nano-W disc specimens are being made for measuring tritium permeating [3]. Figure 2 shows the typical crack occurred after sintering the nano W powders. Experiments have indicated that the crack appears in the low density region of the green compact. This should be improved by increasing the flow-ability of the nano W powders, such as granulation. Figure 3 demonstrates the morphology of fracture surface of the sintered specimens with grain size of ~ 200 nm.

Figure 2. Nano W disc sintered at 1100°C for 1 hour.

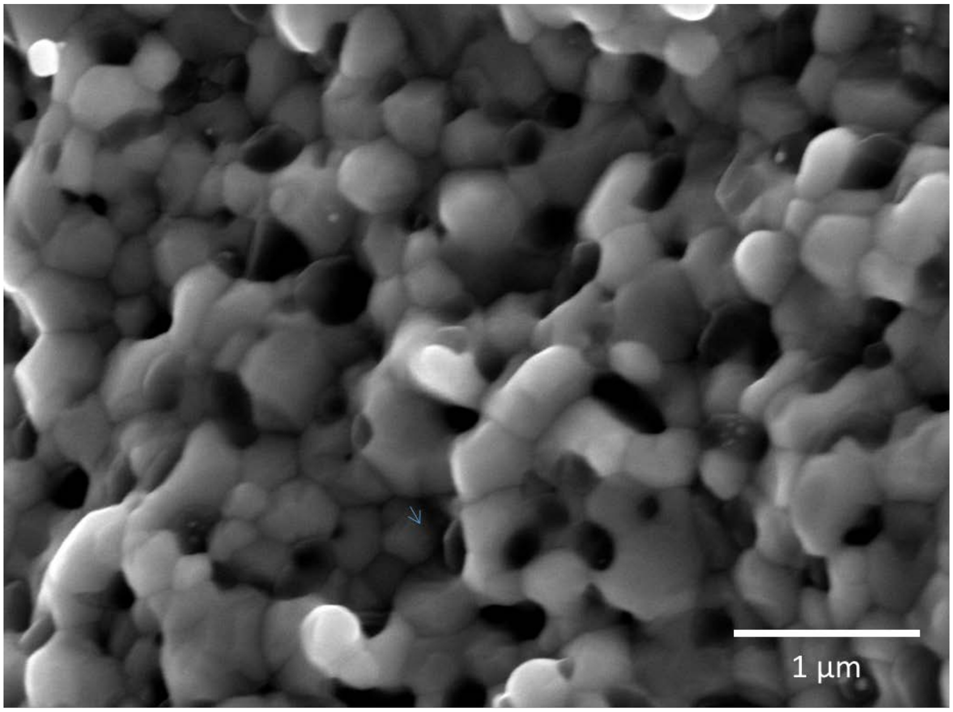

Figure 3. SEM micrograph of Nano W disc sintered at 1100°C for 1 hour.

FUTURE WORK

The processes will be further optimized to achieve high quality test specimens of the nano W alloys. Then the properties of nano W (including mechanical properties and hydrogen permeation) will be evaluated.

REFERENCES

[1] X. Wang, Z. Fang. Fusion Materials Semiannual Report DOE/ER-0313/53 (2013) 40.
[2] X. Wang, Z. Fang. Fusion Materials Semiannual Report DOE/ER-0313/54 (2013) 108.
[3] D. Buchenauer, et al. "Development of plasma driven permeation experiment for TPE". Fusion Engineering and Design, 2014, In press.

4.4 PROPERTIES OF IRRADIATED TUNGSTEN AND RECOVERY ON ANNEALING -

L. Garrison, X. Hu (Oak Ridge National Laboratory), and M. Fukuda (Tohoku University, Japan)

OBJECTIVE

The objective of this work is to understand the impact of neutron irradiation on the mechanical properties of single crystal tungsten and how annealing may recover these properties.

SUMMARY

Samples of (110) single crystal tungsten (SCW) were irradiated in HFIR at 70 to 900^{o}C and fast neutron fluences of 0.01 to 20 ×10^{25} n/m^{2} at E>0.1 MeV [1]. A subset of eleven samples from this group with fluences up to 7×10^{25} n/m^{2} have been selected for the annealing study within the PHENIX collaboration. Hardness testing and positron annihilation spectroscopy (PAS) have been completed on unirradiated control samples. The irradiated samples are being polished in preparation for the upcoming tests.

PROGRESS AND STATUS

Introduction

Tungsten may be used as a plasma-facing material in future fusion devices. However there is a lack of fundamental understanding of the behavior of tungsten under neutron irradiation. To design and build successful fusion devices, more must be known about the effects of irradiation on tungsten's properties. This study aims to further the understanding of microstructure and defect structures in irradiated tungsten and how these defects contribute to irradiation hardening. It is also important to understand if annealing may recover the mechanical properties to pre-irradiation values by healing some of the irradiation induced defects.

Experimental Procedure

The samples in Table 1 have been identified in LAMDA and selected for the annealing study. The samples have been measured, and it was determined that samples 1W05 and 1W25 are large enough to perform PAS. All the samples will be polished and hardness tested. Then, each sample will be annealed for one hour at its respective irradiation temperature. After the annealing, the hardness testing and PAS will be repeated.

Table 1: Samples currently in LAMDA selected for the annealing study.

HFIR Rabbit Capsule	Sample ID	Target Irradiation Temperature (^{o}C)	Fluence 1x10^{25} n/m^{2} (E>0.1 MeV)
TB-300-1	1W01-A	300	0.02
PC1A 'N'	1W05	90	0.02
T9G-11	1W07-A	300	2.82
T9C-14	1W17	500	2.20
TB-500-3	1W20	500	9.00
TB-650-1	1W23	650	0.13
PC2A 'Q'	1W25	90	0.10
PCV4A'V'	1W43-A	90	1.95
TB-300-2	1W47	300	0.10
TB-500-2	1W51	500	0.54
TB-650-2	1W53	650	0.46

Results and Discussion

Unirradiated control samples have been analyzed with PAS and hardness tested. Positron annihilation spectroscopy (PAS) was performed on a SCW (110) sample; the <110> direction was in the plane of the sample. The PAS measured 223.3 ps for the di-vacancies in the control sample (Figure 1).

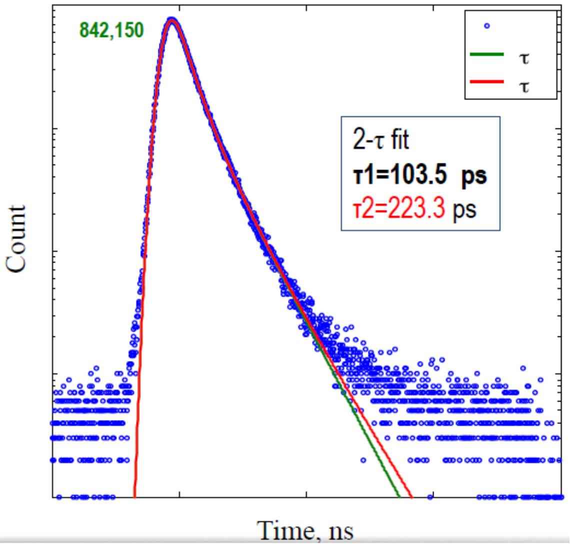

Figure 1. PAS performed on unirradiated SCW (110) sample revealed a value of 223.3 ps for di-vacancies.

Nanohardness of a SCW (110) sample was measured using the Wilson nanohardness indenter with a 10 second dwell time and varying the load between 0.050 and 1 kg (Figure 2). The hardness depends on the indentation load until the load reaches 0.2 kg after which point the hardness plateaus. Future nanohardness tests on tungsten samples should be completed with at least 0.2 kg as the indentation load.

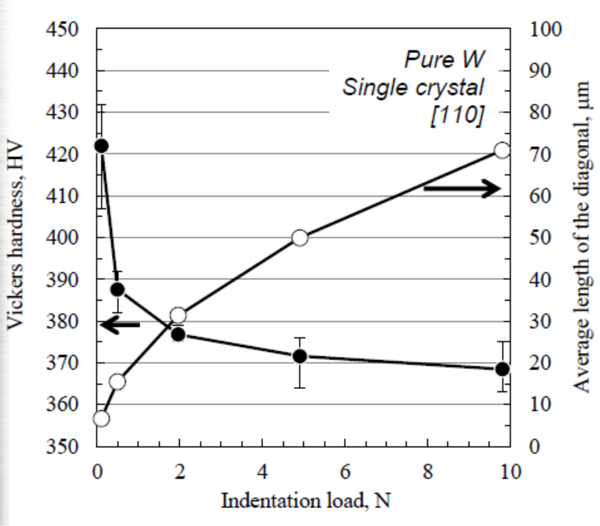

Figure 2. Nanohardness measurement of a SCW (110) sample show that the hardness becomes insensitive to the indentation load above 1.96 N (0.2 kg).

The hardness is also sensitive to the surface polish of the tungsten samples. A sample polished with a final polish step of larger than 3 µm diamond paste showed differing hardness values with rotation of the SCW sample (Figure 3). However when the surface polish was increased to a 1 µm diamond paste, the orientation dependence is largely absent (Figure 3).

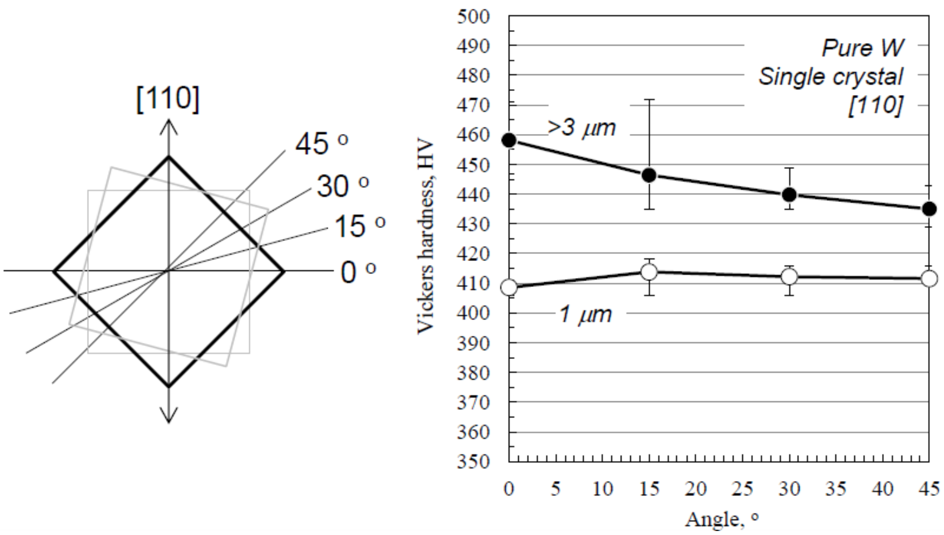

Figure 3. On the sample that was polished with greater than 3 µm paste, a difference in hardness value with orientation was observed.

Electron backscattered diffraction (EBSD) was performed on the SCW sample that showed a change in hardness value with rotational angle of indentation. The SCW samples originated from a grown cylindrical crystal with <110> along the axis of the cylinder. To produce samples, the cylinders are sliced parallel to the cylinder axis and then cut perpendicular to the first direction to create rectangular samples. Thus, it is known that the <110> direction is along one edge of the samples, but EBSD was needed to determine the plane on the face of the samples. Although the sample is a single crystal, the surface finish is not perfect and the slight damage in the polishing scratches can be seen in the EBSD scan, which interpreted the different regions between the scratches as different grains with slightly different orientations (Figure 4). When the orientations of all the "grains" identified by the EBSD are plotted on an inverse pole figure, it can be seen that there is a slight spread in orientations around (889) with data points in other areas of the figure are noise from the scratched regions (Figure 5). The average orientation of the sample surface was determined to be (889) with the <81$\bar{8}$> direction parallel to the vertical direction in the image (Figure 4). The sample is known to have the <101> direction along the edge that is identified as <81$\bar{8}$>, so the 5 degrees difference in the rotational orientation of the plane identified by EBSD is likely due to a slight rotation in the mounting of the sample in the instrument.

Connecting this information with the difference in hardness with rotation, the 0 degrees indentation in Figure 3 would have essentially the same rotational orientation in Figure 4, with the diagonals vertical and horizontal on the page. This orientation of the indentation had the highest hardness value. For the 0 degrees indent, the diagonals of the hardness indenter would have been essentially parallel to [101] family directions on the sample surface. For the other orientations of the indenter, the diagonals would not have been aligned with a principle direction on the sample surface.

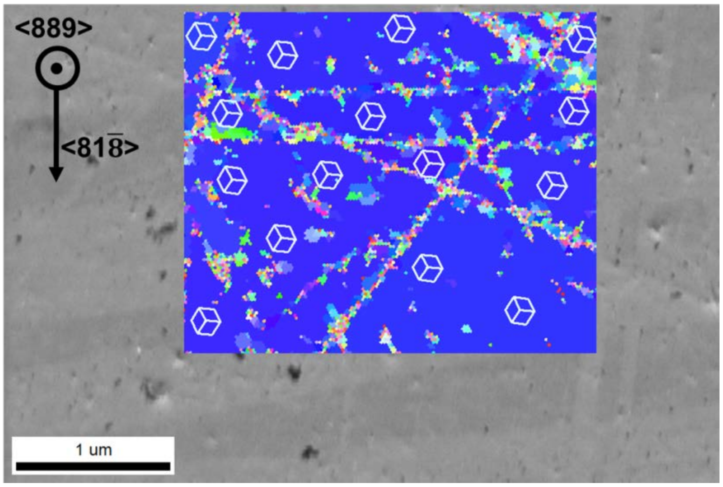

Figure 4. EBSD revealed the surface plane on the SCW sample to be (889).

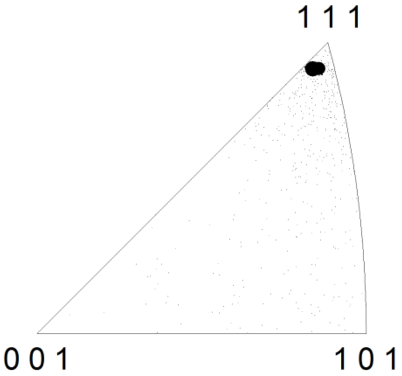

Figure 5. The large spot on the EBSD inverse pole figure for the SCW sample shows the orientation of the face of the sample to be approximately (889), while the smaller data points in other regions of the figure are noise from the scratched regions of the sample.

REFERENCES

[1] Y. Katoh, J.L. McDuffee, Fusion Materials Semiannual Progress Report for Period Ending June 30, 2013, DOE/ER-0313/54, 229-232.

4.5 MECHANICAL PROPERTIES OF NEUTRON IRRADIATED TUNGSTEN

—L. L. Snead, L. M. Garrison, N.A.P. Kiran Kumar, T. S. Byun, M. R. McAlister, and W. D. Lewis (Oak Ridge National Lab)

OBJECTIVE

The objective of this work is to inform plasma-facing component development by creating a basic understanding of the effect of neutron irradiation on the mechanical properties and microstructure of tungsten.

SUMMARY

Tungsten samples of types [110] single crystal tungsten (SCW), [100] SCW, wrought tungsten foils, and annealed tungsten foils were irradiated in HFIR at temperatures from 70 to 900°C and fast neutron fluences of 0.01 to 20 $\times 10^{25}$ n/m^2 at E>0.1 MeV. Samples that were irradiated at 2×10^{25} n/m^2 and below were previously tensile and hardness tested at 300°C and below [1]. In this period samples irradiated at 2×10^{25} n/m^2 and below at temperatures between 300 and 650°C were tensile tested at high temperatures. Annealed and wrought tungsten foils were hardness tested. A sample irradiated to a dose of 2.2dpa at 725°C was analyzed in the TEM.

PROGRESS AND STATUS

Introduction

Tungsten is a material of interest for high heat flux applications such as the divertor of fusion tokamaks. In this position in a fusion device, the material will be exposed to neutron irradiation at high temperatures. While tungsten has several beneficial properties such as a low sputtering yield, it has a small temperature operating window bounded by the ductile to brittle transition temperature on the low end and the recrystallization temperature on the high end. The behavior of tungsten under neutron irradiation needs to be better understood, especially the property changes with temperature. In this study, samples of single crystal tungsten and tungsten foils that had been irradiated in HFIR were analyzed in the LAMDA laboratory. Transmission electron microscopy was utilized to analyze the defect structure and phases. Hardness testing was performed using a microhardness indenter. Tensile test were performed in a vacuum furnace at 300, 500, and 650°C.

Results and Discussion

TEM observation of tungsten single crystal samples

Microstructural analysis on the high dose, high temperature irradiated specimens showed voids with diameter ranging from 3 to 9 nm (Figure 1). The size of voids increases with the irradiation dose and temperature. Figure 2 shows the voids in the 2.2 dpa sample. Fine needle or platelet-like precipitates were observed in specimen irradiated to a dose of 2.2 dpa at 725°C. Scanning mode TEM with energy dispersive spectroscopy (EDS) analysis showed that the precipitates are rhenium rich (χ phase) platelets formed due to transmutation of tungsten to rhenium during irradiation (Figure 3). The length of the transmuted χ phase precipitates ranged from 2 to 28 nm with an average length of 20 nm in material irradiated to 2.2 dpa at 725°C. Based on the transmutation calculations, the predicted amount of tungsten to rhenium transmutation after irradiation in HFIR to a fluence of 7×10^{25} n/m^2 (E>0.1 MeV) is ≈3 at% [2]. The amount of rhenium in the sample is being calculated to compare with that prediction.

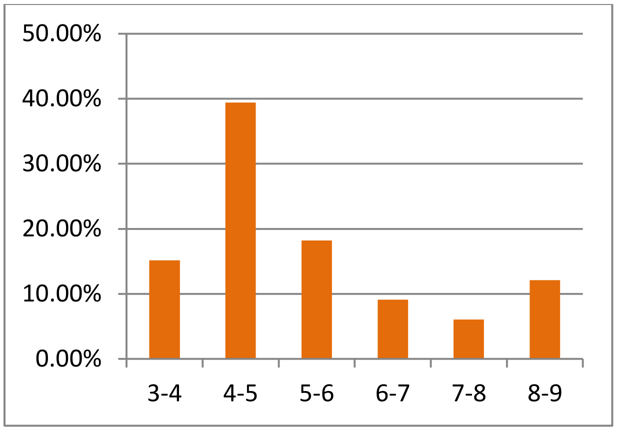

Figure 1. Void size distribution plot for sample irradiated to 2.2 dpa at 725°C.

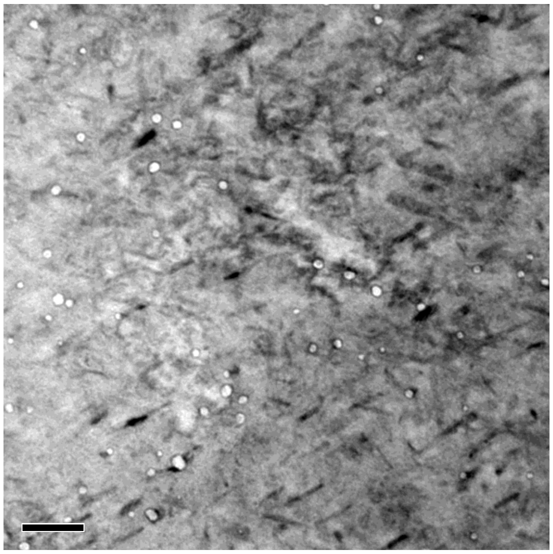

Figure 2. Under-focused TEM image showing the voids in a sample irradiated to 2.2 dpa at 725°C.

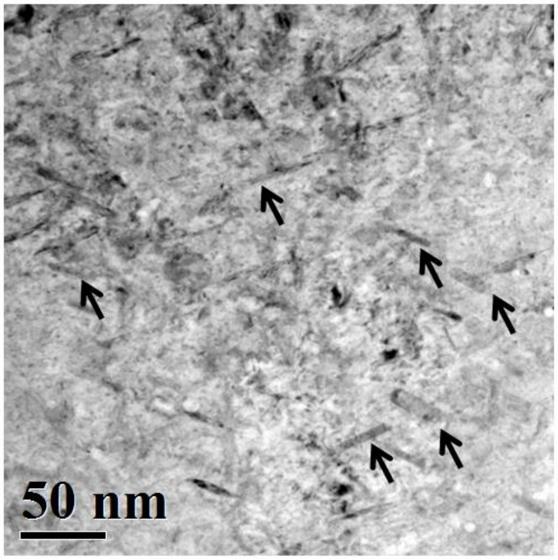

Figure 3. TEM micrograph of single crystal tungsten specimen irradiated to a dose of 2.2 dpa at 725°C. The χ-phase platelets, indicated by arrows, formed due to transmutation of tungsten to rhenium during neutron irradiation.

<u>Hardness testing of irradiated foils</u>

Wrought foil and annealed foils were hardness tested after irradiation to 0.02×10^{25} n/m^2 (E>0.1 MeV) and 0.1×10^{25} n/m^2 (E>0.1 MeV) at 90°C. For both irradiation doses, the wrought foil has a higher hardness than the annealed foil (Figure 4). The annealed foil is insensitive to the irradiation dose with both hardness values being approximately 400. The wrought foil showed a significant increase in hardness from 470 at 0.02×10^{25} n/m^2 to 610 at 0.1×10^{25} n/m^2.

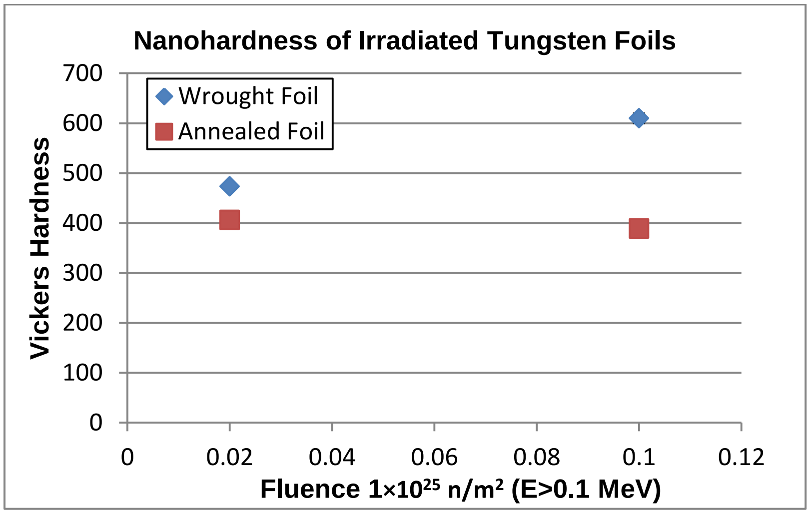

Figure 4. Hardness values for wrought and annealed foil samples after irradiation.

Comparing the hardness values of the foils with the SCW [100] and [110] values reported previously [1], the annealed foil hardness at 0.02×10^{25} n/m^2 is very close to the hardness values for both orientations of SCW irradiated to the same fluence. The annealed foil irradiated to 0.02×10^{25} n/m^2 has a slightly lower hardness value than the SCW samples at that fluence (Figure 5). The wrought foil has a higher hardness value than the SCW samples of both orientations at both fluences tested.

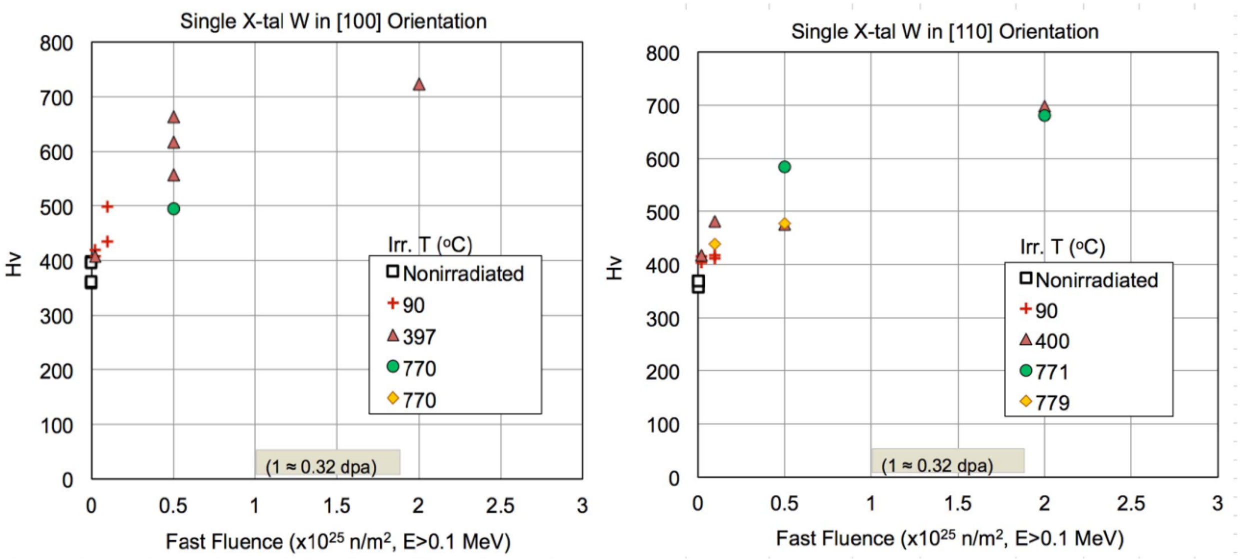

Figure 5. Hardness values of irradiated single crystal tungsten samples in orientations [110] and [100], for a range of neutron fluences and temperatures. Reprinted from Reference [1].

Tensile properties at high temperatures

Samples of SCW with orientation <110> along the axis of the tensile bars were tested at high temperatures. The irradiation temperatures of all irradiated tungsten samples were calculated from dialometry of silicon carbide (SiC) temperature monitors present in each irradiation rabbit capsule. Each temperature determined has a spread on the order of 50°C due to the temperature profile inside the rabbit capsule. The average temperature from the SiC monitors are used here as the temperature of the samples.

Figure 6 compares the results for samples tested at 300°C. The samples were irradiated to fluences from 0.02 to 2×10^{25} n/m^2 at temperatures from 337 to 408°C. Results for an unirradiated sample are included for comparison. The unirradiated sample had significant elongation, at least 50% before failure. As the irradiation fluence was increased, the yield stress also increased. However the elongation did not follow a simple trend with increasing fluence. The sample 1W02, irradiated to 0.02×10^{25} n/m^2, had less elongation than the sample 1W49, irradiated to 0.5×10^{25} n/m^2. The sample 1W08 irradiated to the highest fluence of 2×10^{25} n/m^2 was fully brittle and fractured at the yield strength.

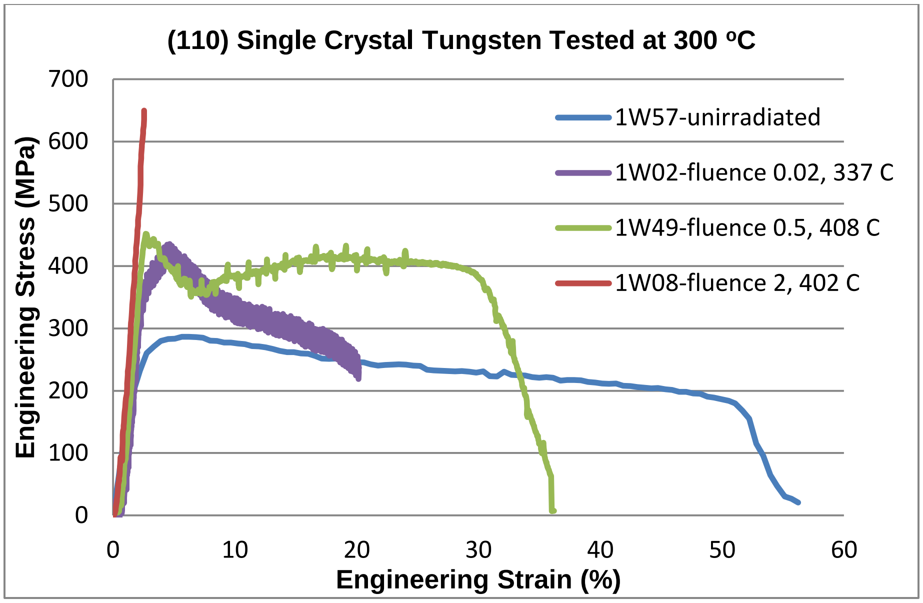

Figure 6. Samples tensile tested at 300°C after irradiation. Fluences are in units $1{\times}10^{25}$ n/m^2 (E>0.1MeV). Irradiation temperatures of the samples are indicated in the figure legend.

The samples tested at 500°C show a clear trend of increasing yield stress and decreasing total elongation with increasing fluence (Figure 7). These samples were irradiated to fluences of 0.1 to $2{\times}10^{25}$ n/m^2 at temperatures from 616 to 740°C. Sample 1W18 irradiated to $2{\times}10^{25}$ n/m^2 at 634°C had the highest ultimate tensile strength of all of the samples tested at 300, 500, and 650°C. Comparing sample 1W52 tested at 500°C to 1W49 tested at 300°C after both were irradiated to $0.5{\times}10^{25}$ n/m^2, sample 1W52 had a yield stress higher by about 50 MPa but also had significantly less elongation, only around 13% compared to at least 30% in sample 1W49.

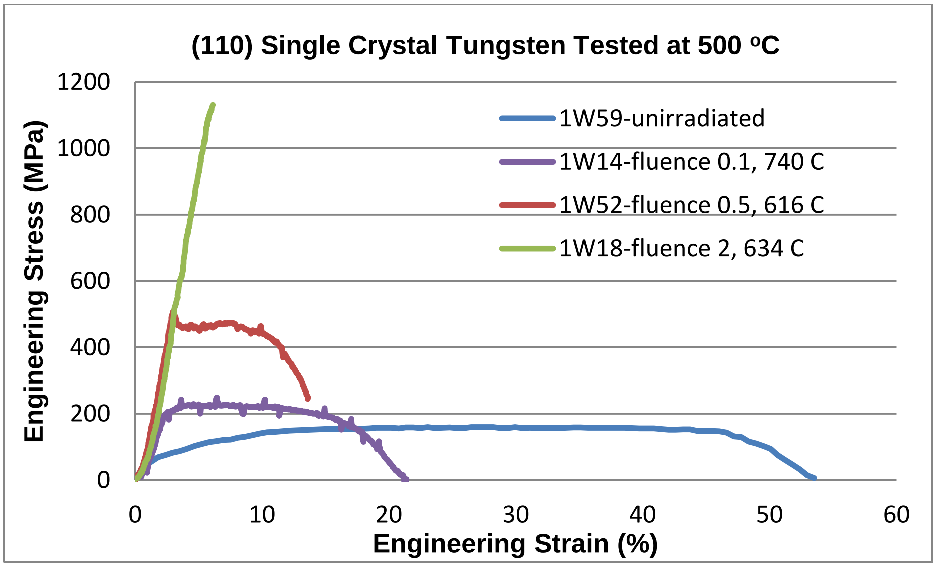

Figure 7. Samples tensile tested at 500°C after irradiation. Fluences in the figure legend are in units $1{\times}10^{25}$ n/m^2 (E>0.1MeV). Irradiation temperatures are indicated in the figure legend.

The samples irradiated to fluences of 0.1 and 0.5×10^{25} n/m^2 at 710 and 675°C, respectively, and tensile tested at 650°C showed a similar trend to the samples tested at 300°C, in that the sample irradiated to 0.5 ×10^{25} n/m^2 had a higher yield stress than the sample irradiated to 0.1×10^{25} n/m^2 but the higher fluence sample had greater elongation. Sample 1W24 irradiated to 0.1×10^{25} n/m^2 and tested at 650°C exhibited only around 13% elongation and an ultimate strength of approximately 280 MPa, while sample 1W14 irradiated to the same fluence but tested at 500°C had close to 20% elongation and an ultimate strength of nearly 220 MPa. The samples irradiated to 0.5×10^{25} n/m^2 showed the opposite relationship with test temperature; sample 1W54 has a lower ultimate strength and the greater total elongation than 1W52.

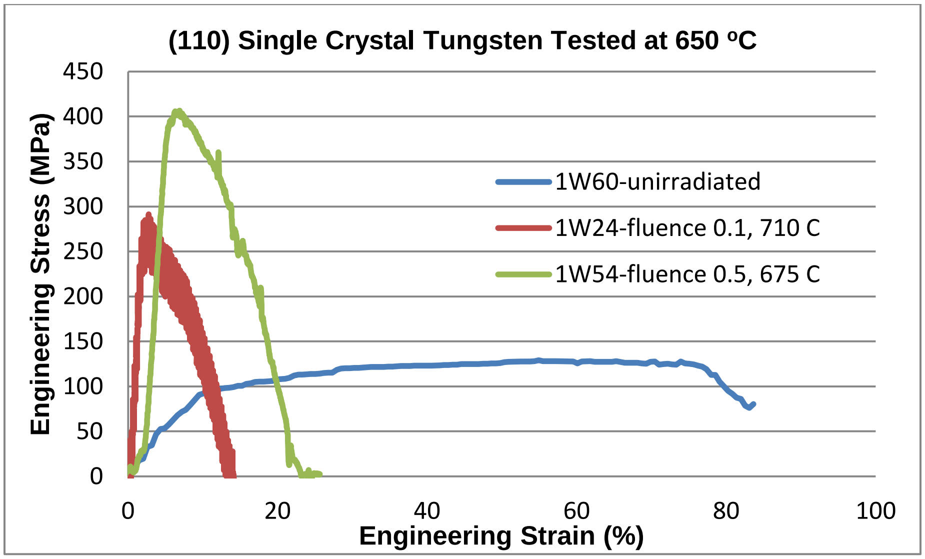

Figure 8. Samples tensile tested at 650°C after irradiation. Fluences in the figure legend are in units 1×10^{25} n/m^2 (E>0.1MeV). Irradiation temperatures are indicated in the figure legend.

REFERENCES

[1] L.L. Snead, L.M. Garrison, T.S. Byun, N.A.P. Kiran Kumar, W.D. Lewis, Fusion Materials Semiannual Progress Report for Period Ending December 31, 2013, DOE/ER-0313/55, 40-47.
[2] L.R. Greenwood, F.A. Garner, J. Nucl. Mater., 212-215 (1994) 635-639.

4.6 HIGH-HEAT FLUX TESTING OF LOW-LEVEL IRRADIATED MATERIALS USING PLASMA ARC LAMPS — A.S. Sabau, E.K. Ohriner, Y. Katoh, and L.L. Snead (Oak Ridge National Laboratory)

OBJECTIVE

The objective of this work is testing of irradiated materials that are candidate of divertor component materials and mock-up divertor components under high-heat flux using Plasma Arc Lamps (PAL).

SUMMARY

In this reporting period high-heat flux testing of six samples, which were supplied by the Japanese collaborators in the PHENIX program, was conducted at ORNL in collaboration with Dr. Kazutoshi Tokunaga of Kyushu University, Japan. As part of the joint US/Japan PHENIX program, Dr. Tokunaga was on assignment at ORNL for four weeks. During this high-heat flux testing, several fixtures for specimen clamping were evaluated for their performance.

PROGRESS AND STATUS

Effort was conducted on three main areas: (a) enhancing the measurement accuracy of the sample temperature, (b) conducting high-heat flux testing with non-irradiated specimens for the joint US/Japan PHENIX program, and (c) enhancing the radiation safety during testing of irradiated specimens.

Temperature measurement and specimen clamping

The current efforts for enhancing the temperature measurement during testing of irradiated specimens included: (a) fabrication of fixtures that would enable specimen onto the substrate and (b) clamping or bolting the thermocouples that would be in direct contact with the specimen. In this reporting period, several attempts were made to fabricate such fixtures for the high-heat flux testing that was conducted in January/February 2014 at ORNL in collaboration with Dr. Kazutoshi Tokunaga for the PHENIX program (Figures 1 and 2).

Clamping the specimen onto the substrate is the best option for high-heat flux testing as the specimen will be pushed onto the substrate, ensuring (a) consistent sample contact with the cooling surface for different specimens and (b) a good contact to the thermocouple for estimating the sample temperature. However, due to the large area covered by the incident heat flux from the plasma-arc lamp, the design of the clamping fixtures is not trivial as the clamping fixtures would be heated directly by the PAL during testing, while on the other hand, the clamping fixtures would not be directly cooled. Moreover, due to different thermal expansion of specimen holder and specimen itself, the clamping fixture cannot be bolted to both sample and cooling rod, resulting in lack of disk clamping for cooling. Thus, the design of the clamping fixtures had to strike an appropriate energy balance between the thermal radiation heating and limited cooling available.

In Figure 1, the drawing of a fixture for specimen clamping is shown. The following features can be pointed out for this design:

- Springs allow the control of the clamping force, for fixed clamping, the springs can be removed
- Springs were placed in low temperature regions for durability and performance
- Top disk may still absorb more energy that it can dissipate by thermal radiation
- The top surface includes a conical area to reduce energy absorption
- Disk cutouts will further minimize energy absorption

The Gen 4 washer clamp fixture, which is sketched in Figure 2, would allow higher-sample temperature at high clamping load, similar to that used for e-beam testing. The Gen 4 of Mo holder is based on clamping the specimen using a washer, allowing high clamping loads, similar to that used for e-beam testing, and high sample temperatures. The Gen 5 of Mo holder is based on clamping the specimen using a scalloped disk and springs, allowing the control of the clamping loads. It is expected that higher heat fluxes would be used for Gen 4 than for Gen 5 Mo holders as the clamping disk used in Gen 4 Mo holder is directly cooled unlike the scalloped disk used in Gen 5 Mo holder. One Gen 3 of Cu rod (7mm diameter of the thread) was fabricated for use with both Mo holders (Figure 1 and 2).

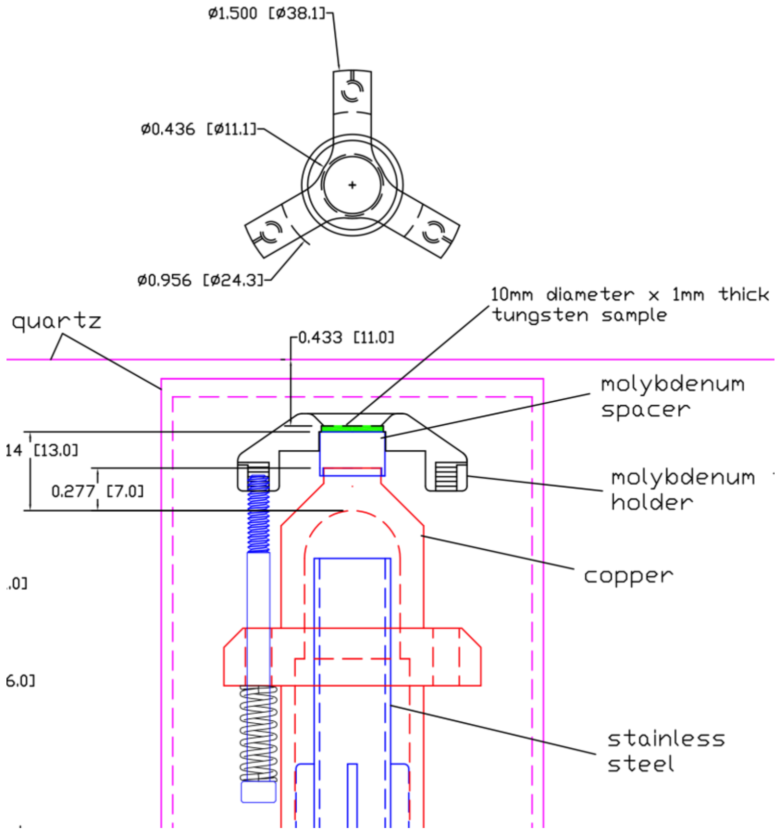

Figure 1. Drawing of a scalloped disk clamp fixture (Gen 5 Mo holder).

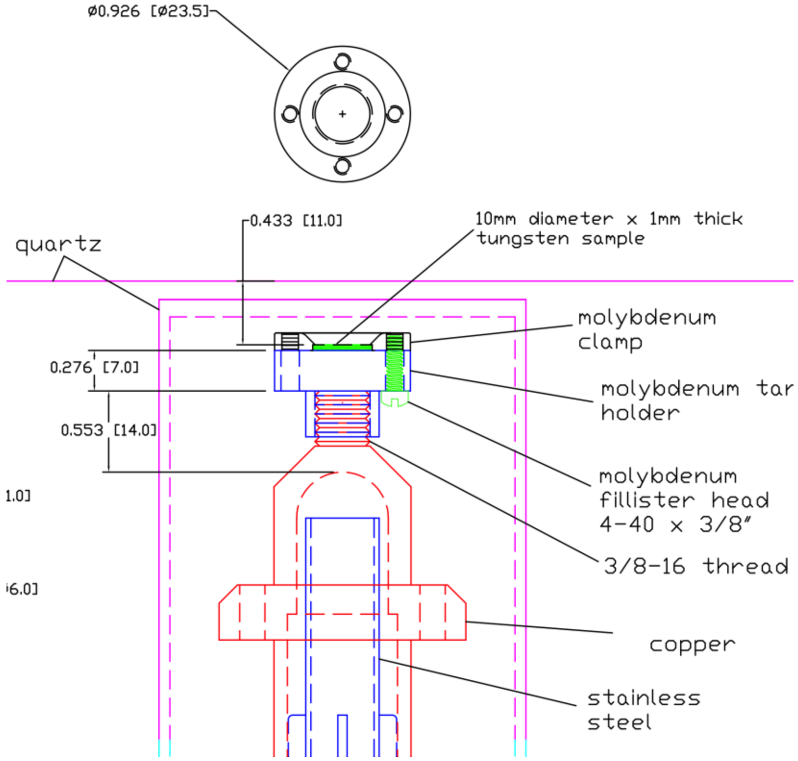

Figure 2. Drawing of a disk clamp fixture bolted from the top (Gen 4 Mo holder).

High-heat flux experiments

In this reporting period, the several high-heat flux experiments were conducted during the visit of Dr. Kazutoshi Tokunaga of Kyushu University, Japan as part of the joint US/Japan PHENIX program. Six samples, which were supplied by the Japanese collaborators in the PHENIX program, were exposed high-heat fluxes at ORNL (Table 1). Each sample was exposed to corresponding high-heat fluxes that would limit the sample temperatures to allowable maximum temperatures for each sample type.

Table 1. Specimens exposed to high-heat flux testing.

Specimen	Materials	Diameter [mm]	Thickness [mm]	Target Max. Temp. [°C]	No. Cycles	Cycle duration [s]	Comments
1	[1]W	6	1	1,200	8		Sample heavily oxidized due to loss of vacuum
2	W	6	1	1,200	61	20-25	Gen 3 cooling rod
3	[2]W/F82H		2	550	76	25	Gen 3 cooling rod
4	[2]W/F82H	10	2	550	75	20-25	Gen 2 cooling rod
5	[2]W/F82H	6	2	550	203	25	Gen 2 cooling rod
6	W	6	1	1,200	42	25	Gen 2 cooling rod

[1] – ITER grade
[2] –Thickness W and F82H steel was 1 mm, respectively.

The temperature results, which were obtained for the first PHENIX sample and are shown in Figure 3, indicate that the accurate data was measured by the bolted thermocouple as it showed the expected temperature range while the unbolted thermocouples indicate similar lower temperatures as before. Both the specimen and Mo holders were oxidized during this preliminary run. However, the rate of heat removal by the Gen 3 cooling rod is lower than that of the Gen 1 cooling rod as the heat exchange area between the Mo holder and Cu rood was limited to that of a disk of 7mm diameter. These temperature results obtained with Gen 3 cooling rod indicate an inefficient cooling of the specimen holder and specimen, as the specimen holder makes good contact only over a 7mm diameter disk. Thus, the Gen 2 cooling rod was used in subsequent runs. It has to be noted that a coolant flow rate of 5 GPM, which is approximately 10 times larger than that for the Gen 1 cooling rod, was attained for both Gen2 and Gen3 cooling rods. The contact surface between the Gen 2 cooling rod and specimen holder was the same as that for the Gen 1 cooling rod, which was previously used in the project.

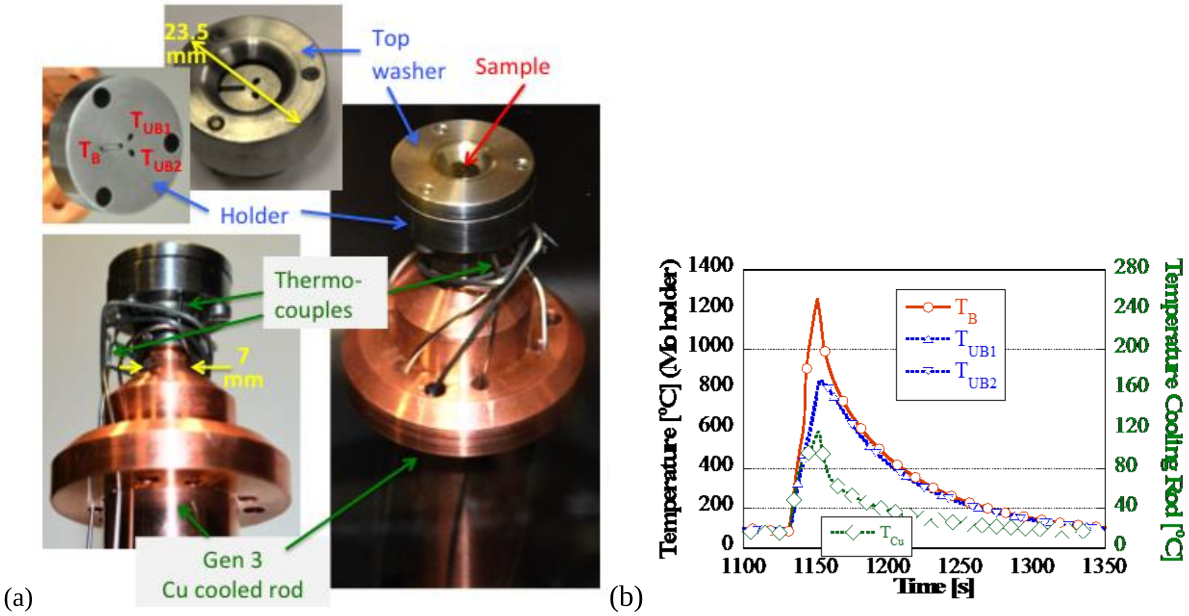

Figure 3. Use of Gen 4 sample holder and gen 3 cooling rod and sample 1 and sample 2: (a) thermocouple location and clamped specimen, and (b) temperature results obtained for sample 1 using bolted thermocouple (T_B) and unbolted thermocouples (T_{UB1}, T_{UB2}), and temperature in the cooling rod.

The temperature results for the second PHENIX sample, which are shown in Figure 4, are lower than those for sample 1 (Figure 3), indicating that a the thermocouples were not in good contact with the specimen. This poor contact noticed for the Gen 5 of specimen holder was due to two factors: (1) the Mo holder – below the disk – was too narrow to allow a horizontal groove to be machined and (2) the Inconel set screws partially melted and the scalloped disk did not clamp the specimen for the entire test duration (i.e., maintain a good contact with the specimen).

(a)

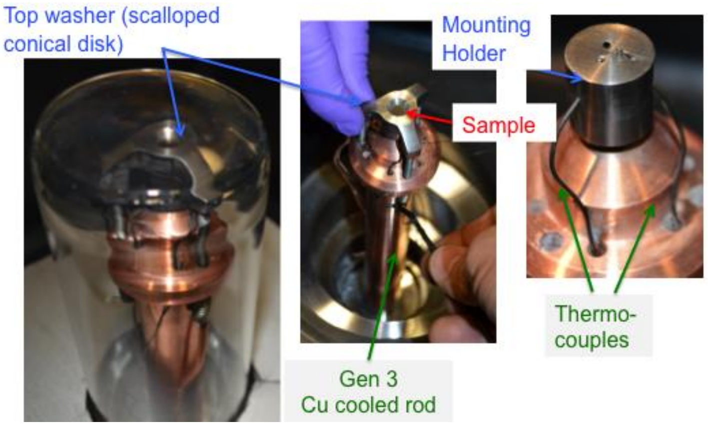

(b)

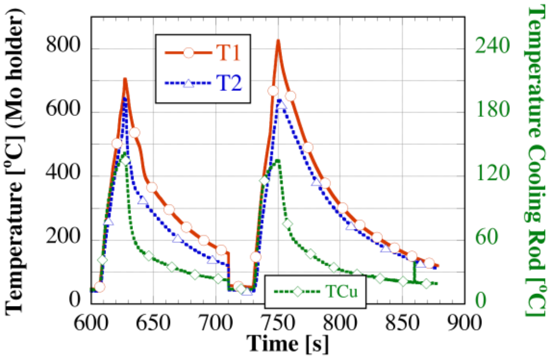

Figure 4. Use of scalloped disk fixture (Gen 5 Mo holder) with Gen 2 cooling rod for sample 2: (a) experimental setup and thermocouple location, and (b) temperature results obtained for sample 2 using un-bolted thermocouples (T_1, T_2), and temperature in the cooling rod.

The temperature results for the sixth PHENIX sample are shown in Figure 5. For this specimen, the disk was bolted from the Mo holder (Gen 4b of specimen holder, similar to the Gen 4 of specimen holder, which was bolted from the top disk, as shown in Figure 2 and 4). The Gen 2 cooling rod was also used in order to provide a larger contact cooling area to the Mo holder than that of the Gen 3 cooling rod that was used for Specimen 1 and 2. The temperature results indicate that maximum temperature reached was approximately 900 °C.

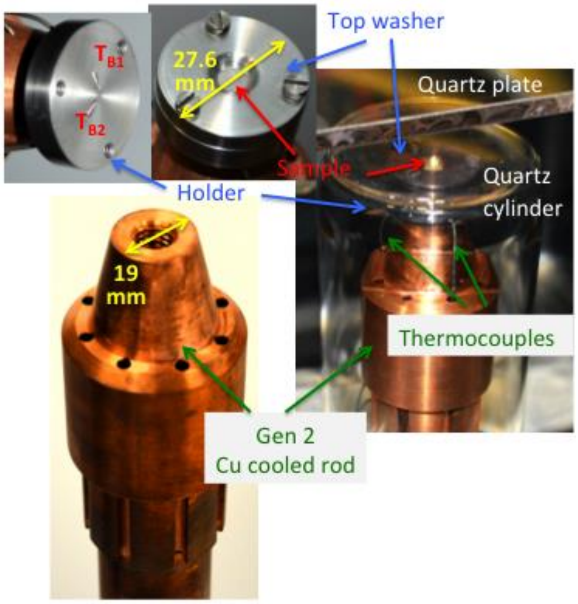

(a)

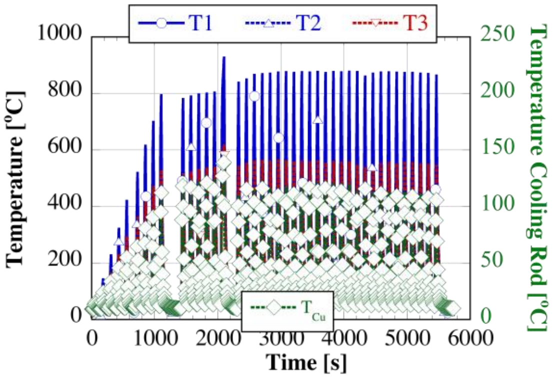

(b)

Figure 5. Use of clamped disk fixture (Gen 4b sample holder), bolted on the Mo support, with Gen 2 cooling rod for sample 6: (a) thermocouple location and clamped specimen, and (b) temperature results obtained for sample 6 for 42 cycles using bolted thermocouple (T_1, T_2) and unbolted thermocouples (T_3), and temperature in the cooling rod.

The microstructure of top surface of specimen 6 is shown in Figure 6. At higher magnifications (bottom row of pictures), several nano-size particles are evident (white dots) after HHFT (bottom right-hand-side picture).

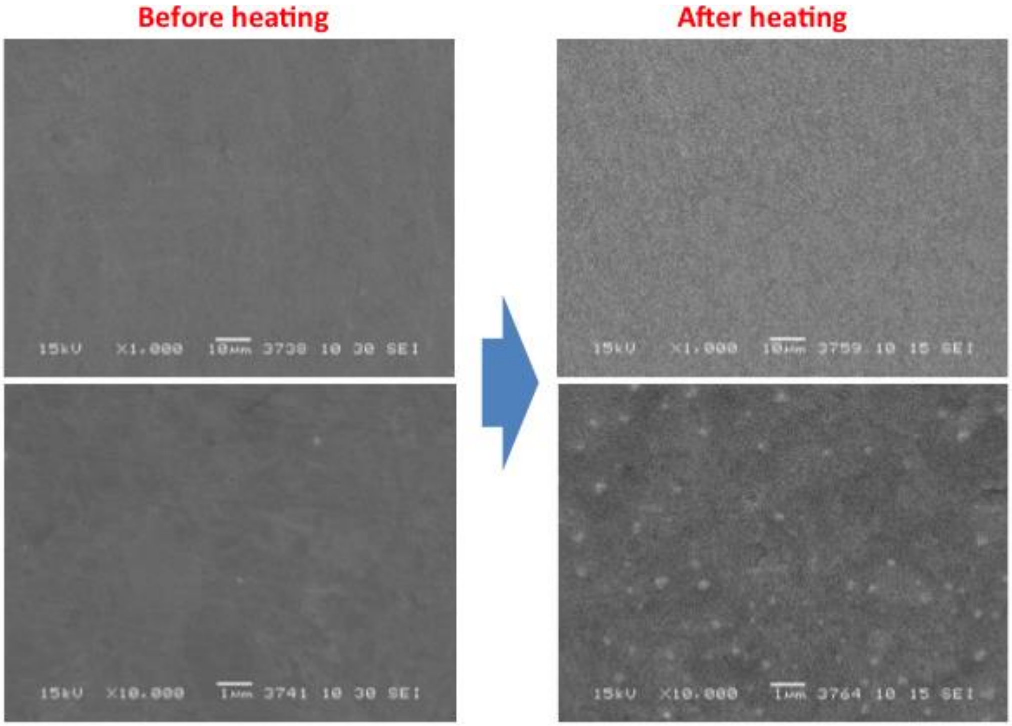

Figure 6. SEM images showing the microstructure of top surface of specimen 6 (provided by Dr. Tokunaga). Different magnifications were used. The left-hand-side pictures were taken before the high-heat flux exposure while the right-hand-side pictures were taken after the high-heat flux exposure.

The sample was clamped as shown in Figure 5. Sample 5 was exposed to a total of 203 cycles. W top surface was not oxidized while the Mo washer was slightly oxidized. These temperature results indicate that the accurate data was measured by the bolted thermocouples as it showed the expected temperature range while the unbolted thermocouple indicate similar lower temperatures consistent with the data recorded previously (Figure 1b and Figure 2). The microstructure analysis of the specimens exposed to high-heat fluxes is ongoing and will be reported in the next reporting periods.

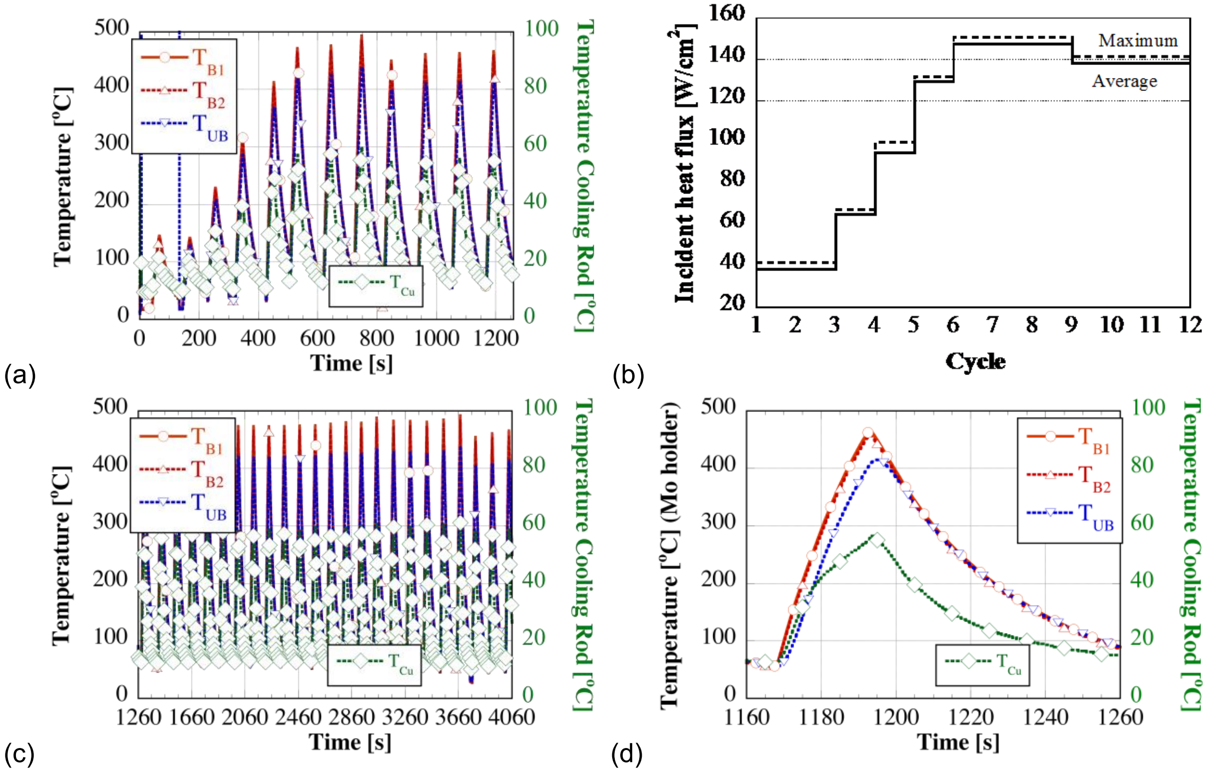

Figure 7. Temperature results obtained specimen 5 (W/F82H, 6mm diameter): using bolted thermocouples (T_{B1}, T_{B2}) and unbolted thermocouple (T_{UB}), and temperature in the cooling rod. (a) cycles 1-12, (b) incident heat fluxes for the first 12 cycles, (b) cycles 13-36, and (c) 12-th cycle considered representative ((525A lamp current, and incident heat flux of 1.4 MW/m^2).

The microstructure of top surface of specimen 5 is shown in Figure 8. After HHFT there is slight change in the microstructure, such as smoothing out of the edges but no cracking was observed. Several considerations have to be made concerning the lack of surface damage at 1.4 MW/m^2: (a) PAL used for the HHFT provides a relatively uniform high-heat flux over the specimen surface, more uniform even than those offered by the neutral beam facilities (e.g., GLADIS), (b) surface damage under more uniform heat sources (e.g. GLADIS) were found to induce surface damage at higher heat fluxes than those by the e-beam. Therefore, for the surface damage for PAL HHFT is expected to occur at larger heat fluxes than those by the e-beam.

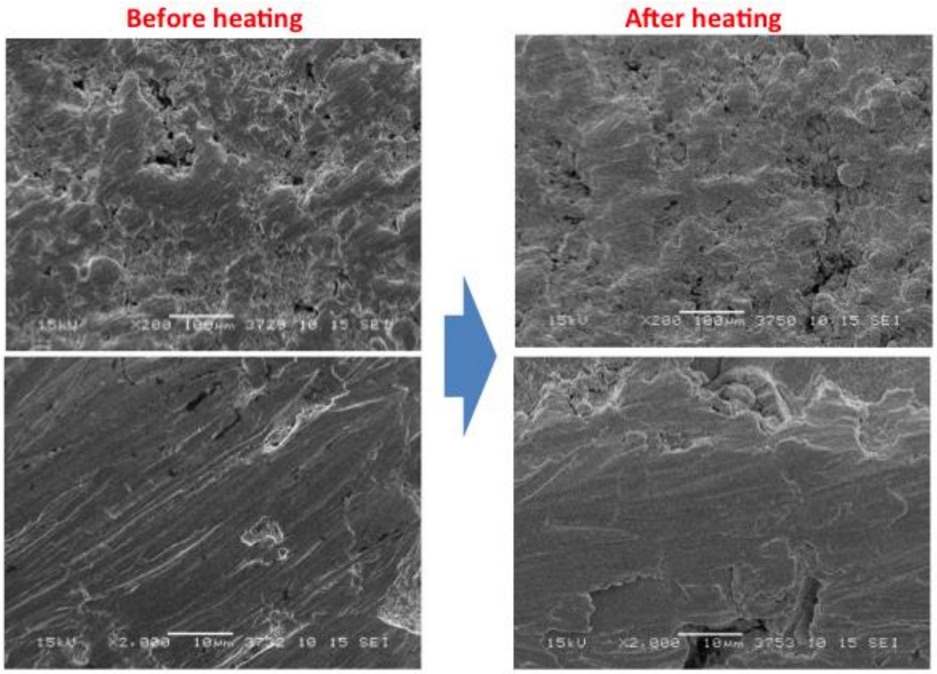

Figure 8. SEM images showing the microstructure of top surface of specimen 5 (provided by Dr. Tokunaga). Different magnifications were used. The left-hand-side pictures were taken before the high-heat flux exposure while the right-hand-side pictures were taken after the high-heat flux exposure.

Enhancing the radiation safety during high-heat flux testing of irradiated specimens

Efforts for enhancing the radiation safety during testing of irradiated specimens include:

- Design of an additional sealed chamber enclosing the cooling rod, specimen holder, and irradiated specimen
- Fabrication of the sealed chamber enclosing the specimen holder and irradiated specimen.

The main test chamber will NOT be contaminated, lowering the maintenance and operational costs. The color legend for the sub-components that comprises the sealed chamber in Figure 9, are as follows:

1. magenta – indicate capped quartz tube surrounding the top region of the cooling rod,
2. light blue – graded quartz to glass region,
3. green – glass region; the glass is fused on the bottom to a steel flange to insure vacuum tight conditions,

The Gen 2 cooling rod that will enable a 3X increase in the coolant flow rate is also shown.

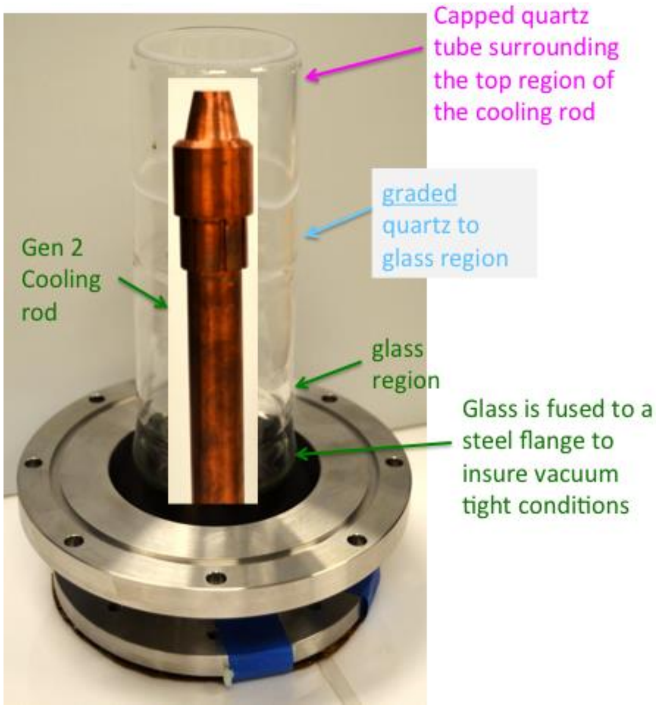

Figure 9. Drawing of the additional sealed chamber to confine contamination to the quartz-glass cylinder surrounding the cooling rod.

Acknowledgments

The authors would like to thank Charles Ross (Chuck) Schaich for assisting with CAD design, fabrication specifications, and assembly; Jim Kiggans for design and fabrication of the Al enclosure, Alta Marie Williams for radiation safety considerations, and David Harper for operating the PAL. We would also like to acknowledge the following Japanese collaborators from the joint US-Japan PHENIX program, Dr. Y. Ueda of Graduate School of Engineering, Osaka University, Osaka, Japan for numerous discussions related to clamped specimens, Dr. K. Tokunaga for assisting with the high-heat flux testing experiments and providing the tungsten specimens, Dr. T. Yokomine of Kyoto University, Kyoto, Japan for presentations made as part of the PHENIX program, discussing high-heat flux testing of He cooled tungsten specimens.

4.7 CHARACTERIZATION OF THERMOMECHANICAL DAMAGE ON TUNGSTEN SURFACES DURING LONG-DURATION PLASMA TRANSIENTS - D. Rivera, A. Sheng, T. Crosby, N.M. Ghoniem (University of California, Los Angeles)

Extended Abstract of an ICFRM-16 paper accepted for J. Nucl. Mater.

Design of plasma facing components for fusion applications requires a detailed knowledge of the damage evolution characteristics of the constituent materials for safe and reliable operation. Tungsten has been declared as a candidate material for many plasma-facing components, and as such, its behavior under simulated fusion conditions must be fully understood before implementation can take place. In an effort to further study the effects mild plasma transients (on the order of 20 MW/m^2) have on plasma facing components, a series of experiments has been conducted in which circular tungsten samples are exposed to cyclic thermal loading. The heat source used is a Praxair SG-100 plasma gun whose output heat flux was measured both by water calorimetry and a specially designed heat flux sensor.

After exposure, samples are subsequently characterized by fabricating micro-pillars on the affected surface as seen in figure 1. These pillars are then tested under compression, and stress vs. strain data is generated as seen in figure 2. Although there is a definite size effect associated with compression of such small pillars, the generated data can be analyzed in a relative sense when compared to the data garnered from pristine pillars. The results indicate the onset of recovery mechanisms within the material as a function of the pulse number. This is evidenced by the reduction of the yield point, and the increase in curvature of the plastic portion of the stress vs. strain curves after exposure. This result is further corroborated by the change in deformation mode of the exposed pillars relative to their pristine counterparts. The deformation mode changed from a barreling type seen in the pristine pillars to one characterized by shear banding typical of well annealed crystals [1] as seen in figure 3. This behavior would indicate that initially the dislocation density in the preferred slip system for tungsten ({110}<111>) was too high for adequate dislocation slip, however after exposure, and the subsequent isothermal anneal, sufficient recovery of the microstructure was able to take place, allowing free dislocation movement in the aforementioned slip system. This is further corroborated by XRD data showing that the material is highly oriented in the <002> direction. Since the shear bands are oriented at 45^{O} from the axis of the pillar, we conclude that the dislocation lines are indeed moving in the (110) planes.

Furthermore, scanning electron microscopy images of the exposed surface reveal the onset of small fractures initiated as a result of thermal cycling; these features can be seen in Figure 4. In order to gain a better understanding of the stress state leading to the surface fracture of the samples during a transient event, a finite element (FE) thermo-elastoplasticity model was developed. The results indicate that upon application of a heat load, compressive stresses build up in the center of the sample, leading to plastic deformation of the surface as can be seen in the von Mises stress map in figure 5. Upon the cooling phase of the cycle, however, the recovered elastic strain of the cooler parts of the sample exceeds that from parts that deformed plastically, resulting in a tensile surface self-stress (residual surface stress), which correlates with the surface fracture seen in the SEM analysis.

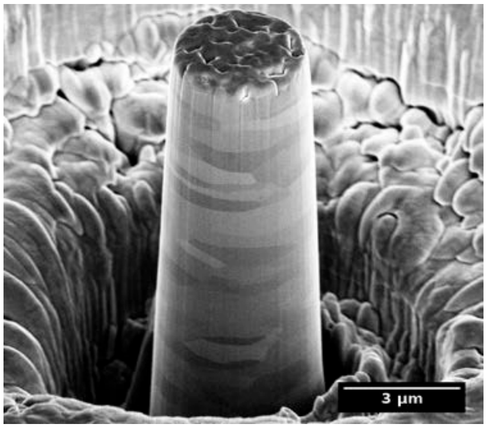

Figure 1. Newly fabricated pillar

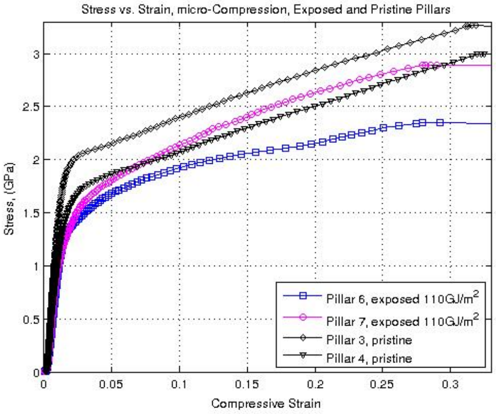

Figure 2. Stress vs. strain data for pillars fabricated from both pristine and exposed material, the stress state is compressive

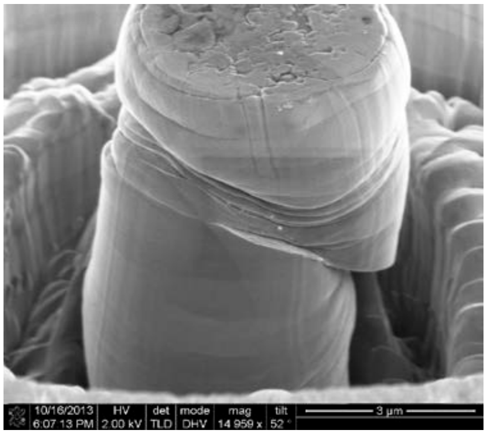

Figure 3. Shearing deformation mode resulting from high exposure to plasma transients.

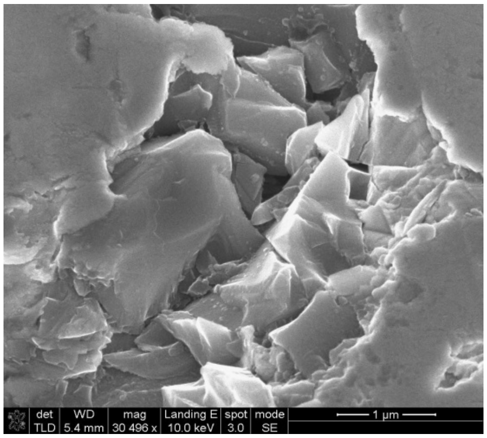

Figure 4. Brittle surface fracture of exposed specimen after 1000 cycles of 25 MW/m^2, each with a pulse duration of 4 s for a total absorbed energy density of 100 MJ/m^2.

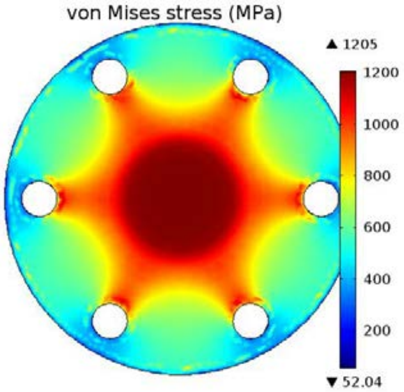

Figure 5. von Mises stress plot of the surface of the test sample during exposure to a 20 MW/m^2 heat pulse.

REFERENCES

[1] Reed-Hill, R. E. and Abbaschian, R, 1994, *Physical Metallurgy Principles,* PWS Publishing Co, Boston, MA, p. 725.

5.1 IRRADIATION RESPONSE OF NEXT GENERATION HIGH TEMPERATURE SUPERCONDUCTING RARE-EARTH AND NANOPARTICLE-DOPED $YBa_2Cu_3O_{7-X}$ COATED CONDUCTORS FOR FUSION ENERGY APPLICATIONS -

K.J. Leonard, T. Aytug, Fred. A List III, Yanwen Zhang (Oak Ridge National Laboratory),A. Perez-Bergquist, W.J. Weber (University of Tennessee), A. Gapud, N.T. Greenwood, J.A. Alexander and A. Khan (University of South Alabama)

OBJECTIVE

The goal of this work is to evaluate the irradiation response of the newest generation of coated conductors based on rare earth and nanoparticle doping of the $YBa_2Cu_3O_{7-x}$ (YBCO) high temperature superconductors. The materials under investigation represent different methods for enhanced flux pinning for improved performance under externally applied magnetic fields. Ion irradiation was used to perform an initial evaluation of the materials electrical response, and is currently being followed up by neutron irradiation testing.

SUMMARY

During this reporting period, electrical characterization work was completed on the ion irradiated superconducting films. Detailed electrical characterization of the materials response was performed at the University of South Alabama. This contribution highlights results of a forthcoming paper concluding the electrical characterization of the ion irradiated materials. Based on this work, the Zr-doped $(Y,Gd)Ba_2Cu_3O_{7-x}$ and $(Dy,Y)Ba_2Cu_3O_{7-x}$ (DyBCO) materials were selected for neutron irradiation studies. Ion irradiation results for the $GdBa_2Cu_3O_{7-x}$ conductor did not show a significant improvement over second-generation YBCO materials in terms of J_c improvement with irradiation. However, irradiated T_c remained higher than for YBCO. The neutron irradiation exposures are being planned for the July-August 2014 cycle at HFIR. Information on the irradiation capsules and preliminary results will be included in the next semi-annual report.

EXPERIMENTAL

The high temperature superconducting (HTS) coated conductors consisted of metal organic chemical vapor deposition Zr-doped $(Y,Gd)Ba_2Cu_3O_{7-x}$ (Zr-YBCO) and $GdBa_2Cu_3O_{7-x}$ (GdBCO) films fabricated by SuperPower Inc., and metal organic deposition Dy-doped $YBa_2Cu_3O_{7-x}$ (DyBCO) films processed by American Superconductor Corporation. The HTS conductors were fabricated in long-lengths, but with individual test samples sectioned from the processed tapes.

Ion irradiation of the HTS materials was performed at the University of Tennessee Ion Beam Materials Laboratory using 5 MeV Ni and 25 MeV Au ions. The energies were selected to provide a range of damage effects in order to examine conductor response. This range was also selected to avoid implantation in the conductor and avoid columnar defect formation, which appear at electron energy loss values (S_e) around 20 keV/nm (S_e, of the Ni and Au ions was 1.8 and 6 keV/nm, respectively). Irradiations were performed at room temperature, normal to the tape surfaces to fluences of 10^{11} and 10^{12} cm^{-2} for 25 MeV Au ions, producing 0.003 and 0.03 displacements per atom (dpa), and with $5.5x10^{11}$ cm^{-2} for 5 MeV Ni ions producing 0.004 dpa in the Zr-YBCO and GdBCO films and 0.005 dpa in the DyBCO films.

Transport measurements were performed at the University of South Alabama on 1.7 cm long samples patterned with a 1-mm-long, narrow bridge with a width of either 1.00 mm or 0.20 mm. For each current contact to the probe, a strip of indium was applied to the Ag pads at pressed copper injection areas, which limited the contact resistance to between ~ 10^{-6} and 10^{-4} Ω. The probe was placed in a variable-temperature cryostat with the field of a 9-Tesla superconducting magnet applied normal to the tape plane (approximately parallel to the crystal *c*-axis). Temperature- and field- dependence of resistivity, $\rho(T, H_o)$ was measured for each constant field H_o over a slow rate of change of temperature T, never more than 0.2 K/min, such that there was negligible difference between the data for cooling and for warming. Critical temperature for each field, $T_c(H_o)$, was determined using the resistivity criterion of 10^{-9} Ωcm, and the locus of all points $T_c(H_o)$ constituting the irreversibility line in the range of fields H_o = 0 to 9 Tesla. For measurements of J_c, the system is designed to provide pulsed DC currents of up to 10 A, each with a duration of up to 50 ms, which, together with low contact resistance, effectively eliminates any significant joule heating [[1]]. Critical current was defined using the standard voltage criterion of 1 μV/cm.

RESULTS

An example of the temperature dependent resistivity in self-field is shown in Figure 1a for the Zr-YBCO conductor. This example represents a common trend of the normal-state resistivity of the conductors with resistivity increasing and critical temperature T_c decreasing with higher dpa. The residual resistivity, ρ_i, obtained from a fit to the $\rho \sim T^2$ portion of the curves extrapolated to the intercept at zero temperature as postulated in Mathiessen's Rule, $\rho = \rho_i + \rho_n(T)$ for the different irradiation conditions is shown for the Zr-YBCO, where ρ_n is the temperature dependent normal-state resistivity. The values for the GdBCO conductor where not obtainable through this method, due to the negative curvature of the plotted data, so resistivity at T=100K, or the ρ_{100} value were compared for the three conductors in Figure 1b. This figure also provides a summary of the changes in T_c, ρ_i and ρ_{100} values for the three conductors with irradiation. For doses up to 0.005 dpa changes are very modest. For the higher fluence 25 MeV irradiations to 0.03 dpa, T_c reduction was within 1% of the unirradiated value, with DyBCO having the smallest reduction of -0.3% and GdBCO with the larger of about -1%. A comparative plot of ρ_{100} data for the three conductors and traditional YBCO films grown on single crystal $SrTiO_3$ (STO) and irradiated by 6 MeV He, 25 MeV O, and 120 MeV Kr are shown in Figure 2. The values for electronic energy loss, S_e, for He and O irradiations were slightly lower than those of the 5 MeV Ni and 25 MeV Au, but resulted in a greater degradation in materials properties in the YBCO films. Values for nuclear energy loss, S_n, were greater in the case of the 5 MeV Ni and 25 MeV Au (0.29 and 1.4 keV/nm, respectively, compared to 0.02 keV/nm or less for other studies). Despite these higher values, the relative lack in property changes may be attributed to the reduced number of defect sites in the YBCO films grown on the single crystal STO substrates that include, grain boundaries, domain boundaries, intergrowths and secondary phases that act as sinks for irradiation damage. Furthermore, it has been also experimentally observed that the YBCO films are more sensitive to electronic interactions over that of nuclear [[2]]. The S_e/S_n ratios for the irradiations of this study are below 9, while the ratios for 25 MeV O and 6 MeV He are calculated at 100 and 1350, respectively. This difference between the irradiation responses of the conductors of this study to that of YBCO films on STO substrates is further evidenced by the changes in T_c as a function of dose. For 1 MeV Ne and 2 MeV Ar irradiations (S_e = 1.6 and 2.3 keV/nm, respectively) of YBCO films on STO, values of $-\Delta T_c/T_{co}$ were as high as 54 and 80%, respectively for dpa values near 0.026 [[3]]. Whereas, in this study, T_c fall-off was within 7% of the unirradiated values for all three conductors irradiated to 0.03 dpa. This is likely an effect of the high S_e/S_n values creating defect sites that may be different than those observed at lower ratios.

A plot of the change in critical current density, represented as the ratio of irradiated to unirradiated values (J_c/J_c^o) as a function of applied magnetic field is shown in Figure 3. The GdBCO conductors response to irradiation by 5 MeV Ni and 25 MeV Au up to 0.004 dpa is very similar and shows a slight decrease in the *H//c* properties up to 8 Tesla in comparison to the unirradiated values. At higher dpa, the properties show a significant drop mainly from the disappearance of the Gd_2O_3 nanoparticles dispersed along the *ab* directions in the conductor. The Zr-YBCO conductor shows somewhat interesting results, in that J_c values are reduced in the 0.003 dpa 25 MeV Au irradiated material and increase to near unirradiated values at the higher dose levels. As observed in the angular field dependence of critical current [[5]], along with transmission electron microscopy studies [[6]], there is a significant improvement in *H//ab* pinning due to the development of intergrowths at the interface of the $BaZrO_3$. However, there is also a loss in the length of the c-axis oriented $BaZrO_3$ particles which may lead to the reduction in low field properties at low damage levels that can be recovered on the formation of smaller radiation-induced defects that were observed at the higher dpa levels. The DyBCO conductor shows relatively unchanged values over the unirradiated condition up to 0.005 dpa at the low field conditions. However at high field, all irradiation conditions show a large improvement over the unirradiated J_c values. Currently, efforts are underway to identify the defects or features responsible for the increase in the high field conditions.

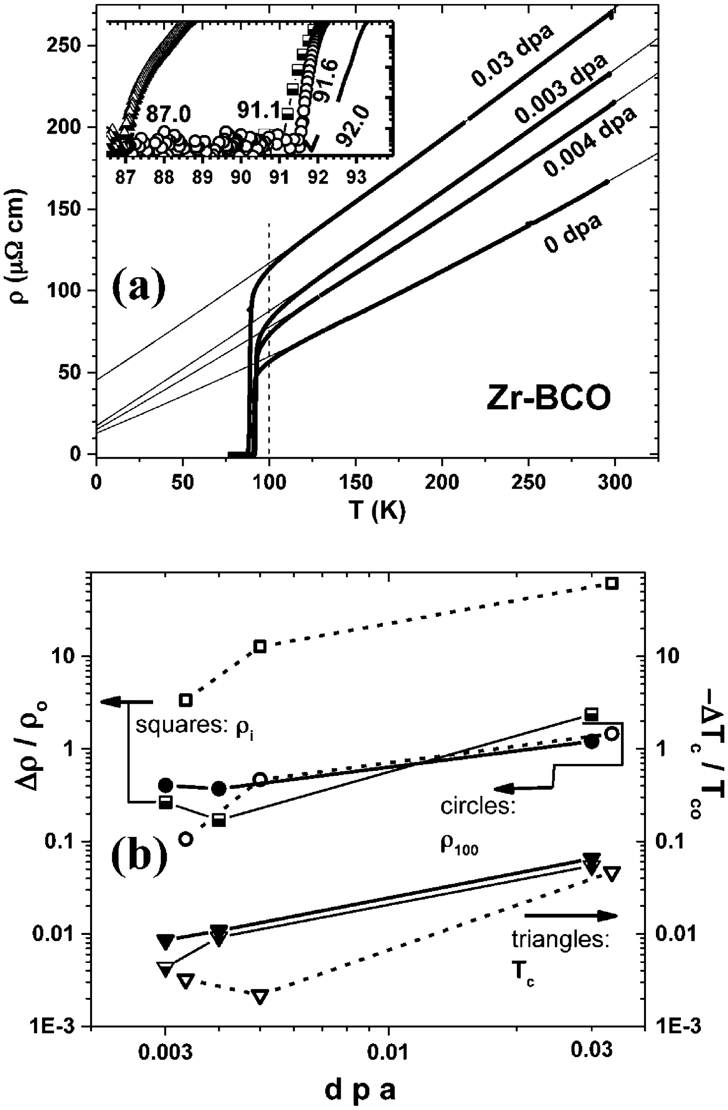

Samples	*Irradiation:* Displacements per atom (dpa), Line+symbol legend		
Label	25 MeV Au $10^{11}/cm^2$	5 MeV Ni $5.5x10^{11}/cm^2$	25 MeV Au $10^{12}/cm^2$
Gd-BCO	0.003dpa —●—	0.004dpa —■—	0.03dpa —▲—
Zr-BCO	0.003dpa —◒—	0.004dpa —⬓—	0.03dpa —△—
Dy-BCO	0.003dpa - -○- -	0.005dpa - -□- -	0.03dpa - -△- -

Figure 1. (a) Resistivity as a function of temperature and dpa for the Zr-YBCO conductor, with the intercept showing the residual resistivity (ρ_i) and resistivity at a temperature of 100 K (ρ_{100}). (b) Fractional shifts relative to the unirradiated state of the ρ_{100} value and the critical temperature T_c.

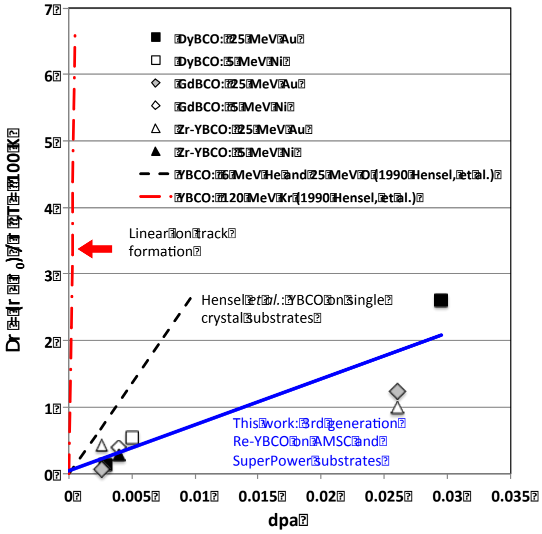

Figure 2. The ρ_{100} values as a function of dpa for the conductors of this study compared to that of YBCO films on single crystal $SrTiO_3$ [[2]]. Electron energy loss energies for the He and O ions are lower than that used in this study, while the 120 MeV Kr irradiation was at the known threshold that produces linear track formation in the YBCO film.

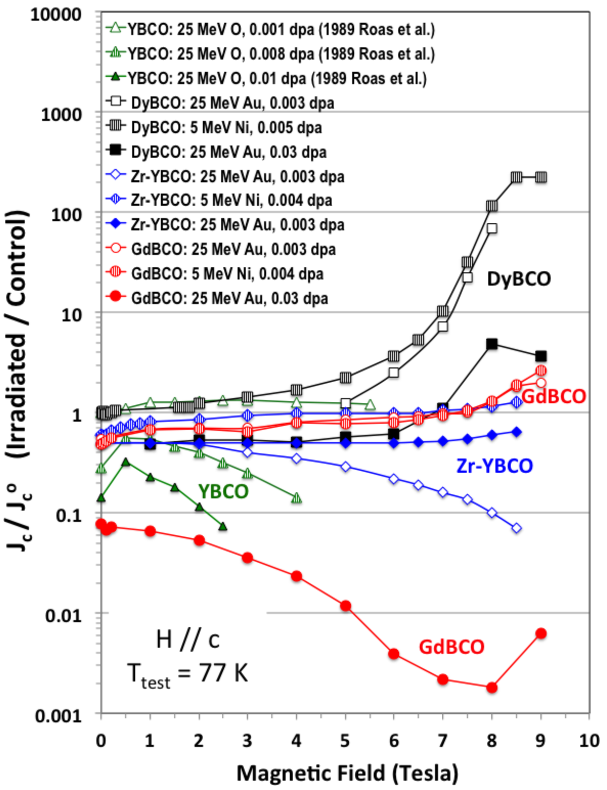

Figure 3. Plot of the changes in critical current density between the irradiated and unirradiated condition for the tested conductors as a function of applied magnetic field. Comparative data from YBCO films on STO substrates is also plotted [[4]].

As the changes in $J_c(H)$ correlate with the overall pinning force density ($F_p = J_cH$), there is normally a maximum pinning force F_p^{max} at a specific field condition. These are plotted as a function of dpa in Figure 4. Initial values of F_p^{max} are significantly higher for the DyBCO and Zr-YBCO conductors than that of the GdBCO, for all irradiation conditions except the low dpa 25 MeV Au irradiations. The field H_{max}, plotted also in Figure 1, is often associated with the "matching field" where the pinning structure becomes optimized for a certain applied flux. While H_{max} reduces for GdBCO with dose, there is an increase in the Zr-YBCO. However, the DyBCO is unique in that it shows a strong initial increase followed by decreasing values with dose, suggesting the pinning that is optimal for a specific field is not necessarily the strongest. There are clearly issues related to the pinning force and matching field that require further examination through microstructural examination.

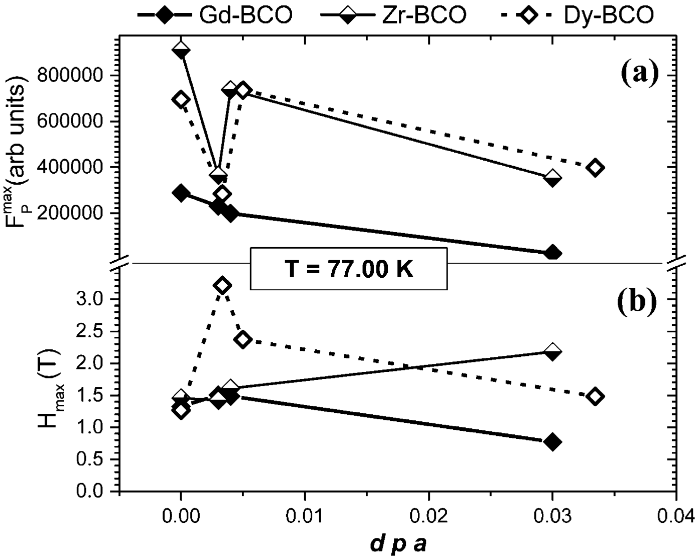

Figure 4. The dependence of the (a) maximum pinning force, F_p^{max}, and (b) the corresponding applied field H_{max} for the three conductors investigated.

The magnetic phase diagram, *H(T)* shown in the inset in Figure 5 for the DyBCO conductor, provides information on the irreversibility line (IL) between the state where vortices are free to move under the slightest applied current (vortex state) and the state where vortices are pinned ($J_c>0$). Also shown in the inset is the upper critical field $H_{c2}(T)$ as well as the IL line for a typical YBCO conductor (in red). The IL can be described as the depinning line, in which conditions to the left side of the line (lower H and T) vortices are pinned and the J_c is non-zero. The unirradiated DyBCO conductor shows a shift in the IL with respect to that of YBCO, with further enhancements observed with irradiation. However, at the high dose 25 MeV Au irradiation, the IL curve dips towards lower T_c values for given fields showing a loss in pinning at the low field conditions. The pinning is recovered above 6 Tesla as nanoscale radiation-induced defects observed through transmission electron microscopy become more favorable pinning locations at high fields.

The phase curves illustrating the change in the IL as a function of the percent shifted T_c are plotted for the three conductors studied in Figure 5. The line at $\Delta T=0$ demarcates between irradiation degradation ($\Delta T<0$) and enhancement ($\Delta T>0$). In general, a good correlation between the IL data and that of the $J_c(H)$ plots are observed. It can be further iterated that the low dose response of the GdBCO shows a slight reduction in the IL, but is further recovered at higher field strengths. However, significant degradation in the IL and $J_c(H)$ properties occurs following 0.03 dpa for the GdBCO. As observed in the $J_c(H)$ data, the IL data for the Zr-YBCO conductor shows a degradation occurring following just 0.003 dpa, believed to be related to the changes observed in the size distribution of the $BaZrO_3$ particles which are more effective in pinning at low applied fields. While there is not a significant difference in dpa between the 5 MeV Ni irradiations to 5.5×10^{11} cm^{-2} as compared to the 25 MeV Au irradiations to 1×10^{11} cm^{-2}, the Ni ions produce a larger S_e/S_n ratio than that of Au ions (8.6 compared to 4.8). This may create more ballistic mixing effects related to changes in the $BaZrO_3$ particles for the Au irradiations and less site occupancy defects within the matrix than is produced in the Ni irradiations. Furthermore, with ion irradiation performed normal to the tape surface, the c-axis aligned $BaZrO_3$ particles may be more sensitive than to irradiations performed at off angles, or by neutron irradiation. This is currently being examined through microstructural examination. As also demonstrated in the $J_c(H)$ data, the DyBCO data for the low fluence Au and Ni irradiations show an enhancement in pinning properties. Only the 0.03 dpa 25 MeV Au irradiation shows degradation in the low field properties that are quickly recovered above 6 Tesla. This suggests a substantial effect of ion irradiation on the Dy_2O_3 at high fluences, but with a substantial improvement in *H//c*. It remains to be determined through microstructural analysis if any realignment of the Dy_2O_3 particles occurs with ion irradiation or if this enhancement also in part to intergrowth and defect formations in the matrix portion of the conductor.

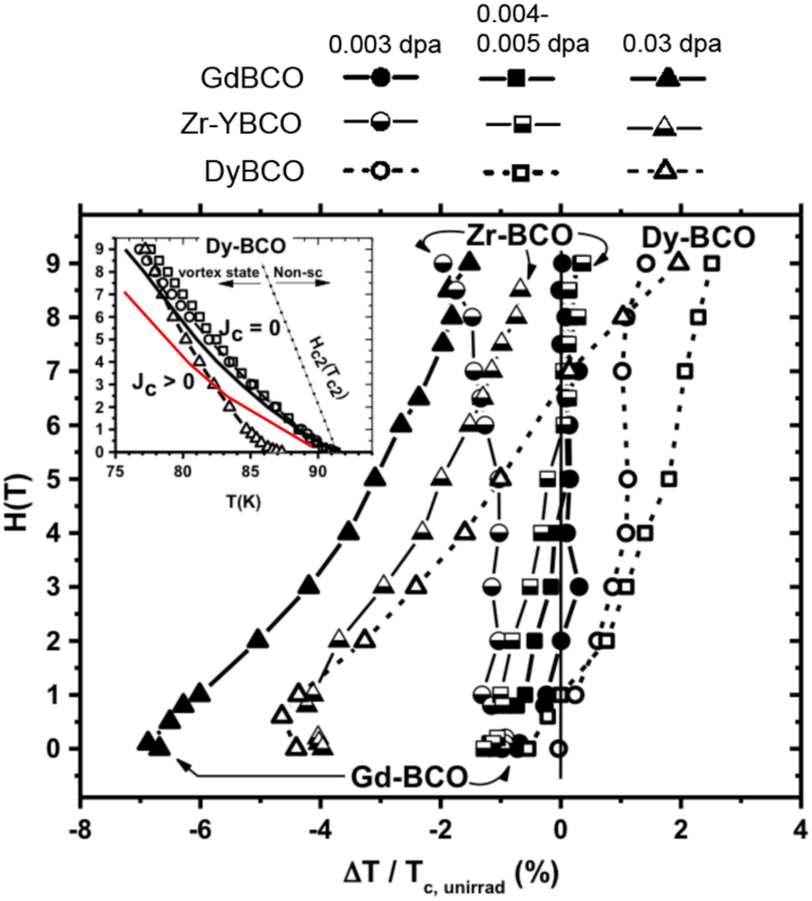

Figure 5. The changing irreversibility line versus the percent change in T_c as a function of irradiation exposure for the three conductors studied. The inset shows the irreversibility, upper critical field $H_{c2}(T)$ as well as the IL line for a typical YBCO conductor (in red) as compared to the data for the DyBCO conductor.

The vortex creep rate, *S*, can be calculated for T=77 K through the power law relationship between the voltage associated with dissipative vortex motion and the applied current ($V \alpha I^n$). Where *n* is the slope of the same *logV-logI* curves used in determining the Ic at T=77 K, with the analysis being only performed to the lowest irreversibility field for dpa < 0.03 at this temperature which is 7.5 Tesla. The relationship [[7],[8]] between the power law relationship and the vortex creep rate is found in the conjunction with the Maxwell Equation, $V \propto -\frac{d\phi}{dt} \propto -\frac{dI}{dt}$, which leads to the vortex creep rate, $S = -\frac{dlnI}{dlnt} = \frac{1}{n-1}$. The normalized vortex creep rate for the irradiated conductors at T =77 K is shown in Figure 6. A lower vortex creep rate is favorable as it demonstrates the stability of the pinning centers in the material. Therefore, for the normalized creep rate, the greater the value above unity the less favorable. As expected the high dose GdBCO has the highest *S* value at low applied fields due to the loss of the Gd_2O_3 particles in the conductor film. At lower damage levels the GdBCO and Zr-YBCO conductors behave comparable to the unirradiated material. However, the value of *S* is lower in the irradiated DyBCO films following irradiation.

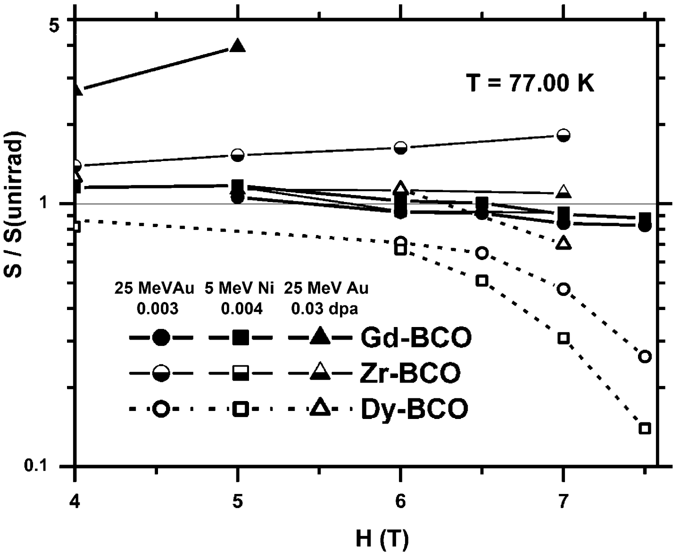

Figure 6. The normalized vortex creep rate as a function of applied field for the various irradiation conditions.

CURRENT AND FUTURE WORK

Current work being performed involves investigating the microstructural link between the changes observed between the unirradiated and irradiated materials. The work on the GdBCO conductor is completed, while specific issues regarding the DyBCO and Zr-YBCO conductors are being addressed through further high-resolution electron microscopy at the Advanced Characterization Laboratory at ORNL. Specific issues currently being investigated through aberration corrected and more conventional TEM methods include the nature of the small radiation-induced stacking-fault-like defects observed in the high fluence 25 MeV Au irradiation, the initial drop in pinning force with irradiation observed in both the Zr-YBCO and DyBCO conductors. Related to the later is the investigated of the differences between the lower fluence 5 MeV Ni and 25 MeV Au irradiations and how the difference in S_e/S_n ratio affects the microstructures in each very different conductor.

Current work that will continue involves the first neutron irradiation testing of these materials. Specially designed capsule inserts have been built to accommodate the tape samples and to allow for controlled handling and processing of the samples through the irradiation and post-irradiation testing. Samples are expected to undergo irradiation in the July-August 2014 HFIR schedule. Irradiation capsules will be initially cut open at the hot cell, but with the internal holders sent to LAMDA for further disassembly and post-irradiation examination. Basic electrical characterization is planned along with TEM examination of the microstructures.

REFERENCES

[1] V. Rouco, E. Bartoloma, A. Palau, M. Coll, X. Obradors and T. Puig, Superconductor Science and Technology, 25 (2012) 122001.
[2] B. Hensel, B. Roas, S. Henke, R. Hopfengartner, M. Lippert, J.P. Strobel, M. Vildic and G. Saemann-Ischenko, Phys. Rev B42, 7, 4135 (1990).
[3] G.J. Clark, A.D. Marwick, R.H. Koch and R.B. Laibowitz, Appl. Phys. Lett. 51 (1987) 139.
[4] B. Roas, B. Hensel, G. Saemann-Ischenko, and L. Schultz, Appl. Phys. Lett., 54, (1989) 1051.
[5] K.J. Leonard, T. Aytug, A.A. Gapud, F.A. List III, N.T. Greenwood, Y. Zhang, A.G. Perez-Bergquist and W.J. Weber, Fusion Science and Technology, (2014) awaiting publication.

[6] K.J. Leonard, ORNL Fusion Materials Program Semi-annual, summer 2013.
[7] J.R. Thompson, Ö Polat, D.K. Christen, D. Kumar, P.M. Martin and J.W. Sinclair, Applied Physics Letters 93 (2008) 042506.
[8] H. Yamasaki and Y. Mawatari, IEEE Transactions on Applied Superconductivity, 9 (1999) 2651.

5.2 IRRADIATION EFFECTS ON MICROSTRUCTURE AND OPTICAL PERFORMANCE OF MULTILAYERED DIELECTRIC MIRRORS

N.A.P. Kiran Kumar, K.J. Leonard, G.E. Jellison and L.L. Snead (*Oak Ridge National Laboratory)*

OBJECTIVE

The goal of this work is to evaluate the upper neutron irradiation dose and thermal limits of two promising dielectric mirrors types, through an investigation of the radiation and thermally induced microstructural and optical property changes. While specifically of interest for use in laser control of inertial confinement fusion systems, the examination of the radiation induced structural changes in the films will be beneficial for the development of other thin-film based electronic components and sensors used in nuclear applications.

SUMMARY

Specifically engineered Al_2O_3/SiO_2 and HfO_2/SiO_2 dielectric mirrors grown on sapphire substrates and exposed to neutron doses of 1 and 4 dpa at 458±10 K in the High Flux Isotope Reactor (HFIR), resulted in reductions in optical reflectance, indicating a failure of the multilayer coating. HfO_2/SiO_2 mirrors failed completely when exposed to 1 dpa, whereas the reflectivity of Al_2O_3/SiO_2 mirror reduced to 50%, eventually failing at 4 dpa. Transmission electron microscopy (TEM) observation of the Al_2O_3/SiO_2 specimens showed defects increase in size with irradiation dose from 1 to 4 dpa. Heavy interdiffusion leading to formation of Al-Si rich phase and cracking of some of Al_2O_3 layers was observed across the Al_2O_3/SiO_2 mirrors; however the interdiffusion is less evident in HfO_2/SiO_2 mirrors. Delamination at the interface between the substrate and first layer was typically observed in both 1 and 4 dpa HfO_2/SiO_2 specimens, where buckling type delamination was a major observation at all doses.

PROGRESS

Introduction

Dielectric mirrors (also known as Bragg reflectors) are considered as one of the crucial components for both inertial and magnetic confinement fusion systems where they function as transmitters of electromagnetic energy with extremely low losses. These mirrors are made up of thin alternating layers of high and low refractive index dielectric material deposited on a substrate. The refracted light from these 1/4λ thick layers results in constructive interference producing high levels of reflectance. Changes to the number, type and thickness of layers allow mirror tuning to a specific wavelength and working range of peak reflectance [1]. While the as-irradiation performance is critical for fusion application, dielectric mirrors have historically performed poorly under irradiation due to their underlying constituents. High quality mirrors are required for diagnostic and remote handling applications in fusion reactors [2]. Any limitations in the mirrors would severely impact the efficiency of the mirror considered for fusion systems.

The present study was performed on Al_2O_3/SiO_2 and HfO_2/SiO_2 dielectric mirrors exposed to neutron doses of 1 and 4 dpa at 185±10°C in the High Flux Isotope Reactor (HFIR). This study is an extension of our previous study on the low dose irradiated dielectric mirrors where the Al_2O_3/SiO_2 mirror showed an impressive radiation resistance at 0.1 dpa and HfO_2/SiO_2 mirror showed loss in reflectivity following post irradiation annealing due to crystallinity changes [3, 4]. The objective of this work is to continue beyond the earlier low dose studies (0.1 dpa and less) to fully understand the failure mechanisms that were beginning to be observed in earlier studies. Understanding the origin of coating damage would not only provide important information for the development of future multilayer mirrors but also helps in producing coating with improved irradiation stability.

Experimental Procedure

The Al_2O_3/SiO_2 and HfO_2/SiO_2 mirrors were obtained from Spectrum Thin Films Inc. The mirrors were produced with ion-assisted electron beam vapor deposition. This deposition method has been the standard process for fabricating multilayer optical coatings due to its ability to scale-up to large substrate sizes and its flexibility for complex designs at relatively low cost. Sapphire was used as a substrate for both the mirrors and all the mirrors used in the present study were designed for an optimum reflectivity at 248 nm. Al_2O_3/SiO_2 mirror consist of 30 bi-layers and HfO_2/SiO_2 consist of 11 bi-layers with the high index layers such as Al_2O_3 and HfO_2 being the first and last layers of the respective mirrors. The sapphire substrates are of 6 mm in diameter and 2 mm in thickness with a surface roughness <10A°.

Earlier studies on the samples involved the neutron irradiation of the mirrors samples to 0.001, 0.01 and 0.1 dpa at 448±10 K. The current work involves the irradiation of a second set of samples to higher doses followed by analysis of the optical and microstructural changes to the mirrors. Irradiations to $1x10^{26}$ and $4x10^{26}$ n/m^2 (E>0.1 MeV) at 458±10 K, corresponding to approximately 1 and 4 dpa, were completed in the peripheral hydraulic tube at the HFIR. The samples are encapsulated in specialized 1100 grade Al holders to eliminate damage to the mirror surfaces, while targeting the appropriate irradiation temperature. The sample holders were unloaded in the LAMDA lab to ensure proper handling of the mirrors.

Optical examination of the samples included measuring changes in the relative spectral reflectance versus wavelength and the absolute reflectivity at 248 nm for the irradiated and post-irradiated annealed specimens. The optical changes are correlated to microstructural changes in the films examined through transmission electron microscopy (TEM) and compared to the unirradiated controls in order to elucidate strain effects at the film/substrate interface.

Results and Discussions

Microstructure of As-received Dielectric Mirrors

Figure 1 shows the cross-sectional bright-field images with the layered structure of the as-received Al_2O_3/SiO_2 and HfO_2/SiO_2 mirrors. Al_2O_3/SiO_2 mirrors consist of 30 bi-layers and HfO_2/SiO_2 mirrors consist of 11 bi-layers. Each layer of Al_2O_3/SiO_2 mirrors showed amorphous structure and the average layer thicknesses of the Al_2O_3 and SiO_2 films in the TEM images are 33 nm and 40 nm, respectively. The as-deposited bi-layers of HfO_2/SiO_2 mirror comprise of polycrystalline HfO_2 layers, showing monoclinic structure with some amorphous regions between the grains, and amorphous SiO_2 layers with average layer thicknesses of 26 nm and 40nm, respectively. The average crystallite size of polycrystalline HfO_2 layers is 13 nm. The films show clear and smooth layers with no intermixing. The high resolution TEM micrograph in Figure 1 (d) shows the grain orientations of polycrystalline HfO_2 layer. HfO_2 grains showed no orientation preference within the HfO_2 layers.

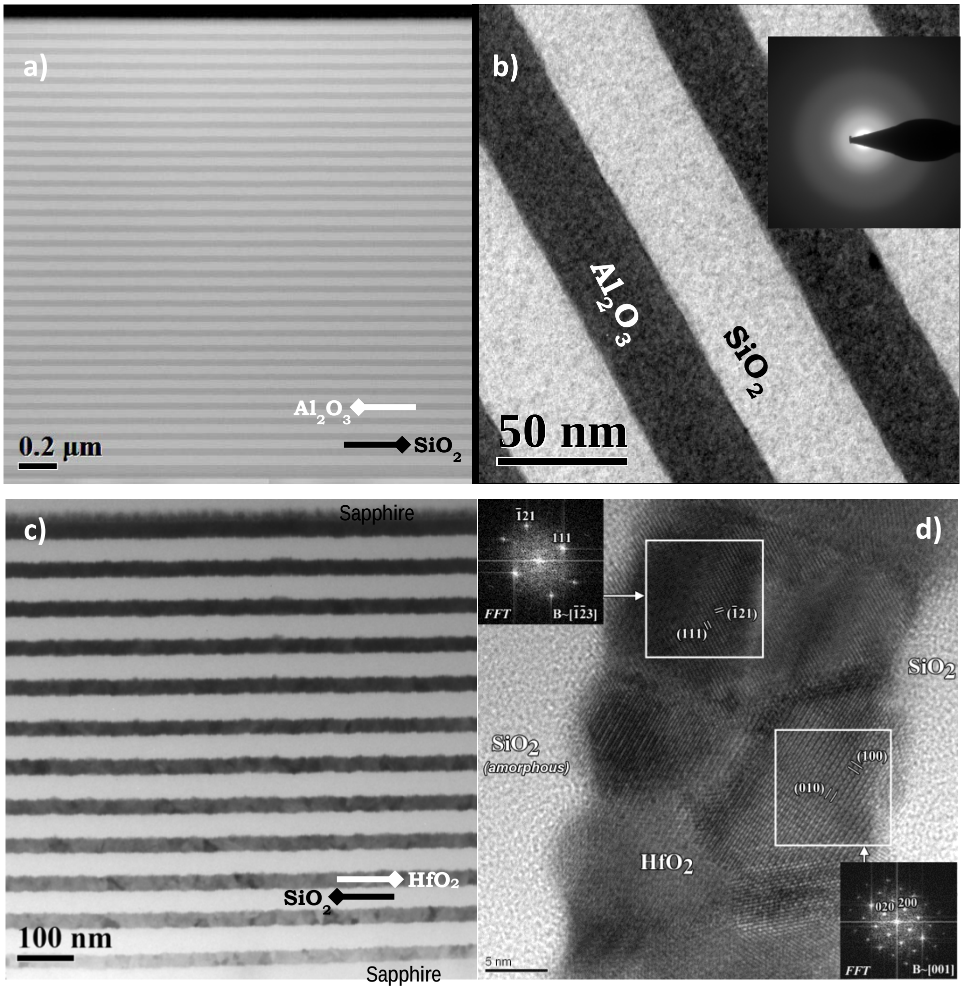

Figure 1. Cross-section TEM micrographs of a) Al_2O_3/SiO_2 mirror showing layered structure, b) High resolution image of Al_2O_3/SiO_2 mirror with an embedded diffraction pattern confirming the amorphous structure of the layers c) HfO_2/SiO_2 mirror showing layered structure d) High resolution image of HfO_2/SiO_2 mirror showing the grain orientation (Insert is the fast Fourier-transformation (FFT) showing the crystal orientation).

<u>Optical Properties of the Irradiated Dielectric Mirrors</u>

Both Al_2O_3/SiO_2 and HfO_2/SiO_2 mirrors were specifically designed to exhibit maximum reflectivity at wavelength of 248 nm. Figure 2 shows the measured reflectance spectrum of two types of mirrors exposed to different irradiation doses. The measurements performed with a spectrophotometer has been normalized to the absolute reflectivity of each sample measured specifically using a NeCu laser (Photon Systems, deep UV NeCu laser, 248.6 nm wavelength). Minimal or no noticeable change in reflectivity was observed following neutron irradiation to 0.1 dpa. Detailed study on optical behavior of low dose irradiation mirrors can be found elsewhere [4]. A drastic drop in reflectance was observed in the specimens subjected to 1 dpa and 4 dpa. HfO_2/SiO_2 mirrors failed completely when exposed to 1 dpa, whereas the reflectivity of Al_2O_3/SiO_2 mirror reduced to 50% at 1 dpa and the mirror failed at 4 dpa. The loss in optical reflectivity indicates the failure of multilayer coating at higher doses. Generally, the optical reflectivity of the dielectric mirrors depends on several factors such as interface roughness and non-uniform layer thickness. In addition, preferential swelling in the layers, leading to flaking off of the film layers could also impact the reflectivity of the multilayers [5]. However, visual inspection of the mirrors after higher dose irradiations showed no signs of crazing or large scale pealing of the mirror layers, but did show localized speckling indication that the drop in reflectance of high dose irradiated mirrors is more due to local microstructural changes rather than broad scale changes related to substrate / film strain influences.

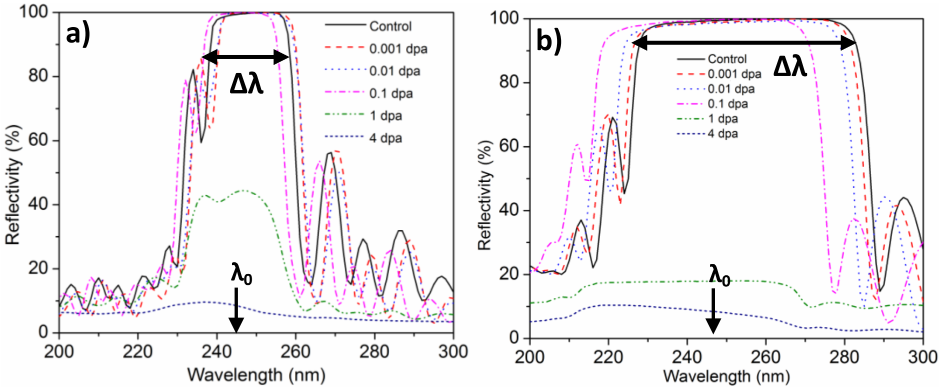

Figure 2. Reflectance of the mirrors compared with low dose results a) Al_2O_3/SiO_2 mirrors b) HfO_2/SiO_2 mirrors

Microstructural Changes in Irradiated Al_2O_3/SiO_2 Mirrors

TEM observation of the irradiated Al_2O_3/SiO_2 specimens showed partial crystallization of Al_2O_3 layers. Selected area electron diffraction pattern revealed a pattern indicative of crystalline structure which could be indexed as cubic γ-Al_2O_3. Figure 3 shows the layered structure and diffraction pattern of the Al_2O_3/SiO_2 mirror exposed to 1 dpa. The γ-Al_2O_3 is described as a defect spinel structure with several cation site vacancies. The amorphous Al_2O_3 (α-Al_2O_3) transform to crystalline γ-Al_2O_3 at elevated temperatures [6, 7]. Furthermore, radiation induced structural transformation of thermodynamically stable α-Al_2O_3 into metastable polymorphs such as κ-, γ-, δ-,θ-Al_2O_3 has also been well established [8, 9]. In contrast, limited studies have been performed to investigate the structural changes in α-Al_2O_3 after irradiation with particles such as ion, neutron and electron. Few studies showed the transformation of α-Al_2O_3 to γ-Al_2O_3 occur under electron irradiation by breaking and rearrangement of unstable Al-O bonds [10-12]. Similar phase transformation was also observed after high energy ion irradiations on α-Al_2O_3 films [13, 14]. The metastable nature of the γ-Al_2O_3 equally promotes reverse transformation of γ-Al_2O_3 to α-Al_2O_3 under irradiation [14]. Therefore, additives such as Si increase the stability of γ-Al_2O_3 [15, 16] where, Si cations occupy the vacancies in γ-Al_2O_3 leading to formation of strong and short Si-O bonds consequently stabilized the γ-Al_2O_3 phase. Although, the overall mechanism leading α-Al_2O_3 to γ-Al_2O_3 structural change under irradiation is still not clear. In the current study it was believed that the atomic rearrangement during irradiation lead to transformation of α-Al_2O_3 to γ-Al_2O_3, where the latter phase is stabilized by diffusion of Si atoms.

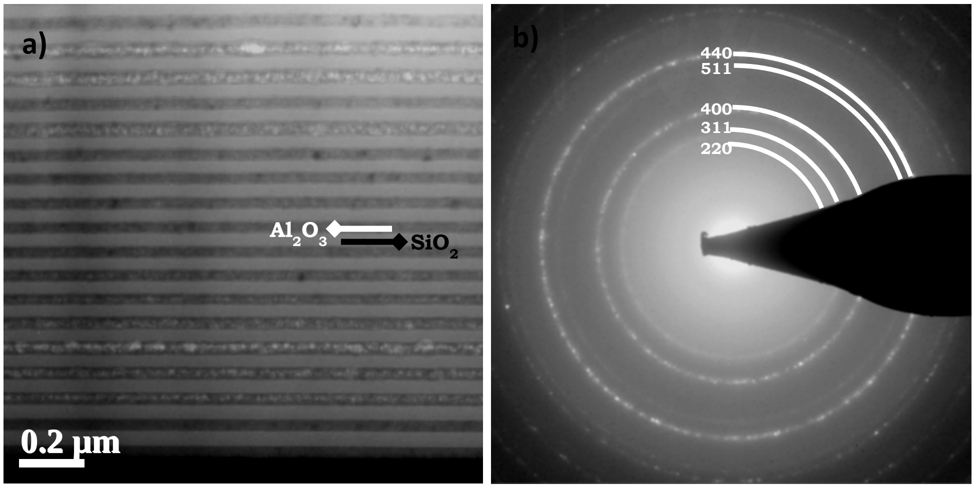

Figure 3. Al_2O_3/SiO_2 mirror after 1 dpa exposure. a) Layered structure b) Diffraction pattern

Al_2O_3 and SiO_2 interdiffusion

Low temperature solid state diffusion is a typical phenomenon observed in irradiated materials. The diffusion rates of Al and Si atoms differ significantly and several factors such as irradiation temperature and irradiation dose influence the diffusion process [17]. Severe interdiffusion was observed in Al_2O_3/SiO_2 mirrors after irradiations (see Figure 4 and 5). The formation of Al-Si rich regions on the Al_2O_3 layers was typically observed at both doses. However, uniformity in the second phase formation was not observed. Only few Al_2O_3 layers were found to have Al-Si rich regions, whereas in the other Al_2O_3 layers less segregation was observed. In addition, SiO_2 layers adjacent to Al-Si rich Al_2O_3 layers shrunk more than other SiO_2 layer in the specimen lead to non-uniform layer thickness of the SiO_2 layers.

The partial crystallization of α-Al_2O_3 to γ-Al_2O_3 could be the reason for this complex behavior of the Al_2O_3/SiO_2 mirrors under high dose irradiations. In general, the energy required to displace an atom from the lattice site of any material depends on factors such as bonding strength and the ability of the material to accommodate an interstitial atom in the structure. The aluminum and oxygen ions in Al_2O_3 have threshold displacement energies of 20 and 65 eV whereas silicon and oxygen atoms in SiO_2 have displacement energies of 20 and 10 eV, respectively [18,19]. In addition, the ionic material such as Al_2O_3 show higher binding energy than covalent bonded SiO_2. Accordingly irradiation would introduce nonstoichiometric numbers of Si, O and Al atoms and also due to weak bonding structure of SiO_2, more Si and O atoms will be displaced than Al atoms. Therefore, during irradiation gradual transformation of α-Al_2O_3 to γ-Al_2O_3 occurs by inward diffusion of excess oxygen atoms produced from SiO_2 layers. Further, the transformed γ-Al_2O_3, with a defect structure and cation vacancies, would act as precursor for the diffusion of silicon atoms, where the enhanced diffusion leading to formation of Al-Si rich phase was observed. The segregation at the other sites where the Al_2O_3 still shows amorphous structure is much less.

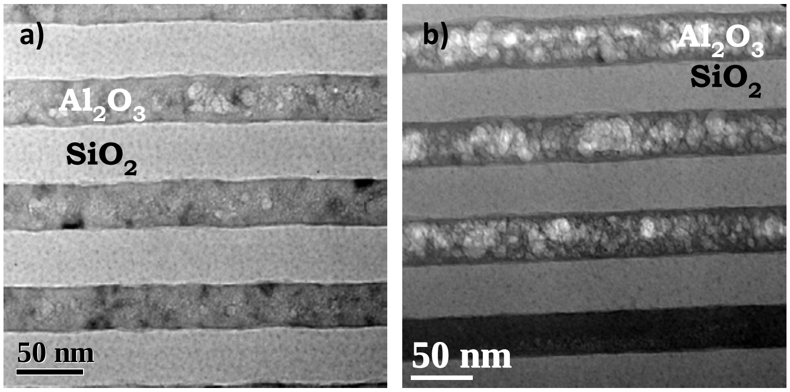

Figure 4. Al_2O_3/SiO_2 mirror exposed to 1 dpa showing non-uniform second phase formation on Al_2O_3 layers a) Less segregation b) Heavy segregation

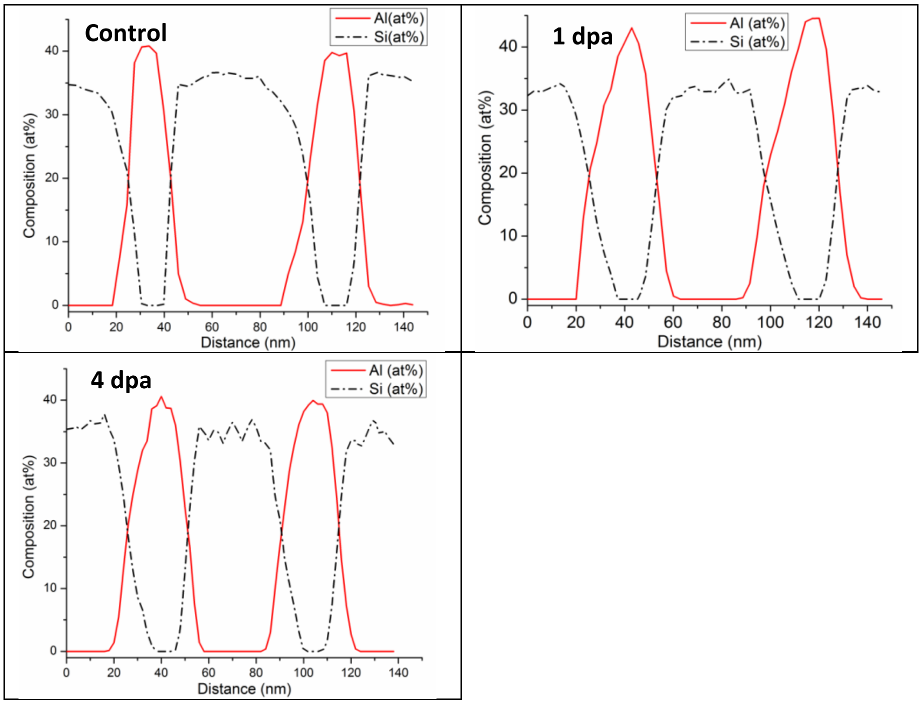

Figure 5. Energy dispersive spectrometry plots of constituent layers of the Al_2O_3/SiO_2 showing interdiffusion with the increase in irradiation dose.

Swelling defects

Apart from the Al/Si interdiffusion, new types of swelling defects were observed in SiO_2 layers of irradiated Al_2O_3/SiO_2 mirrors (see Figure 6). The typical size of each defect was ≈8 nm in 1 dpa and ≈ 42 nm in 4 dpa specimens. The defects in 1 dpa specimen were observed at the Al_2O_3/SiO_2 layer interface and with the increase in irradiation dose further growth of swelling defects occur in the SiO_2 layer. Energy dispersive spectrometry measurements along the SiO_2 layers did not yield any conclusive results due to its weak signal strength at the swelling region. The increase in the size of swelling defects with the irradiated dose suggests that the Al/Si interdiffusion plays a vital role at higher doses in Al_2O_3/SiO_2

mirrors. In addition, an increase in thickness of SiO_2 layer at the swelling region creates a small deviation in the subsequent Al_2O_3 layers. In general, increase in thickness of SiO_2 layer would produce a shift in the working range to slightly longer wavelengths. This is difficult to see based on the misshapen reflectance curves in Figure 1a as compared to the control. The irregularity in the 1 and 4 dpa reflectance curves are likely due to the observed features in the SiO_2 layers. Further work on understanding the swelling defects and the influence of these defects on the optical reflectivity is planned.

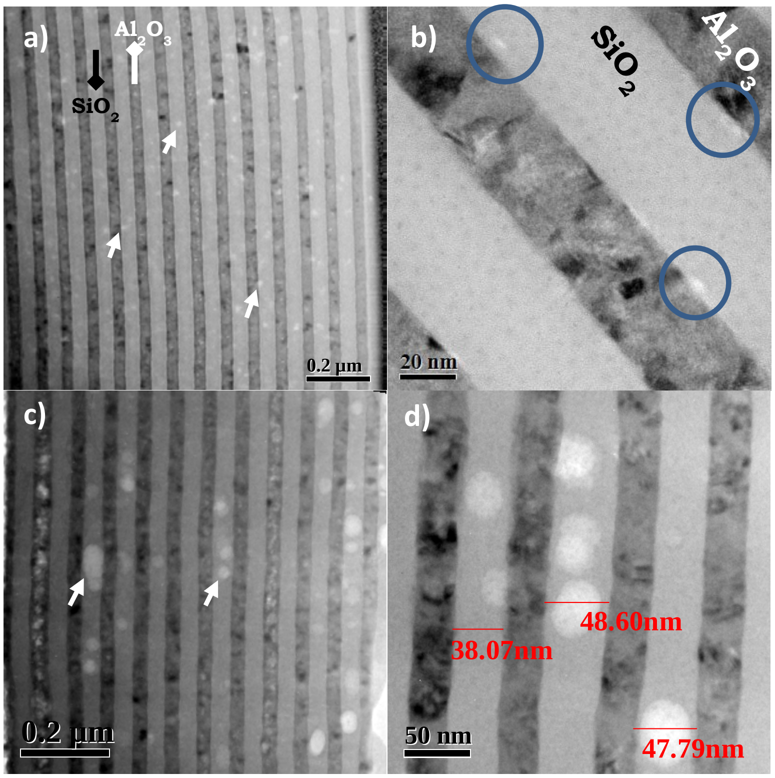

Figure 6. TEM micrographs showing the swelling defects in Al_2O_3/SiO_2 mirror, a), b) low and high magnification TEM micrographs in mirrors after 1 dpa dose, c), d) low and high magnification TEM micrographs showing swelling defects in mirrors after 4 dpa dose.

Microstructural Changes in Irradiated HfO_2/SiO_2 mirrors

Drastic drop in reflectivity was observed in the HfO_2/SiO_2 mirrors exposed to doses of 1 and 4 dpa. The loss in reflectance is attributed to the change in microstructure of the mirrors under high dose irradiations. Figure 7 shows the TEM micrographs of irradiated HfO_2/SiO_2 mirrors. Complete crystallization of the HfO_2 layer with the disappearance of amorphous regions was observed on irradiation to 1 and 4 dpa. The dominance of monoclinic reflections was still observed in HfO_2 layers. An increase in average grain size of HfO_2 layers to 20 nm at 4 dpa from 13 nm in a control sample was observed. The grain growth in metallic oxides is usually not expected in the low-temperature regime of <0.1 T_m (T_{irr}=185±10°C). However, previous work has shown that in nanocrystalline metallic systems at low temperatures the grain growth is driven solely by the reduction in grain boundary area by thermal spikes during displacement cascade [20]. In addition, other studies on ceramic materials have presented similar observations [21, 22]. This suggest that even in HfO_2 films irradiation-induced grain growth is believed to be the dominating mechanism behind the enormous increase in grain size under irradiation at T_{irr}=185°C.

Mirrors after irradiation showed more columnar morphology that extends through the film thickness. In addition, formations of twins were also observed in the HfO_2 layers. In the present case, the formation of nanotwins can be ascribed to the growth encounter during irradiation-induced grain growth, which is restricted to one direction by the thickness of the film layer.

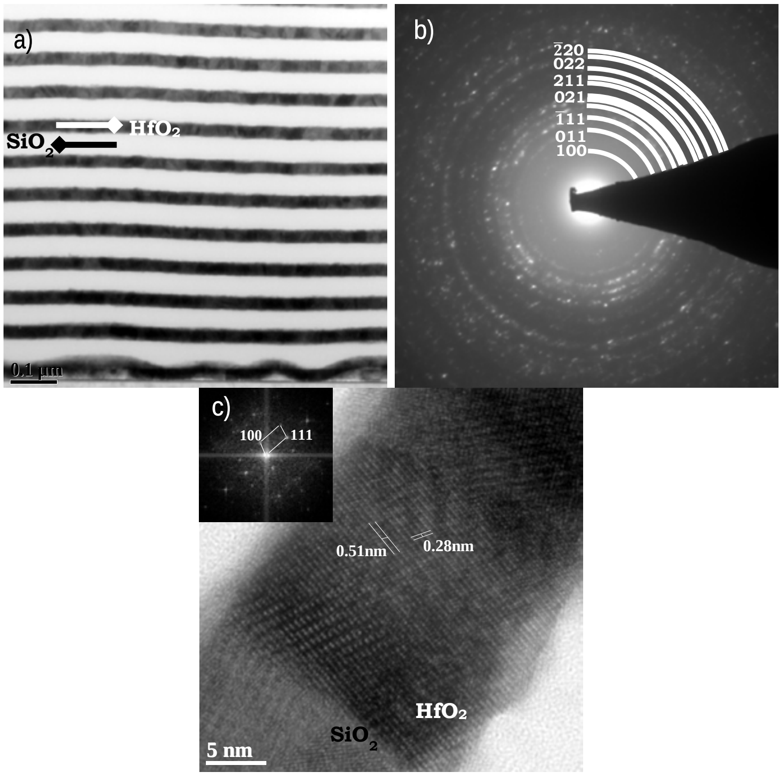

Figure 7. Cross-section TEM micrographs a) layers of HfO_2/SiO_2 mirror Irradiated to 1 dpa b) diffraction pattern showing monoclinic structure of HfO_2 films c) columnar grain structure of HfO_2 layer.

Delamination

Figure 8a is a low magnification TEM micrograph showing all the layers of HfO_2/SiO_2 mirror exposed to a dose of 4 dpa. Buckling type delamination and wrinkling of the HfO_2/SiO_2 bilayers was observed. In addition, non-uniform SiO_2 layer thickness was observed close to the interface layer and is attributed to the release of stresses at the detached region (see Figure 8b). Usually the grain geometry, average grain size and the grain size distribution have a strong influence on the mechanical properties of the polycrystalline thin films. In the case of HfO_2 films, the enormous grain growth during high dose irradiations lead to redistribution of grain boundaries and will produce differences in strain at the boundary compared to the initial fabricated condition. While the densification of SiO_2 films with the irradiation dose (approx. 2.7% volume contraction after exposures above 0.1 dpa (see Figure 9)) could introduce compressive stresses within the SiO_2 films. An imbalance between compressive stresses in SiO_2 layers and grain growth tensile stresses in HfO_2 layers coupled with weak film/substrate interface bonding could possibly lead to a buckle-type delamination and the disruption in the subsequent layers above the delaminated interface layer could lead to wrinkling of the multilayers.

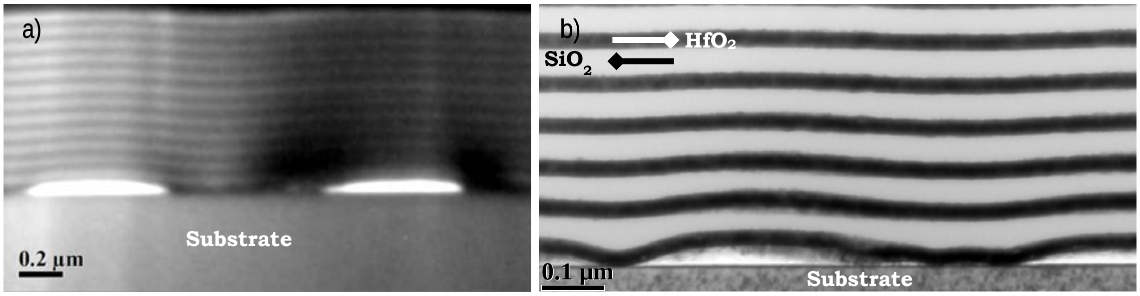

(a)

Figure 8. a) Low magnification TEM micrograph showing the buckle-type delamination at the substrate layer interface and wrinkling of the subsequent film layers, b) High magnification showing the disruption in subsequent layers.

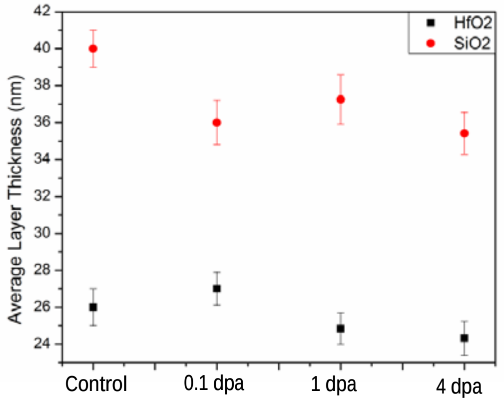

Figure 9. The average thickness of the constituent film layer in the HfO_2/SiO_2 mirrors at different irradiation doses (Densification of SiO_2 under irradiation was observed and the amount of densification reached a saturation limit at 0.1 dpa)

FUTURE WORK

Further analysis using Electron Energy Loss Spectroscopy (EELS) is being performed on the film layers to map the swelling defects observed in Al_2O_3/SiO_2 mirrors in order to understand the possible mechanism behind the defect formation. TEM examination of high dose irradiated mirrors is ongoing. A publication titled “Irradiation Effects on Microstructure and Optical Performance of Multilayered Dielectric Mirrors” is under preparation and the results will be presented at the ANS winter conference- 21st Topical Meeting on the Technology of Fusion Energy (TOFE).

REFERENCES

[1] S.J. Orfanidis, *Electromagnetic Waves and Antennas.*, Rutgers University, (2008).
[2] R.L. Bieri, M.W. Guinan, Fusion Technol., 19 (1991), 673.
[3] L.L. Snead, K.J. Leonard, G.E. Jellison Jr., M. Sawan, T. Lehecka, Fusion Sci. Technol., 56 (2009) 1069.
[4] K.J. Leonard, G.E. Jellison, N.A.P. Kiran Kumar, L.L. Snead, J. Nucl. Mater., 445 (2014) 281.
[5] E.H. Farnum, F.W. Clinard Jr., S.P. Regan, B. Schunke, J. Nucl. Mater., 219 (1995) 224.
[6] Y.T. Chu, J.B. Bates, C.W. White and G.C. Farlow, J. Appl. Phys., 64 (1988) 3727.
[7] I.Levin and D.Brandon, J. Am. Ceram. Soc. 81 (1998) 1995.
[8] M. Ohkubo and Y. Seno, Philos. Mag. Lett. 59 (1989) 171.

[9] K. Jiang, Al2O3 Think Films: Relations between structural evolution, mechanical properties and stability, PhD Thesis (2011).
[10] R. Nakamura, M. Ishimaru, H. Yasuda and H. Nakajima, J. Appl. Phys., 113 (2013) 064312.
[11] C. Pan, P. Shen and S.Y. Chen, J. Cryst. Growth, 299 (2007) 393.
[12] J. Murray, K. Song, W. Huebner and M. O'Keefe, Mater. Lett. 74 (2012) 12.
[13] S. Nakao, P. Jin, G. Xu, M. Ikeyama et al. J. Cryst. Growth, 237 (2002) 580.
[14] N. Yu, P.C. Mclntyre, M. Nastasi and K.E. Sickafus, Phys. Rev. B, 52 (1995) 17518.
[15] S. Blonski, S.H. Garofaline, Chem. Phys. Lett., 211 (1993) 575.
[16] F. Nahif, D. Music, S. Mraz, M. Baben and J.M. Schneider, J. Phys. Condens. Matter, 25 (2013) 125502.
[17] T. R. Allen, G.S.Was, Radiation Effects in Solids, NATO Science Series, 235 (2007) 123.
[18] G.P. Pells, J. Am. Ceram. Soc., 77 (1994) 368.
[19] G. Pacchioni, L. Skuja and D.L. Griscom, Defects in SiO2 and Related Dielectrics: Science and Technology, NATO Science Series, (2000).
[20] D. Kaoumi, A.T. Motta, R.C. Birtcher, J. Appl. Phys., 104 (2008) 073525.
[21] Y. Zhang, W. Jiang, C. Wang, F. Namavar, P.D. Edmondson, Z. Zhu *et al,* Phys Rev B, 82 (2010) 184105.
[22] Y. Zhang, P.D. Edmondson, T. Varga, S. Moll, F. Namavar, C. Lan *et al,* Phys. Chem. Chem. Phys., 13 (2011) 11946.

6.1 LIQUID METAL COMPATIBILITY

S. J. Pawel (Oak Ridge National Laboratory)

OBJECTIVE

The objective of this task is to identify potential structural materials having sufficient compatibility with flowing Pb-Li eutectic that the maximum metal temperature for operation can be increased to improve overall system efficiency.

SUMMARY

Operation of the first thermal convection loop (TCL) using dispersion strengthened FeCrAl (Kanthal APMT) tubing and specimens was completed in this reporting period. The working fluid in the TCL was eutectic Pb-17at%Li, and the peak temperature (550˚) and temperature gradient (116˚C) was maintained without interruption for 1000 h. When operation was terminated, a problem with complete draining of the Pb-Li from the loop was encountered, which delayed retrieval of specimens exposed in the hot leg of the TCL; however, analysis of specimens from the cold leg has been initiated.

PROGRESS AND STATUS

Introduction

Currently, the maximum allowable wall temperature for the dual coolant lead-lithium (DCLL) blanket concept is set at 475˚C based primarily on corrosion limitations of the structural containment materials. To increase overall system efficiency, potential structural materials are being sought with a combination of high strength and creep resistance with simultaneous resistance to dissolution in eutectic Pb-Li at temperatures > 500˚C. Preliminary research using static capsule exposures has indicated that dispersion strengthened FeCrAl (Kanthal APMT) may be resistant to dissolution in eutectic Pb-Li at temperatures in the range of 600-800˚C, at least in part due to the stability of an Al-rich oxide film. However, corrosion data in a flowing system must be generated to analyze the potential for issues associated with thermal gradient mass transfer – relatively high dissolution in hotter portions of the flow system with concomitant deposition in the colder portions – which has been known to disrupt heat transfer and even plug flow paths completely in some temperature gradient/material combinations.

Thus, thermal convection flow loops (TCLs) are being incorporated as the follow-on step to capsule testing for evaluation of liquid metal compatibility. The initial laboratory testing associated with this effort utilized a mono-metallic TCL fabricated of Kanthal APMT with APMT specimens inserted within each of the hot leg and cold leg of the TCL for use in post-exposure evaluation. Fabrication of the first such TCL utilizing APMT tubing (26.7 mm OD, 3.1 mm wall), which evaluated welding and heat treatment procedures to be used in subsequent TCL construction with this alloy, was successfully completed in the prior reporting period.

Results

Figure 1 shows a schematic of the APMT loop alongside a photo of the loop just prior to operation. The loop was about 1 m tall and 0.5 m wide in the flow path. Heating on one side of the loop (the “hot” leg) caused the density of the liquid Pb-Li material to decrease relative to the liquid in the unheated leg; the density difference drives flow (down on cooled side, up on heated side) once a steady temperature gradient is established. [In the schematic diagram, the liquid metal flow direction would be counterclockwise.] The loop contained two specimen chains – one in each vertical leg of the loop. Test coupons of APMT were prepared in the form of miniature tensile specimens which were strung together with APMT wire (see Figure 2). Most of the APMT test specimens received the same high temperature oxidation treatment afforded the loop itself (slow cooled following 8 h in air at 1050˚C), but a few of the specimens were exposed in the as-machined (no oxide) condition to permit ready comparison of compatibility with Pb-Li as a function of temperature around the loop. In addition to APMT coupons, a few small rectangular specimens of commercially pure tungsten were used at the bottom of each specimen chain to act as a "sinker" to keep the relatively low density specimen chains from floating in the Pb-Li test fluid, and to act as "spacers" to keep the specimen chain centered within the tubing and liquid metal flow path.

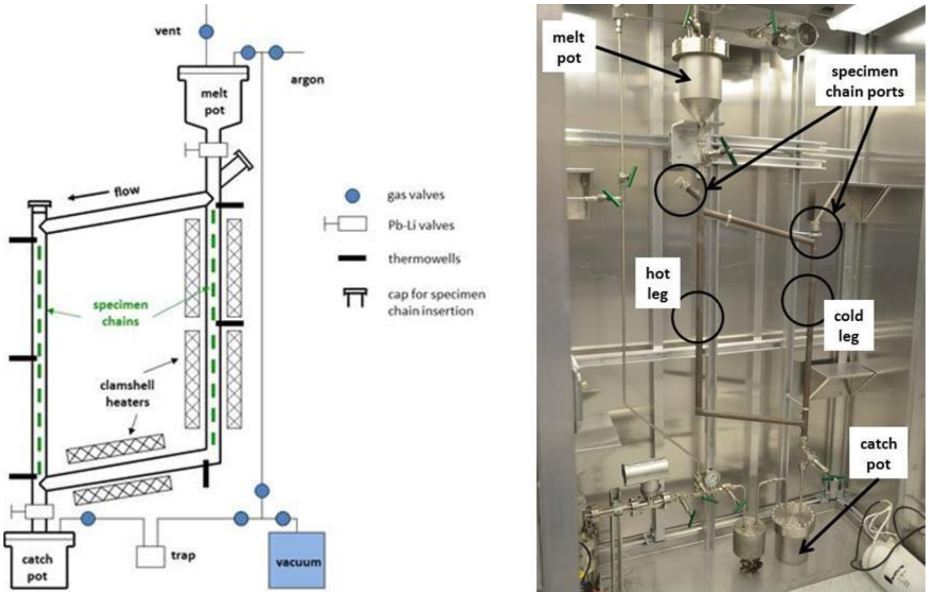

Figure 1. Schematic of the thermal convection loop for Pb-Li experiments and a photo of the actual loop prior to installation of furnaces and insulation. Actual dimensions are approximately 1 m x 0.5 m in the liquid metal flow path around the loop.

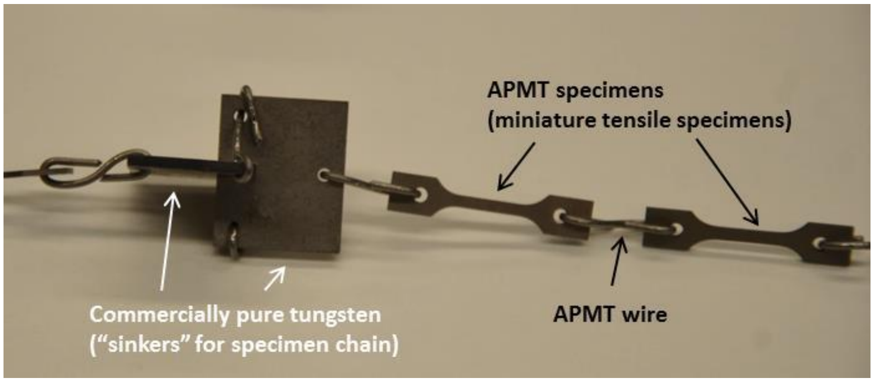

Figure 2. Representative portion of a specimen chain showing APMT miniature tensile specimens ("SS3" design) wired together (also APMT) and pieces of tungsten acting as "sinker" weights and as spacers to assure centering of the specimen chain within the tube. The tensile specimens are about 25 mm long, 5 mm wide, and 1 mm thick.

Table 1 shows the average temperatures achieved at each measurement position around the loop, which were thermowells that protruded about 0.3 cm into the flow path of the working fluid. Following stabilization of the loop (minor adjustments to heaters and insulation over the first 24 h or so), the temperatures at each position remained constant (± 1˚) at the average values for 1000 h until the loop operation was terminated.

Table 1. Average temperatures recorded at ley thermocouple positions around the loop.

Loop Position	Temperature (˚C)
Top of Hot Leg	550
Middle of Hot Leg	484
Bottom of Hot Leg	456
Top of Cold Leg	496
Middle of Cold Leg	461
Bottom of Cold Leg	434

The flow rate within the loop was estimated twice during the 1000 h operation interval using a "hot spot" test. In this evaluation, a small section of insulation on the approximately horizontal section of the loop was removed to expose the loop tubing. Next, the flame of a gas torch was held within 2-3 cm of the exposed tubing for a period of about 15 seconds to increase the Pb-Li temperature significantly in a very localized volume of material. Subsequently, as the P-Li flowed around the loop, a brief temperature spike was detected at each thermocouple location in sequence, and the time required for the temperature spike to travel the distance between detection points was used to estimate the flow rate. Figure 3 is a representative example of data collected in this manner, which displays the modest temperature spike at each location in sequence around the loop. Using this method, the flow rate was estimated to be approximately 0.4 m/min at both measurement events. This value is somewhat lower than that observed in this laboratory for recent TCLs of the similar size/design and temperature gradient utilizing sodium as the working fluid, which exhibited flow rates between 0.8-0.9 m/min. Significantly, the density difference of sodium between 450 and 550˚C (roughly the temperature gradient of interest) is 2.9% while it is only 1.7% for Pb-Li over the same temperature range. As a result of a ~ 70% greater density change, flow rate should be somewhat faster for Na compared to Pb-Li, but flow rate incorporates factors other than fluid density.

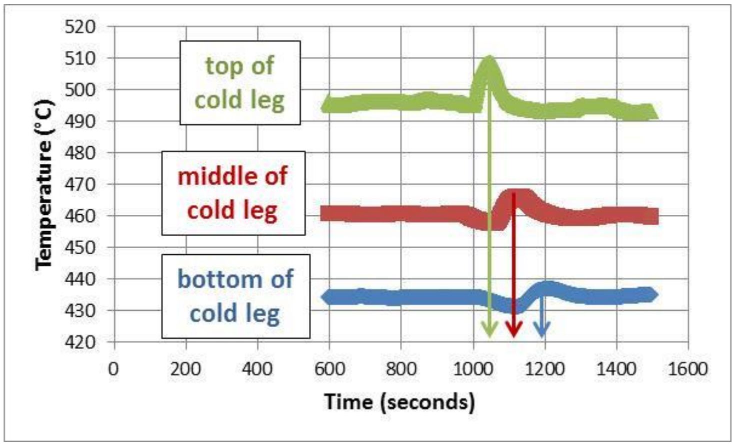

Figure 3. Representative example of data collected in "hot spot" test to estimate flow velocity of Pb-Li within the TCL.

The data in Figure 3 reveal another feature of the hot spot test. Note that for each of the cold leg positions indicated, the temperature decreases slightly prior to the temperature increase associated with the hot spot. The reason is that the application of the hot spot flame decreases the flow rate temporarily due to the imbalance created in liquid metal density at the top portion of the loop. As a result of this flow disruption, the Pb-Li in the cold leg spends a few more seconds there than normal and thus cools a few more degrees than normal. As soon as the flame is removed, however, normal flow is quickly re-established, and the hot spot travels around the loop immediately preceded by a slight dip in temperature.

Following 1000 h of operation, the loop was terminated with the initial attempt to drain the loop of Pb-Li into the dump tank positioned at the bottom of the cold leg. Unfortunately, problems were encountered with a cold spot within the very thick lid of the dump tank. After allowing all of the remaining Pb-Li to freeze in place within the loop, it was confirmed that the Pb-Li froze in this cold spot location after only partially draining from the loop. Other difficulties were encountered upon reheating of the loop to liquefy the Pb-Li and again attempt to drain it from the loop, including a small leak that developed – apparently in the thermowell weld at the top of the cold leg (analysis just beginning) – and a somewhat surprising incomplete draining of the hot leg (despite thermocouple data indicating drainage had occurred). The latter difficulties have delayed removal of specimens from the hot leg of the TCL, but analysis of cold leg specimens has begun. Curiously, the activities designed to complete removal of the hot leg specimens seem to suggest the possibility that the specimen chain, rather than hanging straight in "single file" orientation, is perhaps in a knot at about the midpoint of the hot leg. If this is confirmed, it would potentially account for reduced flow rate via adding substantial flow resistance at this location within the TCL.

Cold-leg specimens were soaked in cleaning solution (1:1:1 mixture of ethanol, hydrogen peroxide, and acetic acid) while within the loop (as an assembled chain) and again upon removal from the loop (as individual specimens). The cleaning solution readily dissolves residual Pb-Li rendering weight change measurements more meaningful. Following exposure to the cleaning solution, the specimens were ultrasonically cleaned in acetone followed by air drying prior to photography and weighing.

Figure 4 shows the mass change as a function of temperature (position) for the cold leg specimens following cleaning. The approximate temperature of each specimen location was estimated by linear extrapolation as a function of position between thermowell locations at which the temperature was known. Weight change from two starting points is given in Figure 4; that based on original (as-received) specimen weight, and that based on specimen weight following a pre-oxidation heat treatment intended to form an aluminum-rich oxide on the surface (same treatment as received by the completed loop). It is plotted both ways (slopes of the weight change are identical) to emphasize the fact that all specimens except the one at the bottom of the cold leg reveal a net weight loss, but the total weight loss is less than the mass gained as a result of the pre-oxidation step for temperatures below about 473˚C.

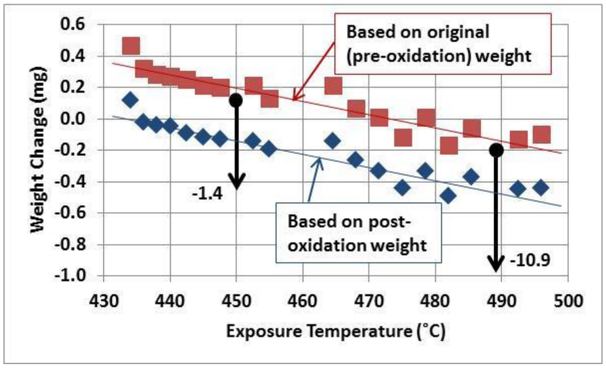

Figure 4. Weight change of specimens as a function of exposure temperature in the Pb-Li thermal convection loop. Black/round points correspond to specimens that were not given the pre-oxidation heat treatment.

The values of net weight change for the heat treated APMT specimens are quite modest. The highest weight loss, approximately 0.5 mg, can be converted to an average uniform dissolution rate using specimen density (~ 7.2 g/cm^3), specimen area (2.0 cm^2), and exposure time (1000 h), which yields a value of approximately 3 µm/y (0.1 mil/y).

Also shown in Figure 4 are the data points for two APMT specimens that were exposed without the pre-oxidation treatment afforded the rest of the specimens and loop tubing. Note that the weight loss for these specimens is a strong function of temperature – much more weight loss at the higher temperature – and substantially greater than the oxidized specimens immediately adjacent to the as-received specimen. An estimate of the uniform dissolution rate for the specimen with no pre-oxidation treatment exposed at 489˚C (10.9 mg net weight loss) yields a dissolution rate more than 25 times higher than that of the surrounding specimens. This indicates that the pre-oxidation treatment to develop aluminum oxide is an important feature of the compatibility of APMT with PbLi at these temperatures.

Note that, as in all TCL experiments, the weight change of any individual specimen is determined by the competition between dissolution activity and precipitation reactions. Additional analysis of the cold leg specimens – and the hot leg specimens when they are retrieved – will be necessary to determine additional compatibility characteristics.

Figure 5 shows the cold leg specimens after cleaning. Note that all of the specimens have varying degrees of discoloration, suggesting variable degrees of oxide film removal and/or variable degrees of deposit quantity or composition. In a qualitative sense, the relatively dark areas on each cold leg specimen seem to be relatively adherent (light scraping with sharp tweezers does not remove material), but in this manner some material is removed from the specimens without a pre-oxidation heat treatment, again suggesting a potentially significant consequence of the pre-oxidation treatment. The variable appearance of the specimens further emphasizes the need for surface analysis and metallurgical examination following tensile testing of the specimens.

Figure 5. Appearance of cold leg specimens following 1000 h exposure and cleaning. Approximate exposure temperature is given adjacent to each specimen. The specimen slightly out of line with the array of specimens is one that was not given a pre-oxidation heat treatment prior to exposure.

As funding allows, additional analysis will be pursued on all specimens (weight change, tensile testing, cross-section metallography, and SEM/microprobe assessment) as they become available.

7.1 EFFECTS OF ION IRRADIATION ON BAM-11 BULK METALLIC GLASS –

A. G. Perez-Bergquist[1,2], J. Brechtl[2], H. Bei[1], Y. Zhang[1,2] and S. J. Zinkle[1,2] ([1]*Oak Ridge National Laboratory,* [2]*University of Tennessee)*

OBJECTIVE

The goal of this study is to investigate the radiation behavior of the bulk metallic glass BAM-11 and to determine if it is a viable candidate for high-radiation structural applications in fusion systems.

SUMMARY

Bulk metallic glasses are intriguing candidates for structural applications in nuclear environments due to their good mechanical properties along with their inherent amorphous nature, but their radiation response is largely unknown due to the relatively recent nature of innovations in bulk metallic glass fabrication. Microstructural and mechanical property evaluations have been performed on as-cast and heat-treated $Zr_{52.5}Cu_{17.9}Ni_{14.6}Al_{10}Ti_5$ bulk metallic glass (BAM-11) irradiated with 3 MeV Ni^+ ions to 1 and 10 dpa. TEM showed no evidence of radiation damage or crystallization following ion irradiation, and changes in hardness and Young's modulus were 10-15%. In addition, irradiation-induced damage was seen to saturate at or below the 1 dpa dose level.

PROGRESS AND STATUS

Introduction

Amorphous metallic glasses were first synthesized in the 1960s [1] and have since received considerable scientific attention due to their appealing properties, including their good thermal conductivity, high strength, good ductility, and corrosion resistance [2-4]. Metallic glasses are an intriguing candidate for use in radiation environments due to their lack of crystalline structure, which prohibits the formation of conventional radiation defects such as vacancy-interstitial Frenkel pairs and dislocation loops that occur in crystalline solids. A more thorough review of radiation effects in bulk metallic glasses is available in the previous semi-annual report (for period ending December 31, 2013).

In the first portion of this study, we investigated ion irradiation effects in the bulk metallic glass BAM-11 (Composition: $Zr_{52.5}Cu_{17.9}Ni_{14.6}Al_{10}Ti_5$). Specimens were irradiated with 3 MeV Ni^+ ions to 0.1 and 1.0 dpa at room temperature and 200°C. Nanoindentation hardness and Young's modulus both decreased by 6 to 20% in samples irradiated at room temperature, with the sample irradiated to 1.0 dpa experiencing the greatest change in mechanical properties. However, no significant changes in properties were observed in the samples irradiated at 200°C, and transmission electron microscopy showed no visible evidence of radiation damage or crystallization following ion irradiation at any of the tested conditions.

Here, we continue the work on this bulk metallic glass and investigate the effects of higher irradiation doses on the material and the effects of pre-irradiation heat treatments.

Experimental Procedures

A $Zr_{52.5}Cu_{17.9}Ni_{14.6}Al_{10}Ti_5$ alloy (BAM-11) was fabricated by arc melting in an argon atmosphere using a mixture of base metals with the following purities: 99.5% Zr, 99.99% Cu, 99.99% Ni, 99.99% Al, and 99.99% Ti. The alloy was then remelted and drop cast in a Zr-gettered helium atmosphere. The rod was then cut into sections of 8 by 3 by 1 mm and mechanically polished to a mirror finish. Some samples were given a 48 hour heat treatment at 300°C, well below the material's glassy transition temperature of 393°C [5].

After fabrication and heat treatment, BAM-11 specimens were ion irradiated with 3 MeV Ni^+ ions at perpendicular incidence. Samples were irradiated to fluences of 4.2 x 10^{14} and 4.2 x 10^{15} ions/cm^2, or peak damage levels of 1 and 10 dpa at the University of Tennessee/ORNL Ion Beam Materials Laboratory (IBML). Ion range and damage event profiles were used to determine the fluence to dpa conversion and were generated by the SRIM software using an average displacement energy of 40 eV [6]. The most common ion range depth was calculated to be 1.36 µm, with implanted Ni concentrations reaching 5.5 x 10^{18} atoms/cm^3 at this depth. Damage levels at the sample surface were calculated to be about 40% of peak levels.

Post-irradiation microstructural characterizations of the irradiated bulk metallic glass specimens were performed via transmission electron microscopy (TEM). TEM foils were fabricated using an FEI Quanta Dual-beam focused ion beam (FIB)/SEM with a final thinning step of 2kV Ga^+ ions at a glancing angle of about 4° in order to minimize ion beam milling damage. Samples were then analyzed in a Phillips CM 200 TEM operating at 200 kV using the techniques of bright field (BF) imaging, selected area electron diffraction (SAED), high resolution TEM (HRTEM), and x-ray energy dispersive spectroscopy (EDS) performed in scanning TEM (STEM) mode.

Hardness and elastic modulus were measured using an MTS XP nanoindenter, with the indentations performed normal to the mechanically polished control and irradiated surfaces [7]. All tests were performed using a Berkovich diamond indenter (3 sided pyramidal tip) in continuous stiffness measurement mode at a constant indentation rate [(dP/dt)/P] of 0.05/s with a maximum applied load of 15 mN, resulting in a maximum indentation depth of ~350 nm. For statistical purposes, each sample was indented a total of ~16 times in different locations and the averages of those results are reported here. Hardness and elastic modulus were calculated using the Oliver and Pharr method [8,9]. The area function of the tip and machine stiffness of the nanoindenter were calibrated by indenting on a standard fused silica sample [10].

Mechanical Properties

Hardness and elastic modulus data generated through nanoindentation tests are shown as a function of indenter depth in Figure 1. Average data for an indenter depth of 200 nm, which represents a compromise in depth to minimize surface effects while also minimizing contributions to the data from unirradiated regions, is presented in Table 1.

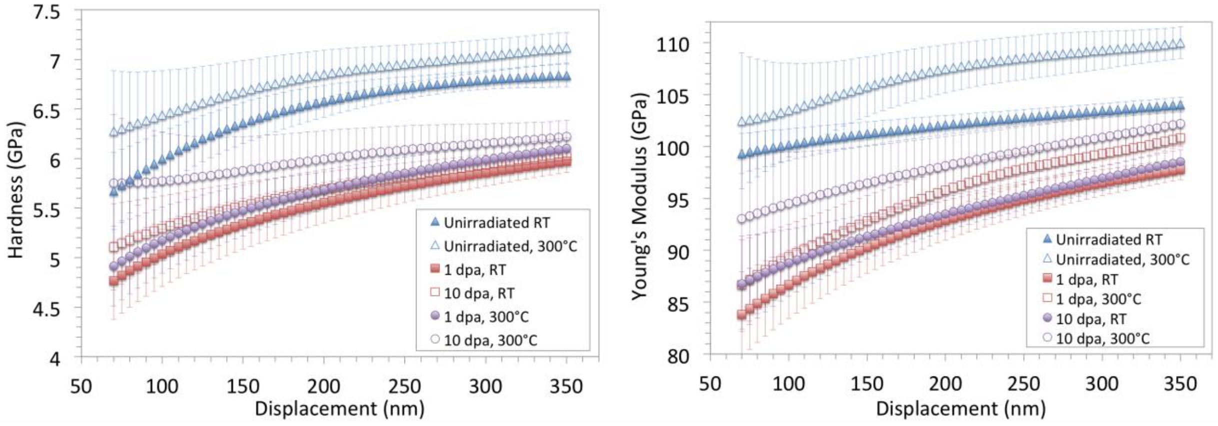

Figure 1. Hardness and elastic modulus as a function of indenter depth in the unirradiated and irradiated BAM-11 specimens.

Table 1. Summary of nanoindentation results on virgin and irradiated BAM-11 at a depth of 200 nm.

	Unirr.	Unirr., HT	1.0 dpa, RT	10 dpa, RT	1.0 dpa, HT	10 dpa, HT
Average Hardness* (GPa)	6.6	6.9	5.6	5.7	5.7	6.0
Std. Dev. Of Hardness (GPa)	0.2	0.2	0.2	0.2	0.2	0.3
Average Young's Modulus* (GPa)	102.1	107.5	92.9	93.5	95.8	98.1
Std. Dev. Of Young's Modulus (GPa)	0.9	2.3	1.9	1.7	2.0	2.8

For both heat-treated and as-cast samples, hardness and modulus dropped for the irradiated specimens as compared to the sample in the unirradiated condition. There was also a slight increase in hardness and modulus in the heat-treated condition as compared to the virgin condition for all samples. The drop in hardness following irradiation for both the as-cast and heat-treated samples was on the order of about 15%, while the drop in modulus was on the order of about 10%.

While hardness and modulus values were observed to drop, the irradiation-induced change does not markedly differ between the samples tested at 1 and 10 dpa, indicating a saturation of irradiation damage in the bulk metallic glass. This indicates that BAM-11 may be resistant to much higher radiation doses than those tested here.

Microstructure

Similar to the previous thrust in which samples were irradiated to a maximum of 1.0 dpa, no significant microstructural changes were observed in the BAM-11 BMG samples after irradiation to 1 or 10 dpa in either the as-cast or heat treated conditions. TEM revealed the samples to be feature-free, and diffraction showed the samples to be amorphous. HRTEM confirmed that no crystallites were present in the sample. Additionally, no dislocations or point defect-like structures were visible upon tilting on two different axes in the TEM. EDS performed on the samples did not reveal any surprises in terms of the elements in the specimens. Microstructures of the as-cast and heat-treated samples are shown in Figure 2.

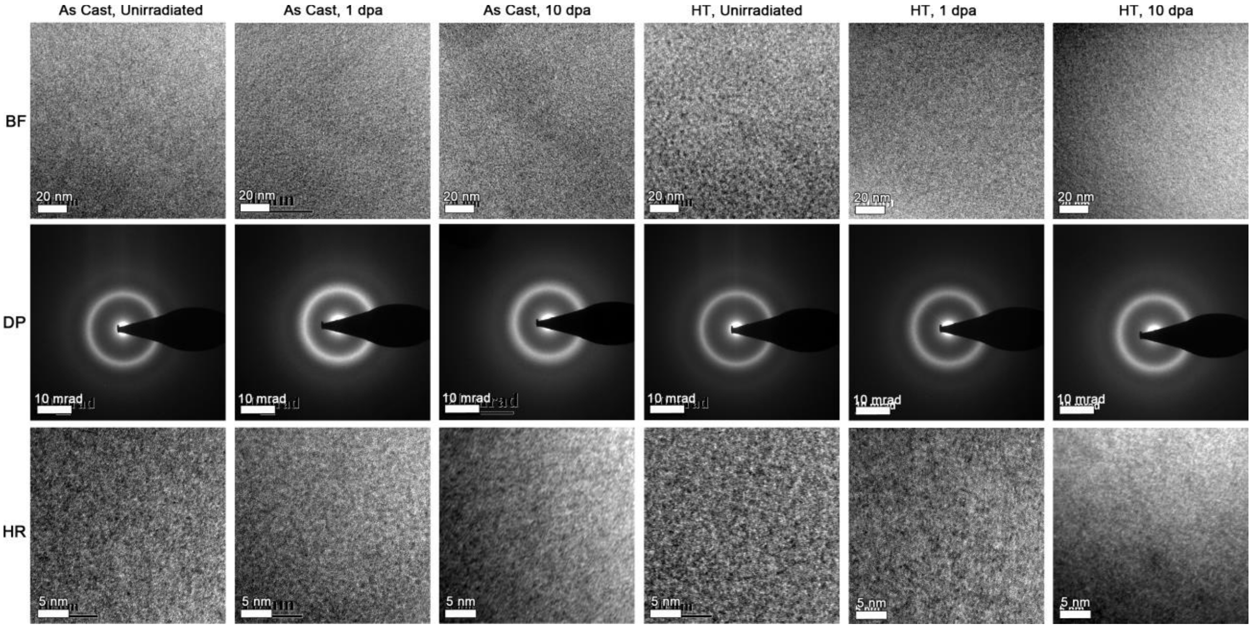

Figure 2. TEM micrographs consisting of BF images at 135kx, diffraction patterns, and high resolution images at 580kx of as-cast and heat-treated ion-irradiated BAM-11 irradiated to 1 and 10 dpa. No changes in crystallinity or any defect structures were observed.

CONCLUSIONS

After irradiation with 3 MeV Ni^+ ions to dose levels of 1 and 10 dpa at room temperature, both as-cast and heat-treated amorphous BAM-11 bulk metallic glass specimens were found to exhibit no observable changes in microstructure and only minor (10-15%) drops in hardness and elastic modulus. In addition, damage in the material seems to saturate at or below the 1 dpa dose level based on mechanical property measurements.

Overall, the favorable constitutive response of BAM-11 following irradiation to low fluence levels indicates that the alloy may have applications as a structural material in nuclear applications, albeit only in low temperature scenarios where the alloy stays below its glassy transition temperature. Further testing of the bulk metallic glass at dose levels up to 100 dpa may be necessary to ensure that irradiation damage does indeed saturate as expected.

REFERENCES

[1] W. Klement, R.H. Wilens, and P. Duwez, Nature **187** (1960) 869-870.
[2] R.W. Cahn, Nature **341** (1989) 183-184.
[3] P. Chaudhari and D. Turnbull, Science **199** (1978) 11-21.
[4] A.L. Greer, Science **267** (1995) 1947-1953.
[5] C.T. Liu, L. Heatherly, D.S. Easton, C.A. Carmichael, J.H. Schneibel, C.H. Chen, J.L. Wright, M.H. Yoo, J.A. Horton, and A. Inoue, Metall. Mater. Trans. A **29A** (1998) 1811-1820.
[6] J.F. Ziegler, J.P. Biersack, U. Littmark. The Stopping and Range of Ions in Solids, Pergamon Press, New York (1985). Also see: http://www.srim.org.
[7] H. Bei, Z. P. Lu, E. P. George, Phys. Rev. Lett. **93** (2003) 125504.
[8] W.C. Oliver and G.M. Pharr, J. Mater. Res. **7** (1992) 1564-1583.
[9] W.C. Oliver and G.M. Pharr, J. Mater. Res. **19** (2004) 3-20.
[10] W. Li, H. Bei, Y. Tong, W. Dmowski, and Y.F. Gao, Appl. Phys. Lett. **103** (2013) 171910.

7.2 EFFECTS OF NEUTRON IRRADIATION ON Ti-Si-C MAX-PHASE CERAMIC MICROSTRUCTURES –

A. G. Perez-Bergquist[1,2], Y. Katoh[1], C. Shih[1], and S. J. Zinkle[1,2] ([1]*Oak Ridge National Laboratory,* [2]*University of Tennessee)*

OBJECTIVE

The goal of this study is to investigate the neutron irradiation behavior of the MAX-phase ceramic Ti_3SiC_2 and to determine if it is a viable candidate for high-radiation structural applications in fusion systems.

SUMMARY

MAX phase ceramics are intriguing candidates for structural applications in nuclear environments due to their unique mixture of metallic and ceramic properties. Specifically, their potential to retain adequate thermal conductivity after high levels of irradiation damage may make them an attractive alternative to SiC in fusion environments. In this study, we investigate samples containing MAX phase Ti_3SiC_2 after neutron irradiation to 3.4 and 5.0 dpa at temperatures of 500 and 800°C. Ti_3SiC_2 in the 500°C sample appeared to decompose into TiC under irradiation, whereas the Ti_3SiC_2 in the 800°C sample did not. Limited radiation damage was visible in the 800°C sample.

PROGRESS AND STATUS

Introduction

MAX phase ceramics are a family of ternary compounds with the general composition of $M_{n+1}AX_n$ where n = 1, 2, or 3, M is early transition metal, A is a Group A element, and X is carbon, nitrogen, or both. These unique carbide and nitride ceramics were first discovered in the 1960s [1], but interest in them was minor until the mid 1990's when Barsoum and El-Raghy first synthesized relatively phase-pure samples of Ti_3SiC_2 [2]. Work in MAX phase materials has since intensified greatly, with MAX phase ceramics being reported to exhibit high modulus, low specific gravity, adequate machinability, outstanding tolerance against oxidation and thermal shock, good thermal conductivity, moderate ductility, and the capacity to maintain strength up to about 1300°C [2-6]. Recently numerous ion irradiation studies have been performed on Ti_3SiC_2 and Ti_3AlC_2. A more thorough review of MAX phase Ti_3SiC_2 and ion irradiation studies in this material are available in the previous semi-annual report (for period ending December 31, 2013).

In this work, we investigate the effects of neutron irradiation on both phase-pure and phase-impure Ti_3SiC_2.

Experimental Procedures

MAX phase Ti_3SiC_2 was fabricated in the seams of joined SiC plates via two different methods. In one set of samples, a 20 µm pure titanium foil was used to diffusion bond the SiC plates. The bond was formed by inserting the foil between the plates and hot pressing at 1170°C at 20 MPa for 3 hours in an argon atmosphere, producing Ti_3SiC_2/Ti_5Si_3 in the joints. In the second set of samples, a tape calendaring process using organic binders and a mixture of TiC and Si powders (99.99% purity, TiC:Si ratio of 3:2) was used. 200 µm thick calendared tapes were pressed and heated between two SiC plates at 1425°C at 30 to 40 MPa applied pressure for 2 hours, producing Ti_3SiC_2/SiC in the joints. Samples were then neutron irradiated at the Flux Trap Facility in the High Flux Isotope Reactor (HFIR) at Oak Ridge National Laboratory to 3.4 dpa and 5.0 dpa at temperatures of 500 and 800°C, respectively.

Post-irradiation examination was carried out in the Low Activation Materials Development and Analysis (LAMDA) laboratory at ORNL. Detailed examination in LAMDA included torsional shear strength evaluation and cross-sectional microstructural and micro-chemical analyses. Details of the shear strength test procedure are given in reference [7]. Scanning electron microscope (SEM) examinations and analyses were performed using field-emission-gun SEM Hitachi Models S4700 and S4800 equipped with energy dispersive X-ray spectroscopy (EDS) systems. Transmission electron microscopy (TEM) foils were fabricated using an FEI Quanta Dual-beam focused ion beam (FIB)/SEM with a final thinning step of 2kV Ga^+ ions at a glancing angle of about 4° in order to minimize ion beam milling damage. Samples were then analyzed in a Phillips CM 200 TEM operating at 200 kV using the techniques of bright field (BF) imaging, selected area electron diffraction (SAED), high resolution TEM (HRTEM), and EDS performed in scanning TEM (STEM) mode.

Mechanical Properties

Torsional tests to determine joint shear strength of the irradiated samples was performed and recorded in the previous semi-annual report. Results are shown here as a reminder in Table 1.

Table 1. Torsional test (shear strength) results.

Joint	Strength, Unirradiated (MPa)	Failure Location, Unirradiated	Irradiation Condition	Strength, Irradiated (MPa)	Failure Location, Irradiated
Ti_3SiC_2/Ti_5Si_3	124 (23)	Joint (Full/Partial)	500°C, 3.4 dpa	125 (36)	Joint (Full/Partial)
Ti_3SiC_2/SiC	117 (10)	Basal Plane	800°C, 5.0 dpa	98 (22)	Joint (Full)

Microstructure

In the previous semi-annual report, we reported on microcracking and radiation-induced defect formation in the Ti_3SiC_2/Ti_5Si_3 sample. At that point, TEM analysis had yet to be performed upon the Ti_3SiC_2/SiC sample. That work will be discussed shortly, but some incongruous results between the two samples forced us to reconsider the work that had already been done.

Shown in Figure 1 is the sample irradiated at 500°C to 3.4 dpa that was ostensibly comprised of Ti_3SiC_2/Ti_5Si_3. The image shows a portion of a Ti_5Si_3 grain, which shows no irradiation defects at any diffraction or tilt conditions, and the presumed Ti_3SiC_2 grain, which exhibited a number of planar defects oriented along certain crystallographic directions in the material. However, the diffraction patterns taken did not correspond to an HCP material, the known crystal structure of Ti_3SiC_2 is, but rather an FCC material. Figure 1b was taken at a [110] FCC zone axis. Figure 2 shows the same diffraction pattern indexed with proper orientations, as well as the diffraction pattern taken from the same grain after orientation to the FCC [112] zone axis. Given the crystal type, the grains which had been presumed to be Ti_3SiC_2 were clearly not, instead they were likely FCC TiC.

EDS performed on the grains had initially been inconclusive, in part possibly due to inaccuracies in the estimated carbon concentration due to carbon being at the tail end of the EDS detector's range of detectability. EDS performed on unirradiated Ti_3SiC_2 had thus shown slightly higher than expected Ti and Si concentrations. Ti concentrations were measured at 60 at% versus 50 at% expected and Si was measured at 25 at% versus 17 at% expected, while C measured at just 16 at% versus 33% expected. Initial EDS measurements on the irradiated, presumed Ti_3SiC_2 grains had instead shown even higher than expected Ti concentrations, high C concentrations, and low Si concentrations. Reanalysis using a tighter beam area with a strict distinction between data points gathered in the bulk of the crystal versus in the planar defect areas resulted in the measurements shown in Table 2. Points noted in Table 2 refer to distinct spots shown in the HAADF image in Figure 3. EDS results showed the bulk of the grain to contain less than 5 at% Si, while the planar defects regions contained no carbon at all, instead appearing to be fully Ti and Si in a concentration that would indicate perhaps Ti_3Si_2.

Overall, this is a very interesting result because pre-irradiation characterization of the joint indicated combined concentrations of Ti_3SiC_2 and Ti_5Si_3 of greater than 99% in the joint. To find TiC with a form of titanium silicide inclusions indicates phase decomposition of the MAX phase during neutron irradiation. Further investigation is currently underway to confirm the TEM results via other experimental methods and to determine the reason for the transformation.

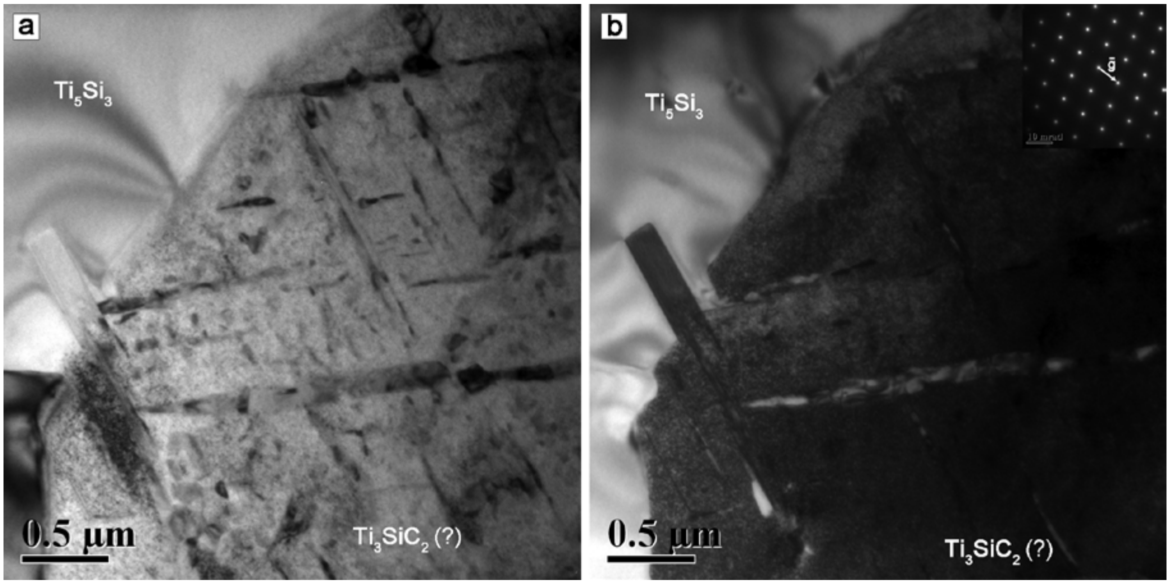

Figure 1. BF TEM images from the 'Ti_3SiC_2/Ti_5Si_3' sample irradiated to 3.4 dpa at 500°C. a) Both types of grains at an aribitrary diffraction condition. b) The same area tilted on zone with diffraction pattern inset.

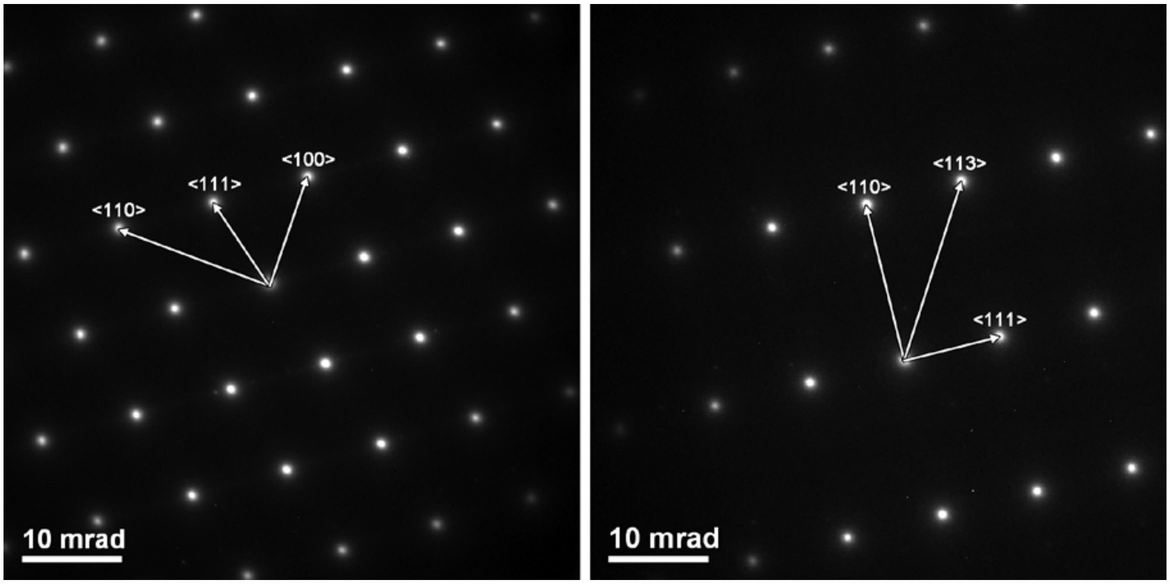

Figure 2. Diffraction patterns from the TiC grain – previously thought to be Ti_3SiC_2. At left, the FCC [110] zone axis. At right, the FCC [112] zone axis.

Table 2. Concentrations of elements measured by EDS in STEM mode from selected spots in Figure 3.

		Weight %:	Atomic %:			Weight %:	Atomic %:
1	Ti	92.1	76.3	3	Ti	69.6	57.4
	Si	1.3	1.8		Si	30.4	42.6
	C	6.6	21.9		C	-	-
2	Ti	89	71.2	4	Ti	69.8	57.5
	Si	3.4	4.6		Si	30.2	42.5
	C	7.6	24.2		C	-	-

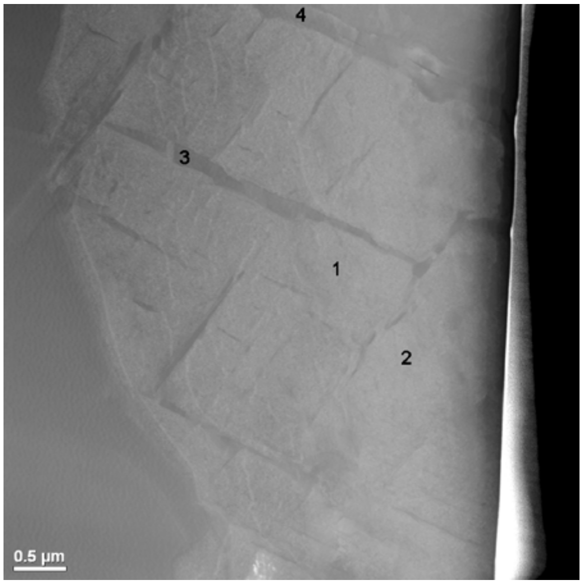

Figure 3. High angle annular dark field (HAADF) of the TiC grain showing spots chosen for EDS analysis, shown in Table 2.

The behavior of the Ti_3SiC_2 irradiated to 3.4 dpa at 500°C is more interesting when viewed in contrast to the sample irradiated to 5.0 dpa at 800°C. In this latter sample, EDS confirmed the presence of Ti_3SiC_2, with MAX phase grains containing concentrations of Ti, Si, and C all within a couple % points of the readings measured from the unirradiated MAX phase material. Due to the smaller size of the grains in this sample, individual diffraction patterns could not be taken and indexed, but grains were not so small as to produce quality ring patterns. Therefore, we have thus far not been able to confirm the phase of the grains via diffraction.

Overall, the 5.0 dpa sample was fairly unremarkable throughout. Microcracking was less significant in this sample than in the one irradiated to 3.4 dpa at 500°C with no cracks observed to propagate throughout the entire TEM sample. Numerous dispersed and disconnected cracks ranging from ~70 nm to several microns in length were noticed with a maximum observed transverse crack width of ~40 nm. Similar to the Ti_3SiC_2/Ti_5Si_3 sample, cracking was primarily transgranular, though a limited sample set of cracks made quantification of the precise amount difficult. While some radiation-induced defects were spotted both in the Ti_3SiC_2 and SiC portions of the sample, the density of the defects was fairly low, with black spot damage and stacking faults the primary defects spotted (Figure 4). The overall density of defects was much lower that seen in the TiC grain in the other sample.

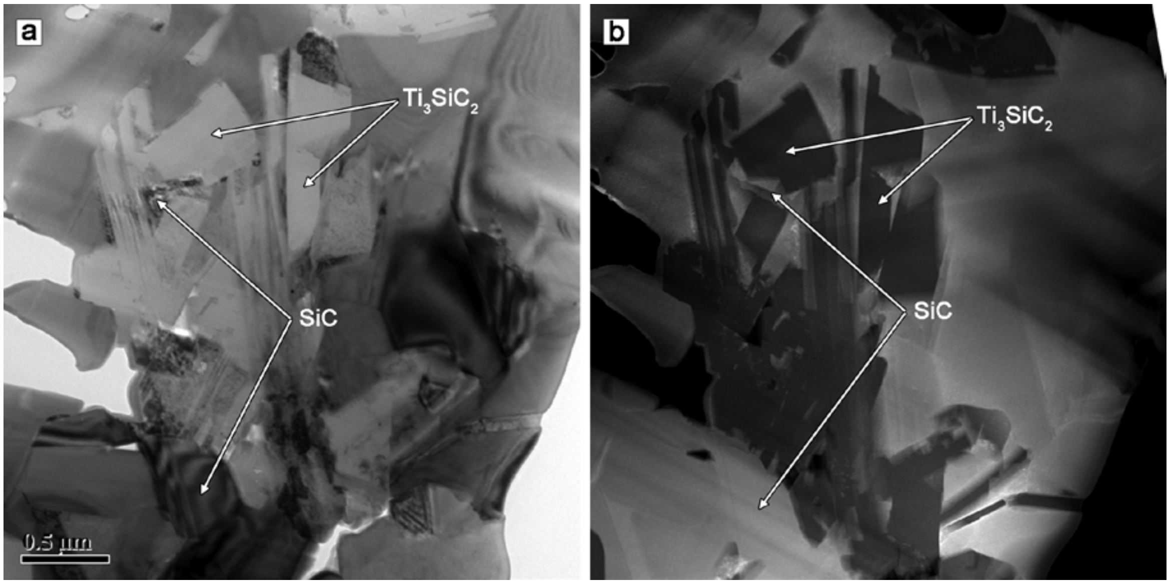

Figure 4. TEM images of the samples irradiated to 5.0 dpa at 800°C. a) BF and b) HAADF images. There was limited visible irradiation damage in the Ti_3SiC_2 grains, though some black spot damage and stacking faults were observed.

CONCLUSIONS

Microstructural evaluations showed a phase change in the Ti_3SiC_2/Ti_5Si_3 sample to TiC/Ti_5Si_3. This is an interesting development that merits further research and thought, especially given that Ti_3SiC_2 in the Ti_3SiC_2/SiC sample retained its phase following irradiation. Further work may be needed to determine the role of temperature in the irradiation-induced phase instability of Ti_3SiC_2.

REFERENCES

[1] W. Jeitschk and H. Nowotny, Monatsh. Chem. **98** (1967) 329-337.
[2] M.W. Barsoum and T. El-Raghy, J. Am. Ceram. Soc. **79** (1996) 1953-1956.
[3] M.W. Barsoum, Prog. Soild State. Chem. **28** (2000) 201-281.
[4] N. Tzenov and M.W. Barsoum, J. Am. Ceram. Soc. **83** (2000) 825-832.
[5] M.W. Barsoum and T. El-Raghy, American Scientist **89** (2001) 334-343.
[6] P. Eklund, M. Beckers, U. Jansson, H. Hogberg, and L. Hultman, Thin Solid Films **518** (2010) 1851-1878.
[7] M. Ferraris, M. Salvo, V. Casalegno, A. Ventrella, and M. Avalle, Int. J. Ceram. Appl. Technol. **9** (2012) 795-807.

7.3 EFFECTS OF HELIUM-DPA INTERACTIONS ON CAVITY EVOLUTION IN TEMPERED MARTENSITIC STEELS UNDER DUAL ION-BEAM IRRADIATION

- Takuya Yamamoto, Yuan Wu, G. Robert Odette (University of California Santa Barbara), Sosuke Kondo, Akihiko Kimura (Kyoto University)

OBJECTIVE

The objective of this research is to characterize how cavity and other microstructural evolution in irradiated candidate ferritic and martensitic structural alloys are influenced by the starting microstructure and irradiation variables, including displacements per atom (dpa), dpa rate and the helium/dpa (He/dpa) ratio.

SUMMARY

Cavity evolution in normalized and tempered martensitic steel (TMS) F82H under Fe^{3+} and He^{+} dual ion beam irradiation (DII) at 500°C was characterized over a wide range of dpa, He and He/dpa. Transmission electron microscopy (TEM) showed that DII up to ≈ 60 dpa and ≈ 2400 appm He produced a significant population of non-uniformly distributed cavities with bimodal sizes, ranging from ≈ 1 nm He bubbles to ≈ 20 nm faceted voids, resulting in observed swelling of up more than 3%. The incubation dpa for the onset of void swelling decreased linearly with increasing He/dpa in both IEA and mod.3 heats of F82H.

BACKGROUND

Predicting and mitigating the effects of a combination of large levels of transmutant He and displacement damage (dpa), produced by high energy neutrons, on the dimensional stability and mechanical properties of structural materials is one of the key grand challenges in the development of fusion energy [1]. The fundamental overriding questions about He and dpa effects and their synergisms include: a) what are the basic interacting mechanisms controlling He and displacement defect transport, fate and consequences; b) how are the resulting cavity and other evolutions influenced by the starting microstructure and irradiation variables, including, displacements per atom (dpa), dpa rate, He/dpa ratio and irradiation temperature; and, c) how can the detrimental effects of He-dpa synergisms be mitigated and managed by proper microstructural designs?

We have previously demonstrated that in situ He implantation (ISHI) in mixed spectrum fission reactor irradiations provides a very attractive approach to assessing the effects of He-dpa synergisms, while avoiding most of the confounding effects associated with Ni- or B-alloy doping type experiments [1-8]. Another approach is to use dual ion beam irradiations (DII) to simultaneously implant He and produce displacement damage [1,9-12]. Note, the two techniques are complementary, but manifest many differences that, in the case of DII, include: a) much higher dpa rates; b) non-uniform spatial distributions of dpa and He; and, c) the proximity of a free surface. Notably, the spatial variations of He and dpa in DII permits assessing the effects of a wide range of He and dpa conditions as they vary with ion penetration depth. Over the last five years we have carried out 8 DII studies at 500°C in DuET facility in Kyoto University at various nominal He/dpa and dpa rates (defined at the depth of 600 nm) in F82H Mod.3 and at subset of conditions in F82H IEA with and without cold work. In this report we focus on the growing database on DII cavity evolution (and swelling) trends in F82H Mod.3 encompassing a very wide range of dpa, He and He/dpa. Note that since very similar trends were observed in the as-tempered F82H IEA heat, they are not summarized in this brief report.

Experimental Procedure

The alloys studied were two variants of tempered martensitic steel (TMS) F82H, namely F82H IEA and F82H Mod.3. The F82H alloy series includes several variants of a base 8Cr TMS, widely studied in a variety of irradiation experiments, including those characterizing He effects [1,3,7,11-19]. The F82H Mod.3 variant adjusted the base composition of a large program heat F82H-IEA, by reducing the N and Ti, while increasing Ta (nominal in wt.%, 7.5Cr, 2W, 0.2V, 0.1C, 0.1S,i 0.02, 0.001Ti, 0.1Ta, 14ppm N, bal.

Fe) [13]. The heat treatment schedule was: austenitizing at 1040 °C for 30 min, followed by normalizing (air cooling), with a final tempering treatment at 740°C for 1.5 h. The F82H microstructure consists of packets of fine ≈ 1 μm laths contained in prior-austenite grain sizes of ASTM 9.5 for F82H Mod.3 and size 3 for F82H IEA. F82H also contains a variety of carbide precipitates with a wide range of sizes [14]. The 9Cr class TMS alloys have good unirradiated strength (yield stress ≈ 500 MPa) [13] and toughness (100 MPa√m temperature of T_o ≈ -100°C [19]) properties, and can be fabricated and joined to serve in first wall and blanket structures [13]. Along with other TMS alloys, like Eurofer97, F82H is a reference structural steel for fusion applications. Notably TMS alloys are resistant to swelling at low He levels, but experience: a) irradiation hardening and embrittlement, below about 400 °C; b) irradiation creep over a wide range of temperatures; and, c) high temperature thermal creep and corrosion. A key objective is to establish the T-dpa-He window for TMS. This window may be severely restricted at high fusion relevant He levels.

DII were carried out on 0.2 mm thick 3 mm diameter disks or 0.5 mm thick ≈ 1x20 mm rectangular coupons mechanically- and electro-polished prior to irradiation. The DII were performed in DuET facility located at the Institute of Advanced Energy, Kyoto University in Japan. Here, Fe^{3+} and He^{+} ions are accelerated to 6.4MeV and 1MeV, respectively [20]. Table 1 summarizes nominal He and dpa conditions, at the reference 600 nm depth, that is encompassed by the current database. The irradiations targeted two nominal doses, three He/dpa and two dpa rate conditions. Taking advantages of the varying spatial distributions of dpa and He, we characterized the microstructures over a very wide range of He-dpa, as shown in Figure 1a; Figure 1b shows the corresponding dpa-dpa rates, including the low ISHI conditions in HFIR. The dpa are based on SRIM using the Kinchin-Pease displacement energy of 40 eV [21,22].

TEM on FIBed lift outs was performed on the FEI T20 and Titan instruments in the UCSB Microstructure and Microanalysis Facility. Through focus bright field imaging was used to characterize the cavities. We avoided regions that suffer the effects of surface proximity and injected self-interstitials, respectively..

Table 1. Irradiation conditions analyzed in this report.

Exp ID	TMS Alloys	T (^{o}C)	Nominal Condition (@550-650nm)				Peak He (@1000-1100nm)		
			dpa	He (appm)	He/dpa	dpa/s	dpa	He (appm)	He/dpa
DI10B1	F82H mod.3	500	26	1210	47	5.0×10^{-4}	45	2100	47
DI10B2			9.9	457	46	5.2×10^{-4}	17	795	46
DI10B3			10	480	47	5.1×10^{-4}	18	840	47
DI13A1	F82H mod.3	500	26	390	15	5.1×10^{-4}	44	670	15
DI13B1	F82H mod.3, F82H IEA	500	30	848	29	1.5×10^{-3}	51	1467	29
DI14A1	F82H mod.3, F82H IEA	500	30	1200	45	1.3×10^{-3}	52	2400	45

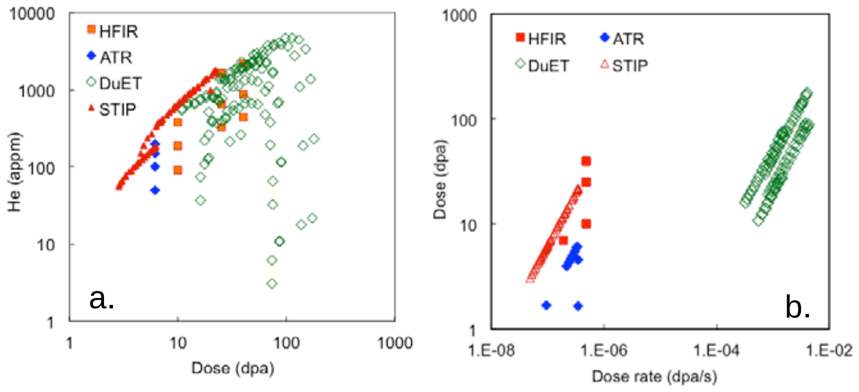

Figure 1. a) A map UCSB irradiation experiments using various techniques, including DII DuET at discrete depth sections: a) a He-dpa map; and, b) a dpa-dpa rate map.

RESULTS

Figure 2a shows a typical cavity microstructure profile from the surface at the left to the depth of ≈ 2 μm at the right. Figure 2b shows the dpa and implanted He as a function of depth over the range shown in Figure 2a. Thin foil energy degraders produced four He ion energy bands with a combined broad concentration peak around ≈ 1.2 μm, shown as the black dashed line. The dpa peaks at ≈ 1.5 μm and reaches a depth of ≈ 2 μm as shown by the red solid line. These two profiles result in an approximately constant He/dpa ratio from ≈ 0.4 to ≈ 1.1 μm, at ≈ 47 appm/dpa in this example, as shown by the green dotted line. The dpe-He profile generally results in cavity number density and sizes that increase with depth up to ≈ 1.2 μm. Figure 2c and 2d compare the cavity microstructures at 0.6 to 0.7 μm. at an average 25 dpa, 1150 appm He and 46 appm/dpa, to those at a depth of 1.1 to 1.2 μm, at 52 dpa, 2060 appm He and 39 appm/dpa. Clearly, larger cavities are found at higher damage levels at the deeper location. This is quantified by the corresponding cavity size distributions shown in Figure 2e. Figures 3a and b show cavity microstructures at a similar dpa ≈ 45 but for a He/dpa ratio of ≈ 15 (Figure 3a) and 47 (Figure 3b), respectively. Figure 3c shows the corresponding cavity size distributions. At lower He/dpa there is a bimodal cavity distribution with peaks at d ≈ 2-2.5 nm and d ≈ 5.5 nm. At the higher He/dpa almost all the bubbles have converted to growing voids peaked at ≈ 5.5 nm. These results are fully consistent with critical bubble models of cavity evolution and void swelling [1]

Swelling Trends

We have quantitatively characterized the cavity evolution trend as a function of dpa, He and He/dpa in terms of their average size, <d>, number density, N, and volume fractions f, previously [23]. Notably <d> and N vary significantly for similar irradiation conditions. This is largely due to the effects of the local microstructure. However, the corresponding variations in f are less. This reflects the fact that variations in the corresponding void $<d_v>$ and N_v are also less, and that the total $f \approx f_v$. Here we assume separation of voids from bubbles at a (≈ critical) size of 4 nm, corresponding to the dip between the two peaks in the cavity size distributions at various conditions.

To date we have collected data on 72 dpa-He-dpa rate DII conditions for F82H Mod.3 and 32 conditions for F82H IEA. Figure 4a shows void volume fraction, f_v, as a function of dpa and He/ dpa ratio in F82H Mod.3. The data show a clear shift of swelling and incubation dpa to lower values with increasing He/dpa. As shown in Figure 4b, a combined damage-dose parameter, dpa* = dpa/[1 + 0.0225 (50 – He/dpa)] collapses the f_v trend at various He/dpa. Figure 4c also shows that the dpa* scaling also collapses the ISHI F82H Mod.3 and Eurofer 97 f_v data at various He/dpa [24]. The ISHI f_v is shifted to lower dpa* compared to the DII cruve indicating a possible dose rate effect. However, more research, especially at higher ISHI dpa and He, is needed to confirm this trend.

Figure 5a shows the corresponding f_v versus dpa plots at various He/dpa in F82H IEA after DII. The data suggest high post incubation swelling rates and swelling levels. The lines are eyeball fits for post-incubation swelling for each of the defined He/dpa groups. Figure 5b shows the dpa at both f_v = 0 (incubation dpa_i) and 1.5%, respectively, decreases linearly with the He/dpa. The swelling rates (slope of the lines) are ≈ 0.11±0.03%/dpa, excluding 5 appmHe/dpa case. This rate is about half of that proposed by Garner for ferritic-tempered martensitic alloys [25]. Figure 4c plots f_v vs. dpa – dpa_i(He/dpa = 30). The f_v do not collapse fully but rather show a trend to higher swelling at lower He/dpa, suggesting that there are secondary effects of He/dpa on the post-incubation swelling behavior. Notably, the swelling levels reach ≈ 3.5%. Even at a nominal He/dpa ≈ 10 appm He/dpa the swelling would reach ≈ 14% at 200 dpa. On the other hand the corresponding swelling is predicted to be minimal at less than 70 dpa. However, dpa rate and other CPI versus DII effects have not been considered in these estimates.

We must close this section with a caveat. The data shown in Figure 5 include different DII runs and intrinsically different regions of the alloy microstructure samples. Thus to the extent that there are small difference in the irradiation conditions and variations background microstructures, these results must be viewed with caution and subject to further verification.

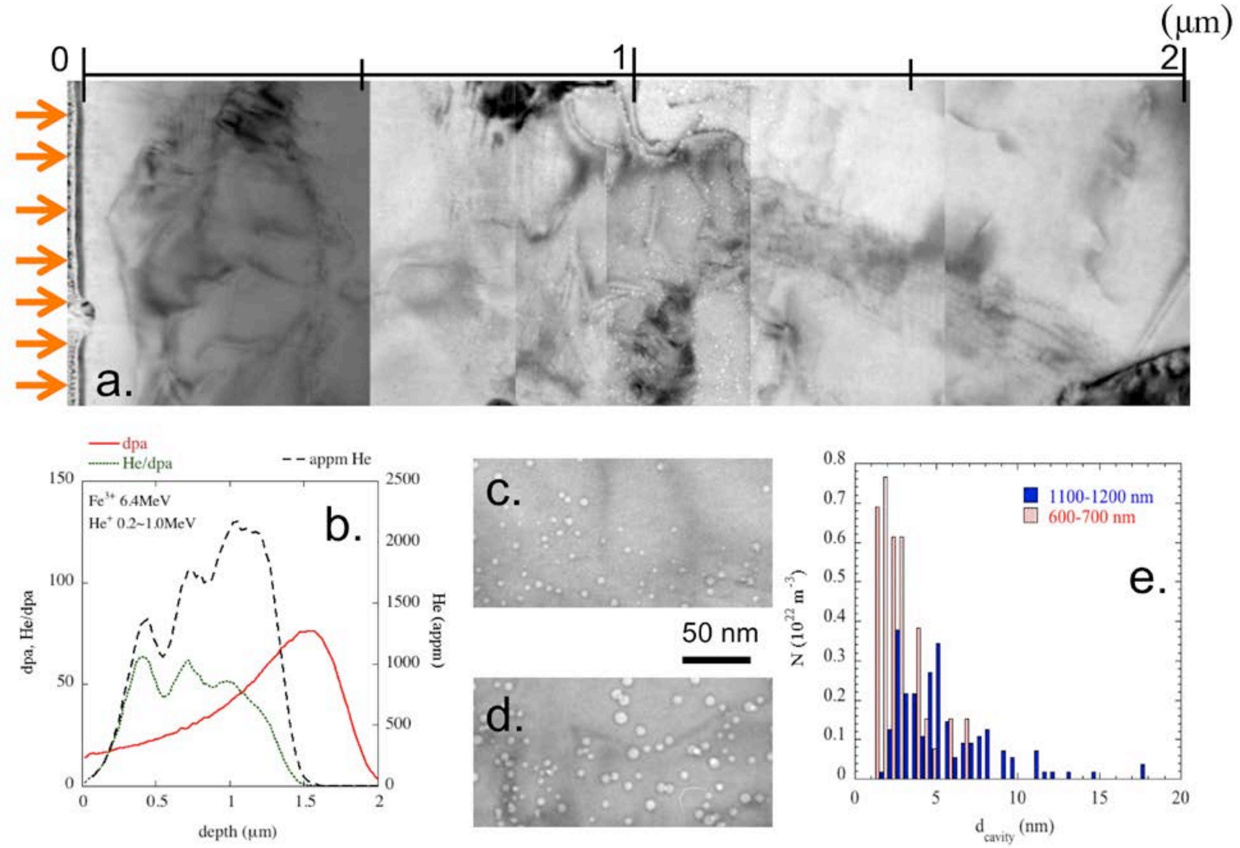

Figure 2. a) The microstructure profile in the DII of F82H Mod.3; b) the dpa (red solid line), He (black dashed line) and He/dpa ratio as functions of depth; c) and d) the cavity microstructures in 0.6 to 0.7 µm and in 1.1 to 1.2 µm sections, respectively; e) the corresponding cavity size distributions.

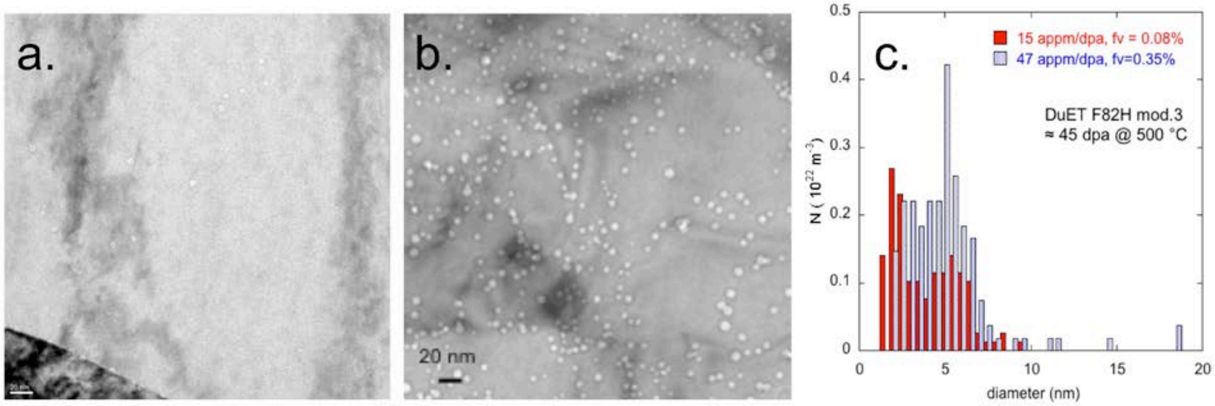

Figure 3. Cavity microstructures in F82H mod. Irradiated at 500°C to ≈ 45 dpa with He/dpa ratios of: a) ≈ 15 and b) ≈ 47 appm He/dpa, respectively; and, c) the corresponding cavity size distributions.

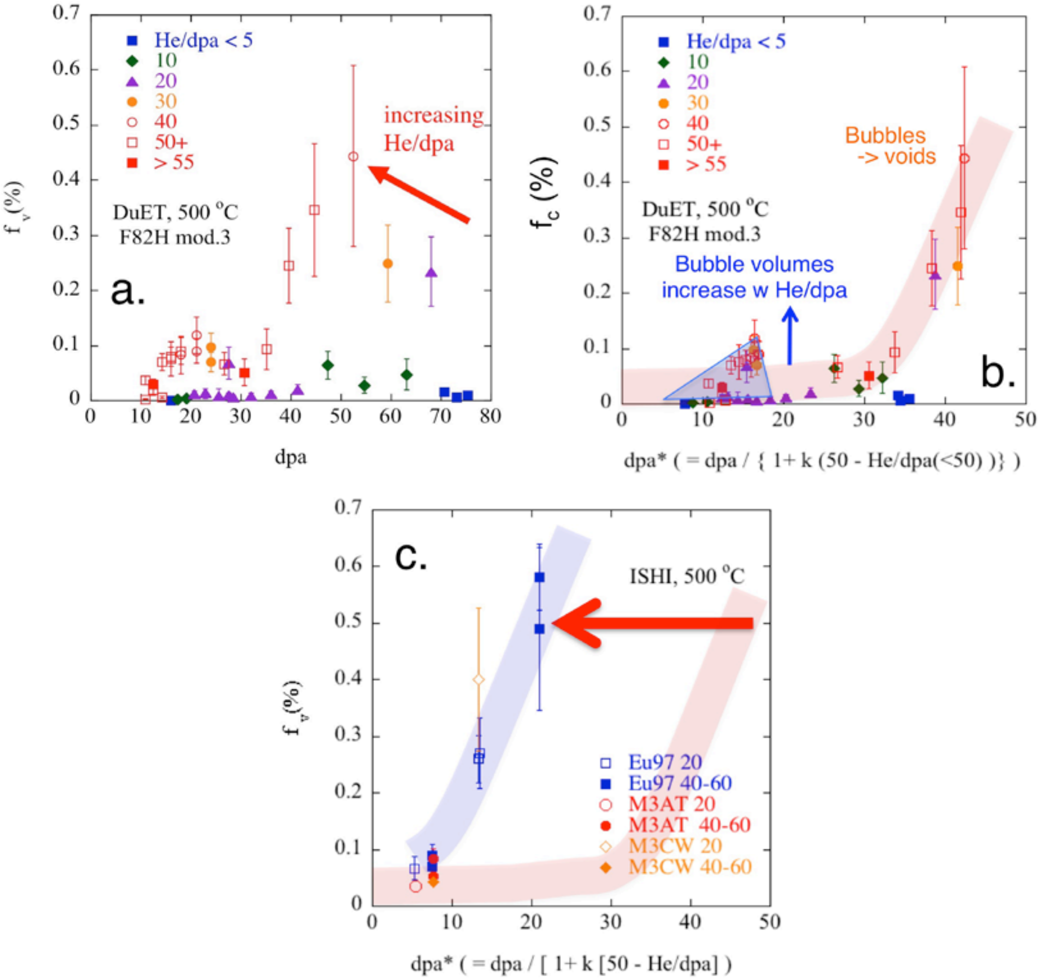

Figure 4. a) The void volume fraction (f_v) versus dpa at various He/dpa ratios in DII F82H Mod. 3; b) the f_v trend on a dpa* scale that collapses He/dpa effects; and, c) f_v versus dpa* in ISHI and DII DuET irradiations.

SUMMARY

Cavity evolutions in normalized and tempered martensitic steel (TMS) F82H under Fe^{3+} and He^{+} dual ion beam irradiations (DII) at 500°C were characterized over a wide range of dpa, He and He/dpa. Transmission electron microscopy (TEM) showed that DII of F82H at 500°C to up to ≈ 60 dpa and ≈ 2400 appm He, produced a moderate number density of non-uniformly distributed cavities with bimodal sizes ranging from ≈ 1 nm He bubbles to ≈ 20 nm faceted voids, and swelling up to ≈ 3.5%. Higher He/dpa systematically accelerates the onset of void swelling and may have a second order effect on rapid post-incubation swelling. Differences between DII and ISHI, including the effects of dpa rate, are critical unresolved issues.

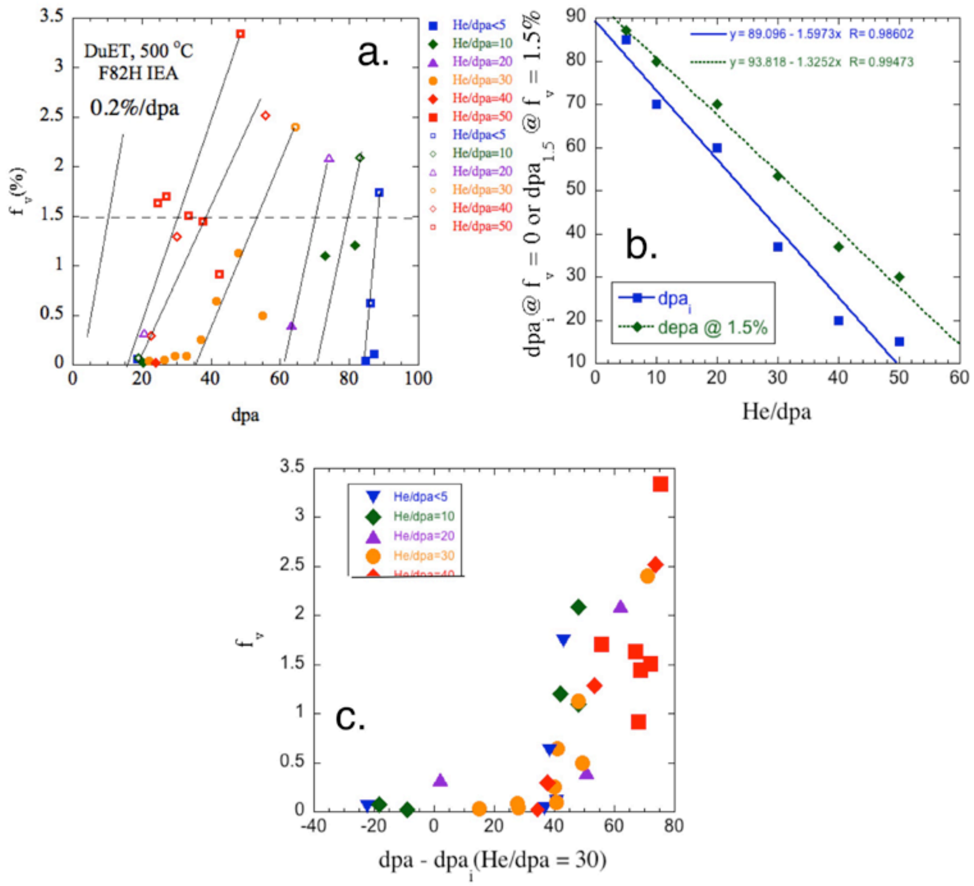

Figure 5. a) Swelling (f_v) as a function of dpa for various He/dpa ratios; b) the dpa at the onset of swelling and f_v = 1.5%; and, c) f_v on a dpa - dpa_i(He/dpa) scale.

ACKNOWLEDGEMENTS

The dual ion-beam irradiations were conducted under the support of the "Joint Research Program on Zero-Emission Energy Research, Institute of Advanced Energy, Kyoto University (ZE26A-16, 25A-19, 24A-13 and 23B-3). The work performed at UCSB was supported by the U. S. Department of Energy, Office of Fusion Energy Sciences, under contract DE-FG03-94ER54275. We acknowledge the contributions of the NSF sponsored UCSB Microstructure and Microanalysis Facility. We are also grateful for generous support of research materials, F82H mod.3 from Dr. K. Shiba, (JAEA, Japan).

REFERENCES

[1] Y. Dai, G.R. Odette, T. Yamamoto, The Effects of helium on irradiated structural alloys, in Comprehensive Nuclear Materials, R. Konings, T. R. Allen, R. E. Stoller, S. Yamanaka Eds. Elsevier (2012).Chap 5

[2] T. Yamamoto, G.R. Odette, L.R. Greenwood, Fusion Materials Semiannual Report 1/1 to 6/30/2005 DOE/ER-313/38 (2005) 95.

[3] T. Yamamoto, G.R. Odette, P. Miao, D.T. Hoelzer, J. Bentley, N. Hashimoto, H. Tanigawa, R. J. Kurtz, J. Nucl. Mater., 367-370 (2007) 399.

[4] R.J. Kurtz, G.R. Odette, T. Yamamoto, D.S. Gelles, P. Miao, B.M. Oliver, J. Nucl. Mater. 367-370 (2007) 417.

[5] G.R. Odette, M.J. Alinger, and B.D.Wirth, Annu. Rev. Mater. Res. 38 (2008) 471.
[6] T. Yamamoto, G.R. Odette, P. Miao et al., J. Nucl. Mater., 386-388 (2009) 338.
[7] D.J. Edwards, R.J. Kurtz, G.R. Odette et al., Fusion Materials Semiannual Report 12/31/2009 DOE/ER-313/47 (2010) 59.
[8] G.R. Odette, P. Miao, D.J. Edwards et al., J. Nucl. Mater., 417 (2011) 1001.
[9] E.H. Lee, J.D. Hunn, T.S. Byun and L.K. Mansur, J. Nucl. Mater. 280 (2000) 18.
[10] H. Kishimoto, K. Yutani, R. Kasada and A. Kimura, Fusion Eng. Des. 81 (2006) 1045.
[11] R. Kasada, H. Takahashi, H. Kishimoto et al., Materials Science Forum 654-656 (2010) 2791.
[12] T. Yamamoto, Y. Wu, G.R. Odette et al., Fusion Materials Semiannual Report 12/31/2010 DOE/ER-313/49 (2011) 1.
[13] K. Shiba, M. Enoeda, S. Jitsukawa, J. Nucl. Mater., 329-333 (2004) 243.
[14] R. Schaublin, P. Spatig, M. Victoria, J. Nucl. Mater., 258-263 (1998) 1178.
[15] A. Kimura, R. Kasada, K. Morishita et al.,,, J. Nucl. Mater., 307-311 (2002) 521.
[16] G.R. Odette, T. Yamamoto, H.J. Rathbun et. al., J. Nucl. Mater., 323 (2003) 313.
[17] T. Yamamoto, G.R. Odette, H. Kishimoto et al., J. Nucl. Mater., 356 (2006) 27.
[18] Z. Tong, Y. Dai, J. Nucl. Mater. 385 (2009) 258.
[19] G.R. Odette, T. Yamamoto, H. Kishimoto et al., J. Nucl. Mater., 329-333 (2004) 1241
[20] A. Kohyama, Y. Katoh, M. Ando and K. Jimbo, Fusion Eng. Des. 51-52 (2000) 789.
[21] ASTM E521-96 (2009), ASTM
[22] R.E. Stoller, M.B. Toloczko, G.S. Was et al., Nuc. Instr. Methods in Phys. Res B 310 (2013) 75.
[23] T. Yamamoto, Y.Wu, G.R. Odette et al, J. Nucl. Mater. 445 1-3 (2004) 190.
[24] G.R. Odette, T. Yamamoto, Y. Wu et al., Fusion Materials Semiannual Report 12/31/2011 DOE/ER-313/51 (2012) 90.
[25] F.A. Garner, M.B. Toloczko, B.H. Sencer, J. Nucl. Mater., 276 (2000) 123.

7.4 EFFECTS OF HELIUM ATOMS ON THE STRENGTH OF BCC Fe GRAIN BOUNDARIES –

Xiaoxun Zhang, Jiansha Ji, Fang Ma (Shanghai University of Engineering Science), G. R. Odette (University of California Santa Barbara), R. J. Kurtz, F. Gao (Pacific Northwest National Laboratory)

OBJECTIVE

The objective is to study the nucleation and growth of helium clusters at grain boundaries (GBs) and their effects on the cohesive strength of GBs in bcc Fe under uniaxial straining.

SUMMARY

The effects of helium atoms and the formation of helium clusters on Σ3 <110> {111}, Σ3 <110> {112} and Σ5 <100> {310} symmetric tilt GBs in bcc iron were studied by the molecular dynamics simulation method. We found that helium atoms are deeply trapped at the GBs during annealing at 300 K, and that two or more helium atoms aggregate to form a small helium clusters. The helium atom and small clusters act as a failure initiation site under uniaxial straining. We show that helium atoms decreases cohesive strength and ductility of all the grain boundaries in bcc Fe that were studied.

PROGRESS AND STATUS

Introduction

In fusion reactor environments helium decreases fracture toughness, creep rupture strength and promotes swelling [1]. However, the mechanisms and processes of helium effects are still not completely understood. There have been a large number of atomistic modeling studies of He in bulk bcc Fe [1-4]. On the other hand the literature on He atoms at Fe GBs is limited [5-9]. In the present study, the effects of helium atoms at various GBs are simulated under uniaxial straining using a new interatomic potential for Fe-He interactions, which is based on the electronic hybridization between Fe d-electrons and He s-electrons [10]. The migration of helium atoms and the formation of helium clusters on the Σ3 <110> {111}, Σ3 <110> {112} and Σ5 <100> {310} symmetric tilt GBs were investigated using molecular dynamics simulations. We found that two or more helium atoms aggregate to form small helium cluster and that the helium atoms and clusters decrease the cohesive strength and ductility of bcc Fe GBs.

Simulation Methods

The Fe-Fe potential developed by Ackland et al. [11], the He-He potential developed by Aziz et al. [12], and the Fe-He potential developed by Gao et al. [10] were combined and used in the present atomistic calculations. The supercells containing two grains of bcc Fe [13] are shown in Figure 1. The Σ3 <110> {111}, Σ3 <110> {112} and Σ5 <100> {310} symmetric tilt GBs were investigated to determine the cohesive strength of helium-loaded GBs under tensile deformation. The simulation cell sizes of Σ3 <110> {111}, Σ3 <110> {112} and Σ5 <100> {310} GBs were 21 Å × 110 Å × 21 Å, 20 Å × 112 Å × 21 Å and 20 Å × 110 Å × 18 Å, respectively. Periodic boundary conditions were imposed in the x and z directions, and uniaxial straining boundary conditions were applied along the y direction, where the x, y and z represent the [11-2], [111] and [1-10] directions in the Σ3 <110> {111} GB model, [1-11], [-112] and [-1-10] directions in the Σ3 <110> {112} GB model, and [031], [0-13] and [100] directions in the Σ5 <100> {310} GB model.

Different concentrations of helium atoms were inserted randomly around the GB plane (within 5 Fe layers on either side of the GB plane). The percentage of helium atoms was taken as a fraction of the Fe atoms within 5 layers near the GB plane. After the helium atoms were inserted, the system was quenched to 0 K, followed by a temperature rescaling to 300 K for 20 ps. Then, tensile displacement with a strain increment of 0.001 at each time step of one femto-second was applied to the atoms in the top and bottom regions of the model to drive the deformation of the simulation volume containing helium-loaded GBs.

The corresponding tensile stress and strain induced by the applied deformation were calculated as $\sigma = F/A_{xz}$ and $\varepsilon = (H - H_0)/H_0$, respectively, where F is the force acting in the y direction on the end plane, A_{xz} is the xz cross-section area of the model, H is the height of the model and H_0 is the initial height of the model. After each strain increment, energy minimization at 300 K was performed.

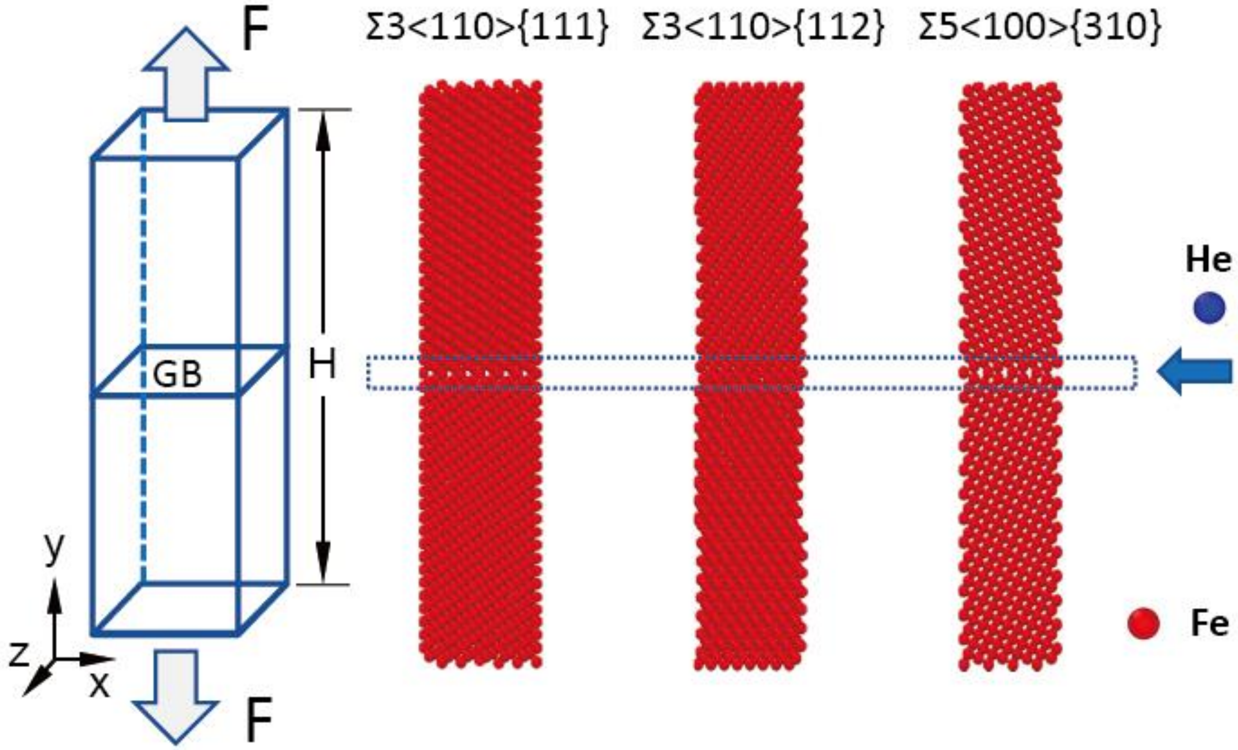

Figure 1. GB model under uniaxial load and different concentrations of helium atoms are inserted randomly around the GB plane (within 5 layers of Fe atoms)

Results

Clusters formation during the annealing

Helium atoms inserted interstitially into the nearby region, quickly move to and are trapped on the GB. Two or more helium atoms the aggregate to form small helium clusters. Figure 2a shows that twenty randomly helium atoms (10% He) migrate to form three helium clusters on the Σ3 <110> {112} GB at 300°K, with sizes of 5, 5, and 10, respectively. Figure 2b shows that twenty-four helium atoms (20% He) form three helium clusters on the Σ5 <100> {310} GB at 300 K, with sizes of 5, 9, and 10, respectively.

Evolution of helium clusters during uniaxial straining at 300°K

The GB helium atoms and small clusters act as a failure initiation sites. Figure 3a shows the failure initiation sites of 10% He loaded Σ3 <110> {111} GB at a strain of 0.0581. Figure 3b shows that that nucleation and propagation of a nano-crack occurred in the 5% He loaded Σ3 <110> {112} GB at a strain of 0.0974.

Figure 4 shows the evolution of helium clusters in a 10% He loaded Σ3 <110> {112} GB during uniaxial straining. Figure 4a shows that there are three isolated helium clusters A, B, and C 0 strain, and Figure 4b that cluster A approaches cluster B at a strain of 0.0357. Figure 4c shows that the three helium clusters connect since there are many nano-cracks produced (as displayed in Figure 3) just before the fracture of the GB (strain < 0.073). Finally, the three helium clusters aggregate to a large cluster just after the fracture of the GB (strain > 0.073).

Figure 5 shows the evolution of helium atoms and clusters in a 20% He loaded Σ5 <100> {310} GB. The number and distribution of the helium clusters in the Σ5 <100> {310} GB remain almost unchanged up to a just before the fracture at a strain of ≈ 0.049.

Effects of helium concentration on GB cohesive strength and ductility in bcc Fe

Figure 6 shows the stress-strain curves obtained for different GBs as a function of helium concentration. For clean GBs, the stresses increase linearly at the elastic regime followed by plastic deformation at constant stress in some GBs at higher strain. Fracture occurs when a second region of elastic strain reaches a critical value on the order of G/4 to G/3. The Σ3 <110> {112} and Σ5 <100> {310} clean GBs show extensive plastic deformation while the Σ3 <110> {111} clean GB does not exhibit an obvious yield point. The stress-strain curves for clean GBs presented here are very similar to those of Terentyev and He [14].

The presence of helium clusters in the GB results in a gradual decrease of the strength and ductility with increasing helium concentration. For example, GB loading of 0.68%, 4.8%, 10, and 20% helium in the Σ3 <110> {111} GB, results in a linear decrease in the fracture stress of 19.17, 15.80, 11.31 and 5.16 GPa, respectively. The corresponding maximum strains are 0.119, 0.096, 0.061, and 0.046, respectively (see Figure 6a). Notably, the curves are insensitive to the helium GB loading up to stresses and strains just before fracture. The fracture stresses and strains as a function of He loading are more clearly shown in Figures 7 and 8. The Σ3 <110> {111} is generally the weakest GB and suffers the largest fractional loss of strength at the highest helium loading, by a factor of 4. The drop in fracture strains in the GB is associated with fracture stresses that are less than needed for plastic yielding.

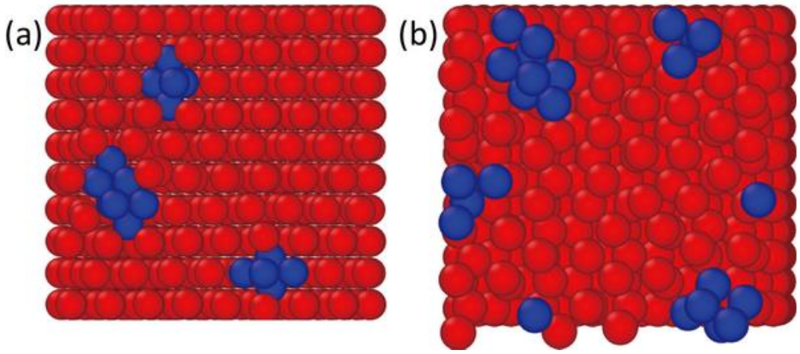

Figure 2. Helium atoms aggregate in small He clusters at 300 K of (a) 10% He loaded Σ3 <110> {112} GB and (b) 20% He loaded Σ5 <100> {310} GB in bcc Fe. (The red is Fe and the blue is He; the He atoms are drawn larger for clarity)

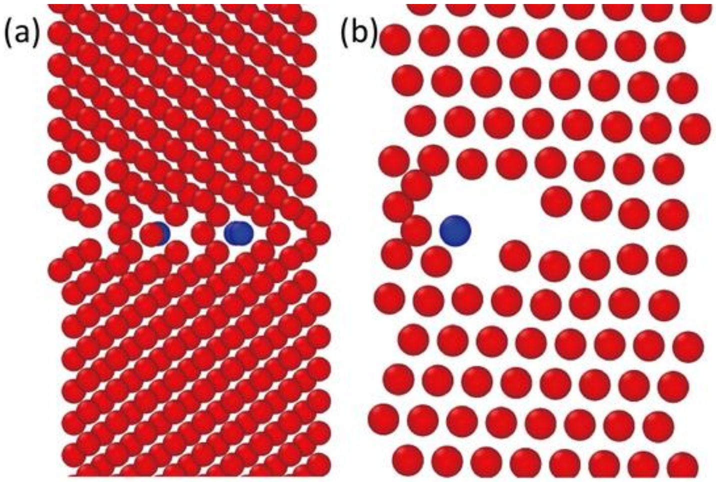

Figure 3. A single helium atom or small helium cluster at the grain boundary becomes a failure initiation site during the tensile loading:(a) 10% He loaded Σ3 <110> {111} GB at the strain of 0.0581 and (b) 5% He loaded Σ3 <110> {112} GB at the strain of 0.0974.

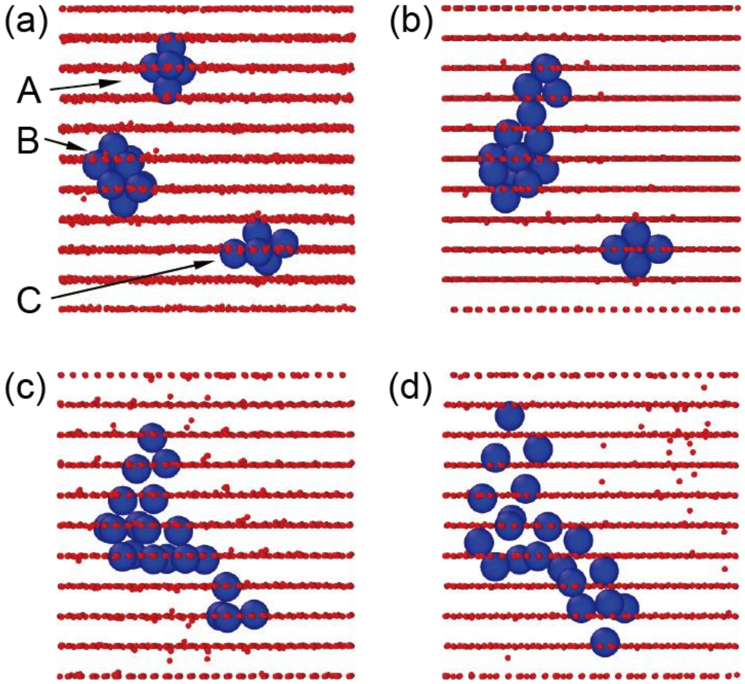

Figure 4. Evolution of helium clusters in a 10% He loaded Σ3 <110> {112} GB in bcc Fe during uniaxial straining to: (a) 0, (b) 0.0357, (c) just before fracture at 0.073), (d) just after fracture.

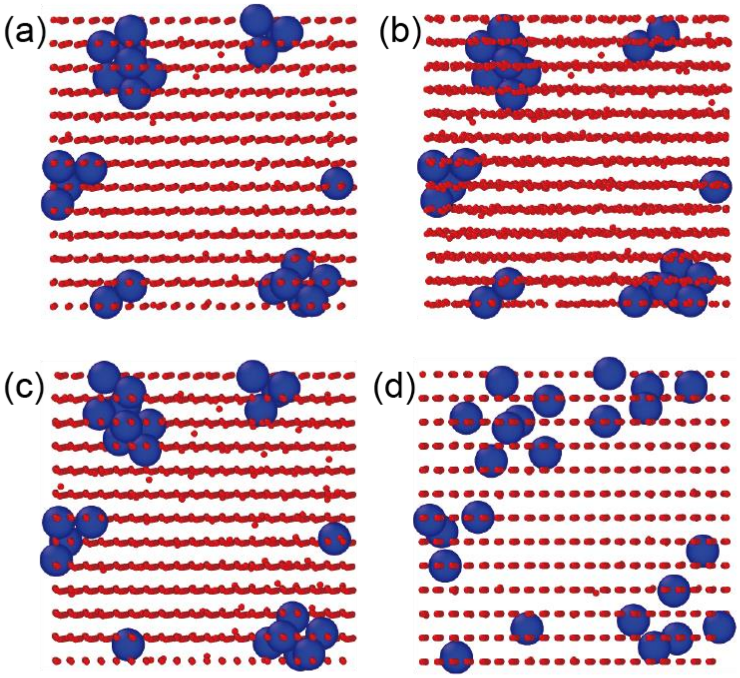

Figure 5. Evolution of helium clusters in a 20% He loaded Σ5 <100> {310} GB in bcc Fe during uniaxial straining to (a) 0, (b) 0.0189, (c) just before fracture at 0.049 and (d) just after fracture.

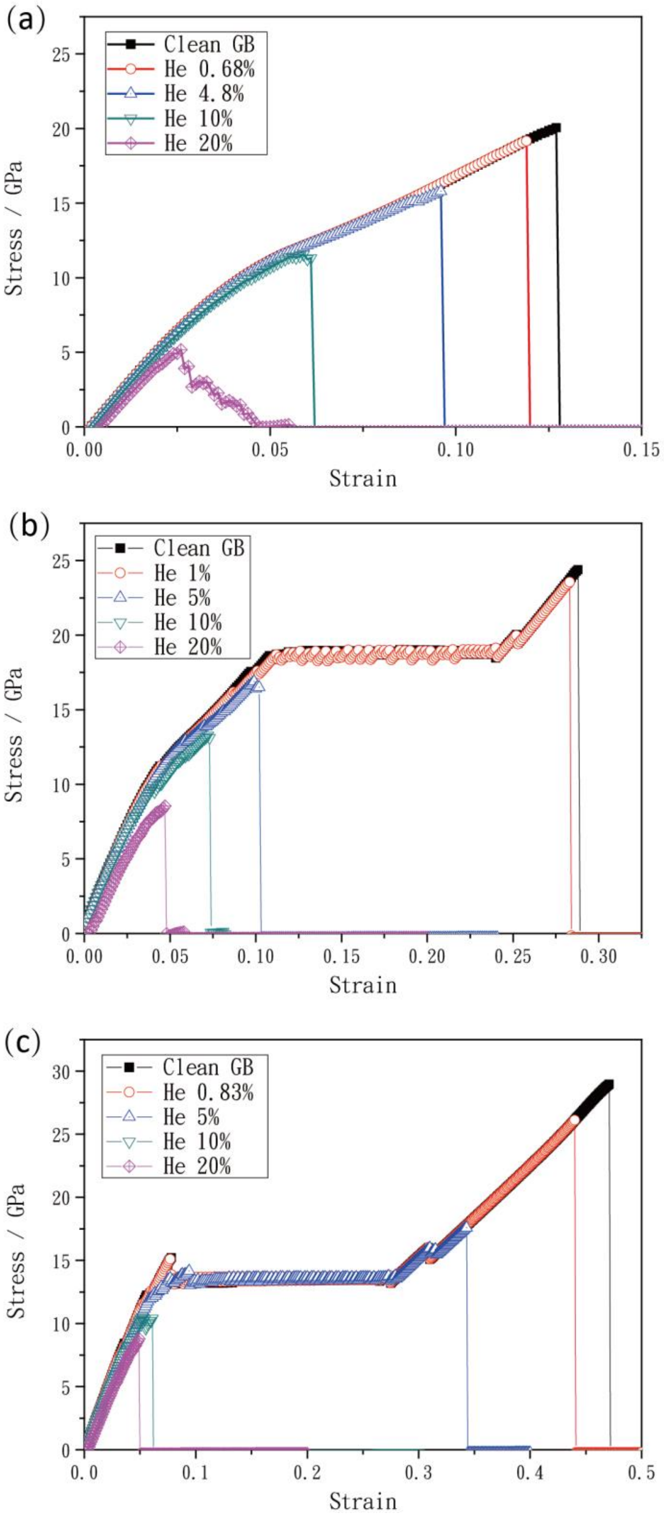

Figure 6. Stress-strain curves for the: (a) Σ3 <110> {111}, (b) Σ3 <110> {112}, and (c) Σ5 <100> {310} GB with different helium loadings.

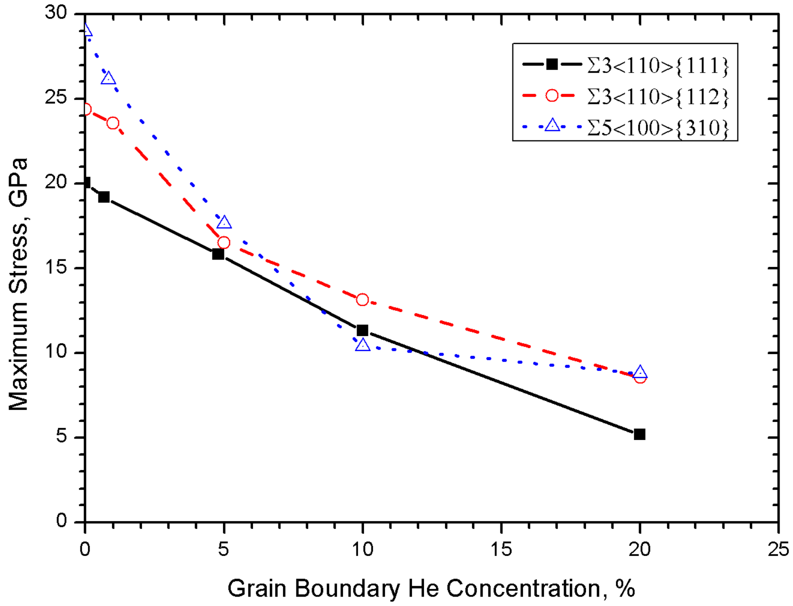

Figure 7. The effect of helium loading on the fracture stress of: Σ3 <110> {111}, Σ3 <110> {112} and Σ5 <100> {310} GB.

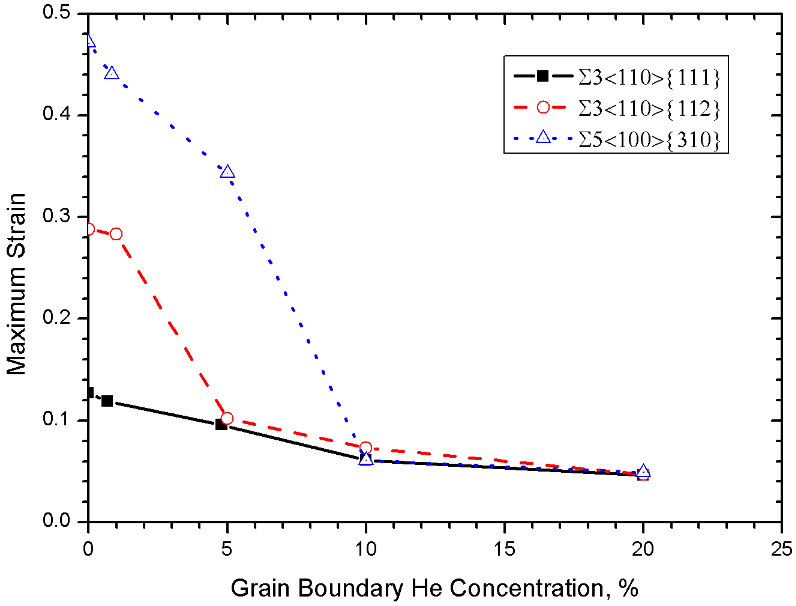

Figure 8. The effect of helium loading on the fracture strain of: Σ3 <110> {111}, Σ3 <110> {112} and Σ5 <100> {310} GB.

Discussion

Increasing loading of three special GB with helium results in large reductions in the fracture stress and strains of up to a maximum of ≈ 4 and 8, respectively. The reduction in strength is not associated with a uniform distribution of helium on the GB leading to a simple reduction of cohesive stress. Rather Helium introduced near GB is quickly trapped and forms clusters on the GB. Both helium atoms and especially small clusters act as sites for the formation and propagation of nano-cracks leading to GB fracture. Even at high helium loading the fracture stresses are very large with a minimum value of ≈ 5 GPa in the Σ3 <110> {111} GB. It is important to note that these results must be viewed as being qualitative and aimed at revealing phenomena rather than precise numbers. The simulations are affected by a variety of approximations compared to reality, including size, strain rate and use of simple many body potentials. Further, it will be important to explore the influence of other variables such as temperature, applied strain rate (including static vs. dynamic), hold periods and so on.

Acknowledgements

The lead author Professor Zhang was supported by SUES Innovation Project under grant 14KY0505 and supported by Science Foundation for the Youth Scholars of Shanghai Municipal Education Commission under Grant ZZGJD12081.

REFERENCES

[1] M. Samaras, Multiscale modelling: the role of helium in iron, Mater Today, 12(11), 46-53 (2009).
[2] S.J. Zinkle, Fusion materials science: Overview of challenges and recent progress, Phys. Plasmas, 12, 058101 (2005).
[3] M.J. Caturla, C.J. Ortiz, C.C. Fu, Helium and point defect accumulation: (ii) kinetic modeling, C. R. Phys., 9,(2008), 401-408.
[4] S.L. Dudarev et al., The EU programme for modelling radiation effects in fusion reactor materials: An overview of recent advances and future goals, J. Nucl. Mater., 386-388, (2009), 1-7.
[5] R.J. Kurtz, H.L. Heinisch, The effects of grain boundary structure on binding of He in Fe, J. Nucl. Mater., 329-333, (2004), 1199-1203.
[6] F. Gao, H.L. Heinisch, R.J. Kurtz, Diffusion of He interstitials in grain boundaries in α-Fe, J. Nucl. Mater., 351,(2006), 133-140.
[7] F. Gao, H.L. Heinisch, R.J. Kurtz, Migration of vacancies, He interstitials and He-vacancy clusters at grain boundaries in α-Fe, J. Nucl. Mater., 386-388, (2009), 390-394.
[8] Y. Zhang et al., First-principles study of helium effect in a ferromagnetic iron grain boundary: Energetics, site preference and segregation, Nucl. Instrum. Methods Phys. Res. B, 267, (2009), 3200-3203.
[9] T. Suzudo, H. Kaburaki, M. Yamaguchi, Modeling of the grain boundary segregation of helium in α-Fe, J. Nucl. Mater., 417, (2011), 1102-1105.
[10] F. Gao, Huiqiu Deng, H.L. Heinisch, R.J. Kurtz, A new Fe-He interatomic potential based on ab initio calculations in α-Fe, J. Nucl. Mater., 418, (2011) 115-120.
[11] G.J. Ackland, M.I. Mendelev, D.J. Srolovitz, S. Han, A.V. Barashev, Development of an interatomic potential for phosphorus impurities in α-iron, J. Phys.: Condens. Mater., 16, S2629 (2004).
[12] R.A. Aziz, A.R. Janzen, M.R. Moldover, Ab Initio Calculations for Helium: A Standard for Transport Property Measurements, Phys. Rev. Lett., 74, (1995), 1586.
[13] D. Terentyev, X. He, A. Serra, J. Kuriplach, Structure and strength of <110> tilt grain boundaries in bcc Fe: An atomistic study, Computational Materials Science, 49, (2010), 419-429.
[14] D. Terentyev,X. He, Effect of Cr precipitates and He bubbles on the strength of <110> tilt grain boundaries in BCC Fe: An atomistic study, Computational Materials Science, 50, (2011), 925-933.

8.1 INFLUENCE OF MASS ON DISPLACEMENT THRESHOLD

—W. Setyawan, A. P. Selby, G. Nandipati, K. J. Roche, R.J. Kurtz (Pacific Northwest National Laboratory, Richland, WA 99352) and B. D. Wirth (University of Tennessee, Knoxville, TN 37996)

OBJECTIVE

The objective of this research is to investigate how displacement threshold energy changes with atomic mass for the same interatomic potential.

SUMMARY

Molecular dynamics simulations are performed to investigate the effect of mass on displacement threshold energy in Cr, Mo, Fe and W. For each interatomic potential, the mass of the atoms is varied among those metals for a total of 16 combinations. The average threshold energy over all crystal directions is calculated within the irreducible crystal directions using appropriate weighting factors. The weighting factors account for the different number of equivalent directions among the grid points and the different solid angle coverage of each grid point. The grid points are constructed with a Miller index increment of 1/24 for a total of 325 points. For each direction, 10 simulations each with a different primary-knock-on atom are performed. The results show that for each interatomic potential, the average threshold energy is insensitive to the mass; i.e., the values are the same within the standard error. In the future, the effect of mass on high-energy cascades for a given interatomic potential will be investigated.

PROGRESS AND STATUS

Introduction

We have started to explore displacement cascade morphologies and their implications on defect creation and defect clustering by simulating cascades in W as a function of the kinetic energy of the primary knock-on atom (PKA). In our previous report [1], it was found that the dependence of the number of surviving Frenkel pairs (N_{FP}) on the PKA energy (E), exhibits three different characteristic domains presumably related to the different cascade morphologies that form. In the sub-threshold regime with $E <$ 0.2 keV (region 1), the cascade is characterized by a hit-or-miss type of Frenkel pair (FP) production near the displacement threshold energy (E_{d}). For E in the range of 0.3 – 30 keV (region 2), the defect production curve exhibits a sublinear dependence, $N_{\mathrm{FP}} \sim E^{0.74}$, associated with a compact cascade morphology. For $E >$ 30 keV (region 3), the cascade morphology consists of complex branches or interconnected damage regions. In this interconnected morphology, large interstitial clusters form from superposition of interstitials from nearby damage regions. In this regime, a superlinear dependence is observed, $N_{\mathrm{FP}} \sim E^{1.36}$. On a log-log scale, one may determine the intersection of the fit lines of region 2 and region 3. The PKA energy at this intersection is defined as the transition energy. It is expected that the transition energy is higher for higher E_{d}. The exact relation is still under investigation. In addition, E_{d} may not be the only factor determining the transition energy. Mass may also play a role. In this report, we firstly investigate how changing the mass affects the threshold energy itself within the same interatomic potential. In this report, the results for Cr, Fe, Mo and W are presented.

Simulation Details

The molecular dynamics (MD) technique is employed to calculate the threshold energy. The MD simulations are performed using the LAMMPS code [2]. The interatomic forces are derived mostly from Finnis-Sinclair (FS) potentials [3] which have been modified and extended for cascade simulations; Fe by Calder et al. [4], Mo by Salonen et al. [5, 6] and W by Juslin et al. [6, 7]. For Cr, the FS potential developed by Bonny et al. is employed [8] with the short-range extension done by Juslin.

Periodic boundary conditions are applied along all axis coordinates. We use an orthorhombic box of 20×18×16 supercells (along x, y, and z, respectively) to avoid the self-interaction of the SIA moving along the <111> directions due to the periodic boundaries. The box contains 11,520 atoms. In test runs using 10 PKAs in each direction of [100], [110], [111], and [136], a smaller box size of 18×16×14 is used and the results are the same within the standard error as with the 20×18×16, giving a confidence that the 20×18×16 box is sufficient. We have also verified visually that replacement events are contained within the box when an SIA is created. Before a displacement is initiated, the system is equilibrated at 10 K and zero pressure for 20 ps with a Nosé-Hoover thermostat with a 1-ps time constant.

For the displacement simulations, a border region is defined with two atomic layers as shown in Figure 1 (black atoms). Note that due to the periodic boundaries, the border region would completely enclose the active region (gray atoms). The simulation cell shape and volume are fixed at the value obtained from the equilibration run. The atoms in the active region are evolved in a microcanonical (*NVE)* ensemble. A Nosé-Hoover thermostat at 10 K with a time constant of 0.1 ps is applied to the atoms in the border region to model the heat extraction. From visualization, it is evident that a 3 ps run is appropriate for observing defect creation. Therefore, the simulation is followed up to 3 ps with 1-fs time step. In the test runs as described previously, we have also verified that simulations up to 5 ps give the same results.

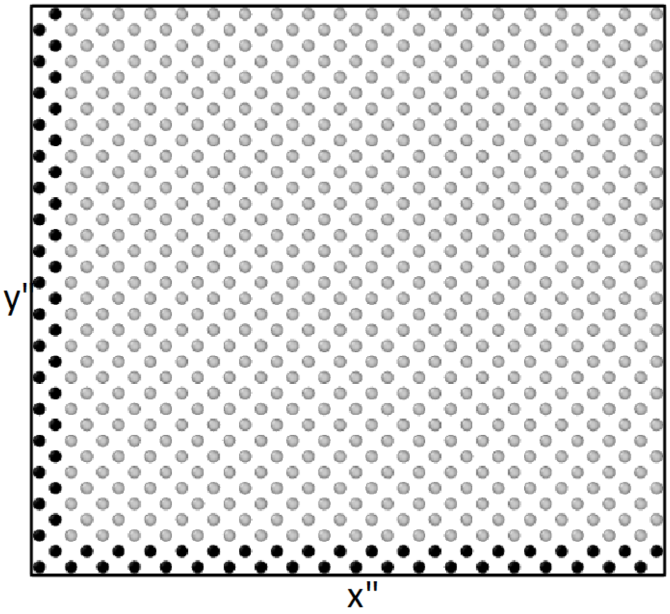

Figure 1. Setup of the simulation cell for the displacement simulations constructed from 20×18×16 supercells along x, y and z respectively. The box contains 11,520 atoms. Border atoms are plotted in black and thermostated at 10 K to model heat extraction. Periodic boundaries are applied in all axes.

The average displacement threshold energy is defined as

$$E_d = \frac{1}{4\pi}\int_0^{4\pi} E_d(\Omega)\,d\Omega. \quad (1)$$

From a point symmetry consideration, the average E_d can be calculated within the set of irreducible crystal directions (ICD). The ICD and the PKA direction grid used in this study are shown in Figure 2a. If the ICD is employed, it is necessary to account for the different multiplicity of each grid point to correctly calculate the average. The multiplicity represents the number of equivalent directions of a grid point. In Figure 2b, the multiplicity of each point is shown as the number following the x character within the parentheses. The grids are constructed with a Miller index increment of 1/24 resulting in a total of 325 points. Note that these points are not located on the surface of a sphere centered at the origin. Therefore, an appropriate weight due to the different solid angle of each point needs to be taken into account. The solid angle of point-i, $\Delta\Omega_i$, is calculated as the solid angle enclosing a small sphere with a diameter D = 1/24 (i.e. the sphere fits in to each grid) centered at grid point-i, as illustrated in Figure 2a. Finally, Equation 1 becomes

$$E_d = \sum_i E_{d,i} P_i \Delta\Omega_i / \sum_i P_i \Delta\Omega_i \tag{2}$$

$$\Delta\Omega_i(h,k,l) = 2\pi\left(1 - \frac{\sqrt{h^2+k^2+l^2}}{\sqrt{h^2+k^2+l^2+D^2/4}}\right) \tag{3}$$

where P_i denotes the number of equivalent directions for grid point-i.

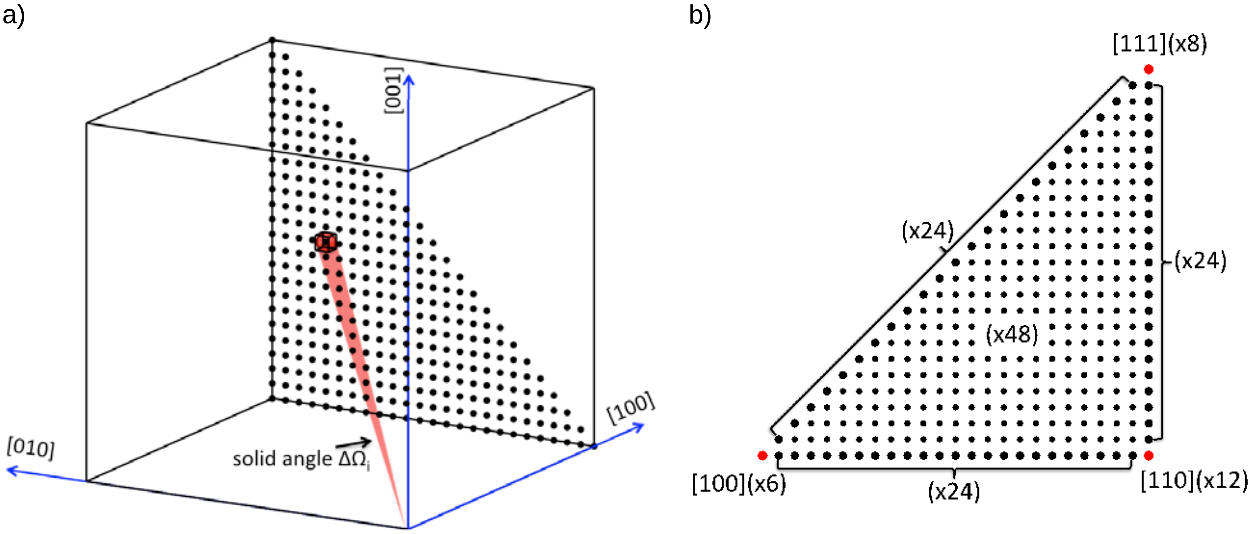

Figure 2. a) The irreducible part of the crystal directions and the grid points for the PKA directions. The grids are constructed with a Miller index increment of 1/24 resulting in a total of 325 points. b) The number of equivalent directions of each point is shown as the number following the x character within the parentheses.

Results

For each direction, the threshold energy is averaged over 10 simulations using a different PKA chosen near the center of the box. To search for the threshold energy, the PKA energy is incremented by 5 eV until a defect is detected, then decremented by 1 eV until no defects are detected. The threshold energy for a specific simulation is taken to be the minimum energy where a defect is created. Wigner-Seitz cell occupancy is used to recognize defect creation. The average threshold energy calculated with Equation 2 for all combinations of masses and interatomic potentials used in this study is presented in Table 1. For each interatomic potential, the results show that the displacement threshold energy is insensitive to mass, i.e. the values are the same within the standard error. In the future, the effect of mass on high-energy cascades for a given interatomic potential will be investigated. In high-energy cascades, the mass is expected to play a more important role than in sub-threshold displacement events due to the larger volume of material involved affected by cascade damage.

Table 1. Calculated average of the displacement threshold energy, in eV, as a function of interatomic potential (row-wise) and mass (column-wise). The mass is given in parentheses. Standard error of the threshold energy is included.

	Cr (52.00)	Fe (55.85)	Mo (95.94)	W (183.85)
Cr potential	34.4 ± 1.5	33.4 ± 1.5	34.0 ± 1.5	33.8 ± 1.4
Fe potential	41.4 ± 1.6	41.8 ± 1.6	41.8 ± 1.7	41.3 ± 1.3
Mo potential	78.6 ± 2.8	77.4 ± 2.9	78.7 ± 2.9	77.9 ± 2.9
W potential	123.6 ± 4.4	123.7 ± 4.2	122.7 ± 4.1	122.6 ± 4.4

We would like to acknowledge the contributions from N. Juslin in improving the short-range of the Cr potential [8]. Computations were performed on Olympus supercomputer (FUSION account) at Pacific Northwest National Laboratory.

REFERENCES

[1] W. Setyawan, et al., Fusion Reactor Materials Program Semiannual Report 54 (2013) 201.
[2] S. Plimpton, J. Comp. Phys., 117, (1995), 1.
[3] M. W. Finnis and J. E. Sinclair, Phil. Mag. A 50, (1984), 45.
[4] A. F. Calder and D. J. Bacon, J. Nucl. Mater., 207, (1993), 25.
[5] E. Salonen, T. Järvi, K. Nordlund and J. Keinonen, J. Phys. Cond. Mat., 15, (2003), 5845.
[6] G.J. Ackland and T. Thetford, Phil. Mag. A 56, (1987), 15.
[7] N. Juslin and B.D. Wirth, J. Nucl. Mater., 432, (2013), 61.
[8] G. Bonny, R. C. Pasianot, D. Terentyev, and L. Malerba, Phil. Mag. 91, (2011), 1724.

8.2 IMPLEMENTATION OF FIRST-PASSAGE TIME APPROACH FOR OBJECT KINETIC MONTE CARLO SIMULATIONS OF IRRADIATION

—G. Nandipati, W. Setyawan, H. L. Heinisch, K. J. Roche, R. J. Kurtz (Pacific Northwest National Laboratory) and B. D. Wirth (University of Tennessee)

OBJECTIVE

The objective of the work is to implement a first-passage time (FPT) approach to deal with very fast 1D diffusing SIA clusters in *KSOME* (kinetic simulations of microstructural evolution) [1] to achieve longer time-scales during irradiation damage simulations. The goal is to develop *FPT-KSOME*, which has the same flexibility as *KSOME*.

SUMMARY

This is a work in progress and in this report we present basic implementation details of the first-passage time (FPT) approach to deal with very fast 1D diffusing SIA clusters in *KSOME* (kinetic simulations of microstructural evolution) and the status of its development.

PROGRESS AND STATUS

Introduction

From the test simulations of irradiation in bulk tungsten carried out using the *KSOME* code we find that one-dimensionally (1D) diffusing SIA clusters, due to very low migration barriers, will limit the achievable simulation time and radiation dose. In this case most of the computational time is spent moving around SIA clusters that are far away from other defects, in the empty space of a simulation box. In order to avoid simulating these numerous individual diffusive hops by SIA clusters we let them do multiple nearest neighbor jumps simultaneously, depending on conditions in their neighborhood, and calculate the time for this jump using a well-known analytical expression for mean first-passage time (MFPT) for a 1D diffusing walker. [2, 3] SIA clusters that are very close to other defects and all other types of defects will perform regular KMC moves. A full FPT approach, where all defects are treated using FPT approach was employed previously to accelerate irradiation simulations [4] and we take a similar approach in implementing FPT in *KSOME.* In contrast to previous approaches, to reduce overhead, *FPT-KSOME* will be hybrid of FPT and traditional KMC methods.

Implementation of FPT Approach

In our first-passage-time approach, detailed 1D motion of an SIA cluster is replaced by a calculation of its overall first-passage time for ``absorption" at the boundaries of an interval whose length is determined based on how far it is from the nearest defect. Diffusive moves of other types of defects with barriers that are significantly higher than the migration barrier for SIA clusters are treated as regular KMC moves. The intent is that the bigger the difference between the migration rates of SIA clusters and other defects in the simulation the bigger will be the gain in decreased simulation time.

A key point is that the use of the FPT approach to accelerate KMC adds significant overhead. Therefore the best approach to achieve significant speedups is to treat only frequently occurring low-barrier events with the FPT approach while other events are treated as regular KMC events [3,4,5]. In addition, only SIA clusters that are farther than a certain user specified distance from a defect are allowed to make multiple nearest neighbor jumps, while other SIA clusters will perform regular KMC hops. Therefore diffusion of an SIA cluster will switch back and forth from multiple hop (FPT) to single hop (KMC) diffusion depending on how far it is from another defect. In order to further reduce the overhead we take the less rigorous approach of using average FPT instead of randomly selecting the FPT from an appropriate probability distribution function.

Calculation of Average First-passage Time For a 1D Diffusing SIA

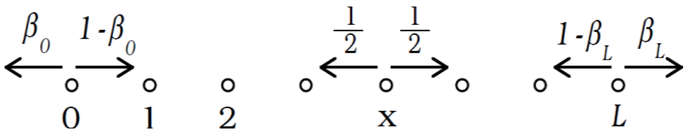

Figure 1. Schematic showing 1D random walker diffusing between partially absorbing boundaries at 0 and L with absorption probabilities β_0 and β_L, respectively [2].

In our case a 1D diffusing SIA cluster is mapped to a 1D random walker diffusing between two boundaries. For a 1D diffusing SIA cluster we treat both of the boundaries of the interval (see Figure 1) as perfectly absorbing, meaning β_0 $(\beta_L) = 1$. Then

$$n(x) = x(L - x) \qquad (1)$$

Where L is the interval length and x is the location of the 1D random walker in the interval. In our implementation we assume for simplicity that SIA clusters are initially always at the middle of the interval, that is at $x = L/2$ i.e., an SIA has equal probability to reach or escape from either end of the interval. The mean first passage time $\tau(x)$ to escape the interval from $[0,L]$ is given by

$$\tau\left(\frac{L}{2}\right) = L^2/8D_{SIA} \qquad (2)$$

Where D_{SIA} is the diffusion rate of an SIA cluster. For verification we can easily see that $L = 2$ and $x = 1$ represents a regular KMC jump. For this case, using Eqs (1) & (2) one can see that $n(1) = 1$ and $\tau(1) = 1/2D_{SIA}$ clearly represents a regular KMC jump.

If L is too short we may not see any significant speed up due to the overhead, but if it is too large we may miss important reaction events. The design of the simulation code has to be such that an appropriate interval length L is determined for each individual SIA cluster depending on its neighborhood. We use the distance of an SIA from its nearest defect and the sum of their capture radii to determine the interval length L. Each L is calculated as

$$\boldsymbol{L} = \boldsymbol{R} - (\boldsymbol{R_a} + \boldsymbol{R_b}) \qquad (3)$$

where R is the distance of the SIA from its nearest defect, while $\boldsymbol{R_a}$ and $\boldsymbol{R_b}$ are the capture radii of the SIA cluster and its closest neighbor respectively. This condition ensures that the capture radii of the SIA and its nearest defect never touch or overlap. Note that although the length of the interval is L, an SIA cluster will only move a distance of $L/2$ from its present location. Then the average first-passage time $\boldsymbol{\tau}\left(\frac{L}{2}\right)$ for the diffusion event along with times for all other possible processes an SIA cluster can perform are calculated. The SIA is moved to either end of the interval with equal probability if $\boldsymbol{\tau}\left(\frac{L}{2}\right)$ is the smallest time and the simulation clock is updated to $\boldsymbol{\tau}\left(\frac{L}{2}\right)$**.** If a non-diffusive process is selected then the position of the SIA cluster is updated within its interval before the non-diffusive process is performed and then a new interval length and $\boldsymbol{\tau}\left(\frac{L}{2}\right)$ are calculated. An SIA can perform two non-diffusive processes, emission and rotation. As mentioned earlier only SIAs that are far away from other defects are allowed to perform FPT moves while others will perform regular KMC moves. Accordingly, as SIA clusters move away from other defects they switch from KMC to FPT diffusion and if they move closer to other defects then it switches back from FPT to KMC diffusion. This switch from FPT to KMC diffusion and back is necessary to take care of reaction events properly.

Time-based KMC

Only hops to direct nearest neighbors *(L = 2)* are exponentially distributed. The lack of an exponential probability distribution disqualifies FPT diffusion steps to be used in the classical KMC algorithm (rate-based approach). [3] In order to implement the FPT approach we will use a time-based rather than a rate-based KMC method. [2,4] In this case events are chronologically ordered and the event with smallest time is executed. Each individual 1D diffusing SIA cluster has its own time. In addition to maintaining a list of first-passage times for all 1D diffusing SIA clusters, after each event we also update the total rate for all regular KMC moves $\boldsymbol{R_{KMC}} = \sum \boldsymbol{n_i}\,\boldsymbol{R_i}$ (where $\boldsymbol{R_i}$ is the rate for a process of type *i*, and $\boldsymbol{n_i}$ is the number of processes of this type). This rate is then used to calculate the time before the next regular KMC event given by $\boldsymbol{\Delta t_{KMC}} = -\mathbf{ln}(\xi)/\boldsymbol{R_{KMC}}$, where ξ= a uniform random number between [0,1]. This time is then compared with the time of the earliest FPT event (which will be selected using another binary tree). If the event type corresponds to a regular KMC event, then the specific event is selected randomly from all of the possible events of this type.

Benchmarking Tests

The basic *FPT-KSOME* code has been completed and it is being tested and benchmarked using data from single cascade annealing in tungsten at various PKA energies and temperatures obtained using *KSOME.* [6] Figure 2 compares the results from *KSOME* and *FPT-KSOME* for surviving fraction of defects during single cascade annealing in bulk tungsten at 300 K for PKA energies of 60 and 75 keV. L_{max} represents the maximum allowable interval length (L), which is a user-defined parameter. Each data point is an average of 300 runs. As can be seen from Figure 2 we have obtained reasonable agreement between FPT and regular KMC results.

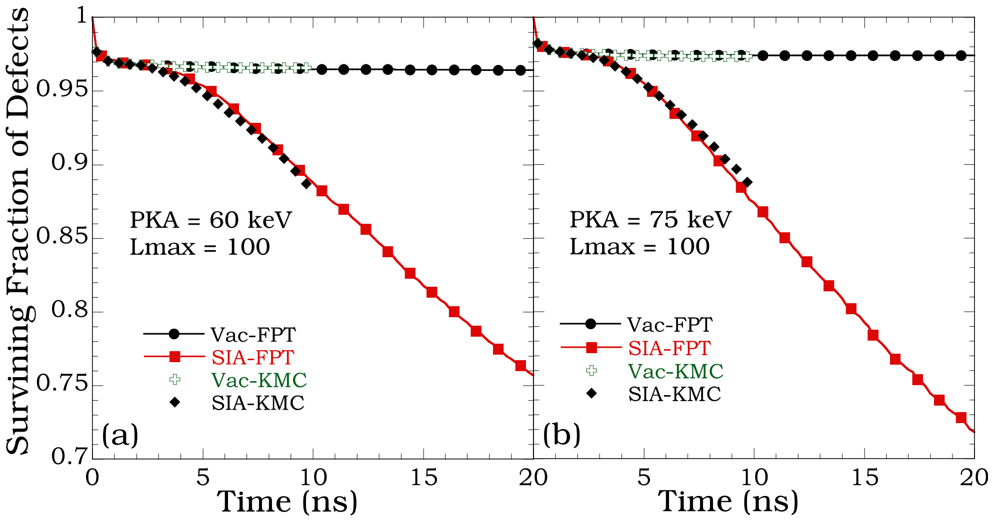

Figure 2. Comparison of regular OKMC and FPT OKMC for surviving fraction of defects during annealing of single cascades in tungsten at 300 K for PKA energies of (a) 60 and (b) 75 keV.

For the two cases shown in Figure 2 an average of 1.5 X 10^6 diffusive steps are performed to reach a simulation time of 10 ns. In case of *FPT-KSOME*, the same simulation time is reached on average a sum of 4 x 10^4 diffusive steps. Further reduction in the number of diffusive steps can be obtained if L_{max} is increased further than 100. As expected due to overhead resulting from additional bookkeeping associated with determining interval length and calculation of first-passage times, for annealing simulations of single cascade we have not seen a significant speed up compared to regular KMC simulations. A small speed up of 1.6X was obtained. However for irradiation simulations, which require achieving much longer times and involve a significant number of KMC steps compared to single cascade aging simulations, we expect to see significant speed up compared to regular KMC simulations.

FUTURE WORK

FPT-KSOME requires further testing of various aspects of the code. It been tested at 300 K where the rotation and dissociation of SIA clusters is negligible and therefore further testing is required to make sure that the code performs correctly at all temperatures. It also requires further testing to determine the optimum criteria to determine when to switch SIA diffusion from FPT-to-KMC and back to make sure that reaction events are properly handled. Note that we have conservatively chosen the length of the interval to be the distance between an SIA cluster and its nearest neighbor minus the sum of their capture radii, but the maximum allowable interval length is twice this value. Therefore we plan to carryout test simulations to determine the optimum value of L_{max} to obtain maximum computational efficiency.

Once the code is completely tested and benchmarked, it will be used to perform long-time scale irradiation simulations in bulk tungsten at various PKA energies and temperatures using the same database of cascades used in the cascade aging simulations.

Acknowledgement

This work was performed by Pacific Northwest National Laboratory, which is operated by Battelle for the United States Department of Energy under Contract DE-AC05-76RL01830. This study was supported by the U.S. Department of Energy, Office of Fusion Energy Sciences and Office of Advanced Scientific Computing Research through the SciDAC-3 program. All computations were performed on CARVER at National Energy Research Scientific Computing Center (NERSC).

REFERENCES

[1] G. Nandipati *et al* Semiannual Progress Report DOE/ER-0313/54, June 2013, 179-183.
[2] A. El-shehawey, J. Phys. A 33, 9005 (2000).
[3] G. Nandipati, Y. Shim, and J. G. Amar, Phys. Rev. B 81, 235415 (2010).
[4] A. Donev, *et al*, J. Comput. Phys. 229, 3214 (2010).
[5] A. Bezzola, B. B. Bales, R. C. Alkire, and L. R. Petzold, J. Comput. Phys. 256, 183 (2014).
[6] G. Nandipati et al., Semiannual Progress Report DOE/ER-0313/55, December 2013, 161-166.

8.3 AN INITIAL ATOMISTIC-BASED EQUATION OF STATE FOR HELIUM IN IRON - R. E. Stoller and Y. N. Osetskiy (Oak Ridge National Laboratory)

OBJECTIVE

The objective of this research is to determine the equation of state of helium in radiation-induced bubbles in iron-based alloys. Properties of He-bubbles significantly affect the evolution of the microstructure and mechanical properties under radiation damage conditions.

SUMMARY

An equation of state that accurately reproduces the pressure-volume relationship of helium is necessary to understand and predict the behavior of He-vacancy defects in irradiated materials. We have used *ab initio* calculations to determine the energetics of helium-vacancy clusters and applied the results to develop a new three-body interatomic potential that describes the behavior of helium in iron. The potential was employed in molecular dynamics simulations to determine the conditions for mechanical equilibrium between small helium-stabilized bubbles and an iron matrix, and to systematically map the pressure-volume relationship for the bubbles at a range of temperatures. These atomistic results are compared to an existing equation of state and a modification is proposed for bubbles with high helium densities.

PROGRESS AND STATUS

Introduction

The helium produced in irradiated metals and alloys by (n,α) transmutation reactions strongly influences microstructural and mechanical property changes. Helium is a particular concern for DT fusion reactor conditions because this environment will lead to significantly higher levels of He production than in fission reactor irradiation experiments where most data on radiation effects has been obtained. A prominent result of high He levels is the formation of very high densities of small He-vacancy clusters that can evolve into larger bubbles and voids. A computational model capable of predicting the behaviour of these small cavities requires an accurate equation of state to reproduce the pressure-volume relationship. Previous research has employed equations of state of varying complexity, including the ideal gas, van der Waals, and hard sphere models. Recent advances in high performance computing have made it possible to employ ab initio calculations to determine the energetics of larger and more complex atomic systems. Such calculations were used as the basis for development of a new three-body interatomic potential that accurately describes the behaviour of helium as either a substitutional or interstitial impurity in iron [1,2]. Molecular dynamics simulations employing this potential have been used to determine the conditions for mechanical equilibrium between small helium-stabilized bubbles and the iron matrix, and to systematically map the pressure-temperature relationship for He-filled bubbles. These atomistic results build on our previous research [3,4], and are compared to a hard-sphere equation of state we have used previously [5,6]. A modification of the hard-sphere model is proposed for bubbles with high helium densities.

Simulation Method

Molecular dynamics (MD) simulations were carried out at constant volume using a bcc iron system size of 128,000 iron atoms (40 lattice parameters cubed) containing helium-filled bubbles consisting of 9 to 44,399 vacancies, corresponding to nominal radii (r_b) from ~0.25 nm to ~5.0 nm. The appropriate lattice parameter was used for each simulation temperature in the range from 300 to 1000 K. The helium density in the bubbles was the primary simulation variable, with the density expressed as either the helium-to-vacancy ratio or the number of helium atoms per unit volume. Note that when the bubble volume is required, it is calculated based on the number of vacancies in the bubble and the atomic volume, i.e. $V_b = n_v\Omega$, and not as a sphere of radius r_b. This distinction is particularly important for small bubbles. The interatomic potentials employed were those of Ackland and co-workers for iron [7] and the ORNL three-body He-Fe potential [2]. For each simulation condition, the simulations were carried out long enough (see below) to obtain an accurate determination of the bubble pressure. There is a slight linguistic ambiguity in the following discussion. When carrying out MD simulations, it is common to use the term "equilibration" to describe the process of carrying out a simulation long enough for the total system energy to be equally distributed between kinetic and potential energy. We follow this convention here. However, we also wish to determine the equilibrium state of bubbles as discussed in the next paragraph. The latter we refer to as a condition of mechanical equilibrium. Although the MD simulations do not account for any influence of quantum effects that may occur with helium at high densities, previous work indicated that these effects are not significant above about 50 K even for very high pressures [8].

Results

The helium density is a useful parameter for determining the helium inventory in irradiated materials, and is a critical parameter in any equation of state. The helium-to-vacancy ratio for equilibrium bubbles is shown in Fig. 1. The temperature dependence in the ratio is not strong, except for the 0.25 nm

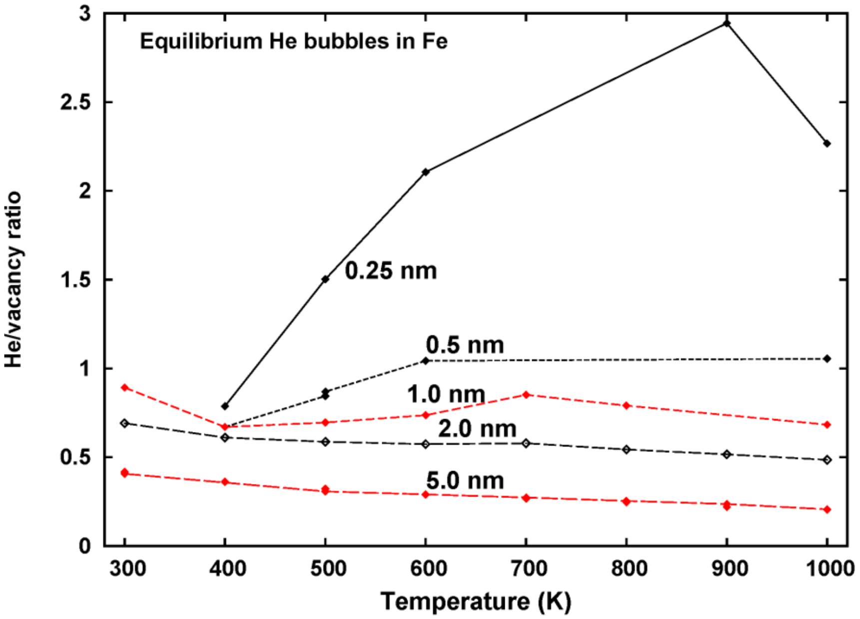

Figure 1. Helium-to-vacancy ratio for bubbles with radius shown, in mechanical equilibrium with the iron lattice for the indicated conditions.

bubbles. The ratio varies from 0.69 to 0.48 and 0.4 to 0.2 between the temperatures of 300 and 1000 K for 2 and 5 nm bubbles, respectively. There is a stronger dependence on bubble radius, ranging from 0.4 to 0.9 and from 0.2 to 1.0 between 5 nm and 0.5 nm at 300 and 1000 K, respectively. The results for 0.25 nm bubbles exhibit a stronger temperature dependence and higher values than the bubbles with larger radii. This may be related to a He phase change within the bubbles as discussed by other researchers [9-11]. In an initial assessment of the pair correlation functions obtained for He in these small bubbles, the He appears to be in the gas phase for 2 and 5 nm bubbles at all temperatures and in 1 nm bubbles at high temperatures. For the 0.25 and 0.5 nm bubbles and 1 nm bubbles at low temperatures the structure observed in the pair correlations is consistent with liquid or solid-like behavior. A more detailed analysis of the pair correlations and He diffusion behavior is underway and will be reported elsewhere. Note that there are two closely spaced data points at 500 K for the 0.5 nm radius. Only this very small difference was observed between MD equilibrations that started at different points to assess of the accuracy of the calculated values.

The He compressibility is defined as the ratio of the bubble pressure obtained from the MD simulations to the ideal gas pressure for the same bubble size, temperature, and helium content. The compressibility of bubbles in mechanical equilibrium with the iron lattice is shown as a function of bubble radius in Fig. 2a and as a function of the He/vacancy ratio in 2b. All temperatures are included for each radius and the line connects values at 500 K as a guide to the eye. There is a clear increase in scatter for He/vacancy ratios greater than about 0.7 (compressibilites greater than about 8) in Fig. 2b. This may be related to the He phase change mentioned above. Additional analysis of bubble behavior for higher He/vacancy ratios is underway and will be published elsewhere.

Brearley and MacInnes developed a hard-sphere equation of state (HSEOS) for helium based on the formalism of Carnahan and Starling [12]. Although the simple form of the equation neglects some of the potentially significant correction terms discussed by Wolfer, et al. [13] and Trinkaus, et al. [14,15], their model predicted compressibilities (Z) in good agreement with a somewhat limited amount of relatively low temperature (~65°C), high pressure helium data [5]. The equation of state has the following form:

$$Z = \frac{PV}{mkT} = \frac{(1 + y + y^2 - y^3)}{(1 - y)^3} \qquad (1)$$

where y is proportional to the helium density: $y=(\pi d_g^3/6)\cdot(m_{He}/V_b)$, d_g is the effective hard sphere diameter of the He atoms, m_{He} is the number of He atoms, and V_b is the bubble volume in nm^3. The hard sphere diameter is determined by the interatomic potential assumed; Brearley and MacInnes employed a modified Buckingham potential leading to a four-parameter expression for $d_g=0.3135\ [0.8542 - 0.03996\ ln(T/9.16\ K)]$ nm. This equation of state was adopted previously for use in models of bubble evolution and void swelling [6]. For comparison with the hard-sphere equation of state, compressibilities were calculated as the ratio of the bubble pressure obtained from the MD simulations to the ideal gas pressure for the same bubble size, temperature, and helium content. Because the values cover a range of discrete conditions (radii, helium densities, and temperatures), they are plotted as individual data points in Fig. 3a. Perfect agreement between the HSEOS and MD results would follow the 1:1 in Fig. 3a.

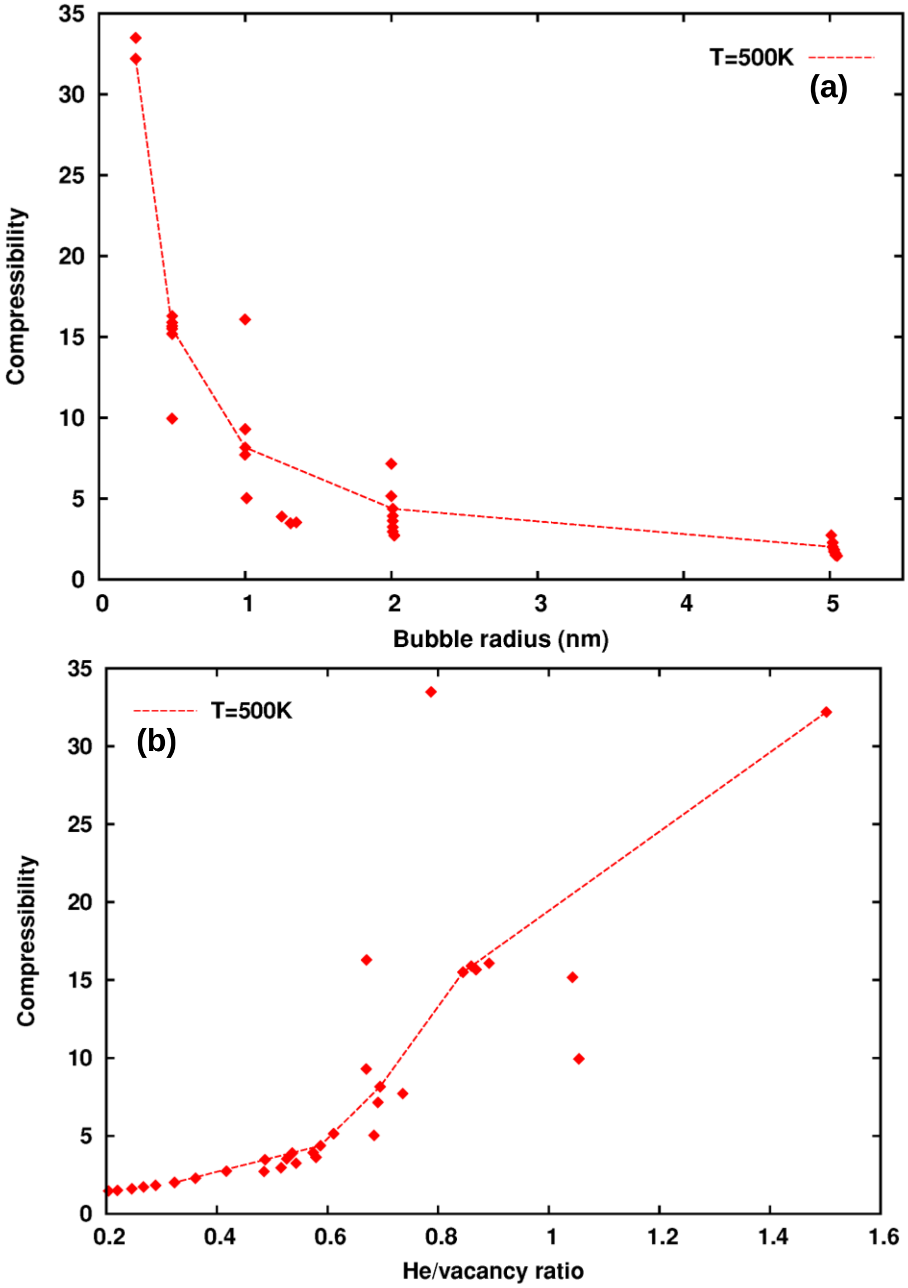

Figure 2. Compressibility of bubbles in mechanical equilibrium with the iron lattice as a function of bubble radius (a) and He/vacancy ratio (b), all temperatures are shown for each radius and line connects values at 500 K. Compressibility defined as the pressure from MD simulations divided by ideal gas pressure.

For compressibility values less that about 2, there is reasonable agreement between the MD and HSEOS results. However, the MD-based compressibilities are significantly greater for higher helium densities. Moreover, the results become increasingly scattered as the bubble radius decreases. This appears to be a result of two aspects mentioned previously: (1) the statistical difficulties associated with small

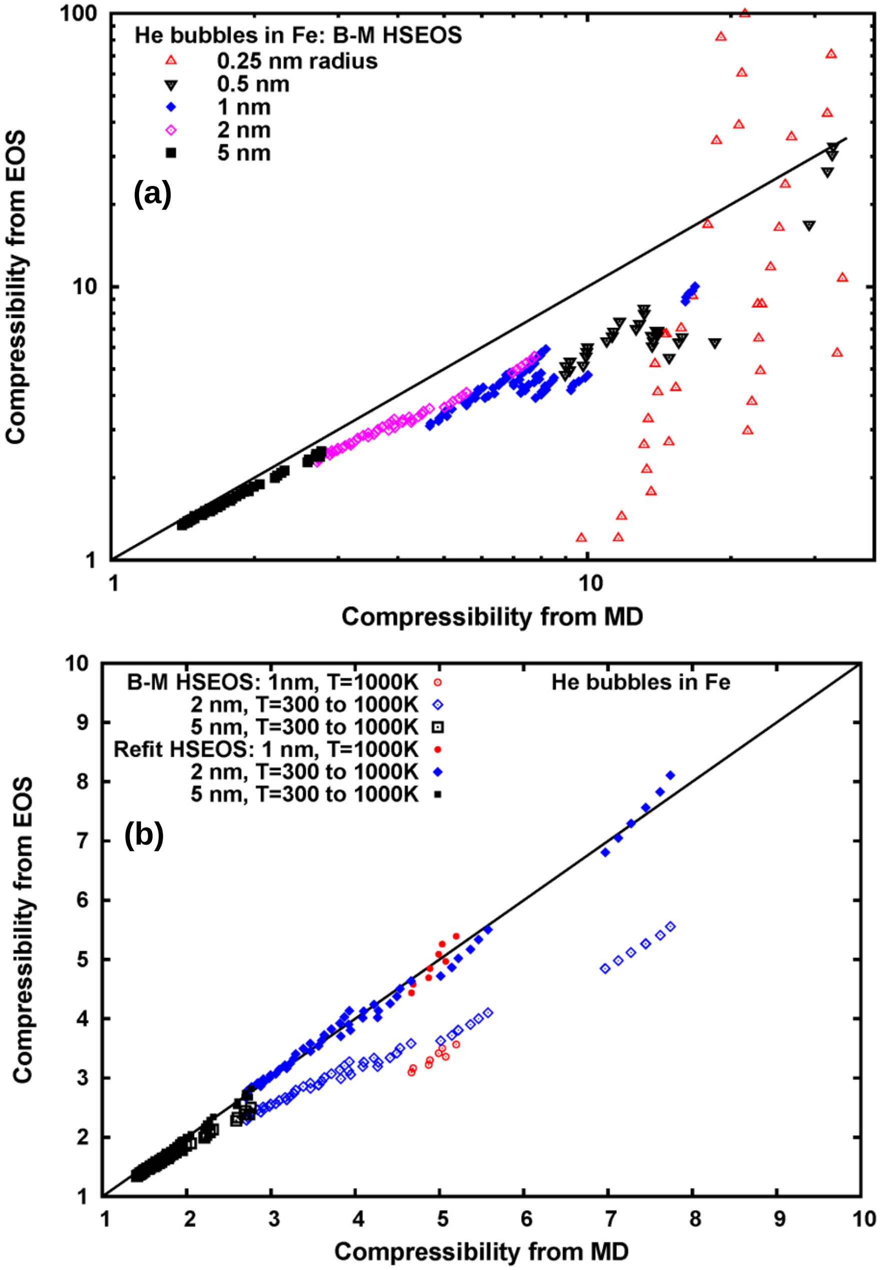

Figure 3. Comparison of compressibility obtained from MD simulations with those calculated using the Brearley-MacInnes hard-sphere equation of state [4]: (a) original parameters for all conditions, and (b) comparison of original parameters with those obtained from the non-linear fitting process as discussed in the text, see Table 1.

numbers of vacancies and He atoms in the smallest bubbles, and (2) the apparent phase change associated with the highest pressures. In addition, as reported previously [2,3], He atoms do not uniformly fill the bubble volume due to a strong, short-range Fe-He repulsion. A small radial gap is observed between the time-averaged position of the outermost He atoms and the bubble surface. This effectively reduces the active bubble volume and increases the pressure. Since the gap is nearly independent of the bubble radius, the relative impact is larger for smaller bubbles.

In order to provide an improved description of the MD results, the data was used as the basis for refitting the parameters in the HSEOS. The non-linear generalized reduced gradient method implemented in the Microsoft Excel *Solver* function was employed in the fitting process. The fitting parameters were the four coefficients in the hard sphere diameter d_g listed above and the size of the radial gap (Δr) between the He atoms and the bubble surface. As discussed above, the bubble volume in the HSEOS is determined by the number of vacancies rather than the nominal radius. The impact of Δr was accounted for in the context of an effective change in the atomic volume of the bubble which scaled as the cube of the corrected to nominal radius: $V_b^{eff} / V_b = (r_b - \Delta r)^3 / r_b^3$. Based on the systematic trends on the MD results that have already been discussed, the fitting database included all results for 2.0 and 5.0 nm bubbles and the 1000 K results for 1.0 nm bubbles. The results of the fitting process are shown in Fig. 3b, which clearly demonstrates the improved agreement. The applicable range of the compressibilities in Fig. 3b includes most conditions of interest to reactor materials. Future work will examine scenarios for extrapolating the HSEOS to higher compressibilities. The coefficents obtained in the fitting process are listed in Table 1.

Table 1. Coefficients obtained from fitting the HSEOS to the MD results

Fitting Parameter	**Original HSEOS**	**Refit HSEOS**
a_1	*0.3135*	0.319332
a_2	*0.8542*	0.865456
a_3	*0.03996*	0.041802
a_4	9.16	9.228038
Δr	n/a	0.057389
Hard-sphere gas atom diameter: $d_g = a_1 [a_2 - a_3 \ln(T(K)/a_4)$, *T= temperature in K* Effective reduced bubble volume: $V_b^{eff} / V_b = (r_b - \Delta r)^3 / r_b^3$		

Comparison with Experiments

The MD simulations employing the ORNL three-body He-Fe potential [1] indicate that the helium-to-vacancy ratio for equilibrium bubbles large enough to be visible in the transmission electron microscope is in the range of 0.3 to 1.0. Values greater than 1.0 are obtained only for bubbles with radii less than 1 nm. This result is consistent with recent experimental measurements using electron energy loss spectroscopy to determine the helium-to-vacancy ratio for small helium bubbles in ferritic-martensitic steels [16,17]. The helium density results of Wu et al. for a 1.3 nm bubble lead to a He/vacancy ratio ~0.6 [17], and earlier measurements by Frechard et al. for bubbles between 2 and 5 nm for which the He/vacancy ratio was in the range of 0.25 to 0.85 [16].

REFERENCES

[1] T. Seletskaia, Yu. N. Osetsky, R. E. Stoller, and G. M. Stocks, Phys. Rev. Lett. 94 (2005) 046403:1-4.
[2] R. E. Stoller, S. I. Golubov, P. J. Kamenski, T. Seletskaia, and Yu. N. Osetsky, Philos. Mag. 90 (2010) 923-934.
[3] D. M. Stewart, Yu. N. Osetskiy, and R. E. Stoller, "Atomistic studies of Formation and Diffusion of Helium Clusters and Bubbles in BCC Iron," J. Nucl. Mater. 417 (2011) 1110-1114.

[4] D. M. Stewart, Yu. N. Osetsky, R. E. Stoller, S. I. Golubov, T. Seletskaia, P. J. Kamenski, Philos. Mag. 90 (2010) 935-944.

[5] I. R. Brearley and D. A. MacInnes, J. Nucl. Mater. 95 (1980) 239-252.

[6] R. E. Stoller and G. R. Odette, J. Nucl. Mater. 131 (1985) 118-125.

[7] G. J. Ackland, D. J. Bacon, A. F. Calder, T. Harry, Philos. Mag. A 75 (1997) 713-732.

[8] Y. Song and E. Mason, Phys. Rev. E 47 (1993) 2193-2196

[9] S. M. Hafez Haghighat, G. Lucas, and R. Schaublin, EPL 85 (2009) 600081-5.

[10] A. Caro, J. Hetherly, A. Stukowski, M. Caro, E. Martinez, S. Srivilliputhur, L. Zepeda-Ruiz, M. Nastasi, J. Nucl. Mater. 418 (2011) 261-268.

[11] T. Jourdan and J.-P. Crocombette, J. Nucl. Mater. 418 (2011) 98-105.

[12] N. F. Carnahan and K. E. Starling, J. Chem. Phys. 51 (1969) 635-636.

[13] W. G. Wolfer, B. B.Glasgow, M. F. Wehner, and H. Trinkaus, J. Nucl. Mater. 122 & 123 (1984) 565-570.

[14] H. Trinkaus, Rad. Eff. Def. Sol. 78 (1983) 189-211.

[15] R. Manzke, W. Jager, H. Trinkaus, G. Crecelius and R. Zeller, Solid State Commun. 44 (1982) 481.

[16] Y. Wu, G. R. Odette, T. Yamamoto, J. Ciston, and P. Hosemann, “An Electron Energy Loss Spectroscopy Study of Helium Bubbles in Nanostructured Ferritic Alloys,“ Fusion Reactor Materials, Semiannual Progress Report DOE/ER-0313/54, Oak Ridge National Laboratory (2013) pp. 173-179.

[17] S. Fréchard, M. Walls, M. Kociak, J.P. Chevalier, J. Henry, and D. Gorse, J. Nucl. Mater. 393 (2009) 102.

8.4 A STOCHASTIC NONLINEAR DIFFERENTIAL EQUATIONS APPROACH TO THE SOLUTION OF THE HELIUM BUBBLE SIZE DISTRIBUTION IN IRRADIATED METALS-

D. Seif (University of California, Los Angeles), N.M. Ghoniem (University of California, Los Angeles)

Extended Abstract of an ICFRM-16 paper submitted to J. Nucl. Mater.

A rate theory model based on the theory of nonlinear stochastic differential equations (SDEs) is developed to estimate the time-dependent size distribution of helium bubbles in metals under irradiation. Using approaches derived from Ito's calculus [1], rate equations for the first five moments of the size distribution in helium-vacancy space are derived, accounting for the stochastic nature of the atomic processes involved. Fluctuations and the spread of the distribution about the mean are obtained by white-noise terms in the second-order moments. Physically, these are driven by fluctuations in the general absorption and emission of point defects by bubbles and fluctuations stemming from collision cascades. This statistical model for the reconstruction of the distribution by its moments is coupled to a previously developed reduced-set rate theory model [2], which has been shown to adequately describe the nucleation and growth phases of average-sized bubbles in irradiated metals.

As an illustrative case study, the model is applied to a tungsten plasma-facing component under irradiation, at a dose rate of $5X10^{-3}$ dpa/s and with a He/dpa ratio of 5 appm/dpa. The results of a simulation at 1800 K are shown in figure 1, showing the evolution of the distribution in the first 200 seconds of irradiation time. Projections of the vacancy and helium profiles of the distribution are seen in blue and red, respectively, and the mean bubble radius and mean pressure ratio, P/P_{eq}, are plotted in the inset plot on the left and right ordinate axes, respectively. In the very early stages of irradiation, we observe a rapid spreading of the distribution in the vacancy direction, which continues to grow, stabilizing after about 100 seconds of irradiation. This rapid dispersion stems from the increased effect of the stochastic fluctuations when bubble sizes are very small. The stabilization begins to occur as the average bubble size increases. In these early times, from the nucleation regime until the average bubble reaches roughly 3 nm, bubbles are observed to be highly pressurized ($P/P_{eq}>>1$). Due to the large difference in mobilities, when bubble concentrations and sizes are small, helium atoms can more effectively find their way to bubbles leading to these large pressures. However, as the internal helium interstitial population decreases due to bubble capture, the vacancy capture rates become large enough to keep the pressures low. The steady state bubble pressures are strongly controlled by the helium generation rate, H, and the re-solution parameter, b, which can be tuned to replicate specific experimental data. Figure 2 shows the time evolution during the simulation of the moments of the distribution (m_{10}, m_{01}, m_{20}, m_{02}, and m_{11}, where m_{ij} is the i^{th} moment in the helium direction and j^{th} moment in the vacancy direction).

The primary advantage of the method is the necessity for only a small set of rate equations to construct the entire distribution. This relies on the assumption of a Gaussian distribution as a first approximation. For increased resolution, discussion is given into how a path integral solution may be incorporated. Our findings highlight the important role of stochastic atomic fluctuations on the evolution of helium-vacancy cluster size distributions. The model is formulated in a general way, capable of including point defect drift due to internal temperature and/or stress gradients, which in practice arise from such issues as pulsed irradiation and both externally applied stresses or internally generated non-homogeneous stress fields, respectively. Discussion is given into how the stochastic terms may be modified to include additional physics governing the evolution of bubbles in irradiated materials and how the model can easily be extended to include full spatial resolution.

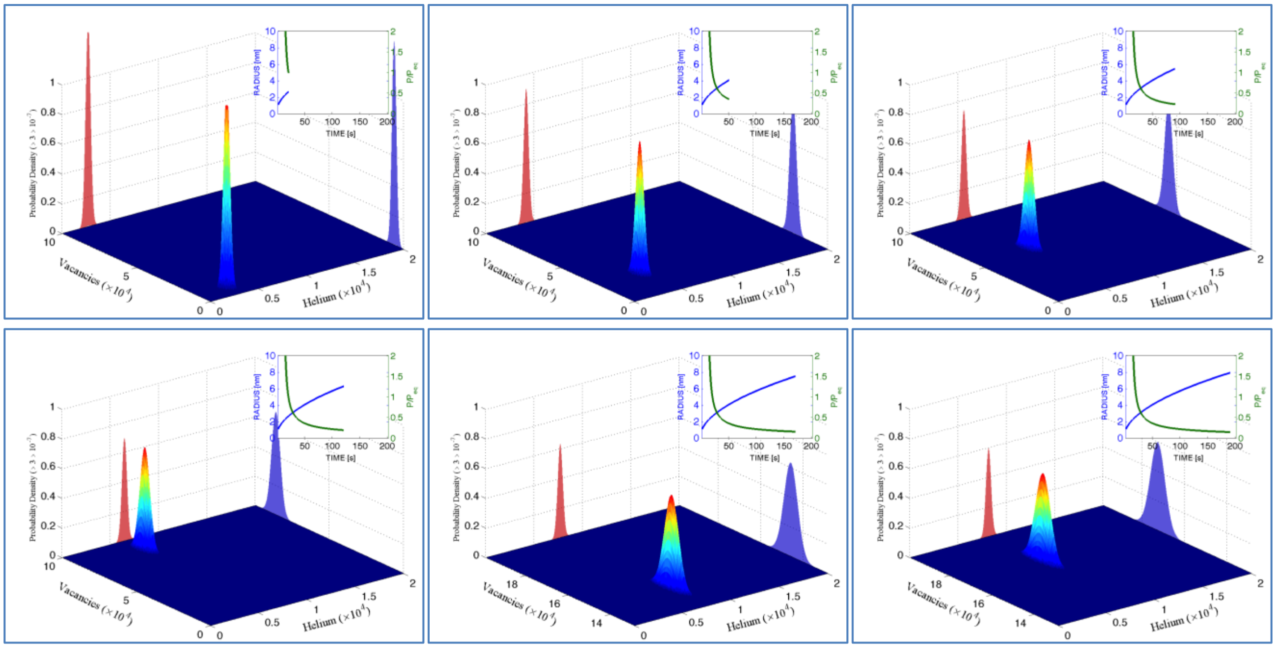

Figure 1. Evolution of the helium-vacancy size distribution spanning the first 200 seconds of irradiation time. The distribution is normalized by an arbitrary value (3X10^{-7} for plotting purposes. Projections of the vacancy and helium profiles of the distribution are seen in blue and red, respectively, and the mean bubble radius and equilibrium bubble pressure ratio, are plotted in the inset plot on the left and right ordinate axes, respectively.

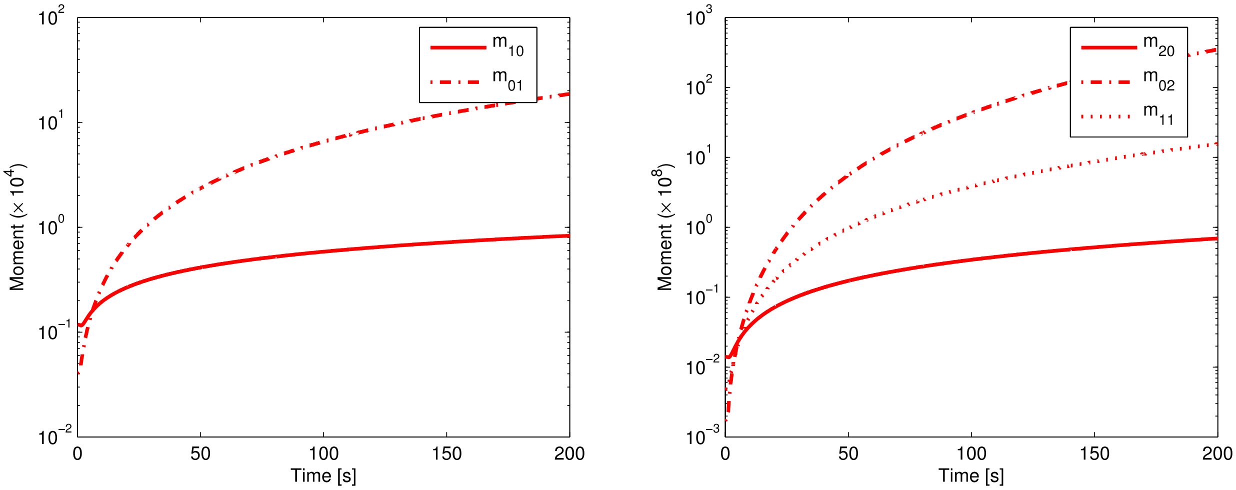

Figure 2. Log-scale plot of the moments of the size distribution versus time spanning the first 200 seconds of irradiation. The first order and second order moments are shown in the left and right plots, respectively.

REFERENCES

[1] K. Ito, Proc. Jap. Acad. Series A, 20 (1944) 519-524.
[2] N. M. Ghoniem, J. N. Alhajji and D. Kaletta, J. Nucl. Mater., 136 (1985) 192-206.

8.5 ATOMISTIC STUDIES OF GROWTH OF HELIUM BUBBLES IN α-FE—F. Gao, L. Yang, and R. J. Kurtz (Pacific Northwest National Laboratory)

OBJECTIVE

The clustering and growth of He bubbles in bcc Fe are simulated using molecular dynamics. We found that the creation and evolution of defects due to the growth of He bubbles depends on the separation distance between helium bubbles. A 1/2<111> interstitial loop is always created by a single helium cluster, but a <100> loop is formed under special conditions.

SUMMARY

Experimental results and atomistic simulations demonstrate that nucleation and growth of He bubbles in α-Fe will contribute to embrittlement and is a significant material problem for development of fusion power. Understanding the nucleation growth of He bubbles in steels is one of the most important issues in nuclear fusion technology. In order to understand the formation and evolution of self-interstitials (SIAs) caused by He bubble growth under He-rich/vacancy-poor conditions, the clustering of He and growth of He bubbles in bulk Fe is currently being investigated by inserting He atoms one by one into one or two He clusters. We find that a 1/2 <111> dislocation loop is formed and eventually punched out by a single He cluster, but when two He clusters are present the configuration of the SIA loop formed depends on the distance between the two He clusters. A <100> cluster is created when the distance between the He clusters is less than about $6a_0$ and eventually grows into a <100>{100} dislocation loop.

PROGRESS AND STATUS

Introduction

Ferritic/martensitic steels and alloys have been used for structural materials in current nuclear fission reactors and proposed as candidate first wall materials in future fusion energy facilities. Thus, a large number of experimental and computer simulation studies have focused on the irradiation damage of Fe-based bcc materials [1,2], including the production of self-interstitial atoms (SIAs), vacancies, He and H atoms. The behavior of He in irradiated materials is of interest because high concentrations of He created by transmutation are known to induce the formation of He bubbles with existing and radiation-induced defects, and significantly degrade the mechanical properties of first-wall structural materials.

Modeling of the nucleation and growth of He bubbles in irradiated metals began a few decades ago. Atomic simulation is a useful tool to explore the kinetic process of initial clustering of He to a nanometer sized bubble. Processes of He bubble growth in bcc Fe and Fe-alloys have been simulated at the atomistic level. By loading He atoms into a pre-existing bubble seed in pure Fe and an Fe-Cr alloy, 1/2<111> interstitial dislocation loops are emitted during the relaxation procedure [3]. After randomly adding He atoms in bcc Fe, which simulates a He-rich and vacancy-poor condition, SIAs or 1/2<111> interstitial dislocation loops appear due to the clustering of He [4]. In addition, the formation of 1/2<111> dislocation loops during He cluster growth has also been observed by inserting He atoms one by one. The transformation of the SIA clusters into a 1/2<111> dislocation loop is similar to the previous study in [3]. However, the numbers of SIAs created differ using different Fe-Fe, Fe-He and He-He interatomic potentials [5]. Up to now, only 1/2 <111> dislocation loops, due to the clustering of He, were reported in bulk Fe and Fe alloys in the simulations. However, after He implantation, two sets of interstitial dislocation loops, with Burgers vectors of 1/2<111> and <100>, were identified in oxide dispersion strengthened ferritic steel using transmission electron microscopy (TEM) [1]. Also, the predominant types of loops found in irradiated reduced activation ferritic/martensitic (RAFM) steels were <100> {100} and ½<111>{111} [5]. We have studied the accumulation and clustering of He atoms at grain boundaries (GBs) in bcc iron. Some <100> dislocation loops are directly formed at the GB that are confined between He clusters, and they are very stable, even at high temperatures. However, the formation mechanism of those <100> dislocation loops is unclear.

Simulation Methods

The potentials used in this work are the same as those used in Ref. 6. The Fe-Fe, Fe-He and He-He interactions are described by the interatomic potentials of Ackland et al., Gao et al., and Aziz, respectively. An MD box of $50a_0 \times 50a_0 \times 50a_0$ with 250,000 Fe atoms is used to simulate the formation and growth of He clusters in bulk iron, where a_0 is the lattice constant of perfect bcc Fe (2.8553Å). Periodic boundary conditions are applied along all three directions. The NVT (constant number of atoms, volume and temperature) ensemble is chosen in the present simulations with a time step of 1 fs. At first, the growth of one He bubble in the box is simulated by the following procedure: He atoms are inserted one by one into the He cluster. After each He atom insertion, the configuration is quenched to 0 K, followed by a temperature rescaling to 300 K and annealing at that temperature for 100 ps. For the insertion of the next He atom, the configuration is quenched back to 0 K and the procedure is repeated. The growth of two He bubbles in the simulation box are investigated using a method similar to the one above, but He atoms are inserted one by one into the two He clusters, respectively.

Results and Discussion

One He ClusterEvolution

We firstly investigated the growth of one He cluster (or bubble), which corresponds to the condition of a low density of He bubbles growing in bulk Fe. Recent studies show that single He interstitials and small He clusters (He_2, He_3) quickly diffuse through the lattice at 300 K, and thus, the simulation is initialized with four He atoms (He_4) located at a tetrahedral interstitial site in the center of the simulation box. It is found that the He_4 cluster is also able to migrate away from the initial site without creating an SIA. Upon adding the fifth He, the He_5 cluster pushes the nearest Fe atom off its lattice site along the <111> direction, creating more space for the He cluster, but the emission of an SIA does not occur. After inserting two more He atoms, the displacements of the Fe atoms around the He cluster increases. However, an Fe atom is kicked out from the cluster when the number of He atoms increases to eight, forming a He_8V cluster and an SIA. The SIA appears as a <111> crowdion at a distance of about 3.5 Å from the center of the He cluster, but the <111> crowdion can also transform to the <110> dumbbell during annealing. We observed that the minimum number of He atoms in the cluster required to create an SIA is slightly different from other simulation results. With different potentials, Morishita et al. [7] found that the pressure of a six He atom cluster was large enough to push an Fe atom off from its normal site and create a Frenkel pair. Gao et al. [8] also predicted that a He_6 cluster would create an SIA with <111> crowdion configuration, but Guo et al. [9] observed that three He atoms were sufficient to create an SIA in their simulations. Our result is close to the prediction of Stewart et al. [10], in which a Frenkel pair can be produced by a cluster containing ten He atoms at 200 K, and nine He atoms at 400 K. The insertion of the eleventh He atom followed by annealing at 300 K causes a second SIA to be emitted with a <110> dumbbell configuration. These SIAs collect at the periphery of the He-V cluster. After insertion of 13 He atoms, all the SIAs move to the same side of the cluster, rather than remaining uniformly distributed over the cluster surface, which is consistent with Morishita's observations in Fe [7] and Wilson's results in Ni [11]. A fourth SIA is emitted from a 15 He atom cluster and then the four SIAs spontaneously transform into $[1\bar{1}1]$ crowdions during annealing.

Insertion of additional He atoms results in the accumulation of more SIAs at the periphery of the cluster. Several snapshots of the configurations produced by continuously adding He atoms are shown in Figure 1, where all the insets are viewed normal to the <111> direction. When the 23rd He atom is introduced, eight SIAs align along the same <111> direction as crowdions, forming a well-defined SIA cluster attached to the He-V cluster, as shown in Figure 1(a), where the inset is the configuration of the SIAs, vacancies and He atoms projected on the {111} plane. A 1/2<111> dislocation loop with N_I = 16 (the number of SIAs) is formed after the insertion of 35 He atoms. The inset in Figure 1(b) shows the 16 SIA cluster configuration on the {111} plane, which arranges to form part of a hexagonal dislocation loop. The open circles represent empty positions in this loop. It should be noted that the dislocation loop is still attached to the He cluster. After the 41st He atom is inserted into the cluster, a dislocation loop with N_I =

18 is able to move away from the He cluster along a <111> direction. The configurations of the He cluster and nearby defects following 10 ps annealing are shown in Figure 1(c).

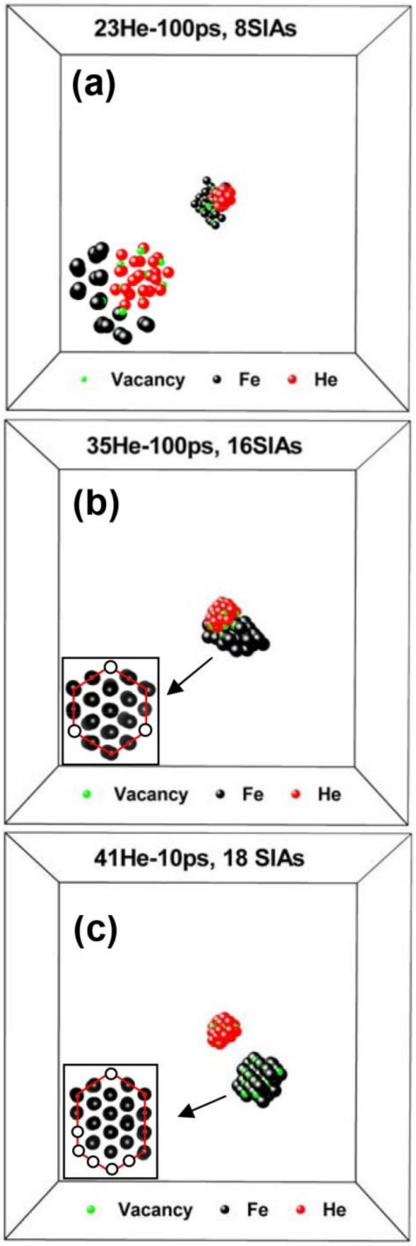

Figure 1. Atomic configurations of the He cluster and it's nearby displaced Fe atoms after adding He atoms followed by annealing 0.1 ns at 300 K: (a) 7He, (b) 8He, (c) 11He and (d) 13He, where large black, medium red and small green spheres present SIA, He and vacancies, respectively.

<u>Two He Bubbles</u>

Three different models involving two He clusters separated at different distances are considered. Two He clusters are inserted along the [001] direction with separation distances of $10a_0$ and $6a_0$, respectively, and another is inserted along the [111] direction with a separation distance of $6a_0$. Figure 2 shows three snapshots of the atomic configuration with two He clusters including 3 He atoms (a), 30 He atoms (b) and

62 He atoms (c) in each cluster, where the initial distance between the two He clusters is $10a_0$. Without special notation, the number of He atoms in the following text means the number in each He cluster. We find that by adding 30 He atoms, some SIAs are created with either <111> crowdion or <110> dumbbell orientation, resulting in SIA clusters on one side of the He clusters. After insertion of 62 He atoms, a large <111> SIA cluster with 28 SIAs forms near the lower He cluster, but an SIA cluster composed of <111> and <110> SIAs is attached to the top He cluster. The formation and evolution of SIAs are similar to those observed for growing He clusters in bulk Fe. It is of interest to note that adding one more He in each He cluster induces the SIAs near the He cluster (A) in Figure 3 to migrate along a <111> direction, joining the SIAs near the He cluster (B) to form an interstitial loop with 55 SIAs. The interstitial loop is much larger than that created by one He cluster consisting of 63 He atoms in bulk Fe. The Fe atoms at the periphery of the top He cluster almost return to their lattice sites. The configuration of defects around the lower He cluster, which is marked by the yellow circle in (a), is shown on the (100) and (111) planes in Figs. 3 (b) and (c), respectively. It is clear that the SIA cluster is a <111> dislocation loop. During growth of the He clusters, the centers of the two He clusters remain near their initial positions.

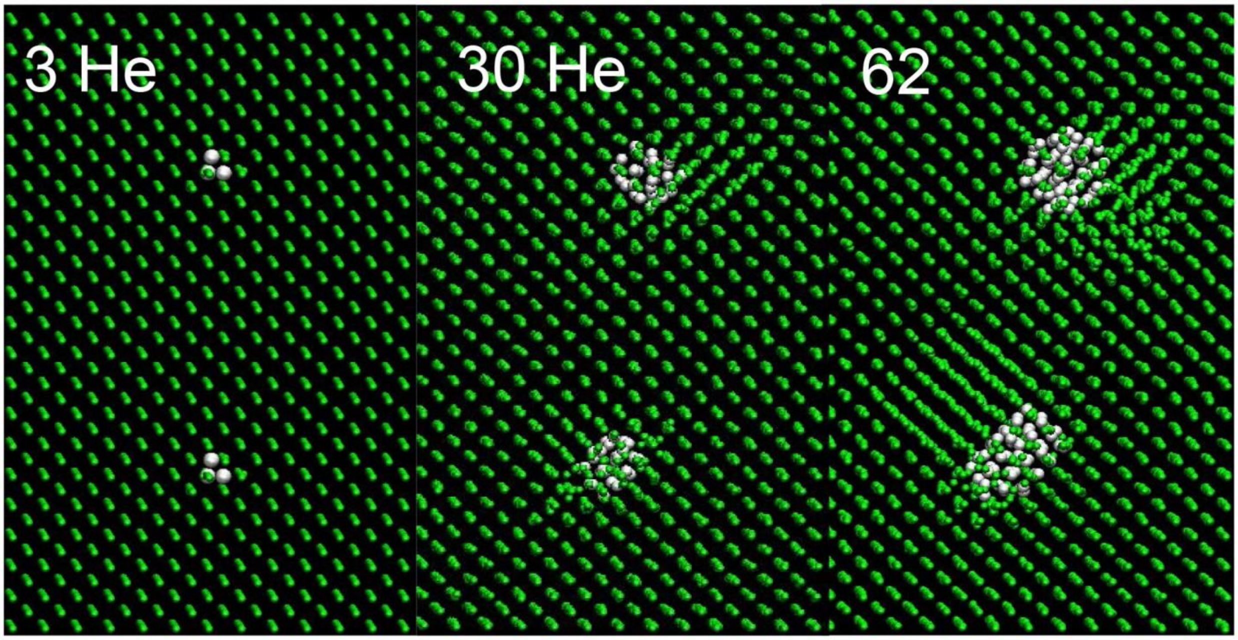

Figure 2. Configurations of the He clusters in bulk Fe, as viewed in the (001) plane, where green spheres are Fe atoms and grey He atoms: (a) 3 He atoms, (b) 30 He atoms, and (c) 62 He atoms in each cluster.

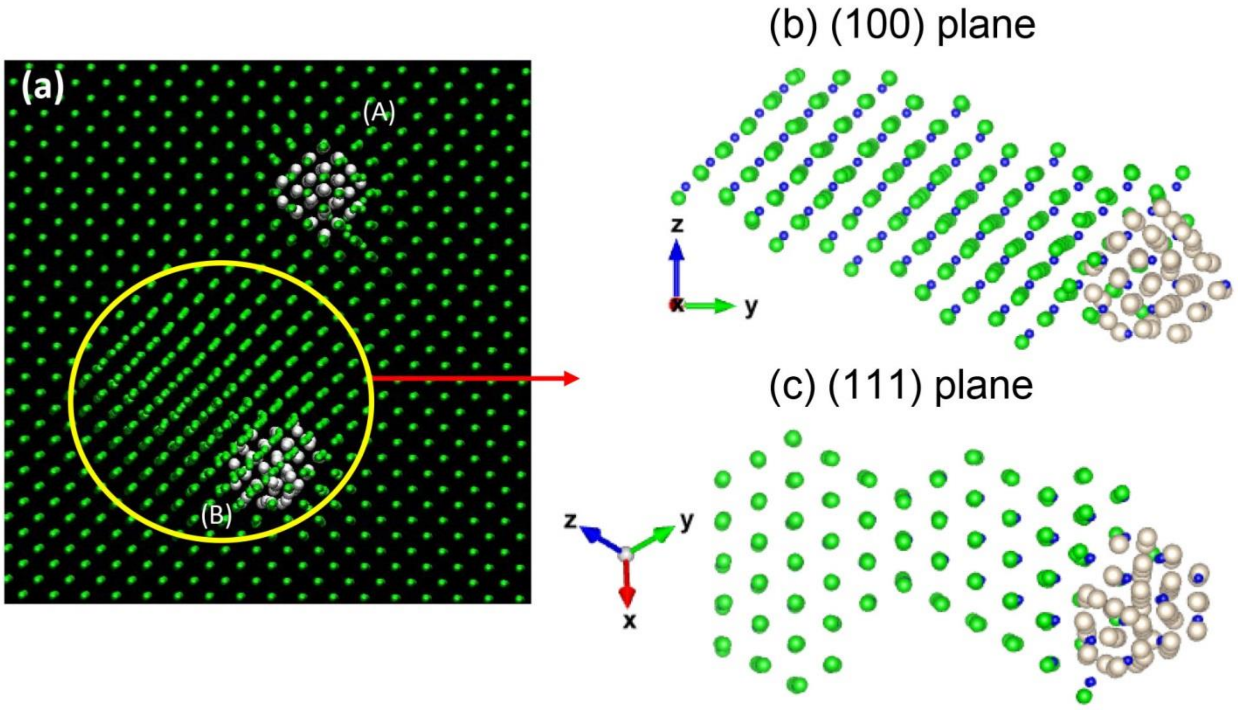

Figure 3. (a) Configurations of He clusters with 63 He atoms in bulk Fe, where green spheres are Fe atoms and grey He atoms. Configurations of defects in the region marked by yellow circle in (a): (b) view on the (100) plane and (c) on the (111) plane, where green spheres are Fe interstitial, blue and grey spheres are vacancies and He atoms, respectively.

By decreasing the initial distance between the two He clusters, a different defect evolution process is observed. Figure 4 shows the configurations of the He clusters and SIAs created for an initial distance of $6a_0$ between the two He clusters, as viewed on the (001) plane, where green spheres are Fe interstitials, and blue and grey spheres are vacancies and He atoms, respectively. It is clearly seen that after adding even He atoms to each He cluster, one of the He_7 clusters emits a Fe atom, forming a He_7V cluster and a <110> crowdion SIA, but the other cluster pushes the nearest Fe atoms off their lattice sites along the <111> direction and creates more space within the He cluster without emitting a SIA, as shown in Figure 4. The SIA initially appears as a <111> crowdion, but transforms to a <110> dumbbell during annealing. The SIA moves around the He-V cluster as the next He atom is added to both clusters. After the insertion of the 11th He atom, the two He clusters seem to attract each other and move closer. A third SIA is emitted to form a <110> dumbbell configuration. From Figure 4, it is of interest to note that most SIAs congregate in the region between the two He clusters after adding 13 He atoms. Three SIAs at the center between the two He clusters transform to <100> dumbbells, but the other surrounding SIAs maintain <111> and <110> configurations. Simultaneously, the lower He cluster further moves towards the top He cluster, decreasing the separation distance between the two clusters to 1.5 nm. With increasing numbers of He atoms, more <111> crowdions transform to <100> dumbbells in the region between the two He clusters, but most SIAs remaining at the periphery of the two clusters are still <110> and <111> crowdions, which can be seen in the snapshots of 21 and 43 He atoms in Figure 4. As a result, a <100> SIA loop with 30 SIAs is directly formed after the insertion of 43 He atoms. The size of the <100> SIA loop increases with increasing numbers of He atoms in the clusters, because more <111> crowdions transforms to the <100> dumbbells. However, the emission of a dislocation loop does not occur even if the number of He atoms in the clusters reaches 63 atoms.

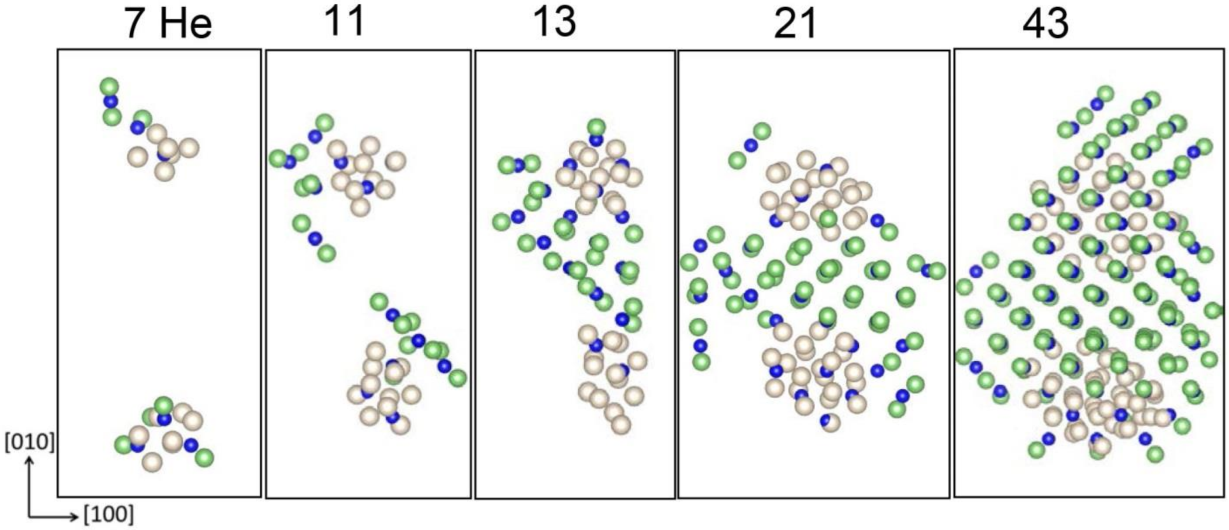

Figure 4. Configurations of He clusters and SIAs viewed on the (001) plane, where green spheres are Fe interstitials, blue and grey spheres are vacancies and He atoms, respectively.

CONCLUSION

The growth of He clusters or nano-scale bubbles in bulk Fe is studied by molecular dynamics approach. The evolution of SIA defects associated with the growth of He bubbles is analyzed in detail. It is found that the formation and evolution of SIA dislocation loops strongly depends on He cluster spacing. A 1/2 <111> dislocation loop forms at the periphery of a single He cluster and the loop is eventually emitted with increasing numbers of He atoms in the cluster. The growth and defect evolution of two He clusters is explored using a similar method, but He atoms are inserted one by one at the same time into both of the clusters. It is interesting to observe that the configuration of the SIA loops formed depends on the initial separation distance between the two clusters. A <100>{100} dislocation loop is created when the distance between the two He clusters is about $6a_0$, whereas a <111> loop forms when the initial cluster separation distance is $10a_0$.

REFERENCES

[1] J. Chen, P. Jung, W. Hoffelner and H. Ullmaier, Acta Mater. 56 (2008) 250.
[2] H.X. Xu, R.E. Stoller, Y.N. Osetsky and D. Terentyev, Phy. Rev. Lett. 110 (2013) 265503.
[3] A. Caro, J. Hetherly, A. Stukowski, M. Caro, E. Martinez, S. Srivilliputhur, L. Zepeda-Ruiz and M. Nastasi, J Nucl. Mater. 418, (2011), 261.
[4] L. Yang, H. Q. Deng, F. Gao, H.L. Heinisch, R.J. Kurtz, S.Y. Hu, Y.L. Li and X.T. Zu, Nucl. Instr. and Meth. B 303, (2013), 68.
[5] B. Yao, D. J. Edwards and R. J. Kurtz, J. Nucl. Mater. 434, (2013), 402.
[6] L. Yang, F. Gao, H.L. Heinisch, R.J. Kurtz, In DOE/ER-0313/50-Volume 51 Semiannual Progress Report December 31, 2011.
[7] K. Morishita, R. Sugano and B.D. Wirth, J. Nucl. Mater., 323, (2003), 243.
[8] N. Gao, H. Van. Swygenhoven, M. Victorian and J. Chen, J. Phys.,Condens. Matter, 23, (2011), 442201.
[9] S.H. Guo, B.E. Zhu, W.C. Liu, Z.Y. Pan and Y.X. Wang, Nucl. Instr. and Meth. B, 267, (2009), 3278.
[10] D. Stewart, Y. Osetskiy and R. Stoller, J. Nucl. Mater., 417, (2011), 1110.
[11] W.D. Wilson, C.L. Bisson and M.I. Baskes, Phys. Rev. B 24, (1981), 5616.

8.6 RELATIVE STABILITY OF HELIUM AND HYDROGEN IN NANO-STRUCTURED FERRITIC ALLOYS — B. Tsuchiya, T. Yamamoto, G. R. Odette, (University of California, Santa Barbara); K. Ohsawa (Kyushu University)

OBJECTIVE

Ab-initio Density Functional Theory (DFT) calculations were carried out to assess the energies of He and H at various locations in $Y_2Ti_2O_7$ and compared the corresponding energies in matrix Fe.

SUMMARY

First principle calculations were carried out for tetrahedral- and octahedral-interstitial sites in $Y_2Ti_2O_7$, and tetrahedral- and octahedral-interstitial as well as substitutional sites in Fe, in order to assess the energetics of He and H in Fe containing $Y_2Ti_2O_7$. The formation energies of He at tetrahedral- and octahedral-interstitial sites in $Y_2Ti_2O_7$ were 1.59 and 1.02 eV, respectively, which were much lower than the corresponding energies (4.47, 4.67, and 2.23 eV) in tetrahedral-, octahedral-interstitial and substitutional sites in Fe. On the other hand, the formation energies of H at tetrahedral- and octahedral-interstitial sites in $Y_2Ti_2O_7$ were 2.87 and 3.01 eV, respectively, which are much higher than the corresponding energies (0.11, 0.24, and 0.41 eV) at tetrahedral-, octahedral-interstitial and substitutional sites in Fe. Thus He and H in NFAs partition to the oxide and Fe, respectively.

PROGRESS AND STATUS

Introduction

Nano-structured ferritic alloys (NFAs), containing a very high density of nanometer-sized pyrochlore-type Y-Ti-O oxide ($Y_2Ti_2O_7$) nanofeatures (NFs), are a leading candidate structural material for advanced fission and fusion energy applications [1-3]. The oxide particles act as obstacles for dislocation motion, increasing the alloy strength, and are expected to act as recombination centers for point defects and trapping sites for helium (He) atoms that are produced by nuclear transmutation reactions to restrain the swelling. Our results confirm and extend previous first principal studies that He prefers substitutional sites in bcc iron (Fe) and individual octahedral-interstitial sites in $Y_2Ti_2O_7$ [4, 5]. Thus the oxides are sites for bubble formation that largely suppress swelling [2]. In this work we also extend the assessment of site-specific energies to hydrogen (H).

Calculation Methods

Figure 1 shows configurations of the ideal pyrochlore-type $Y_2Ti_2O_7$ with lattice constants of 0.9974 nm for a, b, and c axes. The structure has an isometric with space group of $Fd\bar{3}m$: 227 and possess eight molecules consisting of 16 pieces of Y^{3+} cations, 16 pieces of Ti^{4+} cations, and 56 (=48+8) pieces of O^{2-} anions in the unit cell (16+16+56=88 cations and anions; large size of the unit cell). Each cation and anion in the conventional cell locate at the following Wyckoff positions: Y^{3+} at 16*d* (1/2, 1/2, 1/2), Ti^{4+} at 16*c* (0, 0, 0), O^{2-} at 48*f* (*x*, 1/8, 1/8) in a tetrahedron coordinated to two Y^{3+} and two Ti^{4+} cations and at 8*b* (3/8, 3/8, 3/8) in a tetrahedron formed by four Y^{3+} cations, where the displacement of each O-site due to the neighboring unoccupied tetrahedron formed by four Ti^{3+} cations, *x*, is the only internal free parameter [2, 6]. Figure 2 shows configurations of Fe bulk having body-center cubic (bcc) crystal structure with lattice constants of 0.2842 nm for a, b, and c axes and space group of $Im\bar{3}m$: 229 and containing 128 pieces of Fe^{4+} cations in the supercell [2, 4, 7-13]. The Fe^{4+} cations locate at the Wyckoff position of 2*a* (0, 0, 0). All structural relaxations and energetic calculations were carried out using periodic primitive cells and supercells, the DFT code – VASP ver. 4.6, a plane-wave basis generated with valence configurations of H-$1s^1$, He-$1s^2$, O-$2s^2 2p^4$, Ti-$3s^2 3p^6 3d^2 4s^2$, Fe-$3d^6 4s^2$, and Y-$4s^2 4p^6 4d^1 5s^2$ and the projector augmented wave method (PAW) [14, 15]. One He or H atom was inserted in the center of (a) tetrahedron and (b) octahedron, surrounded by four Ti atoms and three Y and three Ti atoms, respectively, in bulk $Y_2Ti_2O_7$, as shown in Fig. 1. The energy cutoff was set at 650 eV for He and 500 eV for H and a 5×5×5 Monkhorst-Pack k-mesh was used for the unit $Y_2Ti_2O_7$ cell, because of approximately 1.5 times as much as maximal plane-wave kinetic energy (e.g; 479 eV for He, 400 eV for O, 275 eV for Ti, 250 eV for H, 212 eV for Y). The period of the first principal calculation was 24 hrs for the oxide and the three rounds was carried out to obtain the values. On the other hand, it was also shown in Fig. 2 that various defect structures, including interstitial He and H at tetrahedral- and octahedral-interstitial sites, a He or H atom occupying a Fe vacancy site (i.e. substitutional He or H) were modeled. The energy cutoff was set at 350 eV for He and H and 7×7×7 Monkhorst-Pack k-mesh was used for Fe in its 4×4×4 bcc supercells. The calculation for 120 hrs was repeated until three rounds. Spin-polarised calculations were performed for Fe and non-spin-polarised calculations in the case of $Y_2Ti_2O_7$.

The formation energies of He and H defects at interstitial sites in $Y_2Ti_2O_7$, $E_{\text{defect}}^{\text{He in } Y_2Ti_2O_7}$ and $E_{\text{defect}}^{\text{H in } Y_2Ti_2O_7}$, are defined, as given in Eqs. (1) and (2).

$$E_{\text{defect}}^{\text{He in } Y_2Ti_2O_7} = E_{\text{He in } Y_2Ti_2O_7} - E_{Y_2Ti_2O_7} - E_{\text{He}}, \tag{1}$$

$$E_{\text{defect}}^{\text{H in } Y_2Ti_2O_7} = E_{\text{H in } Y_2Ti_2O_7} - E_{Y_2Ti_2O_7} - E_{H_2}/2, \tag{2}$$

where $E_{\text{He in } Y_2Ti_2O_7}$, $E_{\text{H in } Y_2Ti_2O_7}$, and $E_{Y_2Ti_2O_7}$ are the total energies of the He- and H-doped defective and defect-free unit $Y_2Ti_2O_7$ cells, respectively, that consist of 16 Y, 16 Ti, and 56 O atoms. E_{He} and E_{H_2} represent the total energies (E_{He}=-0.000448 eV/formula unit, E_{H_2}=-6.7449 eV/formula unit) of a cubic box with 1 nm sides that contains an isolated He atom and gaseous hydrogen molecule (H_2), respectively, which have been calculated using the energy cutoffs of 650 eV for He and 350 eV for H and 1×1×1 Monkhorst-Pack k-mesh. As denoted at the third term of Eq. (2), it was assumed that half the total energy of H_2 indicated to the total energy of an isolated H atom, $E_{\text{H}} = E_{H_2}/2$ =-3.3725 eV/atom, which corresponded to the calculated binding energy of the $H_2/2$ molecule [13, 16]. The bond length of H_2 was calculated to be 0.0751 nm, which was in fairly good agreement with the other calculated (0.0750 nm) [8] and experimental data (0.0741 nm) [17]. Similarly, the formation energies of substitutional He and H in Fe, $E_{\text{defect}}^{\text{He in Fe}}$ and $E_{\text{defect}}^{\text{H in Fe}}$, are defined in the same manner as follows;

$$E_{\text{defect}}^{\text{He in Fe}} = E_{\text{He in Fe}} - E_{\text{Fe}} - E_{\text{He}}, \tag{3}$$

$$E_{\text{defect}}^{\text{H in Fe}} = E_{\text{H in Fe}} - E_{\text{Fe}} - E_{H_2}/2, \tag{4}$$

where $E_{\text{He in Fe}}$, $E_{\text{H in Fe}}$, and E_{Fe} are the total energies of the He- and H-doped defective and defect-free supercells that consist of 128 Fe atoms, respectively. In addition, the defect formation energies of He- and H-occupying Fe-vacancy sites, $E_{\text{defect}}^{\text{He}}$ and $E_{\text{defect}}^{\text{H}}$, are defined in the same manner as follows:

$$\begin{aligned} E_{\text{defect}}^{\text{He}} &= E_{\text{defect}}^{\text{He+V}} - E_{\text{defect}}^{\text{V}} \\ &= \left(E_{\text{He+V in Fe}} - mE_{\text{Fe}}/128 - E_{\text{He}}\right) - \left(E_{\text{V in Fe}} - mE_{\text{Fe}}/128\right) \\ &= E_{\text{He+V in Fe}} - E_{\text{V in Fe}} - E_{\text{He}}, \end{aligned} \tag{5}$$

$$\begin{aligned} E_{\text{defect}}^{\text{H}} &= E_{\text{defect}}^{\text{H+V}} - E_{\text{defect}}^{\text{V}} \\ &= \left(E_{\text{H+V in Fe}} - mE_{\text{Fe}}/128 - E_{H_2}/2\right) - \left(E_{\text{V in Fe}} - mE_{\text{Fe}}/128\right) \\ &= E_{\text{He+V in Fe}} - E_{\text{V in Fe}} - E_{H_2}/2, \end{aligned} \tag{6}$$

where $E_{\text{defect}}^{\text{V}}$ and $E_{\text{V in Fe}}$ are the formation and total, respectively, energies of a vacancy in Fe bulk, and $E_{\text{defect}}^{\text{He+V}}$ is the addition of $E_{\text{defect}}^{\text{He}}$ to $E_{\text{defect}}^{\text{V}}$. $E_{\text{He+V in Fe}}$ and $E_{\text{H+V in Fe}}$ are the total energies of the defective supercells that include each one He and H atom with *m* Fe atoms, *m*=127.

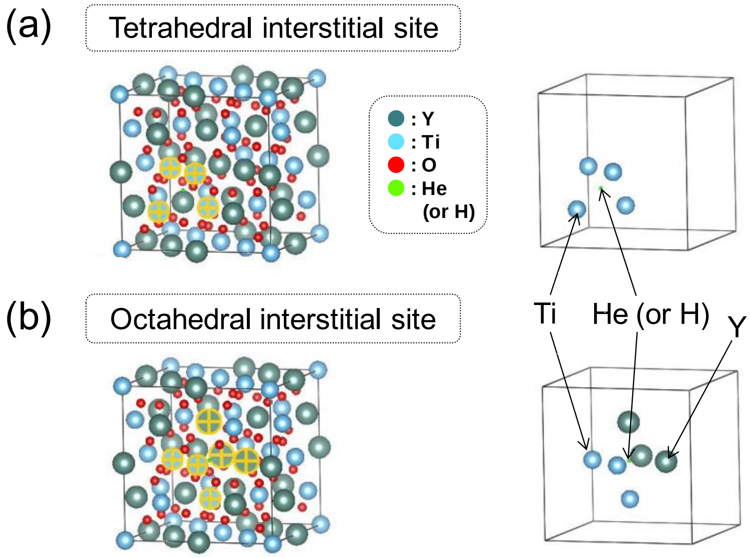

Figure 1. Configurations of various He and H in (a) tetrahedral- and (b) octahedral-interstitial sites surrounded by four Ti^{4+} cations and three Y^{3+} and three Ti^{4+} cations, respectively, in bulk $Y_2Ti_2O_7$.

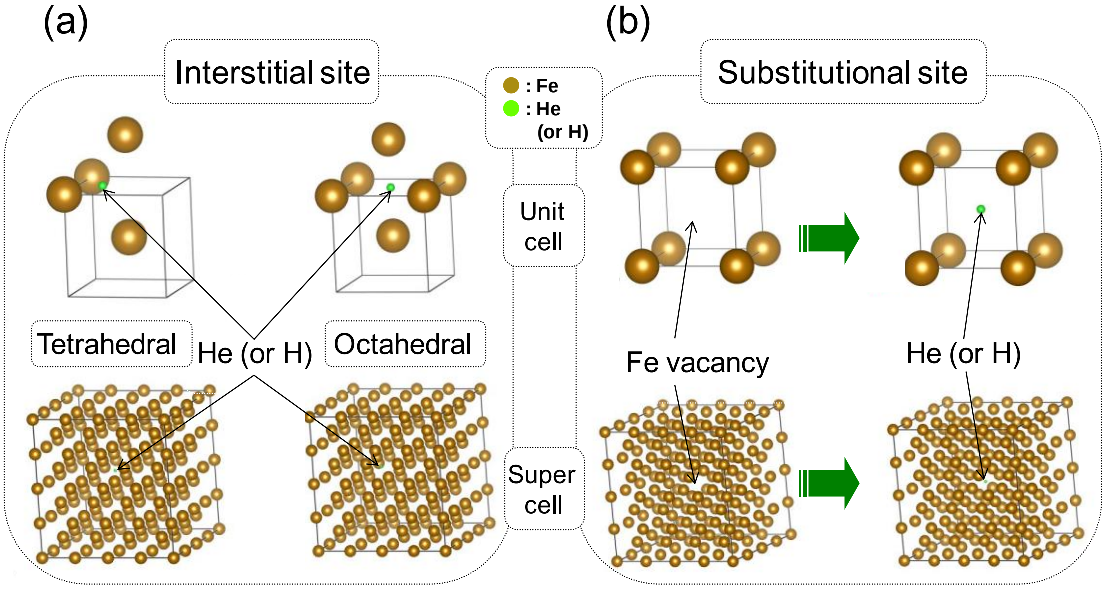

Figure 2. Configurations of various He and H in (a) tetrahedral- and octahedral-interstitial sites and (b) a Fe vacancy (substitutional site).

Results and Discussion

Figure 3 shows calculated formation energies of He and H in tetrahedral- and octahedral-interstitial sites in $Y_2Ti_2O_7$, which have been obtained using Eqs. (1) and (2), where the horizontal axis represents the number of just one He or H atoms in the interstitial sites for the present study. Table 1 summarizes our calculated formation energies of all these defect structures, as shown in Fig. 1, and compared to the other calculated data for only He-dopant, which have already been reported by L. Yang [2]. The doped-He atom prefers to occupy octahedral-interstitial site in $Y_2Ti_2O_7$ to tetrahedral-one, with resulting defect formation energies of $E_{\mathrm{defect}}^{\mathrm{He\,in\,Y_2Ti_2O_7\,(octa.)}}$=1.02 eV and $E_{\mathrm{defect}}^{\mathrm{He\,in\,Y_2Ti_2O_7\,(tetra.)}}$=1.59 eV, respectively, which are in good agreement with the other data within a little bit deviation of less than approximately 0.084 eV. The deviation may be caused by the differences of the set energy cut-off of 650 eV for this work and 500 eV for L. Yang, and the total calculation time of 72 hrs for this work and unknown time for L. Yang. On the other hand, the doped-H atom prefers to occupy tetrahedral-interstitial site to octahedral-one, with resulting defect formation energies of $E_{\mathrm{defect}}^{\mathrm{H\,in\,Y_2Ti_2O_7\,(tetra.)}}$=2.87 eV and $E_{\mathrm{defect}}^{\mathrm{H\,in\,Y_2Ti_2O_7\,(octa.)}}$=3.01 eV, respectively. In addition, the formation energies of H defects are much higher than those of He ones. The result indicates that He atoms can trap at interstitial sites in $Y_2Ti_2O_7$ easier than H.

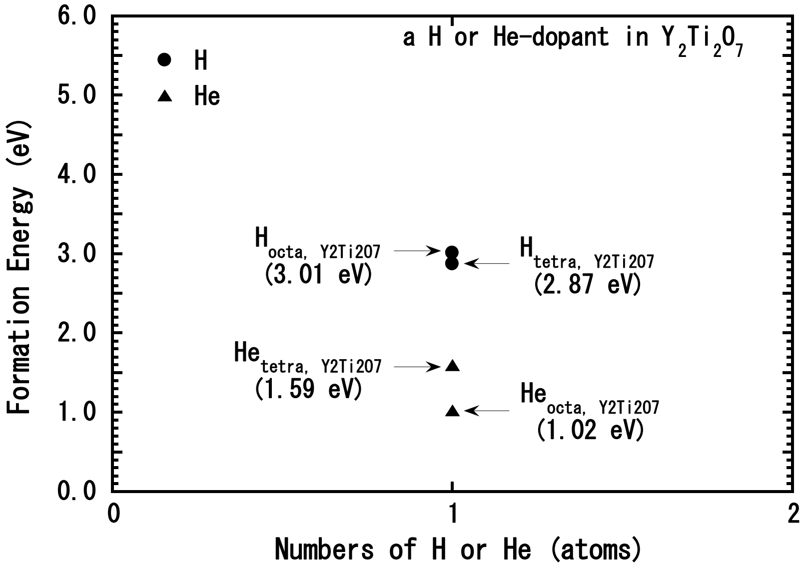

Figure 3. Calculated formation energies of (▲) He and (●) H in tetrahedral- and octahedral-interstitial sites in $Y_2Ti_2O_7$.

Table 1 Calculated formation energies of He and H tetrahedral- and octahedral-interstitial sites in $Y_2Ti_2O_7$, as compared to those of He defects which have been reported by L. Yang.

	Tetrahedral-interstitial site		Octahedral-interstitial site	
	$E_{\mathrm{defect}}^{\mathrm{He\,in\,Y_2Ti_2O_7\,(tetra.)}}$ [eV]	$E_{\mathrm{defect}}^{\mathrm{H\,in\,Y_2Ti_2O_7\,(tetra.)}}$ [eV]	$E_{\mathrm{defect}}^{\mathrm{He\,in\,Y_2Ti_2O_7\,(octa.)}}$ [eV]	$E_{\mathrm{defect}}^{\mathrm{H\,in\,Y_2Ti_2O_7\,(octa.)}}$ [eV]
This work	1.59	2.87	1.02	3.01
Theory by L. Yang [2]	1.51		0.94	

Figure 4 shows calculated formation energies of (a) He and (b) H defects in $Y_2Ti_2O_7$ compared to in Fe, in order to estimate the relative stability of He and H in $Y_2Ti_2O_7$ and Fe. The He atom energy in the octahedral site in $Y_2Ti_2O_7$ is much lower than the corresponding energy in tetrahedral-, octahedral-interstitial, and substitutional, sites in Fe, at 4.47, 4.67, and 2.23 eV, respectively. The calculated formation energy of a vacancy in Fe bulk, $E^{\mathrm{V}}_{\mathrm{defect}}$=2.08 eV, is less than the half of those of interstitial He. These results are consistent with DFT calculations of the reported ones [2, 5], as denoted in Table 2. In contrast, the H atom energy in tetrahedral-, octahedral-interstitial, or substitutional, sites in Fe, at 0.11, 0.24, and 0.41 eV, respectively, which are close to the reported ones [8, 10-12], is much lower than in $Y_2Ti_2O_7$. It is suggested from these results that just one He or H atom in NFAs prefers to occupy individual octahedral-interstitial sites in $Y_2Ti_2O_7$ and tetrahedral-interstitial sites in Fe, respectively. This calculation result indicates that the simultaneous He- and H-induced synergistic effect in void and bubble growths, dislocation bias, and swelling [18], in NFAs does not occur due to dispersion of the nanometer-sized oxide particles in Fe.

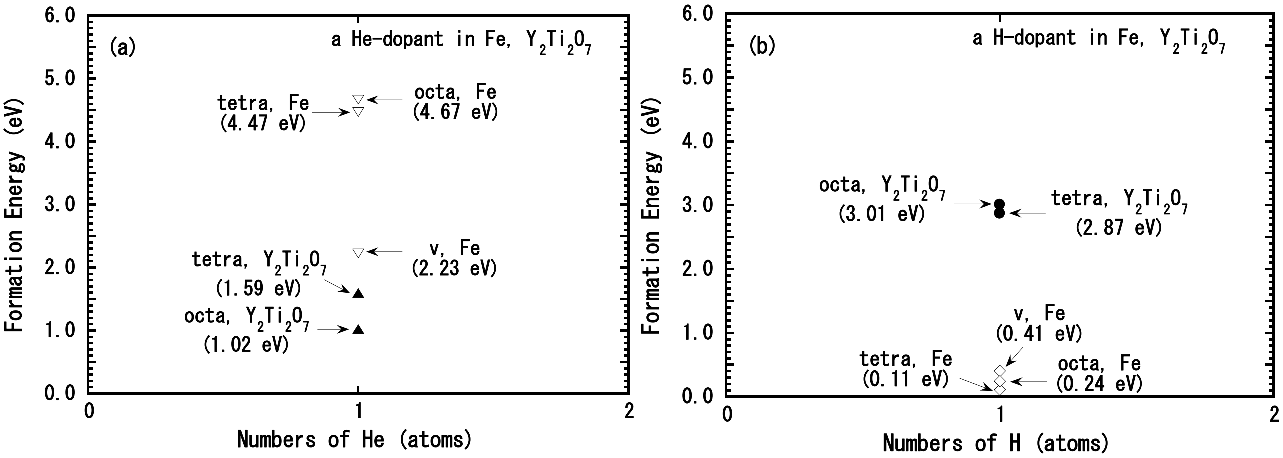

Figure 4. Calculated formation energies of (a) He and (b) H in $Y_2Ti_2O_7$ as compared to those in Fe.

Table 2 Calculated formation energies of He and H IN tetrahedral-, octahedral-interstitial, substitutional sites in Fe, as compared to the references.

	Tetrahedral-interstitial site		Octahedral-interstitial site		Substitutional site	
	$E_{\text{defect}}^{\text{He in Fe (tetra.)}}$ [eV]	$E_{\text{defect}}^{\text{H in Fe (tetra.)}}$ [eV]	$E_{\text{defect}}^{\text{He in Fe (octa.)}}$ [eV]	$E_{\text{defect}}^{\text{H in Fe (octa.)}}$ [eV]	$E_{\text{defect}}^{\text{He in Fe (v)}}$ [eV]	$E_{\text{defect}}^{\text{H in Fe (v)}}$ [eV]
This work	4.47	0.11	4.67	0.24	2.23	0.41
Theory by L. Yang [2]	4.63		4.83		2.28	
Theory by C. C. Fu [5]	4.40		4.58		2.09	
Theory by D. E. Jiang [8]		0.30		0.43		
Theory by S. K. Desai [10]		0.26		0.39		
Theory by W. A. Counts [12]		0.21		0.34		0.57
Experiment by F. Besenbacher [11]						0.63

REFERENCES

[1] G. R. Odette, M. J. Alinger, and B. D. Wirth, Annu. Rev. Mater. Res. 38, (2008), 471-503.

[2] L. Yang, Y. Jiang, G. R. Odette, T. Yamamoto, Z. Liu, and Y. Liu, J. Appl. Phys. 115, (2014), 143508.

[3] P. Erhart, J. Appl. Phys. 111, (2012), 113502.

[4] T. Seletskaia, Y. N. Osetsky, R. E. Stoller, and G. M. Stocks, Phys. Rev. Lett. 94 (2005) 046403.

[5] C. C. Fu and F. Willaime, Phys. Rev. B. 72, (2005,) 064117.

[6] J. M. Pruneda and E. Artacho, Phys. Rev. B 72, (2005), 085107.

[7] T. Seletskaia, Y. N. Osetsky, R. E. Stoller, and G. M. Stocks, J. Nucl. Mater., 351, (2006), 109-118.

[8] D. E. Jiang and E. A. Carter, Phys. Rev. B 70, (2004), 064102.

[9] E. J. Song, H. K. D. H. Bhadeshia, and D. W. Suh, Corrosion Science 77, (2013), 379-384.

[10] S. K. Desai, T. Neeraj, and P.A. Gordon, Acta Materialia, 58, (2010), 5363-5369.

[11] F. Besenbacher, S. M. Myers, P. Nordlander, and J. K. Nørskov, J. Appl. Phys. 61, (1987), 1788.

[12] W. A. Counts, C. Wolverton, and R. Gibala, Acta Materialia 58, (2010,) 4730-4741.

[13] M. L. Fullarton, R. E. Voskoboinikov, S. C. Middleburgh, J. Alloys Comp. 587, (2014), 794-799.

[14] G. Kresse and J. Hafner, Phys. Rev. B 47, (1993), 558.

[15] G. Kresse and J. Furthmüller, Phys. Rev. B 54 (1996) 11169.

[16] G. Herzberg, Molecular Spectra and Molecular Structure: Spectra of Diatomic Molecules, 2nd ed., Krieger, 1989.

[17] K. P. Huber and G. Hertzberg, Molecular Spectra and Molecular Structure IV: Constants of Diatomic Molecules (Van Norstrand Reinhold, New York, 1979).

[18] T. Tanaka, K. Oka, S. Ohnuki, S. Yamashita, T. Suda, S. Watanabe, E. Wakai, J. Nucl. Mater., 329-333, (2004), 294-298.

8.7 STRENGTHENING DUE TO HARD OBSTACLES IN FERRITIC ALLOYS- Y. N. Osetskiy and R. E. Stoller (Oak Ridge National Laboratory)

OBJECTIVE

The purpose of this research is to understand atomic level hardening mechanisms in materials with rigid precipitates such as ODS alloys. Because of the lack of interatomic potentials, direct modeling of such systems is not yet possible. We therefore have developed a model of rigid uncompressible precipitates embedded in a metallic matrix interacting via an empirical EAM potential.

SUMMARY

We have developed a molecular dynamics (MD) based model to simulated dislocation dynamics in the presence of rigid, impenetrable inclusions. These inclusions simulate rigid oxide particles as obstacles to dislocation motion. Interactions between a moving edge dislocation ½<111> {110} and rigid inclusions was modeled over a wide range of parameters such as inclusion size, temperature, strain rate and interaction geometry. It was found that the interaction mechanism depends strongly on the inclusion size and interaction geometry. Some new mechanisms were observed and are now under detailed investigation.

PROGRESS AND STATUS

Introduction

ODS materials have a number of properties making them very attractive for nuclear energy applications [1, 2]. Some of these such as interactions between oxide-particles and other solute elements are strongly related to chemical properties. For example it is expected that existence of small oxide-particles may suppress He-bubble formation and growth. However due to significant complications in describing interatomic interactions such studies are mainly limited by low-scale firs-principle DFT calculations of elementary interactions between constituting elements but not modeling real oxide particles [3, 4]. However, in application to mechanical properties of ODS materials the problem can be resolved in a relatively simple and accurate way. The main issue here is the dislocation interaction with oxide particles and the fact that these particles are much harder than the metallic, e.g. Fe, matrix material. Oxide particles are “strong” obstacles that interact with moving dislocations by the Orowan-like mechanism and the important is not the behavior of dislocations inside the particle or on its interface but the self-interaction of dislocation segments heavily-curved around the obstacle. Therefore, omitting the details of particle-matrix interface does not affect the dislocation particle interactions.

Simulation method

We have developed a molecular dynamics (MD) based model to simulated dislocation dynamics in the presence of rigid, impenetrable inclusions. These inclusions simulate rigid oxide particles as obstacles for dislocation motion. At the MD scale such an inclusion is considered as a super-atom of the corresponding size whose motion follows the usual Newtonian equations. Modeling of atomic-scale dislocation dynamics is a very resource-demanding process for a) the simulated crystal should be large to accommodate long enough dislocation which can be strongly curved around the large obstacle and b) large number of time steps should be integrated to model a relatively slow dislocation. In practice, the largest obstacle we simulate at the moment, 7 nm in diameter, needs ~6.3 million mobile atoms integrated over a few million steps to model dislocation moving at about 1 m/s. Using this model we are studying dislocation – rigid inclusion interactions over a wide range of parameters such as inclusion size, interaction geometry, dislocation velocity and applied deformation strain rate, ambient temperature etc.

Current progress

For the last six months we have continued modeling of the largest at that time obstacles, 6 nm in diameter and have started a larger, 7 nm, inclusion. The necessity of this came from the observation that the mechanism of interaction between a moving dislocation and rigid inclusion depends very much on the obstacle size. More precisely it depends on the inclusion curvature and therefore on the cross-section of the inclusion in the dislocation glide plane. We therefore investigate this particular effect and have found that it is more important for large inclusions. The results were treated and we have found that the obstacle critical resolved shear stress (CRSS) follows the dependence versus the actual obstacle size where it is intersected by the dislocation slip plane. A certain asymmetry was found for the obstacle above the slip plane, which is stronger than the equivalent obstacle below the slip plane. An example of CRSS dependence as a function of the interaction geometry is presented in Figure1. We explain this by the fact that interatomic potentials are asymmetric as well and the absolute value of forces generated during compression is higher than that for tension. This therefore affects to the obstacle strength through the compression and tension regions around edge dislocations. We do not expect a similar effect for screw dislocations. It is interesting that not only CRSS depends on the interaction geometry but also the interaction mechanism itself. This is illustrated in Figures 2 and 3. Thus in Figure 2 shows the edge dislocation ½<111>(110) and 6 nm inclusion with its equator in the dislocation slip plane before (a) and after (b) interaction. The Orowan sheared loop shown in Figure 2b is formed due to this interaction. This mechanism provides the maximum strengthening as shown in Figure 1.

Figure 3 show the same obstacle but in the configuration when its equator is half of the radius below the dislocation slip plane and the corresponding CRSS in Figure 1 is for R=0.5. The position of slip plane can be clearly seen on Figure 3a as a red line and it moves from left to right.

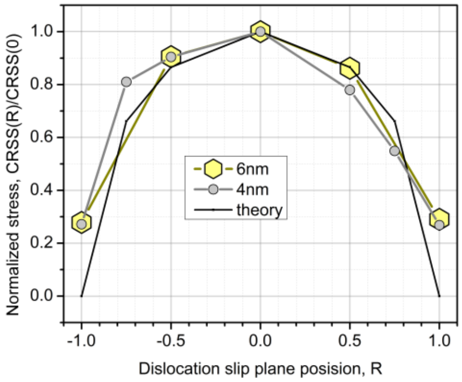

Figure 1. Dependence of the CRSS vs distance between the inclusion equator and dislocation slip plane. Black solid line shows the estimation based on the area of the corresponding cross-section through the inclusion.

The configuration obtained after the dislocation bypassed the inclusion is shown in Figure 3b. One should take into account that in this figure dislocation is seen again on the left side of the obstacle where it appeared due to periodic boundary conditions in the slip plane. A small interstitial loop is left behind the inclusion and the corresponding negative superjog was created on the dislocation line. This can be seen more clearly in Figure 3c where the view along the dislocation Burgers vector is shown. The loops size and shape is approximately equivalent to the upper part of the inclusion above the dislocation slip plane.

These examples demonstrate clearly how the interaction mechanism depends on the interaction geometry. The mechanism on Figs.3 is observed for the first time and was not described yet in the literature. The usual deformation mechanisms result in formation vacancy-type defects because this is energetically more favorable. Formation of interstitial-type defects occurred on these inclusions is because they are very strong obstacles. In fact, they are obstacles of maximum possible strength. We are going to investigate these mechanisms in more details because we think they should have important influence to the creep behavior of ODS alloys.

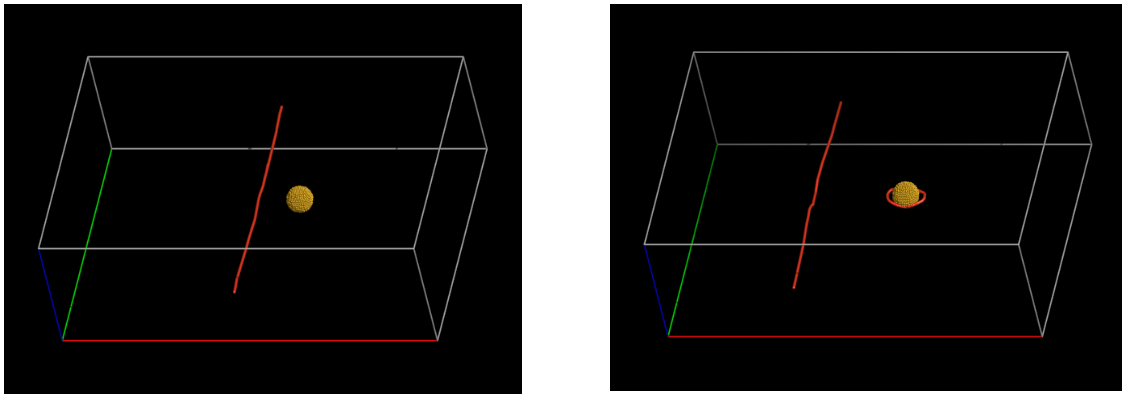

Figure2. Edge dislocation ½<111>(110) and 6nm inclusion with its equator in the dislocation slip plane before at) and after (b) interaction. The Orowan sheared loops shown on the right is formed due to this interaction. This mechanism provides the maximum strengthening.

We have also concluded that 6 nm obstacle might be too small for the treatment within the continuum approach to find out the general description of the effect. So we have launched a new series of deformations for 7 nm rigid particle. The full set of parameters to be studied includes temperature: 100, 300, 450 and 600 K, different levels of the dislocation slip plane relatively to the particle equator: 0, +-0.5R, +-0.75R and +-R, where R=7 nm is the particle radius and applied strain rates: 1, 2 and 5 in units of 10^6 s^{-1}. This work is in progress now.

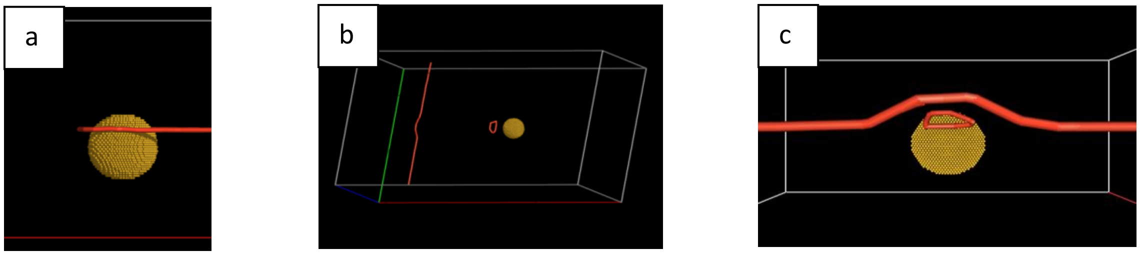

Figure 3. Edge dislocation ½<111>(110) and 6nm inclusion with its equator half of the inclusion radius below the dislocation slip plane. a – view to the inclusion along the dislocation slip plane where red line is the bowing around. Dislocation glides from left to right. Centre – total view to the crystal after the interaction. Dislocation has a negative created due to an interstitial dislocation loop left behind the inclusion. Right – view along the dislocation Burgers vector.

REFERENCES

[1] X.L. Wang,∗, C.T. Liu, U. Keiderling, A.D. Stoica, L. Yang, M.K. Miller, C.L. Fu, D. Ma, K. An, “Unusual thermal stability of nano-structured ferritic alloys”, Journal of Alloys and Compounds 529 (2012) 96– 101.

[2] M.K. Miller, D.T. Hoelzer, E.A. Kenik, K.F. Russel, “Stability of ferritic MA/ODS alloys at high temperatures”, Intermetallics 13 (2005) 387–392.

[3] C.L. Fu, M. Krcmar, G.S. Painter, & X.Q. Chen, “Vacancy mechanism of high oxygen solubility and nucleation of stable oxygen-enriched clusters in Fe”. Phys. Rev. Lett. 99, 225502 (2007).

[4] J. Brodrick, D.J. Hepburn, G.J. Ackland, “Mechanism for radiation damage resistance in yttrium oxide dispersion strengthened steels”, J. Nucl. Mater., 445 (2014) 291–297.

8.8 SIMULATION OF TRIPLE ION-BEAM IRRADIATION IN Fe SINGLE CRYSTALS USING STOCHASTIC CLUSTER DYNAMICS -

Jaime Marian, Tuan Hoang (Lawrence Livermore National Laboratory)

OBJECTIVE

The objective of this work is to ascertain the status of modeling with respect to triple ion-beam irradiations (self-ions, He and H ions) in ferritic steels and their derivative materials. To this end we use stochastic cluster dynamics modeling parameterized with the latest energetics data obtained with electronic structure calculations and state-of-the-art atomistic semiempirical potentials.

SUMMARY

Helium and hydrogen are produced at rates of about 10 and 40 appm per dpa during fusion reactor operation. Although, the effects of He and H on microstructure are more or less well understood independently, their combined action under irradiation has not been established yet and the experimental evidence obtained over three decades of research is inconclusive. In recent years, electronic structure calculations have shed some light on the joint effect of He and H on defect cluster stability, and the associated energetics has begun to be used in long-term models of damage accumulation. In this work, we present stochastic cluster dynamics (SCD) simulations of triple (Fe/He/H) ion beam irradiations of pure single crystal Fe. With SCD we can perform simulations of multiple damage species up to doses beyond the 1-dpa limit. We calculate the amount of swelling as a function of temperature and point to the limitations of the He/H interaction model by comparing and discussing the experimental data.

Introduction: Fusion structural materials

One scientific challenge for fusion energy is to develop an understanding of the response to radiation damage accumulation of the first wall and breeding-blanket materials that will likely determine the operating parameters and hence the energy efficiency (operating temperature) and overall lifetime of any fusion reactor. The structural materials of a fusion reactor are exposed to a hard neutron spectrum that results in atomic displacement cascades and transmutation nuclear reactions. The displacement cascades produce vacancies, interstitials, and a variety of extended defects, but of particular concern is the simultaneous production of helium and hydrogen at dose rates and accumulated concentrations for which the materials and engineering communities have little practical experience and hence little understanding.

Displacement damage and the generation of He and H

The rate of atomic displacements per atom (dpa) will amount to 20-30 dpa/year in steels, while the He and H gas produced by transmutation nuclear reactions will be 10-15 appm and 40-50 appm per dpa respectively, all of which are produced continuously and simultaneously. There is considerable experience both experimental and modeling for low dpa production simultaneously with He that is relevant to fission reactors [1]. In fusion conditions, the dpa and He rates an one to two orders of magnitude greater, and whose effects are the object of careful experimental characterization [2], but the simultaneous transmutation production of H introduces a new variable for which little experimental data and modeling exist.

Transmutation production of gas atoms

Nuclear reactions (n,α), (n,p), and (2n,p) from neutrons result in the transmutation production of the gas atoms He and H. In a comparison of a fission reactor neutron spectrum and a computed DEMO neutron spectrum it is observed that the fluxes per lethargy unit are greater for the fusion spectrum at all energies above 2 MeV [3]. It is noted in [4] that because of inadequacy of the modeling of the DEMO spectrum, the fusion flux below 2 MeV may also be greater than the fission spectrum. Moreover because every fusion reaction yields a 14.1 MeV neutron there is a peak in the neutron spectrum at that energy.

The production and retention of H in combination with He in fission reactor fcc austenitic steels has been established experimentally [5], along with some early evidence for the synergistic consequences of simultaneous H and He production together with displacement damage. While this discovery identified interesting degradation of the irradiated steels associated with the synergy of H and He, in fusion the consequences of transmutation gas production are unknown, although it would not be unreasonable to expect them to result in more serious problems because of the much higher production rates and the much greater desired lifetime doses.

Experimental evidence for He-H synergies

In a 1994 report to General Atomics, Bullough reviewed the current understanding of possible radiation effects in vanadium alloy and in the ferritic-martensitic (F/M) steel 9Cr-1Mo known as T91 (also P91). It is noted that dual ion-beam data on pure vanadium shows evidence for both helium and hydrogen leading to significant swelling in pure vanadium in the presence of simultaneous production of atomic displacement damage from heavy ion irradiation [6]. It is emphasized in this report that an important issue for F/M steel application as the fusion first wall material was (and still is today) “Resistance to irradiation damage in the presence of the helium and hydrogen that will be produced by the high-energy fusion neutrons…” [6]. While the development of core materials for fast fission reactors benefited from the availability of testing reactors, no such facilities exist today for the development of fusion materials. This then leaves us with a strategy of accumulating data from simulation experiments that inform and are understood through coupling to computational models. Unfortunately, this approach is not without uncertainty arising from unexpected phenomena or from the difference between the simulation conditions and those of an actual fusion facility; dose rate, details of the damage cascade arising from the kinetics of the cascade inducing particle, specimen dimensions, and details of the chemistry, phase and microstructural features of the material under test. Early evidence for a He and H synergy in the presence of displacement damage in F/M steel (1986) was given by Farrell and Lee [7] who investigated the combined effects of the high input of He and H along with displacement damage using multiple simultaneous ion beams (MSIB) of He, H, and Fe and reported a rather significant increase in the peak swelling rate in 12Cr-1Mo steel.

It is useful to note that while the primary motive for understanding the synergistic role of displacement damage and He and H production in F/M steels comes from a need to identify radiation tolerant materials for fusion energy this same challenge became a research issue for fission energy austenitic steels when it was suggested that hydrogen might serve the same role as helium in stabilizing small vacancy clusters to form bubbles that once reaching critical size lead to void formation [8]. Because hydrogen is a fast diffuser it was commonly held that hydrogen in austenitic (stainless steels) steels could not be retained at high concentrations and would diffuse out. Experimental work led to the discovery that hydrogen, which is produced by nuclear reactions but which is also introduced into steels by a variety of other processes both nuclear and chemical, is retained when helium nucleated cavities become a significant part of the microstructure [9].

Modeling triple Fe/He/H implantation

Experimental and computational evidence of vacancy/He/H interactions in Fe

Results obtained from positron annihilation lifetime and coincidence Doppler broadening measurements indicate that He atoms are more effective for micro-void formation than H atoms [10]. Therefore, He will first form bubbles with existing vacancy clusters. As He bubbles grow due to absorption of more He and vacancies in the volume, their surface areas increase and the surrounding stress fields attract H atoms towards them [11] and form the V-He-H triple clusters. This would also explain the existence of an incubation time for V-He-H clusters to form, and the higher the He^+ damage rate is, the sooner these triple clusters appear. The presence of He within the crystal has been proved experimentally to significantly enhance the trapping of hydrogen, even for periods of years after irradiation [12-14]. Comparing the vacancy cluster number densities in the specimens for the two cases of dual (Fe^{3+}+He^+) ion-irradiation and triple ion-irradiation, we see that the presence of hydrogen under triple ion-irradiation condition has caused a reduction in vacancy cluster and vacancy-He bubble populations.

For its part, the computational characterization of V/He/H interaction effects come from three main sources. Kirsanov et al. [15] noted that the small binding energy of H and its high mobility in bulk Fe allows them to find otherwise mobile He-2V clusters and attach itself to the free vacancy. He-2V clusters are the main carriers of He during gas void formation, and thus one may expect a delay of helium bubble formation caused by H, and an increased number of nucleation sites. Using DFT calculations, Hayward and Deo [16] analyzed the energetics and structure of small V-He-H bubbles, and explained the seemingly observed He/H synergy as a consequence of bubble growth through helium induced loop punching, aided by the presence of H, instead of as a direct interaction between H and He. The H benefits from an increased area of free surface on which to bind. However, we discount this possibility, as it would require insertion doses much in excess of those present in fusion environments. Finally, Ortiz et al. [17] also performed DFT calculations of V-He-H complexes and obtained a weak interaction between H and He in bubbles. This is in contrast to previous DFT results of a strong trapping of H at He. The strong preference of He and H to occupy regions with low electronic density (such as vacancies) explains this discrepancy, with vacancy-He and vacancy-H binding forces screening the repulsive interaction between He and H.

Model of bubble formation in Fe in the presence He and H atoms

Based on the evidence put forward in the preceding section, we implement the following model of V/He/H interaction:

- Both He and H atoms display extremely fast three-dimensional diffusion and cover the entire configurational space very efficiently.
- Small vacancy clusters can attract H atoms. However, these atoms do not occupy substitutional vacant sites. Instead they bind (with binding energy: 0.5 eV) at external tetra or octahedral interstitial positions. Thus, they do not intrinsically stabilize small vacancy clusters.
- He atoms can stabilize small vacancy clusters by occupying vacant sites. However, these V-He complexes can retain some mobility particularly if the number of He atoms is not equal to the number of vacancies.
- If a H finds one of these mobile V-He complexes, turning it into a V-He-H complex, their mobility is then suppressed.
- It is assumed that triple V-He-H clusters are stable across the entire temperature range, such that no vacancies, helium or hydrogen can detrap from these clusters.

The implicit temperature dependence of the above model stems from the competition between two main mechanisms. At lower temperatures, H and He atoms are more strongly bound to V-H and V-He clusters respectively (more potential nucleation points), but the mobility of these clusters is small and there is less coalescence as well as losses to sinks. At high temperatures, nucleated bubbles can coalescence giving rise to larger bubbles, but losses to sinks increase. The optimum compromise is found and the so-called peak swelling temperature.

As well, when we increase the He damage rate, the population of V-He-H clusters also increases. However swelling may decrease because, as more helium is inserted into the volume, the number of nucleated V-He bubbles also increases, but they become smaller because helium atoms will now combine with many smaller vacancy clusters instead of few larger ones. Because of that, the stress fields around these V-He bubbles are weaker, and the amount of hydrogen atoms attracted to them decreases accordingly. As V-He clusters become smaller, the reactions between hydrogen and these clusters are less likely to take place. This leads to the decrease of the stable V-He-H cluster population which is the main cause of volume swelling in materials under multi-ion irradiation. On the other hand, loading more hydrogen into the volume causes more swelling due to the increase of the stable V-He-H triple cluster population. Thus, we can see that the He:H ratio directly effects the amount of volume swelling and the formation of defect clusters in the materials.

Stochastic cluster dynamics method for long-term damage accumulation

Here we use the stochastic cluster dynamics method (SCD) [18] to perform all simulations. SCD is a stochastic variant of the mean- field rate theory technique, alternative to the standard ODE-based implementations, that eliminates the need to solve exceedingly large sets of ODEs and relies instead on sparse stochastic sampling from the underlying kinetic master equation. Rather than dealing with continuously varying defect concentrations in an infinite volume, SCD evolves an integer-valued defect population N_i in a finite material volume Ω, thus avoiding combinatorial explosion in the number of ODEs. This makes SCD ideal to treat problems where the dimensionality of the cluster size space is high, e.g., when multispecies simulations—for example involving energetic particles, He, H, etc., simultaneously—are of interest. SCD recasts the standard ODE system into stochastic equations of the form:

$$\frac{dN_i}{dt} = \tilde{g}_i - \sum_j \tilde{s}_{ij} N_i + \sum_j \tilde{s}_{ji} N_j - \sum_{i,j} \tilde{k}_{ij} N_i N_j + \sum_{j,k} \tilde{k}_{jk} N_j N_k$$

where the set $\{\tilde{g}, \tilde{s}, \tilde{k}\}$ represents the reaction rates of 0th (insertion), 1st (thermal dissociation, annihilation at sinks), and 2nd (binary reactions) order kinetic processes taking place inside V. Calculations involving clusters with three dimensions in the number of species are costly in computation and memory, and have been brought about by the implementation of several enhancements to SCD, such as τ-leaping and volume re-scaling [19].

For the SCD calculations, the baseline parameterization is that used by Marian and Bulatov [18], to which the damage/He/H model described in Section 4.2 is added in terms of additional energetics and specification of extra key reactions. By way of example, we show in Figure 1 the PKA cumulative damage function that defines the source term.

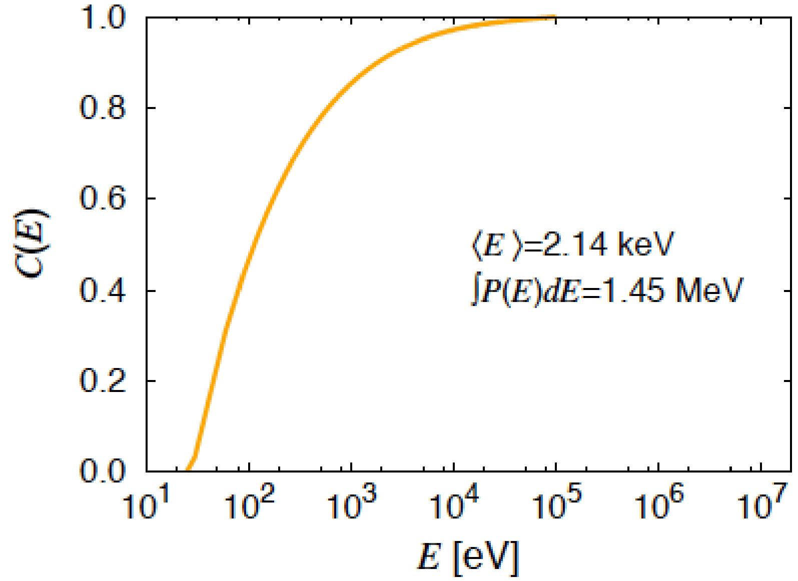

Figure 1. Cumulative damage function for 10.5-MeV Fe ions in Fe from SRIM calculations. The average PKA energy from this function is <*E*> = 2.14 keV, while the total damage energy is 1.45 MeV.

C(*E*) is sampled during every insertion event and defect distributions are generated from existing cascade statistics for every PKA energy *E*. This process is repeated until the total damage energy of 1.45 MeV is reached. This process completes a full insertion event, which occurs at a rate consistent with the prescribed dose rate.

Calculations

The calculations are run up to a total dose of 1 dpa and all defect populations are tallied as a function of dose. Figure 2 shows the evolution of the defect species with dose at a temperature of 510°C. The calculations reveal interesting information, such as the incubation times of each species subpopulation, or the metastability of certain types of clusters.

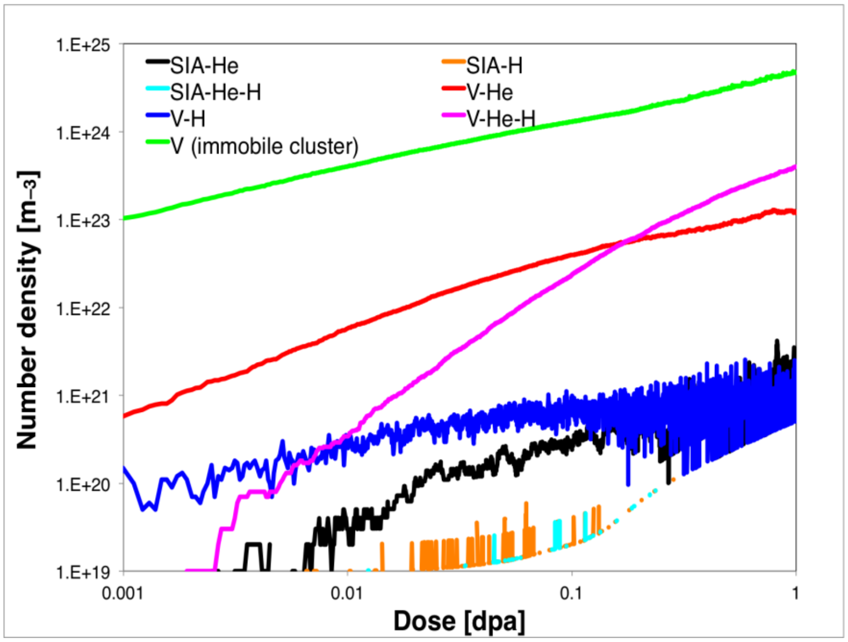

Figure 2. Evolution with dose of all defect species at a temperature of 783 K.

The total amount of swelling can be calculated by summing over the number of vacancies contained in all stable, immobile vacancy clusters, and dividing by the number of lattice sites in the simulation volume:

$$S = \frac{\Omega_a \sum_i^{N_V} n_i}{\Omega \rho_a},$$

where Ω_a and ρ_a are the atomic volume and density respectively. This swelling ratio is plotted in Figure 3 as a function of dose at the four temperatures considered in this study. As the figure shows, the differences are not remarkable, although a clear temperature dependence can be distinguished. This is what is shown in the inset, where a peak swelling temperature of around 800 K can be appreciated for the swelling levels after 1 dpa.

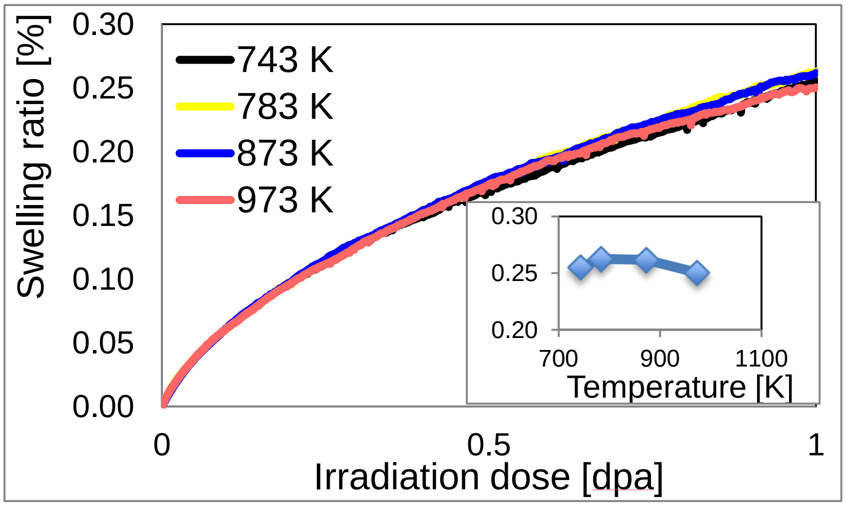

Figure 3. Evolution with dose of the swelling ratio as a function of temperature. The inset shows the amount of swelling after 1 dpa of irradiation.

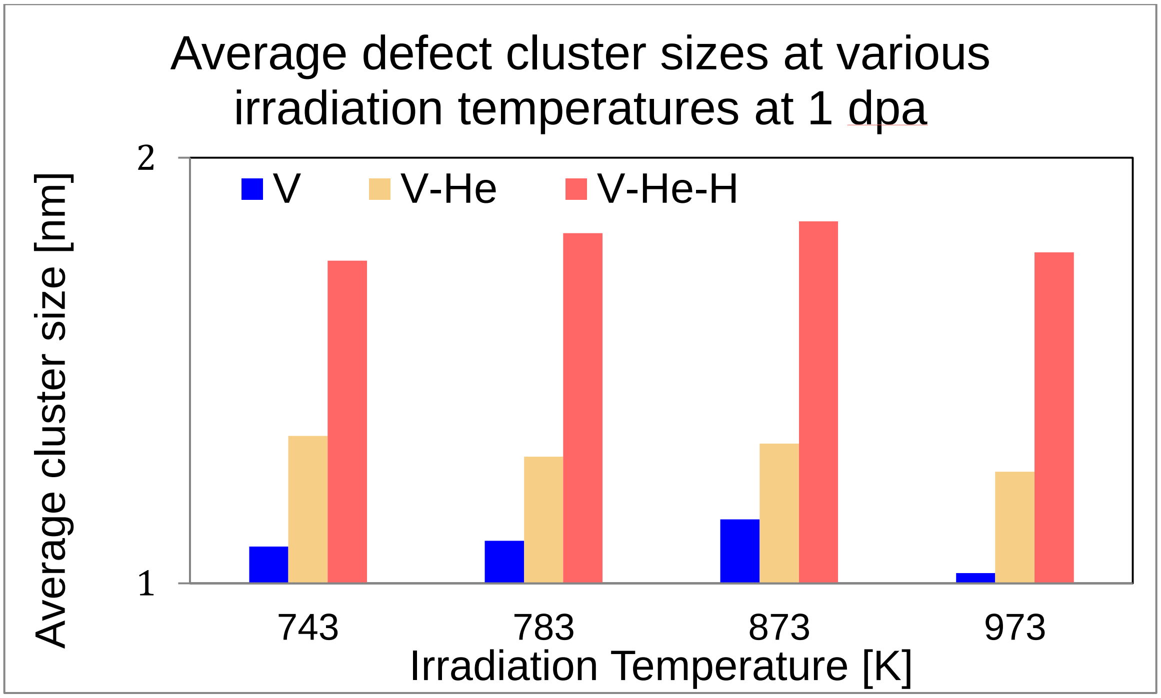

Figure 4. Average vacancy cluster size as a function of temperature after an accumulated dose of 1 dpa.

More striking perhaps is the average bubble size after 1 dpa, shown in Figure 4. There, it can be clearly seen that triple V-He-H clusters are significantly larger than their V-He and pure V counterparts. We note that at this dose level, the average size is still too small to be indicative of anything but bubble growth. In other words, 1 dpa is still well below the required dose to achieve runaway void growth and the bubbles are clearly in their growth phase.

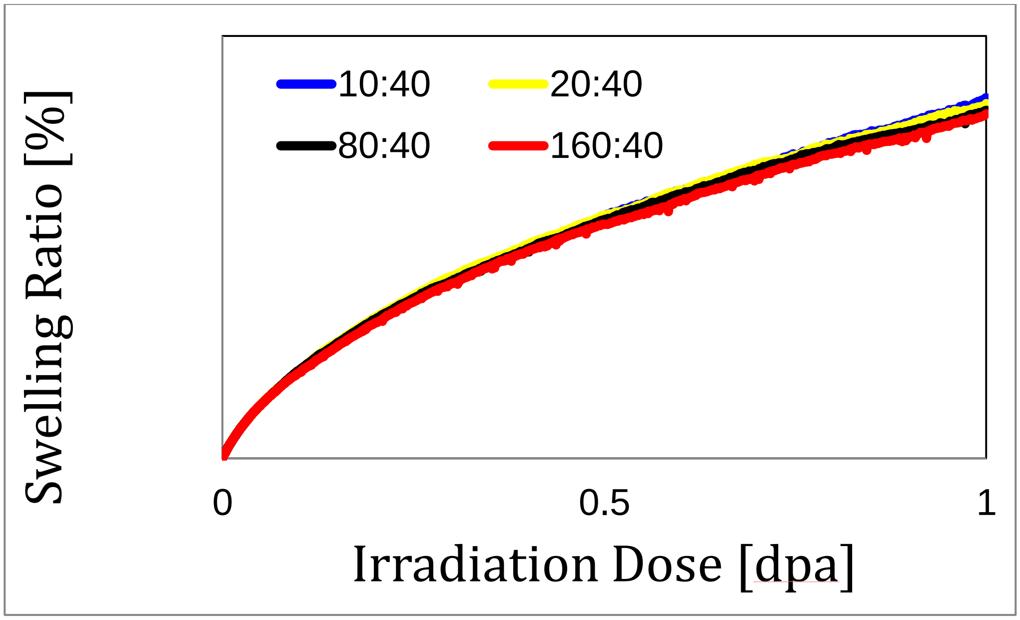

Figure 5. Effect on the swelling ration of the relative amount of He to H injected in the system.

We have also looked at the effect on swelling of the He-to-H insertion ratio. This is what is plotted in Figure 5 in terms of atomic parts per million per dpa for each species. Again, the differences are not remarkable, although clearly the higher the content of He relative to H, the lower the swelling. If one looks at the evolution with dose of the average bubble size with this ratio, shown in Figure 6, this trend is maintained, although it appears that there exists a threshold He-to-H level beyond which the bubble size does no longer change. This is the case for rations of 80:40 and 160:40, where the average diameter saturates at about 1.2 nm, down from 1.8 nm at the fusion ratio of 10:40.

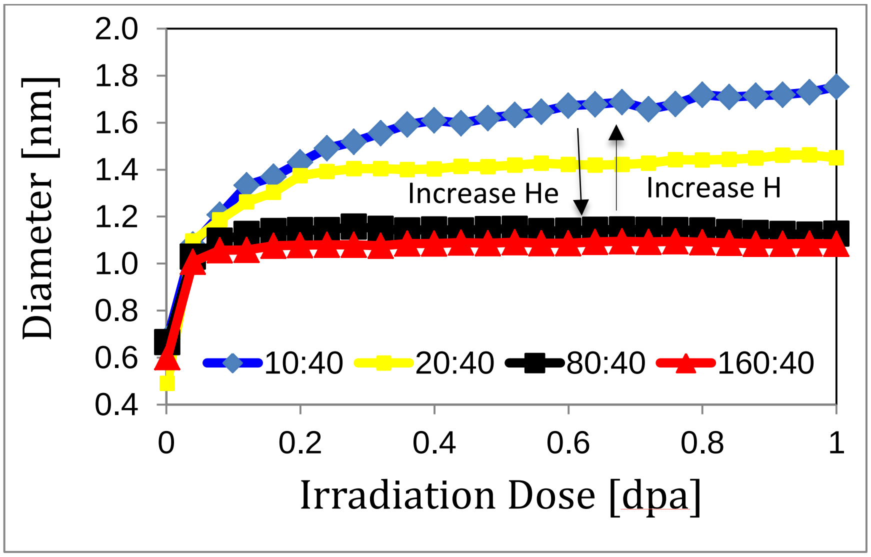

Figure 6. Evolution of the average bubble diameter with dose at 743 K as function of the He-to-H ratio.

Finally, we study the synergistic effect for the model of damage/He/H interaction described here. To this end, we plot in Figure 7 the average bubble size from three different simulations: (i) dual ion beam exposure with self-ions and H ions, (ii) dual ion beam exposure with self-ions and He, (iii) triple ion beam exposure with self-ions, He and H ions. Clearly, the triple beam case results in the largest bubbles (in the form of triple clusters).

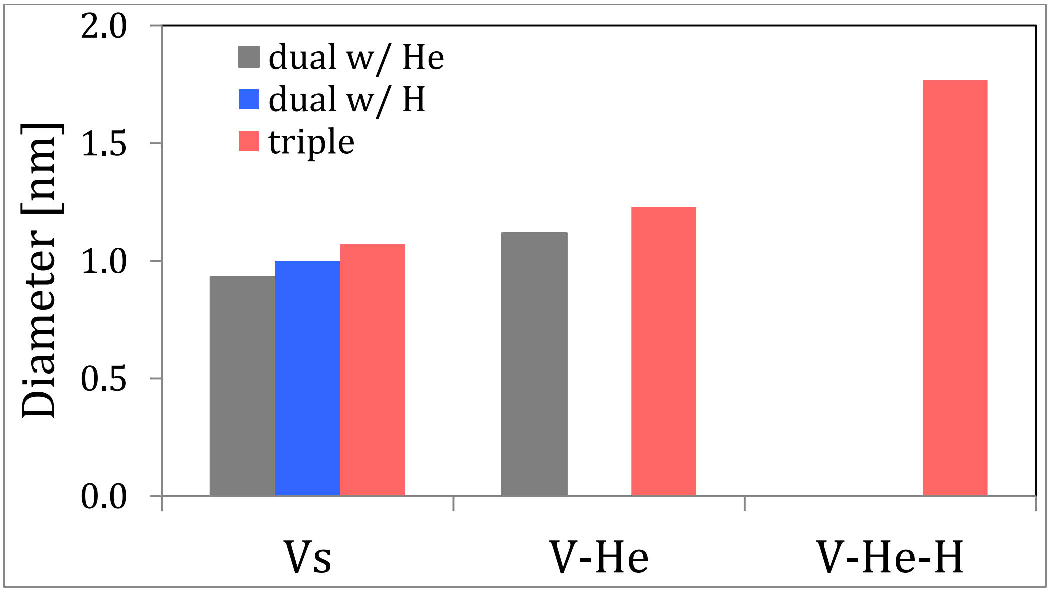

Figure 7. Average bubble diameter after 1 dpa of irradiation at 743 K under dual and triple ion-beam irradiation conditions.

Discussion and Summary

Our results do predict a significant influence of simultaneous He/H co-implantation on the average bubble size although not on the total amount of swelling. The available experimental evidence points to the importance of bubble/void size as the measure responsible for an increased swelling. Coexistence of He and H appears to limit the number density of available nucleation sites, resulting in much larger bubble sizes than when only He is present. This results in a lower cross section for SIA-bubble interaction, and hence and increased probability of SIA-loop trapping at sinks. In any case, the lack of difference in total swelling means that the current simulation model does not provide a mechanism for swelling increases in its present form. More work, both experimental and simulations, will have to be carried out to determine whether synergistic effects do indeed play an important role in the microstructural evolution of irradiated F/M steels.

This work was performed under the auspices of the U.S. Department of Energy by Lawrence Livermore National Laboratory under Contract DE-AC52-07NA27344. This material is based upon work supported by the U.S. Department of Energy, Office of Science, Office of Fusion Energy Sciences. IM code: LLNL-TR-657134

REFERENCES

[1] Haibo Liu, Mohamed A. Abdou, Larry R. Greenwood, Fusion Engineering and Design 88, (2013), 2860- 2864.
[2] G. R. Odette, T. Yamamoto, Y. Wu, E. Stergar, N. J. Cunningham, R. J. Kurtz, D. J. Edwards, Fusion Reactor Materials Program December 31, 2011 DOE/ER-0313/51 - Volume 51, p. 90.
[3] R. Bullough, report: “Factors involved in the use of vanadium alloys and ferritic steels for the ITER first wall/blanket and divertor”, UKAEA FUS 554, EURATOM/UKAEA Fusion, June 2009.
[4] M.R. Gilbert and J. –Ch. Sublet, 2011 Nucl. Fusion 51 043005.
[5] M.R. Gilbert, S.L. Dudarev, S. Zheng, L.W. Packer and J.-Ch. Sublet, Nucl. Fusion 52, (2012), 083019, p. 12.

[6] F.A. Garner, E.P. Simonen , B.M. Oliver , L.R. Greenwood , M.L. Grossbeck , W.G. Wolfer , P.M. Scott , J. Nucl. Mater., 356, (2006), 122–135.
[7] F. Kano, Y. Arai, K. Fukuya, N. Sekimura and S. Ishino. J. Nucl. Mater 203, (1993), 151.
[8] K. Farrell and E. H. Lee, "Ion Damage in a Fe-10Cr-6Mo-0.5Nb Ferritic Steel," Radiation-Induced Changes in Microstructure: I, STP 955, American Society For Testing and Materials, Philadelphia, 1987, pp. 498-507.
[9] F. A. Garner and L. R. Greenwood, Radiation Effects and Defects in Solids, 144 (1998) 251-283.
[10] T. Ishizaki, Q. Xu, T. Yoshiie, S. Nagata, T. Troev, J. Nucl. Mater. 307–311 (2002) 961-965.
[11] G.D. Tolstolutskaya, V.V. Ruzhytskiy, I.E. Kopanets, S.A. Karpov, V.V. Bryk, V.N. Voyevodin, F.A. Garner, J. Nucl. Mater., 356,(2006), 136-147.
[12] F.A. Garner, E.P. Simonen, B.M. Oliver, L.R. Greenwood, M.L. Grossbeck, W.G. Wolfer, P.M. Scott, J. Nucl. Mater., 356, (2006), 122-135.
[13] F.A Garner, B.M Oliver, L.R Greenwood, M.R James, P.D Ferguson, S.A Maloy, W.F Sommer, J. Nucl. Mater., 296, (2001), 66-82.
[14] S. Linderoth, A. V. Shishkin, Philos. Mag. A 55 (3) (1987), 291.
[15] V. V. Kirsanov and M. V. Musina, J. Nucl. Mater. 191-194,(1992), 1318-1322.
[16] E. Hayward, C. Deo, J. Phys.: Condens. Matter 24, (2012), 265402.
[17] C. J. Ortiz, R. Vila, J. M. Pruneda,arXiv:1205.6374v2 [cond-mat.mtrl-sci].
[18] Jaime Marian, Vasily V. Bulatov, J. Nucl. Mater., 415, (2011), 84–95.
[19] T. Hoang, J. Marian, V. V. Bulatov, D. Chrzan, A. Arsenlis, P. Hosemann, submitted to J. Comp. Phys (2014).

8.9 MOLECULAR DYNAMICS MODELING OF ATOMIC DISPLACEMENT CASCADES IN 3C-SiC – G. D. Samolyuk, Y. N. Osetskiy and R. E. Stoller (Oak Ridge National Laboratory)

OBJECTIVE

The objective of this effort is to characterize the nature of primary radiation damage in SiC to provide a basis for understanding the experimentally observed fluence-temperature map of the irradiated microstructure. Recently reported results demonstrated that the most commonly used interatomic potentials (Tersoff [1]) are inconsistent with *ab initio* calculations of defect energetics. In order to demonstrate the sensitivity of cascade recombination to the value of barrier recombination additional cascade simulations have been done with the newly developed Gao-Weber potential [2].

SUMMARY

We demonstrated that the most commonly used interatomic potentials are inconsistent with *ab initio* calculations of defect energetics. Both the Tersoff potential used in this work and an alternate modified embedded atom method potential reveal a barrier to recombination which is much higher than the density functional theory (DFT) results. The barrier obtained with a newer potential by Gao and Weber is closer to the DFT result but the overall energy landscape is significantly different. This difference results in a significant difference in the cascade production of points defects. We have completed both 10 keV and 50 keV pka energy cascade simulations in SiC at temperatures equal to 300, 600, 900 and 1200 K. Results were obtained for the number of stable point defects using the Tersoff/ZBL and Gao-Weber/ZBL (GW) interatomic potentials. In a contrast to Tersoff potential, the GW potential produces almost twice as many C vacancies and interstitials at the time of maximum disorder (~0.2 ps) but only about 25% more stable defects at the end of the simulation. Only about 20% of the carbon defects produced with the Tersoff potential recombine during the in-cascade annealing phase, while about 60% recombine with the GW potential. The GW potential appears to give a more realistic description of cascade dynamics in SiC, but still has some shortcomings when the defect migration barriers are compared to the *ab initio* results.

PROGRESS AND STATUS

Introduction

Irradiation effects in solids have received a great deal of attention since the 1960s. This attention was mostly related to metals. Designing silicon carbide components for fusion reactor blankets requires a basic understanding of defect formation and evolution, and the associated property changes. Despite the large range of phenomenological studies of observed effects, the microstructural origin of these effects is not well understood.

The molecular dynamics (MD) study of cascades evolution, based on application of empirical potential, is an important tool for understanding the irradiation effects. According to our analysis of SiC publications, most of the cascades modeling in SiC was executed with Tersoff potential. However, as we demonstrate in our research, the Tersoff potential gives unphysical large defect migration barriers. Thus, in the current investigation we investigate the number and distribution of stable point defects in cascades in SiC with both Tersoff and GW interatomic potentials.

Simulation Method

The GW potential code was introduced in the LAMMS molecular dynamics (MD) package [3]. The good agreement between MD and first-principles calculated formation energies of twelve most typical defects were demonstrated (see Table 1).

Table 1. The formation energies (in eV) of interstitials (dumbbells C^+-C<100>, C^+-Si<100>, Si^+-C<100>, Si^+-Si<100> and tetrahedral interstitals C_{TC} …), antisite defects (C_{Si}, Si_C) and vacancies (C(V), Si(V)), together with those calculated by *ab initio* methods.

Defects	*ab initio*	Current report
C^+-C<100>	3.16	3.05
C^+-Si<100>	3.59	3.44
Si^+-C<100>	10.05	7.75
Si^+-Si<100>	9.32	5.51
C_{TC}	6.41	4.66
C_{TS}	5.84	4.33
Si_{TC}	6.17	3.98
Si_{TS}	8.71	6.79
C_{Si}	1.32	1.69
Si_C	7.20	7.94
C(V)	5.48	2.77
Si(V)	6.64	3.30

To improve weak repulsive of GW potential at short distances we joined GW with well-established Ziegler, Biersack and Littmark (ZBL) potential at 0.95 Å (see Figure 1).

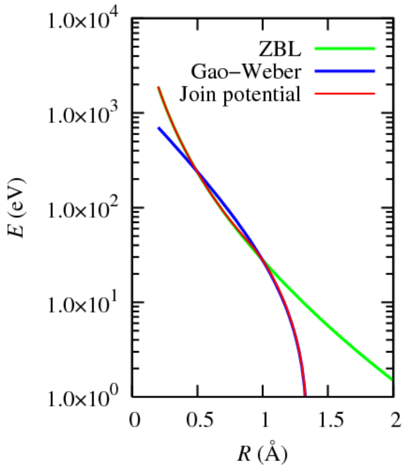

Figure 1. Repulsive Si-C atom interaction. The GW potential is shown in blue, the ZBL in green and the resulting joined potential is shown by the red line.

Simulation cells containing from 80x80x80 unit cells (409,600 atoms) were used for 10 keV primary knock-on atom (PKA) kinetic energy cascades and 120x120x120 unit cells (13,824,000 atoms) for 50 keV PKA cascades. The initial system was equilibrated for 2 picoseconds with time steps of 0.1 femtosecond. Each cascade was initiated by giving a Si atom the kinetic energy of 10 or 50 keV while holding zero total momentum. The cascades evolved for 20 ps and the time step is modified such that the distance traveled by the fastest particle in the system is less than 0.014 Å. Constant volume is held through the iteration and the lattice parameter is chosen for zero system pressure in equilibrium at a particular temperature. The Wigner-Seitz cell analysis method was used to determine defects in the modeling system.

The *ab initio* recombination barrier was calculated within the density functional theory (DFT) was calculated using the Quantum ESPRESSO (QE) package [4]. The calculations have been done using a plane-wave basis set and ultrasoft pseudo-potential [5] optimized in RRKJ scheme [6] (Si.pbe-n-rrkjus.UPF, C.pbe-n-rrkjus.UPF from QE pseudopotentials database). We used Perdew, Burke, and Ernzerhof [7] exchange-correlation functional. The Brillouin zone (BZ) summations were carried out over a 4 × 4 × 4 BZ grid for the system with 64 atoms in a supercell. The electronic smearing with a width of 0.02 Ry was applied according to the Methfessel-Paxton method. The plane wave energy cut off 40 Ry and charge density - 400 Ry allows reaching accuracy 0.2 mRy/atom. Atomic structure was optimized until the forces were smaller than 0.001 Ry/Å.

Results

The 10 keV cascade simulations with Tersoff potential were carried out at a range of temperatures and indicated that in-cascade recombination seemed to be much lower than in metals. Simulations at 50 keV have shown the same behavior as indicated in Figure 2. Figure 2a shows the time dependence of defects obtained in a 50 keV SiC cascade at 600, and Figure 2b shows typical results for similar simulations in iron. Note that the ratio of the peak defect count to the stable defect count at t>10 ps is less than a factor of two in SiC and almost two orders of magnitude in iron.

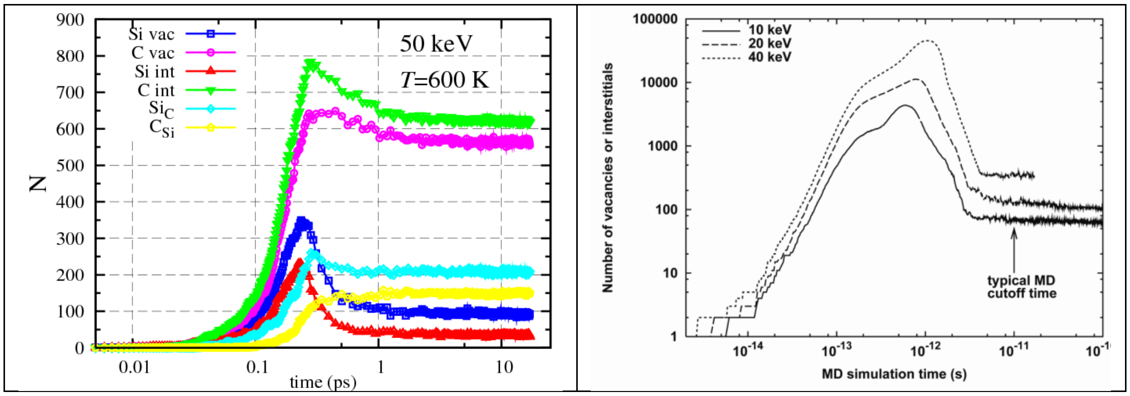

Figure 2. Time dependence of the number of point defects observed in MD displacement cascade simulations: (a) 50 keV SiC cascade at 600 K with Tersoff potential and (b) 10, 20, and 40 keV cascades in iron.

Such significant difference between SiC and Fe results is caused by presence of “empty” spaces in SiC lattice at (1/2, 1/2, 1/2), (3/4, 3/4, 3/4) and symmetry related positions which easily accommodate interstitial atoms.

Point defects in SiC consist of interstitials (I) and vacancies (V) of both carbon and silicon, as well as antisite defects of C on an Si site (C_{Si}) and Si on a C site (Si_C). The carbon defects predominate as shown by the green and purple symbols in Figure 3.

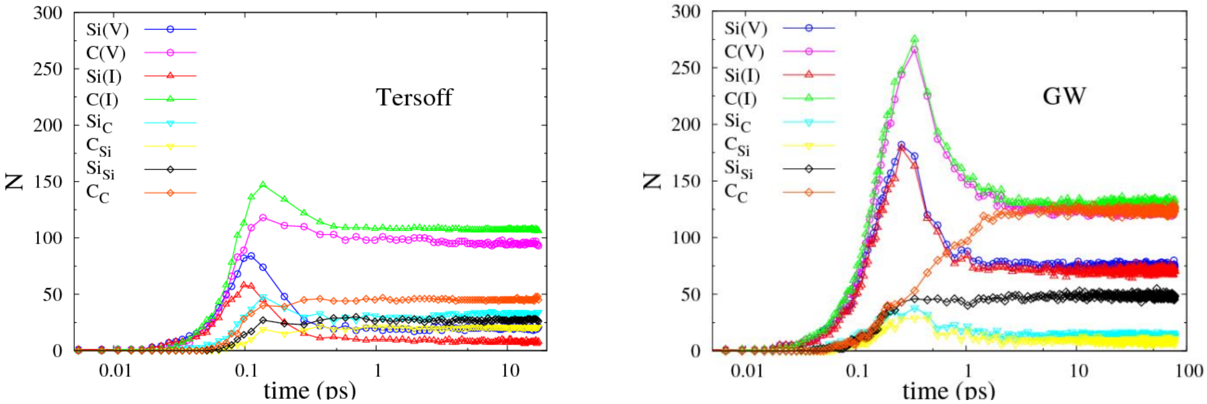

Figure 3. Time dependence of the number of point defects observed in MD displacement cascade simulations 10 keV pka at 300 K: (a) Tersoff potential, (b) GW potential.

This result is qualitatively similar to that obtained with Tersoff potential (Figure 3b). However, in contrast to the simulations with the Tersoff potential, the GW potential (Figure 3b) produces almost twice as many C vacancies and interstitials at the time of maximum disorder (~0.2 ps) but only about 25% more stable defects at the end of the simulation. As a result the ratio of peak-to-stable defects is much higher for the GW potential. This result is more similar to that observed in metals and oxides. Only about 20% of the carbon defects produced with the Tersoff potential recombine during the in-cascade annealing phase, while about 50% recombine with the GW potential.

As discussed in our earlier reports, the energy barrier for carbon V-I recombination with the GW potential is much smaller than with the Tersoff potential barrier, and is closer to results of first-principles calculations (Figure 4). On the basis of these result we can conclude that GW potential gives a much more realistic description of cascade dynamics in SiC and we will use this potential in our continuing work.

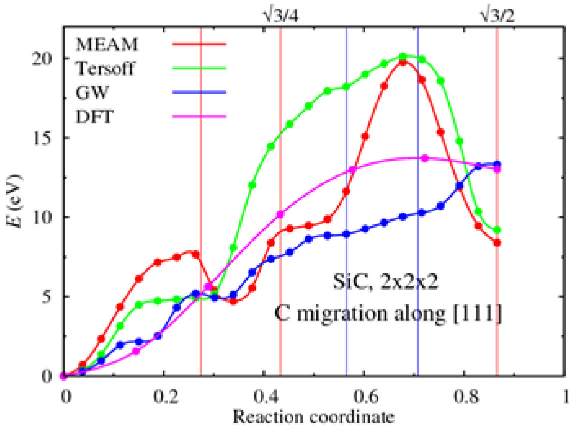

Figure 4. Carbon atom migration barrier in [111] direction.

The results for cluster size distributions at the end of simulation for both potentials are presented in Figure 5. In our analysis we defined group of point defects as a linked cluster if any of them are connected by a distance less than a lattice parameter. Both simulations produce a significant amount of pair clusters and ~ 75 % of these clusters correspond to the same atom type I-V pair. However if in the case of Tersoff potential all **I**-V pair clusters correspond to carbon atoms, in the case of GW potential a significant part of these clusters correspond to silicon.

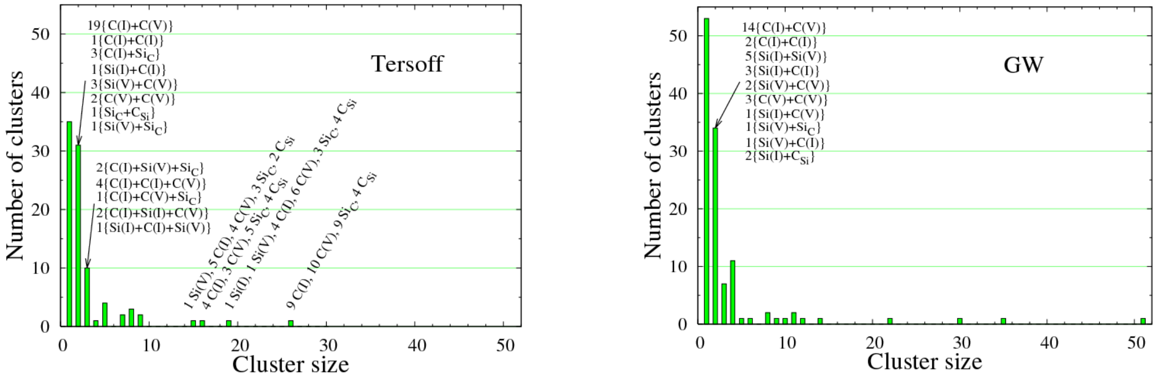

Figure 5. Cluster size distribution at the end of 10 keV Si recoil event in SiC at 300 K: (a) Tersoff potential, (b) GW potential.

Another difference corresponds to large size cluster distributions. Thus in the case of Tersoff potential (Figure 5a) there are only two relatively large clusters containing 19 and 21 defects, in the case of GW potential there are four clusters of size 21, 30, 35 and 51 defects. These large clusters could be discussed as potential amorphisation regions. One of these clusters containing 51 defects is presented in Figure 6, where carbon defects predominate as shown by the green and purple symbols.

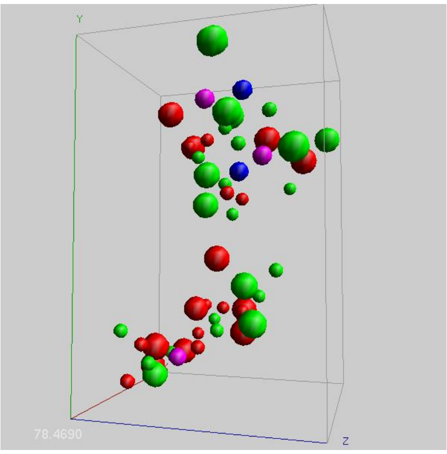

Figure 6. The distribution of carbon (green) and silicon (red) interstitials (large spheres) and vacancies (small spheres) at the end of 10 keV Si recoil event in SiC. Blue and purples spheres correspond to Si$_C$ and C$_{Si}$ antisites, respectively.

The number of defects at the end of cascade evolution is weakly temperature dependent for Tersoff potential, but reduces with temperature for the GW potential. The difference is due to unphysically large migration barriers for Tersoff potential. The increase in the temperature naturally leads to more rapid diffusion of carbon vacancies and interstitials. As a result, more carbon vacancies and interstitial recombine and the number of defects at the end of cascade evolution is reduced with temperature increase. However, the defect migration barriers for Tersoff potential are so large that diffusion is suppressed even at high temperatures such as 1600 K and the number of defects is weakly temperature dependent.

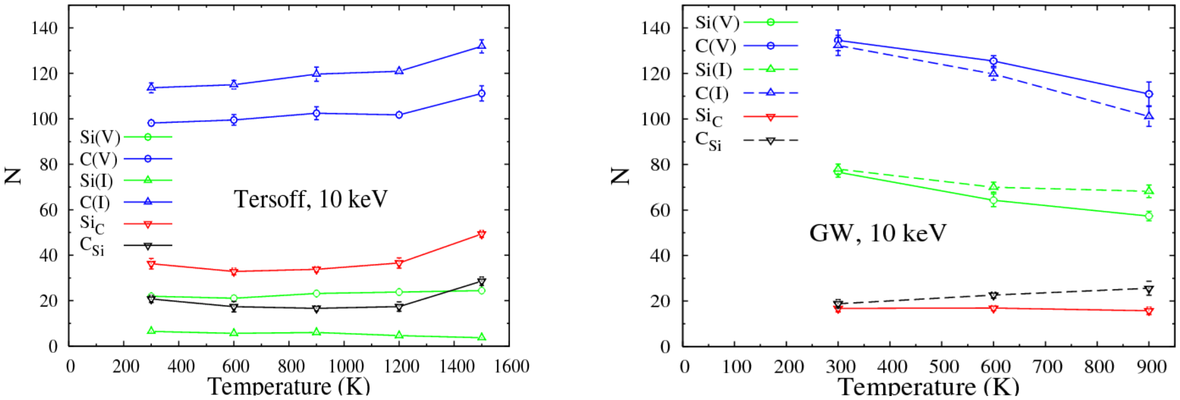

Figure 7. The number of defects at the end of cascade evolution

Additional computational resources have been used for this work through collaboration with JAEA.

REFERENCES

[1] J. Tersoff, Phys. Rev. B 39 (1989) 5566–5568.
[2] F. Gao and W. J. Weber, Nucl. Instr. And Methods in Phys. Research B 191 (2002) 504-508.
[3] S. Plimpton, Fast Parallel Algorithms for Short-Range Molecular Dynamics, J Comp Phys, 117, (1995), 1-19.
[4] P. Giannozzi, S. Baroni, and N. Bonini ... Quantum espresso: a modular and open-source software project for quantum simulations of materials. J of Physics:Condensed Matter, 21, 395502 (2009).
[5] D. Vanderbilt. Soft self-consistent pseudopotentials in a generalized eigenvalue formalism. Phys. Rev. B, 41, (1990), 7892–7895.
[6] A. M. Rappe, K. M. Rabe, E. Kaxiras, and J. D. Joannopoulos. Optimized pseudopotentials. Phys. Rev. B, 41, (1990), 1227–1230.
[7] J. P. Perdew, K. Burke, and M. Ernzerhof. Generalized gradient approximation made simple. Phys. Rev. Lett., 77, (1996), 3865–3868.

8.10 FIRST-PRINCIPLES CALCULATIONS OF CHARGE STATES AND FORMATION ENERGIES OF Mg, Al, and Be TRANSMUTANTS IN 3C-SiC

– S.Y. Hu, W. Setyawan, W. Jiang, C. H. Henager, Jr. and R. J. Kurtz (Pacific Northwest National Laboratory)

OBJECTIVE

To investigate the charge states and formation energies of Mg, Al and Be transmutants in 3C-SiC.

SUMMARY

The Vienna Ab-initio Simulation Package (VASP) is employed to calculate charge states and the formation energies of Mg, Al and Be transmutants at different lattice sites in 3C-SiC. The results provide important information on the dependence of the most stable charge state and formation energy of Mg, Al, Be and vacancies on electron potentials.

PROGRESS AND STATUS

Introduction

Theoretical calculations by Sawan, *et al*. [1] have predicted that at a fast neutron dose of ~100 dpa, there are ~0.5 at% Mg, ~0.15 at% Al, and ~0.2 at% Be generated in SiC through nuclear transmutation. These transmutants are expected to have potentially significant effects on phase stability, oxidation, transport properties (electrical and thermal conductivity), and elevated temperature mechanical properties. As we know, defects in semiconductor materials such as SiC might have different charge states, which depend on the local electron potentials. In order to determine thermodynamic and kinetic properties of defects in SiC, it is necessary to identify the charge states of defects and evaluate their effect on defect properties. This progress report presents possible charge states and formation energies of Mg, Al, and Be transmutants in 3C-SiC, calculated from density functional theory (DFT).

Simulation Method

The method of calculating the formation energy of a charged defect is described in our previous report [2]. In the present simulations, a large supercell $3a_0 \times 3a_0 \times 3a_0$ (about 216 atoms) with a $3\times3\times3$ Monkhorst-Pack k-point mesh for Brillouin-zone sampling is used to minimize the spurious interactions between images of charged defects in periodic simulation cells.

Results

The defect energies of Mg, Al, Be and a vacancy with different charges $(q=-2,-1,0,+1,+2)$ at different lattice sites [Si, C, the tetrahedral center of carbon atoms (TC), and the tetrahedral center of Si atoms (TSi)] in 3C-SiC have been calculated. Figure 2 plots the formation energy $E^f(q)$ with different charge states at different lattice sites as a function of electron potential μ_F. The ionization level $(q/q\pm1)$ can be determined by the intersection between two linear formation energy curves with charge q and $q+1$ $(\text{or}\, q-1)$, respectively. The vertical dashed lines in Figure 2 indicate the ionization levels for different defects. The segments defined by the intersections at ionization levels show the formation energy of the most stable charged defect for a given electron potential. Table 1 summarizes the most stable charge state, the formation energy, and lattice site of Mg, Al, Be and a vacancy for given electron potentials: 0.2, 1.0 and 2.0 eV, respectively.

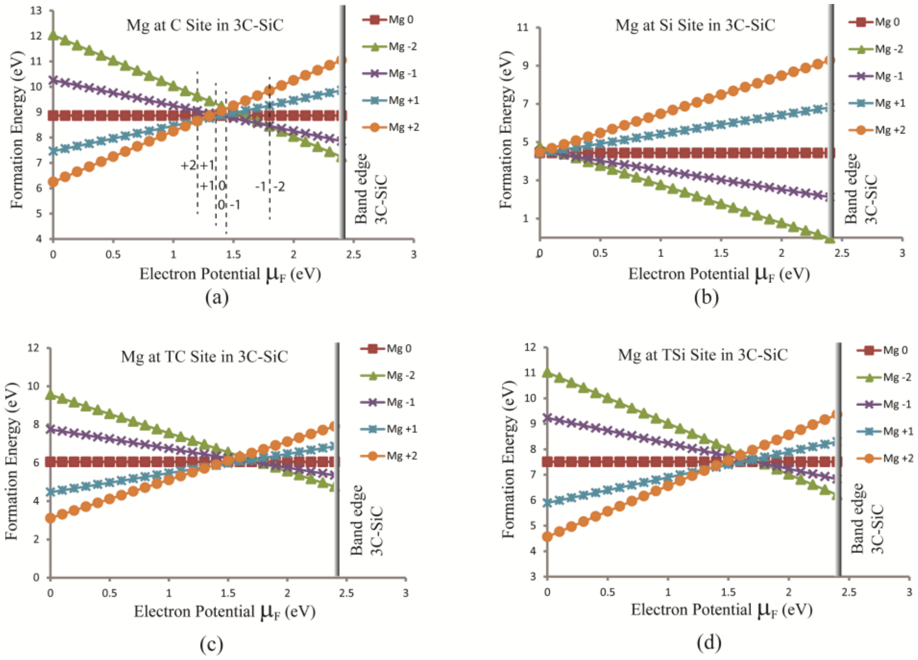

(a) (b)

(c) (d)

(A) Formation energy of charged Mg, (a) at C, (b) at Si, (c) at TC, and (d) at TSi.

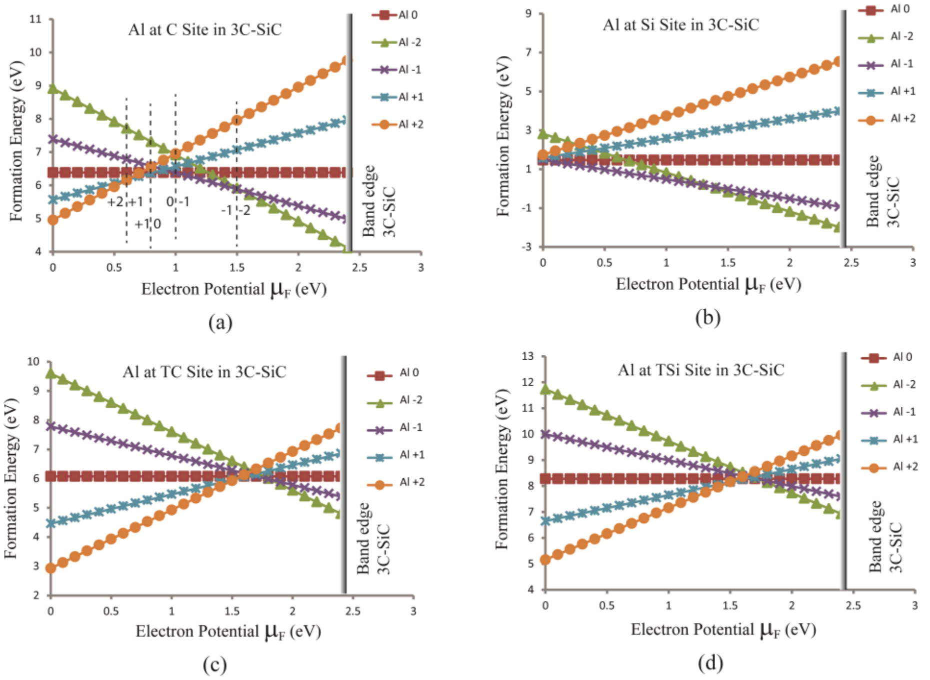

(a) (b)

(c) (d)

(B) Formation energy of charged Al, (a) at C, (b) at Si, (c) at TC, and (d) at TSi.

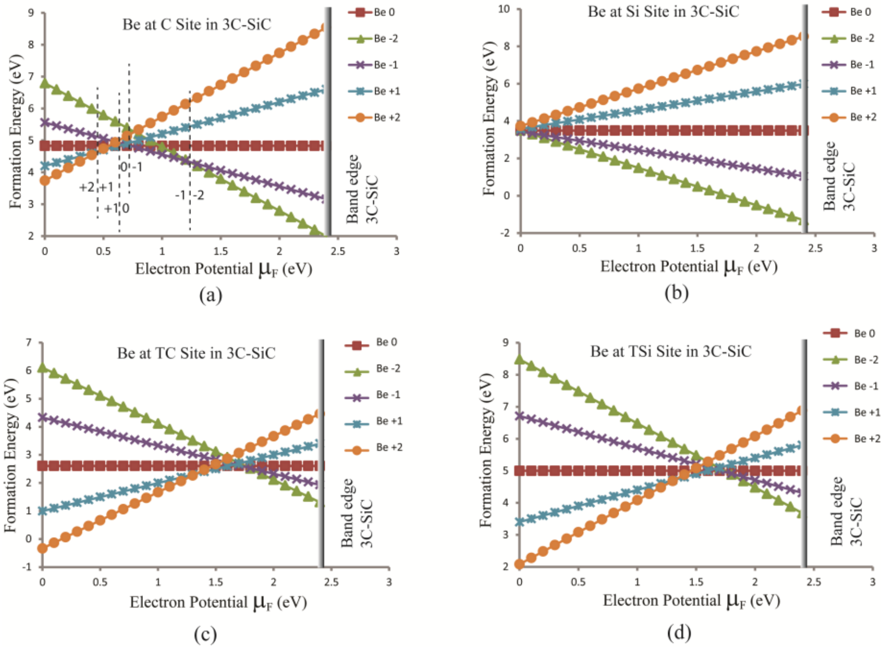

(C) Formation energy of charged Be, (a) at C, (b) at Si, (c) at TC, and (d) at TSi.

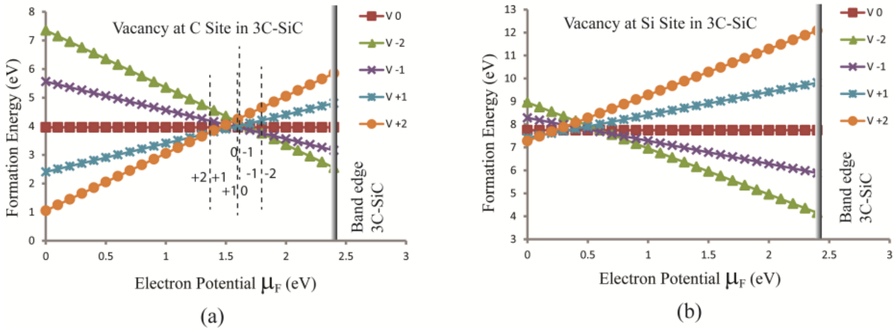

(D) Formation energy of a charged vacancy, (a) at C, (b) at Si, (c) at TC, and (d) at TSi.

Figure 1. Formation energy of charged Mg, Al, Be and Vacancy at different lattice sites under different electron potential. The band gap value is taken as E_{band} = 2.39 eV,determined from experiment. [3]

Table 1. Most stable charged defect and formation energy of Mg, Al, Be and a vacancy under different electron potentials.

Electron potential	Mg		Al		Be		Vacancy	
	Stable defect	Formation energy	Stable defect	Formation energy	Stable defect	Formation energy	Stable defect	Formation energy
0.2eV	Mg_{TC}^{+2}	3.51eV	Al_{Si}^{-1}	1.28eV	Be_{TC}^{+2}	0.07eV	V_{C}^{+2}	1.45eV
1.0 eV	Mg_{Si}^{-2}	2.77eV	Al_{Si}^{-1}	0.48eV	Be_{Si}^{-2}	1.49eV	V_{C}^{+2}	3.05eV
2.0 eV	Mg_{Si}^{-2}	0.77eV	Al_{Si}^{-2}	-1.18eV	Be_{Si}^{-2}	-0.51eV	V_{C}^{-2}	3.35eV

FUTURE WORK

In the future work, we will examine the effect of charge states on migration energies of different defects by DFT calculations, and study the defect evolution kinetics in 3C-SiC by modeling and experiments.

Acknowledgements

This work was performed by Pacific Northwest National Laboratory, which is operated by Battelle for the United States Department of Energy under Contract DE-AC05-76RL01830. This study was supported by the U.S. Department of Energy, Office of Fusion Energy Sciences.

REFERENCES

[1] M. E. Sawan, Y. Katoh, and L. L. Snead, J. Nucl. Mater., 442, (2013), 5370.
[2] S.Y. Hu, W Setyawan, W Jiang, CH Henager, Jr, and RJ Kurtz, Fusion Reactor Materials Program-Semiannual Progress Reports. PNNL-SA-101947.
[3] W.J. Choyke, D.R. Hamilton, L. Patrick, Phyical Review 133, (1964), A1163.

9.1 FUSION MATERIAL IRRADIATION TEST STATION (FMITS) AT SNS –Mark Wendel, Phil Ferguson (Oak Ridge National Laboratory)

OBJECTIVE

The Fusion Materials Irradiation Test Station (FMITS) is a plan for an irradiation facility at the Spallation Neutron Source (SNS). The objective of the current effort is a feasibility study based on a 30% design to quantify the risk to normal operations and safety at the SNS. The deliverables are a Feasibility Study Report, 30% Design Review, and a Preliminary Safety Assessment. The original study of FY2012 estimated a total project cost of $10M over a 3-year schedule. The current estimate for implementation of the FMITS at SNS is $13.4 M including a 25% contingency.

SUMMARY

FMITS irradiations at SNS would occur on samples welded inside an FMITS target harness in two horizontal tubes which project out in front of the mercury target. For these specimen locations, the back-scattering neutron flux spectra should be close to the ITER fusion spectrum. The PKA spectra at the FMITS samples were also compared to those for ITER, and the results show good agreement. Radiation damage rates would be 1.6–5.5 dpa/y for steel, with the range of helium-to-dpa production ratios starting close to those expected in D-T fusion, and increasing toward beam center locations.

The deliverables for the FY14 funding from OFES have all been met:

1. A review of the 30% design for FMITS was conducted on June 2-3,
2. The feasibility study report was completed July 1, 2014, and
3. The preliminary safety assessment was completed July 1, 2014.

The 30%-design review committee found that the FMITS design was feasible in that all of the technical and safety issues were addressed at a level appropriate for a 30% design. Specific recommendations were addressed in the feasibility study report appendices.

Other highlights of the FMITS 30% design progress during the past 6 months include a completed preliminary seal mock-up test, improved remote handling tooling and procedures, and a completed project resource-loaded schedule and contingency analysis.

Progress and Status

During FY14, workable solutions have been identified to the technical engineering challenges for implementation of FMITS. Also, a comprehensive analysis has been completed evaluating the impacts of FMITS on SNS operations and SNS safety. Communication with SNS key operations staff and fusion materials scientists has taken place in monthly meetings and special topical technical meetings on experiment design, instrumentation, mechanical design, remote handling, and safety are conducted as needed. As of July 1, 2014, all of the promised deliverables have been completed.

The FMITS 30% design review committee members were:

- Michael Baumgartner, Chair–Mechanical Systems and Operations Group Leader; SNS, ORNL
- Dr. Jeffrey Binder—Director, Applied Research Institute; University of Illinois
- Dr. David Cook—Safety Basis Authority; Research Reactors Division, ORNL
- Dr. Kenneth Herwig—Instrument Projects and Development Group Leader; SNS, ORNL
- Patrick Hurh—Mechanical Support Department Head; Accelerator Division, FNAL
- Dr. Stuart Maloy—Transmutation Core Materials Technical Lead; FCRD Advanced Fuels Campaign, LANL
- Brad Nelson—US ITER Chief Engineer; US ITER Project Office, ORNL
- Mark Rennich—Target Systems Engineer; Instrument and Source Division, ORNL

- Dr. Steven Zinkle—UT/ORNL Governor's Chair; Dept. of Nuclear Engineering & Dept. of Materials Science & Engineering, University of Tennessee

The broad charge to the committee was to comment on the feasibility of the FMITS design. The committee was also asked to make the following judgments:

1. Identify significant technical challenges and issues that should be addressed.
2. Has the case for technical success of FMITS to fusion materials science been made?
3. Have all of the significant safety concerns (threats to personnel or the environment) been identified and addressed at an appropriate level for this stage of the project?
4. Has the operational risk to the SNS neutron science mission been sufficiently defined, and are the planned mitigation strategies appropriate?
5. Is the FMITS project planning effective and at the appropriate level?

A brief summary of the committee's judgments in response to the charge follows. Detailed discussion and recommendations can be found in the charge sections of the committee report.

In summary, the committee's response is that the FMITS design is feasible. All aspects of the engineering challenges appear to have been addressed. In part this judgment is based on the planned tests and mock-ups intended to resolve the remaining technical challenges and mitigate design risks, specifically those categorized as "itemized technical risks." The committee identified issues associated with minimizing the impact of FMITS on the SNS facility and provided recommendations.

The case for the technical success of FMITS to fusion materials science has been made. FMITS would allow the US to develop a scientific understanding of radiation effects in materials for fusion applications at low doses (~10 dpa) with the concurrent production of helium and hydrogen. This data, when coupled with simulations from physics-based models, would develop insight into fusion-relevant radiation effects for three key phenomena (the listed temperatures are relevant for ferritic/martensitic steels):

- Radiation hardening at low temperatures 250-400°C (synergistic H, He, defect effects),
- Void nucleation and growth leading to swelling at 400-500°C, and
- Helium embrittlement effects above 500°C.

This improved understanding of radiation effects under prototypic fusion conditions gained from low-to-intermediate dose data coupled with modeling results:

- Would help to optimize material choices for near-term machines, such as ITER test blanket materials,
- Would provide important scientific information to guide the development of next-generation ferritic steels specifically tailored for the D-T fusion energy environment,
- Would allow one to systematically explore mechanisms to control effects of He such as trapping on nano-scale particles, and
- Would provide a scientific basis for more informed use of IFMIF or other fusion materials irradiation facility options in the future.

All significant safety concerns have been identified and addressed at a level appropriate for this stage of the project. The set of hazards and associated consequences to the public, onsite workers, and environment were adequately considered and appropriate judgments regarding engineering and administrative controls made. For each of the unmitigated events evaluated as part of the gas system and water system hazard evaluations, numerous methods of detection and minor controls for prevention or mitigation of the events were identified.

The committee determined that the operational risk presented by FMITS to the SNS neutron science mission had been sufficiently defined and that planned mitigation strategies were appropriate for this stage of the FMITS effort. The design would have negligible effect on target system thermal-hydraulic and neutronic performance. The design team identified the operational technical challenges (FMITS harness handling, core vessel seal design, target Imaging system calibration) that remain to be solved and strategies to minimize risk.

The committee found the FMITS project planning effective and at the appropriate level for the pre-CD-1 stage of the design effort. A cost estimate and logic driven schedule were developed from the ~350 project activities associated with the design, fabrication, and installation of FMITS. Derived from the technical scope of work, the overall schedule was reasonable but did not incorporate the resource and facility access constraints of the provisional SNS operating schedule. Similarly, the FMITS cost estimate was reasonable but largely dependent upon successful outcomes resulting from the identified tests and on a funding profile that supported the proposed schedule.

With the FMITS 2014 report and review completed, and the feasibility of FMITS confirmed by the committee, the decision for continuing into the next phase of design and mock-up testing is left to DOE. Specifically, DOE must decide whether FMITS is a viable project at the SNS.

PUBLICATIONS AND REPORTS

1. R. Battle, S. Chae, M. Dayton, J. Denison, V. Graves, T. Lessard, W. Lu, S. Parson, R. Stoller, M. Wendel, SNS Fusion Materials Irradiation Test Station Feasibility Study, SNS-ISDD-NSD-TD-0001-R00, July 1, 2014.
2. D. Freeman and M. Harrington, Preliminary Safety Assessment for FMITS Feasibility Study, SNS-102030102-ES0074-R00, July 1, 2014.

HFIR IRRADIATION EXPERIMENTS – June 30, 2014

Summary of Recent, Current and Planned Fusion Materials Program Experiments

(Sorted by capsule type and sponsoring experimenters)

Experiment Designation	Primary Materials	Specimen Types*	Irradiation Temperature (°C)	Max Exposure (dpa)	Number of Reactor Cycles	Irradiation Period (month/year)		
Beryllium reflector (RB) irradiation positions								
RB-15J	F82H	T, F, FT	300, 400	6	10	6/08	–	12/09
Target zone full-length capsules								
JP-25	F82H	T, FT	300, 500	20	10	2/99	–	1/01
JP-26	F82H	T, FT	300,400,500	9	5	12/03	–	11/04
JP-27	F82H	T, FT	300, 400	21	13	12/03	–	1/08
JP-28	F82H	T, FT	300,400,500	80	46	4/05	–	7/13
JP-29	F82H	T, FT	300,400,500	80	46	1/05	–	7/13
12-DCT	F82H	DCT	50	1.6	1	8/11	–	8/11
JP-30	F82H	T, FT	300,400,650	20	~10	11/11	–	8/13
JP-31	F82H	T, FT	300,400,650	20	~10	11/11	–	8/13

*T = Tensile, F = Fatigue, FT = Fracture Toughness, MC = Multipurpose Coupon, BSR = Bend Stress Relaxation Creep, DCT = Disc Compact Tension, BTC: Bellows-loaded Tensile Creep, UDMC: Uni-directional Mini-composite. Most experiments also contain TEM disks, other special purpose specimens, and monitors occupying small spaces.
**Hydraulic tube – fractional cycle exposures.

Experiment Designation	Primary Materials	Specimen Types*	Irradiation Temperature (°C)	Max Exposure (dpa)	Number of Reactor Cycles	Irradiation Period (month/year)		
Target zone rabbit capsules (DOE-JAEA)								
F8A1	F82H	T, FT	300	50	29	2/09	–	7/13
F8A2	“	“	“	“	“	“	–	“
F8B1	“	“	“	“	“	“	–	“
F8B2	“	“	“	“	“	“	–	“
JCR-1	SiC/SiC	Bend bars	800	30	15	10/04	–	1/09
JCR-2	“	“	“	“	“	“	–	“
JCR-3	“	“	“	“	“	“	–	“
JCR-4	“	“	“	“	“	“	–	“
JCR-5	“	“	“	>50	>25	10/04	–	2/11
JCR-6	“	“	“	“	“	“	–	“
JCR-7	“	“	“	“	“	“	–	“
JCR-8	“	“	“	“	“	“	–	“
JCR-9	“	“	500	30	15	10/04	–	1/09
JCR-10	“	“	“	“	“	“	–	“
JCR-11	“	“	“	“	“	“	–	“
JCR-12	“	“	“	“	“	“	–	“
F11A3	F82H	T, FT	300	20	12	5/11	–	2/13
F11A4	“	“	“	“	“	“	–	“
F11B3	“	“	“	“	“	“	–	“
M4-TEN	F82H	DCT	50	1.6	1	8/11	–	8/11
JCR11-01	SiC/SiC	Bend bars	950	50	25	11/12	–	
JCR11-02	SiC/SiC	Bend bars	950	10	5	10/12	–	8/13
JCR11-03	SiC/SiC	Bend bars	950	30	15	5/13	–	
JCR11-04	SiC/SiC	Bend bars	950	30	15	5/13	–	
JCR11-05	SiC/SiC	Bend bars	950	50	25	10/12	–	
JCR11-06	SiC/SiC	Bend bars	950	10	5	10/12	–	7/13
JCR11-07	SiC/SiC	Bend bars	950	100	50	10/12	–	
JCR11-08	SiC/SiC	Bend bars	950	100	50	10/12	–	
JCR11-09	SiC/SiC	UDMC	950	4	2	6/13	–	11/13
JCR11-10	SiC/SiC	UDMC	950	10	5	6/13	–	
JCR11-11	SiC/SiC	UDMC	950	30	15	6/13	–	
JCR11-12	SiC/SiC	UDMC	950	100	50	6/13	–	
F13A5	F82H	T, FT	300	10	9	1/14	–	
F13A6	F82H	T, FT	300	20	18	1/14	–	
F13B4	F82H	T, FT	300	10	9	1/14	–	
F13B5	F82H	T, FT	300	20	18	1/14	–	

Experiment Designation	Primary Materials	Specimen Types*	Irradiation Temperature (°C)	Max Exposure (dpa)	Number of Reactor Cycles	Irradiation Period (month/year)		
Target zone rabbit capsules (DOE-NIFS)								
T8A1	SiC	BSR	300	0.01	HT**	10/09	–	10/09
T8A2	SiC	BSR	300	0.1	HT	10/09	–	10/09
T8B1	SiC	BSR	500	0.01	HT	10/09	–	10/09
T8B2	SiC	BSR	500	0.1	HT	10/09	–	10/09
T8C1	SiC	BSR	500	~1	1	5/09	–	6/09
T8D1	SiC	BSR	800	0.1	HT	3/11	–	10/09
T8E1	SiC	BSR	800	~1	1	8/09	–	8/09
T8F1	SiC	BSR	1200	~1	1	8/09	–	8/09
T9A1	W, Ni	Discs	90	0.1	HT	1/09	–	10/09
T9A2	W, Ni	Discs	90	1.2	1	1/09	–	1/09
T9C1	Steels	T, MC	500	5.5	3	11/09	–	2/10
T9C2	Steels	T, MC	500	9.6	5	11/09	–	6/10
T9G1	Steels	T, MC	300	1.2	1	6/09	–	8/09
T9G2	Steels	T, MC	300	9.6	8	6/09	–	8/11
MTTN01	Steels	T, MC	300	4.8	4	1/12	–	8/11
300-LD-1	Steels	SSJ, MC	300	2	1	5/12	–	6/12
300-HD-1	Steels	SSJ, MC	300	12	6	5/12	–	2/13
500-LD-1	Steels	SSJ, MC	500	2	1	5/12	–	6/12
500-HD-1	Steels	SSJ, MC	500	12	6	5/12	–	2/13
500-HD-2	Steels	SSJ, MC	500	12	6	5/12	–	2/13
500-HD-3	Steels	SSJ, MC	500	12	6	5/12	–	2/13
650-LD-1	Steels	SSJ, MC	650	2	1	5/12	–	6/12
650-LD-2	Steels	SSJ, MC	650	2	1	5/12	–	6/12
650-HD-1	Steels	SSJ, MC	650	12	6	5/12	–	2/13
650-HD-2	Steels	SSJ, MC	650	12	6	5/12	–	2/13
300-LD-2	Steels, W	SSJ, MC	300	2	2	7/12	–	8/12
300-MD-1	Steels, W	SSJ, MC	300	7	4	7/12	–	2/13
500-LD-2	Steels, W	SSJ, MC	500	2	2	1/13	–	7/13
300-LD-3	Steels, W	SSJ, MC	300	2	2	7/12	–	11/12
300-HD-2	Steels, W	SSJ, MC	300	12	8	7/12	–	2/14
500-LD-3	Steels, W	SSJ, MC	500	2	1	7/12	–	8/12
500-HD-4	Steels, W	SSJ, MC	500	12	6	7/12	–	7/13
650-LD-3	Steels, W	SSJ, MC	650	2	2	10/12	–	7/13
650-HD-3	Steels, W	SSJ, MC	650	12	8	7/12	–	11/13
PC1	Various	SSJ, MC	80/100	0.02	HT	6/12	–	6/12
PC1A	Various	SSJ, MC	80/100	0.02	HT	6/12	–	6/12
PC2	Various	SSJ, MC	80/100	0.1	HT	6/12	–	6/12
PC2A	Various	SSJ, MC	80/100	0.1	HT	6/12	–	6/12
PC3	Various	SSJ, MC	80/100	0.5	HT	6/12	–	7/12

PC3A	Various	SSJ, MC	80/100	0.5	HT	6/12	–	7/12
Experiment Designation	Primary Materials	Specimen Types*	Irradiation Temperature (°C)	Max Exposure (dpa)	Number of Reactor Cycles	Irradiation Period (month/year)		
Continued ***-Target zone rabbit capsules (DOE-NIFS)***								
PC4	Various	SSJ, MC	80/100	2	1	6/12	–	7/12
PC4A	Various	SSJ, MC	80/100	2	1	6/12	–	7/12
PC5	Various	SSJ, MC	80/100	20	9	6/12	–	11/13
TB-300-1	Steels, W	SSJ, MC	300	0.02	HT	8/12	–	8/12
TB-300-2	Steels, W	SSJ, MC	300	0.1	HT	8/12	–	8/12
TB-300-3	Steels, W	SSJ, MC	300	0.5	HT	8/12	–	8/12
TB-300-4	Steels, W	SSJ, MC	300	7	5	7/12	–	6/13
TB-500-1	Steels, W	SSJ, MC	500	0.1	HT	8/12	–	8/12
TB-500-2	Steels, W	SSJ, MC	500	0.5	HT	8/12	–	8/12
TB-500-3	Steels, W	SSJ, MC	500	7	4	7/12	–	2/13
TB-650-1	Steels, W	SSJ, MC	650	0.1	HT	8/12	–	8/12
TB-650-2	Steels, W	SSJ, MC	650	0.5	HT	8/12	–	8/12
TB-650-3	Steels, W	SSJ, MC	650	7	5	7/12	–	6/13
TB-650-4	Steels, W	SSJ, MC	650	20	11	7/12	–	7/14
TTN09	SiC	Joint	500	3.4	2	8/11	–	11/11
TTN10	SiC	Joint	500	4.1	2	8/11	–	11/11
TTN11	SiC	Joint	800	4	2	3/12	–	5/12
TTN01	SiC	BSR	300	1	1	2/11	–	3/11
TTN02	SiC	BSR	300	10	6	2/11	–	12/11
TTN03	SiC	BSR	300	20	11	2/11	–	8/13
TTN04	SiC	BSR	500	10	6	5/11	–	4/12
TTN05	SiC	BSR	500	20	11	5/11	–	8/13
TTN06	SiC	BSR	800	10	6	5/11	–	4/12
TTN07	SiC	BSR	800	20	11	5/11	–	8/13
TTN08	SiC	BSR	1200	10	6	5/11	–	8/12
TTN16	SiC	Fiber BSR	500	1	1	11/11	–	12/11
TTN17	SiC	Fiber BSR	500	10	6	8/11	–	6/12
TTN18	SiC	Fiber BSR	500	20	11	8/11	–	8/13
TTN19	SiC	Fiber BSR	1200	1	1	3/12	–	4/12
TTN20	SiC	Fiber BSR	1200	10	6	3/12	–	11/12

Experiment Designation	Primary Materials	Specimen Types*	Irradiation Temperature (°C)	Max Exposure (dpa)	Number of Reactor Cycles	Irradiation Period (month/year)		
Target zone rabbit capsules (US-NIFS-JAEA)								
T11-01J	V-4Cr-4Ti	BTC	425	2	1	11/12	–	12/12
T11-02J	V-4Cr-4Ti	BTC	425	6	3	1/13	–	7/13
T11-03J	V-4Cr-4Ti	BTC	425	2	1	11/12	–	12/12
T11-04J	V-4Cr-4Ti	BTC	425	6	3	1/13	–	7/13
T11-05J	SiC	BTC	600	2	1	11/12	–	12/12
T11-06J	SiC	BTC	600	6	3	1/13	–	7/13
T11-08J	SiC	BTC	600	6	3	1/13	–	7/13
T11-09J	SiC	BTC	600	2	1	11/12	–	12/12
T11-11J	SiC	BTC	600	2	1	11/12	–	12/12
T11-13J	Graphite	BTC	600	2	1	11/12	–	12/12
T11-14J	Graphite	BTC	600	6	3	1/13	–	7/13
J12-01	F82H	BTC	300	1.5	1	1/13	–	2/13
J12-02	F82H	BTC	300	6	3	5/13	–	7/13
J12-03	F82H	BTC	300	1.5	1	5/13	–	2/13
J12-04	F82H	BTC	300	6	3	1/13	–	6/13
J12-05	F82H	BTC	300	1.5	1	1/13	–	2/13
J12-06	F82H	BTC	300	6	3	5/13	–	6/13
Target zone rabbit capsules (US-IMR)								
MX-1	Ceramics	Various	400	2	1	7/13	–	8/13
MX-2	Ceramics	Various	400	6	3	7/13	–	3/14
MX-3	Ceramics	Various	400	10	6	7/13	–	7/14
MX-4	Ceramics	Various	700	2	1	7/13	–	8/13
MX-5	Ceramics	Various	700	6	3	7/13	–	2/14
MX-6	Ceramics	Various	700	10	5	7/13	–	5/14
MX-7	Ceramics	Various	1000	2	1	7/13	–	8/13
MX-8	Ceramics	Various	1000	6	3	7/13	–	3/14
MX-9	Ceramics	Various	1000	10	5	7/13	–	5/14
Target zone rabbit capsules (US)								
SCJ2-10	Ceramics	Joint	500	3	2	5/14	–	7/14
SCJ2-11	Ceramics	Joint	500	>10	10	5/14	–	
SCJ2-12	Ceramics	Joint	500	3	2	5/14	–	7/14
SCJ2-16	Ceramics	Joint	1000	3	2	6/14	–	8/14
SCJ2-17	Ceramics	Joint	1000	3	2	6/14	–	8/14